

NBSIR 83-1690

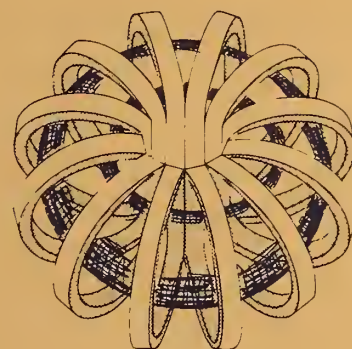
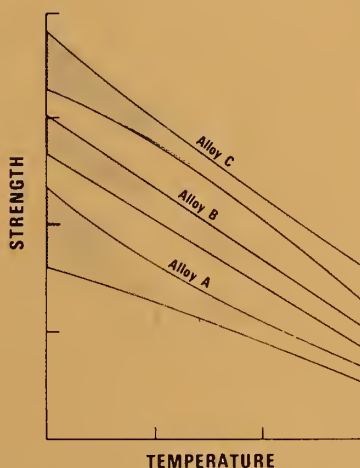
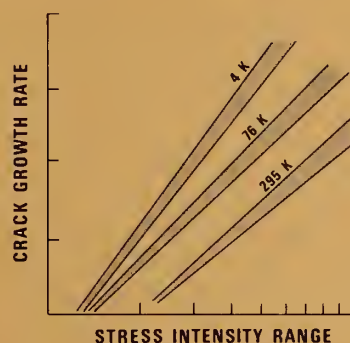
NBS  
PUBLICATIONS

TECHNICAL REPORTS



A11104 529501

# MATERIALS STUDIES FOR MAGNETIC FUSION ENERGY APPLICATIONS AT LOW TEMPERATURES - VI



To  
Department of Energy  
Office of Fusion Energy  
Washington, D.C. 20545

By  
Fracture and Deformation Division  
National Bureau of Standards  
Boulder, CO 80303

QC  
100  
.U56  
83-1690  
1983  
c. 2



NBSIR 83-1690

UC 20b, c

NATIONAL BUREAU  
OF STANDARDS  
LIBRARY

QC100 - Qrc.

U.S.

NO. 83-1690

1983

C.2

TECHNICAL REPORTS

**MATERIALS STUDIES FOR  
MAGNETIC FUSION ENERGY  
APPLICATIONS AT LOW TEMPERATURES - VI**

Edited By

**R.P. Reed and N.J. Simon  
Fracture and Deformation Division  
National Bureau of Standards  
Boulder, Colorado 80303**

**May 1983**

Sponsored By

**Department of Energy  
Office of Fusion Energy  
Washington, D.C. 20545**



U.S. DEPARTMENT OF COMMERCE, Malcolm Baldrige, Secretary

NATIONAL BUREAU OF STANDARDS, Ernest Ambler, Director





## CONTENTS

	<u>Page</u>
SUMMARY. . . . .	v
ORGANIZATIONAL CONTACTS. . . . .	vi
PROGRAM DESCRIPTION. . . . .	vii
HIGHLIGHTS OF RESULTS. . . . .	1
 STRUCTURAL ALLOYS	
STRUCTURAL ALLOYS PROGRAM . . . . .	9
SUMMARY OF MECHANICAL PROPERTY MEASUREMENTS OF STRUCTURAL ALLOYS. . . . .	10
MARTENSITIC TRANSFORMATIONS IN Fe-Cr-Ni STAINLESS STEELS. . . . .	11
A COMPUTER-INTERACTIVE FATIGUE CRACK GROWTH RATE TEST PROCEDURE . . . . .	41
EFFECTS OF SENSITIZATION ON SOME FRACTURE MECHANICS FATIGUE PARAMETERS FOR Fe-18Cr-3Ni-13Mn-0.37N STAINLESS STEEL AT 295 AND 4 K . . . . .	53
EFFECTS OF MAGNETIC FIELD ON TENSILE BEHAVIOR AT 4 K OF ALLOYS 304 AND 310 . . . . .	73
FACTORS INFLUENCING THE LOW-TEMPERATURE DEPENDENCE OF YIELDING IN AISI 316 STAINLESS STEELS. . . . .	87
TEMPERATURE DEPENDENCE OF FLOW STRENGTH OF SELECTED AUSTENITIC STAINLESS STEELS. . . . .	113
PROPERTIES OF AUSTENITIC STAINLESS STEEL AT CRYOGENIC TEMPERATURES. . . . .	127
AUSTENITIC-STEEL ELASTIC CONSTANTS. . . . .	157
ELASTIC CONSTANTS OF AN Fe-5Cr-26Mn AUSTENITIC STEEL, 76-400 K. .	181
 WELDMENTS AND CASTINGS	
WELDMENTS AND CASTINGS PROGRAM . . . . .	197
CORRELATIONS OF FATIGUE CRACK GROWTH RATE PARAMETERS AT CRYOGENIC TEMPERATURES. . . . .	199

## CONTENTS (Cont'd)

	<u>Page</u>
DEFORMATION AND FRACTURE OF STAINLESS STEEL CASTINGS AND WELDMENTS AT 4 K. . . . .	213
MECHANICAL PROPERTIES OF STAINLESS STEEL CASTINGS AT 4 K. . . . .	235
METALLOGRAPHY OF DUPLEX STAINLESS STEEL CASTINGS. . . . .	243
A TRANSMISSION ELECTRON MICROSCOPY STUDY OF CAST DUPLEX AUSTENITIC STAINLESS STEELS WITH VARYING FERRITE CONTENT: AS-CAST AND DEFORMED AT 4 K . . . . .	273
TEXTURE IN STAINLESS-STEEL WELDS: AN ULTRASONIC STUDY. . . . .	339
NONMETALLICS	
NONMETALLICS PROGRAM. . . . .	359
VARIABILITY IN MECHANICAL PERFORMANCE OF G-10CR CRYOGENIC- GRADE INSULATING LAMINATES. . . . .	361
EFFECT OF CRYOGENIC TEMPERATURES ON THE MECHANICAL PERFORMANCE OF GLASS-FABRIC-REINFORCED EPOXY AND POLYIMIDE MATRIX LAMINATES. .	369
ELASTIC STIFFNESS AND LOCAL STRESSES IN WOVEN-FABRIC COMPOSITES AT 77 K. . . . .	375
INFLUENCE OF PLY CRACKS ON FRACTURE STRENGTH OF GRAPHITE/EPOXY LAMINATES AT 76 K . . . . .	385
ORTHOTROPIC ELASTIC CONSTANTS OF A GLASS-FIBER-CLOTH EPOXY- MATRIX COMPOSITE. . . . .	415
CALCULATED ELASTIC CONSTANTS OF COMPOSITES CONTAINING ANISOTROPIC FIBERS. . . . .	429
TECHNOLOGY TRANSFER	
TECHNOLOGY TRANSFER PROGRAM . . . . .	457
INTERNATIONAL COOPERATION IN RESEARCH TO DEVELOP RADIATION- RESISTANT LAMINATES . . . . .	458
ACKNOWLEDGMENT . . . . .	464

## SUMMARY

This report contains results of a research program to produce material property data that will facilitate design and development of cryogenic structures for the superconducting magnets of magnetic fusion energy power plants and prototypes. The program was conceived and developed jointly by the staffs of the National Bureau of Standards and the Office of Fusion Energy of the Department of Energy; it is managed by NBS and sponsored by DoE. Research is conducted at NBS and at various other laboratories through subcontracts with NBS.

The reports presented here summarize the sixth year of work on the low-temperature materials research program. Highlights of the results are presented first. Research results are given for the four main program areas: structural alloys, weldments and castings, nonmetallics, and technology transfer. Objectives, approaches, and achievements are summarized in an introduction to each program area.

The major portion of the program has been the evaluation of the low-temperature mechanical and physical properties of stainless steel base metals, welds, and castings, with particular emphasis on the nitrogen-strengthened stainless steels. Developmental steels with manganese additions are also under investigation. Codes and standards development received increased emphasis this year, especially as related to low-temperature property measurements. Work has been done on the standardization of industrial laminates for low-temperature applications and on the measurement of nonmetallic composite properties at cryogenic temperatures. Modeling of the elastic and fracture behavior of woven fiber-reinforced composites has been initiated this year.

Note: Certain commercial equipment, instruments, or materials are identified in this paper to specify the experimental procedure adequately. In no case does such identification imply recommendation or endorsement by the National Bureau of Standards, nor does it imply that the material or equipment identified is necessarily the best available for the purpose. Papers by non-NBS authors have not been reviewed or edited by the NBS editors. Therefore, the National Bureau of Standards accepts no responsibility for the comments or recommendations contained therein.

## ORGANIZATIONAL CONTACTS

The people responsible for the various major aspects of the program are listed below so that specific technical questions may be directed to them.

Department of Energy, Office of Fusion Energy, Washington, D.C. 20545

Program Monitor	D. Beard	(301) 353-4958 (FTS) 233-4958
-----------------	----------	----------------------------------

National Bureau of Standards, Boulder, Colorado 80303

Program Manager	R. P. Reed	(303) 497-3870 (FTS) 320-3870
-----------------	------------	----------------------------------

Structural Alloys	R. P. Reed	(303) 497-3870
	R. L. Tobler	(303) 497-3421
	J. M. Arvidson	(303) 497-3424
	R. P. Walsh	(303) 497-3537

Elastic Properties	H. M. Ledbetter	(303) 497-3443
--------------------	-----------------	----------------

Welding and Casting	H. I. McHenry	(303) 497-3268
	Y.-W. Cheng	(303) 497-5545
	P. Purtscher	(303) 497-3699

Nonmetallics	M. B. Kasen	(303) 497-3558
	H. M. Ledbetter	(303) 497-3443
	R. D. Kriz	(303) 497-3547

Technology Transfer	N. J. Simon	(303) 497-3687
---------------------	-------------	----------------

Colorado School of Mines, Metallurgy Department, Golden, Colorado

E. L. Brown	(303) 273-3953
-------------	----------------

Rockwell International Corporation, Energy Systems Group, Rocky Flats Plant, Golden, Colorado

T. A. Whipple	(303) 497-4365
---------------	----------------

University of Colorado, Mechanical Engineering Department, Boulder, Colorado 80309

S. K. Datta	(303) 492-7750
-------------	----------------

## PROGRAM DESCRIPTION

The overall objective of the program is to assist in the design, construction, and safe operation of low-temperature magnetic fusion energy (MFE) systems, especially superconducting magnets, through effective materials research and materials technology transfer. The specific steps taken to achieve this objective are: (1) evaluation of low-temperature materials research needs specific to MFE devices; (2) development and monitoring of a research program to acquire the necessary data; and (3) rapid dissemination of the data to potential users through personal contacts, publications, and workshops.

Efforts directed at the first specific objective began with the publication of the "Survey of Low Temperature Materials for Magnetic Fusion Energy" in March 1977. A recent publication updating part of this survey, "Structural Alloys for Superconducting Magnets in Fusion Energy System," was included in Volume IV (1981) of this series. In this volume, reviews of the properties of austenitic stainless steels and of austenitic-steel elastic constants contribute to this objective. Through continuous interactions with all low-temperature design, construction, and measurement programs, such as the Large Coil Project, we are aware of new problems as they arise. This year's contribution to the second objective is described in Table 1 in the form of an outline of the research projects. The results appear later in this report. This year, more emphasis has been placed upon research oriented toward establishment of test standards. The third objective is satisfied, in part, by these annual reports and by the series of NBS-DoE Workshops on Materials at Low Temperatures, which are held biennially in Vail, Colorado. Since 1982, handbook pages presenting the available data for specific materials have been distributed to interested members of the low-temperature materials community.



Table 1. Outline of the NBS/DoE Program on Material Studies for Magnetic Fusion Energy Applications at Low Temperatures.

Program Area	Organization	Program Description
<u>A. Structural Alloys</u>		
1. Development of strong, tough alloys	NBS	Assessment of low -temperature properties of selected austenitic alloys containing varying concentrations of C, N, and Mn with a Fe-Cr base. Assessment of Japanese austenitic alloys with Fe-Mn base.
2. Development of strong, fatigue-resistant alloys	NBS	Assessment of fatigue and fatigue crack-growth rates of candidate structural alloys, including 300 series steels, Fe-Mn base alloys, and age-hardened alloys.
3. Development of low-temperature codes and standards	NBS	Research to establish low-temperature mechanical test standards, now emphasizing tensile, fracture toughness, and fatigue.
<u>B. Weldments and Castings</u>		
1. Austenitic-steel welds	NBS	Evaluation of the strength and toughness properties of the 25Mn-5Cr and 32Mn-7Cr alloys at 4 K. Continuation of studies to understand the mechanisms by which residual delta ferrite affects the deformation and fracture of stainless-steel welds.



Program Area	Organization	Program Description
2. Stainless steel castings	NBS, Colorado School of Mines	Investigation of the metallurgical factors that affect the mechanical properties of stainless-steel castings at cryogenic temperatures, including metallographic observations of duplex austenite/delta-ferrite microstructures in deformed and fractured stainless steels. Study of the effects of ferrite and nitrogen content on the strength and toughness at 4 K.
3. Testing program	NBS	Continuation of mechanical property testing at 4 K of welds and plate material in support of superconducting magnet design and construction.

#### C. Nonmetallics for Magnet Structures

1. Standardization	NBS	Continuing cooperation with industry to establish and refine cryogenic-grade specifications for insulating laminates and coding systems for laminates.
2. Characterization	NBS	Measurement of thermal conductivity of composite components at cryogenic temperatures to aid in establishing models for predicting the thermal conductivity of a variety of laminates. Investigation of failure modes of laminates under compression at cryogenic temperatures.

Program Area	Organization	Program Description
3. Property determination modeling	NBS	Development of dynamic methods to determine elastic properties of laminated composites. For a woven glass-fiber/epoxy composite, experimental determination of the complete nine-component elastic-constant tensor. Study of the local-stress distribution in a glass-fiber/epoxy composite "unit cell" using finite-element methods.

#### D. Technology Transfer

1. NBS/DoE Workshop	NBS	Presentation of research results to the fusion community, discussion of new problems, and interaction between interested parties by means of a biennial workshop.
2. Handbook	NBS	Distribution (1982) of preliminary handbook data pages on mechanical and physical properties of AISI 316 stainless steels. Distribution this year of 21Cr-6Ni-9Mn stainless steel and AISI 304N and 304LN stainless steels data pages. Inclusion of aluminum alloy data in future handbook pages.

## ***HIGHLIGHTS OF RESULTS***



## HIGHLIGHTS OF RESULTS

### STRUCTURAL ALLOYS:

#### Tensile, Fracture, and Fatigue Properties

The studies leading toward development of strong, tough structural alloys for superconducting-magnet use continued, resulting in the following major accomplishments:

1. The temperature dependence of the flow strength,  $\sigma_f$ , of austenitic steels was shown to be best characterized by a linear dependence of the  $\log \sigma_f$  on temperature between 4 and 300 K.
2. Extensive reviews of mechanical properties, martensitic transformations, and elastic properties of austenitic stainless steels were presented.
3. Little effect of magnetic fields on stainless steel mechanical behavior was identified. Studies are continuing.

An extensive program to measure fatigue crack growth rates at low stress intensity factors was initiated. Highlights are:

1. An improved measurement capability was developed, including very sensitive compliance correction terms and computer-interactive operation and analyses.
2. Elastic-modulus corrected measurements of aluminum, titanium, and stainless steels were obtained, adding to calibration of measurements of crack growth.

#### Codes and Standards

Discussions were initiated with the Metals Properties Council to set up a cooperative program leading to the establishment of low-temperature codes and standards. Working groups have been organized into two areas: metals and nonmetals.

#### Elastic Constants of Fe-5Cr-26Mn, 76-400 K

By measuring longitudinal-mode and transverse-mode sound velocities at frequencies near 10 MHz, we determined the complete engineering elastic constants--bulk modulus, shear modulus, Young's modulus, Poisson's ratio--for an Fe-5Cr-26Mn austenitic steel between 76 and 400 K. As the result of a magnetic transition, all elastic constants behave anomalously below about 360 K. The bulk modulus begins to soften during cooling at some higher temperature. All elastic constants except Poisson's ratio resume an apparently normal temperature dependence below the 360-K magnetic transition. After increasing abruptly at the magnetic transition, Poisson's ratio increases with decreasing temperature.

For physical properties, these results imply important consequences. For example, properties such as specific heat and thermal expansivity should also exhibit anomalies near the magnetic phase transition. The overall 300-to-4-K thermal contraction should be much smaller than in conventional 304 stainless steel. Depending on their mechanism, plastic mechanical properties may also behave anomalously.

#### Austenitic-Steel Elastic Constants at Low Temperatures

Ledbetter reviewed his contributions to this topic: altogether 31 manuscripts, many unpublished. Main sections of the review are: variability, alloying, temperature, monocrystal and polycrystal relationships, texture, instability, and binary alloys (Fe-Ni).

### WELDMENTS AND CASTINGS:

#### Austenitic-Steel Weldments

The tensile properties, fracture toughness, and fatigue crack-growth rates of two high-manganese austenitic steels were measured at 4 K. Base plate and weld metal properties were measured in a 25Mn-5Cr alloy, and the base plate properties were measured in a 32Cr-7Mn alloy. The results for both alloys fall near the strength-vs.-toughness trend line developed for austenitic stainless steels.

#### Austenitic-Stainless-Steel Castings

The tensile properties and fracture toughness of a series of five CM8M castings with nitrogen contents varying from 0.02 to 0.20 percent were evaluated at 4 K. The nitrogen and chromium contents of the alloys were varied within the limit of 9 to 11 percent nitrogen and 19 to 22 percent chromium, such that the delta ferrite content remained nearly constant at  $9 \pm 1$  percent. The strength, ductility and toughness did not vary appreciably for nitrogen levels between 0.02 and 0.1 percent. The alloys with higher nitrogen contents had significantly higher yield strength, but lower fracture toughness.

The metallography of CF8M castings with ferrite contents ranging from 1 to 28 percent was studied to determine the influence of delta ferrite on deformation and fracture. Evidence was found for two failure mechanisms: (1) brittle fracture of the delta ferrite mixed with ductile fracture of the austenite, and (2) ductile failure in the austenite near the delta-ferrite interface.

#### Stainless-Steel-Weld Elastic Constants

For shielded-metal-arc E316L welds, we determined ultrasonically the complete set of engineering elastic constants: Young's modulus, shear modulus, bulk modulus, Poisson's ratio. Reflecting texture, the elastic constants depend strongly on direction. Agreeing with many previous studies, we found a strong  $\langle 100 \rangle$ -axis texture perpendicular to the welded plate, in the principal heat-flow



direction. Disagreeing with these studies, we found that another strong texture element must be involved to explain the measurements. We considered carefully the relationship between the macroscopic weld constants and those of the microscopic constituent single crystals. Surprisingly, we found that delta ferrite up to 10.1 volume percent affects the weld elastic constants only negligibly.

## NONMETALLICS:

### Standardization

NBS personnel continue to work with those in the United States laminating industry to provide magnet builders with commercial sources of reliable, characterized nonmetallic structural and insulating materials. Of the two products in commercial production, G-10CR and G-11CR, primary emphasis has been placed on the lower cost G-10CR, refining its specification and characterizing its performance. Preliminary test data had suggested that the higher cost G-11CR product provided little advantage over G-10CR. However, more recent tests at ORNL have indicated that the aromatic amine cure used in G-11CR does provide better radiation resistance than the acid anhydride cure used in G-10CR. Also, there is some evidence that the G-11CR product may have superior dimensional stability. Therefore, steps are being taken to bring the G-11CR specification to the same level of development as the G-10CR specification.

### Characterization

G-10CR products from five manufacturers were tested at 295 and 76 K, and the results were statistically analyzed to determine how much variability could be expected among manufacturers. Data on tensile strength, Young's modulus, compressive strength, Poisson's ratio, and interlaminar shear strength were obtained. The analysis indicated that differences in performance were not statistically significant, suggesting that the specifications are adequate to insure uniformity of product behavior.

A continuing study of the reasons for low interlaminar shear strength of a polyimide-matrix variant of G-10CR has shown that one of the reasons is poor interfacial bonding between the E-glass fibers and the matrix. Results of a fractographic study comparing the failure modes of the standard epoxy product with that of the polyimide variant were presented at the 1982 ICEC9/ICMC conference in Kobe, Japan.

### Property Determination and Modeling

(a) Predicted elastic constants of composites containing anisotropic fibers. By a wave-scattering method, we derived dispersion relationships for waves propagating perpendicular to continuous fibers that are oriented unidirectionally. In the long-wavelength limit we obtained relationships that predict the composite's effective static elastic constants. We compared these relationships with others derived from energy methods to obtain upper and lower bounds of the effective static moduli. We plotted the predicted composite constants for graphite-epoxy over the

full range of fiber volume fractions. We consider the fibers to be anisotropic, but transversely isotropic. Under special conditions, the energy-method upper and lower bounds compare identically with the results of this study. The static properties are, of course, special cases of the more general dispersion relationships. Graphs are given for nine elastic constants: axial and transverse Young's and shear moduli, bulk and plane-strain-bulk moduli, and three Poisson's ratios.

(b) Orthotropic elastic constants of a glass-fiber-reinforced epoxy-matrix composite. For a G-10CR-type composite, we determined ultrasonically the complete nine-component orthotropic-symmetry elastic-constant tensor. Using conventional crystal-physics notation developed for single crystals, we described the elastic constants both as Voigt  $C_{ij}$ 's and  $S_{ij}$ 's and as engineering elastic constants: Young's, shear, bulk moduli, and Poisson's ratio. For the first time, anisotropic elastic strain and stress calculations can be carried out confidently for these materials.

(c) Prediction of local stress in a woven-composite "unit cell." Woven-fabric composites are commonly used in superconducting magnets and in containment of cryogenic liquids. The mechanical response of a plain-weave laminated composite at cryogenic temperatures was studied by predicting the load-deformation response of a fundamental "unit cell." A finite-element model was used to predict three-dimensional stresses and elastic stiffness within the unit cell. Elastic Young's modulus predicted by the finite-element model agreed exactly with that predicted by thin-laminate-plate theory. From parametric studies it was found that the Young's modulus in the thin-laminate plane is reduced 50 percent when the warp fiber bundle orientation is increased from 0° to 45°. Parametric studies also demonstrated that thermal loads induced at 77 K decrease delamination stresses at the fill-warp interface and increase delamination stresses in the matrix region adjacent to the warp fiber bundle. Decreasing warp fiber bundle angle decreases these stresses. Future studies will include stress redistributions caused by fracture of fill fiber bundles.

#### TECHNOLOGY TRANSFER:

Handbook supporting documentation pages have been prepared for AISI 316 stainless steels and distributed in preliminary draft format. Properties covered include: tensile strength, yield strength, elongation, reduction of area, stress-strain curves, elastic constants, impact energy, fracture toughness, stress- and strain-controlled fatigue life, fatigue crack growth rate, and electromagnetic and thermal properties. These pages were also submitted to the advisory committee of the "Materials Handbook for Fusion Energy Systems" and are currently in the review process. Handbook and supporting documentation pages on 21Cr-6Ni-9Mn stainless steels have also been prepared, covering the same properties. The 21Cr-6Ni-9Mn pages have recently been submitted to the advisory committee. Preliminary work on handbook pages covering AISI 304N and 304LN is in progress.

# ***STRUCTURAL ALLOYS***



## STRUCTURAL ALLOYS PROGRAM

LEADER: R. P. Reed, NBS

STAFF: R. L. Tobler, J. M. Arvidson, R. P. Walsh, H. M. Ledbetter, NBS

### OBJECTIVES:

- (1) Development of strong, tough structural alloys for use at 4 K in superconducting magnets.
- (2) Development of strong, fatigue-resistant structural alloys for use at 4 K in pulsed superconducting magnets.
- (3) Development of effective codes and standards related to low-temperature property measurements and structural design.

### RESEARCH PAST YEAR (1982):

- (1) Review of martensitic transformations in austenitic steels.
- (2) Characterization of Japanese Fe-Mn base austenitic steels.
- (3) Preliminary development and review of low-temperature fatigue measurements.
- (4) Reports on effects of magnetic fields on austenitic-steel properties.
- (5) Characterization of low-temperature flow strength of austenitic steels.
- (6) Suggestions of modification of ASTM tensile specifications for testing at 4 K.
- (7) Continued studies on low-temperature elastic properties of austenitic steels.

### RESEARCH THIS YEAR (1983):

- (1) Continued research on effects of magnetic fields on 4-K deformation of austenitic steels.
- (2) Construction of 500 000-N (110,000-lbf) capacity tensile-fatigue testing facility for the temperature range 4 to 300 K.
- (3) Characterization of selected Japanese, United States, and USSR Fe-Mn and Fe-Mn-Cr base austenitic steels.
- (4) Correlation of metallurgical effects with fatigue resistance of AISI 304, 316, and 310.
- (5) Study of tensile strength and fracture toughness of manganese-modified 304LN austenitic steels.
- (6) Development and verification of fatigue test methodology.
- (7) Continued studies on low-temperature elastic properties of austenitic steels.
- (8) Thermal-expansion studies on austenitic steels.



## SUMMARY OF MECHANICAL PROPERTY MEASUREMENTS OF STRUCTURAL ALLOYS

Alloy (Designation)	Country of Supplier	Tensile 295,76,4K	Elastic 295-4K	Fracture Toughness 295,76,4K	Fatigue Crack Growth Rate 295,76,4K	Fatigue S-N 4K	Report Volume* (page)
<u>AUSTENITIC STEELS</u>							
Fe-19Cr-9Ni (304)	U.S.	I,II, III,IV,	I,II, III,IV	I,II,III, IV	II,III,IV	I	I(15,71,213), II(79,149,175), III(15,91,105, 117),IV(37,101, 203,215,227),V(71)
Fe-19Cr-9Ni (304L)	U.S.	II,III, IV	I,II, IV	III,IV	III,IV		I(213),II(79,123, 175),III(15),IV(37, 101,131,302,215)
Fe-19Cr-9Ni-N (304N)	U.S.	I,III, IV	IV	I,III,IV	I,III,IV		I(93),III(15),IV (37,101,203,215)
Fe-19Cr-9Ni-N (304LN)	U.S.	II,III, IV,V	IV	II,III, IV	II,III,IV	II	II(35,79),III(15), IV(37,101,203),V(29)
Fe-19Cr-9Ni- 1 to 8Mn (304LN)	U.S.	IV,V	V	IV,V			IV(77),V(15,59,189)
Fe-17Cr-9Ni-8Mn	U.S.		III				III(91)
Fe-17Cr-13Ni-2Mo (316)	U.S.	I,II, III,IV		I,II	II	I	I(15,71),II(79), III(49,105,117), IV(147),V(185)
Fe-17Cr-13Ni-2Mo (316LN)	U.S.	II		II	II		II(79)
Fe-25Cr-21Ni (310)	U.S.	V	III	V			III(105,117),V(71, 145)
Fe-18Cr-3Ni-13Mn	U.S.	I	III	I	I		I(93),III(91)
Fe-21Cr-6Ni-9Mn (21/6/9)	U.S.	I	III	I		I	I(15,71),III(91)
Fe-21Cr-12Ni-5Mn	U.S.	I,II	III	I,II	I,II		I(93),II(79), III(91)
Fe-13Cr-19Mn	USSR		III				III(79)
Fe-20Cr-16Ni-6Mn	USSR	V	V				V(29,213)
Fe-19Ni-9Co (200-300 grades)	U.S.		IV				IV(237)
Many alloys		Review IV,V	Review IV,V	Review IV,V	Review IV,V	Review IV	IV(17,257),V(171)
<u>ALUMINUM ALLOYS</u>							
Al-4Mg (5083-0)	U.S.	IV				II	II(35),IV(185)
Al-6Cu-0.2Mn-0.1Fe (2219-T87)	U.S.		II	II	II	II	II(19)
<u>SUPERCONDUCTORS</u>							
Nb-45Ti	U.S.		III				III(133)

\*Materials Studies for Magnetic Fusion Energy Applications at Low Temperatures: NBSIR 78-884 (I); NBSIR 79-1609 (II); NBSIR 80-1627 (III); NBSIR 81-1645 (IV); NBSIR 82-1667 (V).



## MARTENSITIC TRANSFORMATIONS IN Fe-Cr-Ni STAINLESS STEELS<sup>+</sup>\*

R. P. Reed  
Fracture and Deformation Division  
National Bureau of Standards  
Boulder, Colorado

### ABSTRACT

Very low-temperature martensitic transformations are of great concern for cryogenic applications and research. The principal transformation characteristics are reviewed and then elaborated. The materials classes or alloy systems that exhibit martensitic transformations at very low temperatures are briefly discussed, and references to reviews and compilations are given. The austenite stability of Fe-Cr-Ni alloys with regard to cooling, elastic stress, and deformation is discussed in detail, and the empirical stability expressions that have been developed are summarized and reviewed. Structural relationships between the face-centered cubic austenite ( $\gamma$ ) and body-centered cubic ( $\alpha'$ ) and hexagonal-close-packed ( $\epsilon$ ) martensite products are examined. Typical stress-strain curves of stable and metastable austenitic alloys are illustrated and analyzed as is the temperature dependence of the flow strength below room temperature. Finally, the influence of martensite transformation upon alloy performance in cryogenic applications is surveyed.

<sup>+</sup> Work supported by Office of Fusion Energy, Department of Energy

<sup>\*</sup> To be published in Austenitic Steels at Low Temperatures, Eds. R. P. Reed and T. Horiuchi, Plenum Press, New York (1983).



## INTRODUCTION

The AISI 300 series stainless steels, especially alloys 304, 310, and 316, are used extensively for cryogenic structures. These alloys have a high elastic modulus, high toughness and ductility, low thermal and electrical conductivity, and good weldability. Because of these characteristics, they are used more than any other alloy class for structures for service at 20 K and below, but their use is complicated by the metastability of the austenitic structure of most alloys of this Fe-Cr-Ni alloy series. The metastability leads to martensitic transformation during cooling, from applied stress or during plastic deformation. The martensitic transformation is a significant design consideration in applications requiring fracture control planning, close dimensional tolerances, the absence of a ferromagnetic phase, and high toughness of weldment, heat-affected zone, and base metal. Consequently, research has been conducted to characterize the transformations and their effects on mechanical and physical properties and in-service performance.

Martensitic transformation initially meant the transformation from face-centered-cubic (f.c.c.) austenite to body-centered-cubic (b.c.c.) or body-centered-tetragonal (b.c.t.) martensite in steels. Gradually, however, metallurgists began to describe newly discovered nonferrous transformations as martensitic in nature, and the term martensitic evolved to describe a class of structural transformations. Cohen et al.,<sup>1</sup> who have presented a thorough discussion of the characterization of martensitic transformation, state "A martensitic transformation is a lattice-distortive, virtually diffusionless structural change having a dominant deviatoric component and associated shape change such that strain energy dominates

the kinetics and morphology during the transformation." Thus, a change of atomic structure that takes place with no atomic diffusion and exhibits a change of shape with an attendant undistorted plane is considered a martensitic phase transformation. In such transformations, the associated strain energy is very significant in the determination of the final product shape and size and in the transformation time and temperature characteristics.

Nucleation restricts the martensitic transformation in all ferrous alloys and in some nonferrous systems. After nucleation, growth to a restricted product morphology usually proceeds very quickly; the rate may approach the speed of sound. Except in certain nonferrous alloys, additional transformation is achieved by the nucleation of new crystals, not by the growth of the existing crystals.

Martensitic transformations occur at very low temperatures in such diverse materials as stainless steels, alkali metals, and solidified gases; therefore, atomic diffusion plays no essential role. Atom transfer from parent to product structures proceeds by shear-like, coordinated motion of many atoms, resulting in a shape change. This shape change is easily observed by using conventional microscopy techniques.

A consequence of the shear-like, coordinated atomic motion is that there are easily defined geometrical relationships between parent and product phases. An orientation relationship exists between all product-phase and parent-phase crystal structures. The interface plane, separating the parent and product phase, is conventionally called the habit plane and is usually unique for a given alloy system. Phenomenological crystallographic theories have been reasonably successful in predicting and explaining the interrelationships of these geometrical parameters, but they are not completely satisfactory. Another consequence of the atom-transfer mode of a martensitic transformation is that the identical atom concentration of the parent phase is preserved in the product phase; there is no composition gradient between the two phases. Finally, locally large stresses, which may exceed the yield strength of the parent material, may result from the shape deformation of the product phase. This is particularly apparent in ferrous-alloy transformations, where extensive slip, faulting, or in special cases, deformation twinning may be induced in the parent phase and where the generation of point defects in the product phase may be about 0.5 at.%.

No review has previously been devoted to martensitic transformations in Fe-Cr-Ni steels. However, here are a number of excellent reviews on martensitic transformations. Especially, the reader is referred to Reed and Breedis<sup>2</sup> for a thorough compilation (702 references) of literature prior to 1966; to Bilby and Christian,<sup>3</sup> Christian,<sup>4</sup> Wayman,<sup>5,6</sup> and Lieberman<sup>7</sup> for excellent descriptions of martensite crystallography; and to Roitburd and



Kurdjumov,<sup>8</sup> Entwisel,<sup>9</sup> Christian,<sup>10</sup> and Kaufman and Cohen<sup>11</sup> for excellent reviews of martensite kinetics. Low temperatures have been emphasized in reviews by Barrett<sup>12</sup> and Reed and Breedis.<sup>2</sup> General books on martensitic transformations include Martensitic Fundamentals and Technology<sup>13</sup> and Christian.<sup>14</sup> There have been excellent international conference proceedings on general martensitic research: Physical Properties of Martensite and Bainite,<sup>15</sup> Mechanism of Phase Transformations in Crystalline Solids,<sup>16</sup> Shape Memory Effect in Alloys,<sup>17</sup> New Aspect of Martensitic Transformations,<sup>18</sup> and Phase Transformations.<sup>19</sup> The International Conference on Martensitic Transformations (ICOMAT) held its third conference in 1979. These ICOMAT conferences bring most of the principal research scientists together every third year. Their proceedings (e.g., Proceedings of the International Conference on Martensitic Transformation, ICOMAT-1979,<sup>20</sup> report current research.

#### AUSTENITE STABILITY

Either on cooling, under applied elastic stresses, or during plastic deformation, the austenite phase ( $\gamma$ ) of Fe-Cr-Ni alloys may transform martensitically to b.c.c. ( $\alpha'$ ) and h.c.p. ( $\epsilon$ ) phases. The alloy composition affects the chemical free-energy difference between the two phases.

The difference in free energy ( $F$ ) between the two phases  $\gamma$  and  $\alpha'$  is:

$$\Delta F^{\alpha' \rightarrow \gamma} = F_T^{\gamma} - F_T^{\alpha'} \quad (1)$$

where  $F_T^{\gamma}$  and  $F_T^{\alpha'}$  are the total free energies of the respective phases. The free energies of mixing,  $\Delta F_m^{\gamma}$  and  $\Delta F_m^{\alpha'}$ , of the two phases may be expressed in terms of the total free energies as:

$$\Delta F_m^{\gamma} = F_T^{\gamma} - \sum X_i F_i^O \quad \text{and} \quad (2)$$

$$\Delta F_m^{\alpha'} = F_T^{\alpha'} - \sum X_i F_i^O \quad (3)$$

where  $X_i$  are the atom fraction of a component,  $i$ , and  $F_i^O$  is the free energy of the pure component,  $i$ , in the standard state. The total free energy of each phase is a sum of the partial molar free energies of each component in an ideal solution of  $\gamma$  or  $\alpha'$ :

$$F_T^{\gamma} = \sum X_i \bar{F}_i^{\gamma} \quad \text{and} \quad F_T^{\alpha'} = \sum X_i \bar{F}_i^{\alpha'} \quad (4)$$

The difference in the free energy of mixing for the two phases is:

$$\Delta F_m^{\gamma} - \Delta F_m^{\alpha'} = F_T^{\gamma} - \sum X_i F_i^O - F_T^{\alpha'} + \sum X_i F_i^O \quad \text{and} \quad (5)$$

$$\Delta F_m^{\gamma} - \Delta F_m^{\alpha'} = F_T^{\gamma} - F_T^{\alpha'} = \Delta F^{\alpha' \rightarrow \gamma} \quad (6)$$

Therefore, from eqs. 4 and 6,

$$\Delta F^{\alpha' \rightarrow \gamma} = \sum X_i (\bar{F}_i^{\gamma} - \bar{F}_i^{\alpha'}) = \sum X_i (\Delta \bar{F}_i^{\alpha' \rightarrow \gamma}). \quad (7)$$

That is, the free energy difference between the two phases can be expressed as the sum of the partial molar free energy differences of each component.

Breedis and Kaufman<sup>21</sup> have derived the expression for  $\Delta F^{\alpha' \rightarrow \gamma}$  for the Fe-Cr-Ni ternary system:

$$\begin{aligned} \Delta F_{\text{Fe,Cr,Ni}}^{\alpha' \rightarrow \gamma} = & (1 - X_{\text{Cr}} - X_{\text{Ni}}) \Delta \bar{F}_{\text{Fe}}^{\alpha' \rightarrow \gamma} + X_{\text{Cr}} \Delta \bar{F}_{\text{Cr}}^{\alpha' \rightarrow \gamma} + \\ & X_{\text{Ni}} \Delta \bar{F}_{\text{Ni}}^{\alpha' \rightarrow \gamma} + X_{\text{Cr}} (1 - X_{\text{Cr}} - X_{\text{Ni}}) (B - A)_{\text{Fe-Cr}} + \\ & X_{\text{Ni}} (1 - X_{\text{Cr}} - X_{\text{Ni}}) (B - A)_{\text{Fe-Ni}} + X_{\text{Cr}} X_{\text{Ni}} (B - A)_{\text{Cr-Ni}} \end{aligned} \quad (8)$$

Here  $X_{\text{Cr}}$  and  $X_{\text{Ni}}$  are the atom fractions, and A and B are interaction parameters. These parameters are described as

$$A = \frac{F_{\text{exc}}^{\alpha'}}{X(1-x)} \quad \text{and} \quad B = \frac{F_{\text{exc}}^{\gamma}}{X(1-x)} \quad (9)$$

where  $F_{\text{exc}}^{\alpha' \rightarrow \gamma}$  is the excess free energy of a binary system.  $\Delta F_{\text{Cr}}^{\alpha' \rightarrow \gamma}$ ,  $\Delta F_{\text{Ni}}^{\alpha' \rightarrow \gamma}$ , and  $\Delta F_{\text{Fe}}^{\alpha' \rightarrow \gamma}$  represent the partial molar free-energy difference between  $\alpha'$  and  $\gamma$  for the pure components chromium, nickel, and iron, respectively.

Kaufman<sup>22</sup> derived free-energy relations for the Fe-Cr binary system and combined these with the previous data for Fe-Ni binary alloys<sup>23</sup> to calculate  $\Delta F^{\alpha' \rightarrow \gamma}$  for stainless steels. On the basis of regular solution and for the temperature range of about 100 to 900 K,

$$\begin{aligned} \Delta F_{\text{Fe,Cr,Ni}}^{\alpha \rightarrow \gamma} = & \Delta F^{\gamma} - \Delta F^{\alpha'} \\ = & (1 - X_{\text{Cr}} - X_{\text{Ni}}) (5036 - 11 \times 10^{-3} T^2 + 6.5 \times 10^{-6} T^3) \\ & + X_{\text{Cr}} (1927 + 4.2T) + X_{\text{Ni}} (-15500 + 2.97 \times 10^{-3} T^2 + 1.64 \times 10^{-6} T^3) + \\ & X_{\text{Cr}} (1 - X_{\text{Cr}} - X_{\text{Ni}}) (-11730 + 3.1T) + \\ & X_{\text{Ni}} (1 - X_{\text{Cr}} - X_{\text{Ni}}) [15080 + 2.4T(1 - \ln T)] \quad \text{J} \cdot \text{mol}^{-1} \end{aligned} \quad (10)$$

For calculations of  $T_{\text{ms}}$  of stainless steels, Kaufman<sup>22</sup> added the term

$$X_{\text{G+N}} (-2346 + 0.175T) \quad \text{J} \cdot \text{mol}^{-1} \quad (11)$$

to account for carbon and nitrogen; the nominal manganese content of 1.5 wt.% was added to the nickel content. Values of  $\Delta F^{\alpha' \rightarrow \gamma}$  ranging from about 2000 J·mol<sup>-1</sup> (475 cal·mol<sup>-1</sup>) for  $T_{\text{ms}} = 100$  K to 1260



$\text{J}\cdot\text{mol}^{-1}$  ( $300 \text{ cal}\cdot\text{mol}^{-1}$ ) for  $T_{\text{ms}} = 550 \text{ K}$  were calculated for typical stainless steel compositions using Eq. 8. (In this paper the temperature of transformation start is labeled  $T_{\text{ms}}$ ; this nomenclature is a compromise between the metallurgical expression,  $M_s$ , and the physics label,  $T_c$ .) Data calculations by Breedis and Kaufman<sup>21</sup> and Rao et al.<sup>24</sup> predict lower values of  $\Delta F_{\text{Fe}}^{\alpha \rightarrow \gamma}$  and would, similarly, result in lower values of  $\Delta F_{\text{Fe,Cr,Ni}}^{\alpha \rightarrow \gamma}$  for the Fe-Cr-Ni ternary system.

An equation analogous to Eq. 10 can be developed for the free energy difference between the  $\epsilon$  and  $\gamma$  phases in Fe-Cr-Ni alloys. Values for  $\Delta F_{\text{Fe}}^{\epsilon \rightarrow \gamma}$  and  $\Delta F_{\text{Cr}}^{\epsilon \rightarrow \gamma}$  were estimated by Kaufman<sup>25</sup> from enthalpy and entropy differences due to structure. Interaction parameter estimates were made by Breedis and Kaufman<sup>21</sup> for Fe-Cr, Fe-Ni, and Cr-Ni binaries. Using these estimates, the following expression is derived for the free energy difference between  $\epsilon$  and  $\gamma$  phases in Fe-Cr-Ni alloys:

$$\Delta F_{\text{Fe,Cr,Ni}}^{\epsilon \rightarrow \gamma} = X_{\text{Fe}} \Delta F_{\text{Fe}}^{\epsilon \rightarrow \gamma} + X_{\text{Cr}} (1095 + 0.628T) - X_{\text{Ni}} (1047 + 1.26T) + 2095(X_{\text{Cr}}^2 - X_{\text{Cr}} + X_{\text{Ni}}^2 - X_{\text{Ni}}) \text{ J}\cdot\text{mol}^{-1}. \quad (12)$$

The partial molar free-energy difference ( $\Delta F_{\text{Fe}}^{\epsilon \rightarrow \gamma}$ ) can be calculated from the graphical presentation by Breedis and Kaufman<sup>21</sup> of  $\Delta F_{\text{Fe}}^{\alpha \rightarrow \gamma}$ , and  $\Delta F_{\text{Fe}}^{\alpha \rightarrow \epsilon}$ . This term becomes positive at temperatures lower than 390 K and equals about  $300 \text{ J}\cdot\text{mol}^{-1}$  at 300 K. Using Eq. 12 and the  $\Delta F_{\text{Fe}}^{\epsilon \rightarrow \gamma}$  data plotted in Fig. 1, the temperature dependence of  $\Delta F_{\text{Fe,Cr,Ni}}^{\epsilon \rightarrow \gamma}$  can be calculated and is plotted in Fig. 1. This indicates that  $\Delta F_{\text{Fe,Cr,Ni}}^{\epsilon \rightarrow \gamma}$  becomes positive near 325 K. Actually,  $\epsilon$  transformation has been observed on cooling below room temperature (e.g., Reed<sup>26</sup>). Alloy additions such as carbon, nitrogen, and manganese move the  $\Delta F_{\text{Fe,Cr,Ni}}^{\epsilon \rightarrow \gamma}$  curve to lower temperatures.

Expressions relating the stability of the austenite and the temperatures of transformation during cooling ( $T_{\text{ms}}$ ) or during deformation ( $T_{\text{md}}$ ) have been developed empirically and are summarized in Table 1. Eichelman and Hull,<sup>27</sup> working with austenitic alloys with 10 to 18% Cr, 6 to 12% Ni, 0.6 to 5% Mn, 0.3 to 2.6% Si, 0.004 to 0.129% C, and 0.01 to 0.06% N, established that all of the above alloying elements stabilize the austenite and thus lower  $T_{\text{ms}}$ . Monkman et al.,<sup>28</sup> using a larger number of specimens with ranges of 5 to 13% Ni, 11 to 19% Cr, and 0.035 to 0.126% C+N, produced a similar analysis and concluded that only to a first approximation was  $T_{\text{ms}}$  linearly dependent on composition. The dependence of  $T_{\text{ms}}$  on carbon and nitrogen concentration seemed to be influenced by chromium and nickel concentration.

Hull<sup>31</sup> completed another study assessing the effects of nickel, chromium, manganese, carbon, nitrogen, silicon, and cobalt (aluminum, thallium, vanadium, and tungsten sometimes were added) on  $\alpha'$

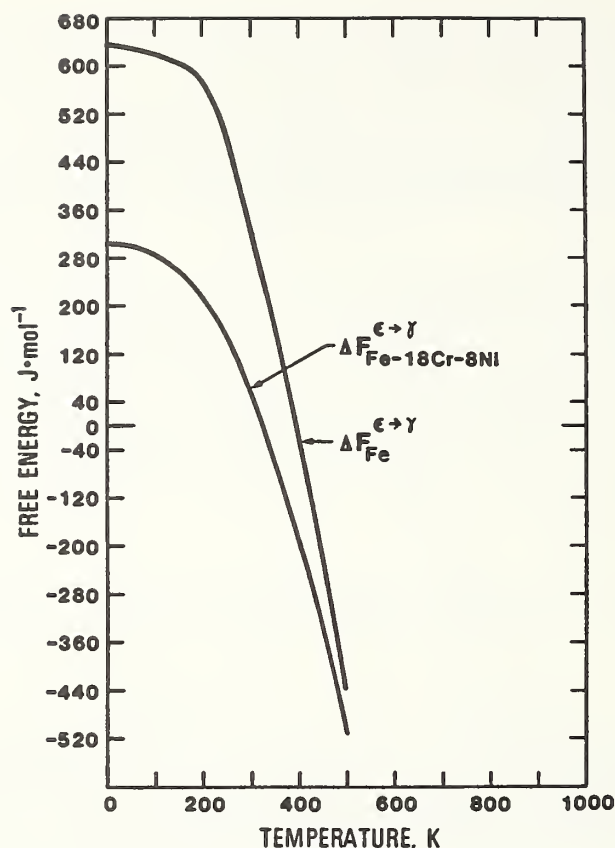


Fig. 1. Temperature dependence of free energy difference of  $\epsilon$  and  $\gamma$  structures of iron and Fe-18Cr-8Ni alloy.

formation during low-temperature cooling-and-deformation experiments and on ferrite retention after cooling to room temperature from the melt. Hull's study reconfirmed that all the above elements suppress low-temperature  $\alpha'$  formation during either cooling or deformation but that chromium, molybdenum, silicon, vanadium, tungsten, niobium, tantalum, and aluminum additions promote the formation or retention of the high-temperature, b.c.c. delta-ferrite phase. To predict the effect of elemental additions on  $T_{ms}$ , Hull assumed that the nickel contribution was the average of the Monkman et al.<sup>28</sup> and Eichelman and Hull<sup>27</sup> results and then compared all the effects of alloying additions with that of nickel. The empirical relationships have been analyzed by King and Larbalestier,<sup>40</sup> who point out some expected deviations in the dependence of  $T_{ms}$  on nickel and chromium when the relationships are used for prediction of the composition range of AISI 300 series stainless steels.

The formulation of Andrews<sup>30</sup> applies to lower chromium and nickel concentrations, thus higher  $T_{ms}$ , and his results are included

in Table 1 to point out the disparity between the high- and low-temperature empirical results. Hammond<sup>29</sup> was the only investigator to include molybdenum with chromium and nickel.

In all these studies, specimens of various composition were prepared and cooled, and their  $T_{ms}$  values were measured. Regression analyses were then used to obtain the empirical relation of the dependence of  $T_{ms}$  on alloy concentration.

Similar experiments have been conducted to assess the influence of cold work (either tensile or compressive) on  $T_{md}$ . Their results are also contained in Table 1. Note that the experimental definition of  $T_{md}$  varied in each study: Angel<sup>32</sup> used 50%  $\alpha'$  at 30% tensile elongation; Williams et al.<sup>33</sup> used 2.5%  $\alpha'$  at 45% compressive elongation; and Hull<sup>34</sup> used the minimum detection level (probably about 1%  $\alpha'$ ) at 50% compressive elongation.

In reviewing the current status of the predictability of Fe-Cr-Ni stability, Collings and King<sup>41</sup> caution that the Breedis and Kaufman<sup>21</sup> free-energy expression for  $T_o$  near 0 K does not have the same chromium and nickel coefficients as the Eichelman and Hull<sup>27</sup> and Monkman et al.<sup>28</sup>  $T_{ms}$  expressions. The latter expressions are based predominantly on chromium and nickel concentrations less than those required for  $T_o$  near 0 K ( $T \approx 300$  K). This raises the question of the usefulness of these  $T_{ms}$  predictive expressions for the normal 18Cr-8Ni stainless steels.

Collings and King<sup>41</sup> also point out that in low-interstitial-austenitic stainless steels (those steels that are most easily welded), there is a higher tendency for isothermal transformation (in the 100 to 200 K range), and these predictive equations are not useful in the estimation of the occurrence of time-dependent  $\alpha'$  transformation (or the separation between athermal and isothermal transformation).

Schramm and Reed<sup>37</sup> used x-ray peak-shift measurements, coupled with previous stacking-fault energy measurements, to estimate the dependence of the stacking-fault energy on chemical composition. This dependence should correspond to the dependence of the  $\gamma \rightarrow \epsilon$  transformation on composition, because a stacking fault represents a local planar area of  $\epsilon$ . Rhodes and Thompson<sup>38</sup> suggested that the stacking-fault energy values of the Schramm and Reed analysis were too large, considering additional weak-beam electron-microscopy data. Weak beam electron microscopy measurements by Bampton et al.<sup>42</sup> confirm that the Schramm and Reed least-square analysis produced stacking fault energies that were excessively large and indicated a data spread of about  $\pm 25\%$  from measurements of individual nodes. Brofman and Ansell<sup>39</sup> added the dependence on carbon. The stacking-fault-energy composition dependences are also included in Table 1. The stacking-fault

Table 1. Temperature equivalents for calculation

Investigator (Year)	Temperature Equivalent					
	Base	Cr	Ni	Mn	Si	C
f.c.c.→b.c.c. ( $T_{ms}$ ), cooling <sup>a</sup>						
Eichelman and Hull <sup>27</sup>	1578	-41.7	-61.1	-33.3	-27.8	-1670
Monkman et al. <sup>28</sup>	1455	-36.7	-56.7			-1460
Hammond <sup>29</sup>	1105	-29	-39			
Andrew <sup>30</sup>	273	-12.1	-17.7	-30.4		-423
Hull <sup>31</sup>	1755	-47	-59	-54	-37	-2390
f.c.c.→b.c.c. ( $T_{md}$ ), deformation <sup>a</sup>						
Angel <sup>32</sup>	686	-14	-9.5	-8.1	-9.2	-46.2
Hull <sup>31</sup>	1655	-23	-59	-41	-20	-777
Williams et al. <sup>33</sup>	686	-6	-25	-16	+21	-222
Magnetic transition (paramagnetic→antiferromagnetic, Néel temperature)						
Warnes and King <sup>34</sup>	90	-1.25	-2.75	+7.75	-14	
Enthalpies of Formation <sup>b</sup>						
Lee et al. <sup>35</sup>	-8168	208	181	1087		3186
f.c.c.→h.c.p. (stacking fault energy at room temperature) <sup>c</sup>						
Dulieu and Nutting <sup>36</sup>	0		5	14		34
Schramm and Reed <sup>37</sup>	-530	7	62	32		
Rhodes and Thompson <sup>38</sup>	12	6	14	177	-47	
Brofman and Ansell <sup>39</sup>	167	9	21			260

a. Numbers in table represent K/wt.%; b. Numbers in table represent J·mol<sup>-1</sup>·wt.%; from enthalpy measurements, lath, and plate α'.



of stability parameters of austenitic steels.

N	Mo	Other	Comments, Composition Range (wt.%)
-1670			21 alloys: 10-18Cr, 6-12Ni, 0.6-5Mn, 0.3-26Si, 0.004-0.12C, 0.01-0.06N
-1460			49 alloys: 11-19Cr, 5-13Ni, 0.035-0.0176(C+N)
	-36		16 alloys: 0-12Cr, 4-8Ni, 0.03C, 2-6Mo, 0-15Co, 1-2Ti
	-7.5		184 alloys from previous studies not in this table. Notice different composition ranges. 0-4.6Cr, 0-5.0Ni, 0.04-4.9Mn, 0.1-1.9Si, 0.11-0.6C, 0-5.4Mo
-3720	-56	-180(Ti), -14(Co)	59Ni = average of Eichelman and Hull <sup>27</sup> and Monkman et al., <sup>28</sup> 29 alloys: 12-24Cr, 0-22Ni, 0-20Mn, 0-4Si, 0-0.1C, 0-0.15N, 0-6Mo, Co, 0-2Ti
-46.2	-18.5		30% tension, 50% $\alpha'$
-315	-24	-12(Co)	50% compression, 60 alloys: 12-24Cr, 0-22Ni, 0-20Mn, 0-4Si, 0-0.1C, 0-0.15N, 0-6Mo, Co
-222	-11		45% compression, 2.5% $\alpha'$ , 25 alloys: 12-25Cr, 9-20Ni, 1-2Mn, 0.1-0.6Si, 0.04-0.25C, 0.01-0.1N, 0.6-2.8Mo
	-5.5		64 commercial and specially prepared alloys: 5-25Cr, 5-32Ni, 0-16Mn, 0-24Si, 0.3Mo
		1137 <sup>d</sup>	48 alloys: 0-18Cr, 0-30Ni, 0-3Mn, 0-0.05Si, 0.01-0.86C, 0.02-0.2Mo
	1	36(Ti), 32(Cu), -055(Co)	Electron microscopy
	93		7 alloys, x-ray, literature data-regression analysis Modified Schramm-Reed approach

c. Numbers in table represent  $\mu\text{J}/\text{m}^2 \cdot \text{wt.}\%$  (ergs/cm<sup>2</sup>·wt.%); d. Represents stored energy



energy is expected to decrease at lower temperatures, and the temperature dependence should approximately follow the form of the  $\Delta F_{\text{Fe,Cr,Ni}}^{\epsilon \rightarrow \gamma}$  curve illustrated in Fig. 1.

In all empirical relations, chromium is shown to increase the stability of austenite relative to either  $\epsilon$  or  $\alpha'$  (Table 1). Although it is not clear at first glance, Eq. 8 (intended for use below 900 K) predicts that chromium will act to suppress the  $\gamma \rightarrow \alpha'$  transformation. At higher temperatures, chromium has the opposite effect and stabilizes the  $\gamma$  structure.<sup>22</sup> However, Eq. 12 predicts that chromium additions act to increase  $\Delta F_{\text{Fe,Cr,Ni}}^{\epsilon \rightarrow \gamma}$ , thus promoting  $\epsilon$  transformation. This contrasts with the regression analyses results of the dependence of the stacking-fault energy on composition (Table 1). Additional study is needed to decide whether to amend the free-energy expressions and whether chromium alloyed with manganese, silicon, carbon, and nitrogen is a stabilizing influence on austenite with respect to hexagonal-close-packed structures.

Warnes and King<sup>34</sup> measured the Néel temperature (paramagnetic-to-antiferromagnetic transition temperature) for a series of Fe-Cr-Ni alloys. Regression analysis of their data has resulted in an expression relating the Néel temperature to composition (Table 1). The magnetic term was considered to be a relatively minor contribution to the free energy of the Fe-Cr-Ni alloy structures (e.g., Breedis and Kaufman<sup>21</sup>). It is of interest, however, that both chromium and nickel act, in the approximately same ratio, to suppress the antiferromagnetic phase and to stabilize the austenite structure.

Calorimetric measurements of the heat evolved during martensite formation were made by Lee et al.<sup>35</sup> for a series of Fe-Cr-Ni alloys. For an Fe-18Cr-8Ni alloy transformed at temperatures ranging from 156 to 293 K, the transformation enthalpy change,  $\Delta H$ , was measured and the average value was found to be  $1920 \text{ J} \cdot \text{mol}^{-1}$ . No temperature dependence of  $\Delta H$  was observed. Results of the regression analysis of all alloys for elemental contributions to the enthalpy change are listed in Table 1. There is a strong similarity between these results and the effect of the contributions of the elements on  $T_{\text{ms}}$ .

## STRUCTURE

Face-centered-cubic austenite ( $\gamma$ ) transforms on cooling to two martensitic products: one b.c.c. ( $\alpha'$ ), the other h.c.p. ( $\epsilon$ ). The h.c.p. phase is associated with extended stacking faults and forms as thin sheets on (111) austenite planes. In most austenitic stainless steels, the  $\alpha'$  product forms as laths. Breedis<sup>43</sup> reported a lath  $\alpha'$  morphology for compositions ranging from Fe-19Cr-11Ni to Fe-10Cr-16Ni; at lower chromium and higher nickel concentrations the  $\alpha'$  morphology changed to a plate-like structure.

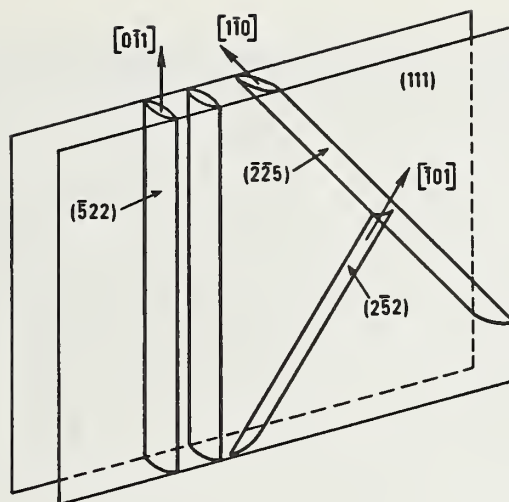


Fig. 2. Schematic representation of  $\alpha'$  laths within a  $\{111\}$  sheet in Fe-18Cr-8Ni alloy.

From Reed,<sup>26</sup> the  $\alpha'$  lath-like structure is parallel to  $\langle 110 \rangle$ , with  $(225)$ ,  $(112)$ , or both habit planes.<sup>44</sup> The laths are restricted within  $\{111\}$  bands, and usually three sets of habit planes form within the band. The schematic in Fig. 2 is a typical representation of  $\alpha'$  laths within a  $\{111\}$  band. For a given  $\langle 110 \rangle$  lath direction, two possible habit planes are possible; for example, for  $[1\bar{1}0]$   $(111)$ , both  $(\bar{2}25)$  and  $(252)$  are possible habit planes. The habit plane observed is the one that makes the largest angle to the confining  $(111)$  band. Many adjacent laths appear to be twin related.<sup>35</sup> Optical photomicrographs of bands of  $\alpha'$  martensite, taken in sequence after polishing and etching, are shown in Fig. 3. Reed<sup>26</sup> notes that during thermal cycling or cooling to a lower temperature, new bands of lath martensite continued to form, and morphological variations were observed. Some lath directions deviated from  $\langle 110 \rangle$ , and the habit plane deviated from  $\{225\}$ . While most laths were confined by  $\{111\}$  bands, some  $\alpha'$  was restricted by  $\{211\}$  bands. Therefore, continued transformation adds considerably to the complexity of the  $\alpha'$  structure.

Transformation during plastic deformation initially results in  $\alpha'$  at intersections of active  $\{111\}$  deformation bands. The  $\alpha'$  assumes the shape of laths along  $\langle 110 \rangle$  common to the two active  $\{111\}$  systems. Figure 4 illustrates  $\alpha'$  formation at slip-plane intersections. Evidence of dislocation pileups at  $\alpha'$  laths is observable. Also, more than one lath may form at each transformation site, and in contrast to the  $\alpha'$  that forms on cooling (Figs. 2 and 3), all laths have the same habit-plane variant. Finally, at several sites, the lath transformation appears irregular or incomplete; there is a lack

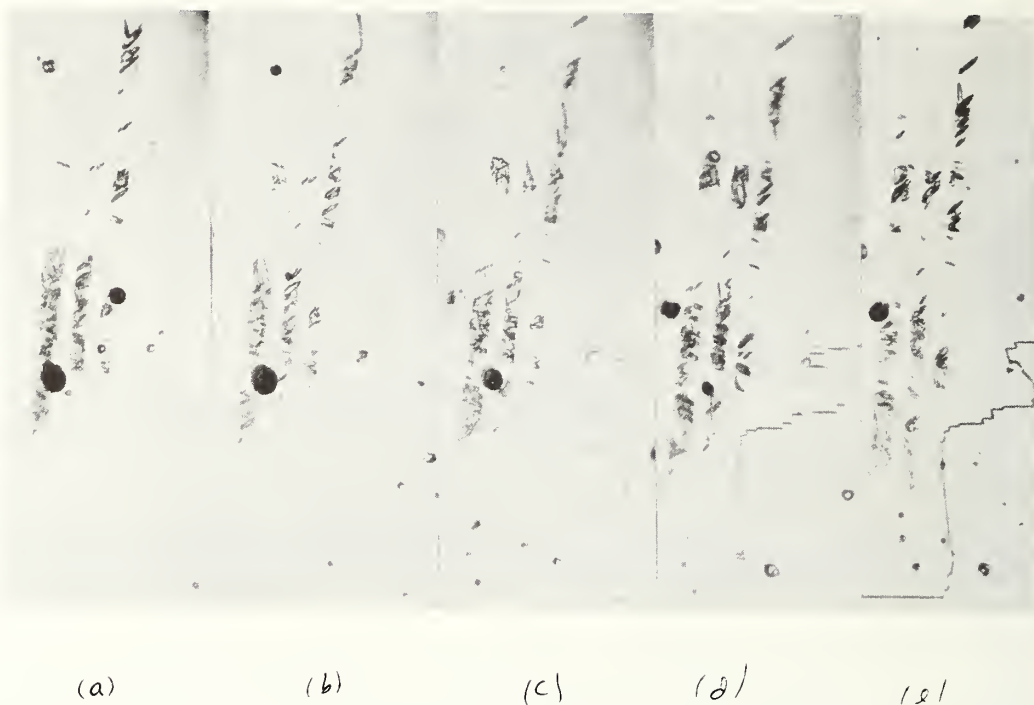


Fig. 3. Optical photomicrographs of sheets of  $\alpha'$  martensite in Fe-18Cr-8Ni taken after sequential electropolishing and etching steps (a to e).

of a well-defined austenite-martensite interface, and the interaction of transformed material with the dislocations in the immediate vicinity is very complex. Growth of the  $\alpha'$  nucleus produces a more distinct and crystallographically regular lath-like product-phase morphology.

There is a considerable amount of accommodation deformation in the austenite after transformation during cooling; it is particularly large within the  $\{111\}$  band containing the  $\alpha'$  laths. This leads one to suspect that lattice deformation is minimized normal to the  $\{111\}$  band that contains the three  $\langle 110 \rangle$  directions and that the lattice-invariant deformation in these  $\langle 110 \rangle$  directions may be very low. The  $\{111\}$  bands contain either  $\epsilon$  martensite or a large amount of stacking faults.<sup>43,44</sup>

The orientation relationships between the  $\gamma$ ,  $\epsilon$ , and  $\alpha'$  phases are:<sup>44</sup>

$$(111)_{\gamma} \parallel (0001)_{\epsilon} \parallel (101)_{\alpha'}$$

$$[1\bar{1}0]_{\gamma} \parallel [1\bar{2}10]_{\epsilon} \parallel [11\bar{1}]_{\alpha'}$$

These relationships are apparently retained regardless of the manner of  $\epsilon$  or  $\alpha'$  formation.

The internal defect structure of the  $\alpha'$  phase in Fe-Cr-Ni steels consists predominantly of dislocations. Wirth and Bickerstaffe<sup>45</sup> have reported the presence of some twins in  $\alpha'$  following increased chromium additions (with 8 wt.% Ni) or increased cooling rates. As chromium is replaced by nickel, Breedis<sup>43</sup> reports that cellular, irregular distributions of dislocations typical of  $\alpha'$  laths change to planar, regular arrays typical of  $\alpha'$  plates. Also, as nickel replaces chromium, the amount of  $\epsilon$  transformation decreases, the sharpness of the h.c.p. reflections decreases, and the f.c.c. twin reflections become more diffuse.<sup>43</sup>

Many metallurgists have been concerned with the role of the  $\epsilon$  transformation: does  $\epsilon$  act as a precursor transformation ( $\gamma \rightarrow \epsilon \rightarrow \alpha'$ ) or is the  $\epsilon$  an accommodation effect ( $\gamma \rightarrow \alpha'$ ,  $\gamma \rightarrow \epsilon$ )? Both effects have been

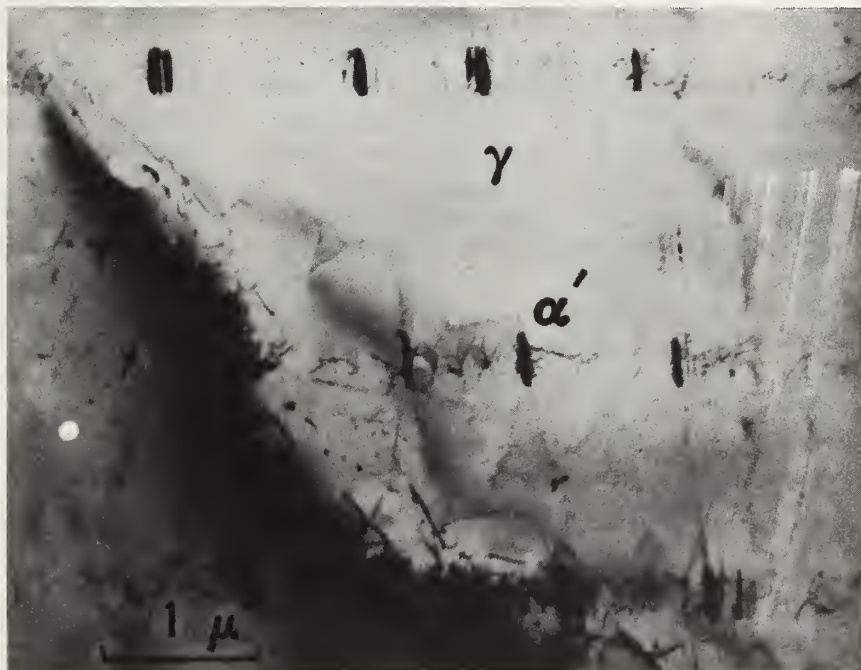


Fig. 4. Fe-18Cr-8Ni austenite strained 0.01 in tension with two active slip systems on  $\{111\}$ . Formation of  $\alpha'$  along  $\langle 1\bar{1}0 \rangle$  intersections of slip planes.



observed. The stainless steels with low stacking-fault energy tend to form  $\epsilon$ , and the  $\alpha'$  tends to form from  $\epsilon$ . Higher stacking-fault-energy alloys require transformation stresses for observable  $\epsilon$  formation.

#### EFFECTS OF TEMPERATURE

The amount of  $\alpha'$  transformation is dependent on temperature, and the kinetics generally follow the form shown in Fig. 5. After cooling below  $T_s$ , holding at constant temperature produces a C curve when temperature<sup>ms</sup> is plotted against holding time for constant  $\alpha'$  product. Suppression of  $\alpha'$  transformation usually occurs below about 100 K.<sup>46</sup> In most of the Fe-18Cr-8Ni (AISI 304L) alloys that have been examined and found to exhibit  $\alpha'$  transformation, cooling to 76 K produces a maximum amount of  $\alpha'$  (usually 5 to 10%). Cooling rapidly to 4 K in some cases suppresses  $\alpha'$  transformation entirely.

Reversion of  $\epsilon$ , formed either from deformation<sup>26</sup> or cooling,<sup>47</sup> to  $\gamma$ , begins when the alloy is heated to about 410 K (see Fig. 6). Reversion of  $\alpha'$ , formed either by cold working ( $\sim 70\% \alpha'$ ), or cooling ( $\sim 7\% \alpha'$ ), begins at a higher temperature, about 770 K as illustrated in Fig. 26.<sup>26</sup> Partial decomposition of the  $\alpha'$  on holding at lower temperatures has been observed.

#### EFFECTS OF AUSTENITE DEFORMATION

Deformation of austenite at temperatures several hundred degrees above room temperature tends to produce a cellular dislocation substructure. At lower temperatures (about one hundred degrees above room temperature) more planar defects, stacking faults, and twins are produced. At still lower temperatures,  $\epsilon$  martensite,  $\alpha'$  martensite, or both form. The exact temperatures depend primarily on the stacking-fault energy. The lower the stacking-fault energy, the higher the deformation temperatures for formation of planar dislocations, stacking faults, and  $\epsilon$  martensite. Since the stacking-fault energy is very dependent on temperature,<sup>42,47</sup> deformation at lower temperatures results in an increase of planar defects.

The formation of planar defects tends to enhance subsequent martensite formation at lower temperatures. In contrast, a cellular dislocation structure suppresses subsequent transformation on cooling below  $T_s$  or during deformation below  $T_{md}$ . Presumably cellular structures only influence the martensitic transformation by raising the strength of the austenitic matrix. Planar defects, with reduced cross-slip, produce high local strain fields, which may serve as nucleation sites. Evidence of austenitic prestrain effects on transformation at lower temperatures confirms the very delicate balance between austenite strengthening and planar-dislocation-induced stress fields.





Fig. 5. Typical martensite-transformation-kinetics for Fe-18Cr-8Ni alloy on cooling below room temperature. The series of curves show the effect of progressively decreasing cooling rates, from (a) to (e).

Small amounts of tensile plastic deformation (0 to 10%) at room temperature stimulate transformation to  $\alpha'$  on cooling to temperatures below  $T_{ms}$ .<sup>26,46,48</sup> Added deformation steadily suppresses transformation. Breedis<sup>48</sup> has reported that the  $\alpha'$  transformation is enhanced in alloys that have a low stacking-fault energy; planar dislocation arrays, as opposed to cellular dislocation substructures, result in more transformation during cooling. Strife et al.<sup>49</sup> have found that prestrain above  $T_{md}$  reduces  $T_{ms}$ , may enhance subsequent transformations, and at larger strains, usually suppresses transformation.

There is ample evidence that deformation-induced defects play a major role in the nucleation of both  $\epsilon$  and  $\alpha'$ . Brooks et al.<sup>50</sup>

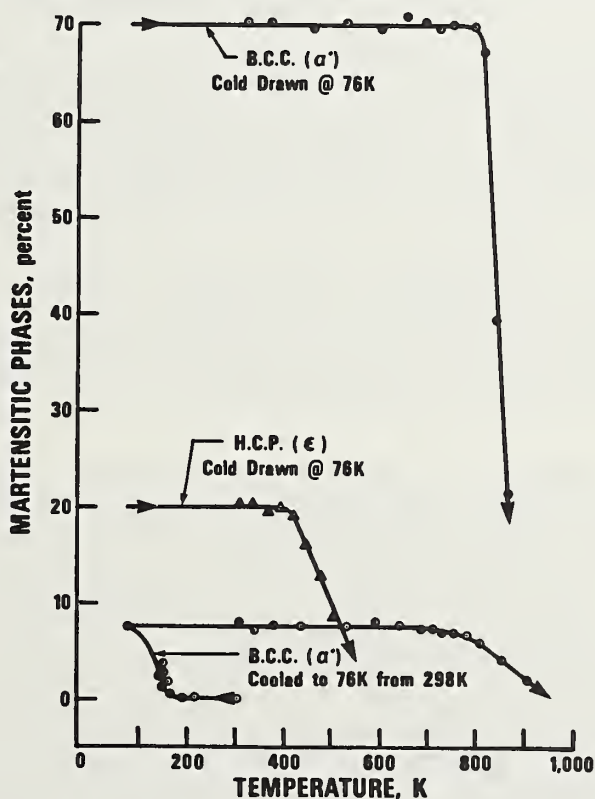


Fig. 6. Reversion of  $\alpha'$  and  $\epsilon$  martensite on warming, following formation at 76 K in an Fe-18Cr-8Ni alloy (AISI 304L).

concluded that the nucleus of the  $\epsilon$  martensite is a single stacking fault and that  $\alpha'$  nucleates from faulted regions in dislocation pileups. Others (Suzuki et al.,<sup>51</sup> Mangonon and Thomas,<sup>52</sup> Lagneborg, Murr et al.<sup>53</sup>) have observed that the formation of strain-induced  $\alpha'$  initially occurs at intersections of two active  $\{111\}$  slip systems (see Fig. 4).

#### EFFECTS ON AUSTENITE DEFORMATION

Below the equilibrium temperature,  $T_0$ , martensite tends to form during (a) cooling, (b) application of elastic stress, and (c) plastic deformation of the austenite. Transformation during cooling and during application of elastic stress (stress-assisted transformation) results in similar martensite morphology. But, as described earlier, strain-induced martensite forms at slip-band intersections. During plastic deformation of metastable Fe-Cr-Ni austenite at low temperatures, two strain-induced martensitic phases form, h.c.p.  $\epsilon$  and b.c.c.  $\alpha'$ .

The AISI 300 series stainless steels used in cryogenic applications range from metastable to stable austenites. Alloys, such as 304, containing 18% Cr and 8% Ni, are metastable, whereas 310, containing 26% Cr and 20% Ni is stable with respect to martensitic transformation. The stress-strain behavior and temperature dependence of the flow strength of these alloys differ and depend on the austenite stability. In the more unstable alloys, both  $\epsilon$  and  $\alpha'$  martensite are formed; in the slightly metastable alloys (e.g., 316), only  $\alpha'$  is formed; and in the stable alloys, neither  $\alpha'$  nor  $\epsilon$  is formed during deformation to fracture at any temperature.

Figures 7 and 8 assist in explaining the role of martensite transformations in austenite deformation. In a metastable alloy at low temperatures (4 to 200 K), three distinct stages are present. A stable alloy only exhibits dislocation work hardening and has "well-behaved" stress-strain characteristics.

Stage I (Fig. 7) of metastable austenite strain-strain behavior represents the microstrain and early macrostrain behavior that includes the 0.2% offset yield strength. The formation of  $\alpha'$  is not thought to occur in this range; perhaps stacking-fault clusters, or the  $\epsilon$  phase, or both contribute to low-temperature deformation in this range. The stacking-fault energy is reduced at low temperatures, and apparently becomes low enough to promote  $\epsilon$  martensite. With x-ray analysis to detect  $\epsilon$  formation during early deformation and creep at low temperatures, Mirzagev et al.<sup>54</sup> related the log of volume fraction of  $\epsilon$  over the volume fraction of  $\gamma + \alpha'$  to the log of the plastic deformation for an Fe-18Cr-13Ni-0.02C steel; other x-ray analysis measurements on similar steels have not confirmed this  $\epsilon$ -strain correspondence.<sup>54,55</sup>

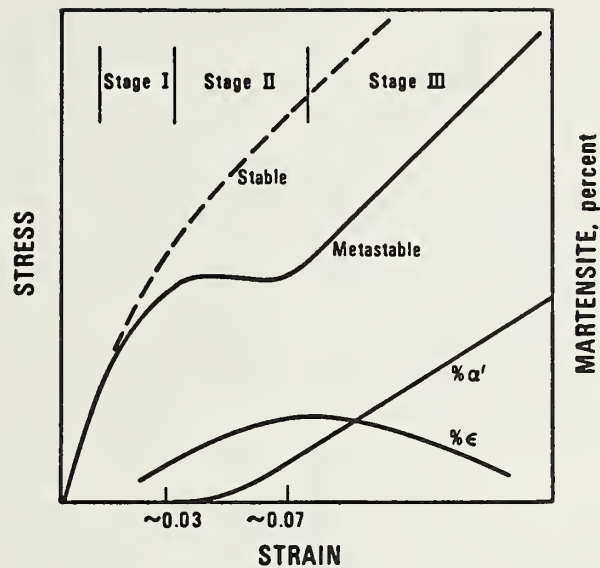


Fig. 7. Typical stress-vs.-strain curves of stable and metastable austenitic Fe-Cr-Ni alloys at low temperatures and associated relative amounts of strain-induced  $\epsilon$  and  $\alpha'$  that form in the metastable alloy.

The temperature dependence of metastable and stable Fe-Cr-Ni alloys in Stage I is illustrated in Fig. 8. There are three regions of the temperature dependence of the flow strength for metastable alloys: (a) the high-temperature range ( $>T_1$ ) that exhibits normal temperature dependence with no detectable martensitic products; (b) the middle region ( $T_2 < T < T_1$ ) in which the flow strength decreases with decreasing temperature; and (c) the low-temperature range ( $<T_2$ ) where flow strength again increases at lower temperatures. The temperature dependence of the flow strength of stable alloys is normal, increasing monotonically with decreasing temperature.

In Stage I,  $\alpha'$  has not been detected. Magnetic torsion-balance measurements<sup>56</sup> do not sense a permeability change until Stage II is reached. Suzuki et al.<sup>51</sup> have also used magnetic measurements to characterize the stress level at which  $\alpha'$  begins to form as a function of temperature; their results are also included in Fig. 8. The stress level at which  $\alpha'$  forms is considerably above the yield strength. At first, the study of Olson and Azrin<sup>57</sup> appears to conflict with these premises. They worked with a less stable Fe-9Cr-8Ni alloy (a TRIP steel) and obtained an excellent correlation between the temperature dependence of the yield strength and the flow strength at which  $\alpha'$  was first detected by using ac permeability measurements. It is likely, however, that martensite formation in their alloy was stress assisted and that  $\epsilon$  did not form.

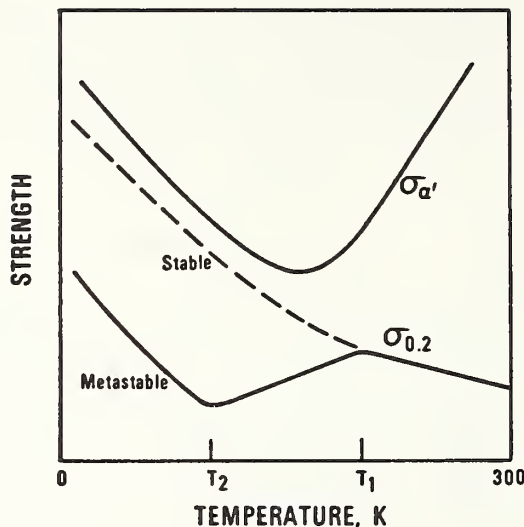


Fig. 8. Temperature dependence of tensile flow strength at 0.2% offset,  $\sigma_{0.2}$ , and estimated strength at which  $\alpha'$  begins to form,  $\sigma_{\alpha'}$ , of stable and metastable Fe-Cr-Ni steels.<sup>51</sup>

Stress-assisted martensite formation or the formation of  $\alpha'$  from preexisting nucleation sites is best illustrated by the study of Breedis and Robertson.<sup>58</sup> They measured the temperature dependence of a metastable single-crystal Fe-16Cr-12Ni and of a stable single-crystal alloy. The critical resolved shear stress of the metastable alloy fell to zero at the  $T_{ms}$  of  $\alpha'$  ( $\sim 240$  K). They detected the presence of both  $\epsilon$  and  $\alpha'$  in the deformed crystals at temperatures above  $T_{ms}$ . The critical resolved shear stress of the stable alloy increased continuously with decreasing temperature. The  $T_{ms}$  of commercially available alloys is normally below 0 K, and therefore, the flow strengths of these alloys are not expected to approach zero.

Stage II, consisting of an "easy glide" range is best correlated with the formation of  $\alpha'$  laths at cross-slip intersections. Suzuki et al.<sup>51</sup> have proposed that such  $\alpha'$  laths, with the long  $\langle 110 \rangle$  direction representing the intersection of two active slip systems, act as windows to assist cross slip. Stage II is most prevalent in the temperature range 76 to 200 K. In this temperature region, the range of strain at which the stress remains relatively constant is large, usually about 0.03 to 0.05.

In Stage III, the rate of work hardening increases to a constant, which is maintained over a relatively large amount of plastic deformation (20 to 40%). The  $\alpha'$  volume percentage is linearly related to plastic deformation in Stage III. The nature of the transition in the roles of  $\alpha'$  formation--from promoting earlier glide in Stage II to being associated with a linear, high rate of work



hardening in Stage III--is not clear. Perhaps in Stage III essentially all active cross-slip sites have been transformed to  $\alpha'$ , and subsequent  $\alpha'$  formation occurs within active glide bands. Such  $\alpha'$  formation would not be expected to promote stacking-fault glide. There is a hint that this sequence may occur: the x-ray data of Reed and Guntner<sup>56</sup> presented schematically in Fig. 7 indicate that a maximum value of the  $\epsilon$  volume concentration occurs at about the transition from Stage II to Stage III. There is apparently no  $\epsilon$  formation during Stage III; the amount of  $\epsilon$  decreases with strain, presumably transforming to  $\alpha'$ .<sup>55</sup> Stages I and II decrease in significance in more stable austenites, but Stage III is retained. For instance, AISI 316 exhibits neither Stage I nor Stage II, but does begin to transform to  $\alpha$  at strains of about 0.02 below 190 K. No  $\epsilon$  martensite has been detected in this alloy.

In this discussion of the influence of martensitic products on plastic deformation, the results of current research indicate that the schematic representations of Figs. 7 and 8 are time-dependent. Further research is necessary to sort out the creep and strain-rate effects and the isothermal characteristics of the strain-induced martensitic transformations.

This discussion has emphasized the roles of the strain-induced martensites. Martensite that forms during cooling below  $T_{ms}$  contributes differently. For many years  $\alpha'$  martensite has been known and used to strengthen steel, and it may be used in a similar way to strengthen Fe-Cr-Ni alloys (e.g., Mangonon and Thomas<sup>52</sup>). With severe rolling to induce a high percentage of  $\alpha'$ , room-temperature yield strengths of about 1.4 GPa ( $2 \times 10^5$  psi) may be achieved at the expense of significant ductility and (probably) toughness.

The complex martensitic transformation characteristics in Fe-Cr-Ni austenitic commercial alloys are summarized in Table 2. Stress-assisted martensite has been reported in single crystals<sup>43</sup> and in Fe-9Cr-8Ni,<sup>57</sup> but has not been observed in Fe-18Cr-8Ni polycrystalline commercial grades. Martensite formed by the application of elastic stress should result in morphology similar to that observed from cooling. The strain-induced transformations have been subdivided into three stages, each contributing distinctly to austenite deformation. The major distinction between the stages is the degree of work hardening. Strain-induced  $\alpha'$  (Stage III) is distinguished from stress-assisted or thermally induced martensite by the location of transformation: strain-induced  $\alpha'$  forms at slip-band intersections, with only one habit-plane variant; stress-assisted or thermally-induced martensite forms in  $\{111\}$  sheets with three habit-plane variants. This review emphasizes one aspect that is not conventionally recognized. It has been thought that stress-assisted transformation lowers the flow strength, and that strain-induced transformation increases the flow strength. The strain-induced martensite at first promotes no work hardening and thus decreases the



Table 2. Summary of martensitic transformation characteristics  
in commercial AISI 300 series steels.

Transformation	Characteristics			Amount (%)	Comments
	Crystal Structure	Morphology	Location		
Cooling	h.c.p.	{111} sheets		0 - 5	
	b.c.c.	$\langle 1\bar{1}0 \rangle$ laths, 3 habit plane variants	Within {111} sheets	0 - 10	Isothermal (more than 76 than 4 K)
Stress assisted	h.c.p.	{111} sheets			
	b.c.c.	$\langle 1\bar{1}0 \rangle$			Not observed in Fe-18Cr- 8Ni or more stable alloys
Strain induced					
Stage I	h.c.p.?	{111} sheets		0 - 5	Work hardening
Stage II	h.c.p.	{111} sheets		0 - 20	Reduces in Stage III
	b.c.c.	$\langle 1\bar{1}0 \rangle$ laths, 1 habit plane variant	Slip-plane intersections	0 - 10	No work hardening
Stage III	b.c.c.		Within {111} sheets	10 - 80	% linear with strain; strong work hardening

flow strength in Stage II, and then in Stage III, it increases the flow strength. This leads one to suspect that the transformation mechanism changes from Stage II to III.

#### INFLUENCE ON PERFORMANCE

Several characteristics of the austenite-to-b.c.c.-martensite transformation in stainless steels cause problems in many cryogenic applications.

The martensitic b.c.c. product has a larger specific volume (+1.7%) than the parent austenite; therefore, these steels expand during transformation. The martensitic product forms as individual crystals, and the associated transformation shear and volume expansion results in localized regions of disruption. For example, in Fig. 9a,  $\alpha'$  formation at the surface is illustrated microscopically. The shape deformation results in local surface upheavals, usually bounded by (111) $\gamma$  planes. In Fig. 9b,  $\alpha'$  formation near or at the surface of the flange caused localized surface upheavals. For service that requires close tolerances, such as valves or bearings, these local surface fluctuations are disastrous.

Welding of austenitic steels tends to produce chemical segregation in the heat-affected zone. Nitrides, in high-nitrogen steels, and carbides tend to form, especially with chromium. The chemically depleted austenitic solid solution has a greater tendency for martensitic transformation on cooling to cryogenic temperatures. Transformation under such circumstances is particularly critical, since it is restricted to the weld heat-affected zone and, therefore, tends to produce high local stresses from the transformation volume expansion and local shear. In a few applications of thin-gauge sheet, through-thickness cracks in the heat-affected zone of the welds or spot welds have resulted.

The transformation at cryogenic temperatures is unpredictable from room-temperature characteristics. The transformation occurs after application of applied stress or local plastic-deformation at low temperatures much more readily than at room temperature. Prevention of in-service transformation depends on proper alloy selection. A good rule to follow is that the more alloying elements one uses (and can afford), the more stable the austenitic stainless steel will be. Therefore, to a first approximation, AISI 310 is stable, AISI 316 has limited strain-induced martensite, and AISI 304 is the least stable. In AISI 304 within the chemical specification limits, martensite may form on cooling and on application of stress and certainly will form with plastic deformation.

Another concern, mostly in design of superconducting magnets, is that the b.c.c. martensitic product is ferromagnetic, whereas the parent austenite is paramagnetic. A simple rule is that each percent

(a)



(b)



Fig. 9. (a) Shape deformation of martensitic transformation in austenitic stainless steel (Fe-Cr-Ni alloy, AISI 304L) on cooling to 76 K (230X). (b) Shape deformation of martensitic transformation in steel (AISI 304) flange previously used in service at 76 K (64X).



of b.c.c. martensite results in a permeability increase of 0.01. Therefore, if time-dependent field changes corresponding to material changes of the order of 0.10 are significant, then alloy selection is important.

Finally, a common design fear has been that martensitic transformation in austenitic stainless steels adversely affects toughness. Experience suggests that this is partly true. Strain-induced martensitic transformation in austenitic stainless steels tends to produce higher toughness. Comparison of the low-temperature toughness of AISI alloy grades 304, 316, 310 indicates that toughness is inversely related to austenite stability (and austenite tensile yield strength). But, if the austenite is sufficiently unstable such that martensite forms on cooling (e.g., in the AISI 400 series steels and in AISI 301), then the martensite is less tough. To summarize: In the more stable austenitic stainless steel grades, martensite does not form during cooling and forms only during deformation. In these alloys, with predominantly austenite plastic deformation, martensitic transformation produces greater toughness. In metastable stainless steels in which the base structure is predominantly martensite prior to the application of stress and, therefore, in which plastic deformation must take place in the martensitic phase, the martensite has a deleterious effect on toughness.

#### REFERENCES

1. Cohen, M., Olson, G. B., and Clapp, P. C., On the classification of displacive phase transformations, in Proceedings of the International Conference on Martensitic Transformations, ICOMAT 1979, Department of Materials Science and Engineering, M.I.T., Cambridge, Massachusetts (1979), pp. 1-11.
2. Reed, R. P. and Breedis, J. F. (1966). Low-Temperature phase transformations, in Behavior of Materials at Cryogenic Temperatures, ASTM STP No. 387, American Society for Testing and Materials, Philadelphia, Pennsylvania (1966), pp. 60-132.
3. Bilby, B. A. and Christian, J. W., The crystallography of martensitic transformations, J. Iron Steel Inst. 197:122-131 (1961).
4. Christian, J. W., Basic crystallography and kinetics, in Martensite Fundamentals and Technology, E. R. Petty, ed., Longman Group, London, 11-41 (1970).
5. Wayman, C. M., Introduction to the Crystallography of Martensitic Transformations, Macmillan Co., New York (1964).
6. Wayman, C. M., The crystallography of martensitic transformations in alloys of iron, in Advances in Materials Research, Vol. 3, H. Herman, ed., Interscience, New York (1968), pp. 147-304.
7. Lieberman, D. S., Crystal geometry and mechanisms of phase transformations in crystalline solids, in Phase Transforma-

- tions, American Society for Metals, Metals Park, Ohio (1970), pp. 1-58.
8. Roitburd, A. L. and Kurdjumov, G. V., The nature of martensitic transformations, Mater. Sci. Eng. 39:141-167 (1979).
  9. Entwisle, A. R., The kinetics of martensite formation in steel, Metall. Trans. 2:2395-2407 (1971).
  10. Christian, J. W., The Theory of Transformations in Metals and Alloys, Pergamon Press, New York (1965).
  11. Kaufman, L. and Cohen, M., Thermodynamics and kinetics of martensitic transformations, in Progress in Metal Physics, Vol. 7, B. Chalmers and R. King, eds., Pergamon Press, New York, (1958) pp. 165-246.
  12. Barrett, C. S., Transformations at low temperatures, Trans. Jap. Inst. Met. 17:465-475 (1976).
  13. Martensite Fundamentals and Technology, E. R. Petty, ed., Longman Group, London (1970).
  14. Christian, J. W., The Theory of Transformations in Metals and Alloys, Pergamon Press, New York (1976).
  15. Physical Properties of Martensite and Bainite, The Iron and Steel Institute Special Report 93, Percy Lund, Hampshires & Co., London (1965).
  16. Mechanism of Phase Transformations in Crystalline Solids, Monograph and Report Series No. 33, Institute of Metals, London, England (1969).
  17. Shape Memory Effect in Alloys, J. Perkins, ed., Plenum Press, New York (1975).
  18. New Aspects of Martensitic Transformations, H. Suzuki, ed., Japan Institute of Metals, Tokyo, Japan (1976).
  19. Phase Transformations, American Society for Metals, Metals Park, Ohio (1970).
  20. Proceedings of the International Conference on Martensitic Transformation, ICOMAT-1979, W. S. Owen, ed., Department of Materials Science and Engineering, M.I.T., Cambridge, Massachusetts (1979).
  21. Breedis, J. F. and Kaufman, L., Formation of hcp and bcc phases in austenitic iron alloys, Metall. Trans. 2:2359-2371 (1971).
  22. Kaufman, L., The free energy changes attending the martensitic transformation in the iron-chromium and iron-chromium-nickel systems, Trans AIME 215:218-223 (1959).
  23. Kaufman, L. and Cohen, M., The martensitic transformation in the iron-nickel system, Trans. AIME 206:1393-1401 (1956).
  24. Rao, M. M., Russell, R. J., and Winchell, P. G., A correlation of thermodynamic variables for iron-rich iron-nickel-carbon alloys, Trans. AIME 239:634-642 (1967).
  25. Kaufman, L., The lattice stability of the transition metals, in Phase Stability in Metals and Alloys, P. S. Fudman, J. Stringer, and R. I. Jaffee, eds., McGraw-Hill, New York (1967), pp. 125-150.
  26. Reed, R. P., The spontaneous martensitic transformations in 18%Cr, 8%Ni steels, Acta Metall. 10:865-877 (1962).



27. Eichelman, G. H. and Hull, F. C., The effect of composition on the temperature of spontaneous transformation of austenite to martensite in 18-8-type stainless steel, Trans. Am. Soc. Met. 45:77-104 (1953).
28. Monkman, F. C., Cuff, F. B., and Grant N. J., Computation of  $M_s$  for stainless steels, Met. Prog. 71:94-96 (1957).
29. Hammond, C. M., The development of new high-strength stainless steels, in Advances in the Technology of Stainless Steels and Related Alloys, ASTM STP No. 369, American Society; for Testing and Materials, Philadelphia, Pennsylvania (1963), pp. 47-53.
30. Andrews, K. W., Empirical formulae for the calculation of some transformation temperatures, J. Iron Steel Inst. 203:721-727 (1965).
31. Hull, F. C., Delta ferrite and martensite formation in stainless steels, Weld. J. Res. Suppl. 52:193-s-203-s (1973).
32. Angel, T., Formation of martensite in austenitic stainless steels, J. Iron Steel Inst. 177:165-174 (1954).
33. Williams, I., Williams, R. G., and Capellaro, R. C., Stability of austenitic stainless steels between 4 K and 373 K, in Proceedings of the Sixth International Cryogenic Engineering Conference, IPC Science and Technology Press, Guildford, Surrey, England (1976), pp. 337-341.
34. Warnes, L. A. A. and King, H. W., The low temperature magnetic properties of austenitic Fe-Cr-Ni alloys in the prediction of Néel temperatures and maximum susceptibilities, Cryogenics 16:659-667 (1976).
35. Lee, S., Millman, S., MacDougall, I. L., Keown, P., and Argent, B. B., Enthalpy of the martensitic transformation in steels containing nickel and chromium, Met. Sci. 11:261-271 (1977).
36. Dulieu, D. and Nutting, J., Stacking fault energy of Fe-Cr-Ni alloys, in Metallurgical Developments in High Alloy Steels, Special Report 86, Iron and Steel Institute, London (1964), pp. 140-145.
37. Schramm, R. E. and Reed, R. P., Stacking fault energies of seven commercial austenitic stainless steels, Metall. Trans. 6A:1345-1351 (1975).
38. Rhodes, C. G. and Thompson, A. W., The composition dependence of stacking fault energy in austenitic stainless steels, Metall. Trans. 8A:1901-1906 (1977).
39. Brofman, P. J. and Ansell, G. S., On the effect of carbon on the stacking fault energy of austenitic stainless steels, Metall. Trans. A 9A:879-880 (1978).
40. King, H. W. and Larbalestier, D. C., Austenitic stainless steels at cryogenic temperatures: The compositional dependence of the  $M_s$ , Cryogenics 21:521-524 (1981).
41. Collings, E. W. and King, H. W., Austenitic stainless steel as magnetic transition metal alloys, in The Metal Science of Stainless Steels, E. W. Collings and H. W. King, eds., Metallurgical Society of the AIME, New York (1979), pp. 1-21.

42. Bampton, C. C., Jones, L. P., and Loretto, M. H., Stacking fault energy measurements in some austenitic stainless steels, Acta Metall. 26:39-51 (1978).
43. Breedis, J. F., Martensitic transformations in iron-chromium-nickel alloys, Trans. AIME 230:1583-1596 (1964).
44. Kelly, P. M., The martensite transformation in steels with low stacking fault energy, Acta Metall. 13:635-646 (1965).
45. Wirth, A. and Bickerstaffe, J., The morphology and substructure of martensite in maraging steels, Metall. Trans. 5:799-808 (1974).
46. Lagneborg, R., The martensite transformation in 18%Cr-8%Ni steels, Acta Metall. 12:823-843 (1964).
47. Abrassart, F., Stress-induced  $\gamma \rightarrow \alpha'$  martensitic transformation in two carbon stainless steels. Application to trip steels, Metall. Trans. 4:2205-2216 (1973).
48. Breedis, J. F., Influence of dislocation substructure on the martensitic transformation in stainless steel, Acta Metall. 13:2359-2371 (1965).
49. Strife, J. R., Carr, M. J., and Ansell, G. S., The effect of austenite prestrain above the  $M_s$  temperature on the martensitic transformation in Fe-Ni-Cr-C alloys, Metall. Trans. 8A:1471-1484 (1977).
50. Brooks, J. W., Loretto, M. H., and Smallman, R. E., Direct observations of martensite nuclei in stainless steel, Acta Metall. 27:1839-1847 (1979).
51. Suzuki, T., Kojima, H., Suzuki, K., Hashimoto, T., and Ichihara, M., An experimental study on the martensite nucleation and growth in 18/8 stainless steel, Acta Metall., 25, 1151-1162 (1977).
52. Mangonon, P. L. and Thomas, G., Structure and properties of thermal-mechanically treated 304 stainless steel, Metall. Trans. 1, 1587-1594 (1970).
53. Murr, L. E., Staudhammer, K. P. and Hecker S. S., Effects of strain state and strain rate on deformation-induced transformation in 304 stainless steel: Part II. Microstructural study, Metall. Trans. 13A:627-635 (1982).
54. Mirzagev, D. A., Goykhanberg, Y. N., Shteynberg, M. M., and Rushchin, S. V., The elasto-plastic strain effects in alloys with low stacking fault energy at temperatures above  $M_s$ , Fiz. Met. Metalloved. 35:1206-1212 (1973).
55. Guntner, C. J. and Reed, R. P., The effect of experimental variables including the martensitic transformation on the low temperature mechanical properties of austenitic stainless steels, ASM Trans. Q. 55:399-419 (1962).
56. Reed, R. P. and Guntner, C. J., Stress-induced martensitic transformations in 18Cr-8Ni steel, Trans. AIME 230:1713-1720 (1964).
57. Olson, G. B. and Azrin, M., Transformation behavior of TRIP steels, Metall. Trans. A 9A:713-721 (1978).

58. Breedis, J. F. and Robertson, W. D., Martensitic transformation and plastic deformation in iron alloy single crystals, Acta Metall. 11:547-559 (1963).



# A COMPUTER-INTERACTIVE FATIGUE CRACK GROWTH RATE TEST PROCEDURE\*+

Yi-Wen Cheng  
Fracture and Deformation Division  
National Bureau of Standards  
Boulder, Colorado 80303

## ABSTRACT

A computer-interactive fatigue crack growth rate testing system has been developed that implements the fatigue crack growth rate testing procedure set forth in ASTM E647-81. The system uses a minicomputer to acquire the load-deflection data as a function of load cycles and to determine the crack length using the compliance technique. The fatigue crack growth rate,  $da/dN$  and the stress intensity range,  $\Delta K$ , are calculated and plotted during the test.

\*Work sponsored by the Department of Interior, Minerals Management Service and Department of Energy, Office of Magnetic Fusion Energy.

Key Words: compliance technique; computer-interactive testing; fatigue crack growth rate; fatigue of materials.





## INTRODUCTION

Fatigue crack growth rate (FCGR) data can be used for material characterization and for fracture mechanics reliability analysis of structures subjected to cyclic loading. The standard test method for measuring FCGR under constant-amplitude loading has been developed and published in the 1981 Annual Book of ASTM Standards under the designation ASTM E647-81 [1]. In this paper, a computer-interactive implementation of the Standards is described.

There are several advantages of using a computer to acquire, analyze, and display FCGR data during the test. First, the time needed for crack length determination and data reduction is greatly reduced. Second, the data scatter is reduced. Third, because the testing is interactive in nature, the procedure is relatively easy to follow. Fourth, subjective interpretation and influence of the experimenter are eliminated.

## THE FCGR TEST METHOD

The requirements of specimen preparation for FCGR tests are described in ASTM E647-81 [1]. The sequence of the FCGR test is: first to obtain the raw data, namely, fatigue crack length,  $a$ , versus elapsed fatigue cycles,  $N$ ; and then to analyze these data to a plot of  $da/dN$  versus  $\Delta K$ , where  $da/dN$  is the FCGR in mm/cycle and  $\Delta K$  is the crack-tip stress intensity range in  $\text{MPa}\cdot\text{m}^{\frac{1}{2}}$ . Typical outputs are presented in Figure 1.

The number of elapsed fatigue cycles is readily available from electronic or mechanical counters. However, the methods of crack length measurement are more complicated and have been a subject of extensive study [2,3]. Although several methods of crack length measurement have been developed, most require specialized equipment commonly not available in mechanical testing laboratories. The compliance technique, however, requires only monitoring of load cell and clip gage deflection, which is routinely achieved in mechanical testing. Compliance is defined as the specimen deflection per unit load, which is a function of crack length. The load and deflection signals (voltages) can also be interfaced to a computer. Because of the simple instrumentation and the need for environmental chambers for cryogenic temperature and saltwater corrosion-fatigue tests, the compliance technique was chosen to measure the crack length.

The most commonly used FCGR test specimen is the compact-tension (CT) type with its well-established crack-tip stress intensity calibration [1] and compliance functions [4]. The data reduction technique is either the secant method (point-to-point method) or the seven-point incremental polynomial method, as recommended in ASTM E647-81 [1].

## THE COMPUTER-INTERACTIVE FCGR TEST

### Equipment and Procedure

A schematic of the computer-interactive FCGR testing system is illustrated in Figure 2. The system consists of a closed-loop servohydraulic mechanical testing machine, a multichannel analog-to-digital (A/D) converter unit, and a minicomputer. Signal amplifiers and the cycle

counter are built into the mechanical testing machine. Included with the minicomputer are a cathode-ray-tube (CRT) terminal, a line printer, a dual floppy disk data storage unit, and a digital plotter.

The current A/D converter unit has a 16-bit resolution with a range of  $\pm 10$  V. This gives a least significant bit a resolution of about 0.3 mV. This level of precision has been found adequate for the present purpose. At the present time, because of a 5-Hz filter associated with the A/D converter unit, the maximum fatigue cycle frequency that the A/D converter can convert enough load-deflection pairs for an accurate crack length measurement is limited to about 0.03 Hz. Consequently, fully automatic testing with higher frequencies is not yet possible, and the test must be periodically interrupted for crack length measurement. A digital memory oscilloscope has been procured and is being incorporated into the testing system. It will enable the testing system to be fully automatic during continuous high-frequency testing.

The procedure for conducting the FCGR test is described as follows. The precracked specimen is fatigue cycled under the prescribed loading conditions and frequency. A typical cycling frequency is 20 Hz. Depending upon the crack length-to-specimen width ratio,  $a/W$ , the fatigue cycling is interrupted after selected increments of crack growth. The instantaneous crack length is then inferred using the compliance technique. For example, in a 25.4-mm-thick CT specimen, crack length measurements at an interval of crack growth between 0.5 mm and 0.76 mm are optimum. The amount of crack length increase during the 20-Hz fatigue cycling can be estimated using a digital indicator, which provides continuous instantaneous readings of the maximum and minimum output voltages from the clip gage at the crack mouth. The difference in maximum and minimum values correlates well with the instantaneous crack length.

During the single 0.02-Hz cycle compliance measurement, the signals of load cell and clip gage are plotted on an X-Y recorder. At the same time, the signals are amplified, digitized by the A/D converter unit, and fed into the computer for compliance calculation. The lower one-third of the compliance signals are dropped to eliminate the possible crack closure effects [5]. The upper two-thirds of the signals are correlated to a straight line using a linear least-squares fit. This is illustrated schematically in Figure 3. A linear correlation coefficient of 0.9999 or greater is generally obtainable. If the linear correlation coefficient drops below 0.999 scatter will increase so the test is terminated. Generally, a drop in linear correlation is obtained at high  $\Delta K$  values in ductile steels because of the development of a large plastic zone ahead of the crack tip. The large plastic zone causes the specimen to behave inelastically resulting in the formation of a hysteresis loop in the load-deflection curve. From the resulting compliance, the instantaneous crack length is computed using the appropriate expression for the compliance calibration of the specimen [4]. The precision of the crack length measurement is typically within  $\pm 0.04$  mm.

The specimen compliance, the least-squares correlation coefficient, and the crack length inference are displayed on the CRT screen and printed on the line printer. After the number of fatigue cycles is manually fed into the computer through the CRT terminal, the computer computes  $da/dN$  and  $\Delta K$ , and the digital plotter plots the data points  $(a, N)$  and  $(da/dN, \Delta K)$  on the  $a$ -versus- $N$  and on the  $da/dN$ -versus- $\Delta K$  graphs, such as those in Figure 1. The line printer also prints the  $da/dN$  and  $\Delta K$  results. All the resulting data are stored on the floppy disk for post-test analyses.

The computer programs for the post-test analysis include the following capabilities:

1. Converting units
2. Plotting data in desired units
3. Plotting data in desired coordinate ranges
4. Plotting data of several different specimens on one graph
5. Calculating the material constants  $C$  and  $m$  in the Paris equation,  $da/dN = C (\Delta K)^m$  [6], and drawing the regression line through the data

All the computer programs, including data acquisition routine, data reduction routine, and the post-test analysis routines, are written in the language of Fortran IV.

## APPLICATIONS

The computer-interactive FCGR testing system has been successfully used for room temperature tests in air, cryogenic temperature tests in liquid nitrogen and in liquid helium, and room temperature tests in saltwater. Special apparatus are needed in the cryogenic temperature tests and in the saltwater tests. The loading apparatus used in the cryogenic temperature tests have been described previously by Fowlkes and Tobler [7]. In the saltwater tests, the clip gage used for deflection measurements is mounted above the saltwater level on a scissors-like extension that protects the gage from the saltwater.

Figure 4 shows a comparison between the results obtained with the computer-interactive FCGR testing system and those obtained without the computer system, using manual data reduction. Good agreement between the two tests is observed, but the computer-interactive testing accomplished the tasks in far less time.

## SUMMARY

A computer-interactive FCGR testing system, which implements the procedure set forth in ASTM E647-81, has been developed and successfully used in room temperature tests in air, in cryogenic temperature tests, and in room temperature tests in saltwater. The system offers considerable time saving in data acquisition and in data reduction. The new test procedure is relatively easy to follow and enables technicians to produce data with less scatter (with respect to the non-computer-aided technique), because no manual data interpretation or fitting to straight lines is done.



## REFERENCES

- [1] Standard Test Method for Constant-Load-Amplitude Fatigue Crack Growth Rates Above  $10^{-8}$  m/cycle, (Designation E647-81) 1981 Annual Book of ASTM Standards, Part 10, American Society for Testing and Materials, Philadelphia, PA, (1981), pp. 765-783.
- [2] The Measurement of Crack Length and Shape During Fracture and Fatigue, C. J. Beevers, ed. Engineering Materials Advisory Services Ltd. Printed by the Chameleon Press, Ltd, UK (1980).
- [3] Advances in Crack Length Measurement, C. J. Beevers, ed. Engineering Materials Advisory Services Ltd., Printed by the Chameleon Press, Ltd, UK (1981).
- [4] S. J. Hudak, Jr., A Saxena, R. J. Bucci, and R. C. Malcolm, "Development of Standard Methods of Testing and Analyzing Fatigue Crack Growth Rate Data," Air Force Materials Laboratory, AFML-TR-78-40, (May, 1978).
- [5] W. Elber, "The Significance of Fatigue Crack Closure," in Damage Tolerance in Aircraft Structures, ASTM STP 481, American Society for Testing and Materials, (1971), pp. 230-242.
- [6] P. C. Paris and F. Erdogan, "A Critical Analysis of Crack Propagation Laws," Transactions of ASME, Journal of Basic Engineering, Series D, Vol. 85, No. 3 (1963), pp. 528-534.
- [7] C. W. Fowlkes and R. L. Tobler, "Fracture Testing and Results for a Ti-6Al-4V Alloy at Liquid Helium Temperature," Engineering Fracture Mechanics, 8 (1976), pp. 487-500.

## LIST OF FIGURES

1. Data outputs from the FCGR test.
2. Schematic of the FCGR testing system.
3. Schematic illustration of the closure effect on the load-deflection curve.
4. Results of FCGR test obtained from the computer-interactive testing system and the non-computer-aided technique: a comparison.

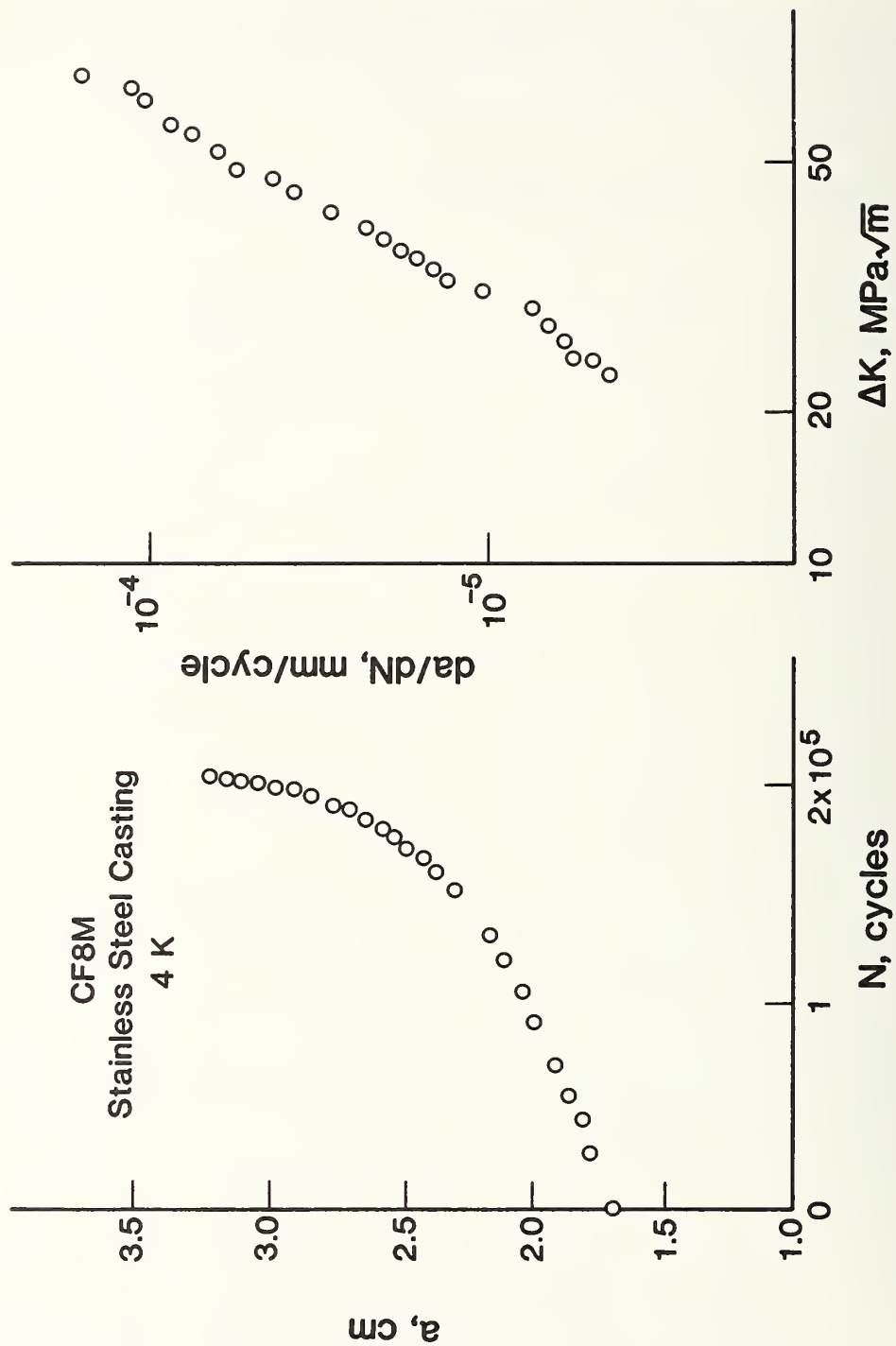


Fig. 1. Data outputs from the FCGR test.

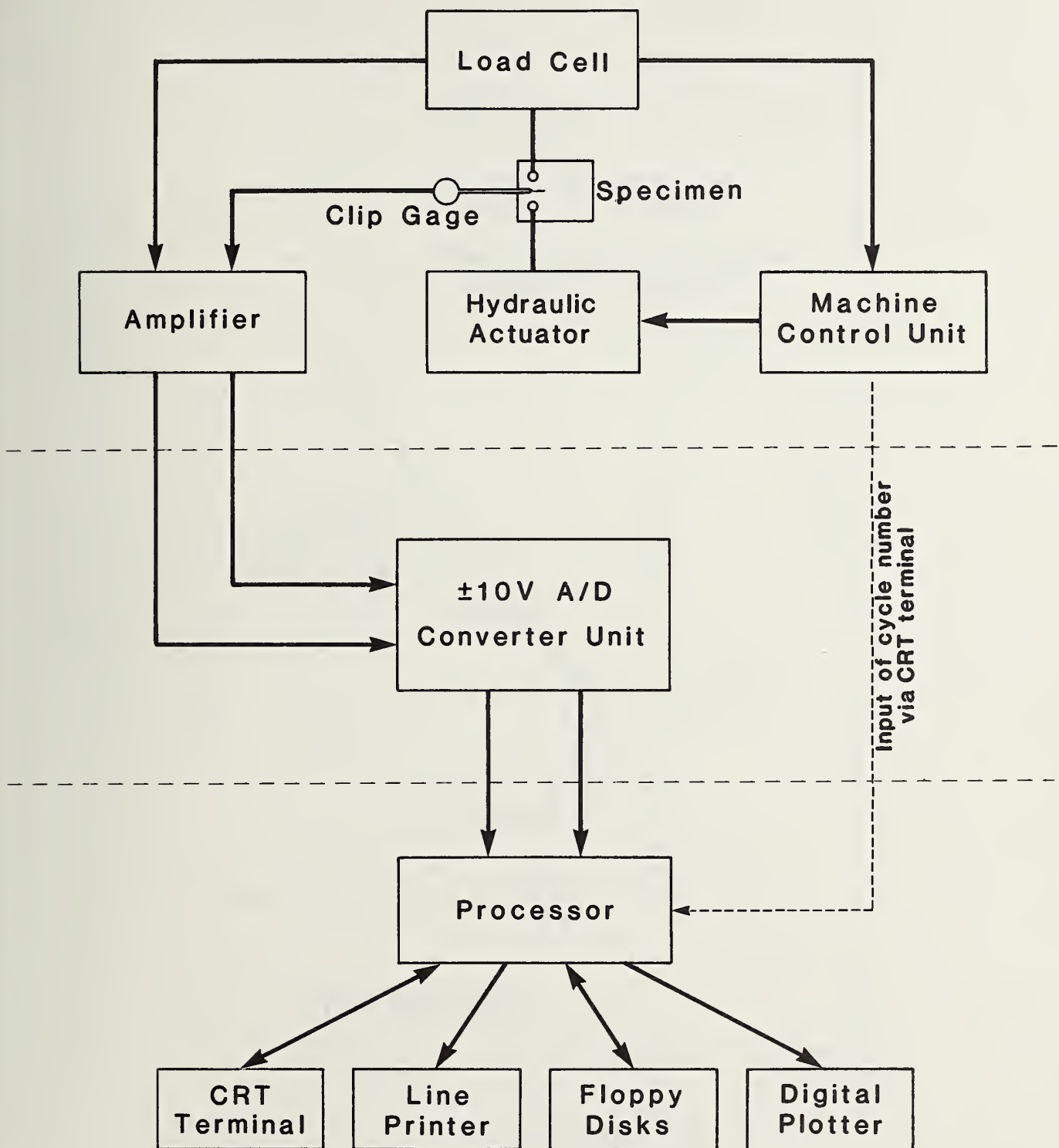


Fig. 2. Schematic of the FCGR testing system.



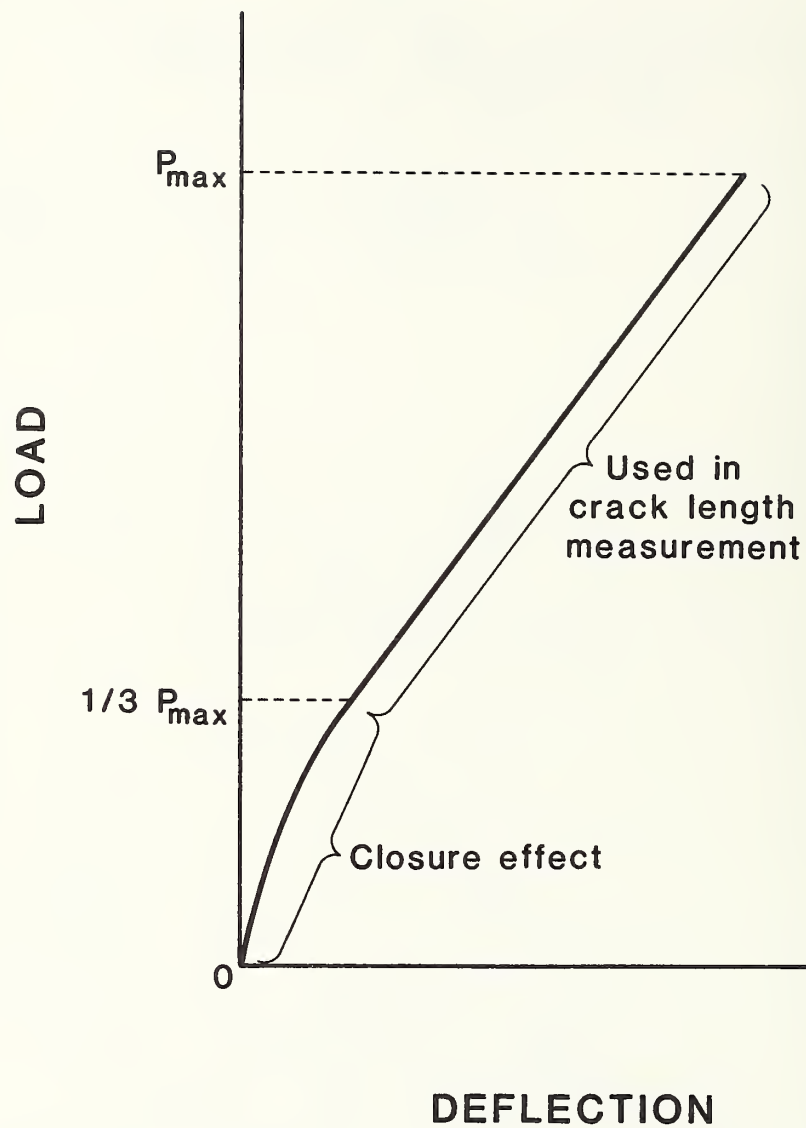


Fig. 3. Schematic illustration of the closure effect on the load-deflection curve.

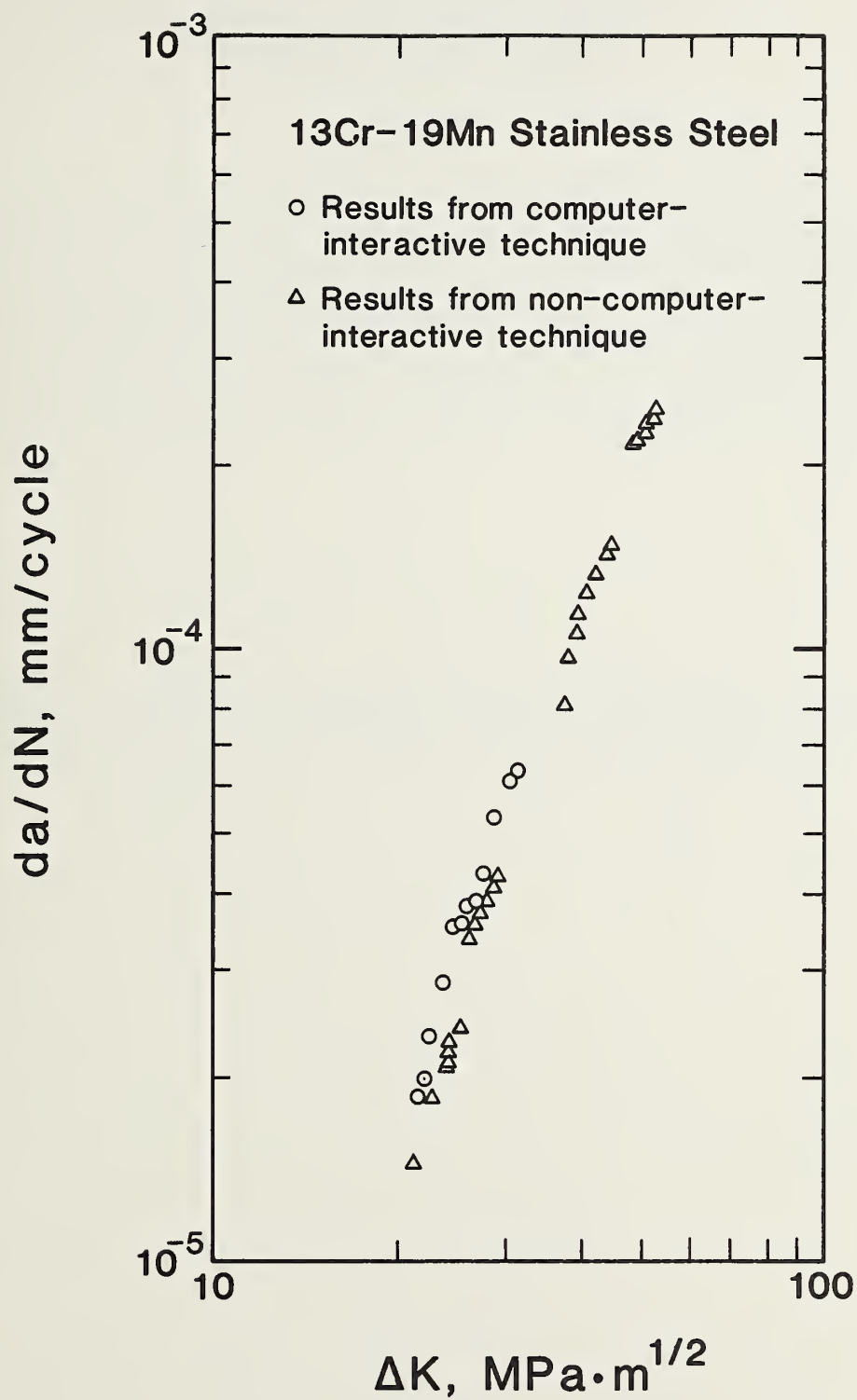


Fig. 4. Results of FCGR test obtained from the computer-interactive testing system and the non-computer-aided technique: a comparison.



EFFECTS OF SENSITIZATION ON SOME FRACTURE MECHANICS FATIGUE  
PARAMETERS FOR Fe-18Cr-3Ni-13Mn-0.37N STAINLESS STEEL  
AT 295 AND 4 K\*

R. L. Tobler  
Fracture and Deformation Division  
National Bureau of Standards  
Boulder, Colorado 80303

ABSTRACT

A nitrogen-bearing austenitic stainless steel (Fe-18Cr-3Ni-13Mn-0.37N) was subjected to fatigue tests at 295 and 4 K. Sensitization (chromium carbo-nitride precipitation) was induced by heating the as-received annealed material for 0.75 or 1.5 h at 977 K. Data comparisons for the sensitized versus the annealed conditions indicate that at 295 K there is little or no difference in the Paris law parameters governing fatigue crack growth rates at intermediate  $\Delta K$ . At 4 K, however, sensitization reduces the fatigue resistance of this steel by adversely affecting all three stages of the fatigue process: crack initiation, crack propagation, and fatigue fracture toughness.

Key words: austenitic stainless steel; chromium carbo-nitride precipitation; fatigue; fatigue crack growth rates; low temperature properties; sensitization.

\*Work supported by Office of Fusion Energy, Department of Energy.





## INTRODUCTION

The austenitic stainless steels are generally regarded as reliable cryogenic structural alloys, but property degradation due to sensitization may limit the performance of some of these materials for specific applications, such as those requiring welding. Sensitization is a metallurgical condition encountered when austenitic stainless steels are heated at temperatures from 700 to 1100 K. After sufficient time at these temperatures, chromium carbo-nitride compounds begin to precipitate, first at the grain boundaries, and then within the austenite grains themselves. This precipitation can ruin corrosion resistance, reduce ductility and toughness, and lower the austenite stability with respect to martensite transformations.

Little is known about the effects of sensitization on the fatigue properties of austenitic stainless steels at cryogenic temperatures. Some steels are more susceptible to sensitization, owing to compositional variations. In this paper some measurements are reported for an Fe-18Cr-3Ni-13Mn-0.37N stainless steel. This relatively high-nitrogen alloyed steel was studied because it was thought to be particularly susceptible to sensitization at 4 K.

## MATERIAL

The test material was a commercial 25-mm plate of austenitic stainless steel, previously tested in the annealed condition and characterized [1] as follows:

As-received condition: annealed, 1080°C, water quenched

Composition: (wt%) Fe-18.09Cr-3.26Ni-13.22Mn-0.37N-0.038C-0.12Mo-0.52Si-0.005S-0.028P

Grain Size: ASTM No. 6 ( $d = 48 \mu\text{m}$ )

Hardness: Rockwell B 93

Mechanical properties: See Table 1

This plate was tested in both the annealed (as-received and not sensitized) and sensitized conditions. To sensitize some of the material, separate portions of stock were cut into blanks and then subjected to either of two thermal treatments:

$S_1$  condition: 977 K, 0.75 h, water quench

$S_2$  condition: 977 K, 1.5 h, water quench

Thus, the annealed condition is unsensitized, while the  $S_2$  condition is more severely sensitized than the  $S_1$  condition. Figure 1 shows the microstructures as revealed by electrolytic etching with 10 % oxalic acid solution for various periods of time. In addition to the usual examination with the light microscope, specimen  $S_1$  was heavily etched and examined in the scanning electron microscope (SEM).

## PROCEDURE

All tests were conducted using compact specimens 25-mm thick and 50.8-mm wide, as shown in Figure 2. The specimen orientation is such that the load is applied in the transverse direction and the crack propagates in the longitudinal direction of the plate. The specimen, clip-gage, and cryogenic apparatus for performing tests in liquid helium at 4 K are described elsewhere [2].

The properties measured in this study included the number of cycles to initiate a fatigue crack from the notch ( $N_i$ ), the fatigue crack growth rates ( $da/dN$ ), and the fatigue fracture toughness ( $K_{fc}$ ). These parameters were measured at selected temperatures and test conditions specified in the text. After failure the specimens were examined with the SEM.

All fatigue tests used a sinusoidal wave form and a 0.1 ratio of minimum-to-maximum fatigue loads. The cycling rate was 20 Hz, except near the end of the tests when higher stress intensity factor (K) levels were approached. Then, the frequency was reduced to values as low as 2 Hz.

The fatigue crack initiation life was determined for two annealed and two sensitized specimens at 4 K by recording the compliance-versus-cycles data and reading the  $N_i$  values from the resulting curves. A marked change in compliance (deflection/load) occurs when a crack develops in this material at 4 K, leading to relatively easy identification of the crack initiation life at this temperature. The notch root radii were  $0.127 \text{ mm} \pm 10 \%$ . The nominal  $\Delta K$  value at initiation was calculated using the starting notch length as the crack length.

Subsequent to fatigue crack initiation, the crack growth rates were measured at 295 or 4 K, using Cheng's computer-aided compliance test method [3]. The expression used to calculate the stress intensity factors is given in reference [4]. The resulting  $da/dN$  - versus -  $\Delta K$  data were plotted on log-log coordinates and the Paris equation parameters C and n ( $da/dN = C \Delta K^n$ ) were determined on the basis of least-squares fits.

Examination of the specimens after testing showed that obtaining uniform crack fronts in this 25-mm thick material at 4 K is a problem. The ratios of edge-to-average crack lengths at 4 K were always less than 0.9. However, it is assumed that any effects of crack front curvature are satisfactorily accounted for in the fatigue crack growth rate tests since the compliance method senses an average crack length.

The fatigue fracture toughness [5],  $K_{fc}$ , was estimated from observations made at the termination of  $da/dN$  tests. Fatigue cycling with periodic compliance readings was continued until fracture occurred, at which time the final cycle number was recorded. The crack length at failure was estimated from the final cycle number and the  $da/dN$ -versus- $\Delta K$  trend for the specimen. Calculations of  $K_{fc}$  were then based on the maximum fatigue load and the estimated crack length at failure. The uncertainty in  $K_{fc}$  due to error in the final average crack length is estimated at  $\pm 10 \%$ .

Fatigue fracture toughness tests were not performed at 295 K because this steel is highly ductile at room temperature. At 4 K this steel exhibits linear-elastic behavior, and the thickness of 25 mm is quite sufficient to satisfy the ASTM E-399-81 [6] size requirements for valid fracture

toughness ( $K_{IC}$ ) tests. (The thickness requirement for the annealed condition at 4 K is only 5.3 mm). Although the amount of crack front curvature at 4 K is sufficient to invalidate  $K_{IC}$  measurements [6], the  $K_{fC}$  measurements of this study are still considered useful as qualitative indicators of the effect of sensitization on toughness.

## RESULTS

**Fatigue Crack Initiation:** The fatigue crack initiation data at 4 K are shown in Figure 3. Tests were conducted for only one nominal  $\Delta K$  value of  $20.5 \text{ MPa}\cdot\text{m}^{\frac{1}{2}}$ , calculated using the initial notch length as the crack length. For two specimens in the annealed (unsensitized) condition, the initiation lives were 95 and 127 kilocycles (kc). Single tests for the sensitized specimens gave  $N_i = 85$  kc for the  $S_1$  condition and  $N_i = 36$  kc for the  $S_2$  condition. The results show that fewer cycles are required to initiate a fatigue crack when the material is sensitized. This effect is observed at  $\Delta K = 20.5 \text{ MPa}\cdot\text{m}^{\frac{1}{2}}$ , but the behavior at other stress intensity factor ranges remains unexplored.

**Fatigue Crack Growth:** Fatigue crack growth rates for the two sensitized conditions at 295 and 4 K are shown in Figure 4. The Paris equation line fits for the  $S_1$  and  $S_2$  conditions at 295 K are essentially equivalent and in agreement with the results for annealed material from the same plate of steel [1]. One explanation for the similar fatigue crack growth rate behavior at room temperature is the constancy of the failure mechanism. Figure 5 is a representative illustration of the transgranular failure mode observed for each condition at room temperature, the distinguishing feature being striation formation. This same failure mode is observed for the steel in all three metallurgical conditions: annealed,  $S_1$  and  $S_2$ . Since this failure mode does not involve crack propagation along grain boundaries, the effect of grain boundary precipitation on the room temperature cracking rates appears to be negligible for the  $\Delta K$  range studied.

The temperature reduction from 295 to 4 K greatly accelerates the fatigue crack growth rates of the Fe-18Cr-3Ni-13Mn-0.37N steel. This is shown clearly for the sensitized conditions (both  $S_1$  and  $S_2$ ) in Figure 4, and it is also reported to be the case for the annealed condition [1]. The change from 295 to 4 K has remarkable effects on the Paris equation parameters also, in that  $C$  decreases while  $n$  increases markedly (Table 2) for both the annealed and sensitized conditions. Changes in the failure modes associated with the temperature reduction are documented in Fig. 6: the ductile striation formation observed at 295 K is replaced at 4 K by more brittle mechanisms which cause higher growth rates. The brittle failure modes at 4 K are distinguished by the following features: 1) cleavage-type facets in the case of the annealed material (Fig. 6A), and 2) varying amounts of intergranular facets in the case of the sensitized material, conditions  $S_1$  (Fig. 6B) and  $S_2$  (Fig. 6C). Thus, the relative brittleness of the fatigue failure mechanisms at 4 K explain the higher growth rates at 4 K, as compared to 295 K.

The fatigue crack growth rates at 4 K for the annealed and sensitized conditions are compared in Figure 7. The data for annealed material derive from tests performed on three specimens, whereas the data for the  $S_1$  and  $S_2$  conditions represent single specimen tests. For the  $\Delta K$  range studied, sensitization tends to increase the  $da/dN$  at 4 K for a given value of  $\Delta K$ . Most of the data for the sensitized conditions lie above the data scatter for the three annealed specimens. The difference in rates varies with  $\Delta K$ , as well as the degree of sensitization. In particular, the



rates for the  $S_2$  condition begin to accelerate well above the rates for both the  $S_1$  and annealed conditions when  $\Delta K$  exceeds  $30 \text{ MPa}\cdot\text{m}^{\frac{1}{2}}$ . As indicated below, the 4 K fatigue fracture toughness of the sensitized material in the  $S_2$  condition is relatively low ( $K_{fc} = 41 \text{ MPa}\cdot\text{m}^{\frac{1}{2}}$ ), and this factor apparently promotes the marked acceleration of  $da/dN$  for  $\Delta K$  above  $30 \text{ MPa}\cdot\text{m}^{\frac{1}{2}}$ .

A summary of the  $da/dN$ -versus- $\Delta K$  results is given in Table 2. The regression statistics listed in Table 2 apply to the Paris equation line fits which are illustrated in Figures 4 and 7.

Fatigue Fracture Toughness: The fatigue fracture toughness estimates,  $K_{fc}$ , indicate that sensitization can significantly decrease the toughness, relative to the annealed condition, if sufficient time (1.5 h) at the sensitizing temperature is allowed. The  $K_{fc}$  values are 61, 61, and  $41 \text{ MPa}\cdot\text{m}^{\frac{1}{2}}$  for the annealed,  $S_1$ , and  $S_2$  conditions, respectively.

Decreased toughness in the sensitized condition was expected, since precipitates in the grain boundaries usually lower the boundary cohesive strength. The results of scanning electron microscopy, Fig. 8, bear this out. These fractographs correspond to the overload failure zones for each specimen condition. In each case the 4 K fracture surface consists of brittle failure modes but there are obvious differences in the fracture features depending on material condition:

- 1) The annealed condition, Fig. 8A, shows a mixed mode consisting of cleavage facets interspersed with dimpled zones. Slip line traces are observable on the facets.
- 2) The  $S_1$  sensitized condition, Fig. 8B, also shows a mixed mode, this time consisting of portions of intergranular failure interspersed with dimpled zones.
- 3) The more severely sensitized  $S_2$  condition, Fig. 8C, exhibits the most brittle behavior of all. Here the intergranular failure is fully developed, predominating over essentially 100 % of the fracture surface. Many of the exposed grains evidence cavities on their boundaries where the carbo-nitride particles had precipitated.

Thus, the effect of sensitization is to lower the fatigue fracture toughness at 4 K by promoting intergranular fracture in this steel.

## DISCUSSION

The purpose of this discussion is to compare the fatigue and static fracture toughnesses of this austenitic steel at 4 K. Sometimes it is assumed that failure will occur when  $K_{max}$  in fatigue equals  $K_{IC}$ . The present data indicate that this is not true for the studied material.

The  $K_{fc}$  value for the annealed specimen at 4 K was  $61 \text{ MPa}\cdot\text{m}^{\frac{1}{2}}$ . For the same heat of Fe-18Cr-3Ni-13Mn-0.37N steel, material condition, specimen thickness, and specimen orientation (TL[6]), three static fracture toughness tests gave  $K_Q$  values of 70, 70, and  $73 \text{ MPa}\cdot\text{m}^{\frac{1}{2}}$  [1]. These are  $K_Q$ , not  $K_{IC}$  measurements, owing to excessive crack front curvature [1,6]. On the other hand, the load-deflection curves are linear-elastic and the thickness criterion is amply satisfied, so that



the  $K_Q$  data do provide qualitative evidence that the static fracture toughness is higher than the fatigue fracture toughness. Apparently then,  $K_{fc} \approx 0.85 K_Q$  for this steel at 4 K.

A plastic zone size correction ( $r_y$ ) to the final crack length and the fatigue fracture toughness value can be made, based on the expression [7]:

$$r_y = \frac{1}{2\pi} \left( \frac{K_{fc}}{\sigma_y} \right)^2$$

This correction raises the  $K_{fc}$  estimate for the annealed condition at 4 K from 61 to 62  $\text{MPa}\cdot\text{m}^{\frac{1}{2}}$ . Since such a correction is not sufficient to account for the difference in toughness between  $K_{fc}$  and  $K_Q$ , it appears from the data for the annealed condition that the static fracture toughness is definitely higher ( $\sim 16\%$ ) than the fracture toughness that is measured during fatigue as the crack grows to critical size at progressively increasing  $\Delta K$  values.

#### SUMMARY AND CONCLUSION

Some effects of sensitization on the fatigue resistance of an austenitic stainless steel at liquid helium temperature were explored using 25-mm thick compact specimens. The test material was nitrogen-bearing Fe-18Cr-3Ni-13Mn-0.37N steel. Fatigue crack growth rates and Paris equation parameters are reported at 295 and 4 K, along with a limited number of fatigue crack initiation and fatigue fracture toughness measurements at 4 K.

For the  $\Delta K$  range 20 to 50  $\text{MPa}\cdot\text{m}^{\frac{1}{2}}$ , sensitization has little or no effect on fatigue crack growth rates at room temperature. At 4 K, however, the rates for sensitized and annealed conditions increase drastically compared to the rates at 295 K, and the effects of sensitization relative to the annealed condition are then quite pronounced. Observations for the Fe-18Cr-3Ni-13Mn-0.37N steel at 4 K are sufficient to demonstrate that sensitization (1.5 h at 977 K) leads to:

- 1) reduced crack initiation resistance ( $\sim 60\%$ )
- 2) reduced crack growth resistance (a factor of 2 or more), and
- 3) reduced fatigue fracture toughness ( $\sim 33\%$ ).

Fractography demonstrates that the grain boundary precipitation resulting from sensitization has little effect on the fatigue behavior at 295 K since the fatigue failures at this temperature occur via a ductile transgranular striation mechanism. During fatigue and fracture testing at 4 K, however, the annealed material exhibits a brittle transgranular failure mode involving cleavage; the effect of sensitization at this temperature is to promote a transition to a still more brittle intergranular failure mode.

In conclusion, a decreased fatigue life at cryogenic temperatures may be anticipated for sensitized Fe-18Cr-3Ni-13Mn-0.37N stainless steel, owing to a combination of effects. Additional data would be necessary to fully quantify the effects of composition, test temperature, severity of sensitization, and magnitude of fatigue stresses.

## ACKNOWLEDGEMENT

The assistance of Mr. P. Purtscher of NBS in preparation of metallographic specimens and fractography is gratefully acknowledged.

## REFERENCES

- [1] Read, D. T. and Reed, R. P., Toughness, Fatigue Crack Growth, and Tensile Properties of Three Nitrogen-Strengthened Stainless Steels at Cryogenic Temperatures, in: The Metal Science of Stainless Steels, E. W. Collings and H. W. King, eds., Met. Soc. AIME, 1979, pp. 92-121.
- [2] Read, D. T. and Tobler, R. L., Mechanical Property Measurements at Low Temperatures, in: Adv. Cryo. Eng. 28, R. P. Reed and A. F. Clark, eds., Plenum 1982, pp. 17-28.
- [3] Cheng, Y. W., A Computer-Interactive Fatigue Crack Growth Rate Test, in this NBSIR volume.
- [4] Hudak, S. J., Jr., Saxena, A., Bucci, R. J., and Malcolm, R. C., Development of Standard Methods of Testing and Analyzing Fatigue Crack Growth Rate Data, Tech. Report AFML-TR-78-40, May 1978, pp. 257, ADA058320.
- [5] Yokobori, T. and Aizawa, T., Rep. Res. Inst. Strength Fract. Mater., Tohoku University, 6, 1970, p. 19.
- [6] Standard Test Method for Plane-Strain Fracture Toughness of Metallic Materials, ASTM Designation E 399-81, 1981 Annual Book of ASTM Standards, Amer. Soc. Test. Mater., Philadelphia, 1981, pp. 588-618.
- [7] Irwin, G. R., Plastic zone near a crack and fracture toughness, in: Proceedings, 7th Sagamore Ordinance Materials Research Conference, Syracuse University Press, Syracuse, NY, 1960, pp. iv63-iv78.

## LIST OF TABLES

1. Mechanical properties for annealed Fe-18Cr-3Ni-13Mn-0.37N stainless steel [1].
2. Fatigue crack growth rate data for Fe-18Cr-13Mn-0.37N stainless steel.

Table 1. Mechanical properties for annealed Fe-18Cr-3Ni-13Mn-0.37N stainless steel [1].

Temperature (K)	Yield Strength, $\sigma_y$ (MPa)	Ultimate Strength, $\sigma_u$ (MPa)	Elongation in 25 mm (%)	Reduction of Area (%)	Young's modulus, E (GPa)	Poisson's ratio $\nu$
295	440	796	56	53	197	0.280
4	1540	1811	4	26	198	0.277

Table 2. Fatigue crack growth rate data for Fe-18Cr-3Ni-13Mn-0.37N stainless steel.

Material Condition	Temperature (K)	No. of Data Pts.	Paris Equation Parameter <sup>a</sup> C	n	Standard Deviation of C	Standard Deviation of n	Correlation Coefficient	$\Delta K$ Range (MPa·m <sup>1/2</sup> )	$K_{fc}^b$ (MPa·m <sup>1/2</sup> )
Annealed <sup>c</sup>	295	57	$0.97 \times 10^{-10}$	3.82	NA	NA	NA	24 to 85	NA
Sensitized, S <sub>1</sub>	295	24	$2.10 \times 10^{-10}$	3.63	0.082	0.052	0.997	23 to 58	NA
Sensitized, S <sub>2</sub>	295	21	$1.35 \times 10^{-10}$	3.70	0.106	0.069	0.998	22 to 54	NA
Annealed	4	41	$1.09 \times 10^{-12}$	5.73	0.355	0.237	0.968	20 to 48	61
Sensitized, S <sub>1</sub>	4	28	$1.29 \times 10^{-11}$	5.18	0.177	0.177	0.993	20 to 50	61
Sensitized, S <sub>2</sub>	4	20	$2.80 \times 10^{-15}$	7.78	0.632	0.443	0.972	20 to 36	41

<sup>a</sup> The Paris equation is  $da/dN = C(\Delta K)^n$ ; the data fit and regression statistics apply to metric units with  $da/dN$  in mm/cycle and  $\Delta K$  in MPa·m<sup>1/2</sup>.

<sup>b</sup>  $K_{fc} = 1.11 \Delta K$  at failure; one test per condition at 4 K.

<sup>c</sup> Values from reference 1.

## LIST OF FIGURES

1. Microstructures of annealed and sensitized Fe-18Cr-3Ni-13Mn-0.37N steel: (A) annealed, 400X; (B)  $S_2$  condition, 150X; (C)  $S_1$  condition, 200X; (D)  $S_1$  condition, 600X; (E)  $S_1$  condition, SEM view after extensive etching, 500X; (F) same as E; pits have formed where the precipitates have been etched out.
2. Compact specimen used in this study.
3. Fatigue crack initiation test results, showing reduced life for the sensitized conditions.
4. Fatigue crack growth rate data for sensitized conditions at 295 and 4 K.
5. Fatigue failure surface at 295 K, showing the ductile transgranular striation mechanism for material in the  $S_1$  condition ( $\Delta K \approx 50 \text{ MPa}\cdot\text{m}^{1/2}$ ), (A) 300X; (B) 1000X.
6. Fatigue failure surfaces at 4 K, showing mixed modes with brittle mechanisms: (A) annealed condition,  $\Delta K \approx 35 \text{ MPa}\cdot\text{m}^{1/2}$ , 500X; (B)  $S_1$  condition,  $\Delta K \approx 25 \text{ MPa}\cdot\text{m}^{1/2}$ , 300X; (C)  $S_2$  condition,  $\Delta K \approx 30 \text{ MPa}\cdot\text{m}^{1/2}$ , 750X.
7. Fatigue crack growth rate data at 4 K.
8. Fatigue surfaces corresponding to overload at 4 K: (A) annealed condition, 500X; (B)  $S_1$  condition, 500 X; (C)  $S_2$  condition, 1000X.



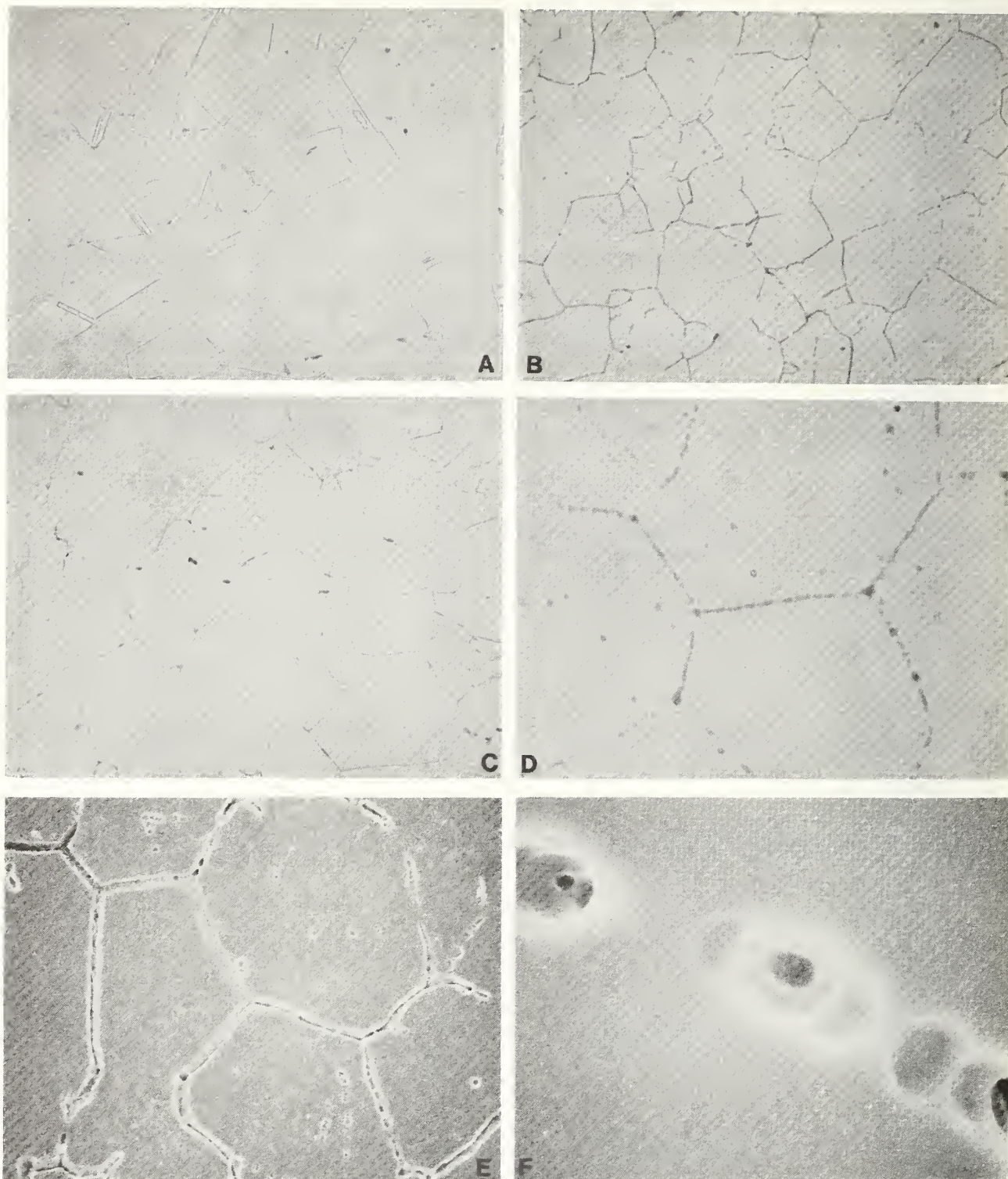
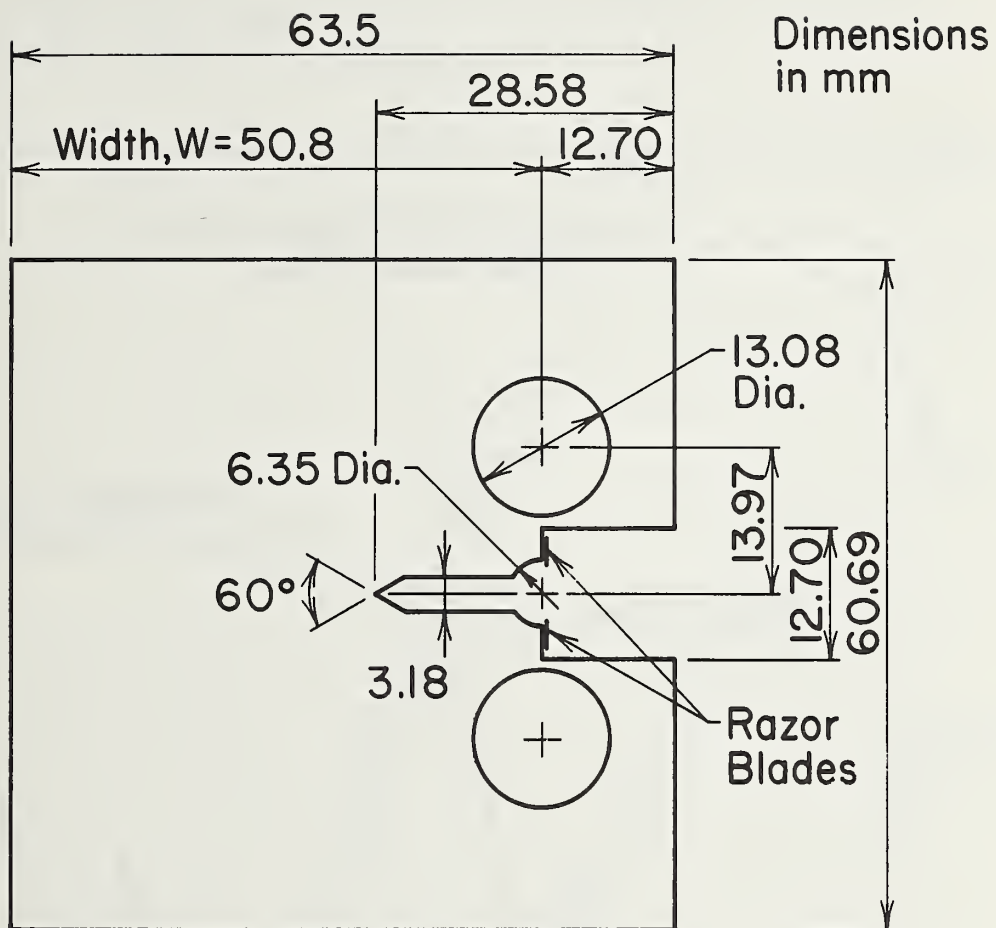


Figure 1. Microstructures of annealed and sensitized Fe-18Cr-3Ni-13Mn-0.37N steel: (A) annealed, 400X; (B) S<sub>2</sub> condition, 150X; (C) S<sub>1</sub> condition, 200X; (D) S<sub>1</sub> condition, 600X; (E) S<sub>1</sub> condition, SEM<sub>1</sub> view after extensive etching, 500X; (F) same as E; pits have formed where the precipitates have been etched out.



**COMPACT SPECIMEN**  
Thickness = 24.5 mm

Figure 2. Compact specimen used in this study.

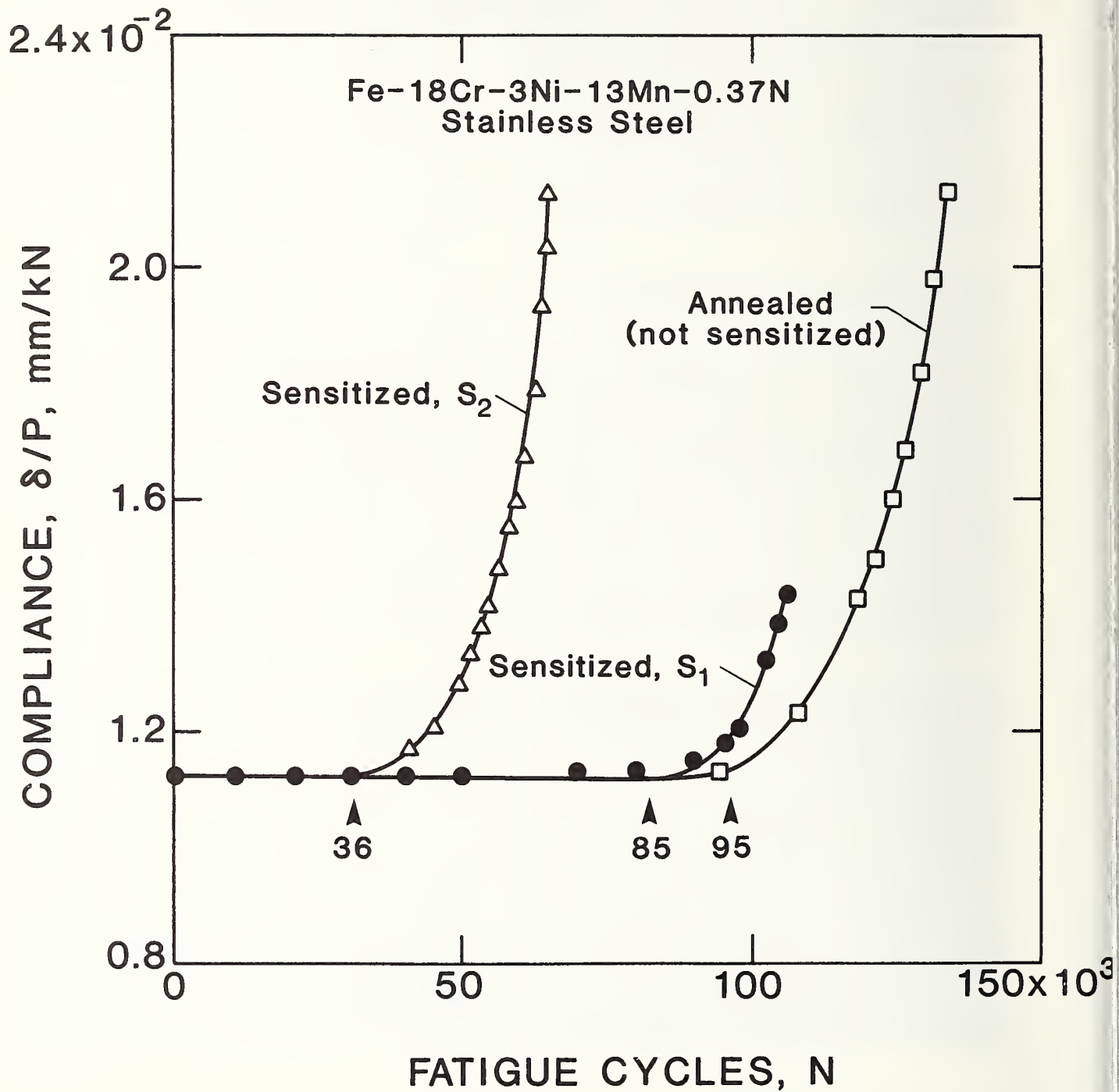
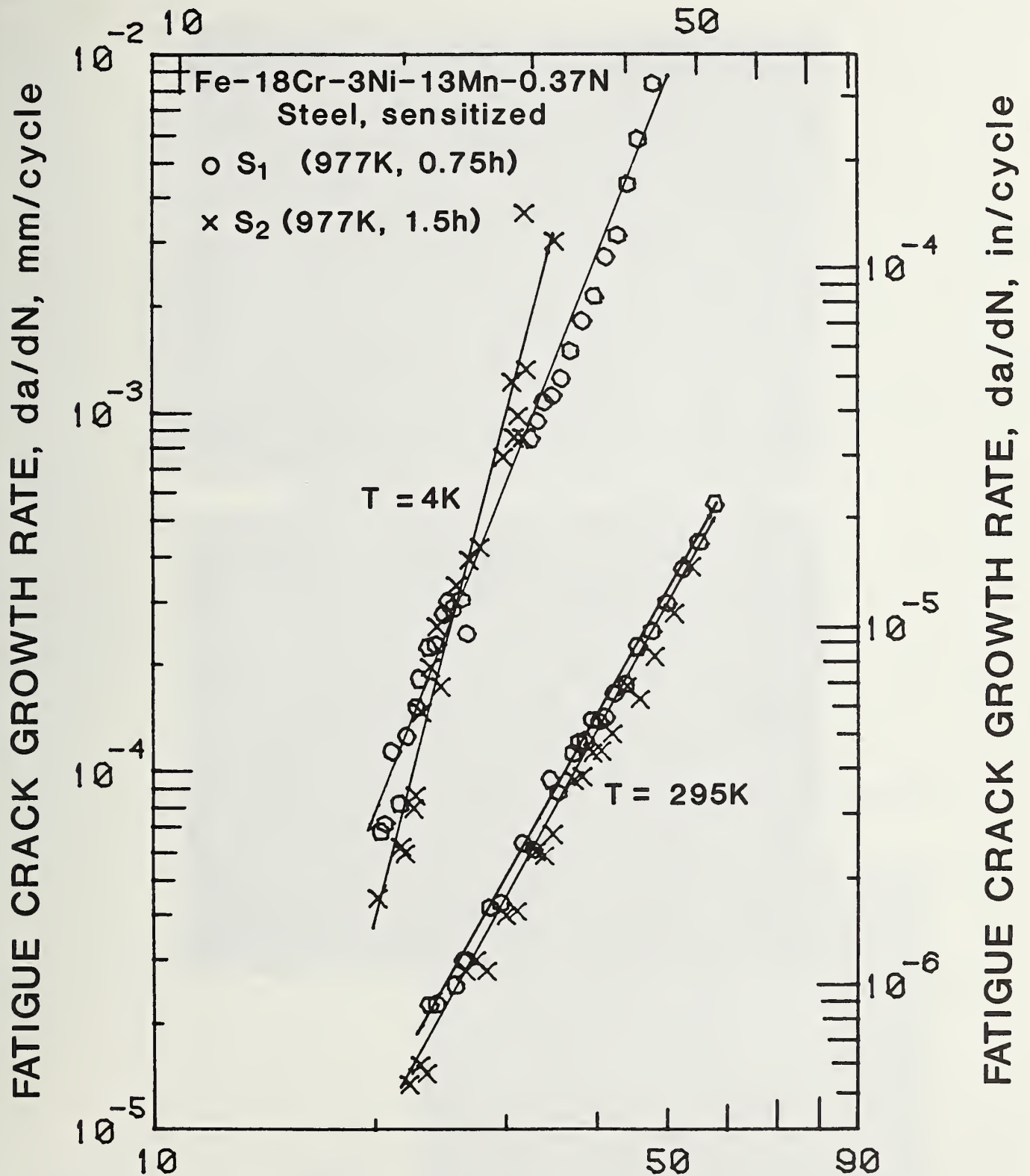


Figure 3. Fatigue crack initiation test results, showing reduced life for the sensitized conditions.

STRESS INTENSITY FACTOR RANGE,  $\Delta K$ ,  $\text{MPa}\cdot\text{m}^{1/2}$



STRESS INTENSITY FACTOR RANGE,  $\Delta K$ ,  $\text{MPa}\cdot\text{m}^{1/2}$

Figure 4. Fatigue crack growth rate data for sensitized conditions at 295 and 4 K.



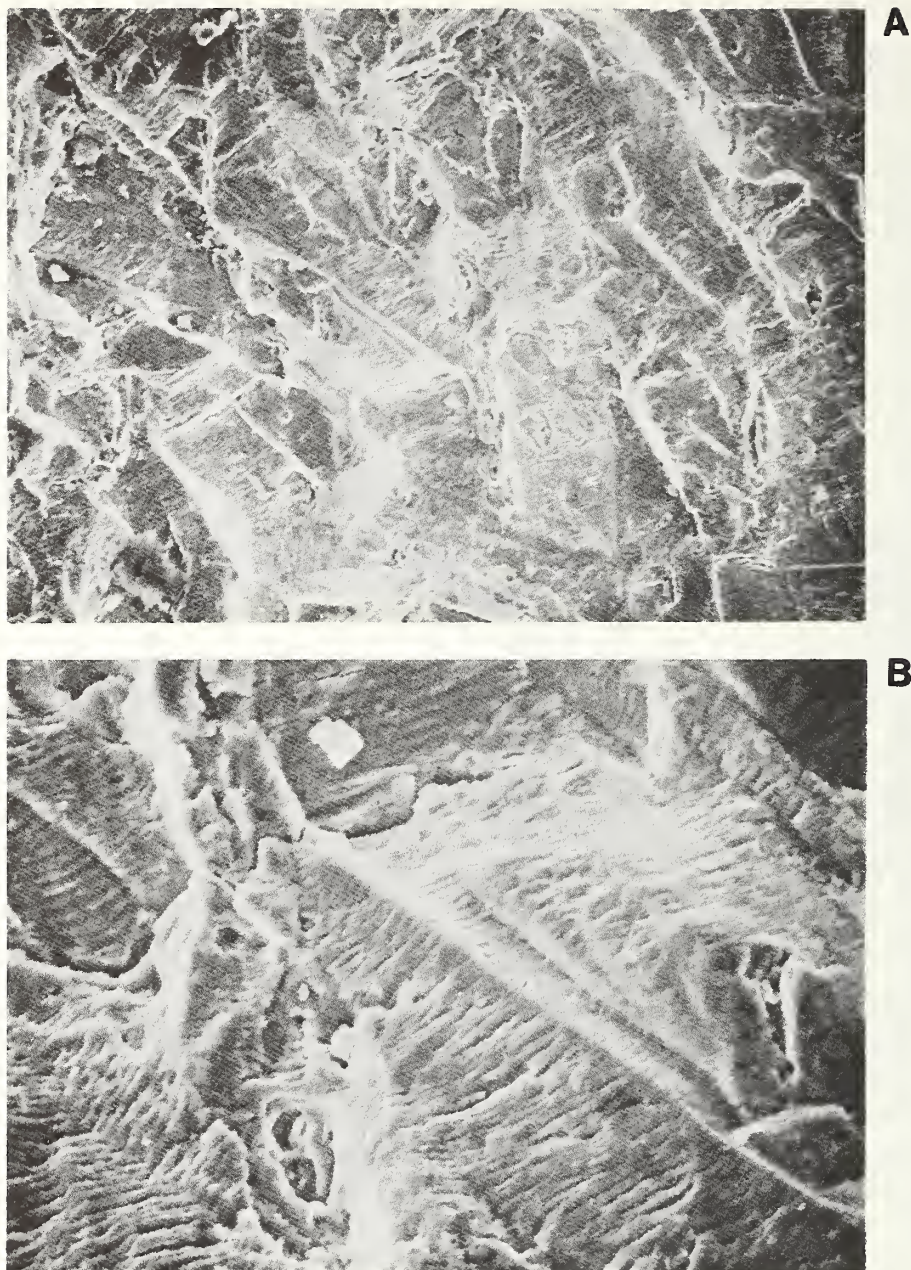


Figure 5. Fatigue failure surface at 295 K, showing the ductile transgranular striation mechanism for material in the  $S_1$  condition ( $\Delta K \approx 50 \text{ MPa}\cdot\text{m}^{1/2}$ ), (A) 300X; (B) 1000X.



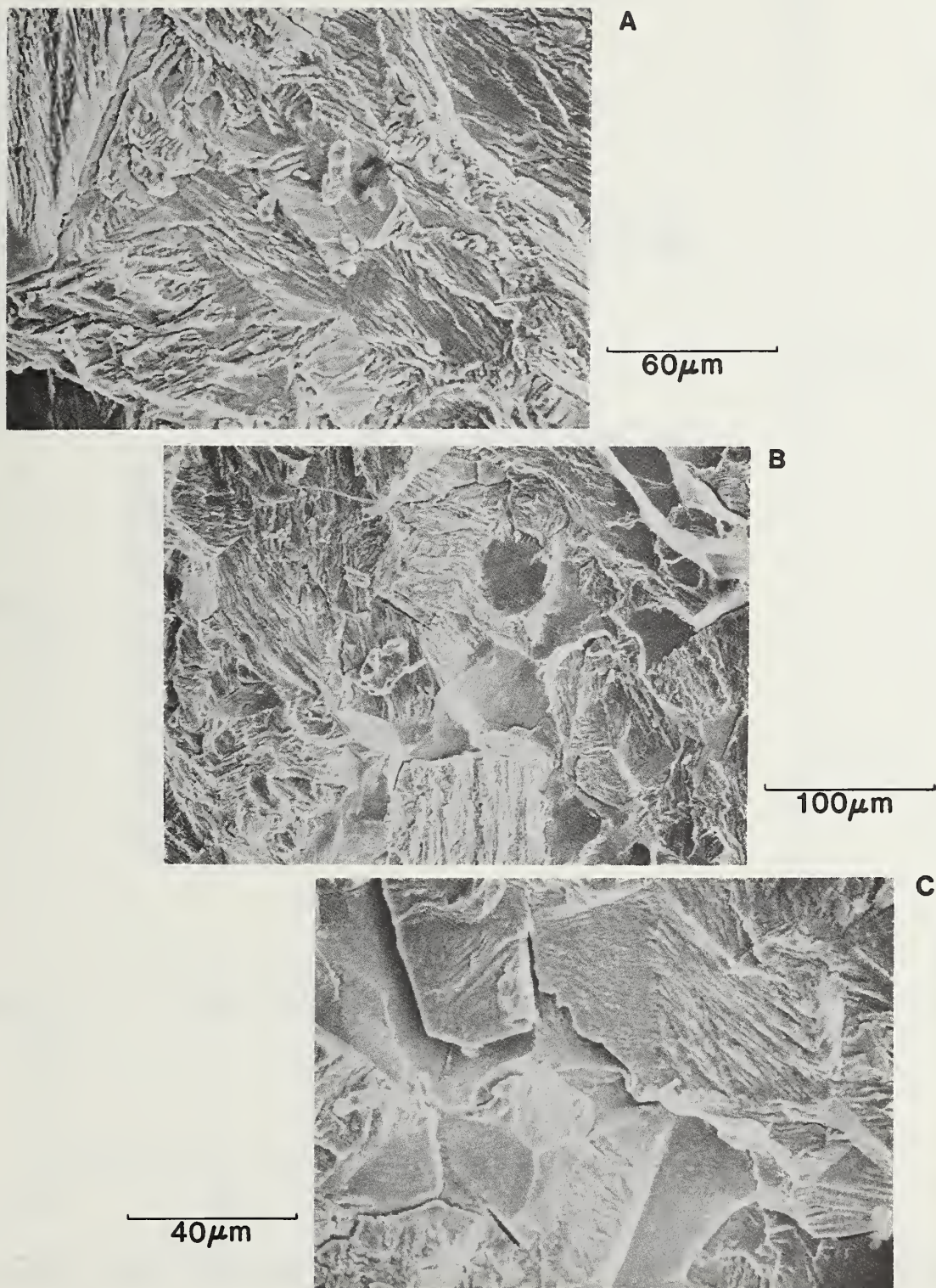


Figure 6. Fatigue failure surfaces at 4 K, showing mixed modes with brittle mechanisms: (A) annealed condition,  $\Delta K \approx 35 \text{ MPa}\cdot\text{m}^{1/2}$ , 500X; (B)  $S_{16}$  condition,  $\Delta K \approx 25 \text{ MPa}\cdot\text{m}^{1/2}$ , 300X; (C)  $S_2$  condition,  $\Delta K \approx 30 \text{ MPa}\cdot\text{m}^{1/2}$ , 750X.

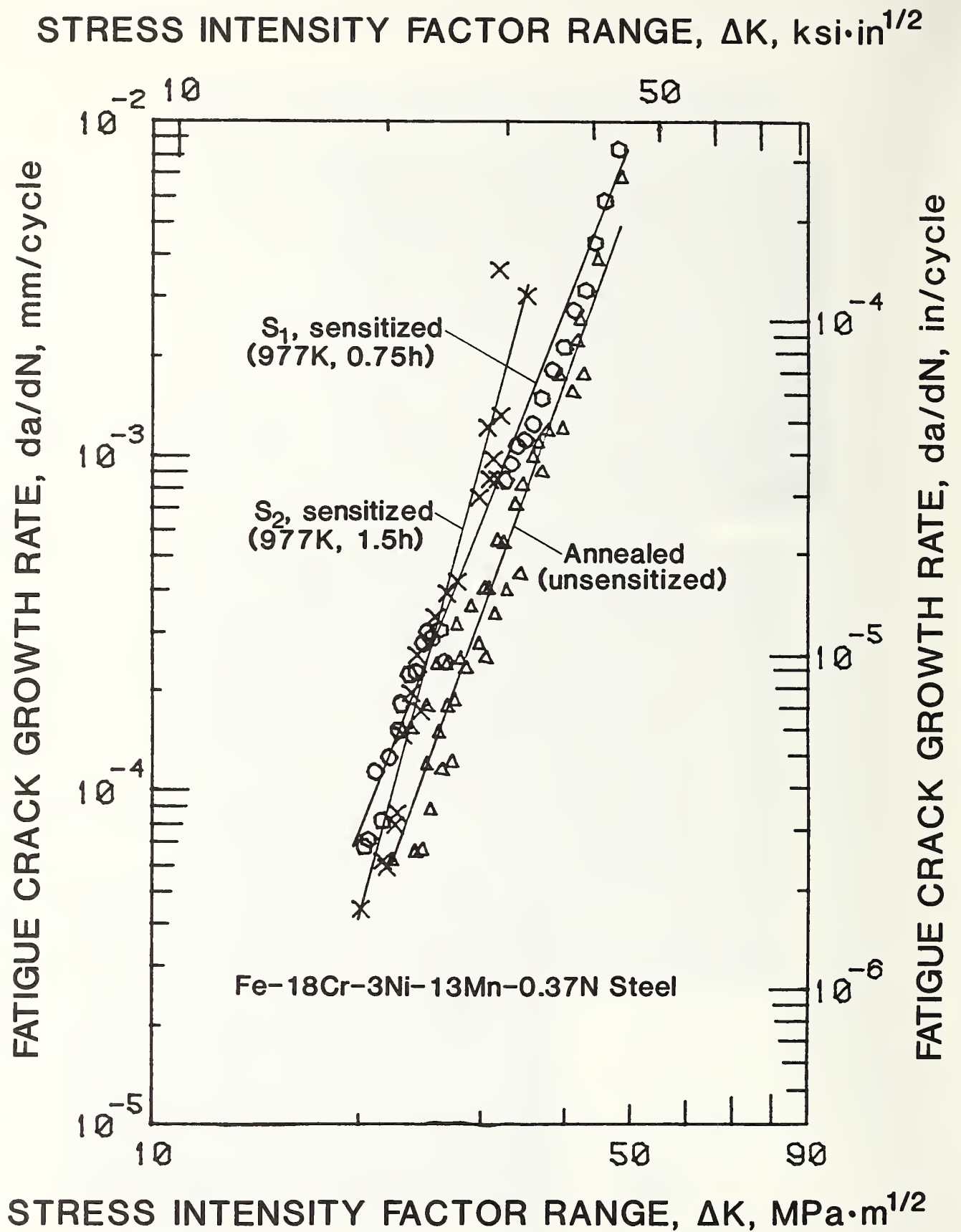


Figure 7. Fatigue crack growth rate data at 4 K.



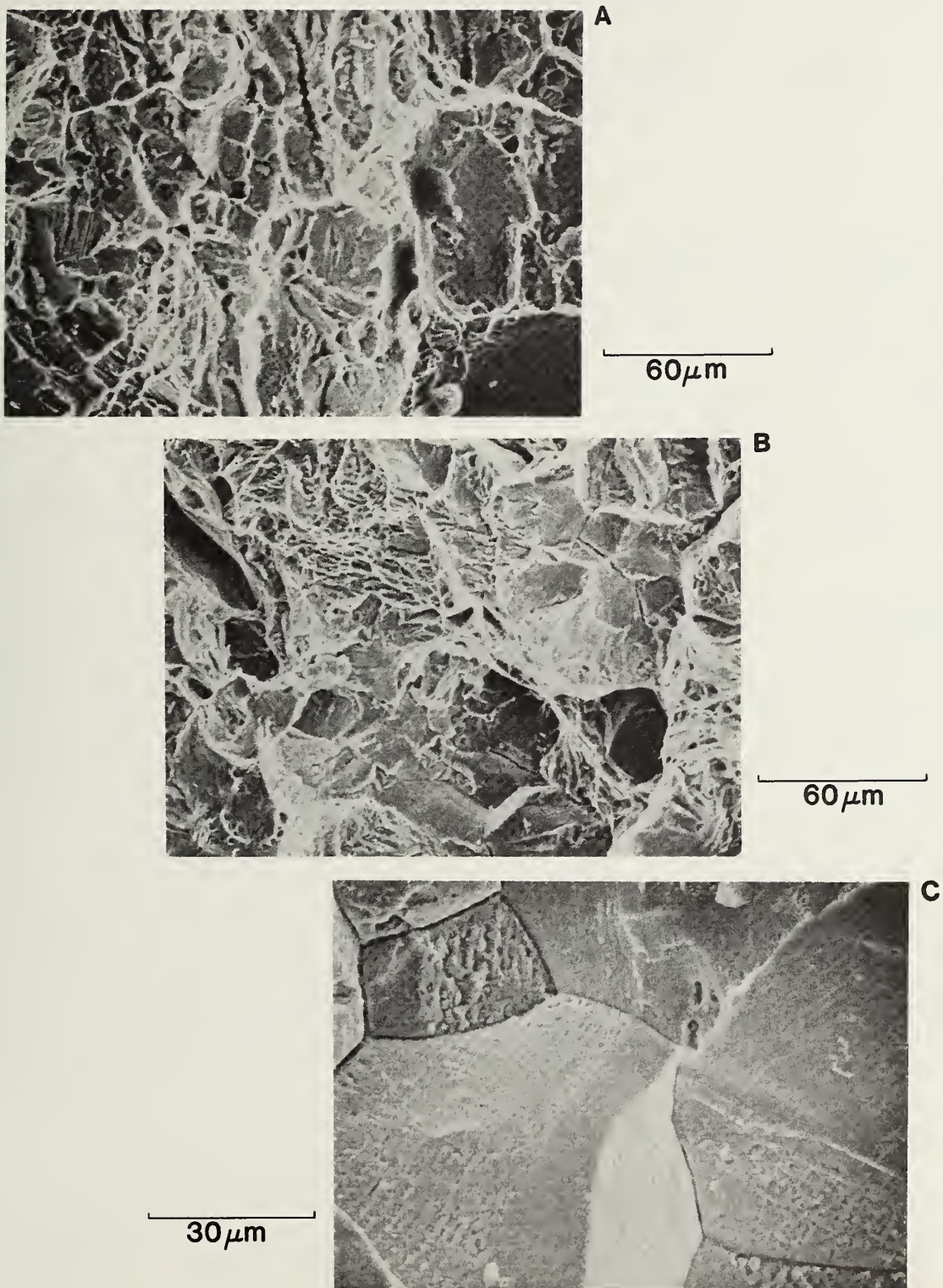


Figure 8. Fatigue surfaces corresponding to overload at 4 K: (A) annealed condition, 500X; (B)  $S_1$  condition, 500 X; (C)  $S_2$  condition, 1000X.



# EFFECTS OF MAGNETIC FIELD ON TENSILE BEHAVIOR AT 4 K OF ALLOYS 304 AND 310+\*

R. P. Reed, J. M. Arvidson, J. W. Ekin, and R. H. Schoon  
National Bureau of Standards  
Boulder, Colorado

## ABSTRACT

The application of magnetic fields has been demonstrated to enhance face-centered cubic to body-centered cubic (bcc) martensitic transformations in ferrous austenitic alloys. In Fe-Ni-Mn alloys higher fields serve to raise the temperature of possible transformation and to increase the amount of transformation. There has been an abundance of papers discussing the use of strong (up to 35 T) pulsed fields to enhance transformation in Fe-Ni, Fe-Ni-Cr and Fe-Mn steels. The plastic deformation of a series of Fe-18Cr, 8-25Ni alloys at 4 K exposed to steady-state and transient magnetic fields has been previously studied and small changes of flow strength were observed that have been attributed to magnetostriction and joule heating effects. Many experiments have shown that martensitic transformations in Fe-Cr-Ni stainless steels affect the low temperature flow strength.

Our experiments were conducted to assess the effects of a steady magnetic field on the austenite stress-strain characteristics at 4 K. Wire specimens (0.64-mm dia) of both a stable Fe-26Cr-20Ni (AISI 310) and metastable Fe-18Cr-9Ni (AISI 304) were measured. A 7 T magnetic field was produced by a split-pair NbTi superconducting magnet with radial access ports and the field was applied perpendicular to the tensile specimen axis. Tests were conducted at 4 K with the field off, with the field on, and with the field switched on and off after prescribed amounts of plastic deformation. The Young's modulus, tensile yield strength and tensile stress-strain curves were measured. The results are summarized here: (1) During magnetic field on/off experiments, no change in austenite flow strength of either alloy was observed from the application or absence of a 7-T field and (2) There was no detectable effect of a constant 7-T magnetic field on the yield strength and Young's modulus of either alloy. However, the specimen-to-specimen yield strength data scatter was large and the application of magnetic field would not necessarily produce changes of flow strength in excess of the data scatter. Discussion is also presented on magnetic field effects on discontinuous yielding and cold worked alloys.

+ Work supported by Office of Fusion Energy, Department of Energy

\* To be published in *Austenitic Steels at Low Temperatures*, Eds. R. P. Reed and T. Horiuchi, Plenum Press, New York (1983).





## INTRODUCTION

Superconducting magnet structures require alloys that have high strength at 4 K in magnetic fields. Since magnetic fields are known to influence martensitic transformation in steels, it is prudent to examine the effect of magnetic field on their strength.

It has been demonstrated that magnetic fields tend to raise the martensitic transformation temperature and to increase the amount of transformation in ferrous alloys. Korenko and Cohen<sup>(1)</sup> have recently studied an Fe-22.5Ni-4Mn alloy and showed that the magnitude of the applied field significantly influences transformation kinetics. For example, no martensite was detected in this alloy on cooling to 190 K; however, a constant 8-T field, applied after cooling, produced 5 percent martensite, and a constant 14-T field produced 35 percent martensite at 190 K.

There has been an abundance of papers<sup>(2-8)</sup> discussing the use of strong (up to 50-T) pulsed fields to enhance transformation in Fe-Ni, Fe-Ni-Cr, and Fe-Mn steels. These studies have established that pulsed magnetic fields raise the temperature of martensitic transformation and, for a given temperature and alloy, there is a minimum critical field to produce martensite. The application of magnetic fields influences only austenite to body-centered cubic (ferromagnetic) martensite, not austenite to hexagonal close-packed (nonferromagnetic) martensite.

---

\*This research was supported by the Office of Fusion Energy, U.S. Department of Energy.

The studies suggest that the primary factor for the influence of magnetic field on transformation is that the thermodynamic stability between the alloy phases has been altered.

Bolshutkin, Desnenko, and Ilichev<sup>(9)</sup> have studied the plastic deformation of a series of Fe-18Cr, 8 to 25Ni alloys at 4 K exposed to steady-state and pulsed magnetic fields. No change of flow strength was observed within experimental uncertainty (3-4 percent) on application of a constant 3.4-T magnetic field. However, when the magnetic field was applied during straining at 4 K, the flow strength of Fe-18Cr, 8 to 15Ni alloys was observed to decrease. The amount of strength decrease was between 1.0 and 5.0 MPa, reaching about 0.6 percent of the flow strength. This decrease of flow strength only became detectable after plastic strains of about 0.05 and increased rapidly with increasing strain to a strain of about 0.10, where the magnitude of the decrease became constant. Conversely, they found that in more stable alloys (Fe, 18Cr, 20-25Ni) the flow strength increased with application of a 3.4-T field during testing. In these steels, the increase of flow strength varied from 2.0 to 3.0 MPa, beginning at strains near 0.01 and saturating at strains near 0.02.

The effect of both longitudinal and transverse, constant 2.5-T magnetic fields on the plastic deformation of high-purity aluminum at 4 K has been studied.<sup>(10)</sup> Increases of flow strength during straining, associated with the application of the magnetic field, were observed. The flow strength increase was associated with increased electron deceleration, which results in reduced dislocation velocity.

The effect of magnetic field on the flow strength at 4 K has been recently studied for a ferromagnetic metal, nickel.<sup>(11)</sup> Magnetic fields were found to increase the flow strength, application of a transverse field had greater influence than a parallel field, and the flow strength increased linearly with field in the range 0 to 4 T. Resistivity measurements as a function of strain provided evidence that the dislocation structure was not affected by magnetic field. The increased flow strength under magnetic fields is attributed to the generation of spin waves by moving dislocations in the ferromagnetic lattice, resulting in reduced dislocation velocity.

This study was initiated to begin assessment of the effects of magnetic fields on austenite-martensite deformation at 4 K in Fe-Cr-Ni alloys. Many experiments have shown that strain-induced martensitic transformations in Fe-Cr-Ni stainless steels affect the low temperature flow strength. At low strains, transformation apparently results in reduced flow strength. However, at larger strains, bcc martensite transformation correlates excellently with increased work hardening.<sup>(12)</sup> Also, elastic property and

susceptibility measurements have indicated the complex magnetic state of Fe-Cr-Ni austenites at low temperatures.<sup>(13)</sup> This state, below the Néel temperature, has been described as varying from longer-range antiferromagnetic ordering in Fe-18Cr-8Ni alloys to shorter-range spin-glass interactions in alloys containing more Cr or Ni. Therefore, two major questions need to be answered: (1) Do applied fields enhance strain-induced martensite transformation in Fe-18Cr-8Ni steels and, if so, how does the magnetic-field-enhanced martensite affect austenite flow strength? (2) How do applied magnetic fields affect the flow strength of austenite as a function of composition?

## MATERIALS

Two stainless steels, AISI 304 (Fe-19Cr-8Ni) and AISI 310 (Fe-25Cr-20Ni) were selected for this test series. AISI 304 is metastable with respect to austenite-to-martensite transformation and transforms during plastic deformation at temperatures below about 200 K; AISI 310 is completely stable with respect to martensitic transformation. Both were obtained as 0.64 mm diameter wire in the cold-drawn condition. Annealing times of 7.5, 15, and 30 min at 1340 K (1950 °F) produced yield strength reductions from 400 to 305, 285, and 290 MPa, respectively, at room temperature for alloy 310. Annealing of alloy 304 at 1340 K (1950 °F) for 30 min resulted in a yield strength reduction from 321 to 233 MPa at room temperature. All annealed wire specimens were produced by heating in a vacuum at 1340 K (1950 °F) for 30 min.

## EXPERIMENTAL PROCEDURE

The apparatus has been described previously by Ekin.<sup>(14)</sup> Tensile load and a magnetic field were simultaneously applied to wire specimens at 4 K. The magnetic field was produced by a 7-T split-pair NbTi magnet with radial access ports, allowing perpendicular application of the field to the specimen. A schematic of the apparatus is shown in Fig. 1. Specimens were tested in straight sections, each with a 27.5-cm-long gage length. The profile of the magnetic field strength over the specimen length is illustrated in Fig. 1. The magnet produces a 7-T field perpendicular to a 6.3-cm length of the specimen at its center. On each side of this central section, the field strength decreased linearly over an 8 cm length to 0 T. Therefore, while only about  $\frac{1}{4}$  of the specimen is exposed to 7 T, the entire specimen is exposed to some magnetic field. Magnetic field accuracy was  $\pm 1.0$  percent, and homogeneity over the sample central section was of the order of  $\pm 1.0$  percent.



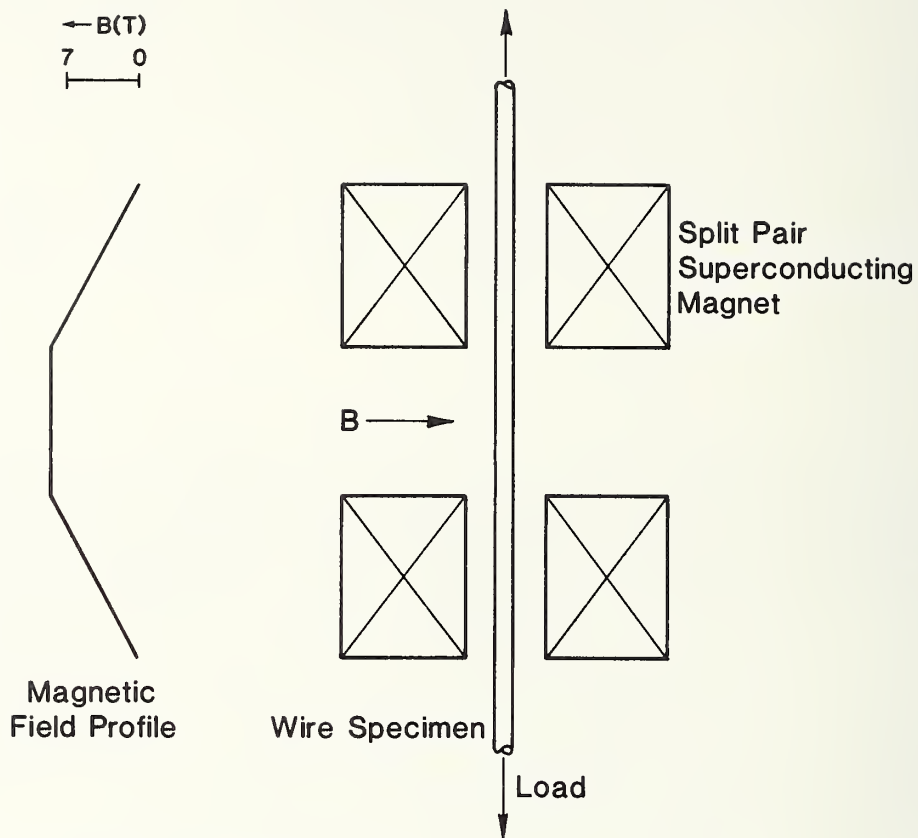


Fig. 1. Schematic of apparatus to apply tensile force and magnetic field to wire specimens.

The specimens were gripped at both ends by soft silver soldering into copper channels, one fixed and one attached to the load train through a self-aligning universal joint. Strain was measured by taking the vertical displacement of the pull rod, as indicated by an LVDT electronic displacement sensor, and dividing by the gage length. The stiffness of the load train, relative to the sample, yields an accuracy in these measurements of  $\pm 0.04$  percent. Load was applied by a 2-kN servohydraulic testing and measured by a compatible load cell in series with the pull rod. Load was measured to within  $\pm 0.2$  percent.

The specimens were strained at a constant rate of 0.002 cm/cm/min using the testing system's interval function generator and a linear ramp wave form. All of the specimens were strained between 0.025 and 0.040 at 4 K. Some experiments were conducted by sequentially turning the magnetic field on and off during the test. In such tests, the specimen was unloaded, but kept at 4 K,

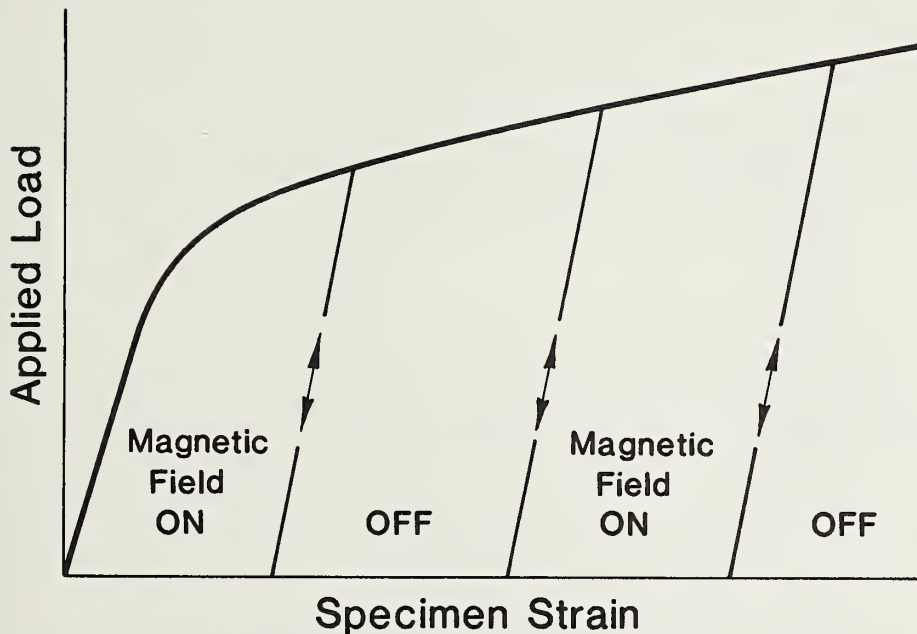


Fig. 2. Schematic of applied tensile load versus specimen strain with magnetic field applied "on", then "off".

prior to field change. A schematic of a typical applied load-specimen-strain curve during these tests is shown in Fig. 2.

To determine the percent (bcc,  $\alpha'$ ) martensite in the specimens at room temperature following deformation, a bar-magnet with a torsion spring was used. This apparatus has been previously described and calibrated.<sup>(15)</sup> The wire specimens had a small diameter compared to the bar magnet. To increase the sensitivity of the measurements, the entire 27.5-cm length of the deformed specimens was cut into smaller lengths, about 2-cm long. Therefore, the magnetic measurements represent an entire specimen average, with sections included over which the field strength varied from 0 to 7 T. Amounts of martensite transformation were estimated<sup>(15)</sup> from the magnetic readings, using earlier established conversions.

## EXPERIMENTAL RESULTS

Experimental data for alloy 310 are tabulated in Table I, and the experimental data for alloy 304 are summarized in Table II. In these tables, ANN refers to annealed, and CD refers to cold

Table I. AISI 310 Stainless Steel Wire\*

Test Temperature, K	Magnetic Field, T	Specimen Condition	Young's Modulus, GPa	Proportional Limit, MPa	Yield Strength (0.2% Offset), MPa	Strain at Onset of Discontinuous Yielding <sup>†</sup>	% Martensite at Onset of Discontinuous Yielding <sup>†</sup>
295	0	CD	186	86	400	--	0
295	0	†	174	134	305	--	0
295	0	§	162	114	285	--	0
295	0	ANN	168	97	290	--	0
4.2	0	CD	206	345	1,120	1.26	0
4.2	0	CD	206	610	1,230	1.45	0
4.2	7	CD	202	386	1,200	1.21	0
4.2	0	ANN	174	252	1,030	*	0
4.2	7	ANN	171	252	1,110	*	0
4.2	7	ANN	186	478	1,000	*	0
4.2	7	ANN	187	478	1,000	*	0
4.2	7	ANN	180	455	1,070	*	0

\* 0.64-mm diameter.

† Annealed at 1339 K (1950 °F) for 7.5 min.

§ Annealed at 1339 K (1950 °F) for 15 min.

† Total strain (elastic/plastic).

x No discontinuous yielding observed to strains of 0.04.

drawn (as received). Small amounts of martensite were detected in all alloy 304 specimens strained at 76 and 4 K, but not in the alloy 304 specimens strained at room temperature. No martensite was detected in alloy 310 specimens. In Table II, the martensite ( $\alpha'$ ) values are reported as percent martensite divided by the specimen elongation; it has been previously found that the amount of  $\alpha'$  is approximately linear with specimen strain.<sup>(12)</sup>

#### Constant-field measurements

There was no detectable effect of a 7-T magnetic field on the yield strength at 4 K of either the 304 or 310 alloys. However, the data scatter is large, and the application of the magnetic field would not necessarily produce changes of flow strength in excess of the scatter of yield strength values. This confirms the findings of Bolshutkin, Desnenko, and Ilichev<sup>(9)</sup> who also could not detect any distinction between zero field and 3.4-T field tensile properties at 4 K for a series of Fe-18Cr-8 to 25Ni alloys.

The magnetic field did not significantly affect the initiation of discontinuous yielding in the cold-drawn 310 alloy. No discontinuous yielding was observed in the annealed 310 alloy to strains of 0.04. In contrast to the 310 alloy behavior, serrated yielding was observed at lower strains for annealed alloy 304, compared with a cold-drawn condition. Data related to the initiation of serrated yielding for alloy 304 (in terms of strains), contained in Table II, are not sufficiently reproducible to permit assessment of the role of applied magnetic fields.

#### Field switching measurements

Experiments were performed in switching the magnetic field from zero to 7 T and from 7 T to zero after the specimens had been partially deformed at 4 K and then unloaded and maintained at 4 K (see Fig. 2). On subsequent reloading after field switching no change of flow strength was observed in either alloy 304 or 310. That is, after application of field, there was no accompanying detectable increase or decrease of flow strength at 4 K. The measurement equipment was capable of detecting changes of about 0.2 percent in flow strength.

During the sequential on-off magnetic field tensile tests, the Young's modulus was measured while the specimen was unloaded and loaded. While absolute values varied for alloy 304 by about  $\pm 13$  percent for five separate specimens, the variation of each measurement on the same specimen is estimated to be  $\pm 1$  percent. The initial data were obtained after the first unloading, usually at plastic strains of 0.001 to 0.003. Subsequent measurements were obtained at field switchings, usually in strain increments of 0.002 to 0.003. The elastic modulus was found to decrease linearly with



Table II. AISI 304 Stainless Steel Wire\*

Test Temperature, K	Magnetic Field, T	Specimen Condition	Young's Modulus, GPa	Proportional Limit, MPa	Yield Strength (0.2% Offset), MPa	Strain <sup>†</sup> at Onset of Discontinuous Yielding	% Martensite % Elongation
295	0	CD	196	104	321	--	0
295	7	ANN	208	91	233	--	0
76	0	ANN	194	86	387	--	1.4
4.2	0	CD	206	138	448	1.60	0.1
4.2	7	CD	213	138	460	1.56	0.1
4.2	7	CD	192	124	470	1.10	0.2
4.2	0	ANN	217	124	623	0.39	2.1
4.2	0	ANN	212	145	575	0.55	2.5
4.2	0	ANN	212	145	538	0.63	1.3
4.2	7	ANN	209	107	480	0.86	1.6
4.2	7	ANN	217	121	529	0.90	1.7
4.2	7	ANN	214	169	614	0.53	1.6
4.2	0/7/0...#	ANN	230	148	523	0.71	1.8
4.2	7/0/7...	ANN	229	169	483	0.81	1.7

\* 0.64-mm diameter.

† ANN: annealed @ 1339K (1950 °F) for 30 min; CD: Cold Drawn (in as-received condition).

‡ All values of Young's modulus were taken at 0.5 - 1.0% strain by unloading and loading.

# Initially the test commenced with field off - at approximately every 0.5% elongation the field condition was alternated between on and off.

increasing plastic deformation in the range between 0.001 to 0.020 strain for both 304 and 310 alloys.

Because the absolute values of the Young's modulus had considerable scatter, the data were normalized to 0.010 strain to values of 210 GPa for alloy 304 and 206 GPa for alloy 310 at 4.2 K. (16) The adjusted Young's modulus data are plotted as a function of strain in Fig. 3 for both zero and 7-T fields. There is no distinction between zero and 7-T field measurements of Young's modulus. Both tend to scatter approximately equally above and below the linear trend line for alloy 304. There is a clear linear dependence of Young's modulus on strain within the strain interval to 0.020. Finally, the Young's modulus for alloy 310 depends slightly less on plastic deformation than for alloy 304.

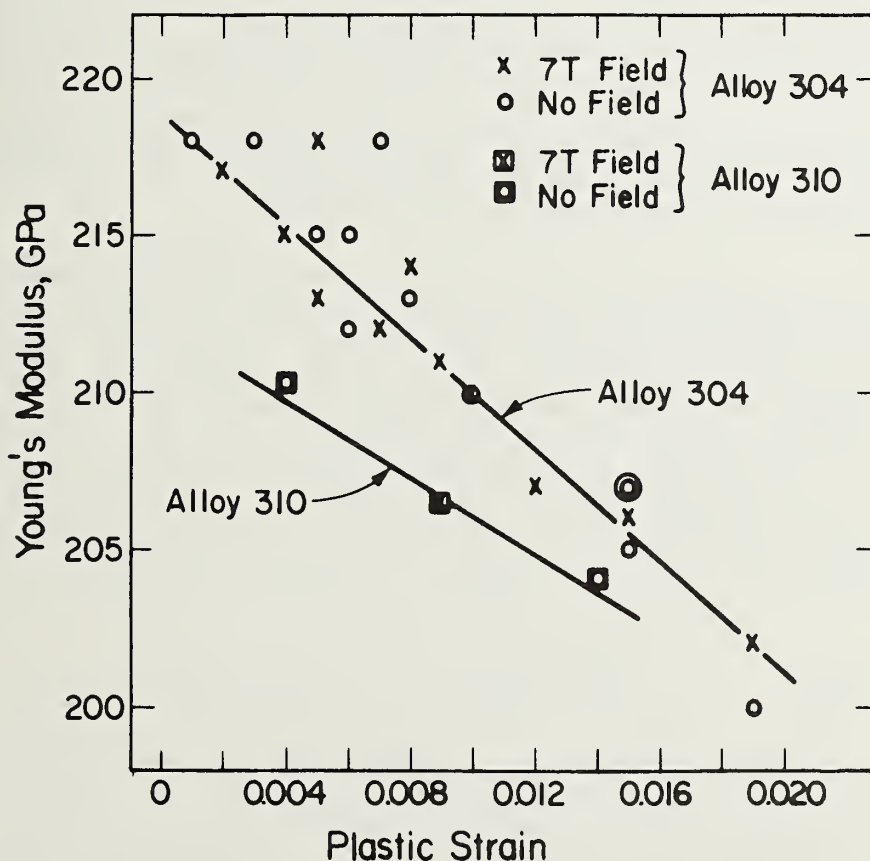


Fig. 3. Dependence of Young's modulus ( $E$ ), measured at 4.2 K, on specimen strain at 4.2 K for alloys 304 and 310 with zero and 7-T magnetic fields. Note that the absolute values of  $E$  are "normalized" to 210 GPa for alloy 304 and 205 GPa for alloy 310 at a strain of 0.010.

## DISCUSSION

No variation in Young's modulus ( $E$ ) with the application of a 7-T transverse magnetic field could be measured. Our Young's modulus measurement sensitivity between tests on a single specimen is estimated to be one percent. Considering that alloy 304 Young's modulus is about 210 GPa, and the measurement is made at flow stresses of about 600 MPa or less, the attendant total specimen strain is  $3 \times 10^{-3}$ . Changes of  $E$  of the order of 2.1 GPa (1 percent) would be reflected in changes of strain of  $3 \times 10^{-5}$ . It follows that the transverse magnetostriction of both alloys must be less than about  $\pm 3 \times 10^{-5}$  for our measurement system not to detect changes of  $E$ .

Similarly, it is unlikely that the magnetostriction of the body-centered cubic ( $\alpha'$ ) martensite phase contributes to distinctions between zero and 7-T field alloy 304 tensile measurements. Only about two percent martensite was detected. Transverse magnetostriction strain contributions of the  $\alpha'$  phase would need to be of the order of  $3 \times 10^{-5}$  per 2 percent martensite =  $1.5 \times 10^{-3}$  to change  $E$  by one percent. Changes of body-centered cubic and face-centered cubic transverse magnetostriction coefficients at room temperature are reported by Bozorth<sup>(17)</sup> not to exceed  $0.02 \times 10^{-3}$  throughout the Fe-Ni composition range.

The flow strength could possibly be influenced by magnetic field enhancement of  $\alpha'$  transformation that, in turn, affects specimen flow strength. The enhancement of  $\alpha'$  formation in Fe-Ni and Fe-Ni-Mn alloy systems has been discussed earlier and, therefore, it is likely that some minimum field strength, field orientation, and/or pulse frequency would produce more martensite transformation. Increased strain-induced  $\alpha'$  transformation is thought to play a significant role in modification of the low temperature stress-strain characteristics.<sup>(12,15)</sup> However, neither the martensite enhancement nor the modification of stress-strain behavior have been detected under the conditions of this experiment.

Finally, the dependences of the Young's modulus on plastic deformation at 4.2 K of both alloys are of interest and have not been previously reported. The linear reduction may either be caused by defect production (at 4.2 K neither point nor line defects can annihilate), by the effect of applied stress or defect production on antiferromagnetic domains or spin-glass clusters, or by dislocation unpinning. It would be of fundamental interest to accurately assess, at 4 K, the roles of applied stress and plastic deformation on elastic constants of austenitic steels.

## REFERENCES

1. Korenko, M. K. and Cohen, M., "Martensitic transformation in high magnetic fields," in Proc. Conf. on Martensitic Transformations, ICOMAT 1979, Massachusetts Institute of Technology, Cambridge, MA (1981), pp. 388-393.
2. Fokima, Y. A., Smirnov, L. V., and Sadovskiy, V. D., "Effect of a pulsating magnetic field on the position of the martensitic transformation range in steel," *Fiz. Met. Metalloved.*, Vol. 19, No. 4 (1965), pp. 592-595.
3. Fokima, Y. A., Smirnov, L. V., and Sadovskiy, V. D., "Destabilization of austenite by a strong pulsating magnetic field," *Fiz. Met. Metalloved.*, Vol. 19, No. 5 (1965), pp. 722-725.
4. Fakidov, I. G., Voronchikhin, L. D., Zavadskiy, E. A., and Barkhanov, A. M., "The variation in the magnetic intensity of austenitic steel exposed to a strong pulsating magnetic field," *Fiz. Met. Metalloved.*, Vol. 19, No. 6 (1965), pp. 852-857.
5. Vornochikhin, L. V. and Fakidov, I. G., "Determining the latent heat of the martensitic transformation induced by a magnetic field in steel," *Fiz. Met. Metalloved.*, Vol. 21, No. 3 (1966), pp. 436-441.
6. Malinen, P. A., Sadovskiy, V. D., and Sorokin, I. P., "Effect of magnetic field on the martensitic transformation in alloys of the  $N_{23}G_4$  type," *Fiz. Met. Metalloved.*, Vol. 24, No. 2 (1967), pp. 305-309.
7. Voronchikhin, L. D., Romashev, L. N., and Fakidov, I. G., "Influence of the initial state of austenitic steel on the martensitic transformation in a strong magnetic field," *Fiz. Met. Metalloved.*, Vol. 26, No. 5 (1968), pp. 948-951.
8. Malinen, P. A. and Sadovskiy, V. D., "Effect of magnetic field on the  $\epsilon$ - $\alpha$  transformation in Fe-Mn alloys," *Fiz. Met. Metalloved.*, Vol. 28, No. 6 (1969), pp. 1012-1017.
9. Bolshutkin, D. N., Desnenko, V. A., and Ilichev, V. Ya., "Low temperature plastic deformation of Fe-Cr-Ni steels in magnetic fields to  $2.71 \times 10^6$  AM-1," *Cryogenics*, Vol. 19 (1979), pp. 231-234.
10. Gotishcheve, V. I., Glinik, R. A., Petrovskii, M. L., and Khazov, V. N., "Effect of magnetic field on the plastic deformation of aluminum at 4.2 K," *JETP Letters*, Vol. 30, No. 2 (1979), pp. 92-96.
11. Lebedev, V. P., Khotkevich, V. I., Krylovskiy, V. S., and Philips, A. H., "Deformation of nickel in a steady magnetic field," *Fiz. Met. Metalloved.*, Vol. 48, No. 5 (1979), pp. 1108-1111.
12. Reed, R. P. and Tobler, R. L., "Deformation of metastable austenitic steels at low temperatures," R. P. Reed and A. F. Clark, eds., in Advances in Cryogenic Engineering-Materials, Vol. 28, Plenum Press, New York (1982), pp. 49-56.



13. Collings, E. W. and King, H. W., "Austenitic stainless steels as magnetic transition metal alloys, E. W. Collings and H. W. King, eds., in The Metal Science of Stainless Steels, Metallurgical Society (AIME), New York (1978), pp. 1-21.
14. Ekin, J. W., "Fatigue and stress effects in NbTi and Nb<sub>3</sub>Sn multifilamentary superconductors," in Advances in Cryogenic Engineering-Materials, Vol. 24, Plenum Press, New York (1978), pp. 306-316.
15. Reed, R. P. and Guntner, C. J., "Stress-induced martensitic transformations in 18Cr-8Ni Steel," Trans. AIME, Vol. 230 (1964), pp. 1713-1720.
16. Ledbetter, H. M., "Stainless-steel elastic constants at low temperatures," J. Appl. Phys., Vol. 52 (1981), pp. 1587-1589.
17. Bozorth, R. M., Ferromagnetism, Van Nostrand Co., New York (1951), p. 669.

FACTORS INFLUENCING THE LOW-TEMPERATURE DEPENDENCE OF YIELDING  
IN AISI 316 STAINLESS STEELS\*

R. L. Tobler, D. H. Beekman, and R. P. Reed  
Fracture and Deformation Division  
National Bureau of Standards  
Boulder, Colorado

ABSTRACT

Tensile tests at temperatures between 323 and 4 K were performed on one heat of AISI 316 austenitic stainless steel having the composition Fe-17.34Cr-12.17Ni-1.55Mn-2.16Mo-0.051C. The temperature dependences of the yield and flow strengths at plastic strain increments from 0.2 to 3.65 % are analyzed. At the yield strain (0.2 %), no body-centered cubic (bcc) martensite phase transformation is detected. At higher strains ( $\sim 3.2 \pm 0.6$  %), bcc martensite forms from the parent austenite phase at test temperatures below 175 K, but there are no discontinuities in the temperature dependence of flow strength. A review of data available for three heats of AISI 316 at temperatures between 973 and 4 K reveals that deviations from thermally-activated plastic flow theory occur at temperatures below 175 K, apparently depending on heat-to-heat compositional variations. Grain size and magnetic transition effects on the yield strength are discussed.

\* To be published in Austenitic Steels at Low Temperatures, Eds. R. P. Reed and T. Horiuchi, Plenum Press, New York (1983).



## INTRODUCTION

The mechanical behavior of the AISI 300 series austenitic stainless steels over a broad range of temperatures is a subject of interest to designers of superconducting and nuclear energy devices. In this paper, factors influencing the initial yielding and stress-strain behavior of AISI 316 stainless steel are described. AISI 316 stainless steel is a metastable Fe16-18Cr, 10-14Ni, 1Mo steel that may undergo a partial austenite-to-martensite phase transformation during deformation at low temperatures, the probability of which increases with increasing strain, decreasing temperature, and decreasing alloy content.

When transformation occurs in Fe-Cr-Ni austenitic stainless steels, two martensitic phases may be formed: the hexagonal close-packed (hcp)  $\epsilon$  martensite and the body-centered cubic (bcc)  $\alpha'$  martensite. The  $\epsilon$  phase usually forms first, then  $\alpha'$  appears [1]. The  $\epsilon$  phase is difficult to detect in small quantities, whereas the  $\alpha'$  phase is ferromagnetic and easy to detect using a magnetometer [2]. For AISI 316, it is reported that no  $\alpha'$  forms spontaneously on cooling to 4 K, but up to 50%  $\alpha'$  forms on straining to failure at 4 K [3].

The published data [4-9] for AISI 316 indicate substantial heat-to-heat variations in yield strength at cryogenic temperatures, presumably due to the broad range of chemical composition allowed in the material specifications. The explanation of such variation is complicated because there has been no systematic study and investigators have not always reported the complete details of material



characterization and test procedure. In particular, the effects of grain size and martensitic phase transformation have never been thoroughly evaluated at cryogenic temperatures.

Soviet authors [10,11] report the existence of three anomalies in the temperature dependence of the yield strength for Fe-18Cr-xNi austenitic stainless steels containing 8, 10, or 20% Ni. These anomalies amount to sharp decreases of the yield strength on the order of 100 MPa, occurring over narrow temperature intervals. The first anomaly occurs between 20 and 4 K and is unexplained. The second anomaly occurs at temperatures between 60 and 35 K and is attributed to the Néel transition (magnetic ordering). The third anomaly occurs in metastable alloys (lower Ni) at temperatures in the martensitic phase transformation range. One aim of this paper is to determine whether such anomalies are evidenced in AISI 316.

Of particular interest is the initiation of martensitic phase transformation, because there is apparently conflicting evidence on its role in affecting the low-temperature yielding and flow behavior of metastable stainless steels. Suzuki et al. [12], measuring the temperature dependence of the 0.2% offset yield strength in an Fe-18Cr-9Ni stainless steel, report a significant decrease in flow strength when the test temperature is lowered from about 260 K. They argue that  $\epsilon$  martensite forms at lower temperatures, reducing the flow strength. Following  $\epsilon$  martensite formation,  $\alpha'$  martensite forms at slip-plane intersections and the  $\alpha'$  lathes along  $\langle 110 \rangle$  act as windows for dislocation pileup release; the result is an "easy-glide" (work-softening) region of the stress-strain curve. This "easy-glide" region had previously been reported by Reed and Guntner [13], who argued that it was caused by strain-induced  $\epsilon$  martensite, since their x-ray and transmission electron microscopy data for an Fe-18Cr-8Ni alloy indicated an increasing concentration of  $\epsilon$  during easy glide. In contrast, Olson and Azrin [14], studying an Fe-9Cr-8Ni alloy, found an excellent correlation between flow strength reduction at lower temperatures and the initiation of  $\alpha'$  martensite. In their experiments,  $\alpha'$  martensite was induced by elastic stresses at low temperatures with attendant reduction of yield strength. The low-temperature martensite transformation was suggested to be stress assisted and to originate from existing nucleation sites. No "easy-glide" region of the stress-strain curve was observed.

To study the above effects, continuous flow-strength measurements as a function of temperature are described here, as an extension of previous work [4]. AISI 316 stainless steel was selected because it exhibits strain and temperature ranges where no martensite forms, while at lower temperatures, body-centered cubic martensite forms at larger strains.

## MATERIALS

The AISI 316 stainless steel tested in this study was obtained in the form of a 38-mm-thick plate. Tensile specimens were machined in the longitudinal orientation in the form of flat coupons having a 50.8-mm gage length and a 2.54-mm x 4.77-mm-gage cross section. The machined specimens were annealed at 1338 K for 0.5 h, producing a Rockwell B ( $R_B$ ) hardness of 71 and an average grain diameter of 55  $\mu\text{m}$  (ASTM grain size number 5.5). The chemical compositions of this steel (denoted heat 2) and other AISI 316 steels referred in this paper are listed in Table 1.

## PROCEDURE

Tensile tests were performed on (1) as-machined and annealed or (2) strained and recrystallized material. The strained and recrystallized material was used to determine grain-size effects. All tensile tests were performed at a crosshead rate of 8.5  $\mu\text{m/s}$  using a screwdriven machine and cryostat [1,16]. Test temperatures of 4 and 76 K were achieved with baths of liquid helium and liquid nitrogen. Other temperatures were achieved by controlled thermal conduction using liquid nitrogen reservoirs and heating wires attached to the specimen grips and load train. Current to the heating wires was varied until thermal equilibrium was reached at the specified test temperature, which was accurate to  $\pm 1.5$  K.

Load-versus-deflection curves were recorded with a commercial load cell and clip-gage extensometer. Clip-gage extensometers permit measurement and magnification of the specimen strain within the (2.5-cm) gage length. Estimated flow-strength measurement inaccuracies are  $\pm 1\%$ , but specimen-to-specimen variations

Table 1. Chemical composition (weight percent) for AISI 316 steel heats referred to in this study.

Heat No. & Reference	Fe	Cr	Ni	Mn	C	P	S	Si	Cu	Mo	Co	N
1 [4]	balance	17.25	13.48	1.86	0.057	0.024	0.019	0.58	--	2.34	--	0.03
2 this study	"	17.34	12.17	1.55	0.051	0.026	0.014	0.68	0.34	2.16	0.19	--
3 [5]	"	16.72	11.27	1.52	0.05	--	--	0.32	--	2.58	--	--
4 [15]	"	17.46	12.93	1.77	0.062	0.030	0.020	0.56	--	2.20	--	--

including both material and measurement variations) may reach  $\pm 5\%$ . As an indication of data scatter, seven tests were performed on the AISI 316 steel at 76 K, resulting in an average yield strength ( $\sigma_y$ ) of 448 MPa and an overall spread of  $\pm 7$  MPa. After plastic strains of 0.002 to 0.038 (mm/mm), the specimens were unloaded, warmed to 295 K, and examined for the presence of ferromagnetic  $\alpha'$  martensite using a torsion-bar magnetometer [2]. X-ray diffractometer measurements were used to try to detect small concentrations of  $\epsilon$  martensite. No  $\epsilon$  was detected and our estimated sensitivity is 2%.

Grain-size variations were obtained by recrystallization treatments. Tensile specimens were plastically strained 20 to 30% at 295 or 76 K and then annealed for 0.25 to 0.5 h in an argon atmosphere at 1233 to 1573 K. These treatments produced grain sizes ranging from 22 to 140  $\mu\text{m}$ . After the recrystallization treatments, the specimen surfaces were cleaned by electropolishing. The recrystallization treatments increased the scatter of yield-strength measurements at 76 K to about  $\pm 15$  MPa. Texture effects were neglected.

A few experiments were performed on the annealed AISI 316 stainless steel to evaluate the strain rate effect. Increasing the crosshead rate by a hundredfold from 0.85  $\mu\text{m/s}$  to 85  $\mu\text{m/s}$  increased the flow strength at strains lower than 0.01 by increments of 6% at 295 K and 3% at 76 K. The effect at 4 K was negligible. Therefore, strain rate does not play a significant part in explaining the variability of results noted in the text.

The  $M_d$  temperature and strain-hardening coefficients were measured after loading a series of specimens to 0.027 or 0.037 plastic strain at low temperatures. The percent  $\alpha'$  was measured at 295 K using a magnetometer; then the  $M_d$  temperature was obtained by extrapolating a plot of  $\alpha'$  per unit strain versus temperature. The strain-hardening coefficients ( $n$ ) at each test temperature were measured as the slope of the  $\log \sigma$ -versus- $\log \epsilon$  plots. Such plots are nearly linear, but only for small strain increments. The values of  $M_d$  and  $n$  apply only for the strain levels studied in this paper.

## RESULTS

The tensile yield strength ( $\sigma_y$ ) and initial stress-strain behavior of the Fe-17Cr-12Ni-2Mo alloy were measured as a function of temperature. Grain size, martensitic transformation, and strain-hardening effects are described in this section.

Table 2. Yield strength measurements at 0.002 plastic strain obtained for AISI 316 (heat 2) of this study.

Test Temperature, T, K	Yield Strength, $\sigma_y$ , MPa*
323	185
295	204
295	198
295	198
240	244
215	281
194	298
192	306
190	307
164	349
154	368
143	380
125	399
100	428
76	456
76	451
76	445
76	450
76	441
76	447
76	448
60	456
39	487
23	528
4	537
4	527

\*To convert from MPa to ksi, divide by 6.895.

### Temperature

Twenty-six  $\sigma_y$  measurements were obtained for annealed AISI 316 stainless steel (heat 2) at seventeen temperatures between 323 and 4 K (Table 2). Magnetometer inspections of the specimens indicated no  $\alpha'$  martensitic transformation for this heat after 0.002 plastic strain, regardless of test temperature. The  $\sigma_y$  data between 295 and 4 K are plotted and compared with previously published data [4-9] in Fig. 1. This figure illustrates significant heat-to-heat variations of  $\sigma_y$ , with considerably greater differences at cryogenic temperatures than at room temperature.



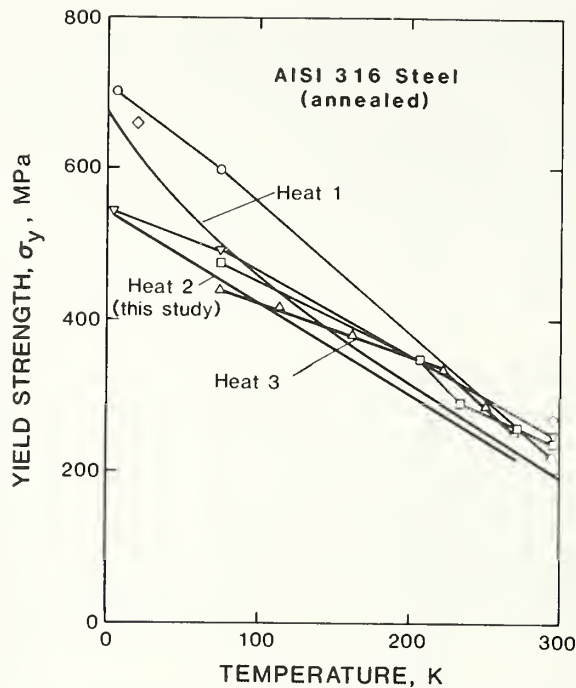


Fig. 1. Yield strength of AISI 316 stainless steels at low temperatures, illustrating heat-to-heat variability. Heat 1 is from Tobler et al. [4]; heat 3 is from Sanderson and Llewellyn [5]. Other data: o - Read and Reed [6];  $\diamond$  - Baughman [7];  $\nabla$  - Tobler et al. [8];  $\square$  - Hoke et al. [9].

To evaluate the data it is first necessary to characterize the temperature dependence. Several references cited in Fig. 1 report data at only a few test temperatures, whereas the functional dependence of  $\sigma_y$  on temperature can be properly identified only by extensive measurements over a broad temperature range. Therefore, relevant data for three heats of AISI 316 are replotted in Fig. 2, which shows that  $\sigma_y$  increases progressively as temperature is lowered. Despite minor variations of grain size, strain rate, and composition, the  $\sigma_y$  values for the three heats exhibit parallel trends between 922 and 175 K, where the test-temperature intervals from different studies overlap. Below 175 K, significant variations of strength and cross-over effects begin to emerge. At still lower temperatures, the variations become more obvious until, at 76 K,  $\sigma_y$  correlates with composition: Fe-17.25Cr-13.47Ni (heat 1) exhibits the highest strength, Fe-17.34Cr-12.17Ni (heat 2) exhibits intermediate strength, and Fe-16.72Cr-11.27Ni (heat 3) exhibits the lowest strength. The evidence that this is a true effect of alloy composition is considered in a later section.

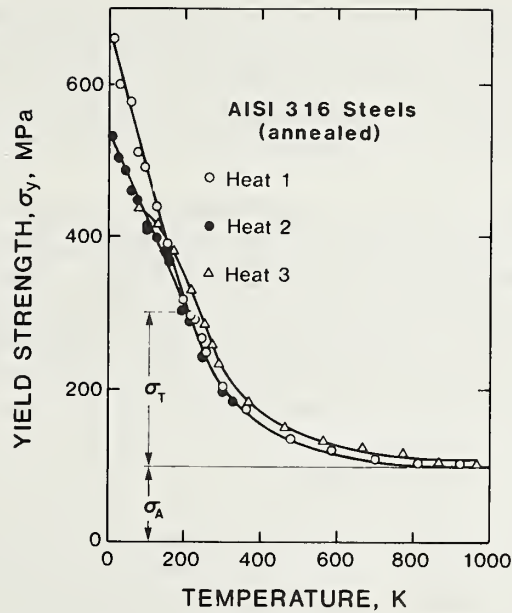


Fig. 2. Yield strength data for AISI 316 stainless steels in the elevated-to-cryogenic temperature range, illustrating overall temperature dependence. The symbols  $\sigma_T$  and  $\sigma_A$  are defined in the Discussion. Heat 1 - Tobler et al. [4]; heat 2 - this study; heat 3 - Sanderson and Llewellyn [5].

Strength variations may arise between specimens from a single heat of steel owing to inhomogeneity or thermomechanical processing effects. As shown in Fig. 1, Read and Reed's data [6] for a 316 stainless steel at 295, 76, and 4 K are 5 to 17% higher than the results of Tobler et al. [4], who tested the same heat. In the former study, the specimens were tested in the as-machined condition, whereas the specimens in the second study were re-annealed (1289 K, 1 h) after machining. This step reduced the hardness at 295 K from  $R_B 79$  to  $R_B 75$  and lowered  $\sigma_y$  by increasing the grain size slightly and removing any residual cold work from the fabrication or machining processes. This effect was also observed by Sikka [17].

#### Grain size

Figure 3 illustrates the effect of grain size on  $\sigma_y$  at 295, 76, and 4 K. The data at each temperature fit an inverse square root dependence on the average grain diameter,  $d$ , in reasonable accord with the Hall-Petch equation:

$$\sigma_y = \sigma_i + kd^{-1/2} \quad (1)$$

Here  $\sigma_i$  refers to the flow strength in the absence of grain boundaries (the "friction stress") and  $k$  is the slope of the  $\sigma_y$ -versus- $d^{-1/2}$  plot and indicates the grain boundary dependence of the yield strength. The values of  $\sigma_i$  and  $k$  are given in the figure for each test temperature (295, 76, and 4 K).

Although the grain size effect is significant at low temperatures, it alone is not sufficient to account for the wide variation in properties for different heats. For example, heat 1 ( $d = 67 \mu\text{m}$ ) has a higher yield strength than heat 2 ( $d = 55 \mu\text{m}$ ) at 4 K, despite its larger grain size. This supports the discussion to follow: that a significant portion of the strength variations at 4 K is due to alloy composition.

#### Martensitic transformation

Specimens (heat 2) deformed at low temperatures were measured using a magnetometer, but no  $\alpha'$  martensite was detected after 0.002 plastic strain. To induce measurable transformation, a series of specimens were loaded to higher strains at 76 K. Figure 4 presents the measured data of the strain dependence of  $\alpha'$ . A plastic strain of about 0.022 is necessary for  $\alpha'$  to form

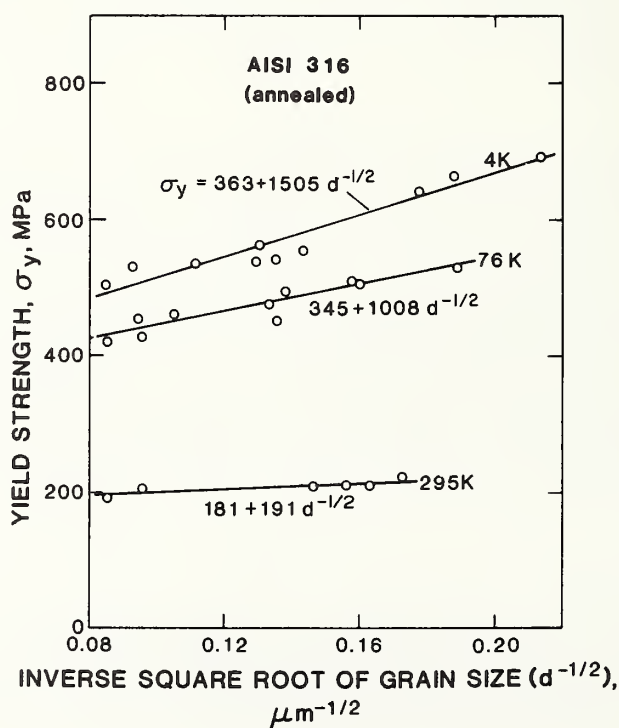


Fig. 3. Effect of grain size on the yield strength at three test temperatures for the Fe-17Cr-12Ni-2Mo alloy.

at 76 K. The dependence of  $\alpha'$  on plastic deformation is linear, at least to 0.05 strain. At larger strains, the dependence apparently increases (more  $\alpha'$  forms per unit strain) since fractured specimens show between 44 and 52%  $\alpha'$  at uniform strains of 0.4 to 0.5.

The relationships between flow stress, plastic deformation, and temperature are presented in Figs. 5 and 6, and Fig. 7 illustrates the experimental method of  $M_d$  determination. From Fig. 7, the quantity of  $\alpha'$  martensite formed after 0.037 plastic strain is negligible for test temperatures between 323 and 175 K. Below 175 K,  $\alpha'$  forms in increasing amounts, and the percent  $\alpha'$  martensite per unit strain is linearly dependent on test temperature. The curves of Figs. 5 and 6 represent specimens in various degrees of transformation, containing from 0 to 10%  $\alpha'$  martensite per unit strain, but the stress-strain curves are regular and free from discontinuities. In other words, we see that the martensitic transformation in this steel apparently occurs gradually with no anomalous decrease of strength. These findings contrast with the behavior of Fe-18Cr-8Ni and Fe-18Cr-10Ni stainless steels that exhibit: (1) irregular yield and flow strength temperature dependences owing to the initiation of  $\epsilon$  and  $\alpha'$  phase transformations [10], and (2) suppression of  $\alpha'$  martensite at 4 and 20 K, compared with that at 76 K [13].

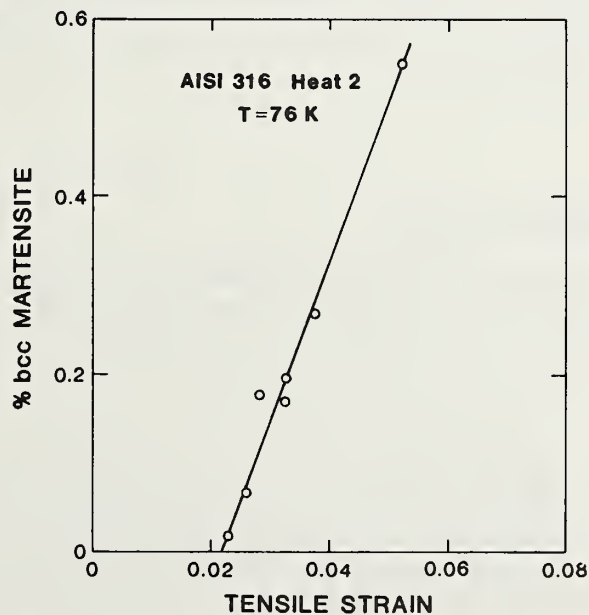


Fig. 4. Dependence of bcc ( $\alpha'$ ) martensite on tensile plastic strain. Martensite was detected by using a bar magnet and torsion balance beam.



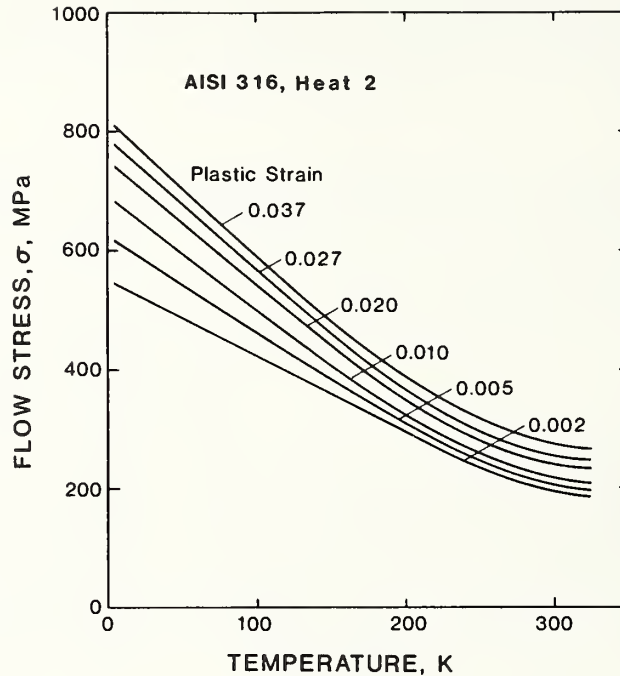


Fig. 5. Temperature dependence of the yield and flow stresses for AISI 316 stainless steels, showing no evidence of anomalies despite martensitic phase transformation occurring at higher strain increments and lower test temperatures.

#### Strain-hardening behavior

Two parameters of strain hardening,  $n$  and  $\Delta\sigma$ , are plotted versus temperature in Fig. 8. A simple and convenient measure of strain hardening is  $\Delta\sigma$ , taken as the difference in flow strength at plastic strains of 0.0275 and 0.002 ( $\Delta\sigma = \sigma_{0.0275} - \sigma_{0.002}$ ). The

$\Delta\sigma$  remains constant between 295 and 175 K, then increases below 175 K. From Figs. 7 and 8 we see corresponding trends for  $\Delta\sigma$  and the  $\alpha'$  transformation: both increase linearly with temperature below 175 K. The strain-hardening coefficient,  $n$ , exhibits a minimum when plotted versus temperature, and it also begins to increase at temperatures near 175 K. We conclude that the onset of  $\alpha'$  transformation in AISI 316 causes the increased strain hardening, and that the degree of strain hardening is proportional to the amount of  $\alpha'$  martensite formed at these low strains.

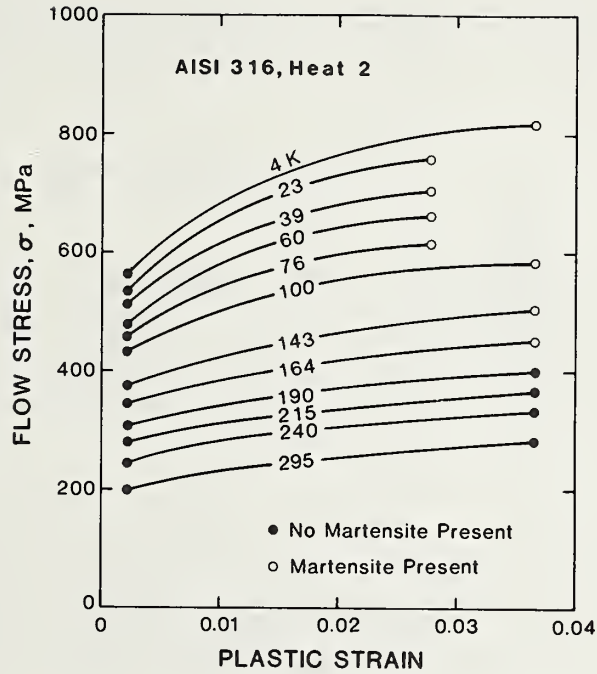


Fig. 6. Stress-strain curves for AISI 316 stainless steels at various test temperatures, showing no evidence of anomalies despite martensitic phase transformations occurring at higher strain increments and low temperatures.

## DISCUSSION

### Thermally activated flow

The behavior of  $\sigma_y$  for AISI 316 stainless steels is consistent with equations based on thermally activated plastic flow. According to Seeger [18],  $\sigma_y$  may be separated into two components:

$$\sigma_y = \sigma_A + \sigma_T \quad (2)$$

Here, the athermal component,  $\sigma_A$ , is a long-range stress-field contribution in which the stresses are large compared with thermal fluctuations and where  $\sigma_A/G$  ( $G$  = shear modulus) is independent of temperature. Other dislocations on parallel slip planes may contribute to  $\sigma_A$ . The thermal component,  $\sigma_T$ , is a short-range stress-field contribution in which the obstacles to dislocation movement may be overcome with the aid of thermal fluctuations.

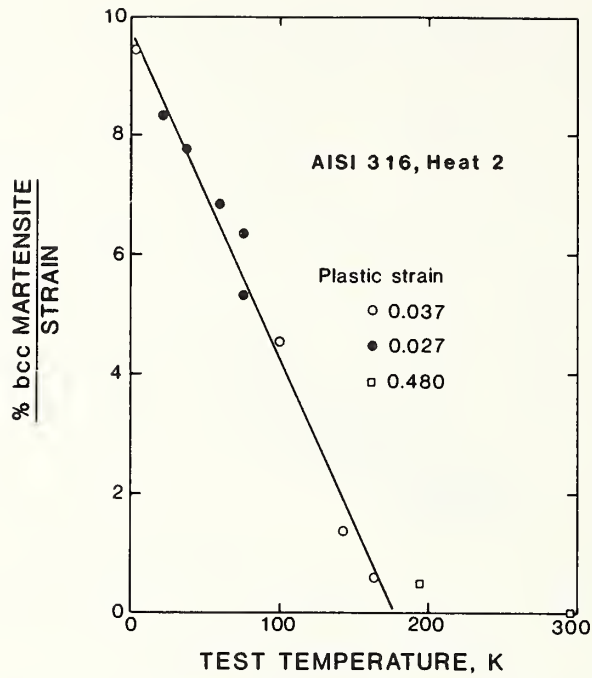


Fig. 7. Amount of bcc martensite per unit strain in AISI 316 specimens deformed to plastic strains of 0.0275 or 0.0365, indicating clear evidence of martensitic phase transformation at cryogenic temperatures. Extrapolated temperature of 0% bcc martensite is about 175 K.

Contributions to the short-range stress fields come from forest dislocations, solute atoms, small jogs in dislocations, and the Peierls-Nabarro stress [19].

In Fig. 9 the  $\sigma_y$  data for the three AISI 316 steels have been normalized to the shear modulus and plotted versus temperature, which is normalized to the melting point,  $T_M = 1658$  K. (Shear modulus data at cryogenic temperatures were taken from Ledbetter [15] and at elevated temperatures from Moore [20]). These data indicate that  $\sigma_T$  becomes active at temperatures lower than about  $1/3 T_M$ . The divergences of the thermal components at low temperatures are observable in Fig. 2.

The following expression derives from thermodynamics and thermally activated plastic flow theory [21]:

$$\sigma_T = (\sigma_0 - \sigma_A) \exp(-CT) \quad (3)$$

Here  $\sigma_0$  is the extrapolated value of  $\sigma_y$  at zero temperature and  $C$  is a materials constant related to activation energy. A complete expression of  $\sigma_y$  is then:

$$\sigma_y = \sigma_A + (\sigma_0 - \sigma_A) \exp(-CT) \quad (4)$$

In a study of alternative equations and curve-fitting techniques, Tobler showed that Eq. (4) best characterized the  $\sigma_T$ -versus- $T$  data for AISI 316 [4]. In this equation, the  $\sigma_A$  values require no correction for the shear modulus, but are estimated from  $\sigma_y$  at elevated temperatures (Fig. 2). The estimates for heats 1, 2, and 3 are 100, 95, and 113 MPa, respectively.

Data that agree with Eq. (4) exhibit a linear trend when plotted using semilogarithmic coordinates, assuming a single rate-controlling thermally activated plastic flow mechanism is operative over the entire temperature interval. Or, if different processes are rate controlling for specific temperature intervals, the trend will consist of several linear segments.

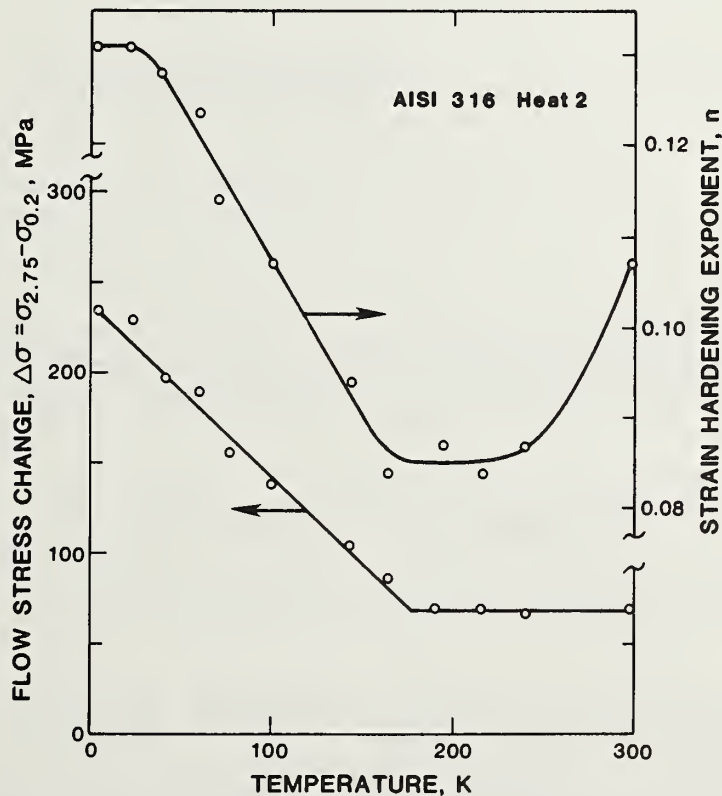


Fig. 8. Temperature dependence of strain-hardening parameters.



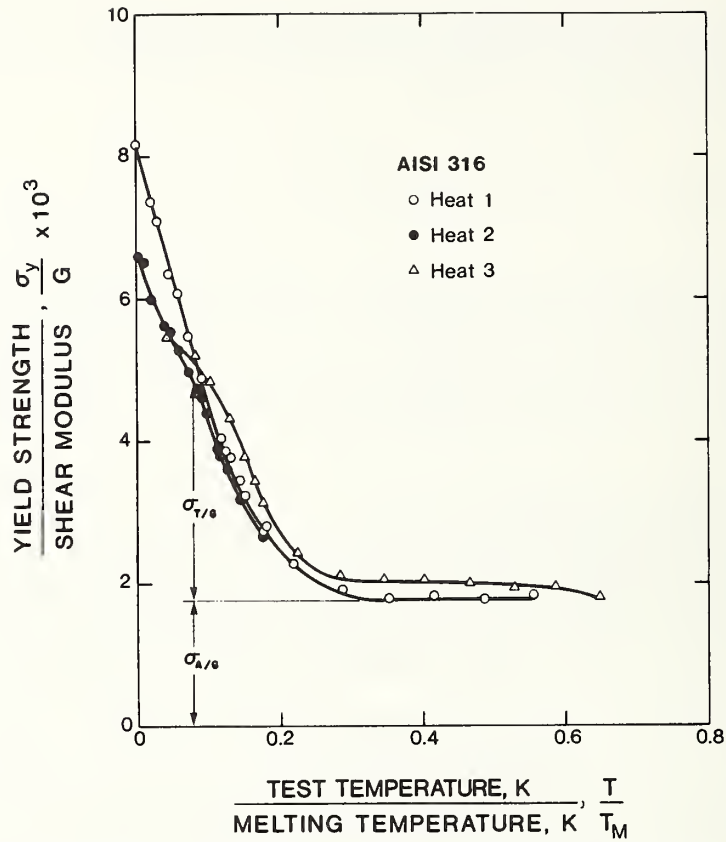


Fig. 9. Normalized yield strength versus normalized temperature for three AISI 316 stainless steel heats, showing variations in thermal and athermal stress components.

As illustrated in Fig. 10, Eq. (4) does adequately characterize the data at elevated and cryogenic temperatures. The data for all three heats can be fit using bilinear trends, where a slope transition occurs at about 60, 150, or 175 K, depending on the heat.

The main trend of data for heat 1 fits the expression:

$$\sigma_y = 100 + 700 \exp(-6.2 \times 10^{-3} T) \quad (5)$$

Deviation from this equation begins at about 60 K, reflecting a change in the exponential.

One consequence of the slope transition is that  $\sigma_0$  is lower (17 and 33% for heats 1 and 2) than would otherwise be the case.

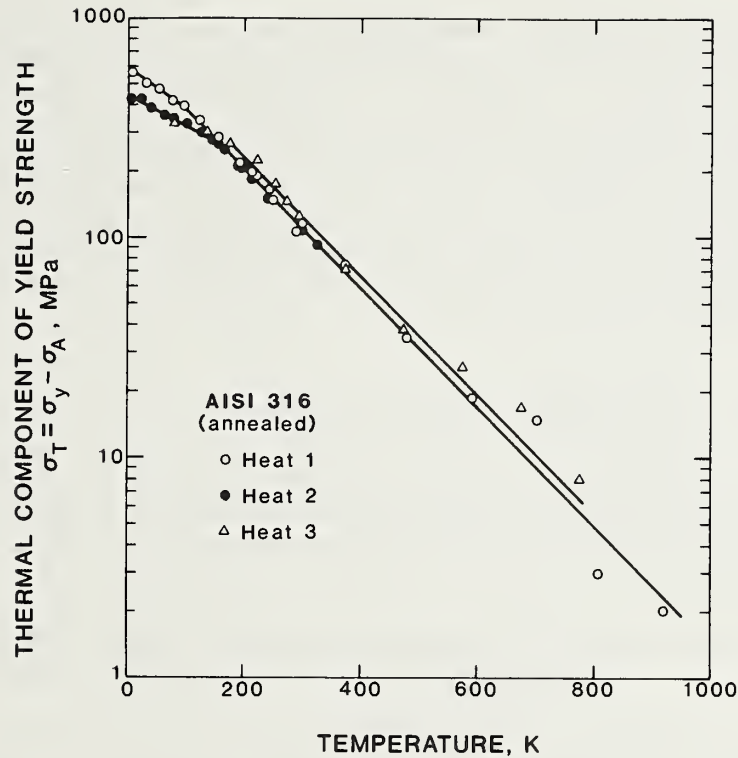


Fig. 10. Temperature dependence of the thermal-stress component, illustrating applicability of thermally activated plastic flow theory at temperatures between 900 and 175 K.

This has practical implications for alloy design. For example, in applications requiring maximum strength at extreme cryogenic temperatures, it would be desirable to suppress or eliminate the inflection point in  $\ln \sigma_T$  for these steels. Our data indicate that this can be done by raising the Ni content to the maximum allowable limit of the material specification.

What can be said about the cause of the slope transitions in Fig. 10? It was suggested previously that dislocation tunneling, magnetic ordering, and adiabatic heating processes may affect  $\sigma_y$  at temperatures approaching absolute zero [4]. But, since these processes are not operative above 60 K, they cannot account for the deviations observed in heats 2 and 3 at 150 and 175 K.

A more plausible explanation is that the deviations represent a change in mechanism of plastic deformation, which relates to alloy composition. As noted in Fig. 10, the deviations in  $\sigma_T$  for heats 1, 2, and 3 occur at about 60, 150, and 175 K, respectively. This sequence follows the order of decreasing alloy

content (Table 1), decreasing stacking fault energy (Table 3), and decreasing crystal structure stability, as indicated by the  $M_s$  and  $M_d$  temperatures (Table 3). Therefore, it is possible that a second thermally activated deformation mechanism having a lower activation energy becomes rate controlling at low temperatures. If so, a change of slopes as in Fig. 10 would be expected. This could be the case in the present study if faulting of the austenite occurred at low temperature, or if  $\epsilon$  phase formed in quantities too low to be detected. The possible martensite roles are discussed in the next section.

#### Role of martensitic transformation

Martensitic transformations may have the following effects on the low-temperature deformation of AISI 316 alloys: (1) they may be responsible for the slope transitions in plots of  $\ln \sigma_T$  versus

Table 3. Calculated stacking fault energies (SFE) and  $M_s$ ,  $M_d$ , and  $T_N$  temperatures for AISI 316 steel heats of this study.

Heat No. & Reference	SFE, <sup>a</sup> mJ/M <sup>2</sup>	$M_s$ , <sup>b</sup> K	$M_d$ , <sup>c</sup> K	$T_N$ , <sup>d</sup> K
1 [4]	32.3	-226	190	24.7
2 this study	29.3	-126	232	25.5
3 [5]	27.8	- 47	246	7.4
4 [19]	NA	NA	NA	26.4

a. Room temperature values, calculated from equation (1) of Rhodes and Thompson [22]. (The SFE is expected to decrease at lower temperatures).

b.  $M_s$  is the temperature at which martensite starts forming spontaneously on cooling, as calculated from the equation of Larbalestier and King [23].

c.  $M_d$  is the temperature above which no deformation induced martensite is possible, as calculated from the equation of Williams et al. [24].

d.  $T_N$  is the temperature of the onset of antiferromagnetic ordering, as calculated from the equation of Warnes and King [25].

temperature below about 175 K, and (2) they may influence the stress-strain behavior at sufficient strain ( $>0.02$ , Fig. 4) and low temperature ( $>175$  K, Fig. 7).

To provide a relative indication of the austenite stability, the  $M_s$  and  $M_d$  temperatures (Table 3) were calculated on the basis of the Cr, Ni, Mn, Si, C, and Mo contents. The calculated  $M_s$  values are negative, indicating complete stability on cooling to absolute zero, which is consistent with the fact that no  $\alpha'$  martensite was detected after cooling to 4 K. The calculated  $M_s$  and  $M_d$  temperatures are only approximate and relative guides to the behavior of the AISI 316 steels at cryogenic temperatures. Comparison of the measured and calculated  $M_d$  values for heat 2 shows considerable disparity, the calculated value being 57 degrees too high. Absolute agreement is not achieved because the predictive equations were developed on lower alloy steels, in compression tests, for specific levels of martensite, and without consideration of trace element effects. Moreover the  $M_d$  temperature is rather loosely defined, because high strains will produce some transformation at higher temperatures (see the 195-K datum, Fig. 7).

First, it is unlikely that the  $\alpha'$  transformation can account for the observed slope transitions (Fig. 10), since no  $\alpha'$  martensite was detected at the yield strength (0.002 plastic strain). From Fig. 4 it is apparent that no  $\alpha'$  is expected to form at 76 K until a plastic strain of about 0.02 is reached. However, it is possible that martensitic transformation involving small amounts of  $\epsilon$  phase or austenite faulting prior to  $\alpha'$  transformation may be responsible. From Table 3, the calculated stacking-fault energies decrease, but remain positive, with increased deviation of  $\sigma_T$ , as illustrated in Fig. 10. This possibility could not be confirmed, however, since our metallographic and x-ray inspection methods lacked the required sensitivity to detect less than 2% of  $\epsilon$ .

Second, martensite transformations usually influence deformation characteristics. In the commercial Fe-18Cr-8Ni austenitic stainless steel (AISI 304), the  $\epsilon$  and  $\alpha'$  martensitic products apparently contribute to the anomalous temperature dependence of  $\sigma_y$  and to the "easy-glide" portion of the stress-strain curves at temperatures near 77 K [12,13,26]. However, Figs. 4 through 7 suggest that in the alloy of this study (Fe-17Cr-12Ni-2Mo), the temperature dependence of the flow strength (including  $\sigma_y$ ) monotonically increases with strain, and therefore, the  $\alpha'$  martensitic product does not cause anomalous behavior.

With respect to the role of martensitic products in affecting the temperature dependence of the flow strength of Fe-Cr-Ni alloys



at low temperatures, there are two schools of thought: Suzuki et al. [12] argue that the  $\epsilon$  phase causes a reduction of  $\sigma_y$  at low temperatures since in their study  $\alpha'$  martensite was detected only at stresses considerably greater than  $\sigma_y$ . They have argued from metallographic evidence that  $\epsilon$  martensite forms at stress levels near the measured  $\sigma_y$ . Additionally, during the easy-glide portion of the stress-strain curve for their Fe-18Cr-8Ni alloy at low temperatures, they detect  $\alpha'$  martensite and find that it typically forms at slip-band intersections. The reduced flow strength in the easy-glide region is attributed to the strain-induced  $\alpha'$  transformation that forms at slip-band intersections and acts as "windows" for dislocation pileups. Conversely, Olson and Azrin [14] studied a less stable Fe-9Cr-8Ni alloy and obtained excellent correlation between the temperature dependence of  $\sigma_y$  and the flow strength at which  $\alpha'$  martensite was first detected.<sup>y</sup>

From our study, it is apparent that the onset of strain-induced  $\alpha'$  martensite in austenitic Fe-Cr-Ni alloys does not necessarily lead to a reduction of the flow strength at low temperatures. Rather, the formation of  $\alpha'$  in our Fe-17Cr-12Ni steel served simply to cause higher rates of strain hardening. Therefore, in the Fe-Cr-Ni alloy system, great significance attaches to alloy composition, and especially to Ni contents in the range 8 to 14%. This finding raises the question of the nature of the strain-induced martensitic product or products that form(s) during plastic deformation. Conflicting parametric studies and lack of conclusive microscopy at this time preclude a final assessment of the role of  $\epsilon$  and  $\alpha'$  martensites in affecting low-temperature flow strength.

The relationship between the "normalized" percent bcc martensite (percent magnetic martensite divided by plastic strain) and temperature (Fig. 7) deserves additional experimental clarification. It is implied that the temperature of about 175 K represents the onset of strain-induced martensite, and at higher strains and temperatures little magnetic product phase is detected. This behavior was substantiated by a few tests to fracture at 195 and 295 K (Fig. 7). However, the nature of the family of curves that could be generated by taking data at larger strains remains undefined. Similar data for AISI 304 steel indicate the existence of a constant temperature of  $\alpha'$  initiation [27], but a gradual deviation from linearity at larger strains.

#### Role of grain size

Data on the grain-size effect on the yield strength of austenitic stainless steels are rare. The room temperature data of this study indicate a very slight effect, as evidenced by the

low  $k$  value of  $191 \text{ MPa} \cdot \mu\text{m}^{-1/2}$ . This value is in reasonable agreement with the  $221 \text{ MPa} \cdot \mu\text{m}^{-1/2}$  value obtained by Norstrom [28] for a 316L stainless steel. Low  $k$  values are typical for face-centered cubic alloys at room temperature. At cryogenic temperatures, however, the grain-size effect increases significantly. As shown in Fig. 3, the values of  $\sigma_i$  and  $k$  at 4 K are greater by factors of 2 and 5, respectively, than the values at 295 K.

In Fig. 11, the temperature dependences of  $k$  and  $\sigma_i$  from Eq. (1) are plotted, using the 4- to 295-K data from this study combined with the 295- to 875-K data of Norstrom [28]. The  $k$  is strongly temperature dependent at low temperatures, but insensitive to temperature above room temperature. The stress,  $\sigma_i$ , increases markedly with decreasing temperature for temperatures lower than about 500 K. These data clearly imply that grain size has a significant effect on low-temperature flow strength. From

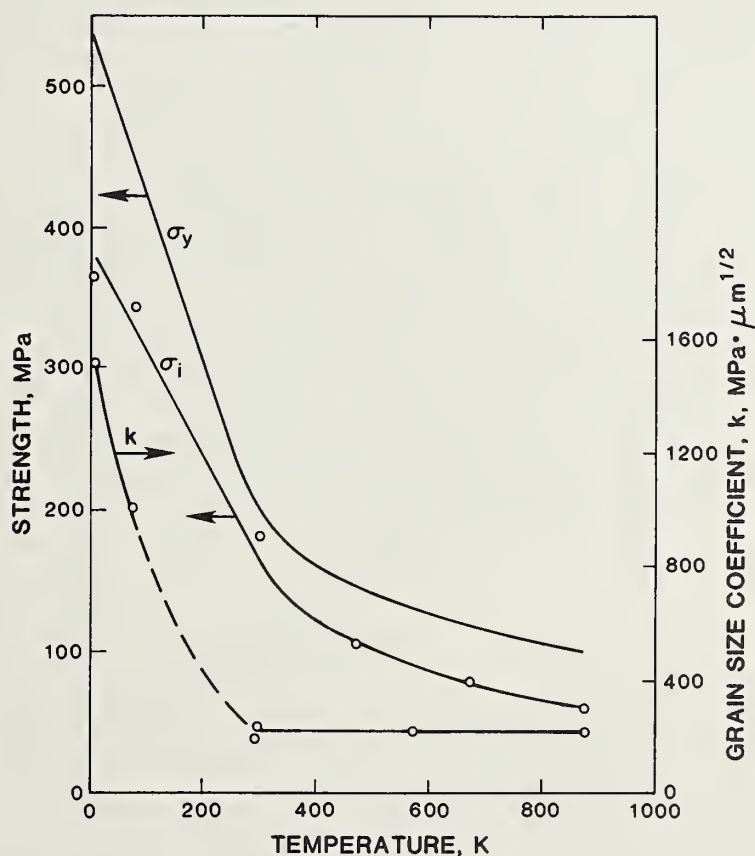


Fig. 11. Dependence of the tensile yield strength,  $\sigma_y$ ; the Hall-Petch parameter,  $k$ ; and the friction stress,  $\sigma_i$ , for AISI 316 steel. High-temperature  $\sigma_i$  data from Norstrom [28] are adjusted to 0.04 weight percent nitrogen.

Fig. 11, the quantity  $(\sigma_y - \sigma_i)$  represents the grain-boundary contribution to flow strength<sup>i</sup> and about 30% of  $\sigma_y$  at 4 K is contributed by grain-boundary strengthening.

#### Role of magnetic transition

Similar to other Fe-Cr-Ni austenitic stainless steels, AISI 316 undergoes a magnetic ordering phenomenon characterized by a change from the paramagnetic to the antiferromagnetic state at low temperatures. Accordingly, a peak occurs in the temperature dependence of magnetic susceptibility at  $T_N$ , the Néel transition temperature, which corresponds to the onset<sup>N</sup> of antiferromagnetic ordering.

Since a decrease of elastic constants occurs at  $T_N$  [29,30], it was suggested that the Néel transition also affects<sup>N</sup> dislocation motion and hence tensile properties [10,11]. On the basis of Soviet experimental data [10,11] for related steels, a sharp decrease of  $\sigma_y$  of about 100 MPa would be expected for our Fe-17Cr-12Ni alloy at  $T_N$ .

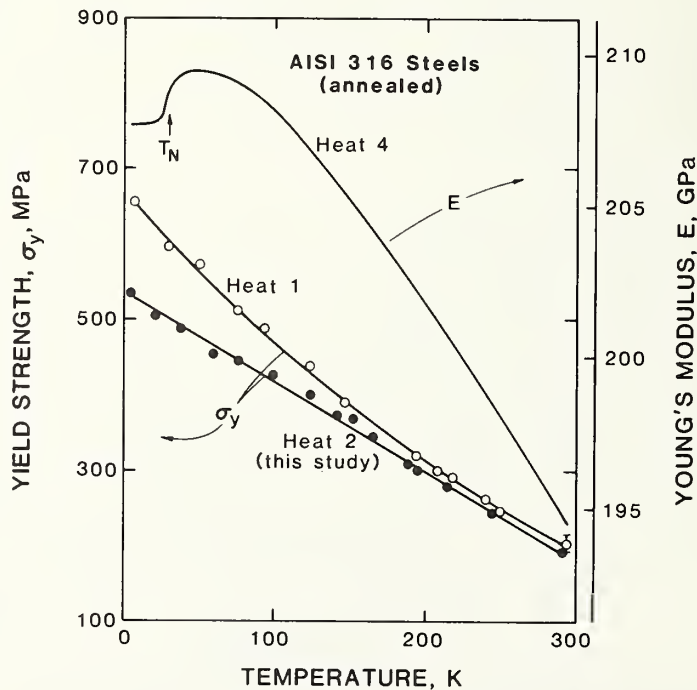


Fig. 12. Temperature dependence of yield strength and Young's modulus for AISI 316 stainless steels, showing no drop in yield strength at the Néel transition temperature.

As shown in Fig. 12, data for an AISI 316 (Fe-17.5Cr-12.9Ni) stainless steel do reveal a measurable drop in Young's modulus ( $E$ ), identifying the Néel transition between 40 and 20 K. But the data of Fig. 12 indicate no decrease of  $\sigma_y$  corresponding to the magnetic transition at  $T_N$ . Nor is there any evidence of an anomalous decrease of  $\sigma_y$  at temperatures between 20 and 4 K. So this study does not support the conclusions of other investigators, and no explanation for the apparent conflict can be offered at this point.

## SUMMARY AND CONCLUSIONS

Tensile tests at temperatures between 323 and 4 K were performed on metastable austenitic AISI 316 stainless steel (Fe-17Cr-12Ni-2Mo). The yield and flow strengths at plastic strains up to 0.037 are analyzed and compared with existing data, noting metallurgical effects. The grain-size effect on yield strength ( $\sigma_y$ ) is weak at room temperature but substantial at cryogenic temperatures. No martensite is detected after tensile loading at low temperatures to 0.002 plastic strain. With further straining ( $\sim 0.03$ ), body-centered cubic ( $\alpha'$ ) martensite forms in the parent austenite phase at test temperatures below 175 K. The initiation of  $\alpha'$  transformation in this steel in tension is associated with increased strain hardening below 175 K, and not with a decrease of flow strength. Significant features of the temperature dependence of flow strength are: 1) a continuous rise of  $\sigma_y$  with decreasing temperature, in accord with thermally activated plastic deformation, 2) an inflection in the thermal component of  $\sigma_y$  at about 150 K, suggesting a change in deformation mechanism, and 3) absence of anomalies due to martensitic transformations, or to magnetic transition at Néel temperature. Comparison of present results with data for other heats indicates a significant variation due to variations in chemical compositions within the material specifications.

## ACKNOWLEDGMENTS

We thank D. Beard, Office of Fusion Energy, DoE for his support and continued encouragement. D. Burkhalter of NBS contributed significantly to this study by conducting tensile tests. Dr. E. L. Brown of NBS, who contributed valuable metallographic assistance and reviews of the manuscript, is also gratefully acknowledged.



## REFERENCES

1. Read, D. T., Reed, R. P., and Schramm, R. E., Low temperature deformation of Fe-18Cr-8Ni steels, in: Materials Studies for Magnetic Fusion Energy Applications at Low Temperatures-II, F. R. Fickett and R. P. Reed, eds., NBSIR 79-1609, National Bureau of Standards, Boulder, Colorado (June 1979), pp. 151-172.
2. Reed, R. P. and Mikesell, R. P., The stability of austenitic stainless steels at low temperatures as determined by magnetic measurements, in: Advances in Cryogenic Engineering, Vol. 4, Plenum Press, New York (1960), pp. 84-100.
3. Larbalestier, D. C. and King, H. W., Austenitic stainless steels at cryogenic temperatures I, structural stability and magnetic properties, Cryogenics 13:160-168 (1973).
4. Tobler, R. L., Reed, R. P., and Burkhalter, D. S., Temperature dependence of yielding in austenitic stainless steels, in: Advances in Cryogenic Engineering, Vol. 26, Plenum Press, New York (1980), pp. 107-113.
5. Sanderson, G. P. and Llewellyn, D. T., Mechanical properties of standard austenitic stainless steels in the temperature range -196 to +800C, J. Iron Steel Inst. 207:1129-1140 (1969).
6. Read, D. T. and Reed, R. P., Fracture and strength properties of selected austenitic stainless steels at cryogenic temperatures, Cryogenics 21:415-417 (1981).
7. Baughman, R. A., Gas atmosphere effects on materials, Progress Report #2, AF 33(616), General Electric Co., Schenectady, New York (November 1958).
8. Tobler, R. L., Mikesell, R. P., Durcholz, R. L., Fowlkes, C. W., and Reed, R. P., Fatigue and Fracture Toughness Testing at Cryogenic Temperatures, NBSIR 74-359, National Bureau of Standards, Boulder, Colorado (March 1974), pp. 182-308.
9. Hoke, J. H., Mabus, P. G., and Goller, G. N., Mechanical properties of stainless steels at subzero temperatures, Met. Prog. 55:643-648 (1949).
10. Ilyichev, V. Ya., Medvedev, Ya. M., Shapovaliev, I. A., and Klimenko, I. N., Low temperature anomaly of the temperature dependence at the flow stresses in iron-chromium-nickel alloys, Phys. Met. Metallogr. 44(1):173-176 (1978).
11. Verkin, B. I., Ilyichev, V. Ya., and Klimenko, I. M., The low-temperature change of the magnetic structure and plastic properties of Fe-Cr-Ni alloys, in: Advances in Cryogenic Engineering, Vol. 26, Plenum Press, New York (1980), pp. 120-125.
12. Suzuki, T., Kojima, H., Suzuki, K., Hashimoto, T., and Ichichara, M., An experimental study of the martensite nucleation and growth in 18/8 stainless steel, Acta Metall., 23:1151-1162 (1972).

13. Reed, R. P. and Guntner, C. J., Stress-induced martensitic transformations in 18Cr-8Ni steel, Trans. AIME, 230:1713-1720 (1969).
14. Olson, G. B. and Azrin, M., Transformation behavior of TRIP steels, Metall. Trans. A, 9A:713-721 (1978).
15. Ledbetter, H. M., Stainless-steel elastic constants at low temperatures, J. Appl. Phys. 52(3):1587-1589 (1981).
16. Reed, R. P., A cryostat for tensile tests in the temperature range 300 to 4 K, in: Advances in Cryogenic Engineering, Vol. 7, Plenum Press, New York (1961), pp. 448-454.
17. Sikka, V. K., Tensile and creep properties of type 316 stainless steels, paper CONF 78 1219-3 (N80-11212), presented at the UK/UKAEA Specialists Meeting on Mechanical Properties, Oak Ridge, Tennessee (Dec. 4, 1978).
18. Seeger, A., The generation of lattice defects by moving dislocations, and its application to the temperature dependence of the flow-stress of FCC crystals, Philos. Mag., 46:1194-1217 (1955).
19. Conrad, H., The cryogenic properties of metals, in: High-Strength Materials, V. F. Zackay, ed., Wiley, New York (1964), pp. 436-509.
20. Moore, T. D., Structural Alloys Handbook, Vol. 2, Battelle's Columbus Laboratories, Columbus, Ohio (1980).
21. Yaroshevich, V. D. and Ryvkina, D. G., Thermal-activation nature of plastic deformation in metals, Sov. Phys.-Solid State (Engl. Transl.) 12(2):363-370 (1970).
22. Rhodes, C. G. and Thompson, A. W., The composition dependence of stacking fault energy in austenitic stainless steels, Metall. Trans. 8A:1901-1906 (1977).
23. Larbalestier, D. C. and King, H. W., Prediction of the low temperature stability of type 304 stainless steel from a room temperature deformation test, in: Proceedings of the Fourth International Cryogenic Engineering Conference, K. Mendelssohn, ed., IPC Science and Technology Press, Guildford, Surrey, England (1975), pp. 338-340.
24. Williams, I., Williams, R. G., and Capellaro, R. C., Stability of austenitic stainless steels between 4 K and 373 K, in: Proceedings of the Sixth International Cryogenic Engineering Conference, ed., K. Mendelssohn, IPC Science and Technology Press, Guildford, Surrey, England (1976), pp. 337-341.
25. Warnes, L. A. and King, H. W., The low temperature magnetic properties of austenitic Fe-Cr-Ni alloys 2, the prediction of Néel temperatures and maximum susceptibilities, Cryogenics 16(11):659-667 (1976).
26. Guntner, C. J. and Reed, R. P., The effect of experimental variables including the martensitic transformation on the low temperature mechanical properties of austenitic stainless steels, Trans. Am. Soc. Met., 55:339-419 (1962).
27. Starr, C. D., Notes on the plastic critical temperature in strain induced martensite reaction, Trans. AIME 197:654 (1953).

28. Norstrom, L. A., The influence of nitrogen and grain size on yield strength in Type 316L austenitic stainless steel, Met. Sci. 11:208-212 (1977).
29. Collings, E. W. and Ledbetter, H. M., Sound velocity anomalies near the spin glass transition in an austenitic stainless steel alloy, Phys. Lett. 72A(1):53-56 (1979).
30. Ledbetter, H. M. and Collings, E. W., Low-temperature magnetic and elastic-constant anomalies in three manganese stainless steels, in: The Metal Science of Stainless Steels, E. W. Collings and H. W. King, eds., Met Soc. AIME, New York (1978), pp. 22-38.

TEMPERATURE DEPENDENCE OF FLOW STRENGTH OF  
SELECTED AUSTENITIC STAINLESS STEELS<sup>+</sup>

R. P. Reed, R. L. Tobler, and J. W. Elmer  
Fracture and Deformation Division  
National Bureau of Standards  
Boulder, Colorado

ABSTRACT

It is important to characterize and to understand the temperature dependence of the tensile flow strength of austenitic steels for efficient design and material selection. Recent studies have suggested the possibility of three anomalies in the temperature dependence of the flow strength of Fe-Cr-Ni and Fe-Cr-Ni-Mn austenitic stainless steels. Reduction of flow strength at decreasing temperature may be associated with the onset of the austenite to martensite transformation ( $\sim 200$  K), the magnetic transition at the Néel temperature ( $\sim 50$  K) and low temperature dislocation dynamics ( $< 20$  K). The tensile flow strength was investigated in the temperature range 4 to 295 K for two annealed polycrystalline alloys: Fe-20Cr-16Ni-6Mn-0.2N steel (produced in the USSR and independently tested by two research laboratories) and Fe-18Cr-10Ni-0.1N steel (AISI 304LN). The former alloy is stable with respect to strain-induced martensitic transformations, the latter metastable.

<sup>+</sup> Work supported by Office of Fusion Energy, Department of Energy

<sup>\*</sup> To be published in Austenitic Steels at Low Temperatures, Eds. R. P. Reed and T. Horiuchi, Plenum Press, New York (1983).





## INTRODUCTION

Austenitic stainless steels are used extensively as the structural material in cryogenic systems, and knowledge of the dependence of their strength on temperature is sometimes essential for proper design. This study addresses the temperature (T) dependence of the tensile flow strength in the range 4 K to room temperature.

Recent studies [1-3] of Fe-Cr-Ni and Fe-Cr-Ni-Mn austenitic stainless steels have reported three anomalies in the temperature dependence of the flow strength. These anomalies consist of sharp decreases of strength on the order of 100 MPa occurring over narrow temperature intervals between room temperature and 4 K. One type occurs only in metastable steels and is associated with the onset of austenite-to-martensite transformation, usually at about 200 K. For both stable and metastable steel compositions, two additional anomalies are reported at temperatures between 60 and 35 K and between 20 and 4 K. The flow strength decrease in the temperature interval 60 to 35 K has been attributed to the paramagnetic-to-antiferromagnetic transition at the Néel temperature, where the elastic constants are known to decrease. It has been suggested that flow strength reductions below 20 K result from possible dislocation tunneling mechanisms [2]. Studies in our laboratory [4-6] have identified the decrease in flow strength associated with austenite instability

---

\*This research was supported by the Office of Fusion Energy, U.S. Department of Energy.

with respect to martensitic transformations. This paper reports on the temperature dependence of the flow strength of two austenitic steels over the entire temperature range between 4 and 300 K. Data are presented for an Fe-20Cr-16Ni-6Mn-0.2N steel (produced in the USSR and independently tested by two research laboratories) and for an Fe-18Cr-10Ni-1.5Mn-0.1N steel (AISI 304LN). The former alloy is expected to be stable with respect to martensitic transformations, the latter metastable.

## MATERIALS

A 25-mm plate of nitrogen-strengthened austenitic stainless steel was obtained from the Paton Institute of Electrowelding, Kiev, USSR. The material was tested in the as-received condition. The characteristics of the alloy are listed here. Composition (wt.%): Fe-20.3Cr-16.4Ni-6.1Mn-0.19N-0.06C-0.21Mo-0.26Si-0.025P-0.026S-0.09Cu. Hardness: Rockwell B88, at 295 K after machining tensile specimens. Microstructure: Equiaxed austenitic grains, free of carbonitride precipitation when viewed at 400X. Grain size: Average grain diameter of 0.039 mm (ASTM No. 6.4).

The AISI 304LN material was received from a U.S. supplier. It was one of nine alloys produced from three 136-kg vacuum-induction-melted heats, split with respect to carbon level, and teemed into 76-cm x 200-cm x 360-cm hot-topped cast-iron ingot molds. The ingots were then reheated and soaked at 1561 K, hot-rolled to 25-mm-thick plates and air cooled. The plate was given a final anneal at 1332 K for one hour and water quenched. The characteristics of the alloy are listed here. Composition (wt.%): Fe-18.0Cr-9.91Ni-1.50Mn-0.016P-0.017S-0.57Si-0.205Mo-0.197Cu-0.037C-0.12N. Hardness: Rockwell B79 at 295 K after machining tensile specimens. Microstructure: Equiaxed austenitic grains. Grain Size: Average grain diameter of 0.105 mm.

## PROCEDURE

In a previous study, unpolished, longitudinally oriented specimens were used to measure tensile yield ( $\sigma_y$ ) and ultimate strengths, as well as ductility, at selected temperatures [5]. In this study, transverse-oriented specimens were used for yield strength measurements at variable temperatures. Both round (6.25 mm diameter) and flat (6.25 mm x 2.50 mm) specimens with 25-mm gage length were used. They were electropolished in perchloric acid solution (70% methanol, 25% glycerol, 5% perchloric acid) to remove scratches and cold-worked material from machining operations. A total of 0.1 mm (4 mils) was

removed from the diameter, which is about four times scratch depth.

Tensile tests used a screw-driven machine at a crosshead velocity of  $8.5 \times 10^{-3}$  mm/s, with apparatus previously described [4,5,7]. Variable temperatures were achieved using controlled thermal conduction from cryogenic fluid reservoirs attached to the load train and electric heaters on the specimen grips. The automatic regulators maintained temperatures to  $\pm 0.2$  K, with an estimated absolute uncertainty of  $\pm 1$  K [5]. A strain-gage extensometer was clipped on the specimen at a gage length of 25 mm.

Specimen-to-specimen scatter of the temperature dependence of the flow strength was eliminated by performing temperature-change tests. To obtain measurements at three to five temperatures, a single specimen was loaded to a strain within the range 0.0005 to 0.002 at  $T_1$ , then unloaded, cooled to  $T_2$ , and reloaded until plastic flow resumed. This procedure is described schematically in Figure 1. Cooling to the lower temperature usually took 10 to 20 minutes. Additional loadings at lower temperatures were also performed, and the flow strength obtained by extrapolating to the 0.002 strain.

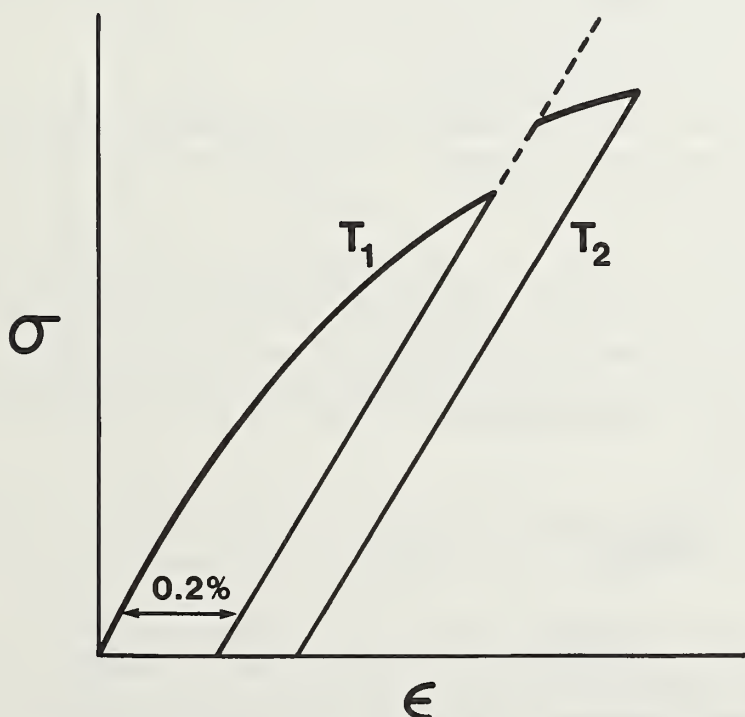


Figure 1. Schematic of test procedures for multiple temperature measurements of flow strength using one specimen.



## RESULTS

Magnetic measurements [4] at 295 K after low temperature (76, 4 K) deformation confirmed that the Fe-20Cr-16Ni-6Mn-0.2N alloy does not exhibit any  $\alpha'$  (body-centered cubic) martensitic transformation and that the Fe-18Cr-10Ni-1.5Mn-0.1N alloy is metastable and partially transformed to  $\alpha'$  martensite. This was expected since calculations listed in Table 1 of  $T_{ms}$  [8] (the temperature at which  $\alpha'$  martensite is expected to begin to transform on cooling), and  $T_{md}$  [9] (the highest temperature of deformation-induced  $\alpha'$  martensite) are both quite low for the Fe-20Cr-16Ni-6Mn-0.2N alloy and  $T_{md}$  for the Fe-18Cr-10Ni-1.5Mn-0.1N alloy is sufficiently high. Stacking fault energy (SFE) estimations [10], listed also in Table 1, indicate that the Fe-20Cr-16Ni-6Mn-0.2N alloy is relatively more stable with respect to the face-centered cubic to hexagonal close-packed ( $\epsilon$ ) strain-induced martensitic transformation.

### Alloy Fe-20Cr-16Ni-6Mn-0.2N

The yield strength results are presented in Figure 2, which compares data from this study with those of our previous study [5] and with the results of Yushchenko et al. [1]. Between 300 and 4 K, the results show approximate conformation to an exponential function given:

$$\sigma_y = 1160 \exp (-4.16 \times 10^{-3} T) \quad (1)$$

Most of the data fit this equation to within about 6 percent, although two points deviate by larger amounts (-10 percent at 295 K, +8 percent at 60 K).

Figure 3 shows only the data at test temperatures between 4 and 100 K. For these results, combined with our previous data, the data spread for five tests at 4 K is  $\pm 55$  MPa, owing primarily to specimen-to-specimen variability. The previously tested specimens [5] were longitudinal and unpolished, but the results are indistinguishable from the electropolished transverse specimens.

Table 1. Austenite Stability and Calculations of Stacking Fault Energy.

Alloy	$T_{ms}$ [8] (K)	$T_{md}$ [9] (K)	SFE [10] ( $10^{-5}$ J/m <sup>2</sup> )
Fe-20Cr-16Ni-6Mn-0.2N	-715	18	79
Fe-18Cr-10Ni-1.5Mn-0.1N	- 84	285	28

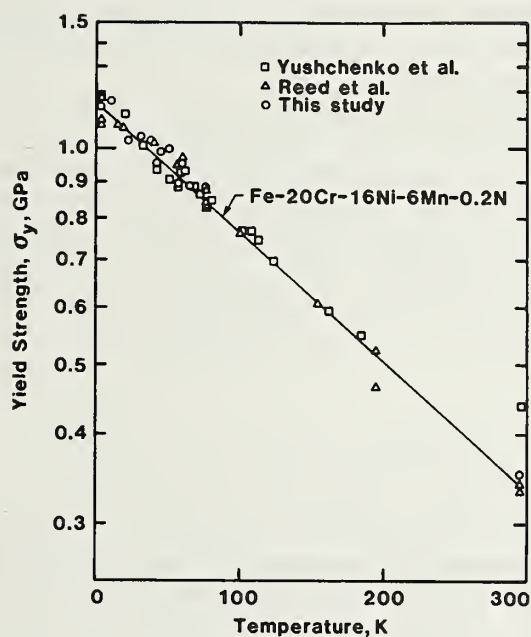


Figure 2. Yield strength versus temperature for Fe-20Cr-16Ni-6Mn-0.2N steel, summarizing data from this study and other studies [1-3,5].

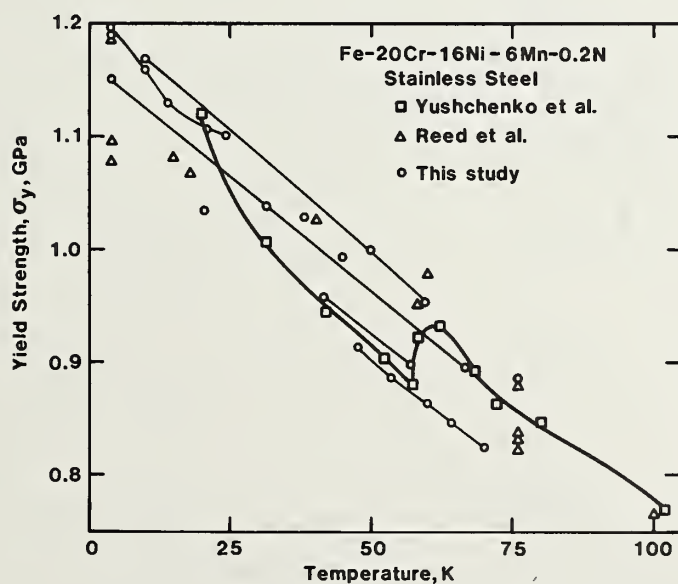


Figure 3. Low temperature yield strength data for alloy Fe-20Cr-16Ni-6Mn-0.2N. Data points connected by lines represent yield strengths obtained from single specimens. Each specimen was initially strained at highest temperature, then cooled and restrained.

The 7-percent drop of  $\sigma_y$  at  $T_N$ , as reported by Yushchenko et al. [1], falls well within specimen-to-specimen variability determined in our study.

To eliminate the obscuring effect of specimen-to-specimen variability, single-specimen temperature-change tests were performed. In Figure 3, the multiple data points from single specimens are linked with straight lines. These trend lines have nearly equivalent slopes, in general do not cross over one another, and include the temperature range (50-65 K) in which strength decreases at lower temperatures have been reported [1-3].

#### Alloy Fe-18Cr-10Ni-1.5Mn-0.1N

Tensile flow strength data at strain offsets of 0.0005 and 0.002 (yield strength) are plotted as a function of temperature in Figure 4. The difference between the flow strengths at 0.002

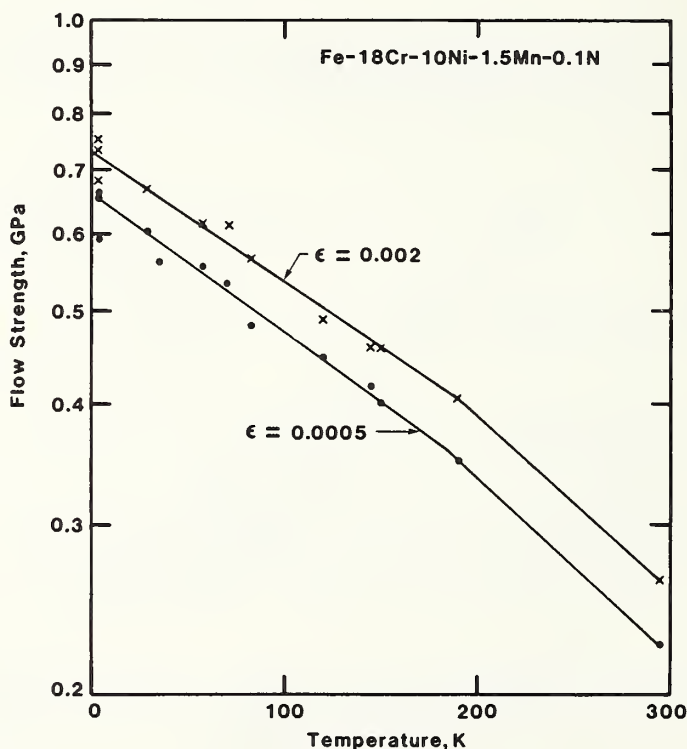


Figure 4. Flow strength at strains of 0.0005 and 0.002 as a function of temperature for Fe-18Cr-10Ni-1.5Mn-0.1N alloy. Solid line represents average temperature dependence from individual specimen measurements, reported in Figure 4.

and 0.0005 strains increases from about 0.038 GPa at 295 K to about 0.070 GPa at 4 K.

Between 300 and 200 K, the yield strength best conforms to:

$$\sigma_y = 900 \exp (-4.22 \times 10^{-3} T) \quad (2)$$

The limited data restrict the assignment of data inaccuracies to this function. Between 4 and 200 K, the dependence of  $\sigma_y$  on T decreases to:

$$\sigma_y = 730 \exp (-3.05 \times 10^{-3} T) \quad (3)$$

The data fit this equation within  $\pm 5$  percent.

Temperature-change experiments were also performed on the Fe-18Cr-10Ni alloy. In Figure 5, the measurements from seven specimens are plotted. For all measurements, the temperature was lowered after reaching strains between 0.0005 and 0.002. The temperature dependence found from single-specimen tests is plotted as a smooth curve in Figure 5. All specimens exhibited normally rising flow strength with a decrease in temperature, with the possible exception of the specimen originally strained at 295 K. The change of strength achieved from the changing of temperature matches that obtained from individual tests at the two temperatures.

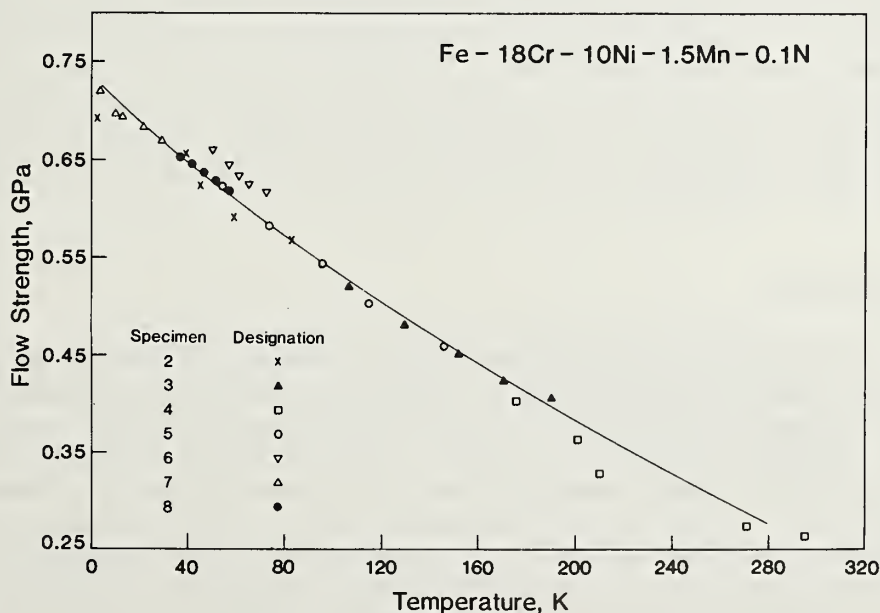


Figure 5. Flow strength of Fe-18Cr-10Ni-1.5Mn-0.1N alloy at strain of 0.002 (yield strength) measured from specimens sequentially cooled and strained.



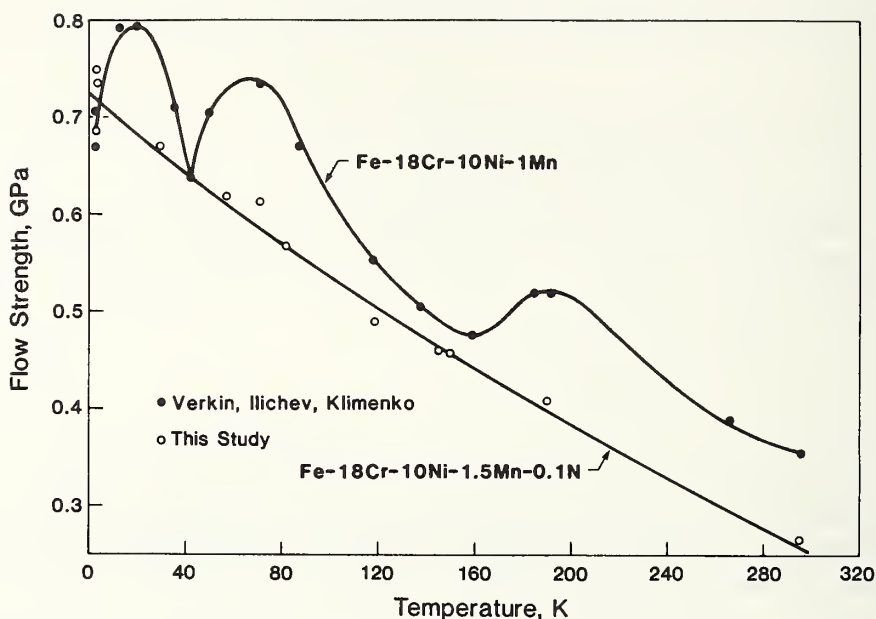


Figure 6. Comparison of data from Verkin et al. [3] and this study for similar Fe-18Cr-10Ni alloys.

Our data and data for a similar Fe-18Cr-10Ni-1Mn alloy [3] are presented for comparison in Figure 6. Three major ranges of strength decrease with decreasing temperature are reported by Verkin et al. [3]. None of the anomalous strength decreases are evident from our measurements on an alloy that is similar in base composition and in total interstitial content. The specimen-to-specimen data scatter for our Fe-18Cr-10Ni-1.5Mn-0.1N alloy is much less than the anomalous decreases reported for the Fe-18Cr-10Ni-1Mn alloy [3].

## DISCUSSION

From Figure 4 the dependence of the flow strength on temperature of the Fe-18Cr-10Ni-1.5Mn-0.1N alloy may be characterized by a change of deformation mechanism below about 200 K, producing two linear regions (4 to 200 K, 200 to 300 K) in the  $\log \sigma$ -T graph. The temperature change experiments (Figures 3 and 5) do not conflict with this characterization. The austenite of the Fe-20Cr-16Ni-6Mn-0.2N alloy is relatively very stable and has higher stacking fault energy and lower  $T_{ms}$  (below 0 K) than the Fe-18Cr-10Ni-1.5Mn-0.1N alloy, owing to higher alloying concentrations (Table 1). It is likely that the strain-induced martensitic transformation (to hexagonal close-packed  $\epsilon$  or  $\alpha'$ ) leads to the change in the temperature dependence of the flow

strength below 200 K in the less stable alloy Fe-18Cr-10Ni-1.5Mn-0.1N. The  $\alpha'$  martensite was detected in Fe-18Cr-10Ni-1.5Mn-0.1N specimens deformed at 76 and 4 K, and the estimated  $T_{md}$  for this alloy is calculated to be positive (Table 1). Conversely, no  $\alpha'$  martensite transformation was detected in the Fe-20Cr-16Ni-6Mn-0.2N alloy and only one linear region of  $\log \sigma$ -T is observed over the entire 4 to 295 K temperature range. However, since  $\epsilon$  and  $\alpha'$  transformation are closely associated in austenitic stainless steels, it is not clear from these data which martensitic product may be associated with flow strength changes in the Fe-18Cr-10Ni-1.5Mn-0.1N alloy.

The single-specimen temperature-change experiment data have been presented in Figures 3 and 5. Clearly there is no distinction at low temperatures (<200 K) in the temperature dependence of the flow strength determined from multiple or single specimen measurements. This indicates that the deformation mechanisms for plastic strain and the defect structures generated during plastic strain are essentially independent of temperature for these two alloys. That is, the same flow strength at a given temperature and strain can be achieved either by straining at the prescribed temperature or by straining to a lower strain at higher temperatures (but <200 K), cooling to the prescribed temperature and straining. This result is a bit unpredictable, since the low temperature deformation mechanisms of the less stable austenitic steel (Fe-18Cr-10Ni-1.5Mn-0.1N) include martensitic transformation. In this discussion, the strain range is limited to  $\leq 0.002$ ; at larger strains with more complex martensitic transformation, the flow strength may not be (strain) path independent.

Finally, this study has failed to confirm the flow strength decreases associated with the Néel transition temperature. The flow strength ( $\sigma_f$ ) is proportional to the shear modulus (G) and the dislocation density ( $p$ ) through the relationship

$$\sigma_f = \alpha G b p^{\frac{1}{2}} \quad (4)$$

where  $\alpha$ , a material constant, usually has a value between 0.2 and 0.5 (e.g., Conrad [11]). The elastic constants for Fe-20Cr-16Ni-6Mn-0.2N steel [12] show a regular, nearly linear increase as temperature is reduced from 300 K, until a plateau is approached below about 76 K. In the 60 to 48 K range, the E and G moduli decrease by about  $\frac{1}{2}$  percent. This decrease marks the Néel temperature,  $T_N$ , at which there is a change in magnetic ordering from paramagnetic to antiferromagnetic conditions. The midpoint of the transition is about 54 K. The  $\frac{1}{2}$ -percent decrease of G measured at  $T_N$  for the Fe-20Cr-16Ni-6Mn-0.2N alloy would not alone be sufficient to account for the 7-percent decrease of  $\sigma_y$ , as reported (Figure 2) by Yushchenko et al. [1] and, for an Fe-18Cr-10Ni-1Mn alloy, the 17-percent decrease reported by

Verkin et al. [3]. Indeed, the  $\frac{1}{2}$ -percent effect is indistinguishable from experimental scatter in  $\sigma_y$  measurements. The single-specimen temperature change test conducted below 60 K shows an increase of  $\sigma_y$  with a magnitude equivalent to that expected from the exponential function of Eqs. (1) and (3).

## CONCLUSIONS

Two austenitic stainless steel alloys have been measured in tension between 4 and 300 K. One alloy contains 20Cr, 16Ni, 6Mn, and 0.2N; the other contains 18Cr, 10Ni, 1.5Mn, and 0.1N and is an AISI 304LN. The results are summarized below:

1. The temperature dependence of the flow strength of the two alloys is best characterized by a linear dependence of  $\log \sigma$  versus  $T$ . The more stable Fe-20Cr-16Ni-0.2N alloy exhibits a linear slope of  $\log \sigma$  versus  $T$  over the entire temperature test range (4 to 295 K). The less stable Fe-18Cr-10Ni-1.5Mn-0.1N alloy exhibits two linear ranges on a  $\log \sigma$  versus  $T$  plot, one from 4 to about 200 K, the other from about 200 to 295 K.
2. Temperature change experiments at low strains ( $\sim 0.002$ ) indicate reversibility of flow strength at temperatures below about 100 K. This implies that the deformation mechanisms do not change under these conditions for these alloys.
3. The reported anomalous low temperature dependences of the flow strength associated with the Néel transition temperature and very low temperatures ( $< 20$  K) for austenitic steels were not confirmed by this study.

## REFERENCES

1. Yushchenko, K. A., Verkin, B. I., Ilichev, V. Ya., and Klimenko, I. N., "The influence of magnetic structure on temperature dependence of the yield strength of 20Cr-16Ni-6Mn steel at low temperatures," in Advances in Cryogenic Engineering-Materials, Vol. 28, Plenum Press, New York, pp. 67-72 (1982).
2. Ilichev, V. Ya., Medvedev, Ya. M., Shapovalov, I. A., and Klimenko, I. N. "Low temperature anomaly of the temperature dependence of the flow stresses in iron-chromium-nickel alloys," *Fiz. Met. Metalloved.* Vol. 44, No. 2, pp. 173-176 (1980).

3. Verkin, B. I., Ilichev, V. Ya., and Klimenko, I. N., "The low temperature change of the magnetic structure and plastic properties of Fe-Cr-Ni alloys," in Advances in Cryogenic Engineering-Materials, Vol. 26, Plenum Press, New York, pp. 120-125 (1980).
4. Reed, R. P. and Simon, N. J., editors, Material Studies for Magnetic Fusion Energy Applications at Low Temperatures - IV, National Bureau of Standards, Boulder, CO, NBSIR 81-1645 (1981).
5. Reed, R. P., Tobler, R. L., Elmer, J. W., McHenry, H. I., and Yushchenko, K. A., "Strength and toughness of USSR Fe-20Cr-16Ni-6Mn-0.2N weldments at cryogenic temperatures," in Proceedings of the Eighth International Cryogenic Engineering Conference, IPC Science and Technology Press, Guildford, Surrey, England, pp. 797-801 (1980).
6. Tobler, R. L., Beekman, D. H., and Reed, R. P., "Low-temperature dependence of yielding in AISI 316 stainless steel" in Austenitic Steels at Low Temperatures, R. P. Reed and T. Horiuchi, editors, Plenum Press, New York (1982).
7. Read, D. T. and Tobler, R. L., "Mechanical property measurements at low temperatures," in Advances in Cryogenic Engineering-Materials, Vol. 28, R. P. Reed and A. F. Clark, editors, Plenum Press, New York (1982).
8. Eichelman, G. H. and Hull, F. C., "The effect of composition on the temperature of spontaneous transformation of austenite to martensite in 18-8-type stainless steel," Trans. Am. Soc. Met., Vol. 45, pp. 77-104 (1953).
9. Williams, I., Williams, R. G., and Capellero, R. C., "Stability of austenitic stainless steels between 4 K and 373 K," in Proceedings of the Sixth International Cryogenic Engineering Conference, IPC Science and Technology Press, Guildford, Surrey, England, pp. 337-341 (1976).
10. Schramm, R. E. and Reed, R. P., "Stacking fault energies of seven commercial austenitic stainless steels," Metall. Trans. Vol. 6A, pp. 1345-1351 (1975).
11. Conrad, H., "The cryogenic properties of metals," in High-Strength Materials, V. F. Zackay, Editor, John Wiley & Sons, New York, pp. 436-509 (1965).



12. Ledbetter, H. M. and Austin, M. W., "Low-temperature elastic properties of an Fe-20-16Ni-6Mn alloy," in Material Studies for Magnetic Fusion Energy Applications at Low Temperatures - V, R. P. Reed and N. J. Simon, editors, National Bureau of Standards, Boulder, CO, NBSIR 82-1667 (1982).

# PROPERTIES OF AUSTENITIC STAINLESS STEEL AT CRYOGENIC TEMPERATURES+\*

H. I. McHenry  
Fracture and Deformation Division  
National Bureau of Standards  
Boulder, Colorado

## ABSTRACT

The low temperature behavior of austenitic stainless steels is reviewed with emphasis on three general classes: 1) the AISI 300-series in the annealed condition; 2) the nitrogen-strengthened grades; and 3) high-strength cold-rolled sheet of the AISI 300-series. Mechanical and physical properties of selected alloys in these classes are presented. Welding, the properties of weldments, and other fabrication considerations are discussed. Recent results on the influence of ferrite content, nitrogen, and sensitization on castings of composition similar to the AISI 300 series are also reviewed.

+ Work supported by Office of Fusion Energy, Department of Energy

\* To be published in Austenitic Steels at Low Temperatures, Eds. R. P. Reed and T. Horiuchi, Plenum Press, New York (1983).



## INTRODUCTION

The austenitic stainless steels are Fe-Cr alloys with sufficient nickel and manganese (and sometimes nitrogen) to stabilize austenite, a face-centered cubic (f.c.c.) phase. Chromium provides corrosion resistance. The most typical austenitic stainless steels are variations of the 18Cr-9Ni alloy. Although none of the commercial alloys were specifically developed for low-temperature service, several of them have been widely used in a variety of cryogenic applications. Their popularity stems from their retention of excellent mechanical properties, particularly toughness, at low temperatures coupled with ready availability, ease of fabrication, and good service experience. Their disadvantages are they are more expensive and have lower yield strength than ferritic Fe-Ni steels and aluminum alloys, and their machinability is poorer than that of aluminum alloys.

The austenitic stainless steels have a wide range of mechanical properties, depending on their chemical composition and thermal-mechanical processing. Three general classes of these alloys are useful for cryogenic applications:

a. The AISI 300-series stainless steels in the annealed condition, particularly types 304 and 304L, are the most commonly used alloys. Consequently, they have the most service experience and coverage in design codes. These grades have moderate strength and excellent toughness, and they are readily available in a variety of product forms. Casting alloys equivalent to the commonly used 300-series grades are used to manufacture complex shapes, such as valve bodies.



b. The nitrogen-strengthened grades are remarkably stronger at cryogenic temperatures and retain most of the advantages of the 300-series grades, except for availability, service experience, and code coverage.

c. The cold-rolled sheets of the AISI 300-series grades have been used as high-strength sheet materials in specialized applications, such as liquid-fueled missile cases.

In addition to the three main classes, there are precipitation-hardened austenitic grades, for example ASTM A 453, which offer promise as high-strength alloys for heavier-gauge applications, but their usage to date has been limited to nuts and bolts. Precipitation-hardened alloys must be selected carefully because these alloys are generally martensitic or semiaustenitic and have low toughness at cryogenic temperatures.

#### ANNEALED AISI 300-SERIES GRADES

The designations and compositions of the most commonly used grades of the AISI 300 series are summarized in Table 1. These grades have moderate strength, excellent toughness, and good fabrication characteristics, and they are readily available in a variety of product forms.

The alloys listed in Table 1 can be compared with AISI-304, the basic 19Cr-9Ni stainless steel. Type 316 contains 2 to 3% Mo to improve

Table 1. Compositions of austenitic stainless steels.

AISI Type No.	Composition (%)			
	Cr	Ni	C, max.	Other
301	16-18	6-8	0.15	
302	17-19	8-10	0.15	
304	18-20	8-12	0.08	
304L	18-20	8-12	0.03	
305	17-19	10.5-13	0.12	
309	22-24	12-15	0.20	
310	24-26	19-22	0.25	1.5 Si, max.
310S	24-26	19-22	0.08	1.5 Si, max.
316	16-18	10-14	0.08	2-3 Mo
316L	16-18	10-14	0.03	2-3 Mo
321	17-19	9-12	0.08	(5 x %C) Ti, min.
347	17-19	9-13	0.08	(10 x %C) Nb+Ta, min.

resistance to pitting in chloride solutions, a property that led to its selection for cargo piping systems aboard liquefied-natural-gas (LNG) ships. Types 304L and 316L are low-carbon modifications of 304 and 316, respectively; low carbon is desirable to avoid sensitization, the grain-boundary precipitation of chromium carbides. Types 321 (alloyed with titanium) and 347 (alloyed with niobium and tantalum) are also sensitization-resistant grades. Type 310S is a 25Cr-20Ni alloy that is a low-carbon version (0.08% C max.) of AISI Type 310 (0.25% C max.). The high-alloy content provides austenite stability, and thus 310S is useful where dimensional stability and nonmagnetic behavior are essential.

The properties of the 300-series austenitic stainless steels have been compiled in cryogenic handbooks,<sup>1,2</sup> in a review article by Brickner and Defilippi,<sup>3</sup> and in suppliers publications.<sup>4,5</sup> In this section, the general trends in strength, toughness, and fatigue resistance are summarized as a function of temperature. Use the data presented here and the data in the handbooks with care because there may be significant heat-to-heat variations in the mechanical properties of the 300-series stainless steels at low temperatures, particularly in the yield strength and toughness. The principal causes of these variations are interstitial content (carbon and nitrogen) and mechanical deformation history, which controls the resulting grain size. The nitrogen content, even within the specification limit of 0.08 wt.%, is particularly significant because higher nitrogen causes substantial increases in yield strength.

### Tensile Properties

The ultimate tensile and yield strengths of AISI grades 304, 310, and 316 are compared in Fig. 1 for temperatures ranging from 4 to 300 K.<sup>6</sup> Notice that type 304 has the lowest yield strength and the highest ultimate strength at all temperatures. The increased ultimate tensile strength of type 304 is due to the martensitic transformation, which occurs more readily in 304 than in 316 or 310. Since the transformation is strain induced, the yield strength is not influenced by martensite, but the ultimate strength is increased.

The ultimate tensile and yield strengths of AISI grade 304L are slightly lower than those of grade 304. The loss of strength associated with reduced carbon content is considered to be characteristic of all the stainless steels (e.g., 304L vs. 304, 316L vs. 316, and 310S vs. 310) and is attributed to the strengthening effect of carbon.

The ultimate tensile and yield strengths of AISI grades 304, 321, and 347 are essentially the same, indicating that the small additions of titanium in type 321 and niobium plus tantalum in type 347 do not influence the mechanical behavior of these alloys at temperatures between 76 and 300 K.

The ductility of the annealed 300-series stainless steels is generally excellent at cryogenic temperatures. Elongation and reduction of area tend to drop with decreasing temperatures, but values generally exceed 30%.

### Toughness

The austenitic stainless steels retain excellent toughness at cryogenic temperatures. The Charpy V-notch impact toughness does decrease with temperature,<sup>2</sup> but in all cases, it still far exceeds the 20-J requirement often used in codes and standards. The Charpy-toughness-vs.-temperature curves are characteristic for f.c.c. alloys; that is, ductile-to-brittle transition does not occur. The minimum temperature for Charpy testing in the United States is 20 K. A test facility for conducting the tests at 4 K is being used in the Soviet

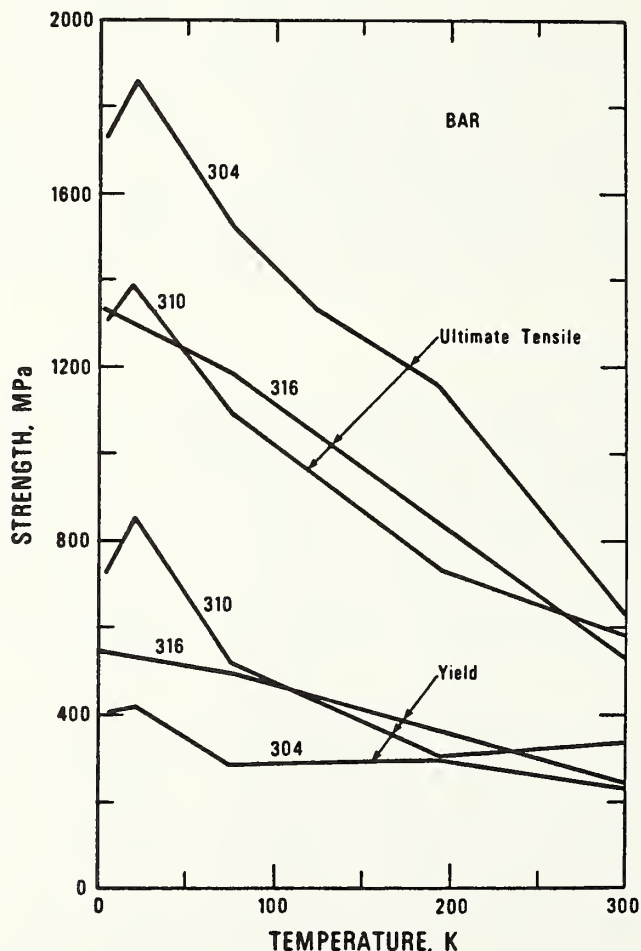


Fig. 1. Tensile and yield strengths of three austenitic stainless steels--AISI types 304, 310, and 316--at temperatures between 4 and 300 K.<sup>2</sup>



Union; however, it is likely that adiabatic heating limits the usefulness of data obtained below 20 K. Low-strain-rate tests using notched tensile specimens indicate that notch sensitivity does not develop at 4 K.<sup>2</sup>

J-integral methods have been used to measure the fracture toughness of AISI grades 310 and 316 at temperatures to 4 K. As shown in Fig. 2, the toughness,  $K_{Ic}$  (J), at cryogenic temperatures exceeds the toughness at room temperature.<sup>1</sup> The ratio of toughness to yield strength [ $K_{Ic}$  (J)/ $\sigma_{ys}$ ] is sufficiently high to ensure gross ductile deformation prior to fracture.

### Fatigue

Strain cycling fatigue properties at 295, 76, and 4 K were measured for AISI grades 304L and 310 by Nachtigall<sup>6</sup> and for grades 304L and 316 by Shepic and Schwartzberg.<sup>7</sup> The results for 304L, which were essentially the same in both investigations, are shown in Fig. 3. The fatigue resistances of 310 and 316 were superior to that of 304L, particularly in low cycle fatigue (less than  $10^4$  cycles). For each alloy, the fatigue resistance at low temperatures was superior to the fatigue resistance at room temperature, except at the highest strain ranges where failure occurred in less than  $10^3$  cycles.

The fatigue crack growth behavior of AISI grades 304, 304L, 310S, and 316 has been determined at 295, 76, and 4 K by Tobler and Reed.<sup>8</sup> The data for 304L are shown in Fig. 4. Notice that the growth rates are essentially the same at 76 and 4 K; similar behavior was observed in each of the other alloys. Also, notice that the growth rates at 76 and 4 K are less than those at room temperature. The best-fit lines through the 304L data at 295 K and at 76 and 4 K form the approximate scatter bands for the data on 304, 310S, and 316 at 295, 76, and 4 K. Thus, it can be concluded that alloy content and temperature have minimal influence on the fatigue crack growth behavior of the 300-series stainless steels.

### Physical Properties

The physical properties of the 300-series stainless steels at 295, 77, and 4 K are summarized in Table 2. The thermal properties have been taken from the best-fit lines used in LNG Materials and Fluids,<sup>1</sup> and the original sources are given for the elastic properties, electrical resistivity, and magnetic permeability.

### ANNEALED NITROGEN-STRENGTHENED GRADES

Nitrogen significantly increases the yield strength of austenitic stainless steels, particularly at cryogenic temperatures. The influence of nitrogen on the low-temperature strength and ductility of AISI 304<sup>12</sup> is shown in Fig. 5. Notice that the 77-K yield strength of 304N (AISI

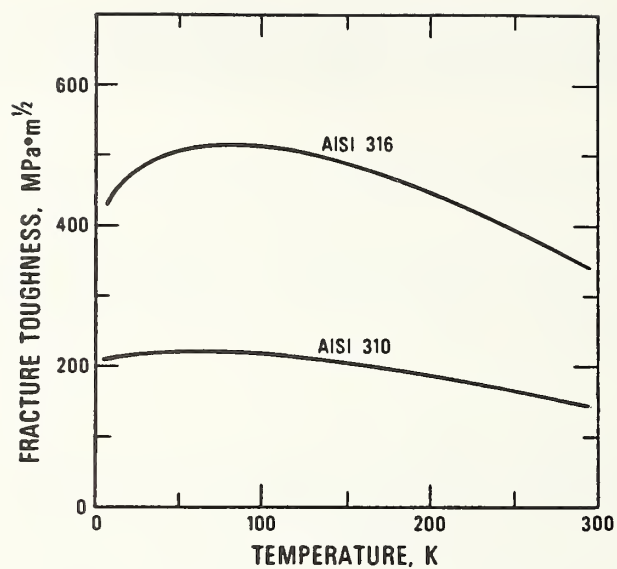


Fig. 2. Fracture toughness of two austenitic stainless steels--AISI types 310 and 316--at temperatures between 4 and 300 K.<sup>1</sup>

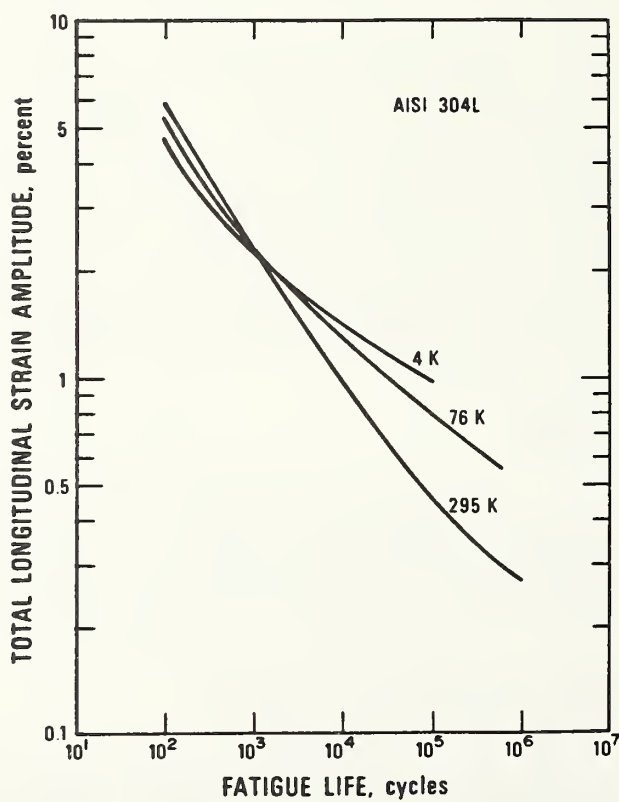


Fig. 3. Strain-cycling fatigue curves for AISI type 304L austenitic stainless steel at 295, 76, and 4 K.<sup>6</sup>



Table 2. Physical properties of austenitic stainless steels.

Stainless Steel and Temperature	Density <sup>a</sup> (g·cm <sup>-3</sup> )	Young's Modulus <sup>a</sup> (GPa)	Shear <sup>a</sup> Modulus (GPa)	Poisson's Ratio <sup>a</sup>	Thermal Conductivity (W·m <sup>-1</sup> ·K <sup>-1</sup> )	Thermal <sup>b</sup> Expansion (mean) (K <sup>-1</sup> ·10 <sup>-6</sup> )	Specific Heat <sup>b</sup> (J·kg <sup>-1</sup> ·K <sup>-1</sup> )	Electrical <sup>c</sup> Resistivity (μΩ·cm)	Magnetic Permeability <sup>d</sup> (initial)
AISI 304									
295 K	7.86	200	77.3	0.290	14.7	15.8	480	70.4	1.02
77 K		214	83.8	0.278	7.9	13.0	--	51.4	--
4 K		210	82.0	0.279	0.28	10.2	1.9	49.6	1.09
AISI 310									
295 K	7.85	191	73.0	0.305	11.5	15.8	480	87.3	1.003
77 K		205	79.3	0.295	5.9	13.0	180	72.4	--
4 K		207	79.9	0.292	0.24	10.2	2.2	68.5	1.10
AISI 316									
295 K	7.97	195	75.2	0.294	14.7	15.8	480	75.0	1.003
77 K		209	81.6	0.283	7.9	13.0	190	56.6	--
4 K		208	81.0	0.282	0.28	10.2	1.9	53.9	1.02

- a. Ledbetter et al.<sup>9</sup>  
b. LNG Materials and Fluids.<sup>5</sup>  
c. Clark, et al.<sup>10</sup>  
d. Efferson and Leonard.<sup>11</sup>

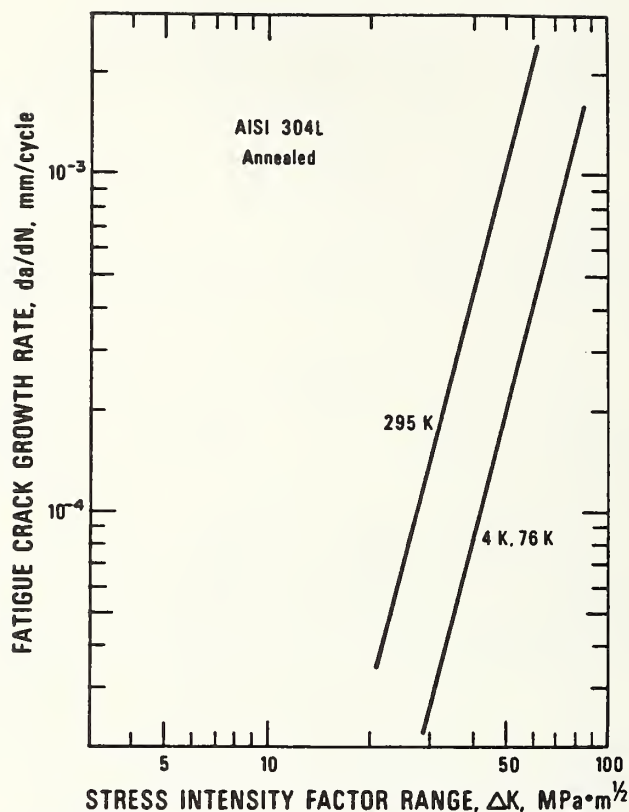


Fig. 4. Fatigue crack growth rates of AISI type 304L austenitic stainless steel at 295, 76, and 4 K.<sup>8</sup>

304 with deliberate additions of nitrogen) is approximately three times greater than the yield strength of 304, their ultimate strengths are approximately equal, and the elongation of the 304N is superior at temperatures below 220 K. This remarkable improvement in mechanical properties occurs in many nitrogen-strengthened grades.

The designations and compositions of the commercially available grades suitable for cryogenic service are summarized in Table 3. They are divided into two basic types: the Cr-Ni-N and the Cr-Ni-Mn-N alloys. The Cr-Ni-N alloys are 300-series stainless steels with deliberate additions of nitrogen. In Europe, nitrogen is deliberately added to several of the common Cr-Ni 300-series stainless steels. The equivalent AISI designations for these European grades are 304LN, 316LN, and 347N. In United States specifications, the nitrogen range is 0.10 to 0.16% for 304N and 316N. The corresponding European specifications permit nitrogen levels to 0.25%. The manganese in Cr-Ni-Mn-N alloys provides austenite stability and can thus be used to replace part of the nickel content. Manganese also increases the solubility of nitrogen in austenite and thus permits higher nitrogen levels; 0.4% N (max.) is typical.

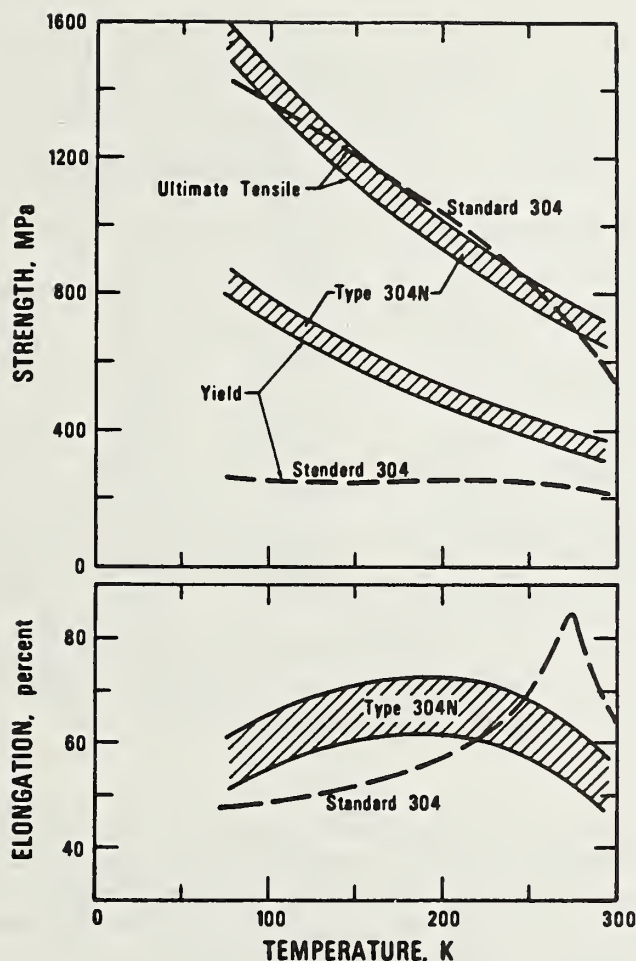


Fig. 5. Tensile properties of two austenitic stainless steels--AISI types 304N (with 0.2% N) and 304--at temperatures between 77 and 300 K.<sup>12</sup>

### Tensile Properties

The yield and ultimate strengths of the Cr-Ni-N 300-series stainless steels are summarized in Fig. 6. The solid lines and the broken lines represent the data of Randak et al.<sup>14</sup> for 304LN and 316LN, respectively.<sup>13</sup> The various symbols depict the data for seven other investigations,<sup>13</sup> each on one of the following alloys: 304LN, 304N, and 316LN. As is the case for 304 and 316 (Fig. 1), alloys 304N and 304LN have approximately 20% greater ultimate strength at cryogenic temperatures than alloy 316LN. All three alloys have essentially the same yield strength at and below room temperature. The nitrogen contents of the 17 heats of test materials range from 0.09 to 0.17%.

With the exception of type AISI 201, the tensile properties of each alloy in Table 3 have been evaluated at cryogenic temperatures. The 21Cr-6Ni-9Mn alloy has been most thoroughly evaluated. Its tensile

Table 3. Compositions of nitrogen-strengthened austenitic stainless steels.

Type	Nominal Composition (%) <sup>a</sup>					
	Cr	Ni	Mn	C, max	N	Other
AISI 201	16-18	3.5-5.5	5.5-7.5	0.15	0.25, max.	
AISI 202	17-19	4-6	7.5-10	0.15	0.25, max.	
AISI 304N	18-20	8-10.5	2.0, max.	0.08	0.10-0.16	
304LN	18-20	8-20	8-12	2.0, max.	0.03	0.10-0.16
AISI 316N	16-18	10-14	2.0, max.	0.08	0.10-0.16	
AISI 316LN	16-18	10-14	2.0, max.	0.03	0.10-0.16	
ASTM XM-10 <sup>b</sup>	19-21.5	5.5-7.5	8-10	0.08	0.15-0.40	
ASTM XM-11 <sup>b</sup>	19-21.5	5.5-7.5	8-10	0.04	0.15-0.40	
ASTM XM-14 <sup>b</sup>	17-19	5-6	14-16	0.12	0.35-0.50	
ASTM XM-19 <sup>b</sup>	20.5-23.5	11.5-13.5	4-6	0.06	0.20-0.40	0.10-0.30 Cb
ASTM XM-29 <sup>b</sup>	17-19	2.25-3.75	11.5-14.5	0.08	0.20-0.40	0.10-0.30 V 1.5-3.0 Mo

a. For each grade: Si = 1.00, max.; P = 0.060, max.; S = 0.030, max.

b. ASTM A412

and yield strength data are summarized in Fig. 7.<sup>8</sup> This alloy typically has about 25% greater yield strength than the Cr-Ni-N alloys. Since yield strength increases and ductility decreases with decreasing temperature, fracture resistance must be considered when selecting these alloys for service at temperatures below 77 K.

### Toughness

The nitrogen-strengthened stainless steels have excellent toughness at room temperature. However, as shown in Fig. 8, significant toughness losses generally occur as the temperature is reduced.<sup>15</sup> At 4 K, the loss in toughness is proportional to the increase in yield strength, as shown in Fig. 9.

### Fatigue

The strain-cycling fatigue behavior of 21Cr-6Ni-9Mn has been measured at 295, 77, and 4 K by Shepic and Schwartzberg.<sup>7</sup> The results, presented in Fig. 10, exhibit crossover behavior similar to that of the 300-series stainless steels; that is, at high-cycle lives (greater than 10<sup>4</sup> cycles), the fatigue strength improves with decreasing temperature, and vice versa at low-cycle lives. A comparison of the results at 4 K (shown in Fig. 11.) indicates that the 21Cr-6Ni-9Mn alloy has fatigue strength better than 304L but not as good as 316.<sup>7</sup> Thus, the significantly higher strength of the nitrogen-strengthened grade does not result in a comparable improvement in fatigue life.

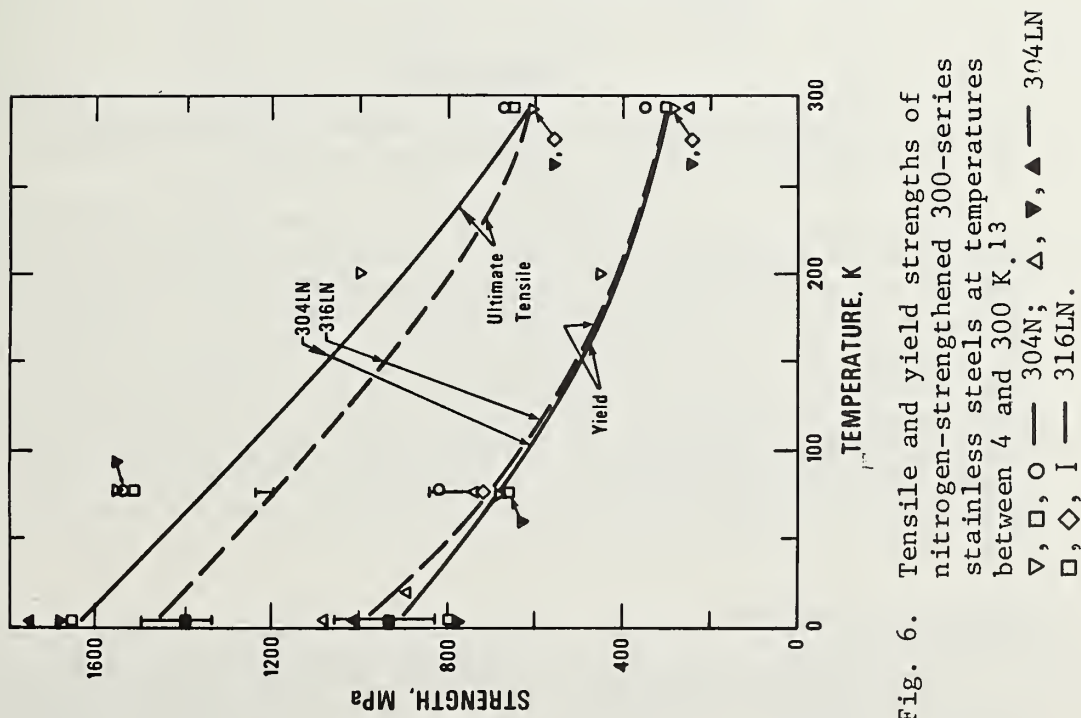


Fig. 6. Tensile and yield strengths of nitrogen-strengthened 300-series stainless steels at temperatures between 4 and 300 K.<sup>13</sup>  
 ▽, ◻, ◊ — 304N; Δ, ▽, ▲ — 304LN  
 ◻, ◊, I — 316LN.

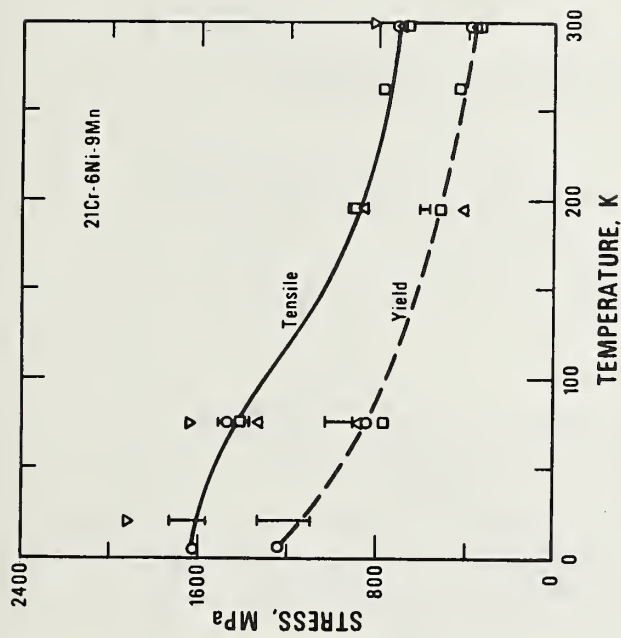


Fig. 7. Tensile and yield strengths of 21Cr-6Ni-9Mn stainless steel at temperatures between 4 and 300 K.<sup>8</sup>



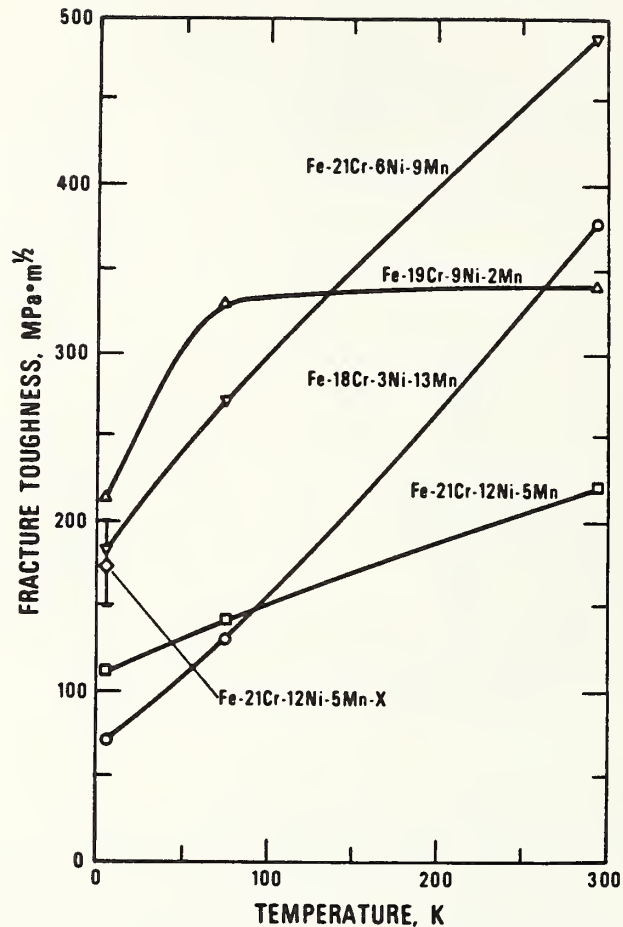


Fig. 8. Fracture toughness of five nitrogen-strengthened austenitic stainless steels at temperatures between 4 and 300 K.<sup>15</sup>

The fatigue crack growth behavior of several nitrogen-strengthened grades has been studied at cryogenic temperatures by Read and Reed.<sup>15</sup> The results at 4 K depend largely on the relative austenite stability of the alloys. For the least stable alloy evaluated, 18Cr-3Ni-13Mn, the fatigue crack growth rates are 6 times greater at 76 K than at room temperature, and even greater at 4 K. For the most stable alloy evaluated, 21Cr-12Ni-5Mn, the fatigue crack growth rates fall within the same scatter band at 295, 76, and 4 K. The fatigue behavior of types 304N and 21Cr-6Ni-9Mn is intermediate: the growth rates are essentially the same at 295 and 76 K, but increase 2- to 3-fold at 4 K.

#### Physical properties

The physical properties of the 300-series nitrogen-strengthened stainless steels are similar to those of the 300-series alloys summarized in Table 2). In the Cr-Ni-Mn grades, anomalies have been observed by Ledbetter<sup>17</sup> in the elastic behavior and by Ledbetter and Collings<sup>18</sup>

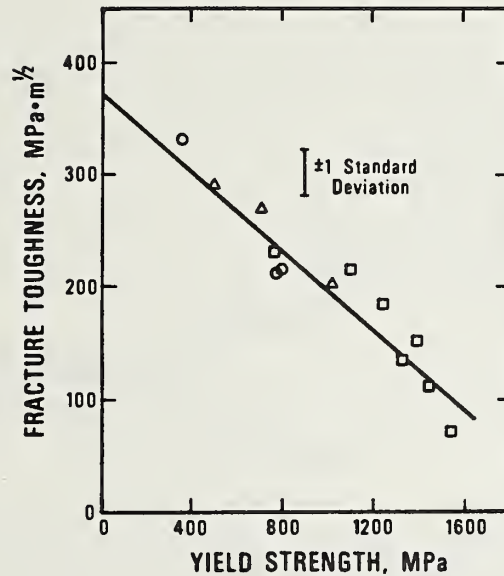


Fig. 9. Trend line for fracture toughness vs. yield strength at 4 K for austenitic stainless steels. o -- 304 (N);  $\Delta$  -- 316 (N);  $\square$  -- other austenitic stainless steels.<sup>16</sup>

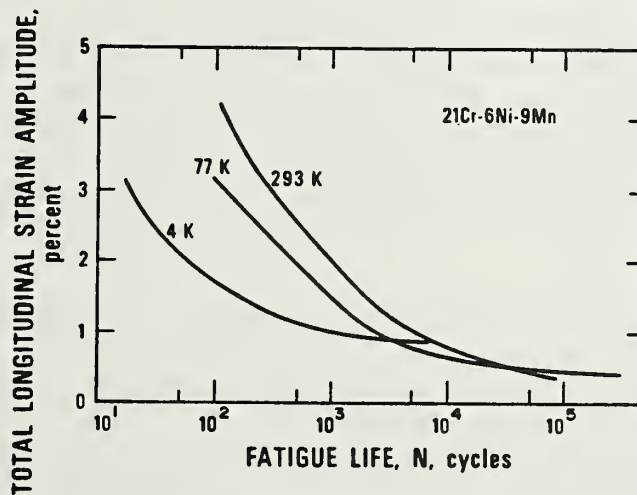


Fig. 10. Strain-cycling fatigue curves for 21Cr-6Ni-9Mn austenitic stainless steel at room temperature, 76, and 4 K.<sup>7</sup>

in some of the magnetic transitions and specific heat. In general, the nitrogen contributes to austenite stability and thus reduces the magnetic permeability induced in some alloys by deformation at low temperatures.

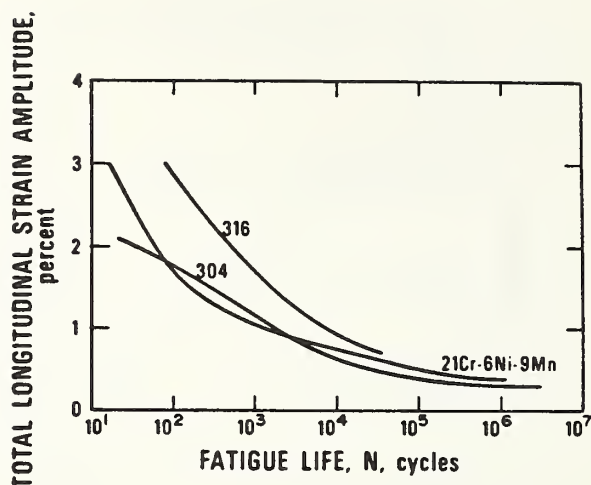


Fig. 11. Strain-cycling fatigue behavior of three austenitic stainless steels--AISI types 304 and 316 and a 21Cr-6Ni-9Mn alloy--at 4 K.<sup>7</sup>

#### HIGH-STRENGTH COLD-ROLLED SHEET

Most austenitic stainless steels are available in the cold-worked condition as sheet, strip, rod, and wire. Heavier product forms, such as plate and bar, are not usually cold-worked owing to the nonuniformity of deformation through the thickness. Cold-rolled sheet has been extensively used at cryogenic temperatures, primarily for missile cases operating at 20 K (liquid hydrogen) or 86 K (liquid oxygen). AISI grades 301, 302, 304L, and 310 have been evaluated for these applications.<sup>19,20</sup>

Cold working increases the strength of stainless steels by strain hardening and, in metastable alloys, by the strain-induced martensitic transformation. Both of these effects are apparent in the tensile properties of annealed stainless steels. Recall from Fig. 1 that the ultimate strength is much greater than the yield strength as a result of strain hardening. The differences between yield and ultimate strength are greatest for alloys that transform to martensite during the test; examples are AISI grades 304, 321, and 347. The strengthening of interest here is the increase in yield strength, which is caused by the cold-working operations, not by the tensile test. Yield strength increases are assumed to be similar for all the AISI 300-series grades.

#### Tensile Properties

Cold rolling causes remarkable increases in yield strength, somewhat less of an increase in ultimate strength, and a severe reduction of ductility. The influence of cold working on the yield strength

and elongation of AISI 310 at room temperature and 20 K is shown in Fig. 12.<sup>21</sup> At 20 K, the yield strength increases 2.4-fold as the cold work increases from 0 to 92%; the corresponding increase in ultimate strength is 1.6-fold. The ductility at 20 K decreases linearly with the percent of cold work, but remains 18% at 60% cold work, the extra-full-hard condition. In contrast, the room-temperature ductility is much lower at all levels of cold work and is only 3% at 60% cold work. Increased ductility at cryogenic temperatures is characteristic of austenitic stainless steels and has been used to advantage in forming operations, referred to as cryoforming.<sup>22</sup>

Metastable alloys, such as AISI grades 301 and 302, exhibit even greater increases in yield strength as a function of cold work owing

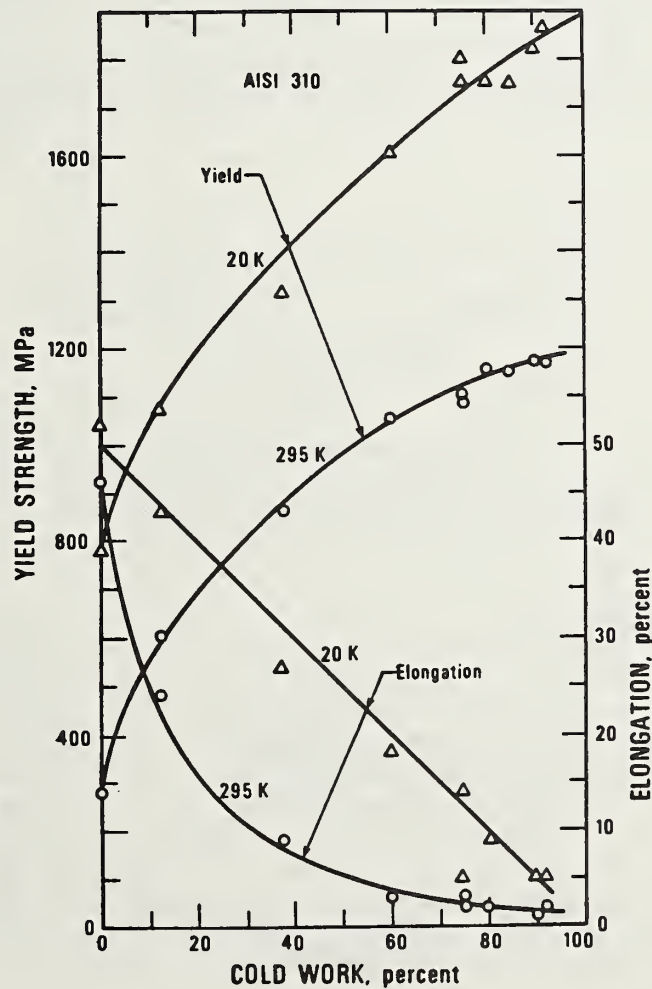


Fig. 12. Tensile yield strength and elongation of AISI type 310 austenitic stainless steel at room temperature and 20 K as a function of percent cold work.<sup>21</sup>

to the strain-induced martensitic transformation. At 60% cold work, the yield strengths at 20 K decrease with increased austenite stability as follows: AISI 301-- $\sigma_{ys}$  = 1940 MPa, AISI 302-- $\sigma_{ys}$  = 1720 MPa, and AISI 310-- $\sigma_{ys}$  = 1600 MPa. The mechanical properties of AISI 301 in the 60% cold-worked condition are summarized in Fig. 13. The drop in elongation that occurs between 76 and 20 K is accompanied by an increase in notch sensitivity and limits the usefulness of this alloy to temperatures 77 K and higher.

### Toughness

Notched tensile tests are usually used to evaluate the toughness of high-strength sheet alloys. Charpy impact tests and plane strain fracture toughness tests have specimen-thickness requirements that limit their applicability to sheet products. The ratio of tensile strengths in notched and unnotched specimens is used as the index of toughness. For stable alloys, such as AISI 310, the notched ( $K_T$  = 6.3)-to-unnotched tensile ratio for room and cryogenic temperatures

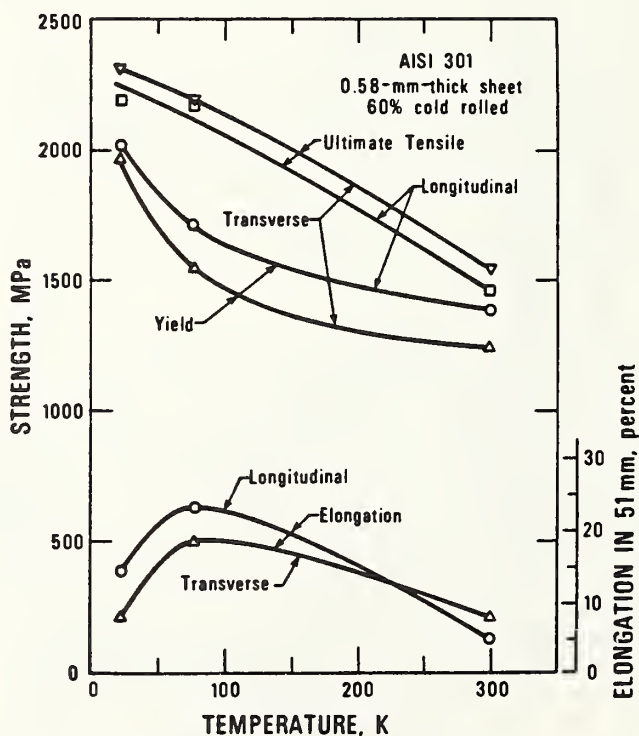


Fig. 13. Tensile properties of AISI type 301 austenitic stainless steel, 60% cold rolled, at temperatures between 20 and 300 K.<sup>19</sup>



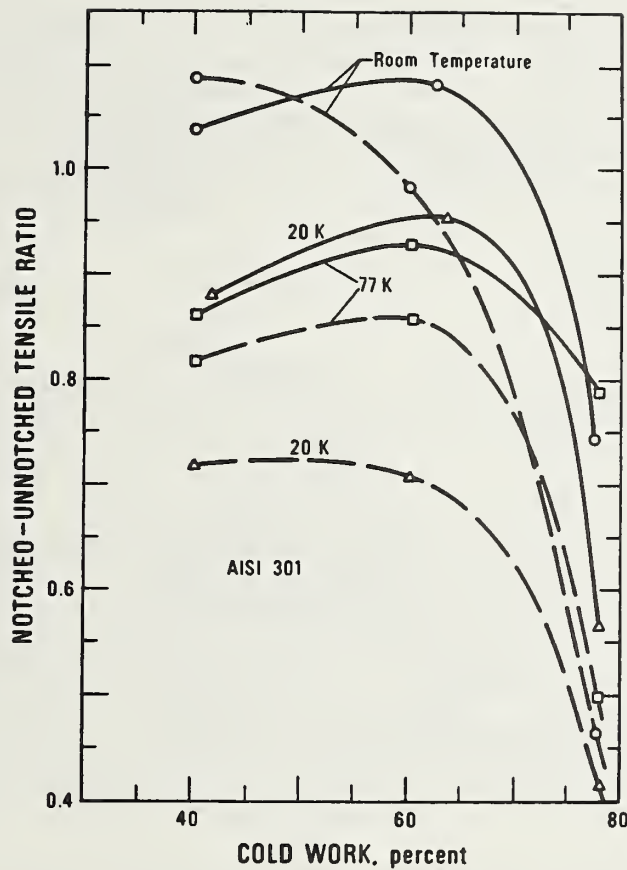


Fig. 14. Notched-unnotched tensile ratio ( $K_T = 6.3$ ) as a function of, cold work for AISI type 301 austenitic stainless steel.<sup>19</sup> Solid line - longitudinal; broken line - transverse.

is equal to  $1 \pm 0.1$  for cold reductions to 92%.\* Such is not the case for metastable alloys. For AISI 301, the notched ( $K_T = 6.3$ )-to-unnotched tensile ratio varies from 0.4 to 1.1, depending on the percent of cold work, test temperature, and specimen orientation, as shown in Fig. 14. Watson and Christian<sup>19</sup> relate this behavior to the martensitic transformation. The maxima in the notched-to-unnotched tensile ratios in Fig. 14 at 50 to 65% cold reduction were attributed to the stabilizing influence (during cryogenic testing) of cold working up to about 60%; cold reductions greater than 60% caused enough martensite to form during rolling to reduce notch strength at all test temperatures. The reduced toughness in the transverse specimens was attributed to the preferred orientation of the martensite rather than to the effects of inclusions.

\*  $K_T$  is the ratio of the maximum stress at the root of the notch to the nominal stress.

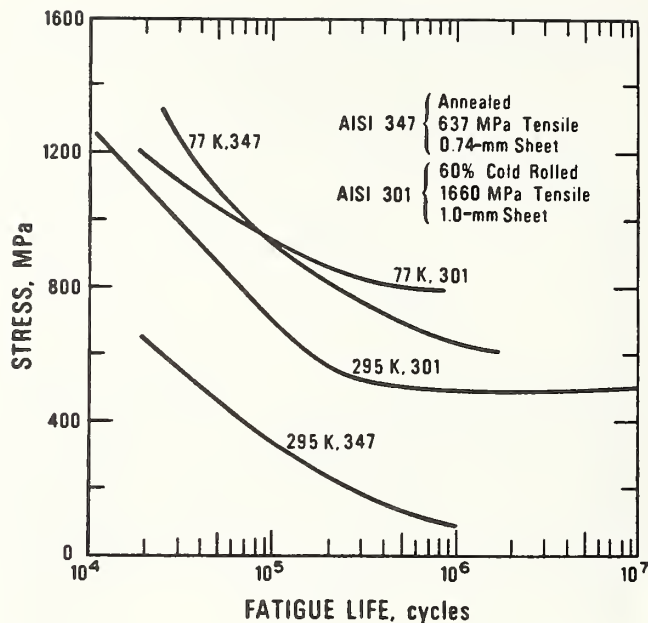


Fig. 15. Flexural fatigue ( $R = -1$ ) strength of two austenitic stainless steels - annealed AISI 347 and 60% cold-rolled AISI 301 - at room temperature and 77 K.<sup>23</sup>

### Fatigue

The cryogenic fatigue behavior of AISI 301 sheet, cold rolled approximately 60%, is shown in Fig. 15.<sup>23</sup> A comparison of these data with similar data on annealed AISI 347, also obtained by Favor et al.,<sup>23</sup> indicates that AISI 301 with a yield strength of 1530 MPa at 295 K has much better fatigue strength at room temperature than annealed AISI 347 with a yield strength of 255 MPa at 295 K. At cryogenic temperatures, however, the differences in fatigue strength are marginal; the annealed AISI 347 has better fatigue strength at fatigue lives less than  $10^5$  cycles and cold-rolled AISI 301 has better fatigue strength at fatigue lives greater than  $10^5$  cycles. At 20 K, the fatigue strength of AISI 347 is superior to that of AISI 301 at all cyclic lives. Thus, in fatigue critical applications at cryogenic temperatures, the increased yield strength of cold-rolled 301 stainless steels is of marginal value.

Notched fatigue ( $K_T = 3.1$ ) tests were conducted on the same materials by Gideon et al.<sup>24</sup> Their results further confirm that the high strength of cold-rolled AISI 301 stainless steel is not beneficial in fatigue critical applications at cryogenic temperatures. The notched fatigue behavior exhibited the same trends apparent in Fig. 15, that is, improved fatigue strength (but to a lesser extent) at room temperature and crossover behavior at approximately  $10^5$  cycles at 77 K.

The applicability of the fatigue test results on AISI 301 to other cold-rolled austenitic stainless steels has not been established. However, the trends discussed should serve as a warning to those who wish to use cold-rolled sheet in highly stressed, fatigue critical applications: Improved tensile strength does not necessarily result in improved fatigue strength, particularly at cryogenic temperatures.

## WELDS

### Welding

The austenitic stainless steels, with and without nitrogen strengthening, are readily weldable by all of the common welding processes, providing the appropriate consumables and procedures are used. The service experience with welded assemblies of the alloys has been satisfactory at cryogenic temperatures. The American Welding Society (AWS) designation system, which is similar to the AISI system for wrought products, is generally used to classify stainless steel filler metals. The AWS designations and chemical compositions of the filler metals commonly used for cryogenic applications are summarized in Table 4.

The strength of stainless steel welds at 4 K generally exceeds the corresponding base metal strength, but toughness is usually significantly lower. Four phenomena that affect the strength and toughness

Table 4. Composition limits of selected filler metals for welding austenitic stainless steels.

AWS Type	Composition (%)			
	Cr	Ni	C, max	Other
<b>Covered Electrodes<sup>a</sup></b>				
E308	18-21	9-11	0.08	
E308L	18-21	9-11	0.04	
E310	25-28	20-22.5	0.20	0.75 Si, max.
E16-8-2	14.5-16.5	7.5-9.5	0.10	0.50 Si, max.; 1-2 Mo
E316	17-20	11-14	0.08	2-2.5 Mo, max.; 1-2 Mo
E316L	17-20	11-14	0.04	
E330	14-17	33-37	0.25	
<b>Rod and Bare Electrodes<sup>b</sup></b>				
ER308	19.5-22	9-11	0.08	
ER308L	19.5-22	9-11	0.03	
ER310	25-28	20-22.5	0.08-0.15	
ER310	18-20	11-14	0.08	2-3 Mo
ER316	18-20	11-14	0.03	2-3 Mo

a. For covered electrodes: Mn = 2.5, max.; Si = 0.9, max.; P = 0.04, max.; S = 0.03, max.

b. For rod and bare electrodes: Mn = 1.0-2.5; Si = 0.25-60; P = 0.03, max.; S = 0.03, max.

of the as-deposited weld metal take on added significance at cryogenic temperatures: sensitization, ferrite content, nitrogen pickup, and oxide inclusions. In addition, heat treatment generally has a stronger influence on the weld metal than on the base metal.

Sensitization, the grain boundary precipitation of chromium carbides, reduces weld-metal toughness at low temperatures.<sup>25</sup> Consequently, weld metals with very low carbon, such as 308L (0.04% C, max.) and 316L (0.03% C, max.) are commonly used for cryogenic applications. Sensitization is most extreme if the weldment is given prolonged exposure in the temperature range 500 to 800°C. In multipass weldments, the underlying weld beads may receive sufficient exposure to these temperatures to cause significant toughness reductions in stainless steels with greater than 0.03% C. Subsequent annealing of the welds at temperatures greater than 950°C dissolves the carbides and improves the toughness.

The ferrite content of as-deposited weld metals can be estimated by using the Schaeffler constitution diagram. To avoid microfissuring, the weld-metal chemistry is usually balanced to provide 4 to 10% ferrite. However, for cryogenic service, there is concern that the ferrite, which is a b.c.c. phase and therefore brittle at low temperatures, may embrittle the weld metal. Szumachowski and Reid<sup>26</sup> have shown that ferrite reduces toughness at 77 K for a wide range of stainless steel weld metals. Read et al.<sup>25</sup> have evaluated the effect of ferrite content on the fracture toughness of shielded metal-arc welds of AWS 316 and 316L; the results at 77 K and 4 K are shown in Fig. 16. Elmer et al.<sup>27</sup> have evaluated the strength and toughness of several fully austenitic weld metals at 4 K. Their results for 20Cr-16Ni-7Mn-2.8Mo-2.1N, 17Cr-16Ni-4Mn-2.2Mo, 18Cr-20Ni-6Mn-0.27Nb, and 16Cr-16Ni-4Mn-1.5Mo indicate that strength and toughness combinations comparable to the base metal properties are possible.

Nitrogen increases the yield strength and decreases the toughness of stainless steel weld metals. When conventional (low-nitrogen) filler metals are used, nitrogen variations of 0.04 to 0.13% may occur, depending on the amount of air that enters the arc-shielding medium. The greatest variations in nitrogen pickup are associated with gas metal-arc (GMA) welding, where the nitrogen content ranges from 0.04 to 0.13%, depending on the type of gas coverage, the electrode extension, and the transfer mechanism (short-circuit is better than spray transfer). In shielded metal-arc (SMA) welding, smaller variations are attributed to electrode coatings; lime coatings generally give better coverage and less nitrogen pickup than titania coatings.

The influence of oxygen content on the toughness of weld metals at cryogenic temperatures has not yet been systematically studied. However, it is well known that oxide inclusions form sites for the initiation of microvoids, and that the ductile fracture resistance



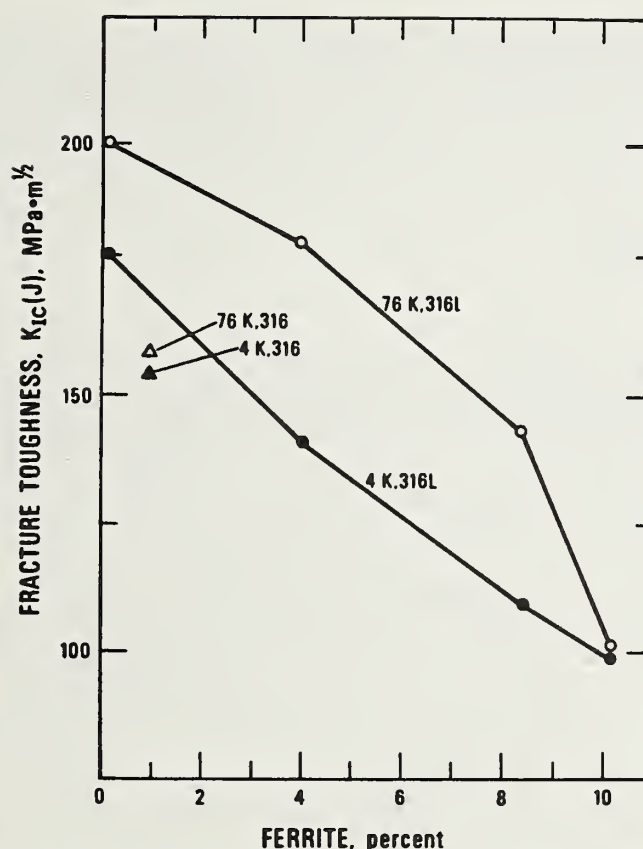


Fig. 16. Fracture toughness of AWS 316 and 316L weld metals at 76 and 4 K as a function of ferrite content.<sup>25</sup>

decreases as the number of microvoids increases. Some evidence on the influence of oxide inclusions comes from a study by Whipple and Kotecki,<sup>28</sup> in which a series of AWS 316L welds were produced using three different welding processes: GMA, gas tungsten arc (GTA), and submerged arc (SA). The toughness at 4 K increased with decreasing inclusion content: SA weld--103  $\text{MPa}\cdot\text{m}^{1/2}$ , GMA weld--161  $\text{MPa}\cdot\text{m}^{1/2}$ , and GTA weld--181  $\text{MPa}\cdot\text{m}^{1/2}$ . Other observations in the literature reveal the importance of inclusions. For example, Szumachowski and Reid<sup>26</sup> found SMA deposits of 316L with a basic coating (lime coating, -15 electrode) generally had superior toughness to those of 316L-16 deposits with a rutile coating; basic coatings are known to have lower oxygen content and oxide inclusions than rutile coatings.<sup>29</sup>

In summary, weld metal toughness can be improved by using low-carbon filler metals to avoid sensitization, by balancing weld-metal chemistry to avoid ferrite, by using low-nitrogen consumables and welding practices, and by using inert-gas-shielded welding processes or basic fluxes to reduce oxide inclusions. However, significant variations in the toughness still arise in ferrite-free welds containing



moderate nitrogen contents (0.004 to 0.007%), that are welded by the same process. As shown in Fig. 17, toughness varies as a function of grain width, a feature of the weld deposit controlled by the heat input and cooling rates.<sup>30</sup> To minimize these toughness variations, it is imperative to qualify the welding materials and procedures used for construction and to ensure that the qualified procedures are used during fabrication.

## CASTINGS

Austenitic stainless steel castings are used for cryogenic equipment having heavy sections or complex geometries that make fabrication from wrought products impractical. Typical examples are valve bodies and piston castings for liquefaction equipment. Several large castings have been used at temperatures down to 2 K for helium bubble chamber

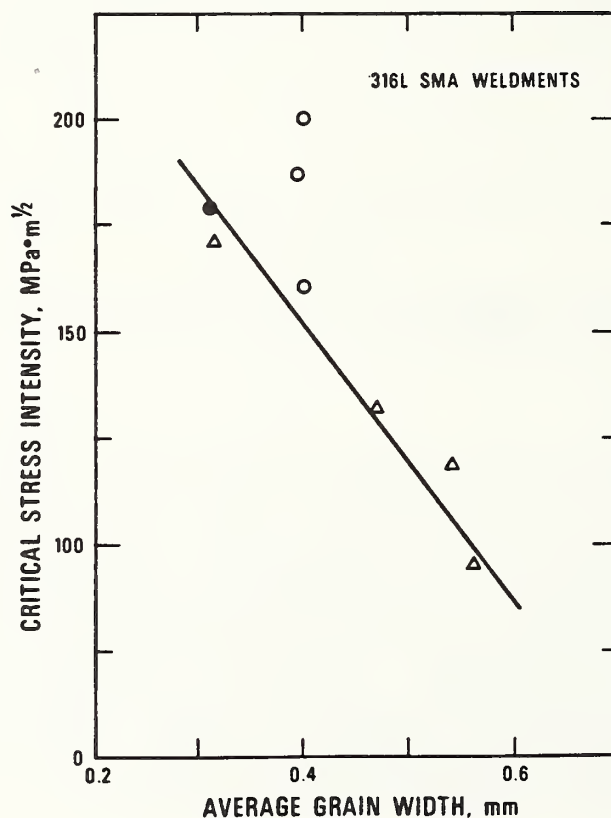


Fig. 17 Fracture toughness of fully austenitic weld metals at 4 K as a function of grain width. • --Read et al.;<sup>25</sup> Δ --LCP; o -- MFTF. LCP and MFTF refer to weld procedure qualification welds prepared for the Large Coil Project, Oak Ridge National Laboratory and the Magnetic Fusion Test Facility, Lawrence Livermore Laboratory.<sup>30</sup>

bodies. The Alloy Castings Institute (ACI) designation system is generally used for stainless steel castings. The ACI types, the equivalent AISI types for wrought products, and the chemical compositions of the casting alloys commonly used for cryogenic applications are summarized in Table 5.

A duplex microstructure of austenite and ferrite is typical of most of the stainless steel casting alloys. The ferrite content of the first six alloys listed in Table 5 may range from 0 to 40%; this is due to chemistry variations within the allowable ranges. The other three alloys (25Cr-20Ni, 20Cr-29Ni, and 16Cr-20Ni-10Mn) are fully austenitic. Ferrite content influences the strength and toughness and thus contributes to the variability observed in the mechanical properties of the castings.

The influence of ferrite content, nitrogen, and sensitization on the toughness of stainless steel castings is similar to their influence on weldments. Whipple and McHenry<sup>31</sup> evaluated the influences of  $\delta$ -ferrite and interstitial nitrogen in the strength and toughness of stainless steel castings at 4 K using nine CF8M (nominally a 19Cr-9Ni-2Mo alloy) castings with controlled chemistries. The chromium and nickel contents were varied to obtain two series of alloys: one series of five alloys had 0.05% N and  $\delta$ -ferrite contents ranging from 0 to 28.5%, the other series of five alloys had 9  $\pm$  1%  $\delta$ -ferrite and 0.02 to 0.20% N. As shown in Fig. 18, an increase in either  $\delta$ -ferrite or nitrogen content increases the yield strength and decreases ductility at 4 K. Fracture toughness decreases with increasing  $\delta$ -ferrite up to

Table 5. Compositions of austenitic stainless steel castings.

ACI Type	Nearest AISI Type	Composition <sup>a</sup> (%)			
		Cr	Ni	C, max.	Other
CF-3	304L	17-21	8-21	0.03	
CF-8	304	18-21	8-11	0.08	
CF-3M	316L	17-21	9-13	0.03	2-3 Mo, 1.5 Si max.
CF-8M	316	18-21	9-12	0.08	2-3 Mo, 1.5 Si max.
CF-8C	347	18-21	9-12	0.08	(8 x %C) Nb, min. or (10%C) Nb+Ta, min.
CF-20	302	18-21	8-11	0.20	
CK-20	310	23-27	19-22	0.20	
CN-7M	---	18-22	27-31	0.07	2-3 Mo, 1.5 Si max. 3-4 Cu

a. For each grade: Mn = 1.5, max.; P = 0.04, max.; Si = 2.0, max.; S = 0.04, max.

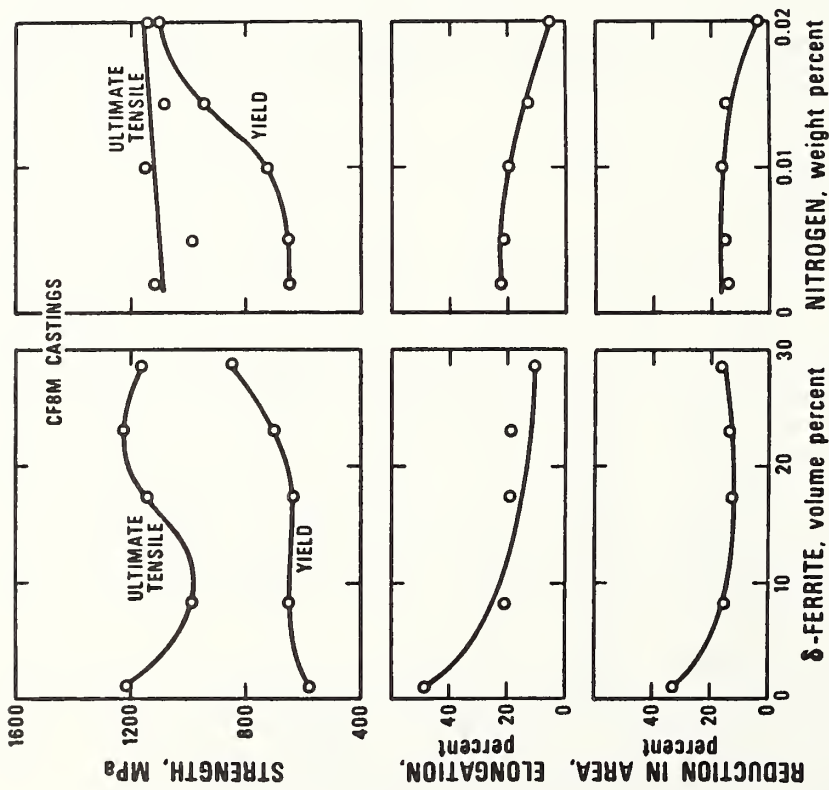


Fig. 18. The effect of  $\delta$ -ferrite and nitrogen content on the tensile properties at 4 K of CF8M austenitic stainless steel castings. The castings in the  $\delta$ -ferrite study contained 0.05% N and the castings in the nitrogen study contained 9  $\pm$ 1%  $\delta$ -ferrite.<sup>31</sup>

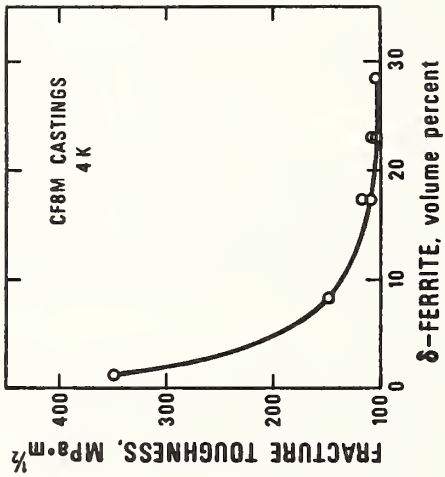


Fig. 19. The effect of  $\delta$ -ferrite on the 4-K fracture toughness of CF8M austenitic stainless steel castings containing 0.05% N.<sup>31</sup>

a  $\delta$ -ferrite content of 17% and then remains constant (Fig. 19). The influence of nitrogen on fracture toughness was not clearly established because the toughness at the 9% ferrite level was already a low value, 126 to 148 MPa·m<sup>1/2</sup> at nitrogen contents of 0.02 to 0.1%. The toughness was substantially lower at higher nitrogen contents: 74 MPa·m<sup>1/2</sup> at 0.14% N and 94 MPa·m<sup>1/2</sup> at 0.20% N.

## SUMMARY

The austenitic Cr-Ni stainless steels have a wide range of mechanical properties at cryogenic temperatures. Depending upon their chemical composition and heat treatment, the yield strengths at 4 K range from 200 to 1300 MPa. The annealed AISI 300-series grades have moderate strength and excellent toughness at low temperatures. Large increases in yield strength can be achieved by alloying with nitrogen or by cold working of selected products, such as sheet. Strength increases are accompanied by decreases in toughness and small changes in fatigue strength. Thus, strength, toughness, and fatigue properties should be balanced, depending on the specific design requirements. Welds and castings can have satisfactory properties at cryogenic temperatures, but the properties vary considerably, depending on metallurgical variables such as ferrite and nitrogen contents.

## REFERENCES

1. LNG Materials and Fluids, D. B. Mann, ed., National Bureau of Standards, Boulder, Colorado (1978).
2. Handbook on Materials for Superconducting Machinery, MCIC-HB-04, Battelle, Columbus, Ohio (1977).
3. Brickner, K. G. and Defilippi, J. D., Mechanical properties of stainless steels at cryogenic temperatures and at room temperature, in Handbook of Stainless Steels, McGraw-Hill, New York (1977), pp. 20-1-20-39.
4. Materials for Cryogenic Service, Engineering properties of austenitic stainless, International Nickel Limited, London (1974).
5. Low Temperature and Cryogenic Steels, Materials Manual, U.S. Steel Corp., Pittsburgh (1966).
6. Nachtigall, A. J., Strain cycling fatigue behavior of ten structural metals tested in liquid helium, liquid nitrogen, and ambient air, in: Properties of Materials for Liquefied Natural Gas Tankage, ASTM STP 579, American Society for Testing and Materials, Philadelphia (1975), pp. 378-396.
7. Shepic, J. A. and Schwartzberg, F. R., Fatigue testing of stainless steels, in: Materials Studies for Magnetic Fusion Energy Applications at Low Temperatures--I, NBSIR 78-884, National Bureau of Standards, Boulder, Colorado (1978), pp. 15-68.



8. Tobler, R. L. and Reed, R. P., Fatigue crack growth resistance of structural alloys at cryogenic temperatures, in: Advances in Cryogenic Engineering, Vol 24, Plenum Press, New York (1978), pp. 82-90.
9. Ledbetter, H. M., Weston, W. F., and Naiman, E. R., Low temperature elastic properties of four austenitic stainless steels, J. Appl. Phys. 46:3855-3860 (1975).
10. Clark, A. F., Childs, G. E., and Wallace, G. H., Electrical resistivity of some engineering alloys at low temperatures, Cryogenics 10:295-305 (1970).
11. Efferson, K. R. and Leonard, W. J., Magnetic Properties of Some Structural Materials Used in Cryogenic Applications, ORNL-4150, Oak Ridge National Laboratory, Oak Ridge, Tennessee (1976), p. 126.
12. Sanderson, G. P. and Llewellyn, D. T., Mechanical properties of standard austenitic stainless steels in the temperature range -196 to +800C, J. Iron Steel Inst. London 207:1129-1146 (1969).
13. McHenry, H. I. and Reed, R. P., Structural alloys for superconducting magnets in fusion energy systems, Nucl. Eng. Des. 58:219-236 (1980).
14. Randak, V. A., Wessling, W., Bock, H. E., Steimaurer, H. and Faust, L., Stahl Eisen 91:1255 (1971).
15. Read, D. T. and Reed, R. P., Toughness, fatigue crack growth and tensile properties of three nitrogen-strengthened stainless steels at cryogenic temperatures, in: The Metal Science of Stainless Steel, American Society of Metals, Metals Park, Ohio (1979), pp. 92-121.
16. Read, D. T. and Reed, R. P., Fracture and strength properties of selected austenitic stainless steels at cryogenic temperatures, Cryogenics 21:415-417 (1981).
17. Ledbetter, H. M., Anomalous low-temperature elastic behavior of a nitrogen-strengthened chromium-manganese stainless steel, Mater. Sci. Eng. 29:255-260 (1977).
18. Ledbetter, H. M. and Collings, E. W., Low-temperature magnetic and elastic-constant anomalies in three manganese stainless steels, in: Metal Science of Stainless Steels, American Institute of Mining, Metallurgical, and Petroleum Engineers, New York (1979).
19. Watson, J. F. and Christian, J. L., Low temperature properties of cold-rolled AISI types 301, 302, 304 ELC, and 310 stainless steel sheet, in: Low-Temperature Properties of High-Strength Aircraft and Missile Materials, ASTM STP 287, American Society for Testing and Materials, Philadelphia (1961), pp. 170-193.



20. Watson, J. F. and Christian, J. L., Mechanical properties of high-strength 301 stainless steel sheet at 70, -320, and -423°F in the base metal and welded joint configuration, in: Low-Temperature Properties of High Strength Aircraft and Missile Materials, ASTM STP 287, American Society for Testing and Materials, Philadelphia, (1961), pp. 136-149.
21. Christian, J. L., Gruner, J. D., and Girton, L. D., The effects of cold rolling on the mechanical properties of type 310 stainless steel at room and cryogenic temperatures, Trans. Am. Soc. Met. 57:199-207 (1964).
22. Schwartzberg, F. R. and Kiefer, T. F., Properties of Cryogenically Worked Metals, NASA contractor report No. NASA-CR-134757, National Aeronautics and Space Administration, Washington, D.C. (1975).
23. Favor, R. J., Gideon, D. N., Grover, H. J., Hayes, J. E., and McClure, G. M., Investigation of Fatigue Behavior of Certain Alloys in the Temperature Range of Room Temperature to -423°F, Report WADD TR 61-132, Battelle, Columbus, Ohio (1961).
24. Gideon, D. N., Favor, R. J., Koppenhafer, A., Grover, H. J., and McClure, M., Investigation of Notched Fatigue Behavior of Certain Alloys in the Temperature Range of Room Temperature to -423°F, ASD-TRD-62-351, Battelle, Columbus, Ohio (1962).
25. Read, D. T., McHenry, H. I., Steinmeyer, P. A., and Thomas, R. D., Jr., Metallurgical factors affecting the toughness of 316L SMA weldments at cryogenic temperatures, Weld. J. 59:104s-113s (1980).
26. Szumachowski, E. R. and Reid, H. F., Cryogenic toughness of SMA austenitic stainless steel weld metals: Part 1-Role of ferrite, Weld. J. 57:325s-333s (1978).
27. Elmer, J. W., McHenry, H. I., and Whipple, T. A., Strength and toughness of fully austenitic stainless steel filler metals at 4K, in: Materials Studies for Magnetic Fusion Energy Applications at Low Temperatures--IV, NBSIR 81-1645, National Bureau of Standards, Boulder, Colorado (1981), pp. 289-302.
28. Whipple, T. A. and Kotecki, D. J., Weld process study for 316L stainless steel weld metal for liquid helium service, in: Materials Studies for Magnetic Fusion Energy Applications at Low Temperatures--IV, NBSIR 81-1645, National Bureau of Standards, Boulder, Colorado (1981), pp. 303-321.
29. Lancaster, J. F., The Metallurgy of Welding, Brazing and Soldering, American Elsevier, New York (1965).
30. Whipple, T. A., McHenry, H. I., and Read, D. T., Fracture behavior of ferrite-free stainless steel welds in liquid helium, Weld. J. 60:72s-78s (1981).
31. Whipple, T. A. and McHenry, H. I., The mechanical properties of stainless steel castings at 4 K, in: Austenitic Stainless Steels at Low Temperatures, Plenum Press, New York (1982).



## AUSTENITIC-STEEL ELASTIC CONSTANTS\*

H. M. Ledbetter  
Fracture and Deformation Division  
National Bureau of Standards  
Boulder, Colorado

### ABSTRACT

We review recent NBS studies on austenitic-stainless-steel elastic constants at low temperatures. By measuring velocities of longitudinal and shear waves, we determined accurately the usual engineering elastic constants: Young's modulus, shear modulus, bulk modulus (reciprocal compressibility), and Poisson's ratio.

Due to magnetic transitions, most of these alloys exhibit low-temperature elastic-constant anomalies. The transitions occur over a temperature range, but show reversible behavior and are probably second-order. A magnetic-susceptibility cusp occurs near the shear-modulus transition temperature. Due perhaps to local moments above  $T_C$ , the bulk-modulus maximum occurs at a higher temperature. Increased nickel content lowers the transition temperature while increased manganese raises it.

At room temperature, twenty different heats of stainless-steel 304 show an elastic-constant variability of about 1.5 percent. For all practical purposes these alloys exhibit elastic isotropy; texture effects, if present, can not exceed 1.0 percent. Surprisingly, at low temperatures, elastic constants vary several percent; this probably reflects steels in different magnetic states.

Surprisingly, interstitial carbon and nitrogen (up to 1.3 atomic percent) do not affect the elastic constants within 0.1 percent. We ascribe this to the interstitial's symmetry; occupying an octahedral site, it produces an isotropic lattice distortion. With increasing manganese content, all the elastic stiffnesses decrease linearly: the bulk modulus most and Poisson's ratio least.

From measured elastic constants of eleven austenitic stainless steels, we deduced the effects of chromium and nickel on the elastic constants. Chromium raises all the constants; nickel lowers them all except Poisson's ratio.

Using Kröner's averaging method, we related polycrystalline elastic constants to monocrystalline values. For certain cases, we describe how the important monocrystalline elastic constants --  $C_{11}$ ,  $C_{12}$ ,  $C_{44}$  -- can be estimated from polycrystalline values.

\* To be published in *Austenitic Steels at Low Temperatures*, Eds. R. P. Reed and T. Horiuchi, Plenum Press, New York (1983).





## INTRODUCTION

We now witness many vigorous attempts to improve the properties of austenitic stainless steels. Mechanical-property and physical-property improvements require two essential ingredients: an understanding based on theory and accurate measurements of important properties.

Recently,<sup>1</sup> the author summarized briefly studies at NBS on the elastic constants of austenitic steels. The present paper extends that review.

Since 1975, the elastic-properties group at NBS produced over thirty manuscripts that relate to stainless-steel physical-mechanical properties, especially the elastic constants. Experimentally, we studied the effects of several variables:

- temperature
- substitutional alloying (Cr, Ni, Mn)
- interstitial alloying (C, N)
- magnetic field
- texture (castings, welds)
- variability, sample-to-sample

Theoretically, several properties interest us:

- monocrystal/polycrystal elastic constants
- monocrystal elastic-constant prediction
- texture effects (Voigt, Reuss, Kröner)

- instability/elastic-constant interrelationships
- fcc Fe elastic constants, monocrystal and polycrystal
- Debye temperature
- second-order phase-transition thermodynamics
- magnetostriction
- theory of 3d metals

## VARIABILITY

The variability of elastic constants in 304 stainless steel was determined by measuring longitudinal and transverse ultrasonic velocities in twenty samples acquired randomly.<sup>2</sup> Three kinds of variations -- sample-to-sample, directional within a sample, and repeated measurements on a single sample -- were reported for four elastic constants: the bulk modulus, Young's modulus, shear modulus, and Poisson's ratio, denoted  $B$ ,  $E$ ,  $G$ , and  $\nu$ . Because of surprisingly small variations, one percent or less, the principal problem became measurement sensitivity and reproducibility. To overcome this problem, a high-resolution measurement system was devised using general-purpose equipment augmented with a very simple impedance-transforming amplifier and an FET transmission gate.

Effects due to frequency and directionality were negligible. Velocity variations were quite small, 0.3 percent for  $\nu_{\parallel}$  and 0.6 percent for  $\nu_{\perp}$ , the longitudinal and transverse sound velocities. Coupled with a 0.6 percent density variation, this leads to elastic-constant variations of 0.9 percent for  $E$ , 1.1 percent for  $G$ , and 1.4 percent for both  $B$  and  $\nu$ . All these are much smaller than variations implied by elastic constants reported in the literature for these alloys. Thus, reported variabilities in these elastic constants must arise from experimental measurement errors, not from the material itself. Texture effects, if present, can not exceed one percent. A similar study involving smaller numbers of specimens gave similar results for 310 and 316 stainless steels.<sup>3</sup> We ascribe the small variability to the thermal-mechanical treatment: high-temperature mechanical deformation and recrystallization.

We attribute the larger variations in  $B$  and  $\nu$  to small differences in the magnetic state, even above the Néel temperature. The magnetic state affects the volume, which in turn affects the elastic constants, especially  $B$ . More than any other elastic constant, the Poisson ratio,  $\nu$ , depends on the nature of the interatomic bonding. Several different magnetic states may occur in these alloys; those suggested include paramagnetic, ferromagnetic, antiferromagnetic, mictomagnetic, spin-glass, and even ferrimagnetic. Thus, details of chemical composition and thermal-mechanical treatment may affect the magnetic state, the interatomic bonding, and Poisson's ratio.

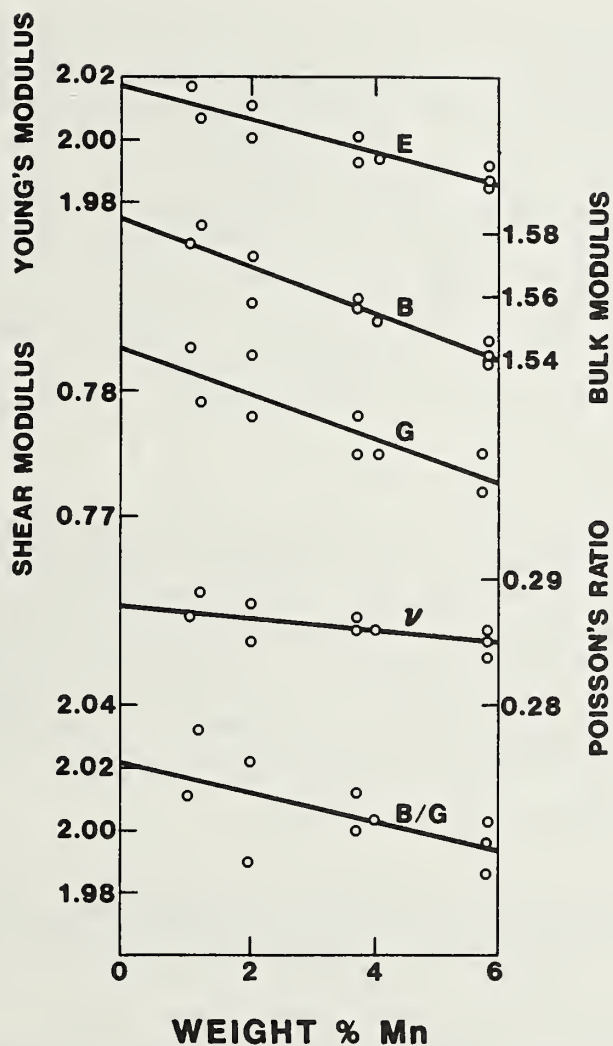


Fig. 1. Compositional variation of elastic constants of Fe-Cr-Ni alloys containing Mn. Units of E, B, and G are  $10^{11}$  N/m<sup>2</sup>.  $\nu$  is dimensionless.

## ALLOYING

### (a) Manganese

Alloying Mn into a 304-type stainless steel decreases all the elastic-stiffness constants and also decreases Poisson's ratio,<sup>4</sup> as shown in Fig. 1. The bulk modulus decreases most, reflecting the high compressibility of Mn atoms. Poisson's ratio and the B/G ratio both vary slowly with Mn concentration. This indicates that Mn does not change the nature of the chemical bonding. Manganese's unusual

bonding characteristics lead one to expect possible changes. By factoring into force constants, the relationship of many-body forces to elastic constants and bonding becomes more clear. Observation shows that  $B/G = 2.005 \pm 0.014$  for all ten alloys. Thus, the marked departure from a two-body-force value of 1.76 shows that many-body forces occur in these alloys. (That many-body forces exist in transition-metal alloys is already well known.) The surprising result is that the ratio is nearly constant for all alloys, indicating no significant change in the character of the chemical bonding. Poisson's ratio is nearly invariant with Mn content:  $\nu = 0.286 \pm 0.001$ , but also different from the  $\nu = 0.261$  predicted for longitudinal-force-constant-only bonding.

#### (b) Chromium and nickel

By accurately measuring the elastic constants of eleven austenitic stainless steels of known chemical composition, we could, by linear-least-squares analysis, determine the separate effects of Cr and Ni on the elastic constants.<sup>5</sup> We found that Cr increases all the elastic constants, including the Poisson ratio and the B/G ratio. On the other hand, Ni decreases all the elastic stiffnesses, but increases both  $\nu$  and B/G. We now try to understand this behavior from the viewpoint of 3d-metal alloy theory.

#### (c) Carbon and nitrogen

Nine stainless-steel 304-type alloys were studied at room temperature.<sup>6</sup> Carbon-plus-nitrogen contents of these alloys ranged from 0.067 to 0.325 weight percent (0.3 to 1.3 atomic percent). Five elastic constants -- longitudinal modulus, Young's modulus, shear modulus, bulk modulus, and Poisson's ratio -- were determined by the pulse-echo ultrasonic method. Within an experimental uncertainty of about 0.1 percent, all the elastic constants remain unaffected by C and N additions. Interstitial atoms, especially those in isotropic, octahedral positions, should affect B more than G because they cannot move under a dilatational force. Yet, among the nine alloys, B and G show the same variations from the mean. Present results contrast sharply with observations reported for ferritic Fe. Carbon added to alpha Fe reduces elastic stiffnesses such as E and G by about five percent per atomic percent C! Indeed, C is the most effective known alloying element in altering alpha Fe's elastic constants. The essential distinction between the ferritic and austenitic cases is the crystal structure. Body-centered-cubic crystals are less accommodating to interstitials than are face-centered-cubic crystals. Carbon alloyed into bcc Fe occupies octahedral interstices that have tetragonal symmetry, which produce a strong tetragonal distortion; no similar distortion occurs in fcc Fe, where C occupies large octahedral interstices and the lattice distortion is isotropic.



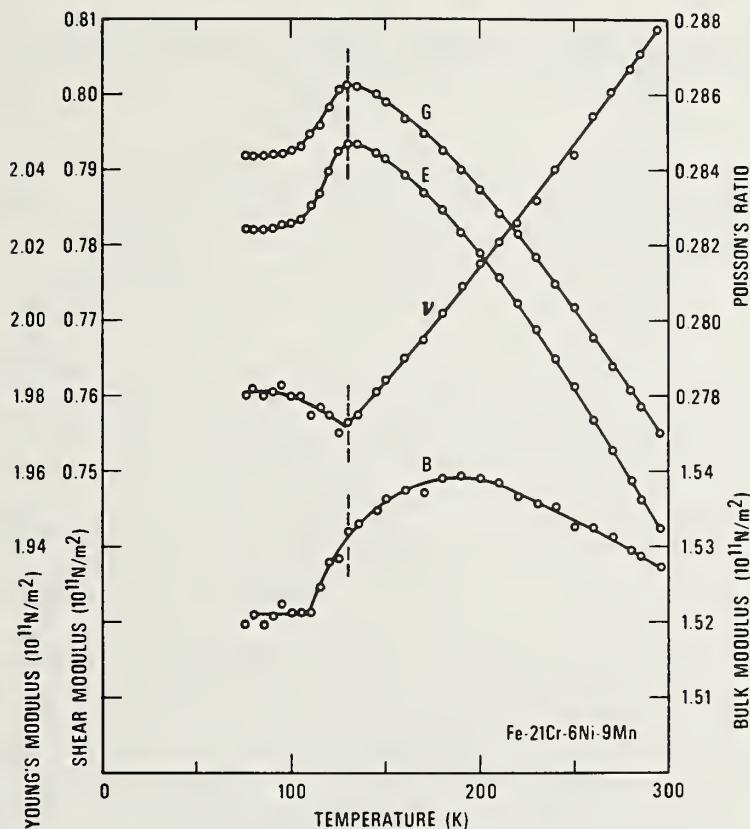


Fig. 2. Temperature variation of elastic constants of Fe-21Cr-6Ni-9Mn.

## TEMPERATURE

Cooling produces dramatic, anomalous changes in the elastic constants of austenitic steels, especially those high in Mn content and/or low in Ni content.<sup>7-19</sup> Figure 2 shows these changes for a nitrogen-alloyed manganese stainless steel, Fe-21Cr-6Ni-9Mn. This anomaly arises from a magnetic transition, reflected in the magnetic susceptibility. The following principal results and conclusions emerge from cooling studies on this and similar alloys:

1. During cooling from ambient to liquid-helium temperature, these steels show anomalies in all their elastic constants. Both the size of the anomalies and the transition temperatures increase with higher Mn content and decrease with higher Ni and Cr contents. High-Mn, low-Ni alloys actually show transition temperatures above ambient.<sup>14,15</sup>
2. At the same time, the alloys undergo sharp antiferromagnetic-like transitions, giving rise to a cusp-like anomaly in the



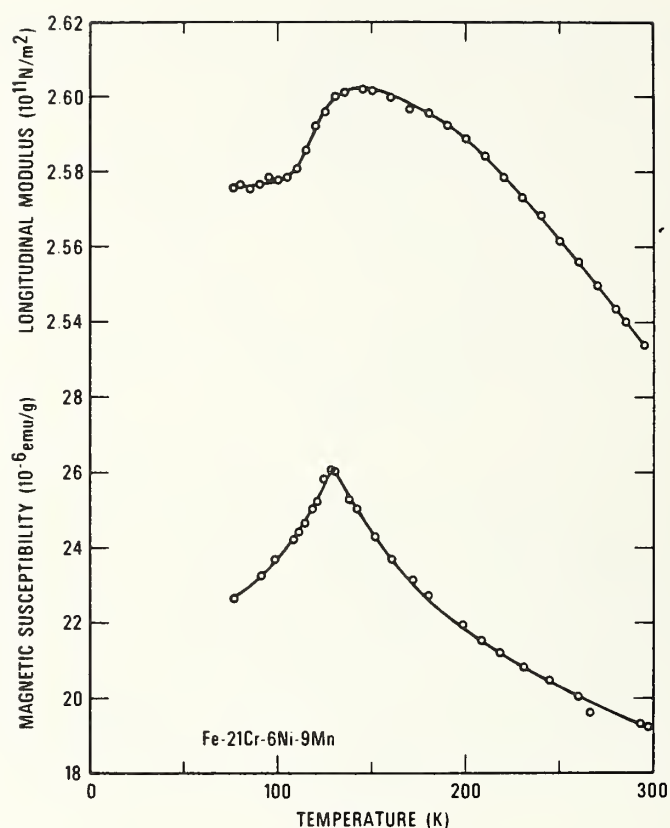


Fig. 3. Temperature variation of longitudinal elastic modulus and magnetic susceptibility of Fe-21Cr-6Ni-9Mn.

magnetic-susceptibility,  $\chi$ . Figure 3 shows the magnetic-susceptibility/temperature curve for Fe-21Cr-6Ni-9Mn. In all these alloys where the  $\chi$ -T curve has been determined, a cusp-like anomaly occurs very near the center temperature of the elastic-constant anomalies.<sup>9,10,17</sup>

3. The shear-type elastic constants (G and E) and Poisson's ratio change sharply near the transition temperature,  $T_c$ . But the dilatation-type elastic constant (B) changes less abruptly and begins to soften at temperatures above  $T_c$ , owing perhaps to local moments above  $T_c$ . This emphasizes that there exists a magnetic-state variable, perhaps the local magnetic moment,  $m$ , that affects physical properties both below and above the paramagnetic-antiferromagnetic transition temperature.

4. The energy terms usually invoked for magnetic transitions cannot explain the anomalous elastic-constant changes with temperature. In terms of conventional ferromagnetic or antiferromagnetic

ordering theory, a possible morphic effect is suggested. By conventional energy terms we mean domain, volume (magnetostriction), and exchange.

5. All alloys studied to date show qualitatively similar behavior. This occurs despite wide chemical-composition variations: 1-21 Ni, 5-25 Cr, and 1-26 Mn. Thus, the elastic-constant anomalies arise as a characteristic of this class of alloys; they do not depend on a particular element such as Mn.

6. Manganese affects the transition temperature more than Ni or Cr. Preliminary results for  $\Delta T_t / \Delta x$  are +11, -3, and -2, respectively, for these three elements, where  $T_t$  denotes transition temperature and  $x$  denotes weight-percent chemical composition.

7. Extrapolations to unalloyed fcc Fe predict that it shows antiferromagnetism at low temperatures. For Fe, the preliminary transition temperature is 80 K.

8. All elastic-constant/temperature curves show complete reversibility upon cooling and reheating. This suggests a second-order transition, which is consistent with the Landau-Lifshitz<sup>32</sup> proof that any magnetic phase transition can be second-order. Also, the bulk modulus decreases during cooling through the transition, as required by second-order-phase-transition thermodynamics.

9. Bulk-modulus softening during cooling is also predicted by quantum-mechanical models. Moruzzi et al.<sup>33</sup> showed for Fe, Cr, and Mn that the effect of magnetic interactions is to increase the volume and decrease the bulk modulus. Although these calculations were done for ferromagnetic spin polarizations, similar repulsive forces should exist in antiferromagnetics. The only requirement is the existence of a magnetic moment over a scale sufficient to establish a band structure (a few atoms).

#### MONOCRYSTAL/POLYCRYSTAL RELATIONSHIPS

Especially for cubic crystal symmetry, the problem of relating the single-crystal elastic constants ( $C_{11}$ ,  $C_{12}$ ,  $C_{44}$ ) to the quasi-isotropic polycrystalline elastic constants ( $B$ ,  $C$ ) has been studied extensively, both theoretically and experimentally. The bulk modulus,  $B$ , because it is a rotational invariant of the elastic-stiffness tensor, is always given by

$$B = (C_{11} + 2C_{12})/3 \quad (1)$$

even for a highly textured material. The expression for the shear modulus,  $G$ , depends on the assumptions of the model. Considering

the self-consistent problem of an anisotropic single-crystal inclusion embedded in a corresponding isotropic matrix, and assuming stress equilibrium at the interface, Kröner<sup>34</sup> showed that

$$G^3 + \alpha G^2 + \beta G + \gamma = 0 \quad (2)$$

where  $\alpha = (5C_{11} + 4C_{12})/8 \quad (3)$

$$\beta = -C_{44}(7C_{11} - 4C_{12})/8 \quad (4)$$

and  $\gamma = -C_{44}(C_{11} - C_{12})(C_{11} + 2C_{12})/8 \quad (5)$

In the forward case, these relationships permit the calculation of B and G from the  $C_{ij}$ 's, the isotropic from the anisotropic, two elastic constants from three.

With one additional piece of information, from either theory or observation, some single relationship among the  $C_{ij}$ 's, the reverse case can be computed also. The  $C_{ij}$ 's can be computed from B and G.

For a relationship among the  $C_{ij}$ 's of 316 stainless steel, we consider the existing  $C_{ij}$  measurements on fcc Fe-Cr-Ni alloys. At least two approximate relationships emerge. First, the elastic anisotropy is relatively constant, being  $3.51 \pm 0.19$ . Second, the  $y = C_{12}/C_{11}$  ratio is relatively constant, being  $0.642 \pm 0.037$ . Ledbetter showed that a slightly better y value results if values for fcc Fe and Ni are also included with these four alloys, the value being  $y = 0.635 \pm 0.031$ .

For B and G values, we use those reported by Ledbetter:<sup>3</sup>  $B = 1.575 \pm 0.014$  and  $G = 0.752 \pm 0.015 \cdot 10^{11} \text{ N/m}^2$ .

Thus, for 316 stainless steel, using  $y_2 = 0.635$ , the results are  $C_{11} = 2.06$ ,  $C_{12} = 1.33$ ,  $C_{44} = 1.19 \cdot 10^{11} \text{ N/m}^2$ . These results are consistent with most existing  $C_{ij}$  measurements on Fe-Cr-Ni alloys. We believe they provide the best available estimate of the monocrystalline 316-stainless-steel elastic constants. The constants serve many purposes, including dislocation calculations and the ultrasonic nondestructive evaluation of welds. Further details on this calculation occur elsewhere.<sup>20,21</sup>

## TEXTURE

Potentially, texture occurs in all polycrystalline aggregates. By texture we mean a nonrandom distribution of crystallite orientations. Texture arises from many sources, including: mechanical deformation, annealing (recrystallization), solidification, electrodeposition, vapor deposition (epitaxy), phase transformation, and

welding. For 316 stainless steel, we studied texture in welds and in castings.<sup>22,23</sup>

First, we describe some theoretical studies,<sup>24-26</sup> principally the case of a 316-stainless-steel weld exhibiting (100) rod texture. One expects that cubic-symmetry crystallites in welds occur either with random orientations or with a single preferred axis parallel to the principal heat-flow direction, denoted  $x_3$ . In the  $x_1$ - $x_2$  plane, crystallites are expected to orient themselves randomly because no preferred heat-flow direction occurs in that plane. Thus, an effective fiber texture occurs with  $x_3$  being the fiber axis. Macroscopically, such a material exhibits transverse-isotropic symmetry, with five independent elastic constants. This is equivalent to hexagonal symmetry. In Voigt's contracted  $C_{ij}$  notation the symmetrical elastic-stiffness matrix is:

$$C_{ij}^H = \begin{bmatrix} C_{11}^H & C_{12}^H & C_{13}^H & 0 & 0 & 0 \\ & C_{11}^H & C_{13}^H & 0 & 0 & 0 \\ & & C_{33}^H & 0 & 0 & 0 \\ & & & C_{44}^H & 0 & 0 \\ & & & & C_{44}^H & 0 \\ & & & & & C_{66}^H \end{bmatrix} \quad (6)$$

where  $C_{66}^H = \frac{1}{2}(C_{11}^H - C_{12}^H)$ . Thus, the theoretical problem is to express the five hexagonal-symmetry elastic constants,  $C_{ij}^H$ , in terms of the three cubic-symmetry elastic constants:  $C_{11}$ ,  $C_{12}$ ,  $C_{44}$ .

Present theory does not permit calculation of the elastic constants of textured polycrystalline aggregates of cubic-symmetry crystallites. This is a special and more difficult case of determining the average elastic constants of a random polycrystalline aggregate. For this latter problem, Landau and Lifshitz<sup>35</sup> remind us that "there is...no general relationship between the moduli of elasticity of a polycrystal and those of a single crystal of the same substance." The fiber-texture case involves a two-dimensional, rather than a three-dimensional, average.

However, elastic-constant bounds can be calculated for textured aggregates. In this study we calculate the Voigt (constant strain)



and Reuss (constant stress) bounds and use Hill's<sup>36</sup> suggestion of an arithmetic average to estimate the elastic constants. This approach turns out to be quite reasonable because the Voigt and Reuss bounds do not differ dramatically (a maximum of 37 percent). And for the important  $\langle 100 \rangle$ -texture case, the bounds coincide for three elastic constants:  $C_{13}^H$ ,  $C_{33}^H$ , and  $C_{44}^H$ . Thus, we know these three constants unambiguously. Kröner and Wawra<sup>37</sup> explain the systematics of this bounds coincidence, and they give the following expressions for the  $C_{ij}^H$ 's:

$$\begin{aligned} C_{11}^H &= C_1 + 3\beta C_3 = \frac{1}{4}(3C_{11} + C_{12} + 2C_{44}) \\ C_{12}^H &= C_2 + \beta C_3 = \frac{1}{4}(C_{11} + 3C_{12} - 2C_{44}) \\ C_{13}^H &= C_2 - 4\beta C_3 = C_{12} \\ C_{33}^H &= C_1 + 8\beta C_3 = C_{11} \\ C_{44}^H &= \frac{1}{2}(C_1 - C_2) - 4\beta C_3 = C_{44} \end{aligned} \tag{7}$$

where

$$\begin{aligned} C_{66}^H &= \frac{1}{2}(C_{11}^H - C_{12}^H) = \frac{1}{4}(C_{11} - C_{12} + 2C_{44}) \\ 5C_1 &= 3C_{11} + 2C_{12} + 4C_{44} \\ 5C_2 &= C_{11} + 4C_{12} + 2C_{44} \\ C_3 &= C_{11} - C_{12} - 2C_{44} \end{aligned} \tag{8}$$

where  $\beta = 1/20$  for  $\langle 100 \rangle$  fiber texture.

Apparently, relationships for the  $S_{ij}^H$ 's, which give the Reuss bounds by matrix inversion, do not occur<sup>11</sup> in the literature. These are:

$$\begin{aligned} S_{11}^H &= \frac{1}{8}(6S_{11} + 2S_{12} + S_{44}) \\ S_{12}^H &= \frac{1}{8}(2S_{11} + 6S_{12} - S_{44}) \end{aligned}$$



$$S_{13}^H = S_{12} \quad (9)$$

$$S_{33}^H = S_{11}$$

$$S_{44}^H = S_{44}$$

$$S_{66}^H = 2(S_{11}^H - S_{12}^H) = \frac{1}{2}(2S_{11} - 2S_{12} + S_{44})$$

In deriving these relationships, one must remember that the inverse  $C_{ijkl}^{-1}$  of a fourth-rank elasticity tensor relates to the inverse  $C_{\alpha\beta}^{-1}$  of its associated  $6 \times 6$  matrix by a factor multiplied times  $C_{ijkl}^{-1}$ . This factor is 4 if both  $\alpha$  and  $\beta$  exceed 3, is 2 if either  $\alpha$  or  $\beta$  exceeds 3, and is 1 if neither  $\alpha$  nor  $\beta$  exceeds 3.

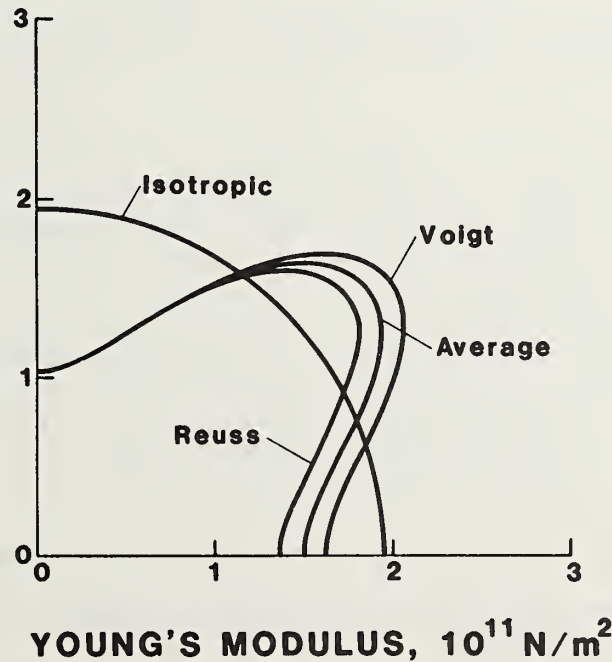


Fig. 4. Angular variation of Young's modulus for 316 stainless steel for  $\langle 001 \rangle$  texture. Vertical direction is  $x_3$  (hex), about which figure has complete rotational symmetry. Average denotes simple arithmetic average of Voigt and Reuss bounds, which correspond to constant strain and constant stress, respectively.

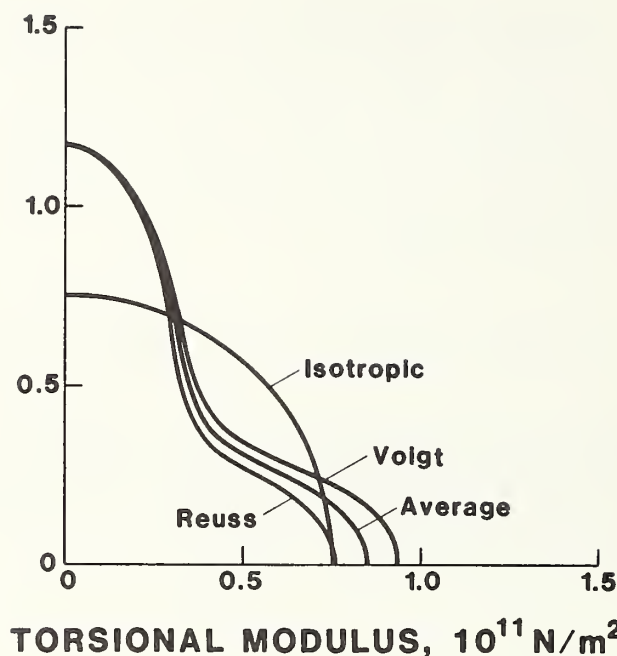


Fig. 5. Angular variation of torsional modulus for 316 stainless steel for  $\langle 001 \rangle$  texture. See figure caption 4.

Table 1 shows the predicted single-crystal elastic constants of 316 stainless steel. Other principal results of the study--elastic stiffness, elastic compliance, and sound velocity--occur in Table 1, which shows Voigt and Reuss bounds together with their arithmetic average for the  $\langle 100 \rangle$  ideal fiber texture. To obtain sound velocities, we used a mass density of  $7.958 \text{ g/cm}^3$ . From these results, the polar plots shown in Figs. 4-6 were determined using well-known relationships. These figures give the angular variation of Young's modulus,  $E$ , torsional modulus,  $T$ , and sound velocities, both longitudinal,  $v_l$ , and transverse,  $v_t$ . All curves in Fig. 6 represent arithmetic averages of Voigt and Reuss bounds.

These calculations show the following principal results:

1. Texture induces large elastic-constant changes (departures from isotropic values).
2. Shear elastic constants,  $C_{44}^H$  and  $C_{66}^H$ , change more than longitudinal constants,  $C_{44}^H$  and  $C_{33}^H$ , and more than the off-diagonal constants,  $C_{12}^H$  and  $C_{13}^H$ .
3.  $C_{44}^H$  offers the best opportunity for detecting texture and estimating its amount.  $C_{44}^H$  corresponds to a shear wave propagated along the fiber axis ( $x_3$ ) and vibrating in the  $x_1$ - $x_2$  plane, which is elastically isotropic.

Table 1. Elastic stiffness, elastic compliance, and sound velocities for 316 stainless steel with <100> fiber texture.<sup>a</sup>

	Voigt	Reuss	Average	Isotropic
$C_{11}^H$	2.473	2.265	2.369	2.577
$C_{12}^H$	0.926	1.133	1.029	1.073
$C_{13}^H$	1.326	1.326	1.326	1.073
$C_{33}^H$	2.072	2.072	2.072	2.577
$C_{44}^H$	1.174	1.174	1.174	0.752
$C_{66}^H$	0.774	0.566	0.670	0.752
$S_{11}^H$	0.617	0.736	0.676	0.514
$S_{12}^H$	-0.029	-0.148	-0.088	-0.151
$S_{13}^H$	-0.376	-0.376	-0.376	-1.515
$S_{33}^H$	0.964	0.964	0.964	0.514
$S_{44}^H$	0.852	0.852	0.852	1.330
$S_{66}^H$	1.293	1.766	1.530	1.330
$v_l(x_1)$	0.557	0.534	0.546	0.569
$v_l(x_3)$	0.510	0.510	0.510	0.569
$v_t(x_1)$	0.312	0.267	0.289	0.307
$v_t(x_3)$	0.384	0.384	0.384	0.307

<sup>a</sup>Units on  $C_{ij}$ ,  $S_{ij}$ , and  $v$  are  $10^{11}$  N/m<sup>2</sup>,  $10^{-11}$  m<sup>2</sup>/N, and cm/ $\mu$ s, respectively.

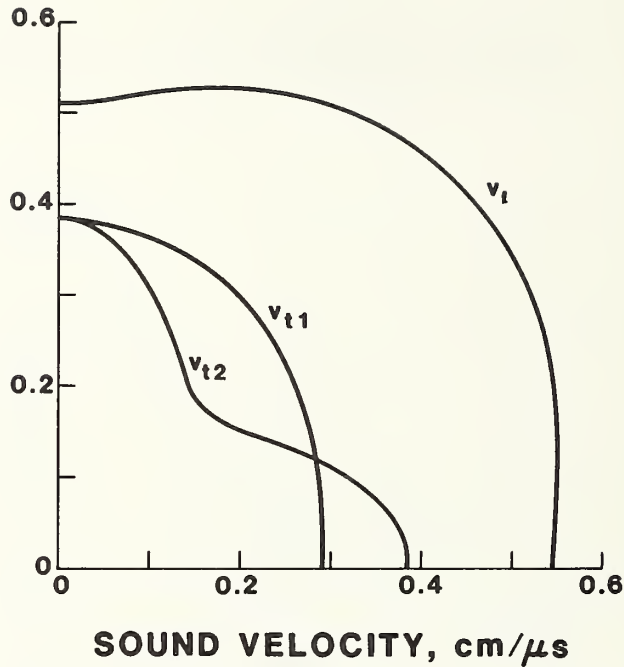


Fig. 6. Angular variation of three sound velocities. See figure caption 4.

4. If high attenuation precludes accurate  $C_{44}^H$  measurement,  $C_{33}^H$  provides a good lower-attenuation alternative.  $C_{33}^H$  corresponds to a longitudinal wave propagating along the fiber axis.

5. For the principal crystallographic directions, with one exception, if texture increases  $v_l$  it decreases  $v_t$ , and vice versa. Hardly surprising, this means simply that stiffening in a particular direction corresponds to softening in transverse directions.

6. Elastic constants affected least by texture are  $C_{66}^H$  and  $S_{66}^H$ . This result, at first surprising since  $C_{66}^H$  depends on the difference between  $C_{11}^H$  and  $C_{12}^H$ , arises presumably because  $C_{66}^H$  represents a shear wave both propagated and polarized in the  $x_1$ - $x_2$  plane, an elastically isotropic plane with properties determined, for all textures, by averaging over all directions perpendicular to the fiber axis.

7. Finally, we remark concerning the bulk modulus of the fiber-textured aggregate. It equals identically the cubic-symmetry bulk modulus,  $\frac{1}{3}(C_{11} + 2C_{12})$ . It is a scalar. Hydrostatic stress would dilate uniformly the textured aggregate. This contrasts sharply with a microscopically hexagonal material that behaves anisotropically, altering its axial length ratio, in response to hydrostatic stress. This means that welds of cubic-symmetry alloys do

not develop pressure-induced internal stresses due to texture. Such stresses would occur, of course, in lower-symmetry-alloy welds.

Another study<sup>26</sup> extends the theory to include [110] and [111] rod textures.

A general conclusion of these studies is that sound velocity provides a powerful probe for detecting, characterizing, and, at least in simple cases, quantifying texture.

## INSTABILITY

Many austenitic steels exhibit crystal-structure instability when subjected to changes of temperature, stress, or pressure. Above, we described the temperature-induced magnetic transitions in these alloys. Without these magnetic transitions, which tend to stabilize the crystal structure, many more crystal-structure instabilities might occur. Thus, magnetic and structural transitions are related; both relate to the elastic constants.

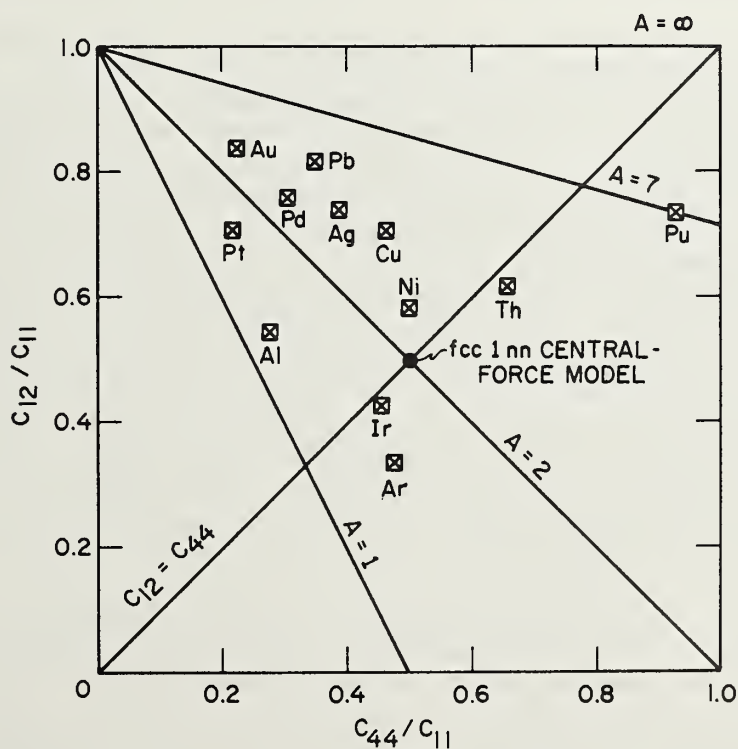


Fig. 7. Reduced monocrystalline elastic stiffnesses for fcc elements.



Recently, Ledbetter<sup>27</sup> conceived a new relationship between monocrystal elastic constants and structural instability. In 1976, Ledbetter and Moment<sup>28</sup> published Fig. 7, a diagram used to describe the unusual elastic behavior of fcc Pu. This figure contains considerable information. For the usual three independent cubic-symmetry Voigt elastic stiffnesses-- $C_{11}$ ,  $C_{12}$ ,  $C_{44}$ --it plots two dimensionless ratios:  $y = C_{12}/C_{11}$  and  $x = C_{44}/C_{11}$ . The Cauchy relationship,  $C_{12} = C_{44}$ , is a straight line from (0,0) to (1,1). The point (0.5, 0.5) identifies the prediction of an fcc nearest-neighbor-only central-force model. Most fcc elements occur in the upper half of the diagram and mostly in the left half. The boundaries  $x = 0$  and  $y = 1$  correspond to mechanical-stability conditions:  $C_{44} > 0$  and  $(C_{11} - C_{12}) > 0$ . The third mechanical-stability condition,  $(C_{11} + 2C_{12}) > 0$ , or  $y > -0.5$ , does not appear in the diagram; but this is of no consequence because no fcc elements exhibit negative  $C_{12}$  values. Straight negative-slope lines emanating from (0,1) correspond to various values of Zener's anisotropy ratio

$$A = 2C_{44}/(C_{11} - C_{12}) \quad (10)$$

All points in the diagram's field correspond to mechanically stable crystal structures.

That Th and Pu occur to the right of  $x = 0.5$  provides a crucial basis for this argument. All elements to the left of  $x = 0.5$  are stable; they exhibit a single crystal structure between  $T = 0$  and the melting point. Both Th and Pu are unstable. At high temperatures, Th transforms to a body-centered-cubic crystal structure. Plutonium is notoriously unstable. Between ambient and melting temperatures it exhibits six allotropes:  $\alpha$  (monoclinic),  $\beta$  (monoclinic),  $\gamma$  (orthorhombic),  $\delta$  (fcc),  $\delta'$  (tetragonal),  $\epsilon$  (bcc). (One can conjecture that lower temperature may reveal further allotropes, perhaps triclinic.) Thus, despite high values of  $x$ , representing high elastic rigidity with respect to (100)[001]-type deformation, both Th and, especially, Pu are unstable. It may be significant that elements on the diagram's left tend to be dominated by s-p electrons in their cohesive properties. In Th and Pu the d and f electrons enter strongly into cohesion. The tendency of Th and Pu toward chemical instability, despite their mechanical stability, encourages one to examine other systems, especially alloys.

Figure 8 shows the variation of  $x$  with Ni content for Fe-Ni alloys. Of course, this composition region is well known for its instability and the incipient fcc-bcc transformation. That  $x$  decreases before the structural transformation occurs suggests a possible magnetic transition that stabilizes the fcc structure for awhile. Magnetic-property measurements between 25 and 35 percent Ni would be very useful in understanding this unusual pretransformation behavior.

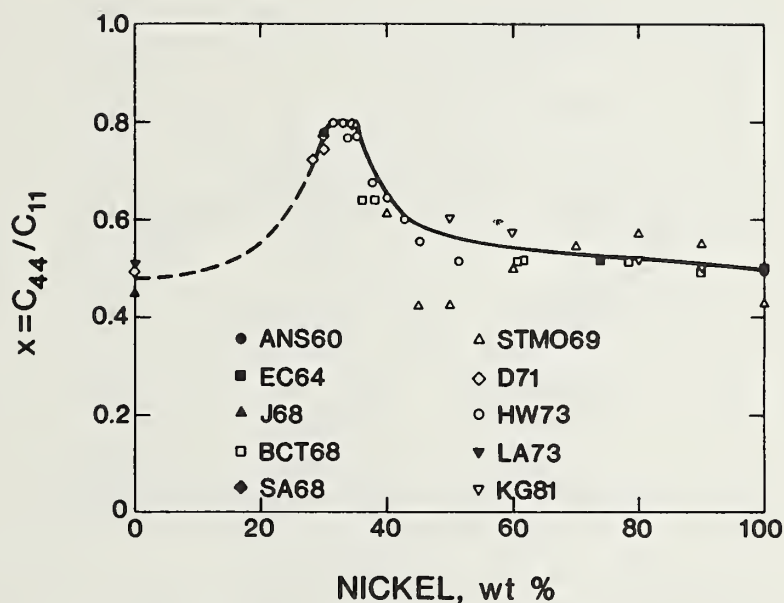


Fig. 8. Variation of  $x = C_{44}/C_{11}$  with Ni content for Fe-Ni alloys.

Figure 9 shows a y-x diagram for austenitic (fcc) stainless steels, which consist mainly of Fe, Cr, Ni, and Mn. These alloys are well known for their instability. At low temperatures they undergo magnetic and/or structural (to bcc) transformations. Plastic deformation of these alloys induces transformations to either bcc or cph (close-packed-hexagonal) structures. This diagram includes points for fcc Fe, Co, and Ni. Iron's allotropic is well known: bcc at low and high temperatures, fcc between. Cobalt, fcc at high temperatures transforms to cph at 603 K. Elastic constants of hypothetical fcc Mn and hypothetical fcc Cr remain, apparently, unestimated. (Recently, Moruzzi et al.<sup>33</sup> estimated the bulk modulus of fcc Mn to be 2.91 Mbar, 95 percent of that for bcc Fe. The bulk modulus equals  $(C_{11} + 2 C_{12})/3$ . Thus, unless the  $C_{44}$  of fcc Mn behaves abnormally, its elastic constants may resemble Fe's.)

A possible explanation of these instabilities lies in the force constants, which relate more directly to forces between pairs of atoms in solids. Details of a force-constant model occur elsewhere.<sup>27</sup>

#### BINARY ALLOYS: Fe-Ni

From a theoretical viewpoint, austenitic steels contain considerable complexity. The four principal constituents--Fe, Cr, Ni,

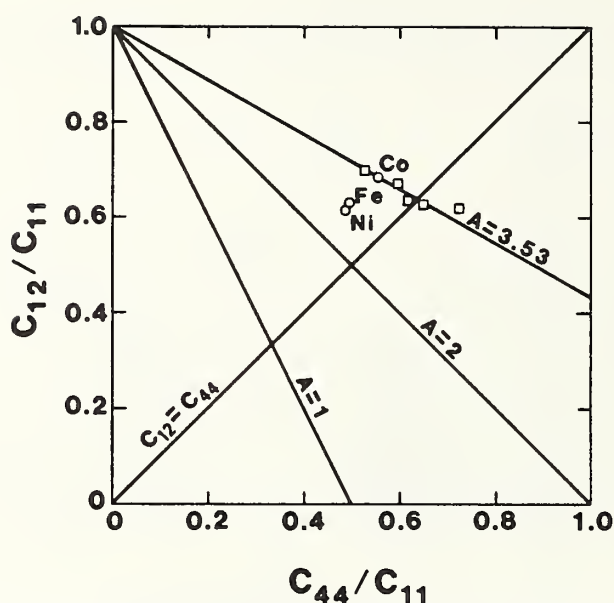


Fig. 9. Reduced monocrystalline elastic stiffnesses for austenitic steels.

Mn--are all 3d transition metals and all are magnetic. Only recently has theory succeeded in predicting the physical properties of these elements and their binary alloys. Thus, to better understand the properties of Fe-Cr-Ni-Mn alloys, we should focus also on simpler binary systems; iron-nickel, for example. Ledbetter and Reed<sup>29</sup> reviewed the elastic constants of these alloys. Ledbetter, Naimon, and Weston<sup>30</sup> measured the low-temperature elastic constants of Fe-30Ni, invar. For these alloys, Fig. 10<sup>31</sup> shows the compositional variation of the Poisson ratio. Within the fcc phase field,  $\nu$  shows both a maximum and a minimum. We pointed out above that  $\nu$ , more than most elastic constants, depends on the nature of the interatomic forces. Figure 10 suggests that with increasing Fe, before the fcc-bcc phase transition, the magnetic state undergoes a change, which stabilizes the fcc. Instead of increasing toward the Born mechanical-instability limit,  $\nu$  turns downward to a value near 0.22. It remains unclear whether the increase in  $\nu$  with further Fe alloying arises because of another magnetic-state change or from the natural result of alloying effects.

#### ACKNOWLEDGMENT

This study arose mainly from research sponsored by DARPA and by the U.S. Department of Energy, Office of Fusion Energy. M. W. Austin of NBS provided much valuable assistance, in particular, highly skilled experimentation.

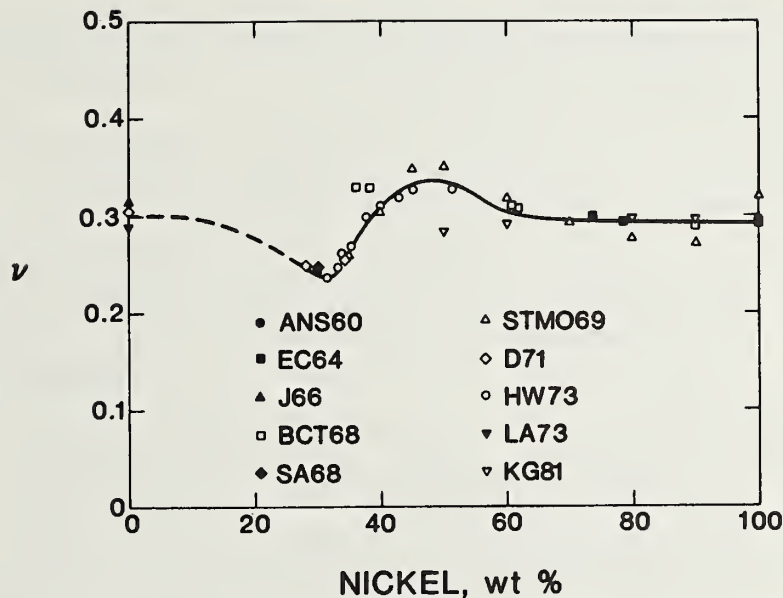


Fig. 10. For Fe-Ni alloys, compositional variation of Poisson ratio.

#### REFERENCES

1. H. M. Ledbetter, Stainless-steel elastic constants at low temperatures: a review, in "Advances in Cryogenic Engineering," Vol. 30, Plenum, New York (forthcoming).
2. H. M. Ledbetter, N. V. Frederick, and M. W. Austin, Elastic-constant variability in stainless steel 304, J. Appl Phys. 51:305 (1980).
3. H. M. Ledbetter, Sound velocities and elastic constants of steels 304, 310, and 316, Metal Sci. 14:595 (1980).
4. H. M. Ledbetter, Manganese contributions to the elastic constants of face-centered-cubic Fe-Cr-Ni stainless steels, submitted for publication.
5. H. M. Ledbetter and M. W. Austin, Elastic constants of polycrystalline austenitic stainless steels, in preparation.
6. H. M. Ledbetter, Effects of carbon and nitrogen on the elastic constants of stainless-steel 304, submitted for publication.
7. H. M. Ledbetter, W. F. Weston, and E. R. Naimon, Low-temperature elastic properties of four austenitic stainless steels, J. Appl. Phys 46:3855 (1975).
8. H. M. Ledbetter, Anomalous low-temperature elastic behavior of a nitrogen-strengthened chromium-manganese stainless steel, Mater. Sci. Eng. 29:255 (1977).



9. H. M. Ledbetter and E. W. Collings, Low-temperature magnetic and elastic-constant anomalies in three manganese stainless steels, in "Metal Science of Stainless Steels," AIME, New York (1980).
10. E. W. Collings and H. M. Ledbetter, Sound velocity anomalies near the spin-glass transition in an austenitic stainless steel alloy, Phys. Lett. 72A:53 (1979).
11. H. M. Ledbetter, Anomalous low-temperature elastic-constant behavior in Fe-13Cr-19Mn, Metall. Trans. 11A:543 (1980).
12. H. M. Ledbetter, Room-temperature elastic constants and low-temperature sound velocities for six nitrogen-strengthened stainless steels, Metall. Trans. 11A:1067 (1980).
13. H. M. Ledbetter, Stainless steel elastic constants at low temperatures, J. Appl. Phys. 52:1587 (1981).
14. H. M. Ledbetter, Low-temperature elastic-constant anomalies in Fe-Cr-Ni-Mn alloys, Physica (forthcoming).
15. H. M. Ledbetter and M. W. Austin, Elastic constants of an Fe-5Cr-25Mn austenitic steel, 76-400 K, submitted for publication.
16. H. M. Ledbetter and M. W. Austin, Anomalous low-temperature elastic-constant behavior of Fe-20Cr-16Ni-6Mn, submitted for publication.
17. H. M. Ledbetter and E. W. Collings, Elastic-constant anomalies at the Néel transition in Fe-18Cr-3Ni-12Mn, submitted for publication.
18. H. M. Ledbetter, Low-temperature variability of stainless-steel-304 elastic constants, submitted for publication.
19. H. M. Ledbetter, Low-temperature elastic constants of a manganese-alloyed stainless steel, in preparation.
20. H. M. Ledbetter, Predicted single-crystal elastic constants of stainless-steel 316, Brit. J. Non-destr. Test. 34:286 (1982).
21. H. M. Ledbetter, Predicted single-crystal elastic constants of 304 stainless-steel, submitted for publication.
22. H. M. Ledbetter and M. W. Austin, Anisotropic elastic properties of 316L welds, in preparation.
23. H. M. Ledbetter and M. W. Austin, Elastic constants and internal friction of some stainless-steel castings, in preparation.
24. H. M. Ledbetter, Single-crystal elastic constants in non-destructive evaluation of welds, in "Review of Progress in Quantitative Nondestructive Evaluation," Plenum, New York (1982), pp. 619-624.
25. H. M. Ledbetter, Single-crystal elastic constants in ultrasonic study of welds, submitted for publication.
26. H. M. Ledbetter, Sound velocity as a texture probe: application to stainless-steel welds, submitted for publication.
27. H. M. Ledbetter, Elastic constants and instability in face-centered-cubic crystals, submitted for publication.



28. H. M. Ledbetter and R. L. Moment, Elastic constants of face-centered-cubic plutonium, Acta Metall. 24:891 (1976).
29. H. M. Ledbetter and R. P. Reed, Elastic properties of metals and alloys, I. iron, nickel, and iron-nickel alloys, J. Phys. Chem. Ref. Data 2:531 (1973).
30. H. M. Ledbetter, E. R. Naimon, and W. F. Weston, Low-temperature elastic properties of invar, in "Advances in Cryogenic Engineering," Vol. 22, Plenum, New York (1977), pp. 174-181.
31. H. M. Ledbetter, Single-crystal and calculated polycrystalline elastic constants of iron-nickel alloys, a review, in preparation.
32. L. D. Landau and E. M. Lifshitz, "Statistical Physics," Pergamon, London (1959).
33. V. L. Moruzzi, J. F. Janak, and A. R. Williams, "Calculated Electronic Properties of Metals," Pergamon, New York (1978).
34. E. Kröner, Berechnung der elastischen Konstanten des Vielkristalls aus den Konstanten des Einkristalls, Z. Phys. 151:504 (1958).
35. L. D. Landau and E. M. Lifshitz, "Theory of Elasticity," Pergamon, London (1959).
36. R. Hill, The elastic behaviour of a crystalline aggregate, Proc. Phys. Soc. A5:349 (1952).
37. E. Kröner and H. H. Wawra, Coincidence of bounds for some elastic moduli of polycrystals with fibre texture, Philos. Mag. A 38:433 (1978).



## Elastic constants of an Fe-5Cr-26Mn austenitic steel, 76 - 400 K

H. M. Ledbetter and M. W. Austin

Fracture and Deformation Division, National Bureau of Standards, Boulder, Colorado 80303, USA

### Abstract

By measuring longitudinal-mode and transverse-mode sound velocities at frequencies near 10 MHz, we determined the complete engineering elastic constants--bulk modulus, shear modulus, Young modulus, Poisson ratio--for an Fe-5Cr-26Mn austenitic steel between 76 and 400 K. Due to a magnetic transition, all elastic constants behave anomalously below about 360 K. The bulk modulus begins to soften during cooling at some higher temperature. Except for Poisson's ratio, below the 360-K magnetic transition, all elastic constants resume an apparently normal temperature dependence. After increasing abruptly at the magnetic transition, Poisson's ratio increases with decreasing temperature.

Key Words: Austenitic steel; bulk modulus; elastic constants; iron alloys; low temperatures; manganese alloys; mechanical properties; physical properties; Poisson ratio; shear modulus; Young modulus.



## Introduction

We now witness much vigorous austenitic-steel research [1,2]. Many new, interesting alloys transcend the limitations of the conventional 304-type stainless steel, Fe-18Cr-8Ni.

Notably, Mn-alloyed austenitic steels provide attractive physical-mechanical properties combined with lower cost due to Ni-content reduction. Although currently much studied, Mn-alloyed austenitic steels were first considered carefully in Germany in the 1930's [3].

Alloying Mn into fcc Fe must cause drastic physical-property changes. Manganese's peculiar elemental properties--a 58-atom unit cell, a bulk modulus 0.35 that of Fe's, antiferromagnetic electronic interactions, negative low-temperature thermal expansivity--preclude any reliable predictions of such effects. Despite the proximity of Mn and Fe in the first long row of the periodic table of elements, their properties differ dramatically. From available elastic constants of fcc Ni and Mn, Vegard's law predicts that Mn lowers all the elastic stiffnesses and Poisson's ratio,  $\nu$ : B by 0.33 percent, E by 0.18 percent, G by 0.18 percent, and  $\nu$  by 0.16 percent per percent solute. Here, we assume that the unknown elastic constants of fcc Fe do not differ significantly from those of fcc Ni; because Fe's atomic volume exceeds Ni's by eight percent, fcc Fe may be slightly softer elastically.

One may ask also whether Mn affects chemical bonding in Fe-Cr-Ni alloys. As described above, Mn is truly a maverick metallic element. In considering chemical bonding in both nonmetals and metals, Pauling [4] referred to "the anomalous Mn radius" and to Mn's "striking abnormality in behavior." We know that elastic stiffness depends relatively sensitively on atomic radius,  $r$ , varying as  $r^{-4}$ . Thus, Mn's larger atomic volume arising from magnetic repulsions explains, in part, its lower elastic stiffness.



Previously, we reported the low-temperature elastic constants of an experimental Soviet austenitic steel, Fe-13Cr-19Mn [5]. Owing to a magnetic transition near 274 K, this steel showed anomalies in all elastic constants. Below the magnetic transition, all constants resumed apparently normal temperature dependence. From other studies [6], we learned that higher Ni content lowers the transition temperature and that higher Mn content raises it.

The present study focused on a high-Mn-content, low-Ni-content alloy, Fe-5Cr-26Mn. Thus, larger anomalies were expected at a higher transition temperature. Especially for cryogenic applications, this alloy offers many desirable properties: stable austenite phase; good strength, ductility, and toughness; relatively low thermal expansivity [7].

#### Material

Samples were obtained from a plate produced in a 45,000-kg commercial pilot electric-furnace heat. Bottom-poured 14,000-kg ingots were reheated to 1200°C and rolled into 4.0-cm plates. These were solution treated at 1050°C for 1.5 h and water quenched. Chemical composition (weight percent ladle analysis) was: 25.6 Mn, 4.67 Cr, 0.97 Ni, 0.86 Si, 0.22 C, 0.043 Nb, 0.040 N, 0.024 P, 0.009 Al, 0.001 S.

#### Measurements

Sound velocities were determined by a method described in detail previously [8]. Briefly, 1.5-cm cubes were prepared by grinding so that opposite faces were flat and parallel within 5  $\mu\text{m}$ . Quartz piezoelectric crystals with fundamental resonances between 4 and 7 MHz were cemented with phenyl salicylate to the specimens. An x-cut transducer was used for longitudinal waves and an ac-cut for transverse waves. Ultrasonic pulses 1 to 2 cycles long were launched into the specimen by electrically exciting the

transducer. The pulses propagated through the specimen, reflected from the opposite face, and propagated back and forth. The pulse echoes were detected by the transducer and displayed on an oscilloscope equipped with a time delay and a microprocessor for time-interval measurements. Figure 1 shows a typical pulse-echo pattern. The sound velocity was computed by

$$v = 2\ell/t \quad (1)$$

where  $\ell$  denotes specimen length, and  $t$  the round-trip transit time. On the oscilloscope,  $t$  was the time between adjacent echoes, the first and second echoes usually being measured, and within these the time between leading cycles. Elastic constants were computed from the general relationship

$$C = \rho v^2 \quad (2)$$

where  $\rho$  denotes mass density. The usual engineering elastic constants are related to the longitudinal and transverse sound velocities,  $v_\ell$  and  $v_t$ , by

$$\text{longitudinal modulus} = C_\ell = \rho v_\ell^2 \quad (3)$$

$$\text{shear modulus} = G = \rho v_t^2 \quad (4)$$

$$\text{bulk modulus} = B = C_\ell - (4/3)G \quad (5)$$

$$\text{Young's modulus} = E = 3GB/(C_\ell - G) \quad (6)$$

$$\begin{aligned} \text{Poisson's ratio} = \nu &= (E/2G) - 1 \\ &= (1/2)(C_\ell - 2G)/(C_\ell - G) \end{aligned} \quad (7)$$

For low-temperature measurements, we used a cryostat similar to one described previously [9] and a cyanoacrylate specimen-transducer adhesive. Above-ambient measurements were made in a stirred, heated mineral-oil bath.

## Results

Table 1 gives for selected temperatures both sound velocities and elastic constants. Figures 2 and 3 show the temperature variations. Maximum uncertainties are believed to be 1.0 percent for  $G$  and  $E$  and 1.5 percent for  $B$  and  $\nu$ .

The results show the following principal features: (1) near 335 K, a transition occurs that affects all the elastic constants; (2) upon cooling through the transition, the bulk, shear, and Young's moduli decrease and Poisson's ratio increases; (3) except for Poisson's ratio, below the transition temperature all elastic constants resume apparently normal temperature variations; (4) at low temperatures, Poisson's ratio,  $\nu$ , shows a nearly linear, but anomalously negative  $d\nu/dT$ ; (5) above the transition temperature, all elastic constants show usual temperature variations, except for the bulk modulus,  $B$ , which shows a nearly zero  $dB/dT$ , which is usually negative, except as zero temperature is approached.

### Discussion

We believe the transition near 335 K is magnetic, the high-temperature phase being paramagnetic. The magnetic state of order in the low-temperature phase remains uncertain. But magnetic-susceptibility measurements on three austenitic alloys--Fe-22Cr-13Ni-5Mn, Fe-21Cr-6Ni-9Mn, Fe-18Cr-3Ni-13Mn--revealed a sharp "antiferromagnetic-like" cusp-like anomaly [6] due perhaps to a spin-glass condensation [10,11]. The elastic-constant-versus-temperature curves for those three alloys resemble strongly the present curves for Fe-5Cr-26Mn.

The magnetic transition is probably second-order. Landau and Lifshitz showed that any magnetic transition can be second-order [12]. The bulk-modulus decreases on cooling, as required by second-order-phase-transformation thermodynamics [13].

Moruzzi et al. [14] showed for Fe, Cr, and Mn that the effect of magnetic interactions is to increase the volume and decrease the bulk modulus. These effects can be quite large. Manganese shows the largest effect. Calculations using a sophisticated density-functional theory, but a nonmagnetic model, predict  $B = 2.91 \cdot 10^{11} \text{ N/m}^2$ . Observation shows [15] that  $B = 0.597 \cdot 10^{11} \text{ N/m}^2$ ,

only forty-three percent of that predicted! These authors considered only ferromagnetic spin-polarization, but they "speculate that similar repulsive forces exist also in antiferromagnets. All that is required is the existence of a magnetic moment over a distance scale sufficient to establish a band structure (a few atoms)... it does not matter if...the moments are disordered or antiferromagnetically ordered instead of being in perfect ferromagnetic alignment...the volume expansion is independent of the spin direction" [16]. Thus, regardless of the low-temperature magnetic-order state, one expects during cooling a volume increase and a bulk-modulus decrease.

Wohlfarth [17] discussed in detail the influence of ferromagnetism on the bulk, shear, and Young's moduli of alloys. The change in elastic constant,  $C$ , at the magnetic transition has four parts:

$$\Delta C = \Delta C_{\lambda} + \Delta C_{\omega} + \Delta C_{\gamma} + \Delta C_m \quad (8)$$

where  $\Delta C_{\lambda}$  arises from linear magnetostriction,  $\Delta C_{\omega}$  from volume magnetostriction,  $\Delta C_{\gamma}$  from shape effects, and  $\Delta C_m$  from magnetization:

$$\Delta C_m = C(M) - C(0) = \frac{1}{2} \frac{\partial^2 F}{\partial \omega^2} M^2 \quad (9)$$

where  $M$  denotes magnetization,  $F$  the magnetic Helmholtz free energy, and  $\omega$  the volume strain.

However, another important influence on  $C$  exists: the dependence of the nonmagnetic bulk modulus on volume. Gilman [18] showed that  $B$  varies as  $r^{-4}$ , where  $r$  denotes atomic radius. Thus, quite apart from  $B$  varying with magnetostriction or with second strain derivatives of the magnetic free energy,  $B$  depends also on volume. The volume expansion on cooling is, as described above, a magnetic effect related closely to the usual spontaneous volume magnetostriction.



It is useful to compare the elastic constants of Fe-5Cr-26Mn with those of the more-familiar 304-stainless-steel alloy [19]. Table 2 shows the comparison as ratios at two temperatures, 0 and 400 K, in the magnetic and nonmagnetic states, respectively. These ratios reflect a general relative elastic softness of Fe-5Cr-26Mn. The nonmagnetic-state lowering of Poisson's ratio is especially interesting. Koster and Franz [15] pointed out that "Poisson's ratio depends to a much greater extent on the conditions of bonding than do the other elastic coefficients." Thus, these two alloys may differ in their paramagnetic-state bonding.

#### Acknowledgment

This study arose from a program sponsored by the U.S. Department of Energy, Office of Fusion Energy.

#### References

1. E. W. Collings and H. W. King (eds.), The Metal Science of Stainless Steels (AIME, New York, 1978).
2. T. Horiuchi and R. P. Reed (eds.), Austenitic Steels at Low Temperatures (Plenum, New York, forthcoming).
3. G. Masing, Lehrbuch der Allgemeinen Metallkunde (Springer-Verlag, Berlin, 1950), pp. 578-580.
4. L. Pauling, The Nature of the Chemical Bond (Cornell U.P., Ithaca, 1960), pp. 254, 419.
5. H. M. Ledbetter, Anomalous low-temperature elastic-constant behavior in Fe-13Cr-19Mn, Metall. Trans. 11A, 543-544 (1980).
6. H. M. Ledbetter and E. W. Collings, Low-temperature magnetic and elastic-constant anomalies in three manganese stainless steels, in The Metal Science of Stainless Steels (AIME, New York, 1978), pp. 22-40.
7. H. Yoshimura, N. Yamada, H. Honma, and T. Ito, Microstructures, low-temperature toughnesses, and thermal-expansion coefficients of high-manganese chromium austenitic steels, Trans. Iron Steel Inst. Japan 16, 98-105 (1976).



8. H. M. Ledbetter, N. F. Frederick, and M. W. Austin, Elastic-constant variability in stainless-steel 304, *J. Appl. Phys.* 51, 305-309 (1980).
9. E. R. Naimon, W. F. Weston, and H. M. Ledbetter, Elastic properties of two titanium alloys at low temperatures, *Cryogenics* 14, 246-249 (1974).
10. E. W. Collings and H. M. Ledbetter, Sound-velocity anomalies near the spin-glass transition in an austenitic stainless-steel alloy, *Phys. Lett.* 72A, 53-56 (1979).
11. E. W. Collings and S. C. Hart, Low temperature magnetic susceptibility and magnetization studies of some commercial austenitic stainless steels, *Cryogenics* 19, 521-530 (1979).
12. L. D. Landau and E. M. Lifshitz, Statistical Physics (Pergamon, London, 1959), p. 445.
13. Ref. 12, p. 438.
14. V. L. Moruzzi, J. F. Janak, and J. R. Williams, Calculated Electronic Properties of Metals (Pergamon, New York, 1978), p. 6.
15. W. Koster and H. Franz, Poisson's ratio for metals and alloys, *Metall. Rev.* 6, 1-55 (1961).
16. Ref. 14, p. 164-166.
17. E. P. Wohlfarth, The influence of ferromagnetism on the bulk, shear, and Young's moduli of alloys, *J. Phys. F: Metal Phys.* 6, L59-L62 (1976).
18. J. J. Gilman, Micromechanics of Flow in Solids (McGraw-Hill, New York, 1969), pp. 29-41.
19. H. M. Ledbetter, Stainless steel elastic constants at low temperatures, *J. Appl. Phys.* 52, 1587-1589 (1981).

#### List of Figures

- Fig. 1. Oscilloscope display of pulse-echo pattern for Fe-5Cr-26Mn. Transit time was measured between crests of leading cycles of consecutive echoes.
- Fig. 2. Temperature dependence of the longitudinal and transverse sound-wave velocities of Fe-5Cr-26Mn.
- Fig. 3. Temperature dependence of four elastic constants of Fe-5Cr-26Mn: E = Young's modulus, G = shear modulus, B = bulk modulus,  $\nu$  = Poisson's ratio.

Table 1. Dynamic elastic properties of Fe-5Cr-26Mn steel  
at selected temperatures

T K	$V_l$ cm/ $\mu$ s	$V_t$	E	G	B	$\nu$
				10 <sup>11</sup> N/m <sup>2</sup>		
395	0.5480	0.3136	1.923	0.765	1.316	0.256
380	0.5486	0.3144	1.932	0.769	1.316	0.255
360	0.5492	0.3151	1.939	0.773	1.317	0.255
340	0.5474	0.3138	1.923	0.766	1.311	0.255
320	0.5389	0.3034	1.817	0.716	1.305	0.268
300	0.5401	0.3037	1.821	0.718	1.313	0.269
280	0.5410	0.3040	1.826	0.719	1.318	0.269
260	0.5422	0.3045	1.832	0.721	1.326	0.270
240	0.5435	0.3048	1.837	0.723	1.334	0.270
220	0.5447	0.3054	1.844	0.726	1.341	0.271
200	0.5458	0.3058	1.851	0.728	1.348	0.271
180	0.5471	0.3064	1.858	0.731	1.355	0.271
160	0.5483	0.3070	1.865	0.733	1.361	0.272
140	0.5492	0.3077	1.873	0.737	1.365	0.271
120	0.5504	0.3082	1.880	0.739	1.372	0.272
100	0.5513	0.3086	1.886	0.741	1.377	0.272
80	0.5524	0.3089	1.890	0.743	1.384	0.272
76	0.5528	0.3071	1.892	0.743	1.387	0.273

Table 2.  
 Ratios of Fe-5Cr-26Mn elastic constants to those  
 of 304-type stainless steel.

T(K)	B	E	G	$\nu$
0	0.88	0.90	0.90	0.98
400	0.84	0.94	0.94	0.87

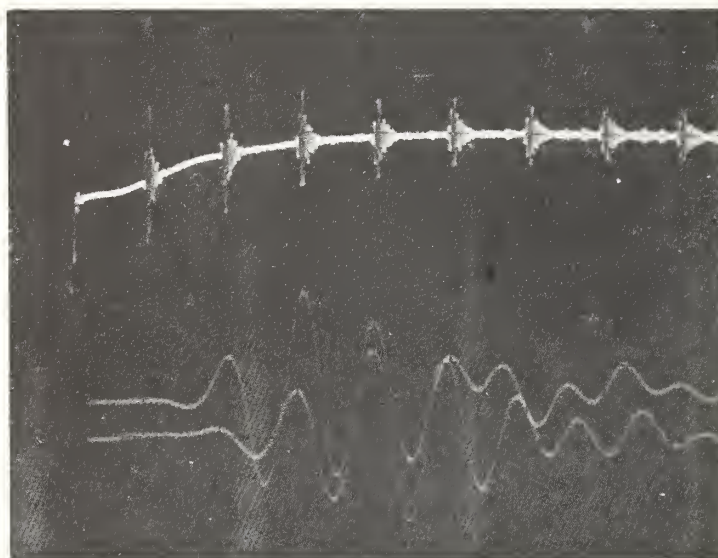


Fig. 1. Oscilloscope display of pulse-echo pattern for Fe-5Cr-26Mn. Transit time was measured between crests of leading cycles of consecutive echoes.

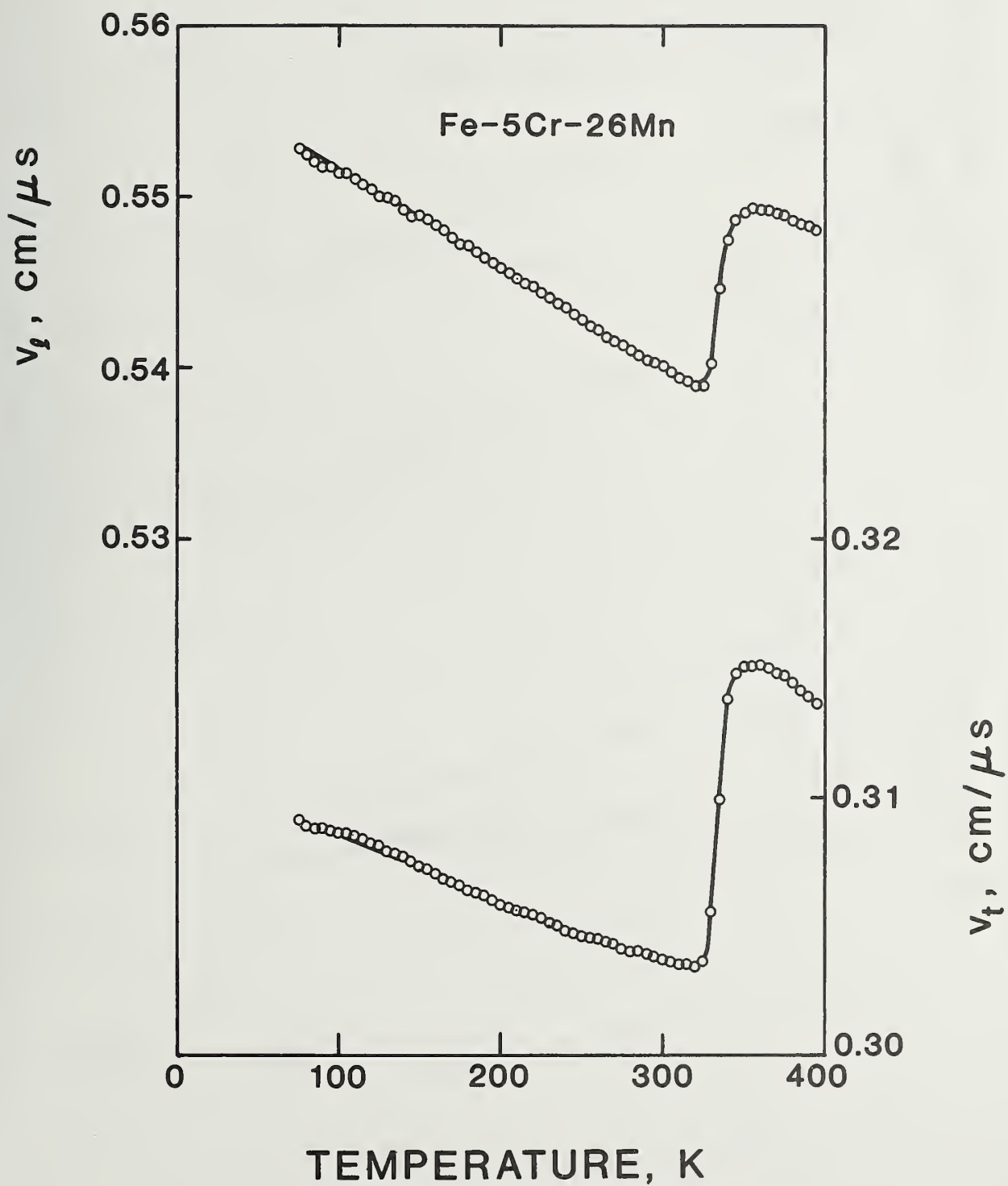


Fig. 2. Temperature dependence of the longitudinal and transverse sound-wave velocities of Fe-5Cr-26Mn.



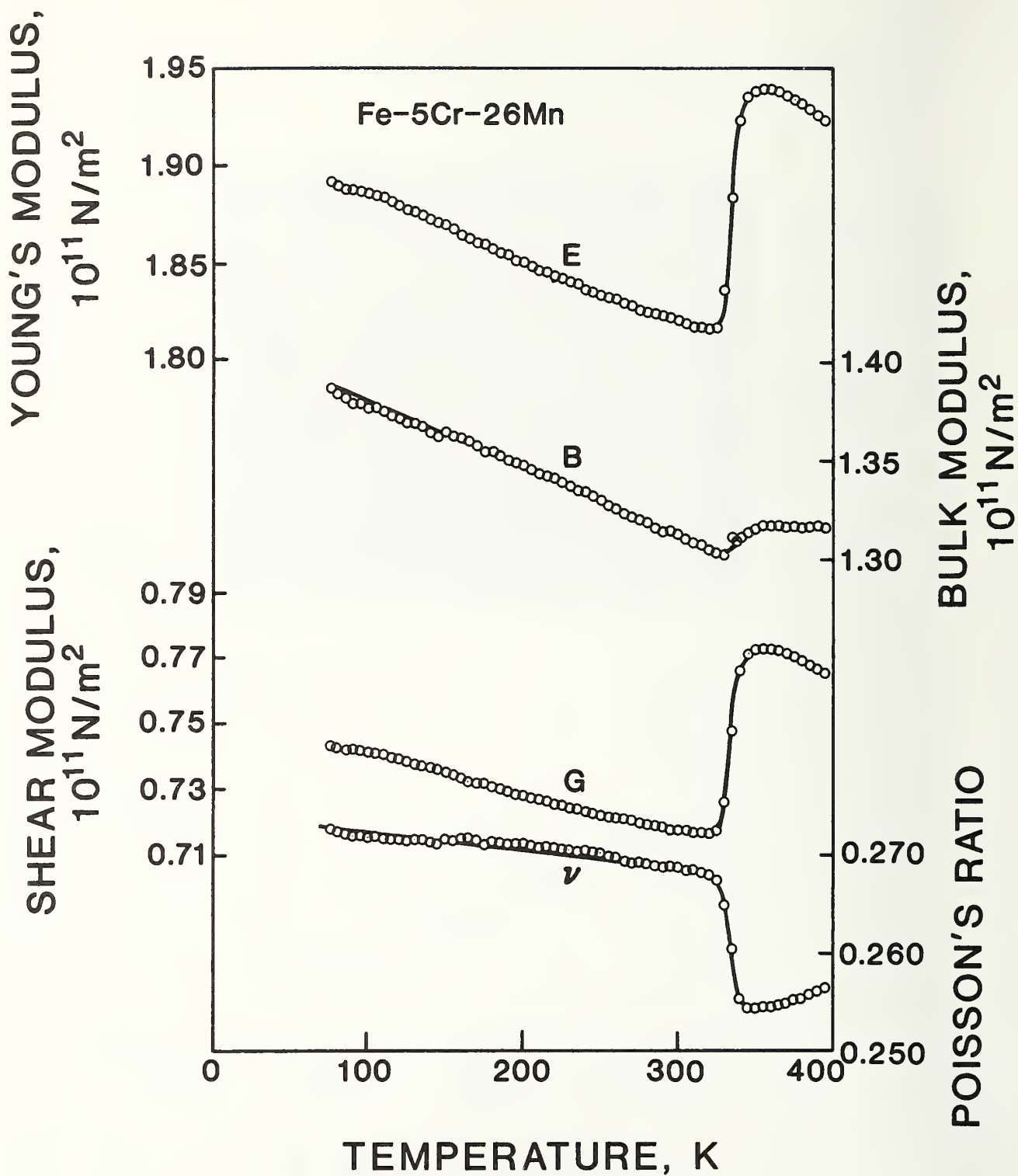


Fig. 3. Temperature dependence of four elastic constants of Fe-5Cr-26Mn: E = Young's modulus, G = shear modulus, B = bulk modulus,  $\nu$  = Poisson's ratio.

## ***WELDMENTS AND CASTINGS***



## WELDMENTS AND CASTINGS PROGRAM

LEADER: H. I. McHenry, NBS

STAFF: Y.-W. Cheng, H. M. Ledbetter, NBS

### OBJECTIVES:

- (1) To investigate the metallurgical factors that affect the mechanical properties of stainless-steel weldments and castings at cryogenic temperatures.
- (2) To contribute to the development of improved filler metals for welding stainless steels for liquid-helium service.
- (3) To evaluate the mechanical properties of weldments and castings at 4 K.
- (4) To develop methods of detecting defects and evaluating their significance in stainless-steel weldments.

### RESEARCH PAST YEAR (1982)

- (1) The five CF8M stainless-steel castings with varying nitrogen contents and constant delta-ferrite content were tested at 4 K.
- (2) The metallographic study on deformed and fractured stainless steels with duplex structures was continued.
- (3) The fatigue crack-growth rates and fracture toughness were measured on the 25Mn-5Cr and 32Mn-7Cr austenitic steels.
- (4) The elastic properties of the CF8M stainless-steel castings were measured ultrasonically.
- (5) Mechanical property testing at 4 K in support of superconducting magnet design and construction continued.

### RESEARCH THIS YEAR (1983)

- (1) The tensile properties and fracture toughness of 25Mn-5Cr weldments produced by three welding processes will be measured at 4 K.
- (2) Fatigue crack-growth rates will be measured in CF8M castings as a function of ferrite content.
- (3) Tensile tests will be conducted on full-thickness stainless-steel welds with the weld reinforcement in place.
- (4) An evaluation of fully austenitic weld metals with low sulfur and phosphorus contents will be initiated.
- (5) A series of stainless steel welds with varying oxygen contents will be produced.
- (6) Mechanical property testing at 4 K in support of superconducting magnet design and construction will continue.





CORRELATIONS OF FATIGUE CRACK GROWTH RATE PARAMETERS  
AT CRYOGENIC TEMPERATURES\*

Y.-W. Cheng and R. L. Tobler  
Fracture and Deformation Division  
National Bureau of Standards  
Boulder, Colorado

ABSTRACT

Fatigue crack growth rate data of ferritic steels, AISI 300 series stainless steels, and austenitic steel welds at 295, 76, and 4 K were collected and analyzed in terms of the exponent in the Paris equation. The data considered pertain to constant amplitude fatigue loading and stress ratio equal to 0.1. It is observed that there is a linear relation between  $\log C$  and  $m$ , the parameters of the Paris equation. The exponent,  $m$ , is insensitive to the variation of fracture toughness and yield strength of the material except in low fracture toughness materials. Temperature effects on  $m$  are observed for ferritic steels but not for austenitic steels.

\* To be published in Proceedings of the ICF International Symposium on Fracture Mechanics, November 22-25, 1983, Beijing, China.



The fracture mechanics approach to the evaluation of fatigue crack growth behavior provides a rationale for material selection as well as design criteria against fatigue failure. For this reason, the materials industry includes fatigue crack growth studies in the materials design and characterization process for a wide variety of component--e.g., aircraft components, nuclear hardware, marine structures, piping, and bridges. Over the past few years, the fatigue crack growth studies at the National Bureau of Standards (NBS) have been used to characterize a wide variety of cryogenic structural alloys and their welds. This work has been spurred by developments in energy-related fields and by magnetic fusion energy programs. This paper summarizes the observed correlations of fatigue crack growth rate parameters of selected materials at room and cryogenic temperatures in terms of the exponent,  $m$ , in the Paris equation,  $da/dN = C(\Delta K)^m$ , where  $da/dN$  is the fatigue crack growth rate in mm/cycle,  $\Delta K$  is the stress intensity range in  $\text{MPa}\sqrt{\text{m}}$ ,  $C$  and  $m$  are material constants.

## MATERIALS

The materials studied include ferritic steels [1-4], wrought AISI 300 series stainless steels [5-12], and austenitic steel welds with various welding processes and filler metals [12-17]. The AISI 300 series stainless steels are commonly used Fe-Cr-Ni alloys. The austenitic steel weld data include data on welds of the AISI 300 series stainless steels, as well as

---

\*Contribution of NBS; not subject to copyright in the U.S.

Table 1. Summary of regression statistics for data of Fig. 1.

	Ferritic Steels	AISI 300 Series Stainless Steels	Austenitic Steel Welds
slope	-1.468	-1.527	-1.474
$\sigma^*$	0.109	0.0753	0.0646
intercept	-3.749	-3.884	-4.247
$\sigma^*$	0.507	0.272	0.291
$R^{**}$	0.966	0.946	0.970

\* $\sigma$ : standard deviation

\*\*R: correlation coefficient;  $R = 1$  implies a perfect correlation

additional Fe-Cr-Ni-Mn, Fe-Cr-Mn, and Fe-Cr-Ni alloys. The testing media are laboratory air, liquid nitrogen, and liquid helium for test temperatures of 295, 76, and 4 K, respectively. The data considered pertain to constant amplitude fatigue loading with a stress ratio equal to 0.1.

The majority of the data collected were obtained in the laboratories of NBS using compact specimens or bend specimens [2-4,6,7,9-11,13-17]. Additional relevant data [1,5,8,12] were included in the analysis for comparison and confirmation. For details of specimen preparation, material compositions and treatment, it is necessary to refer to the original publications.

## RESULTS AND DISCUSSION

### The Relation Between $C$ and $m$

It has been shown that there is an empirical linear relation between  $\log C$  and  $m$  for structural steels at room temperature [18,19]. This study extended the correlation to ferritic steels, AISI 300 series stainless steels, and austenitic steel welds at cryogenic temperatures. The results are shown in Fig. 1. Least-squares regression analyses have been performed for each of the three sets of data of Fig. 1, and the regression statistics are summarized in Table 1. The results indicate that there is a definite linear relation between  $\log C$  and  $m$  for the materials studied.

A linear relation between  $\log C$  and  $m$  has the following implications.

(1) The two constants ( $C$  and  $m$ ) in the Paris equation are not independent

and reduce to one constant ( $C$  or  $m$ ) for a specific class of material.

(2) Materials with higher values of  $m$  have a better fatigue crack growth resistance than those with lower  $m$  values in the lower half of the stress intensity range where the Paris equation applies, or vice versa at the higher stress intensity range.

However, it should be pointed out that different materials with same  $m$  values and different  $C$  values have been observed [20] and the empirical relation between  $\log C$  and  $m$  should be treated as a trend rather than a rule.

### The Relation Between $m$ and Fracture Toughness and Yield Strength

The results of  $m$  vs. fracture toughness and  $m$  vs. yield strength are plotted in Fig. 2. Figure 2a shows that the value of  $m$  is independent of fracture toughness at fracture toughnesses greater than  $90 \text{ MPa}\sqrt{\text{m}}$ . Below  $90 \text{ MPa}\sqrt{\text{m}}$ , high values of  $m$  are observed. The high values of  $m$  in low fracture toughness specimens can be attributed to the concurrent occurrence of monotonic fracture, such as cleavage or intergranular fracture, with fatigue crack growth [20].

As shown in Fig. 2b, the value of  $m$  is independent of yield strength, except that in high yield strength specimens the scatter in  $m$  becomes more pronounced.

### The Relation Between $m$ and Material Type

Examination of Fig. 1 has shown that there is a temperature effect on  $m$  for ferritic steels when temperature decreases from 295 to 76 and 4 K, but not for AISI 300 series stainless steels and austenitic steel welds. The effect of temperature in ferritic steels relates to the effect of fracture toughness on  $m$ , as mentioned in the previous section. Ferritic steels are b.c.c. metals that exhibit ductile-to-brittle transitions when temperature decreases sufficiently. At low temperatures, ferritic steels become brittle (low fracture toughness), and this produces high  $m$  values. No temperature effect on  $m$  is observed in AISI 300 series stainless steels and austenitic steel welds because these f.c.c. metals do not exhibit ductile-to-brittle transitions as temperature is decreased from 295 to 4 K.



Fig. 1 also indicates that the AISI 300 series stainless steels have least spread in  $m$  values and the austenitic steel welds have a higher average  $m$  value than the AISI 300 series stainless steels do (4,43 vs. 3,57).

## CONCLUSION

The following conclusions can be drawn from the present study:

1. There is a linear relation between  $\log C$  and  $m$  in the Paris equation for the cryogenic structural alloys and welds studied.
2. The value of  $m$  is independent of fracture toughness and yield strength of the materials except in low fracture toughness materials; in the latter case,  $m$  increases as fracture toughness decreases below  $90 \text{ MPa}\sqrt{\text{m}}$ .
3. There is a temperature effect on  $m$  for ferritic steels but not for austenitic steels; low temperatures tend to yield higher  $m$  values for ferritic steels.

## ACKNOWLEDGMENTS

This study was supported by the U.S. Department of Energy, Office of Magnetic Fusion Energy.

## REFERENCES

1. V. V. Pokrovski, Strength Mater., 10 (5), 534 (1978).
2. R. L. Tobler, R. P. Mikesell, R. L. Durcholz, and R. P. Reed, in Properties of Materials for Liquefied Natural Gas Tankage, ASTM STP 579, American Society for Testing and Materials, Philadelphia, PA 261 (1975).
3. R. L. Tobler, R. P. Reed, and R. E. Schramm, J. Eng. Mater. Technol., 100, 189 (1978).
4. R. L. Tobler, R. P. Mikesell, and R. P. Reed, in Fracture Mechanics (Eleventh Conference), ASTM STP 677, American Society for Testing and Materials, Philadelphia, PA, 85 (1979).
5. M. W. Mahoney and N. E. Paton, Nucl. Technol., 23 53 (1974).

6. D. T. Read and R. P. Reed, in Materials Studies for Magnetic Fusion Energy Applications at Low Temperatures-I, NBSIR 78-884, National Bureau of Standards, Boulder, Colorado, 93 (1978).
7. D. T. Read and R. P. Reed, in Metal Science of Stainless Steels, Metallurgical Society of New York, 92 (1979).
8. F. R. Schwartzberg, in Materials Research for Superconducting Machinery-II, Semi-annual Technical Report, ARPA-2569, National Bureau of Standards-Advanced Research Projects Agency (1974). Available from NTIS, Springfield, Virginia.
9. R. L. Tobler and R. P. Reed, in Advances in Cryogenic Engineering, 22, 35 (1977).
10. R. L. Tobler and R. P. Reed, in Advances in Cryogenic Engineering, 24, 82 (1978).
11. R. L. Tobler and R. P. Reed, in ASTM 15th Natl. Symp. on Fracture Mechanics, College Park, Maryland (1982).
12. J. M. Wells, R. Kossowsky, W. A. Logsdon, and M. R. Daniel, in Materials Research for Superconducting Machinery-IV, Semi-annual Technical Report, ADA036919, National Bureau of Standards-Advanced Research Projects Agency (1976). Available from NTIS, Springfield, Virginia.
13. H. I. McHenry, J. W. Elmer, and T. Inoue, in Materials Studies for Magnetic Energy Applications at Low Temperatures-V, NBSIR 82-1667, National Bureau of Standards, Boulder, Colorado, 245 (1982).
14. H. I. McHenry and T. A. Whipple, in Materials Studies for Magnetic Fusion Energy Applications at Low Temperatures-III, NBSIR 80-1627, National Bureau of Standards, Boulder, Colorado, 155 (1980).
15. R. L. Tobler, H. I. McHenry and R. P. Reed, in Advances in Cryogenic Engineering, 24, 560 (1978).
16. T. A. Whipple and H. I. McHenry, in Materials Studies for Magnetic Fusion Energy Applications at Low Temperatures-IV, NBSIR 81-1645, National Bureau of Standards, Boulder, Colorado, 273 (1981).
17. T. A. Whipple, H. I. McHenry, and R. T. Read, Weld. J., 60 (4), 72s (1981).
18. K. Tanaka and S. Matsuoka, Int. J. Fract., 13 563 (1977).
19. T. R. Gurney, Fatigue of Welded Structures, 2nd edition, Cambridge University Press (1979).
20. R. L. Tobler and Y. W. Cheng, to be presented at the Symposium on Fatigue at Low Temperatures, Louisville, Kentucky (May 1983).

## List of Figures

- Figure 1(a). Relation between  $\log C$  and  $m$  for the AISI 300 series stainless steels.
- Figure 1(b). Relation between  $\log C$  and  $m$  for austenitic steel welds.
- Figure 1(c). Relation between  $\log C$  and  $m$  for ferritic steels.
- Figure 2(a). Relation between  $m$  and fracture toughness. Note: fracture toughnesses were converted from the J-integral which was obtained from the single specimen test technique.
- Figure 2(b). Relation between  $m$  and yield strength.

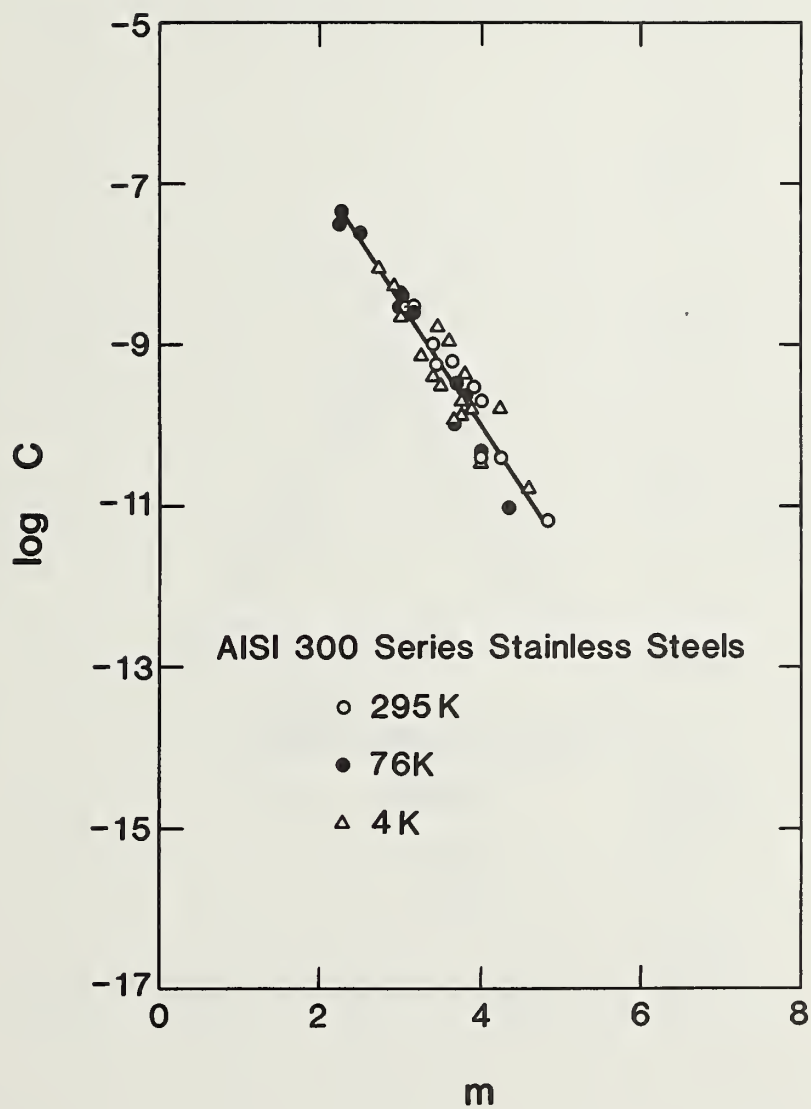


Figure 1(a). Relation between  $\log C$  and  $m$  for the AISI 300 series stainless steels.

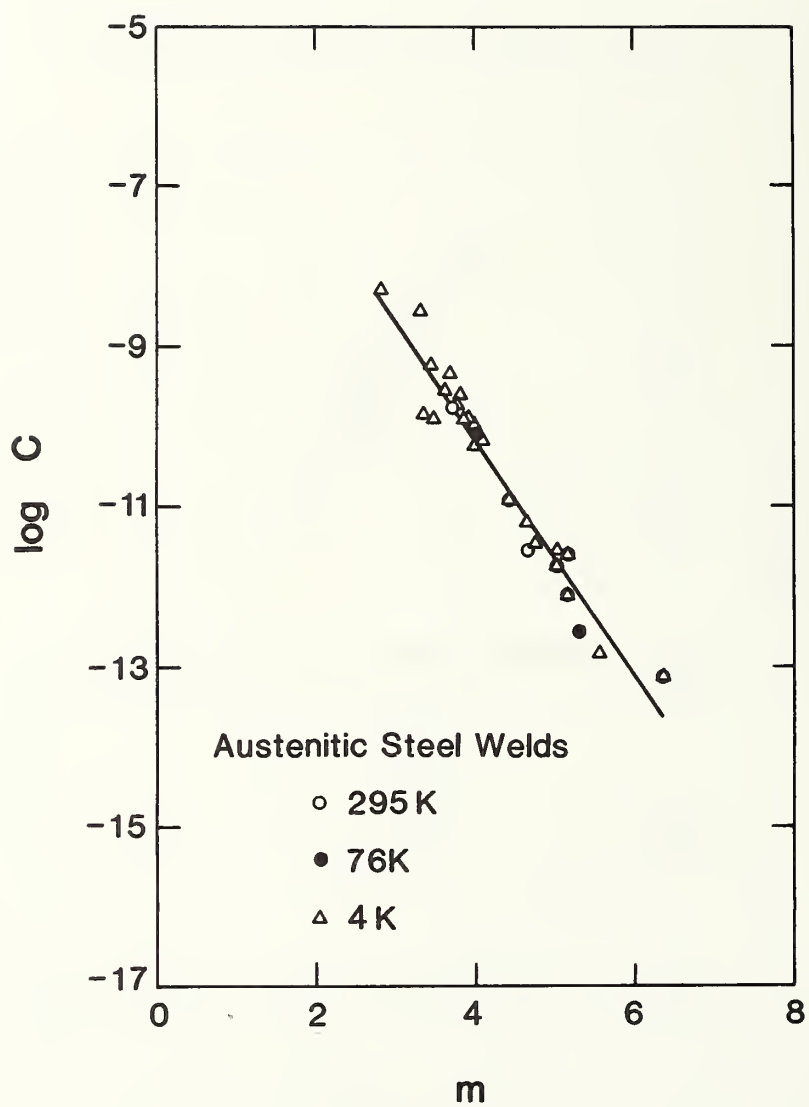


Figure 1(b). Relation between  $\log C$  and  $m$  for austenitic steel welds.



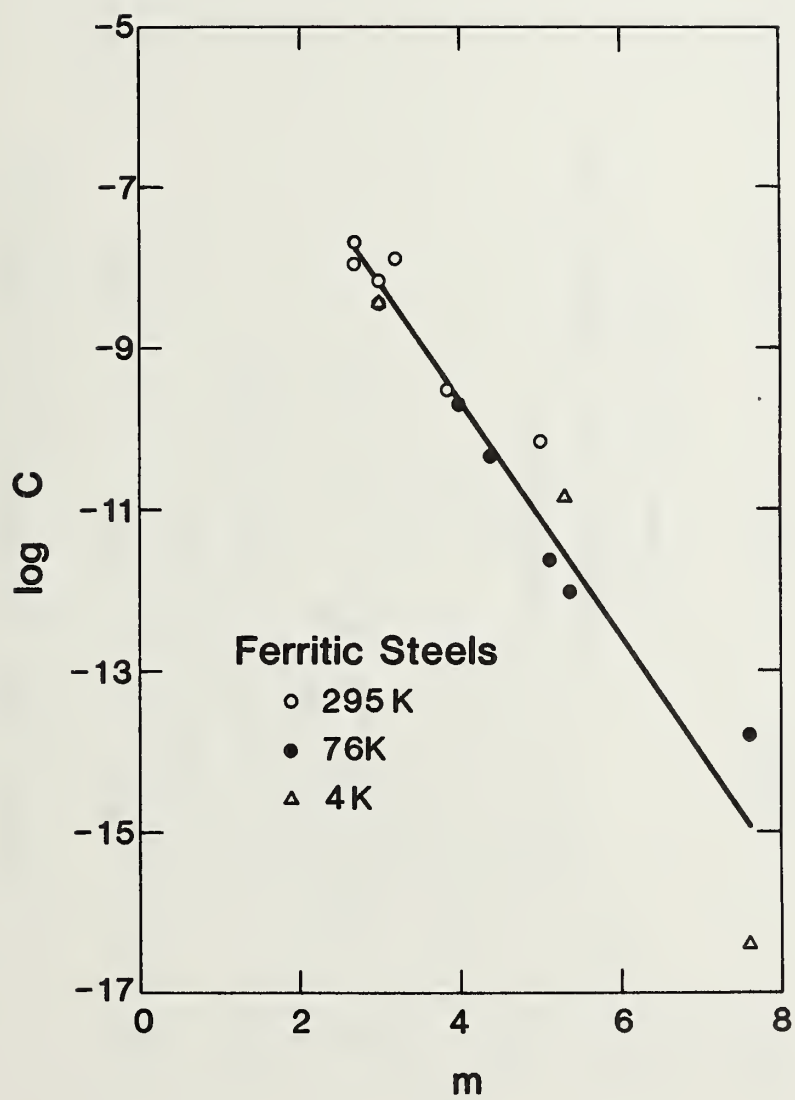


Figure 1(c). Relation between  $\log C$  and  $m$  for ferritic steels.

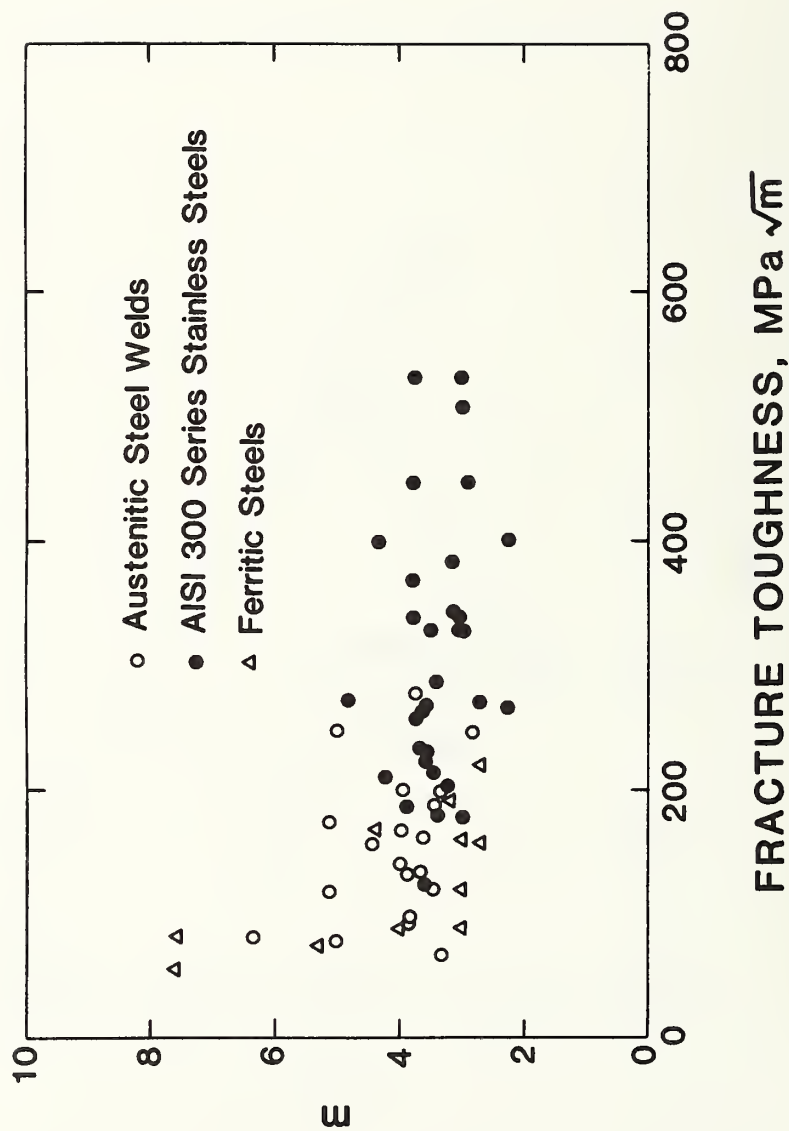


Figure 2(a). Relation between  $m$  and fracture toughness. Note: fracture toughnesses were converted from the J-integral which was obtained from the single specimen test technique.

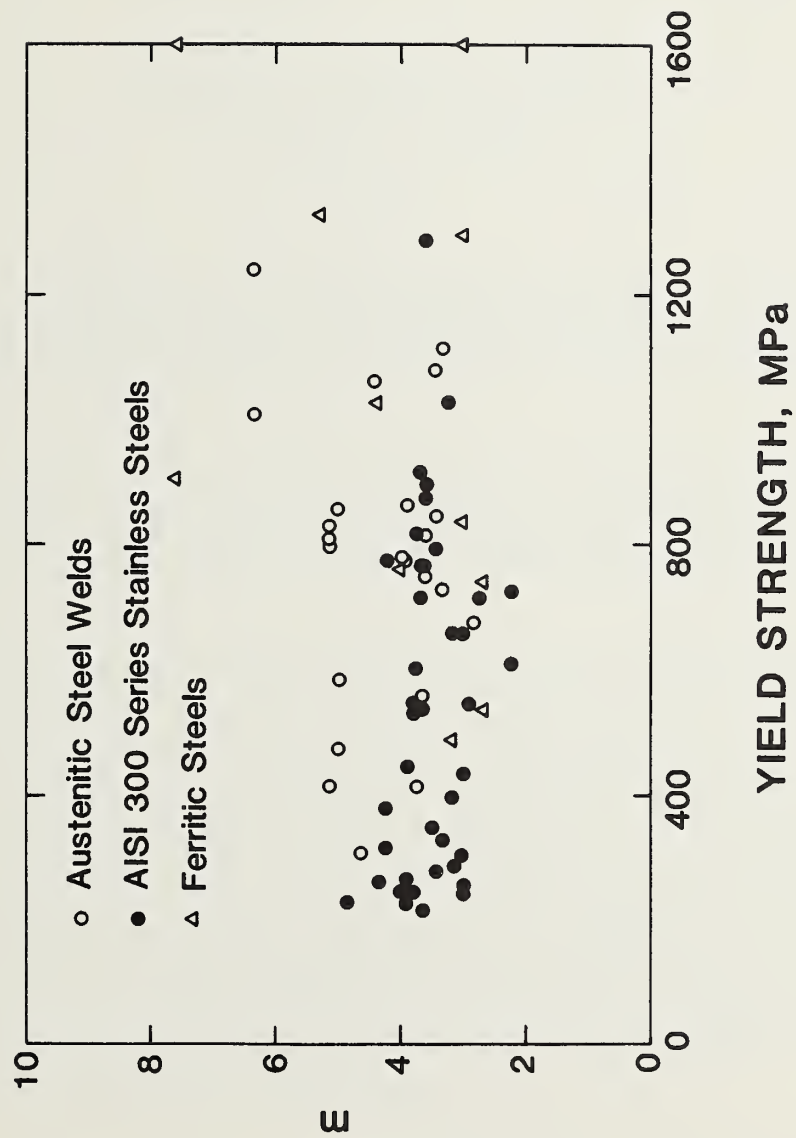


Figure 2(b). Relation between  $m$  and yield strength.



DEFORMATION AND FRACTURE OF STAINLESS STEEL  
CASTINGS AND WELDMENTS AT 4 K\*

T. A. Whipple and E. L. Brown  
Fracture and Deformation Division  
National Bureau of Standards  
Boulder, Colorado

ABSTRACT

A number of stainless steel weldments and castings that were deformed at 4 K have been examined with optical and electron microscopy. The purpose of this investigation was to assess the effects of residual delta-ferrite on the deformation and fracture mechanisms of these materials at cryogenic temperatures.

Weldments and castings have very similar microstructures, but the delta-ferrite in castings is much coarser as a result of slower solidification and cooling rates. This wide variation in the scale of the structure provides a good opportunity for the study of structure and property relationships in these materials.

It has been found that deformation and fracture are greatly influenced by the ferrite morphology. The study of the coarser structure in castings has allowed more direct observation of fracture, which has led to some preliminary conclusions concerning fracture mechanisms. Cleavage fractures of delta-ferrite particles have been observed. It appears that these fractures, although not forming a continuous crack path, assist in the void formation in the ductile austenite matrix. Another observed crack propagation mechanism is that of void nucleation near the austenite delta-ferrite interface. Although interface separation has not been observed, the inhomogeneous deformation near the interface appears to cause premature void nucleation and growth. The occurrence of one of the above mechanisms rather than the other depends on a number of factors, including ferrite morphology and the properties of the two phases. The morphology and properties, in turn, depend on both the alloy composition and solidification conditions.

\* Published in "Trends in Welding Research in the U.S.," American Society for Metals Conference Proceedings, New Orleans, LA, November 16-18, 1981, Editor, S. A. David (American Society for Metals, Metals Park, OH, 1982).





## INTRODUCTION

The structural components for most superconducting magnets are being made of stainless steels. Because of the large structures, high stresses and low operating temperature, welded construction is the most attractive fabrication method. Since the structures are being made of thick plate, fracture toughness is an important consideration. It has been found that stainless steel weldments generally have a much lower cryogenic fracture toughness than the stainless steel base metal (1,2).

To date, three factors have been established that have an effect on the cryogenic fracture toughness of stainless steel weldments: the delta-ferrite content of the weldment, the nitrogen concentration in the weld, and the fusion zone grain size of fully austenitic weldments (1,2,3,4). Nevertheless, it still is not possible to predict the toughness of a stainless steel weldment on the basis of these factors. Apparently there are factors beyond those stated above that cause the observed wide variations in fracture toughness (2,5,6). This paper contains the results of an investigation that is intended to define more precisely the role of delta-ferrite and to identify other factors that have an influence on the cryogenic toughness of stainless steel weldments and castings.

In this investigation qualitative observations were made on various stainless steel weldments and castings which have been tensile and fracture toughness tested at 4K. Also, a series of CF8M castings, with varying delta-ferrite contents, have been tested at 4K. There are presently very few 4 K mechanical property data on castings, but a few initial tests have shown a wide variation in fracture toughness similar to weldments (5). This is not surprising because weldments are actually rapidly solidified castings. Stainless steel castings also generally contain a certain percentage of delta-ferrite, although on a much coarser scale than that of weldments, owing to the slower solidification of castings. Because of the coarser structure and less directional nature of the delta-ferrite in castings, they provide an excellent model material for the study of basic deformation and fracture mechanisms in duplex austenite/delta-ferrite materials. It is anticipated that this study will aid in understanding the causes of the extreme property variations in weldments.

The first part of this investigation was a metallographic and fractographic investigation of stainless steel

weldments and castings, containing delta-ferrite, which were deformed and fractured at 4 K. Secondly, mechanical property tests were performed on a controlled series of CF8M stainless steel castings with varying ferrite contents.

## MATERIALS

The materials for the initial part of this study are stainless steel weldments and castings that have been tensile and fracture toughness tested at 4 K. These materials did not come from a controlled series, however, they all fall into the AISI type 304 or 316 stainless steel composition ranges. These variations in composition, as well as variation in the casting or welding process, are appropriate since the intent of this study was to investigate the possible deformation and fracture mechanisms in duplex austenite delta-ferrite structures at 4 K and not just the mechanism for a specific material. The welding or casting process, delta-ferrite content and alloy are noted within the text as needed.

The chemical composition and delta-ferrite content of the controlled series of CF8M castings are presented in Table 1. The castings were produced by a commercial vendor, and the procedures used have been reported previously (7). The castings were received in the form of 30.5 cm (12 in) X 61.0 cm (24 in). X 10.2 cm (4 in) blocks. All specimens were removed from areas at least 15.2 cm (6 in) from either end and 3.8 cm (1.5 in) from either surface. This was done to avoid any effects of the columnar grain structure near the casting surfaces.

Table 1. Chemical analysis of five heats of CF8M with variable ferrite content.

<u>Heat</u>	<u>C</u>	<u>Mn</u>	<u>Si</u>	<u>Cr</u>	<u>Ni</u>	<u>Mo</u>	<u>N</u>	<u>% Delta-Ferrite*</u>
1	0.06	1.10	0.59	18.04	13.24	2.12	.05	1.1
2	0.06	0.38	1.16	19.62	10.61	2.12	.05	8.2
3	0.06	0.36	1.13	19.23	8.25	2.16	.05	17.2
4	0.06	0.35	0.95	20.40	8.22	2.13	.05	23.1
5	0.05	0.39	1.11	22.54	9.84	2.26	.05	28.5

\*Measured by a metallographic point count.

## PROCEDURES

### Metallographic Specimen Preparation

For this investigation a number of sectioning, metallographic and fractographic techniques were employed. Each technique allows the observation of different phenomena. Macroscopic examination, optical microscopy, and scanning electron microscopy (SEM) were used for making observations.

For the most part metallographic specimens were prepared by using standard mechanical grinding and polishing techniques, but in a few cases electrolytic polishing was used. A 10% oxalic acid electrolytic etch was used as a general purpose etch to reveal delta-ferrite morphology and grain boundaries. A 10 N KOH electrolytic etch was used to reveal the delta-ferrite structure only. This is a deposition etch that colors the delta-ferrite light blue to brown. The main attribute of this etchant is that it does not remove any material; therefore, it will not round the edges of cracks or produce pitting and other etching artifacts. A boiling solution of 1 part  $H_2O_2$  and 2 parts  $H_3PO_4$  was used to reveal strain induced martensite.

### Mechanical Testing

Tensile tests were conducted at 4 K using 2.5-cm (1-in) gage length and 0.64-cm (0.25-in) diameter specimens. The test procedures and the cryostat for the low temperature tests have been described by Reed (8).

Fracture toughness tests were conducted at 4 K using three-point bend specimens with a 2.54-cm (1-in) width and 2.54-cm (1-in) thickness. The single-specimen J-integral procedure (9) was used to determine  $J_{IC}$ , the value of J at the onset of crack extension. The plane strain fracture toughness,  $K_{IC}(J)$ , was determined from  $J_{IC}$  using the relationship proposed by Begley and Landes (10):

$$K_{IC}(J) = \left( \frac{J_{IC} E}{1-\nu^2} \right)^{1/2}$$

where E is Young's modulus and  $\nu$  is Poisson's ratio. Tests were conducted in an electrohydraulic fatigue machine



equipped with the cryostat described by Fowlkes and Tobler (11). The test data is collected and reduced by a laboratory minicomputer. This system has been described by Read (12).

## RESULTS AND DISCUSSION

### Low Temperature Deformation

It is generally true that bcc materials, such as delta-ferrite, go through a ductile-to-brittle transition at low temperatures, whereas fcc materials, such as austenite, do not. The temperature at which this transition occurs in steels is influenced mainly by alloy content and microstructure; a higher nickel content and a smaller grain size lead to a lower transition temperature. Another factor to consider is the increase in strength with a reduction in temperature; bcc materials have a much more dramatic increase in yield strength than fcc materials at low temperatures.

These general observations lead to some expectations for the behavior of duplex stainless steels. At higher temperatures, both austenite and ferrite are ductile and have similar strengths. In this case the amount and morphology of delta-ferrite is expected to have a much smaller effect on strength and ductility than at low temperatures, when the delta-ferrite is strong and brittle. The effect of the property transition in the delta-ferrite should be to increase the strain hardening rate. Data that demonstrate the greater strengthening effect of delta-ferrite at cryogenic temperatures have been presented by Read et al.(1).

Figures 1 and 2 are micrographs of 316L stainless steel weld metal tensile specimens that were tested at room temperature and 4 K, respectively. Note that at room temperature (Figure 1) the delta-ferrite is highly elongated in the direction of the tensile axis and at 4 K (Figure 2) the ferrite maintains its original morphology and shows no indication of elongating with the matrix.

During deformation at low temperatures, austenite can go through a strain induced martensitic transformation. The degree of transformation and the critical strain at which it occurs are a function of the alloy content. Although the stability of the austenite matrix will quantitatively affect the strength and toughness of duplex austenitic stainless steel castings and weldments, it is only of interest in this qualitative discussion in that it provides a method of observing deformation in the austenite.



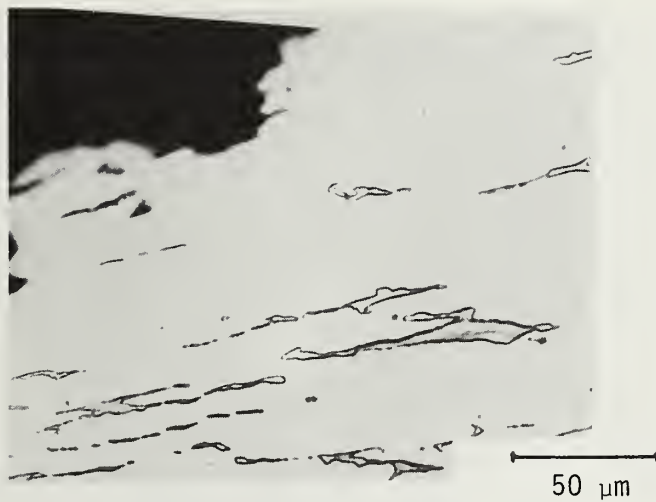


Figure 1. Micrograph of a 316L submerged-arc weld metal tensile specimen, tested at room temperature. KOH etch.

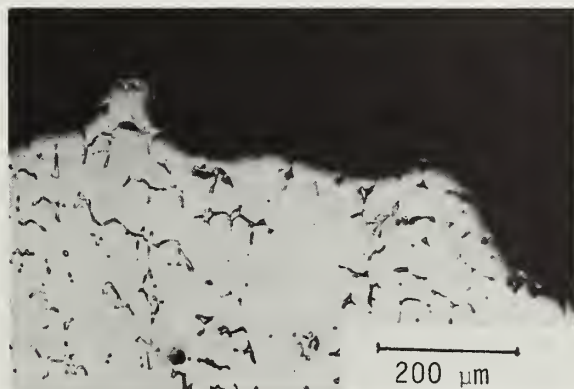


Figure 2. Micrograph of a 316L submerged-arc weld metal tensile specimen, tested at 4K. KOH etch.

Figures 3 and 4 are micrographs of areas near the crack tips in two CF8\* stainless steel castings tested at 4 K.

The intent of these micrographs is to show the inhomogeneity in deformation caused by the presence of delta-ferrite. Figure 3 is from a 0% delta-ferrite casting; the straight lines near the crack tip are strain-induced martensite. Note that the lines are straight and fairly uniform, only changing direction at grain boundaries. This can be contrasted with Figure 4, which is a similar region in a 14.5% delta-ferrite casting. In this case, the martensite formation is nonuniform and seems to be concentrated in association with the delta-ferrite morphology. Another example of the effect of the presence of delta-ferrite on deformation patterns in the austenite matrix is shown in Figure 5. In Figure 5, bending of martensite bands near the delta-ferrite particles can be seen in a CF8M\* casting with 9% ferrite, indicating that the delta-ferrite is nondeforming and the matrix is flowing around it.

Evidence to this point has indicated that delta-ferrite does not deform at 4 K. However, work on the series of CF8M castings has shown this to not be strictly true. As can be seen in Figure 6, the delta-ferrite does deform by a twinning mechanism. The jogs in the delta-ferrite/austenite interface and the fact that the twins are not observed in undeformed structures demonstrate that they are in fact deformation twins. Further evidence for this conclusion is given in Figure 7 in which three twin variants are shown. A stereographic projection of the angles between the three variants shows that they are consistent with (112) twin planes, which is typical for deformation twinning in ferritic materials.

In a macroscopic sense the deformation associated with twinning in the delta-ferrite is small; however it may have some significant secondary effects. One of these effects can be seen in Figure 8. This figure shows bands of intense martensite formation in the austenite at the ends of deformation twins in the delta-ferrite. This intense deformation could create preferred sites for void nucleation in the austenite.

The results of tensile tests on the five CF8M castings at 4 K, are given in Table 2 and shown graphically in

---

\*CF8 and CF8M are ASTM A351 grades of cast stainless steel and are analogous to AISI 304 and 316, respectively.



Figure 3. Area near the crack tip of a 0% delta-ferrite CF8 casting. Oxalic acid etch.

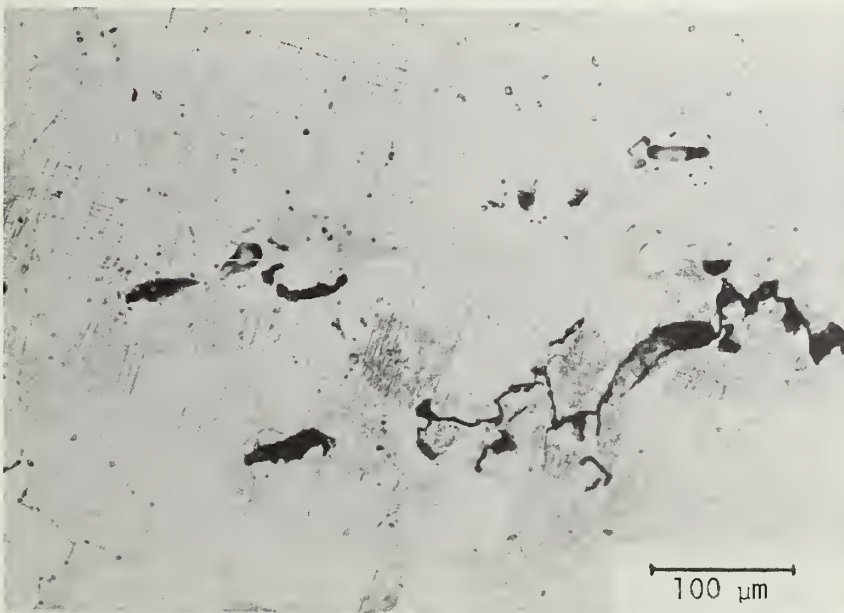


Figure 4. Area near the crack tip of a 14.5% delta-ferrite CF8 casting. KOH and oxalic acid etch.

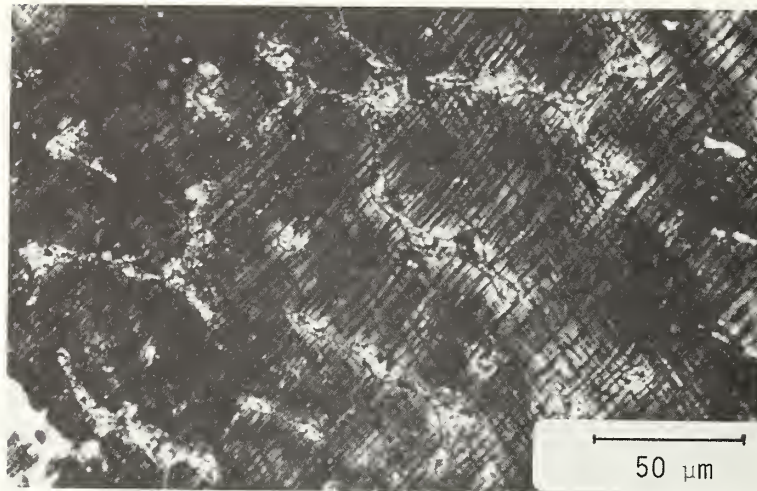


Figure 5. Micrograph of a 9% delta-ferrite CF8M tensile specimen, deformed at 4K.  $\text{H}_3\text{PO}_4$  etch.

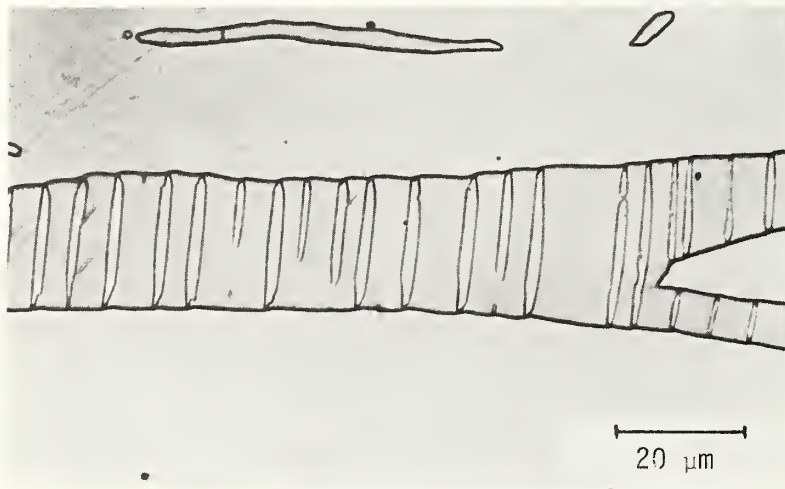


Figure 6. Micrograph of the 28.5% delta-ferrite CF8M casting, showing the deformation twinning that occurs at 4K. KOH etch.



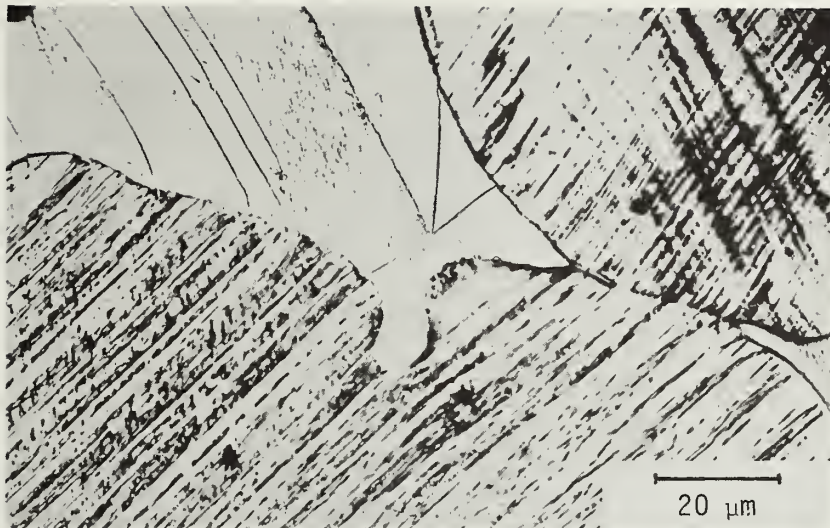


Figure 7. An 8.2% delta-ferrite CF8M casting, showing three deformation twin variants.  $\text{H}_3\text{PO}_4$  etch.

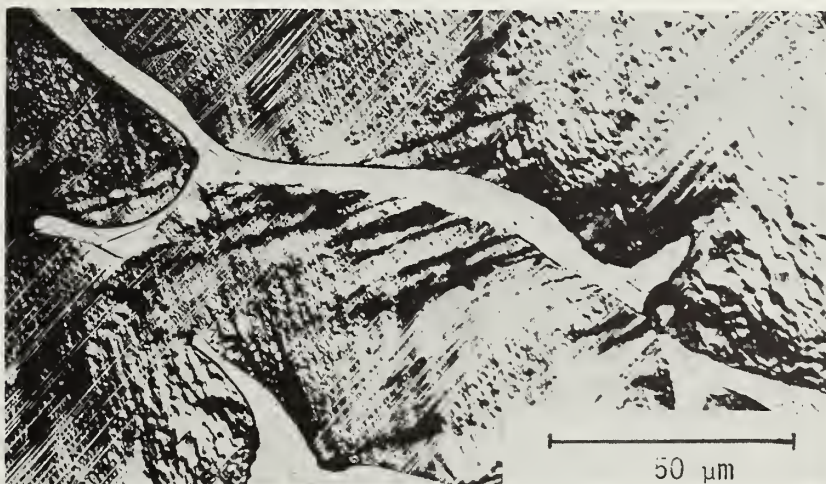


Figure 8. Same specimen as Figure 7, showing austenite deformation associated with twinning in the delta-ferrite.  $\text{H}_3\text{PO}_4$  etch.



Table 2. Mechanical properties of CF8M castings at 4K.

Heat	Yield Strength MPa	U.T.S. MPa	Elong. %	$K_{Ic}$ (J) $MPa\sqrt{m}$
1	581	1215	48	352
2	653	986	21	148
3	641	1143	19	113
4	707	1221	19	106
5	851	1164	11	105

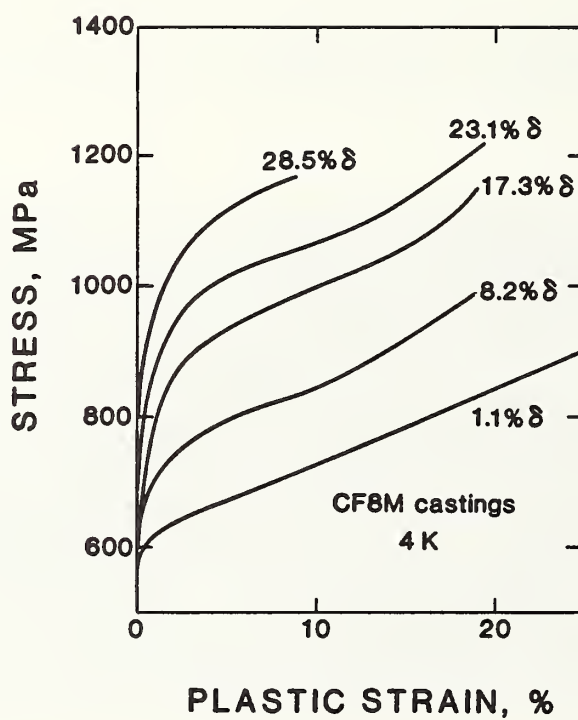


Figure 9. Stress versus plastic strain curves for the five CF8M castings, at 4K.

Figure 9, as stress versus plastic strain. The important feature to note on the stress-strain curves is the significant increase in strain hardening rate at low strains with increasing delta-ferrite content. As mentioned previously this is due to the increasing density of relatively non-deforming delta-ferrite particles which act as barriers to dislocation motion.

### Low Temperature Fracture

As a result of the above discussion on low-temperature deformation, it appears appropriate to classify duplex austenitic stainless steel, at low temperatures, as a ductile matrix composite with hard, brittle discontinuous fibers. This is not an exact classification, since the delta-ferrite does show some evidence of deformation and can be either continuous or discontinuous depending on solidification and cooling conditions, but this classification does provide a good starting point for the discussion of fracture mechanisms. There are three possible mechanisms for the fracture of ductile matrix/hard-discontinuous fiber composites (13).

1. Brittle fracture of the fibers.
2. Matrix/fiber interface separation.
3. Fiber pull-out.

Brittle fracture of the fibers occurs when the local stress in the fiber exceeds its fracture strength. The local stress in the fiber is not necessarily the same as the macroscopic stress on the sample; it can be considerably higher owing to inhomogeneous plastic deformation in the matrix. Interface separation is an important consideration with artificial composites and with metal-matrix/particulate composites; however, the interface between austenite and ferrite appears to be very strong and no evidence of interfacial separation has been observed. Fiber pull-out is sometimes associated with interface separation, but for the purpose of this discussion it means a ductile failure of the matrix near the matrix/fiber interface. This occurs when the fiber does not fracture, but the highly inhomogeneous deformation of the matrix near the fiber results in void nucleation at this location. The occurrence of one of these mechanisms over the other depends on fibre strength, content and morphology.

In this study evidence was found for both fiber fracture and fiber pull-out. Until this investigation there had been

no direct observation of the brittle fracture of delta-ferrite in weldments and castings at 4 K. Although this had long been assumed to be the cause of the reduction in toughness of stainless steel weldments with increasing delta-ferrite content, direct observation was difficult because of the extremely small size of the delta-ferrite in weldments. In this investigation observation were made on both castings and weldments made with high heat input processes. The much slower solidification and cooling rates of these materials results in a coarser structure, which is more easily observed.

With these materials extensive evidence was found of brittle fracture of delta-ferrite in weldments and castings deformed at 4 K. Evidence for cleavage fracture of delta-ferrite is shown in Figure 10 (a micrograph from the 14.5% delta-ferrite CF8 casting). This micrograph shows consistent angular relationships between the fractures, indicating that fracture is occurring on a specific set of crystallographic planes.

Weldments differ from castings mainly in that the solidification and cooling rates are much greater. This results in a more directional solidification pattern and a much finer structure. The greater cooling rate results in less diffusion during the delta-ferrite-to-austenite transformation causing the delta-ferrite to be more closely associated with the original dendritic solidification pattern. When fracture is associated with cracking of the residual delta-ferrite, having continuous delta-ferrite can provide a preferred crack path and lower toughness than occurs for a material of the same delta-ferrite content in a discontinuous morphology.

An example of this preferred crack path is shown in Figure 11 in the crack profile of a fracture toughness specimen from a 316L electroslag weldment. An electroslag weldment experiences a cooling rate greater than that of a casting, but much less than that of other welding processes. This results in a relatively coarse but continuous delta-ferrite morphology. Figure 11 shows that the dendritic growth direction determined the crack propagation direction even though the stress state was such that the crack should propagate straight. The crack was propagated down dendrite cores and secondary dendrite arms.

Further evidence that the delta-ferrite in this weldment fractured in a brittle manner is provided by the SEM fractograph in Figure 12. This fractograph also

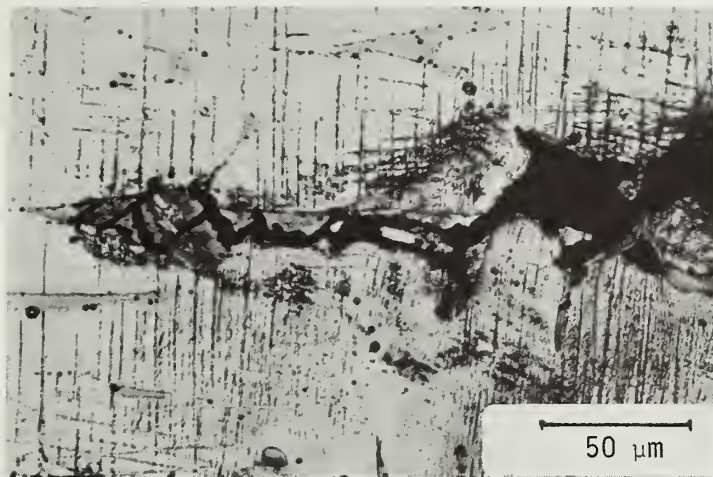


Figure 10. Area near the crack of a 14.5% delta-ferrite CF8 casting. KOH and oxalic acid etch.

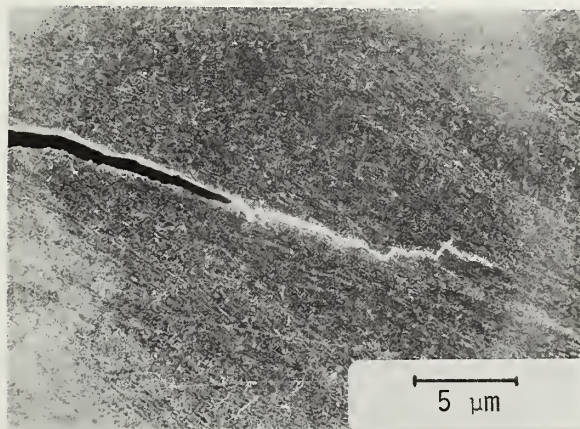


Figure 11. Crack profile of a 316L electroslag weldment. Oxalic acid etch.



demonstrates a mixture of brittle delta-ferrite fracture and ductile austenite failure, which will be discussed later.

As mentioned previously, two possible discontinuous fiber composite fracture mechanisms are of interest: fiber fracture and fiber pull-out. The evidence already presented has shown that fiber fracture does occur in coarse duplex structures. In the case of weldments with much finer structures, limited evidence has been found for both fracture mechanisms. Figure 13 is a fractograph of the fracture surface of a 308L FCMA weldment. The area indicated by the arrow appears to be a subsurface delta-ferrite dendrite, where the inhomogenous deformation nucleated a ductile failure near the delta-ferrite/austenite interface. Composite fracture theory predicts that, for a discontinuous fiber composite, there is a critical aspect ratio (fiber length-to-diameter ratio) at which a transition from fiber fracture to fiber pull-out fracture mechanisms occurs; a high aspect ratio favors fiber fracture. The aspect ratio of fiber is dependent on orientation to the tensile axis: the same fiber will have a high aspect ratio if it is aligned with the tensile axis and a low one if it is perpendicular to the tensile axis. In Figure 13 it is apparent that the dendrite was perpendicular to the tensile axis; therefore fiber pull-out occurred.

From the observations made to date fiber pull-out appears to be the less prevalent of the two fracture mechanisms observed. The most commonly observed mechanism is brittle fracture of the delta-ferrite. If the delta-ferrite is continuous the brittle fracture will result in specimen failure. However, in the case of discontinuous delta-ferrite the brittle fracture of discrete particles will cause stress concentrations that will result in ductile failure of the austenite matrix. An example of this mechanism is shown in Figure 14. This micrograph shows brittle fractures in a delta-ferrite particle with ductile fracture in the austenite between two cracks. This mechanism will result in a fracture surface displaying a mixed mode fracture. This type of fracture has been shown previously (Figure 12) and is commonly observed in these materials.

The deformation twinning in the delta-ferrite does have an effect on the fracture process. The different orientation of the cleavage planes in the twins causes the crack to change direction. This can be seen in the micrograph in Figure 15. The deformation twinning and the change in crack path will result in additional energy being absorbed in the



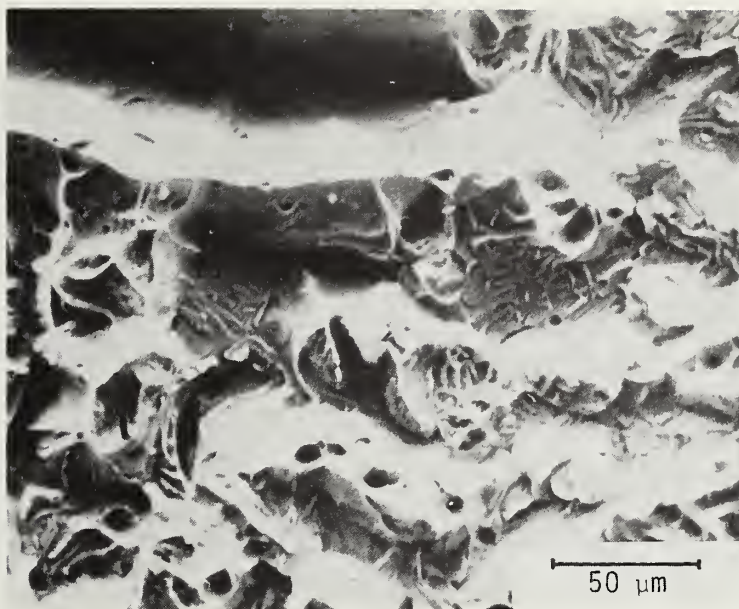


Figure 12. SEM fractograph of the fracture surface of a 316L electrosag weldment.

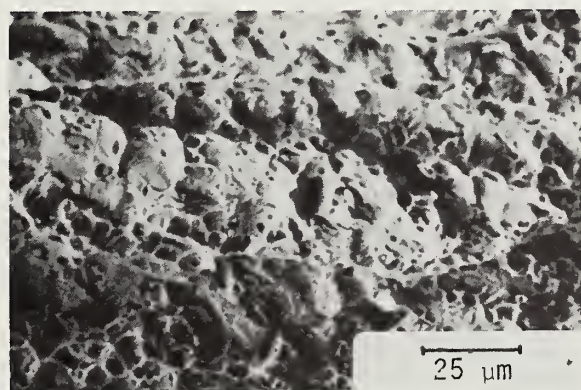


Figure 13. SEM fractograph of a 308L flux - core - metal - arc weldment.

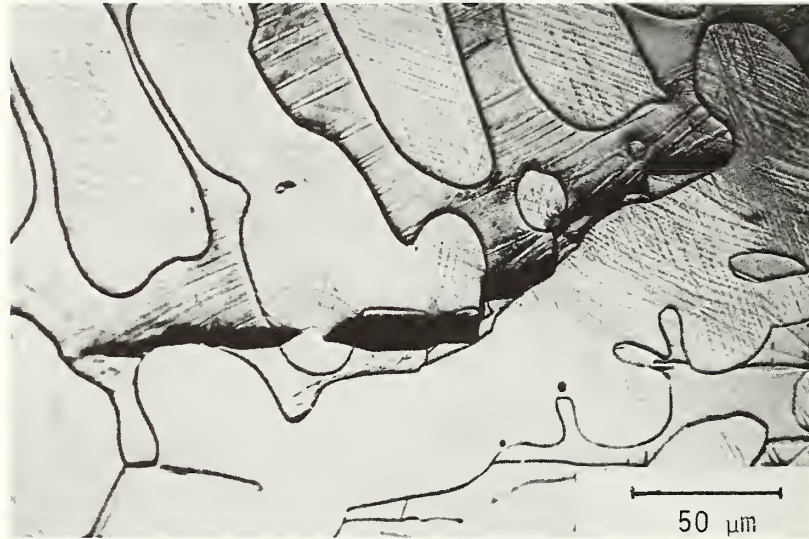


Figure 14. Micrograph of the 28.5% delta-ferrite CF8M casting, showing the combination of ductile and brittle failure.  $\text{H}_3\text{PO}_4$  etch.

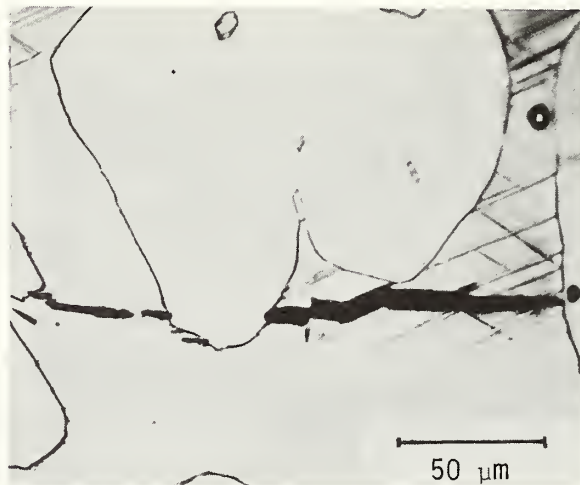
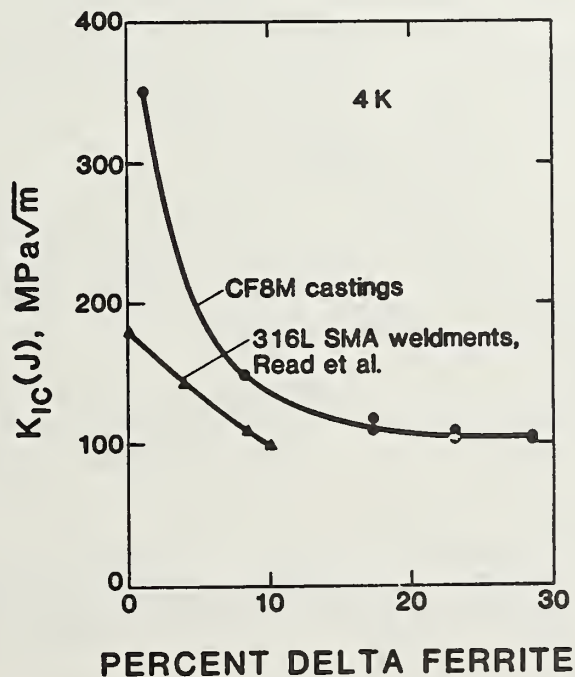


Figure 15. Same specimen as Figure 14, showing the interaction of the cracks with deformation twins.  $\text{H}_3\text{PO}_4$  etch.

fracture process. This will result in a higher fracture toughness. It is not possible, at this time, to determine the quantitative effect that this has on the fracture toughness of these materials.

The results of the fracture toughness testing, at 4 K, on the five CF8M castings are shown in Figure 16. This shows a decrease in fracture toughness with increasing delta-ferrite content up to about 15% delta-ferrite. At higher delta-ferrite contents the fracture toughness is essentially constant. Metallographic and fractographic examination has shown this to be related to the establishment of a continuous delta-ferrite crack path at this delta-ferrite content. Castings with less than 15% delta-ferrite show a mixed-mode ductile/brittle fracture, and those above 15% delta-ferrite show a completely brittle fracture.

Figure 16. The effect of delta-ferrite on the fracture toughness of CF8M castings and 316L weldments.



## SUMMARY

Samples of stainless steel castings and weldments that had been deformed and fractured at 4 K were examined. The thrust of the investigation was to determine the mechanisms by which residual delta-ferrite affects the deformation and fracture of duplex austenite/delta-ferrite structures at cryogenic temperatures. Evidence was presented that indicates that at low temperatures the delta-ferrite acts as a hard, brittle second phase particle. The manner in which these particles affect the mechanical properties of the material depends on the amount, properties and morphology of the second-phase particles. It was observed that the delta-ferrite reinforces the austenite matrix and causes the deformation to be inhomogeneous. Evidence was found for two fracture mechanisms: (1) brittle fracture of the delta-ferrite mixed with ductile failure of the matrix between delta-ferrite fractures and (2) ductile failure in the matrix near the austenite/delta-ferrite interface, which was caused by the highly inhomogeneous deformation in this region. The occurrence of one of these mechanisms over the other depends on the morphology and properties of the delta-ferrite. It was also observed that delta-ferrite deforms by a twinning mechanism at 4 K. These deformation twins have an effect on the crack propagation.

## REFERENCES

- (1) D. T. Read, H. I. McHenry, P. A. Steinmeyer, and R. D. Thomas, "Metallurgical Factors Affecting the Toughness of 316L SMA Weldments at Cryogenic Temperatures," Weld. J. Res. Suppl., 59, 1980, p. 104s.
- (2) T. A. Whipple, H. I. McHenry, and D. T. Read, "Fracture Behavior of Ferrite-Free Stainless Steel Welds in Liquid Helium," Weld. J. Res. Suppl., 60, (4), 1981, P. 72s.
- (3) E. R. Szumachowski and H. F. Reid, "Cryogenic Toughness of SMA Austenitic Stainless Steel Weld Metals: Part I - Role of Ferrite," Weld. J. Res. Suppl., 57, 1978, p. 325s.
- (4) E. R. Szumachowski and H. F. Reid, "Cryogenic Toughness of SMA Austenitic Stainless Steel Weld Metals: Part II - Role of Nitrogen," Weld. J. Res. Suppl., 58, 1979, p. 34s



- (5) T. A. Whipple and H. I. McHenry, "Evaluation of Weldments and Castings for Liquid Helium Service," in Materials Studies for Magnetic Fusion Energy Applications at Low Temperatures-IV, NBSIR 81-1645, 1981, p. 273.
- (6) T. A. Whipple and D. J. Kotecki, "Weld Process Study for 316L Stainless Steel Weld Metal for Liquid Helium Service," in Materials Studies for Magnetic Fusion Energy Application at Low Temperatures-IV, NBSIR 81-1645, 1981, p. 303.
- (7) L. Finch, "The Influence of Ferrite and Nitrogen on Mechanical Properties of CF8M Cast Stainless Steel," in Materials Studies for Magnetic Fusion Energy Applications at Low Temperatures-IV, NBSIR 81-1645, 1981, p. 337.
- (8) R. P. Reed, "A Cryostat for Tensile Tests in the Temperature Range 300 to 4 K," in Advances in Cryogenic Engineering, Vol. 7, Plenum Press, New York, 1962, pp. 448-454.
- (9) G. A. Clarke, W. R. Andrews, P. C. Paris, and D. W. Schmidt, "Single Specimen Tests for  $J_{Ic}$  Determination," in Mechanics of Crack Growth, Proceedings of the 1974 National Symposium on Fracture Mechanics, ASTM STP 590, American Society for Testing and Materials, Philadelphia, PA, 1976, pp. 27-42.
- (10) J. A. Begley and J. D. Landes, "The J-Integral as a Fracture Criterion", in Fracture Toughness, Proceedings of the 1971 National Symposium on Fracture Mechanics, Part II, ASTM STP 514 American Society for Testing and Materials, Philadelphia, PA, 1972, pp. 1-20.
- (11) C. W. Fowlkes and R. L. Tobler, "Fracture Testing and Results for a Ti 6Al-4V Alloy at Liquid Helium Temperatures," Eng. Fract. Mech., 8, 1976, pp. 487-500.
- (12) D. T. Read, "The Computer-Aided J-Integral Test Facility at NBS," in Materials Studies for Magnetic Fusion Energy Applications at Low Temperatures-III, NBSIR 80-1627, 1980, p. 205.





## MECHANICAL PROPERTIES OF STAINLESS STEEL CASTINGS AT 4 K\*

T. A. Whipple and H. I. McHenry  
Fracture and Deformation Division  
National Bureau of Standards  
Boulder, Colorado

### ABSTRACT

In some cryogenic structural applications it would be advantageous to use stainless steel castings, rather than wrought and welded structures. However, to date there are very few data on the mechanical properties of stainless steel castings at cryogenic temperatures. Stainless steel castings usually contain a certain amount of delta-ferrite to prevent hot cracking. The present program was designed to evaluate the effects of delta-ferrite and interstitial nitrogen on the strength and fracture toughness of stainless steel castings at 4 K.

Ten heats of cast CF8M stainless steel, which is the casting equivalent of AISI 316, were produced by a commercial vendor. In five of the heats the chromium and nickel contents were varied to obtain different delta-ferrite contents, ranging from 1.1 to 28.5 percent. The other five heats all had approximately 8 percent delta-ferrite and the nitrogen content was varied from 0.02 to 0.20 percent. As was expected from previous data on weldments and wrought materials, an increase in either delta-ferrite or nitrogen content increases the yield strength. In the five heats with varying nitrogen content the increase in strength resulted in a corresponding decrease in fracture toughness. An increase in delta-ferrite content also gave a decrease in fracture toughness up to approximately 15 percent delta-ferrite. Above this level the fracture toughness remained constant with increasing delta-ferrite content. This has been shown, by metallographic and fractographic evidence, to be due to the establishment of a continuous delta-ferrite crack path, at approximately 15 percent delta-ferrite.

+ Work supported by Office of Fusion Energy, Department of Energy

\* To be published in *Austenitic Steels at Low Temperatures*, Eds. R. P. Reed and T. Horiuchi, Plenum Press, New York (1983).



## INTRODUCTION

The limited use of stainless steel castings for 4-K service is partially due to the limited data available on their mechanical properties at 4 K.<sup>1</sup> The most significant 4-K data available on the tensile and fracture toughness properties of stainless steel castings came from a series of CF8 centrifugal castings with varying delta-ferrite contents.<sup>1,2</sup> There were six heats from three different vendors with delta-ferrite contents ranging from 0 to 14.5 percent. The results generally showed an increase in strength and a decrease in fracture toughness with increasing ferrite content.

The present study was undertaken to evaluate the effects of delta-ferrite and nitrogen on the 4-K tensile and fracture toughness properties of a series of nine CF8M stainless steel castings.

## MATERIALS

The materials used in this investigation were nine CF8M stainless steel castings whose chemical composition and delta-ferrite content are given in Table 1. For the first five castings, the nickel and chromium contents were varied to obtain five residual delta-ferrite contents, ranging from 1.1 to 28.5 percent. For the remaining castings, the nitrogen content was varied and the other elements were balanced to obtain a constant delta-ferrite content.

The castings were produced by a commercial vendor; the procedures used and room temperature mechanical properties have been reported previously.<sup>3</sup> The castings were received in the form of 30.5-cm x 61.0-cm x 10.2-cm blocks. All specimens were removed from

Table 1. Chemical composition\* and delta-ferrite content of CF8M castings.

Heat No.	C	Mn	Si	Cr	Ni	Mo	N	Vol. Percent Delta-Ferrite
47640	0.06	1.10	0.59	18.04	13.24	2.12	0.05	1.1
48988	0.06	0.38	1.16	19.62	10.61	2.12	0.05	8.2
47521	0.06	0.36	1.13	19.23	8.25	2.16	0.05	17.3
47552	0.06	0.35	0.95	20.40	8.22	2.13	0.05	23.1
49021	0.05	0.39	1.11	22.54	9.84	2.26	0.05	28.5
49020	0.07	0.39	1.09	19.32	10.00	2.07	0.02	8.0
47364	0.06	0.40	1.30	19.17	9.14	2.00	0.10	8.5
47390	0.07	0.41	0.98	21.00	9.46	2.13	0.144	9.5
47399	0.06	0.33	1.35	21.66	9.68	2.83	0.20	9.5

\*Chemical composition in weight percent, balance Fe.

areas at least 15.2 cm from either end and 3.8 cm from either surface. This was done to avoid any effects near the casting surface. The test specimens were 0.635-cm smooth bar tensile specimens, with a 2.54-cm gage length.

## PROCEDURES

The tensile tests at 4 K were conducted with the test apparatus and cryostat described by Reed.<sup>4</sup>

For the fracture toughness tests, a test procedure using three-point-bend specimens has been developed.<sup>5</sup> The single-edge-notched three-point-bend specimens were 2.54-cm wide, 2.54-cm thick, with a span of 10.2 cm. A direct measurement of the load-line displacement was made using the comparison bar method developed by Dawes.<sup>6</sup> The test data were acquired and reduced by a laboratory minicomputer, as described by Read.<sup>7</sup>

The volume-percent delta-ferrite was measured metallographically, using a computerized image analyzer. The specimens were electrolytically etched with a 10 N KOH solution, which gives good phase contrast. The values reported for volume percent represent the average for 400 fields at 100 times magnification.

## RESULTS AND DISCUSSION

The results of the 4-K tensile tests are given in Table 2 and shown graphically in Figures 1 and 2. Figure 1 contains the results from the heats with a constant nitrogen content and variable delta-ferrite contents. The yield strength increased with increasing delta-ferrite content. The tensile strength did not show a definite trend with respect to the delta-ferrite content, owing to the decrease in ductility with increasing delta-ferrite.

At low temperature the delta-ferrite, which has a bcc crystal structure, goes through a ductile-to-brittle transition. At 4 K, it



Table 2. Mechanical properties of CF8M castings at 4 K.

Heat No.	Yield Strength MPa	Tensile Strength MPa	Elongation %	Reduction in Area	$K_{IC}$ (J) MPa $\sqrt{m}$
47640	581	1215	49	33	352*
48988	653	986	21	15	148
47521	641	1143	19	13	113
47552	707	1221	19	14	106
49021	851	1164	11	17	104
49020	650	1122	22	14	129
47314	725	1152	20	17	126
47390	951	1086	13	15	74
47399	1100	1138	6	4	94

\*Invalid by specimen size requirements.

is essentially nondeforming, whereas the fcc austenite remains ductile. Therefore, an increase in the delta-ferrite content causes a dramatic increase in the strain-hardening rate of the duplex material. The yield strengths of the 8.2- and 17.3-percent delta-ferrite castings were found to be the same. Further testing in the low-strain region has shown this to be due to a difference in the proportional limit of the austenite matrix.<sup>5</sup> The 17.3-percent delta-ferrite casting had a lower proportional limit and a higher strain-hardening rate.

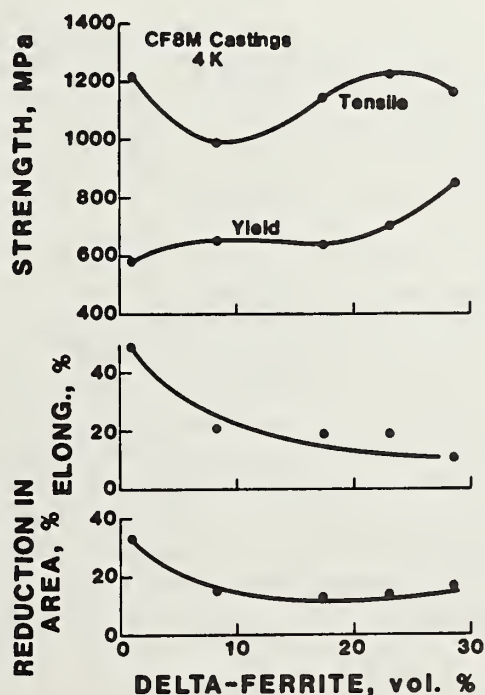


Fig. 1. The effect of delta-ferrite on the tensile properties of castings containing 0.05 percent nitrogen.

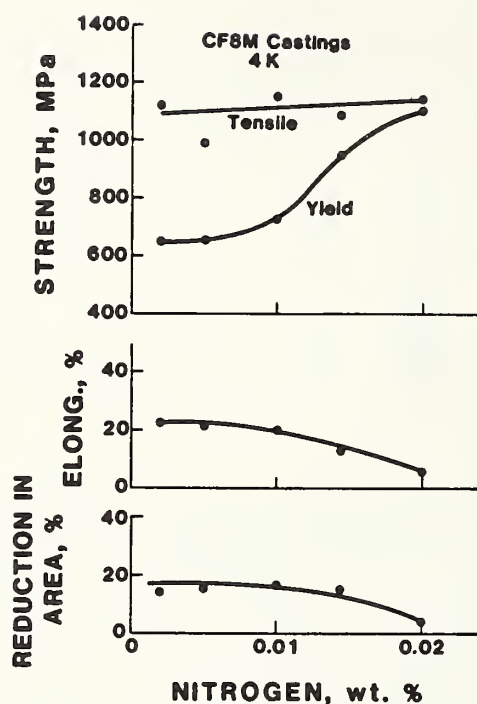


Fig. 2. The effect of nitrogen on the fracture toughness of castings containing  $9 \pm 1$  percent delta-ferrite.

Figure 3 shows the effect of nitrogen on the mechanical properties of CF8M stainless steel castings at 4 K. An increase in the nitrogen content increased the yield strength and reduced the ductility. Again, the tensile strength did not show a trend owing to the difference in ductility. The effect of nitrogen on the tensile properties was small at nitrogen contents below 0.10 percent.

The results of the fracture toughness tests at 4 K are given in Table 2 and shown graphically in Figures 3 and 4. The fracture toughness result on the 1.1-percent delta-ferrite casting is invalid by specimen size requirements and is used here only as an approximate value. However, it can be said that the fracture toughness of this alloy is much higher than the other four heats and is comparable to that of wrought materials of similar compositions. The interesting feature of the fracture toughness data is that the three high delta-ferrite heats (17.3, 23.1, and 28.5 percent) have approximately the same fracture toughness. Metallographic and fractographic observations have shown that this is due to the establishment of continuous delta-ferrite crack path at high delta-ferrite contents.

Figure 4 shows the fracture toughness as a function of nitrogen content. There is a general trend toward decreasing fracture toughness with increasing nitrogen content. The significant scatter in

these results is probably caused by variations in the delta-ferrite content of the castings.

#### CONCLUSIONS

1. An increase in either the delta-ferrite or nitrogen content of CF8M stainless steel castings increases the yield strength and reduces the ductility at 4 K.
2. Increasing the delta-ferrite content of CF8M castings decreases the fracture toughness at 4 K, up to a delta-ferrite content of 17 percent. Above this point, the fracture toughness is constant.
3. Increasing the nitrogen content of CF8M castings above 0.10 percent reduced the fracture toughness.

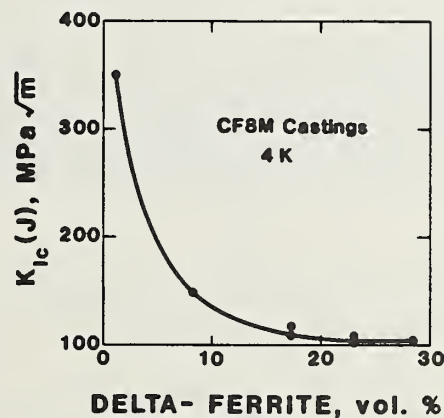


Fig. 3. The effect of delta-ferrite on the fracture toughness of castings containing 0.05 percent nitrogen.

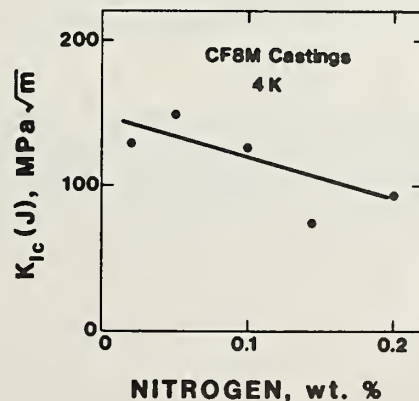


Fig. 4. The effect of nitrogen on the fracture toughness of castings containing  $9 \pm 1$  percent delta-ferrite.

## ACKNOWLEDGMENTS

The authors thank L. Finch of ESCO Corporation for his work in designing the alloy series and R. J. Fields of the National Bureau of Standards for the quantitative metallography work he performed. This research was supported by the United States Department of Energy, Office of Fusion Energy.

## REFERENCES

1. D. Dew-Highes and K. S. Lee, The choice of steel for the Isabelle magnet tubes, in "Advances in Cryogenic Engineering--Materials," Vol. 26, Plenum Press, New York (1981), pp. 151-157.
2. E. L. Brown, T. A. Whipple, and R. L. Tobler, Fracture toughness of CF8 castings in liquid helium, to be published in Metall. Trans.
3. L. Finch, The influence of ferrite and nitrogen on the mechanical properties of CF8M cast stainless steel, in "Materials Studies for Magnetic Fusion Energy Applications at Low Temperatures--IV," NBSIR 81-1645, National Bureau of Standards, Boulder, Colorado (1981), pp. 337-355.
4. R. P. Reed, A cryostat for tensile tests in the temperature range 300 to 4 K, in "Advances in Cryogenic Engineering," Vol. 7, Plenum Press, New York (1961), pp. 448-454.
5. T. A. Whipple, The effect of delta-ferrite on the mechanical properties of CF8M stainless steel castings at 4 K, in "Materials Studies for Magnetic Fusion Energy Applications at Low Temperatures--V," to be published by the National Bureau of Standards, Boulder, Colorado.
6. M. G. Dawes, Welding Institute Research Bulletin No. 7 (1976), p. 185.
7. D. T. Read, The computer-aided J-integral test facility at NBS, in "Materials Studies for Magnetic Fusion Energy Applications at Low Temperatures--III," NBSIR 80-1127, National Bureau of Standards, Boulder, Colorado (1980), p. 205.

## METALLOGRAPHY OF DUPLEX STAINLESS STEEL CASTINGS

E.L. Brown, T.A. Whipple, and G. Krauss  
Colorado School of Mines  
Golden, Colorado 80401

### ABSTRACT

The metallography of duplex stainless steel castings was studied in a series of CF8M alloys with varying ferrite content. Various etching techniques were employed to facilitate microstructural characterization of primary and secondary structures by light microscopy. These observations were then correlated with transmission electron microscopy observations of substructure and selected area electron diffraction studies of the  $\delta \rightarrow \gamma$  transformation. All alloys possessed a significantly recovered dislocation substructure in both the  $\gamma$  and  $\delta$  phases which was correlated with certain microstructural features. The crystallography of the  $\delta \rightarrow \gamma$  transformation was found to be consistent with a Kurdjumov-Sachs type orientation relationship regardless of apparent residual  $\delta$  morphology. On the basis of these observations a model for the evolution of residual  $\delta$  morphology was proposed.





## INTRODUCTION

The solidification behavior of austenitic stainless steels is of concern in both welding and casting technology. The term "austenitic" stainless steel is actually a misnomer with respect to weldment and casting microstructures since these can contain significant amounts of delta-ferrite ( $\delta$ ), the high temperature BCC phase of iron, as well as the FCC austenite phase ( $\gamma$ ). The presence of  $\delta$  can significantly alter the physical and mechanical properties of the  $\gamma$  matrix. Property variations due to  $\delta$  are beneficial or deleterious dependent upon the nature of the material application and its temperature regime. For example, in the case of weldments the presence of 5-10%  $\delta$  has been reported to reduce the incidence of hot cracking(1,2) and microfissuring.(3) At high temperatures ( $>700^{\circ}\text{C}$ )  $\delta$  can transform to the brittle sigma ( $\sigma$ ) phase, resulting in a degradation of mechanical properties(4-6), and in highly corrosive environments it can provide a path for corrosion attack.(7) Ferrite in an austenite matrix also generally increases the strength and lowers the fracture toughness of welds and castings(8), this is especially the case in cryogenic applications. A general review of  $\delta$  in austenitic stainless steel follows. This review will consider the effects of

composition, solidification and solid state transformation on the extent and morphology of  $\delta$  in welds and castings.

### Review of $\delta$ in Austenitic Stainless Steel

Composition Effects. The overwhelming volume of work has been conducted in the area of welding of austenitic stainless steels and, more specifically, concerning the affects of various filler metal compositions on  $\delta$  content. Some additional work has been performed to extend the concepts employed in weldments to castings. The effects of composition on  $\delta$  content are generally embodied in the form of so-called Cr- and Ni-equivalents. The former integrate the effects of ferrite formers and the latter the effects of austenite formers. The Schaeffler and DeLong Diagrams relate  $\delta$  content to Cr- and Ni-equivalents.(9-11) Similar empirical correlations between  $\delta$  content and alloy composition have been established for castings and are contained in the Schoefer Diagram.(12,13) The data contained in these diagrams refer to the  $\delta$  content at ambient temperature, which formed in a non-equilibrium manner. In fact, the equilibrium microstructures of these alloys at ambient temperature generally do not contain any  $\delta$ . The departure from equilibrium can be effected by altering the solidification rate, the cooling rate subsequent to solidification and/or modifying the chemical composition.(14)

Solidification Effects. Numerous investigations have been conducted to elucidate the solidification behavior of this class of stainless steels. The solidification behavior can be divided into primary  $\delta$  and primary  $\gamma$  modes according to the ratio of chromium and nickel equivalents. This division is frequently illustrated by construction of appropriate constant Fe pseudo-binary sections of the Fe-Cr-Ni ternary.(15,16,25) It is important to realize that pseudo-binary sections through ternaries are only qualitative.(2-6) They are, however, useful for qualitatively illustrating solidification modes as a function of composition. A typical pseudo-binary of this sort is depicted in Figure 1.

The two-phase,  $\gamma + L$  and  $\delta + L$  regions are separated by a eutectic triangle of  $\gamma + \delta + L$  region. Below the triangle a  $\gamma + \delta$  phase field exists. It can be seen that if the nominal composition of the steel possesses a low  $Cr_{eq}$  (low proportion of ferrite formers) the primary solid phase is austenite. Similarly, in a steel with a high  $Cr_{eq}$  (high

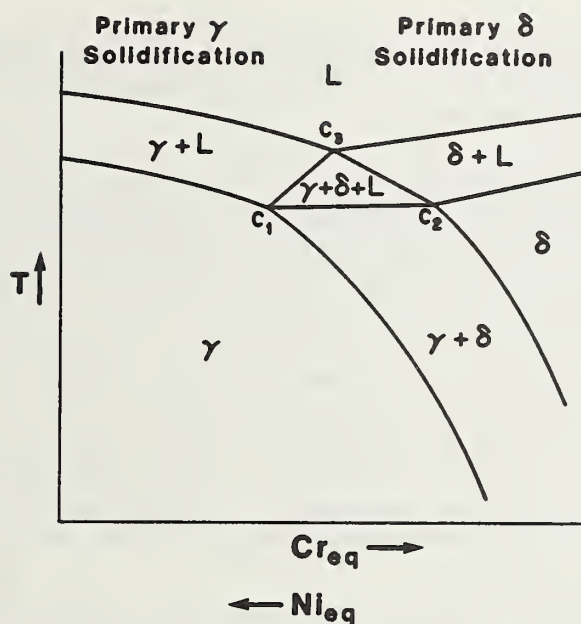


Figure 1. Constant Fe pseudobinary phase diagram

proportion of ferrite formers) ferrite is the primary solid phase. The solidification mode becomes more complex in the vicinity of the eutectic triangle. From nominal compositions  $C_3 > Cr_{eq} > C_1$  the primary solid phase is still austenite, however, ferrite precipitates before solidification is complete. Likewise, for nominal compositions  $C_3 > Ni_{eq} > C_2$  the primary solid phase is ferrite but austenite precipitates prior to complete solidification. As will be discussed later, the microstructures that result from solidification and cooling in the vicinity of the eutectic triangle are also more complex. This finer classification of solidification modes has been described in the literature.(14,17-20,25,27) The ternary eutectic behavior described above is applicable to the majority of commercial austenitic stainless steel grades that contain < 90 w/o iron. In the materials under consideration, the eutectic is of a divorced nature since the amount of liquid at the eutectic composition is generally small. In primary  $\gamma$  solidified alloys the divorced phase at the subgrain and grain boundaries is  $\delta$ . In primary  $\delta$  solidified alloys the divorced phase is  $\gamma$ .(21) Studies of solidification in conventional ingots, complemented by a directional solidification and quenching technique, have confirmed the potentially dynamic nature of the solidification sequence of primary  $\delta$  alloys. (14,16,



25,27,28) Initial precipitation of  $\delta$  could be interrupted by precipitation of  $\gamma$ , in the form of an envelope, before complete solidification.

Concomitant with the evolution of a solidification structure is the redistribution of solute elements, commonly referred to as solute segregation. The various possibilities have been described in detail elsewhere.(29-31) Of course, equilibrium solidification is not a reasonable assumption. A more realistic situation is one in which solid state diffusion is minimal so that coring or microsegregation occurs during solidification.(30,31) Perfect mixing in the liquid and mixing in the liquid by diffusion only represent extreme situations. Real cases probably exist between these two extremes. For the cases described above, the final distributions of solute after normal freezing are depicted in Figure 2.

A generalized theory of primary  $\delta$  solidification of austenitic stainless steel has been formulated for weldments, assuming mixing in the liquid by diffusion only. (15) The transients are associated with the subgrain (dendrite) core and the subgrain boundary (interdendritic) region. Basically, Cr is segregated to the dendrite core and Ni to the interdendritic region. Attempts have been made to experimentally determine solute distribution via electron microprobe and scanning transmission electron microscopy studies.(15,16,18-20,22,23,27,28) Difficulties arise in separating the solute redistribution due to solidification and that due to the solid state  $\delta \rightarrow \gamma$  transformation, without making assumptions regarding the nature of this phase transformation, e.g., no solute redistribution during  $\delta \rightarrow \gamma$  transformation.(15,22,23)

Solid State  $\delta \rightarrow \gamma$  Transformation and Residual Morphologies in Primary  $\delta$  Alloys. The  $\delta$  content of as-solidified primary  $\delta$  alloys can be substantially reduced during cooling and post solidification treatments.(24,32) Therefore, it is obvious that a  $\delta \rightarrow \gamma$  transformation plays a major role in the evolution of microstructure in duplex austenitic stainless steel welds and castings.

A  $\delta \rightarrow \gamma$  transformation only occurs for alloys that undergo primary  $\delta$  solidification and the nature of the transformation appears to vary with composition, cooling rate and perhaps with solidification behavior. It is important to note that a number of labels have been associated with the various observed residual morphologies that are



descriptive in nature but may not accurately describe the source of the morphology.

Primary  $\delta$  alloys remote from the eutectic triangle solidify with almost 100 v/o  $\delta$ ;  $\gamma$  forming interdendritically. In this type of alloy the resultant room temperature microstructure is completely determined by the solid state transformation. The character of the phase transition

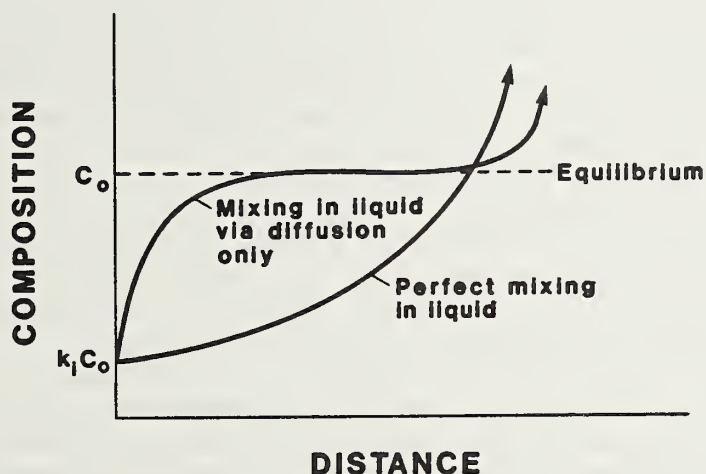


Figure 2 Schematic diagram of solute distribution after normal freezing.

depends essentially on the degree of undercooling, which in turn, depends upon the cooling rate.(14,15) For relatively rapid cooling the  $\delta \rightarrow \gamma$  transformation has been alternatively referred to as a Widmanstatten or an acicular(17,20) morphology. The Widmanstatten phase transformation can be described as a thermally activated, and diffusion controlled reaction in which an orientation relationship between the parent and product phases is established.(33) The residual  $\delta$  product has been termed "lathy".(17,18,20) Microstructural investigation of the lathy morphology in welds(18) has indicated the presence of several differently oriented  $\gamma$ - $\delta$  lath bundles in a given large growth unit. Furthermore, the residual  $\delta$  is not related to the primary  $\delta$  dendritic structure, due to solidification.(14,18,25) At

slower cooling rates the mode of  $\delta \rightarrow \gamma$  transformation in these types of alloys has been termed "equiaxial"(17,20) and it is not exactly clear what type of  $\delta$  morphology this results in.

The majority of primary  $\delta$  alloys of interest intersect the eutectic triangle so that  $\gamma$  envelopes the primary  $\delta$  prior to completion of solidification. The solid  $\gamma$  envelope allows for heterogeneous nucleation of  $\gamma$  during the  $\delta \rightarrow \gamma$  transformation at smaller undercooling (higher temperature). Therefore, the resultant  $\delta$  exhibits less of the Widmanstätten type morphology.(14,16,17,20,25,28) The  $\delta$  morphology that results in this case has been termed "vermicular" because of its so-called roundish appearance.(15,20, 21) A continuous spectrum of ferrite morphology, from vermicular to lathy, has been observed with increasing  $Cr_{eq}/Ni_{eq}$ .(20) Regardless of the observed morphology, the  $\delta$  in primary  $\delta$  alloys is definitely located at the cores or spines of dendrite arms (subgrains).(14,16,17,20,21,25) The progressive growth of  $\gamma$  into the primary  $\delta$  results in segregation of "ferritizers" to the  $\delta$  at the dendrite or subgrain core, thus stabilizing it against transformation.(10,21,22,28) The dendritic form is now easily defined.(14,25) Implicit in this observation is that formation of a  $\gamma$  envelope occurs with attendant segregation of alloying elements. Since diffusion, and hence homogenization of alloying elements is more difficult in austenite, the segregation pattern persists and allows observation of the prior dendritic form at room temperature.(25) In alloys which solidify as virtually 100 v/o  $\delta$  the ease of diffusion in this phase minimizes segregation at high temperature and therefore the dendritic growth form is not observable.

Limited transmission electron microscopy (TEM) observations have shown that lathy  $\delta$  possesses a Kurdjumov-Sachs (K-S) type orientation relationship(34) with austenite, whereas vermicular  $\delta$  possesses no crystallographic relationship with austenite.(20) Angular faceting of  $\delta/\gamma$  interfaces in primary  $\delta$  alloys has also been observed and noted in castings.(21) The observations of primary  $\delta$  alloys described above have all implied a diffusion controlled mechanism for the  $\delta \rightarrow \gamma$  transformation.(16,20)

Some of the observations described above have been synthesized to rationalize the behavior of larger castings and ingots. Castings frequently exhibit a columnar-to-

equiaxed grain transition during solidification, i.e., columnar grains growing inwards from the mold wall and a central equiaxed grain zone. In alloys that solidify almost completely as  $\delta$  the first  $\gamma$  precipitates in the primary grain boundaries and intragranularly as the temperature drops. All of these regions of  $\gamma$  have different orientations and the columnar-to-equiaxed transition is thus observable in the primary (solidification) and secondary (solid state) microstructures.(25) In alloys that intersect the eutectic triangle the columnar-to-equiaxed grain transition is masked by the  $\delta \rightarrow \gamma$  transformation. Austenite begins to solidify from the melt after initial  $\delta$  solidification and prior to completion of solidification. Columnar  $\gamma$  crystals nucleate at high temperature and grow under steep temperature gradients across the entire ingot cross-section. With the high driving force for  $\gamma$  growth thus produced, changes in the original  $\delta$  orientation present no barrier to that growth.(19,28,35) Mixtures of these two modes of behavior are frequently observed in the same ingot. Once  $\delta$  has solidified, the  $\gamma$  envelope necessary for the  $L+\delta \rightarrow L+\delta+\gamma$  transition is difficult to form at high growth rates.(25) Therefore, completely  $\delta$  solidification might be expected in the vicinity of the mold wall and a mixed mode in the ingot interior. Variations in  $\delta$  level through an ingot cross-section must be rationalized in light of the fact that higher  $\delta$  levels, associated with higher cooling rates, can be offset by rapid homogenization in the finer solidification structures.(24,32) Rapid homogenization lowers the  $\delta$  content. As the  $\delta$  levels in welds and castings increase the  $\delta$  phase becomes more continuous.(37) Furthermore, upon dissolution of  $\delta$ , spheroidization can take place concurrently.(24)

The objective of the present investigation was to characterize the microstructure and substructure of CF8M duplex stainless steel castings. Effort was made to correlate microstructural aspects such as  $\delta$  morphology, observed via light microscopy, with substructure, observed by transmission electron microscopy. In addition, the crystallography of the  $\delta \rightarrow \gamma$  transformation was studied by selected area electron diffraction. Structural and crystallographic data were synthesized and a model for the evolution of  $\delta$  morphology proposed.



## EXPERIMENTAL PROCEDURES

### Chemistries and Processing of Alloys

A number of CF8M alloy castings were produced to ASTM specification A351. The alloy designations, their chemical compositions and ferrite content are included in Table I, below. The ferrite contents shown were determined by quantitative metallography techniques. Alloys K-9, K-14 and K-24 were all produced separately as keel block castings (approx. 20 cm x 8 cm x 14 cm) whereas the other alloys were produced together as a series of controlled chemistry castings in which the ferrite content was purposely varied at a constant interstitial content (C+N). This material was produced in the form of fairly large castings (10 cm x 30 cm x 60 cm). The alloy production and castings procedures have been described by Finch.(38) Subsequent to casting, all material was annealed at approximately 1400 K.

TABLE I  
Chemical Composition

<u>Alloy</u> <u>Design-</u> <u>nation</u>	<u>C</u>	<u>N</u>	<u>Mn</u>	<u>Si</u>	<u>Cr</u>	<u>Ni</u>	<u>Mo</u>	<u>v/o</u> <u><math>\delta</math>-ferrite</u>
K-9	0.02	-	1.06	1.10	19.33	11.67	2.14	9
K-14	0.05	-	0.83	1.25	19.50	12.20	2.69	14
K-24	0.07	-	0.52	1.32	21.48	9.48	3.18	24
1	0.06	0.05	1.10	0.59	18.04	13.24	2.12	1.1
2	0.06	0.05	0.30	1.16	19.62	10.61	2.12	8.2
3	0.06	0.05	0.36	1.13	19.23	8.25	2.16	17.2
4	0.06	0.05	0.35	0.95	20.40	8.22	2.13	23.1
5	0.05	0.05	0.39	1.11	22.54	9.84	2.26	28.5

### Light Microscopy

Specimens for light microscopy were ground and lapped to a metallographic finish by standard procedures. Four etching techniques were employed. A deposition color etch composed of 100 ml distilled H<sub>2</sub>O, 20 ml HCl and 2 g potassium metabisulfite was applied as a light etch to delineate the prior solidification structure and as a heavy etch to delineate the macrostructure of the castings. As a light etch, a blue interference layer is deposited on the regions of the original  $\delta$  dendrites (high Cr) and a gold layer on the interdendritic regions (low Cr). The latter actually represent regions of interdendritic liquid. An electro-etch

of 10 g oxalic acid in 100 ml distilled H<sub>2</sub>O (2-6 V and room temperature) was employed to delineate boundaries between  $\delta$  and  $\gamma$  and twin boundaries. When more contrast was required between  $\delta$  and  $\gamma$  a 10N KOH electrodeposition etch was employed to deposit a light blue to light brown film on the  $\delta$  ferrite.

### Transmission Electron Microscopy (TEM)

Thin foils were produced for TEM by cutting wafers  $\sim 0.4$  mm in thickness with a low speed diamond saw. The wafers were reduced to  $\sim 0.07$  mm in thickness by mechanically abrading and 3 mm diameter disks produced by slurry drilling. The latter is a low temperature-low deformation procedure. Foils were produced by electropolishing to perforation in a Fischione twin jet polisher, employing a 5v/o HClO<sub>4</sub> -25v/o glycerin-ethanol electrolyte (40 V- 80 mA at room temperature). Foils were examined in a Philips EM 400 transmission electron microscope, operated at 120 kV.

## RESULTS

### Light Microscopy

Some aspects of the solidification macrostructure are illustrated in the K-9 alloy, light color etched, Fig. 3(a). A columnar-to-equiaxed grain transition occurred, characterized by an increase in interdendritic liquid and detached columnar and equiaxed dendrites. The residual  $\delta$  was seen to exist as networks at the dendrite spines, Fig. 3(b). When a heavier color etch was applied to the same casting section, a coarse columnar grain structure parallel to the direction of maximum heat flow was observed, Fig. 3(c). This columnar grain structure appeared to grow across the previously described columnar-to-equiaxed grain transition. A higher magnification macrograph shows that the dendritic structure, as defined by the residual  $\delta$ , possesses the same orientations across many of the columnar grain boundaries, Fig. 4. In addition, the coarse columnar structure appears composed of a finer scale mosaic of different contrast regions that are faceted on a microscale. The specimens from alloys 1-5 were obtained from regions corresponding the central equiaxed region of the castings. The residual  $\delta$  morphologies in these alloys are generally illustrated in Fig. 5. As the ferrite content is increased



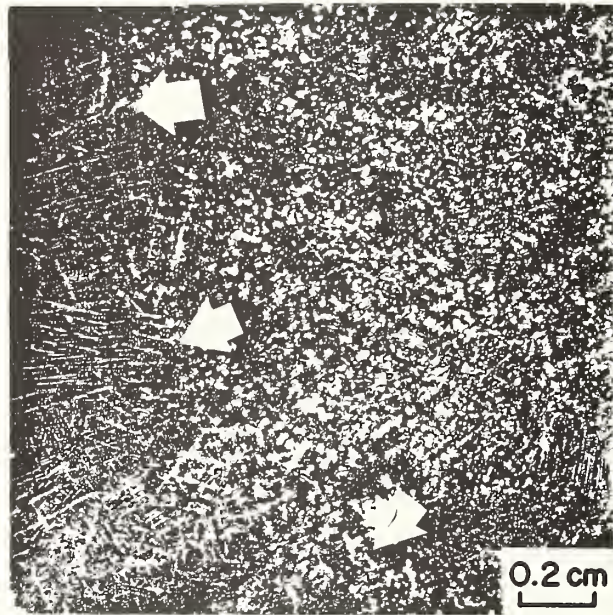


Figure 3(a) Columnar-to-equiaxed grain morphology transition in solidification structure.

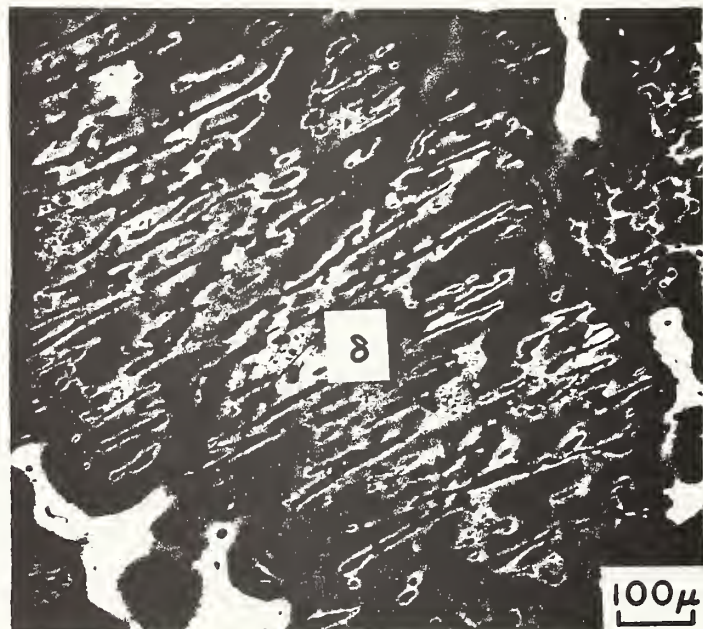


Figure 3(b) Residual  $\delta$  at spines of dendrite arms.



Figure 3(c) Columnar  $\gamma$  crystals formed during  $\delta \rightarrow \gamma$  phase transformation

the ferrite microstructure becomes coarser and exhibits greater continuity. On a given plane of polish the  $\delta$  in the higher ferrite alloys appears composed of either relatively long, filamentary particles or equiaxed cell-like networks. There are also many faceted  $\delta/\gamma$  interfaces. A facet is defined as a straight segment of  $\delta/\gamma$  interphase boundary. Frequently, facets seem to occur at definite, recurring angles to one another on a given plane of polish, suggestive of facet variants. Twinning of the  $\gamma$  matrix was also observed, Fig. 6. The  $\delta/\gamma$  interface morphology is quite intricate and can generally be described as facets connecting curved segments of interface. Closer examination of the interfaces revealed the presence of steps on faceted and curved segments, Fig. 7.

#### Transmission Electron Microscopy

General Features of Substructure. A well recovered dislocation substructure was observed in all castings. Although no quantitative measurements were made, it appeared that the subgrain structure was coarser in the 1.1%  $\delta$  specimen in comparison to those containing higher amounts of ferrite, Fig. 8.

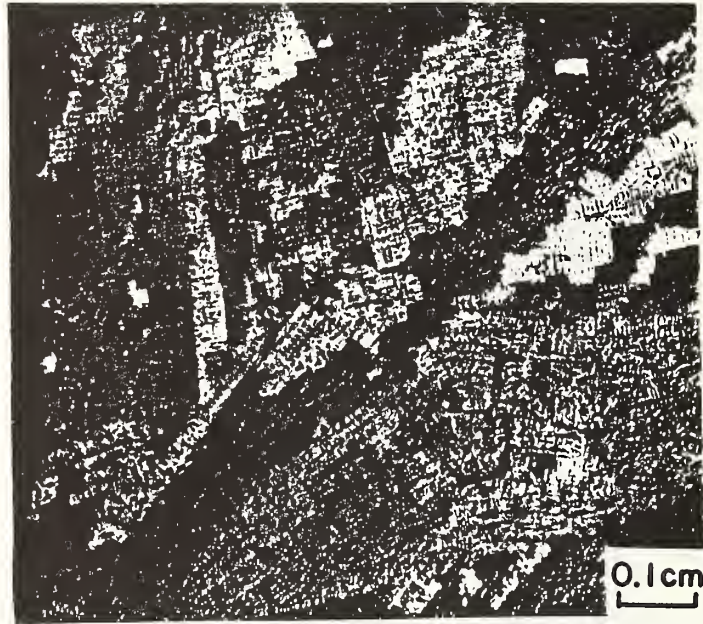


Figure 4 Columnar  $\gamma$  crystal structure showing residual  $\delta$  at spines of dendrite arms and variations in contrast.

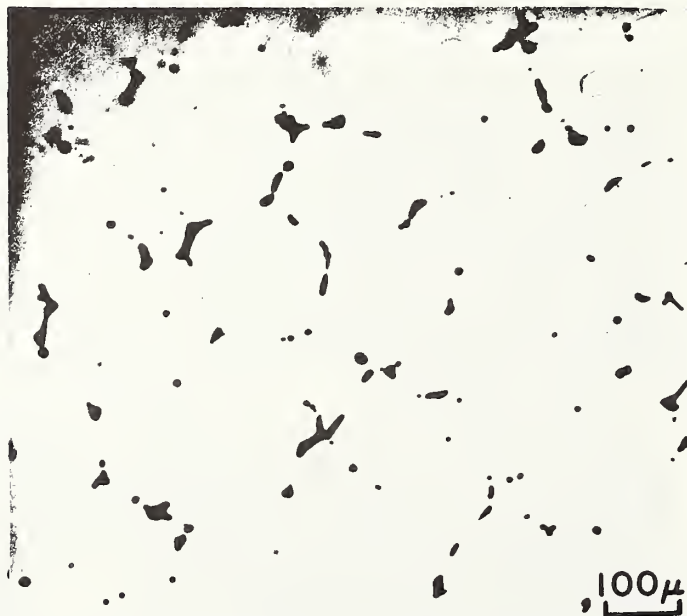


Figure 5(a) Residual  $\delta$  morphology as a function of  $\delta$  content. (a) 1.1%  $\delta$



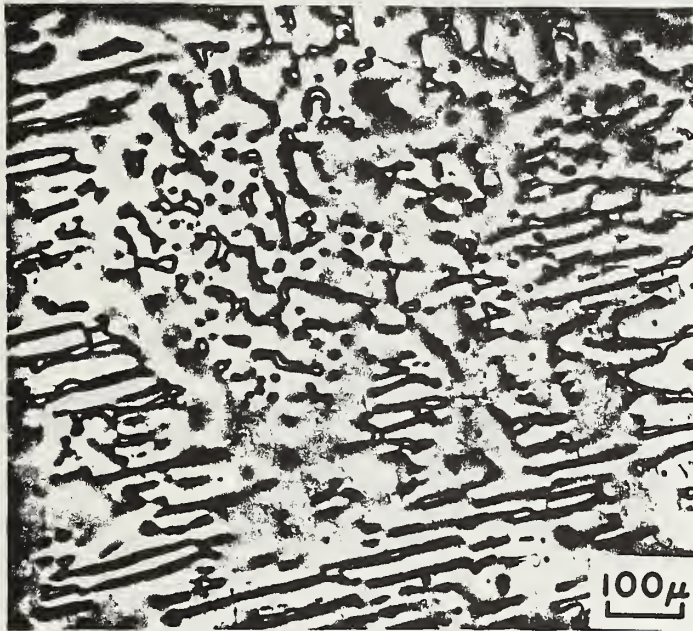


Figure 5(b) 9%  $\delta$

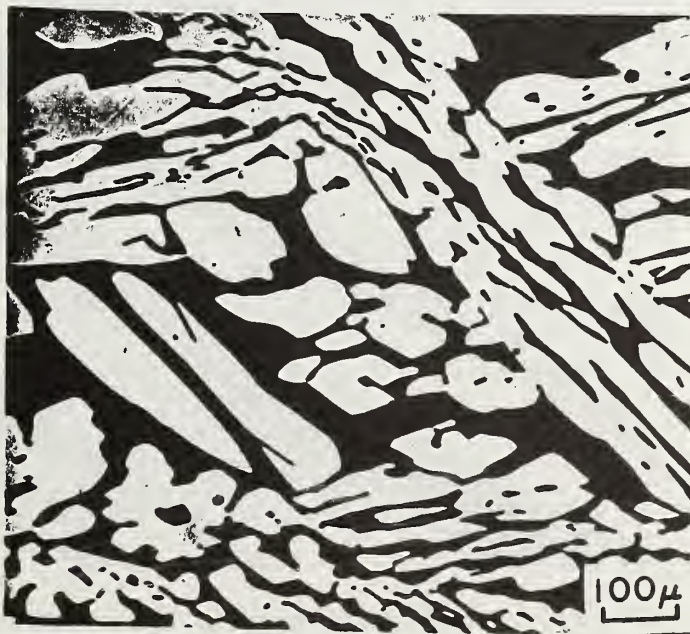


Figure 5(c) 28.5%  $\delta$

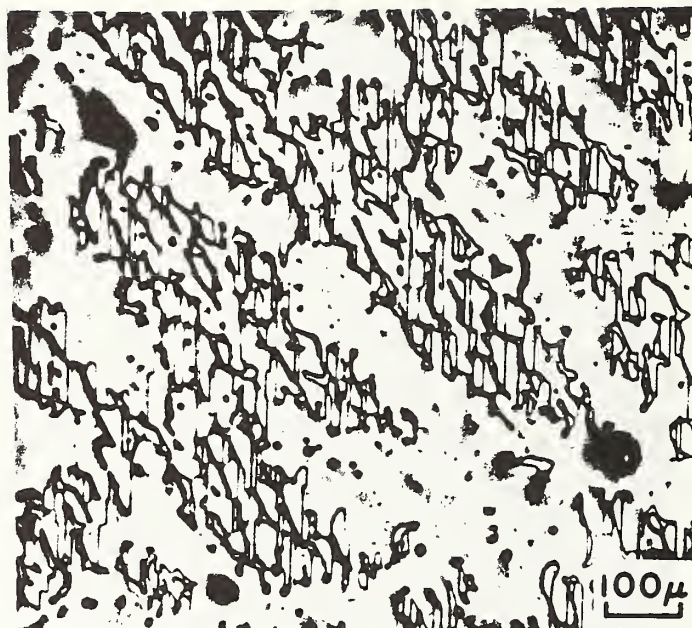


Figure 6 Twinning in  $\gamma$  matrix



Figure 7 Residual  $\delta$  showing ledges on  $\delta/\gamma$  interface.





Figure 8(a) Recovered dislocation substructure  
TEM (a) 1.1%  $\delta$



Figure 8(b) 28.5%  $\delta$

The subgrain boundaries were sometimes composed of dislocation tangles, seemingly "knit" together, while in other instances a well defined dislocation net characterized the boundary, Fig. 9.

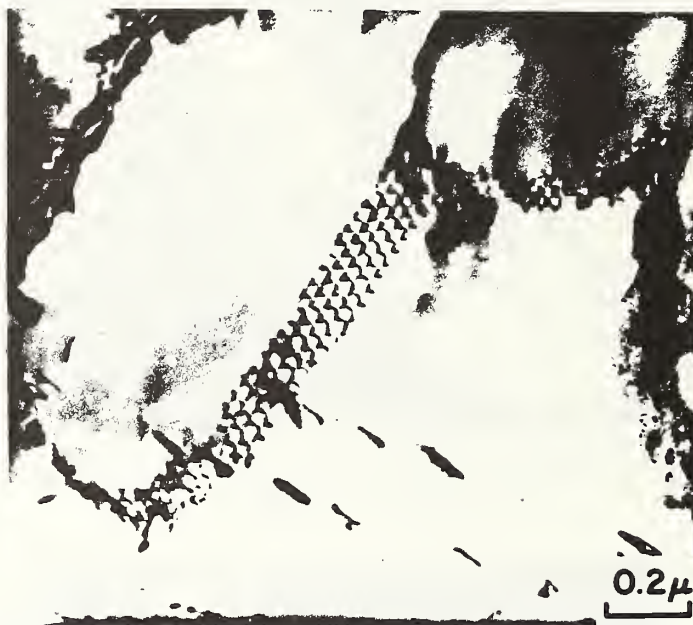


Figure 9(a) Nets of dislocations in subgrain boundaries, 1.1%  $\delta$ ; TEM (a) BF



Figure 9(b) Weak Beam CDF

The ferrite also contained a substantial amount of dislocation substructure. In fact, the 28.5%  $\delta$  exhibited a "bamboo" subgrain structure in the ferrite, Fig. 10. Sub-boundaries were observed to bridge the width of the ferrite region.



Figure 10 Recovered dislocation substructure in  $\delta$ , 28.5%  $\delta$ ; TEM.

In addition to subgrains there were also significant levels of individual dislocations in the subgrain interiors, apparently in the form of debris. The dislocations in the 1.1%  $\delta$  specimen were frequently extended, as evidenced by the extended nodes in the sub-boundary of Fig. 9. There was less evidence of extended dislocations in specimens containing ferrite. There was also more evidence of planar slip in the 1.1%  $\delta$  specimen despite the presence of a recovered subgrain structure, Fig. 11.

Large populations of stacking and twin faults were observed. The diffraction contrast from faulted regions was frequently indicative of overlapping stacking faults, Fig 12(a). These faults were observed to emanate from subgrain boundaries and  $\delta/\gamma$  interfaces. There was also evidence of lamellar twins that were associated with discrete reflections in diffraction patterns Fig. 12(b). Their presence is consistent with the observations of light microscopy. Faults were sometimes associated with edge

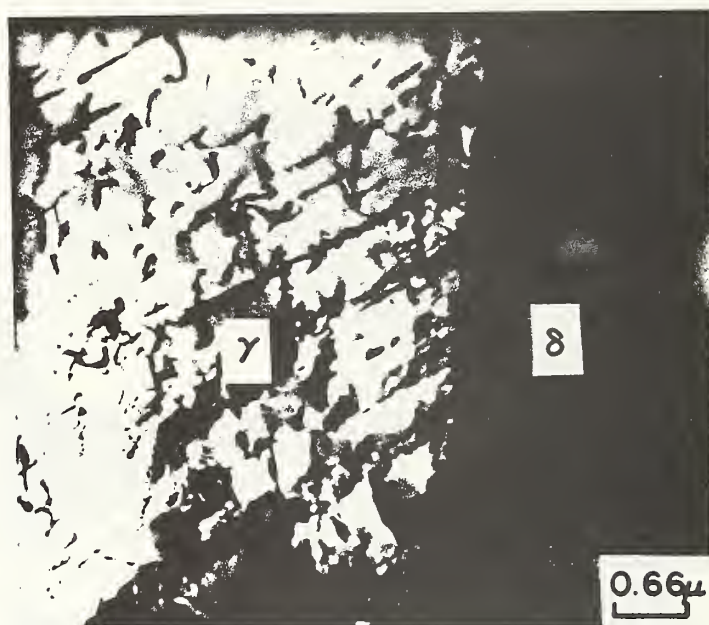


Figure 11 Evidence of planar slip in  $\gamma$ , 1.1%  $\delta$ ; TEM



Figure 12(a) Faulting in  $\gamma$ ; TEM  
(a) Overlapping stacking faults





Figure 12(b) Twin faults.

cracks in the foil. It is difficult to state whether these cracks are actually present in the bulk material or are an artifact of foil making.

Crystallography of the  $\delta \rightarrow \gamma$  Transformation. The crystallography of the  $\delta \rightarrow \gamma$  transformation was studied extensively by TEM of thin foils obtained from the keel block casting containing 9 v/o  $\delta$ . However, the features described below were also observed in specimens containing higher ferrite contents. Observations of the  $\delta/\gamma$  interfacial morphology indicated the presence of many facets and steps. No attempt was made to exactly determine the lattice correspondence between austenite and ferrite. However, SAD evidence was consistent with the widespread occurrence of Kurdjumov-Sachs (K-S) - type orientation relationships, Fig. 13.\* Curved and straight interfaces were examined and the lattice correspondences described above persisted regardless of the extent of boundary curvature. Single surface trace analysis of straight sections of interface indicated habit planes slightly deviated from  $\{111\} \gamma$ . Small facets on the  $\delta/\gamma$  interface were observed and there was some evidence of misfit dislocation structures in the boundaries, Fig. 14.

\*The Kurdjumov-Sachs, Nishayama-Wasserman and Bain orientation relationships, relating bcc and fcc phases, are very similar.





Figure 13(a)  $\delta/\gamma$  Interphase interface, TEM (a) BF

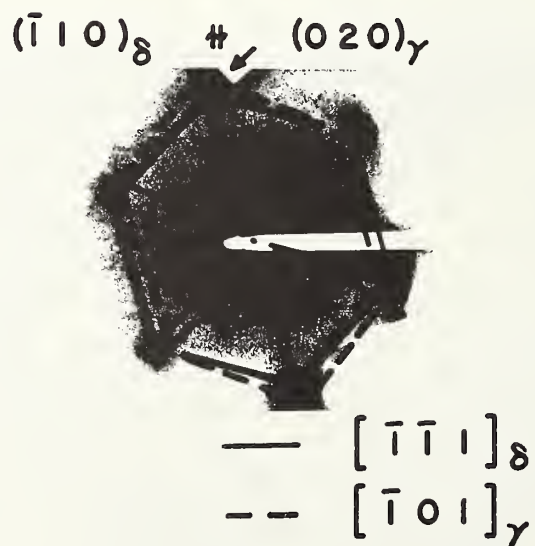


Figure 13(b) SAD consistent with K-S orientation relationship

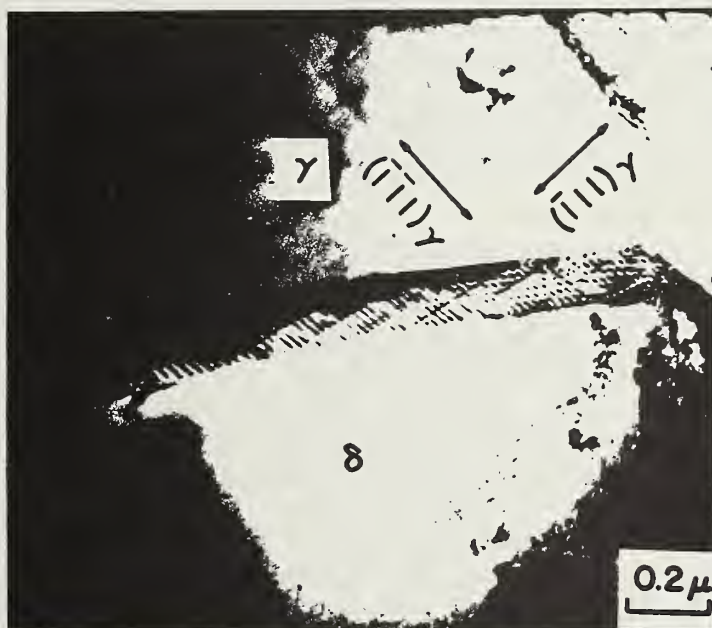


Figure 14(a)  $\delta/\gamma$  Interphase interface, TEM  
(a) Interfacial dislocations

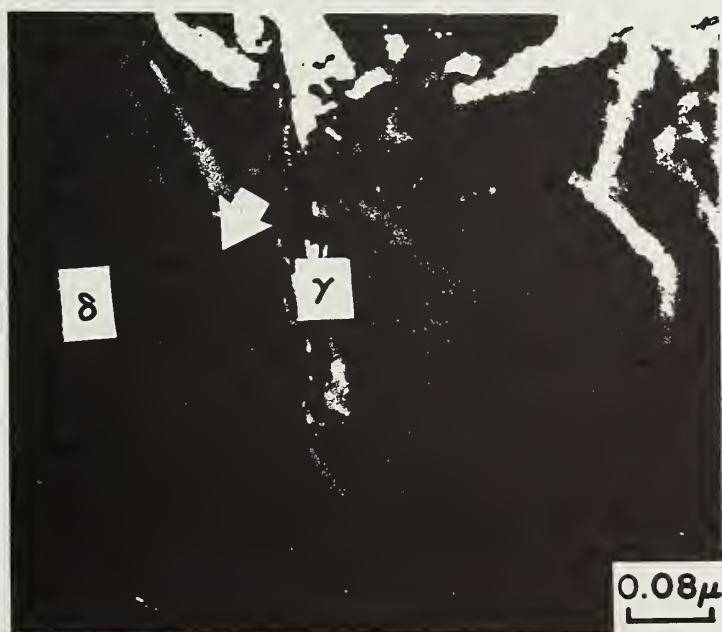


Figure 14(b) Boundary facets.

## DISCUSSION

These CF8M alloys, with the possible exception of the 1.1%  $\delta$  alloy, solidify with  $\delta$  as the primary solid phase, Fig. 3(b). The color etching illustrates that a significant portion of the  $\delta$  that forms upon solidification subsequently transforms to  $\gamma$  during cooling, via a solid state  $\delta \rightarrow \gamma$  transformation. The two macrostructures of Figs. 3(a) and (c) provide important information in further characterizing the transformation sequence. The completely columnar secondary structure of Fig. 3(c) does not exhibit a columnar-to-equiaxed grain transition and therefore must be associated with the solid state  $\delta \rightarrow \gamma$  transformation.(35) The fact that dendrites are observed to grow across the columnar grain boundaries of the secondary structure also supports the assertion that this structure is produced by the  $\delta \rightarrow \gamma$  transformation, Fig. 4. Furthermore, observation of the secondary structure is consistent with the following transformation sequence:  $L \rightarrow L+\delta \rightarrow L+\delta+\gamma \rightarrow \delta+\gamma$ . (14,25) In this case a  $\gamma$  envelope begins to solidify from the melt and columnar  $\gamma$  crystals can nucleate heterogeneously at high temperature and grow with the aid of very steep temperature gradients. Once nucleated under these conditions, a columnar  $\gamma$  crystal will grow right across misorientations between  $\delta$ -ferrite dendrites and parallel to the path of maximum heat flow. It is possible that since the secondary  $\gamma$  structure was not observed in the higher  $\delta$ -ferrite content castings (>20v/o), these alloys possess the following transformation sequence:  
 $L \rightarrow L+\delta \rightarrow \delta+\delta+\gamma$  .

The significant levels and the recovered nature of dislocation substructure might be expected to derive from several sources. Strain can occur due to solidification shrinkage, general thermal strains, differential thermal expansion and transformation strains. It is probable that the total strain induced in the material from all these sources is sufficient to account for the dislocation densities observed. The thermal activation attendant with annealing and cooling is sufficient to recover the dislocation substructure through subgrain formation. The observation of mosaic regions differing in contrast in Fig. 4 might then be rationalized as manifesting an underlying subgrain structure. The evolution of dislocation substructure could also derive from a compromise between the tendency of the  $\gamma$  to grow along a direction of maximum heat flow and its

tendency to grow more readily along certain crystallographic directions. The two directions are not necessarily parallel. One possible way to effect the compromise and accommodate the mismatch is the generation of dislocations. The succeeding discussion on lattice correspondences lends support to the notion of crystallographic directions of easy growth.

The  $\delta/\gamma$  interfacial morphology, viewed via light and transmission microscopy, and diffraction evidence supports the existence of a lattice correspondence between  $\delta$  and  $\gamma$  regardless of the curvature of the interface between the two phases. This lattice correspondence is embodied in a K-S-type orientation relationship ( $\{111\}_\gamma // \{110\}_\delta : \langle 110 \rangle_\gamma / \langle 111 \rangle_\delta$ ) that is associated with a high degree of lattice matching across certain interfaces. If the  $\delta/\gamma$  boundary is oriented favorably a high degree of lattice matching will result in a low specific interfacial energy and, therefore, a facet. In the case of a K-S type lattice correspondence a high degree of atomic matching exists parallel to  $\{111\}_\gamma$  and  $\{110\}_\delta$  in the direction of  $\langle 110 \rangle_\gamma$  and  $\langle 111 \rangle_\delta$  but for only several atomic distances from an arbitrary atomic origin. However, good matching resumes on the next lower or upper  $\{111\}_\gamma : \{110\}_\delta$  pair. The resulting interfacial structure may be thought of as a series of steps or terraces.(39) The macro habit will then be irrational, i.e., not exactly parallel to  $\{111\}_\gamma$ , as was observed in the present investigation. In addition, the interfacial dislocation structures frequently observed in this investigation are generated to accommodate losses in coherency due to lattice mismatch and changes in boundary orientation.

The existence of a K-S-type orientation relationship and a faceted  $\delta/\gamma$  interfacial morphology suggests a general model for the  $\delta \rightarrow \gamma$  transformation analogous to those proposed for diffusion controlled formation of Widmanstatten-type proeutectoid  $\alpha$ .(40-43) A faceted nucleus of  $\gamma$  forms either at solidification subgrain boundaries or on the  $\gamma$  envelope formed by direct  $\gamma$  solidification from the melt. These alternative modes of  $\gamma$  nucleation would not alter the basic morphological evolution. A low energy, faceted interface on the nucleus minimizes total interfacial energy and therefore the activation barrier for nucleation. Growth of nuclei is then accomplished through the movement of curved, incoherent segments of  $\delta/\gamma$  interface. These possess high energy and high mobility compared to the low mobility of the faceted portions of interface. Movement of faceted bound-



aries can occur via movement of interface ledges or steps parallel to the interface. Steps on  $\delta/\gamma$  interfaces have been viewed by light and transmission electron microscopy (Figs. 7 and 14). The features of the residual  $\delta$  microstructure can then be viewed as evolving through the rapid movement of incoherent segments of  $\delta/\gamma$  interface with coherent segments being dragged along behind. The coherent segments move more slowly via a ledge mechanism. A schematic diagram showing the evolution of the residual  $\delta$  morphology is shown in Fig. 15. This schematic emphasizes the continuous nature of the  $\delta$  network and that the appearance of filamentary particles or cell-like networks on a particular plane of polish represent sectioning effects.

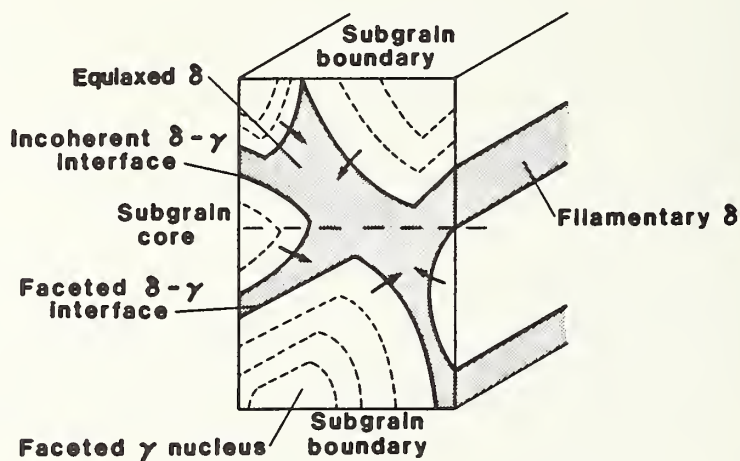


Figure 15 Schematic diagram of evolution of residual  $\delta$  morphology via  $\delta \rightarrow \gamma$  transformation

#### CONCLUSIONS

- (1) All of the alloy castings possessed a recovered dislocation substructure in both the  $\delta$  and  $\gamma$  phases. A recovered dislocation substructure was rationalized on the basis of induced strains due to solidification, thermal expansion, transformation and differential thermal expansion.



- (2) Selected area electron diffraction evidence confirmed the widespread occurrence of a K-S type orientation relationship between  $\delta$  and  $\gamma$ . This prevailed across curved and faceted sections of  $\delta/\gamma$  interface. Data on the faceted segments were consistent with a habit plane which deviated slightly from  $\{111\}\gamma$ .
- (3) In an alloy in which  $\gamma$  precipitation occurred before completion of solidification it was shown that the differences between  $\gamma$  growth along preferred crystallographic directions and in the direction of maximum heat flux might be accommodated by formation of a recovered dislocation substructure.
- (4) The evolution of residual  $\delta$  morphology may be considered as occurring via the rapid movement of incoherent (curved) segments and the relatively slow movement of semicoherent (faceted) segments by a diffusion controlled process. This is accomplished while maintaining a lattice correspondence in a manner similar to the formation of Widmanstätten proeutectoid ferrite from austenite.

#### REFERENCES

1. H.F. Reid and W.T. DeLong, Met. Prog., Vol. 84 (1973), p. 73.
2. H. Fredriks and L.J. VanderTorn, Br. Weld. J., Vol. 15 (1968), p. 178.
3. C.D. Lundin and D.F. Spond, Weld. J. Res. Suppl. Vol. 55 (1976), p. 356-s.
4. R.T. King, N.C. Cole, and G.M. Goodwin, J. Pressure Vessel Technol., Vol. 98 (1976), p. 194.
5. L.R. Poole; Met. Prog., Vol. 65 (1954), p. 108.
6. O.H. Henry, M.A. Cordovi, and G.J. Fisher, Weld. J. Res. Suppl., Vol. 34 (1955), p. 75-s.
7. K.E. Pinnow and A. Moskowitz, Weld. J. Res. Suppl., Vol. 49 (1970), p. 278-s.
8. V.N. Zemsin and G.L. Petrov, Svar. Proisvod., No. 5 (1967), pp. 6-8.
9. W.T. DeLong, Weld. J. Res. Suppl., Vol. 53 (1974), p. 273-s.
10. A. Schaeffler, Metal Progress, Vol. 56, (1949), pp. 680-680B.
11. C. Long and W.T. DeLong; Weld. J., Res. Suppl., Vol. 52 (1973), pp. 281-s-297-s.
12. F.H. Beck, E.A. Schoefer, J.W. Flowers, and M.G. Fontana, in Advances in the Technology of Stainless Steels and Related Alloys, ASTM STP 369, (1965), pp. 159-174.

13. L.J. Schwartzendruber, L.H. Bennett, E.A. Schoefer, W.T. DeLong, and H.C. Campbell, Weld. J. Res. Suppl., Vol. 53 d(1974), p. 1-s.
14. J. Beech: Personal Communication.
15. J.C. Lippold and W.F. Savage; Weld. J. Res. Suppl., Vol. 58 (1979), p. 330-s.
16. S.A. David, G.M. Goodwing, and D.N. Braski, Weld. J. Res. Suppl., Vol. 58 (1979), p. 330.
17. N. Suutala, T. Takalo, and T. Moisio, Met. Trans. A, Vol. 10A (1979), p. 512.
18. N. Suutala, T. Takala, and T. Moisio, Met. Trans. A, Vol. 10A (1979), p. 1183.
19. T. Takalo, N. Suutala, and T. Moisio, Met. Trans. A, Vol. 10A (1979), p. 1173.
20. N. Suutala, T. Takato, and T. Moisio, Met. Trans. A, Vol. 11A (1980) p. 717.
21. M.J. Cieslak and W.F. Savage, Weld. J. Res. Suppl., Vol. 59 (1980), p. 136-s.
22. J.C. Lippold and W.F. Savage; Weld. J. Res. Suppl., Vol. 59 (1980), p. 48-s.
23. C.E. Lyman, Weld. J. Res. Suppl., Vol. 58 (1979), p. 189-S.
24. V.S. Raghunathan, V. Seetharaman, S. Venkadesan, and P. Rodriguez, Mt. Trans A, Vol. 10A (1979), p. 1683.
25. J.M. McTighe and J. Beech, J. Res., SCRATA, No. 37, (1977), p. 43.
26. G. Masing, Ternary Systems: Introduction to The Theory of Three Component Systems, Dover, New York, (1960).
27. O. Hammar and U. Svensson, Solidification and Casting of Metals, Proceedings of an International Conference on Solidification, University of Sheffield, England (1977), p. 401.
28. H. Fredriksson, Met. Trans., Vol. 3 (1972), p. 2989.
29. J.W. Rutter and B. Chalmers; Can. J. Phys., Vol. 31 (1973) p. 15.
30. J.W. Christian, The Theory of Tranformations in Metals and Alloys, Pergamon Press, New York (1965), p. 566.
31. W.A. Tiller, K.A. Jackson, J.W. Rutter, and B. Shalmers, Acta Metall., Vol. 1 (1953), p. 428.
32. Y. Kinoshita, S. Tadedo, and H. Yoshimura, Tesu-to-Hagane, Vol. 65 (1979), pp. 1176-1185.
33. J.B. Newkirk, Precipitation from Solid Solution ASM Seminar, American Society for Metals, (Nov. 1957).
34. G. Kurdjumov and G. Sachs, Ann. Phys., Vol. 64 (1930), p. 325.
35. A. Hultgren, J.I.S.I., Vol. 70 (1929), pp. 69-113.

36. T.P.S. Gill, R.K. Dayal, and J.B. Gnanomoorthy, Weld. J. Res. Suppl., Vol. 58 (1979), p. 375-s.
37. R.G. Berggren, N.C. Cole, G.M. Goodwin, J.O. Stiegler, G.M. Slaughter, R.J. Gray, and R.T. King, Weld. J. Res. Suppl., Vol. 57 (1979), p. 167-s.
38. L. Finch, Materials Studies for Magnetic Fusion Energy Applications at Low Temperatures, NBSIR-1645, (1981), p. 337.
39. M.G. Hall, H.I. Aaronson, and K.R. Kingman, Surface Science, Vol. 31, (1972), pp. 257-274.
40. W.C. Johnson, C.L. White, P.E. Marth, P.K. Ruf, S.M. Tuominen, K.D. Wade, K.C. Russell, and H.I. Aaronson, Met. Trans. A, Vol. 6A (1975), p. 911.
41. H.I. Aaronson, Decomposition of Austenite by Diffusional Processes, The Metal Society, American Institute of Mining, Metallurgical, and Petroleum Engineers, New York (1962), p. 387.
42. H.I. Aaronson, C. Laird, and K.R. Kinsman, Phase Transformations, ASM seminar, American Society for Metals, Metals Park, Ohio, (October 1968) p. 313.
43. H.I. Aaronson, J.K. Lee, and K.C. Russell, Precipitation Processes in Solids, The Metal Society, American Institute of Mining, Metallurgical and Petroleum Engineers, New York (1976).



A TRANSMISSION ELECTRON MICROSCOPY STUDY OF CAST DUPLEX AUSTENITIC STAINLESS STEELS  
WITH VARYING FERRITE CONTENT: AS-CAST AND DEFORMED AT 4 K

E. L. Brown  
Department of Metallurgical Engineering  
Colorado School of Mines  
Golden, Colorado 880401

ABSTRACT

The evolution of dislocation substructure and residual  $\delta$  morphology in the as-cast state was studied by transmission electron microscopy and selected area electron diffraction in a series of CF8M alloys with varying ferrite content. Results were correlated with a previous light microscopy study. A well recovered dislocation substructure existed in both phases and was correlated with the  $\delta \rightarrow \gamma$  transformation and thermal history. The lattice correspondence observed by electron diffraction and habit planes of facets in the  $\delta/\gamma$  interfacial morphology were consistent with a model based on a semicoherent interface. All results were consistent with a proposed model for evolution of residual  $\delta$  morphology analogous to the proeutectoid  $\gamma \rightarrow \alpha$  transformation. The evolution of substructure was detailed in 17.2 volume percent and 28.5 volume percent alloys that were strained at 4 K. Low strain specimens were characterized by dislocation generation in both phases in the vicinity of the  $\delta/\gamma$  interface, dislocation-dislocation interactions and dislocation-sub-boundary interactions in  $\gamma$ . Later stages displayed formation and intersection of shear/deformation bands in  $\gamma$  and was followed by  $\alpha'$  formation at the intersections. Bands of dislocations formed in the  $\delta$  followed by deformation twinning in that phase. The results of  $\gamma$  deformation were considered in light of current theories of the strain-induced  $\gamma \rightarrow \alpha'$  transformation and work hardening in metastable  $\gamma$  in addition to theories regarding plastically non-homogeneous alloys.





## INTRODUCTION

The solidification behavior of 300-series austenitic stainless steels is of concern in both welding and casting technology. In the cast or welded state these alloys can contain up to approximately 30 volume percent delta-ferrite ( $\delta$ ), the high temperature BCC phase of iron. For this reason they are often referred to as duplex stainless steels. The presence of  $\delta$  can significantly alter the physical and mechanical properties of the austenite ( $\gamma$ ) matrix. Property variations due to  $\delta$  can be beneficial or deleterious dependent upon the nature of the material application and its temperature regime. For example, in the case of weldments the presence of 5-10 volume percent  $\delta$  has been reported to reduce the incidence of hot cracking [1,2] and microfissuring [3]. At high temperatures ( $>700^{\circ}\text{C}$ )  $\delta$  can transform to the brittle sigma phase, resulting in a degradation of mechanical properties [4-6], and in highly corrosive environments it can provide a path for corrosion attack [7]. Ferrite in an austenite matrix also generally increases the strength and lowers the fracture toughness of welds and castings [8].

Due to the high strength and toughness of wrought austenitic stainless steels at cryogenic temperatures [9-11], these alloys are currently being considered for applications in the construction of superconducting magnets as both weld filler metals and castings. There is some concern over the usefulness of ferrite containing alloys in cryogenic applications since at these temperatures the ferrite is below its ductile-to-brittle transition. Studies of the strength and fracture toughness of 300-series welds at 4 K indicated the same general trend, cited above, of increasing strength and decreasing toughness with increasing  $\delta$  content [12,13]. There has been considerably less work done to characterize the deformation and fracture behavior of duplex castings at cryogenic temperatures [14-16].

The amount and morphology of  $\delta$  in a weld or casting has been found to depend upon composition, solidification behavior, and a solid state  $\delta \rightarrow \gamma$  phase transformation. The effects of these factors on the extent and morphology of residual  $\delta$  has been extensively investigated and reviewed [17-20]. These alloys can generally be subdivided according to their solidification behavior into primary  $\delta$  and primary  $\gamma$  alloys dependent upon which is the leading phase on solidification. This is determined almost completely by alloy composition. Primary  $\delta$  alloys contain higher levels of ferrite stabilizers, such as chromium, and primary  $\gamma$  alloys contain higher levels of austenite stabilizers, such as nickel. The leading phase and solute redistribution have been found to determine the morphology and location of ferrite in the post-solidification microstructure. In primary  $\gamma$  alloys enrichment of the intercellular or interdendritic regions in chromium stabilizes ferrite in these regions. In primary  $\delta$  alloys chromium is segregated to the dendrite or cell cores during solidification and  $\delta \rightarrow \gamma$  transformation. Therefore, ferrite in primary  $\delta$  alloys is located at dendrite spines. The morphology of the  $\delta$  at dendrite spines in primary  $\delta$  alloys varies from vermicular or roundish, to lathy, to acicular appearing as the nominal alloy composition varies from positions within the eutectic triangle (low contents of ferrite stabilizers) to positions substantially removed from the eutectic triangle (high contents of ferrite stabilizers). Mechanisms to rationalize the evolution of residual ferrite morphology have been formulated on the basis of light and transmission electron microscopy (TEM) [17,19]. However, the majority of TEM studies to date have been mainly concerned with high resolution x-ray microanalysis to determine the nature of solute gradients after solidification.

In an effort to systematically study the effects of ferrite and interstitial content on deformation and fracture of castings at 4 K, a series of controlled chemistry castings were produced and tested. The light microscopy of these alloys has been described previously [17,20] and is characterized by well defined facets on  $\delta/\gamma$  interfaces and regularly occurring angles between facet variants. The deformation and fracture behavior of these castings at 4 K have also been described elsewhere [15,16]. Uniaxial tensile tests were performed in which strain was monitored from the microstrain region to fracture and were characterized by three stages of work hardening, similar to wrought 300-series steels tested at that temperature. Deformation twinning in  $\delta$  and martensitic transformations in  $\gamma$  were observed in the microstructures of strained specimens. The work hardening behavior was found to be dependent upon ferrite content. Fracture toughness was also found to vary with ferrite content in a manner similar to weldments.

Based on the similarities in microstructure and mechanical behavior between welds and castings it may be possible to extend conclusions drawn from microstructural observations of castings to welds. This would greatly facilitate modelling of weld behavior since structural observations in welds are more difficult to accomplish due to their finer microstructure.

The objective of this paper is to describe TEM studies performed to characterize the substructure of as-cast and deformed specimens of cast duplex stainless steel. Effort was made to correlate microstructural aspects such as  $\delta$  morphology, observed previously by light microscopy, with the crystallography of the  $\delta \rightarrow \gamma$  transformation, studied by selected area electron diffraction. The validity of a previously proposed model for the evolution of residual  $\delta$  morphology was investigated. The formation of substructure in  $\delta$  and  $\gamma$ , with strain at 4 K, was observed in addition to the nature of strain-induced martensite ( $\alpha'$ ) formation in  $\gamma$ . Deformation modes in  $\delta$  were also described.

## EXPERIMENTAL PROCEDURES

A number of CF8M alloy castings were produced to ASTM specification A351. The alloy designations, their chemical compositions and ferrite content are included in Table I. The ferrite contents shown were determined by quantitative metallographic techniques. Alloys K-9, K-14, and K-24 were all produced separately as keel block castings (approx. 20 cm x 8 cm x 14 cm) whereas the other alloys were produced together as a series of controlled chemistry castings in which the ferrite content was purposely varied at a constant interstitial content (C+N). The controlled chemistry castings were relatively large (10 cm x 30 cm x 60 cm). The alloy casting procedures have been described by Finch [21]. Subsequent to casting, all material was annealed at approximately 1400 K.

### Mechanical Testing

The details of tensile testing at 4 K have been described previously [15,16]. Specimens of Alloys 3 and 5, strained to levels of 0.005, 0.02, and fracture were sectioned for TEM observation.

Specimen preparation for light microscopy has been described by Brown [17]. Thin foils were produced for TEM by cutting wafers  $\sim 0.4$  mm in thickness with a low speed diamond saw. Wafers from the tensile specimens were removed from the gage section perpendicular to the tensile axis. The wafers from specimens strained to fracture were removed from regions of uniform strain. Wafers were reduced to  $\sim 0.07$  mm in thickness by mechanically abrading and 3 mm diameter disks produced by slurry drilling. The latter is a low temperature, low deformation procedure. Foils were produced by electropolishing to perforation in a Fischione twin jet polisher, employing a 5 volume percent perchloric acid -25 volume percent glycerin-ethanol electrolyte (40 V, 80 mA at room temperature). Foils were examined in a Philips EM 400 transmission electron microscope, operated at 120 kV. Scanning electron microscopy (SEM) and energy dispersive X-ray analysis (EDS) were performed on selected specimens for the purpose of determining the extent of alloying element partitioning between  $\delta$  and  $\gamma$ .

## RESULTS

### Undeformed Specimens

The microstructures of duplex austenitic stainless castings that solidify in a primary  $\delta$  mode have been studied by light microscopy [17,20]. Relevant observations from that work are extracted here. The residual  $\delta$  morphologies were characterized by faceted  $\delta/\gamma$  interfaces. Faceted segments of  $\delta/\gamma$  interface frequently occurred at definite angles with respect to one another on a given plane of polish and high magnification light microscopy has revealed ledges on straight and curved segments, Fig. 1. The habit planes of facet variants could not be determined unambiguously from measurements of inter-variant angles on a given plane of polish since the crystallographic orientation of the plane of polish was not generally known. However, the approximate grouping of inter-variant angles suggested that the habits might be in the vicinity of  $\{110\}\delta$ . Furthermore, the observation of facets and ledges suggested some sort of lattice correspondence between  $\delta$  and  $\gamma$ , namely a Kurdjumov-Sachs (K-S) type orientation relationship.

Another pertinent metallographic result from previous studies regards the observation of columnar  $\gamma$  crystals due to the  $\delta \rightarrow \gamma$  transformation. The origins of columnar  $\gamma$  crystals have been discussed in detail [17,20]. These crystals grow along directions of maximum heat flow and closer examination reveals subtle differences in contrast between regions inside the crystals and dentate boundaries between these regions, Fig. 2. The boundary structure within the columnar  $\gamma$  crystals is reminiscent of subgrain structures observed by other investigators with the aid of polarized light microscopy [22].

A well recovered dislocation substructure in  $\gamma$  was observed in all castings, Fig. 3. The subgrain boundaries were sometimes composed of dislocation tangles, Fig. 4. In other instances a well defined dislocation net characterized the boundary, Fig. 5. Note the extended nodes in the boundary net of Fig. 5, indicative of a low stacking fault energy material. Measurements of the subgrain size, by a linear intercept method, indicated an average subgrain size of  $2-5 \mu$  and no consistent variation with ferrite content. The subgrains also varied in shape from equiaxed to



somewhat elongated. The long segments of elongated subgrains were generally attached to  $\delta/\gamma$  interfaces and stretched across the  $\gamma$  separating two regions of  $\delta$ . This observation was more prevalent in the higher  $\delta$  content alloys. The ferrite also contained a substantial amount of dislocation substructure. In fact, Alloy 5 (28.5 volume percent  $\delta$ ) exhibited a "bamboo" subgrain structure in the ferrite, Fig. 6. The subgrain boundaries in  $\gamma$  and  $\delta$  can produce varying degrees of cusping in the  $\delta/\gamma$  interface where they intersect it, Fig. 7. Another type of  $\gamma$  dislocation network was observed in these alloys that was generally characterized by straight segments of network attached to the  $\delta/\gamma$  interface, Fig. 8. The planes of these networks were consistent with  $\{111\}\gamma$  and  $\{110\}\gamma$ . Similar networks have been observed in lightly deformed austenitic stainless steel and rationalized in terms of interactions between glide and forest dislocations at pile-ups in the vicinity of grain boundaries [23,24]. The presence of  $\{110\}\gamma$  networks may be explained by the fact that  $\{110\}\gamma$  is one of the types of planes of "easy climb" in fcc metals and alloys [25]. Networks are formed by a process called "knitting."

In addition to subgrains in both phases, there were also significant levels of dislocations, in the form of debris. The debris is characterized by individual dislocations, pile-ups, and tangles, indicative of dislocation interactions. Dislocation debris is formed in  $\delta$  and  $\gamma$ . The dislocations are sometimes associated with subboundaries, Fig. 9(a). The dislocations may have been produced at the subboundary or just interacted with it after production elsewhere. Dislocation debris was also observed in association with  $\delta/\gamma$  interfaces, Fig. 6, 9(b). These dislocations were produced at the interface. The tangles of dislocations in  $\delta$  were sometimes very dense and associated with heavily jogged dislocation lines and loops, 9(c). The dislocations in  $\delta$ , indicated at the arrow in Fig. 6, seem to be at an earlier stage of interaction. Dislocations emitted from the subboundary at left are interacting with forrest dislocations. Jogs and dipoles are the result. Overlapping stacking faults were occasionally observed to emanate from  $\delta/\gamma$  interfaces, Fig. 6. It is uncertain whether these are characteristic of the substructure or artifact.

The crystallography of the  $\delta \rightarrow \gamma$  transformation was studied extensively in Alloy K-9 by TEM and selected area electron diffraction (SAD). However, the features described below were also observed in specimens containing higher ferrite contents. Observations of the  $\delta/\gamma$  interfacial morphology indicated the presence of many relatively large facets and steps. No attempt was made to exactly determine the lattice correspondence between  $\delta$  and  $\gamma$ . However, numerous SAD observations were found to be consistent with the widespread occurrence of Kurdjumov-Sachs (K-S)-type orientation relationships, Fig. 10.\* Curved and straight segments of interphase interface were examined and the lattice correspondences described above persisted regardless of the extent of boundary curvature. Single surface trace analysis yielded a population of habit plane trace normals that appeared to cluster in the vicinity of  $(\bar{1}12)\gamma$ , on the boundary of the stereo triangle and near  $(011)\gamma$ , Fig. 11.

---

\*The Kurdjumov-Sachs, Nishayama-Wasserman and Bain orientation relationships, relating bcc and fcc phases, are related to one another by minor rotations.



This data illustrates the irrational nature of the habit plane for "straight" segments of interphase interface. Small steps were observed on the  $\delta/\gamma$  interface, Fig. 12(a). The  $\delta/\gamma$  interface is further characterized by an interfacial substructure, Fig. 12(b).

#### Deformed Specimens

Specimens of Alloys 3 and 5 (17.2 and 28.5 volume percent  $\delta$ ) strained to 0.005, .02 and fracture at 4 K were observed by TEM. The evolution of dislocation substructure and second phase ( $\alpha'$ ) formation with strain was similar for the two alloys; therefore representative observations are presented for the strain sequence.

At a strain of 0.005 dislocation sources in  $\gamma$  are activated in the  $\delta/\gamma$  interface. Dislocations on intersecting slip planes were observed to interact to produce tangled networks, Fig. 13. Note the complicated contrast of the boundary associated with activation of dislocation sources, Figs. 13(c), (d). Dislocations can actually be observed to bow out from the sources in the  $\delta/\gamma$  interphase interface (arrow in Fig. 13(c),(d)). Dislocation sources were also observed in the vicinity of  $\gamma$  subboundary intersections with the  $\delta/\gamma$  interface, Fig. 14. The  $\delta/\gamma$  interface is cusped at this location. These are likely to be regions of high stress concentration due to the overlapping stress fields of dislocations and the torques imposed on the  $\delta/\gamma$  interface. The dislocation density in  $\gamma$  seems to be higher in the vicinity of the  $\delta/\gamma$  interface, where tangles of dislocations were frequently observed, Fig. 15. Glide dislocations have also interacted with subboundaries from the as-cast state, Fig. 16. Actually,  $\delta$  dislocation sources are also activated, as can be seen in Fig. 17, where dislocations are observed to bow out into both phases from the  $\delta/\gamma$  interface.

The structures of specimens strained to 0.02 were characterized by intersections of deformation or shear bands, Fig. 18. The deformation bands appear to be composed of a higher density of dislocations from intersecting slip planes than observed at lower strain. Some of the other bands appear to be associated with stacking fault fringe contrast. These might contain  $\epsilon$ -martensite, although none was detected by electron diffraction. Martensite has begun to form at the intersections of deformation and shear bands, Fig. 19. There is considerable accommodation strain associated with  $\alpha'$  formation as evidenced by dislocations generated in the vicinity of intersections with  $\alpha'$ , Fig. 20. The  $\alpha'$  thus formed sometimes possessed projected images polyhedral in morphology, Fig. 19(a). Most of the  $\alpha'$  formed at intersections possessed a single habit variant. However, there were some regions in which bands of  $\alpha'$  formed, containing multiple  $\alpha'$  habit variants, Fig. 21. The bands are bundles of faults bounded by  $\{111\}_\gamma$ . In the  $\delta$ , dislocation pile-ups were observed at the  $\delta/\gamma$  interfaces, Fig. 22. These dislocations probably emanated from the interface. The dislocations in the pile-ups are jogged and there is a mottled contrast that appears crystallographically arranged (at arrow in Fig. 22). Since the trace of this contrast is consistent with  $\{110\}_\delta$  it is probably due to dislocations viewed end-on. The jogs may be due to interactions with the end-on dislocations. This strain level also appeared to signal the onset of deformation twinning in the  $\delta$ , Fig. 23. Note the kink at the  $\delta/\gamma$  interface induced by twin (arrow).

Specimens strained to fracture were characterized by a greater number of shear/deformation band intersections and, therefore,  $\alpha'$  formation. The 17.2 volume percent  $\delta$  alloy (Alloy 3) displayed regions, sometimes in close proximity, of widely varying degrees of  $\alpha'$  formation, Fig. 24. The upper region of  $\gamma$  contains  $\alpha'$  forming at shear/deformation band intersections, Fig. 24(b). The lower  $\gamma$  region has been almost totally transformed to  $\alpha'$ , Fig. 24(c). Selected area electron diffraction of the  $\alpha'$  in this region indicated variants that are twin related. There may also be fine twins in plates of  $\alpha'$ . The 28.5 volume percent  $\delta$  alloy (Alloy 5) was not generally characterized by as much  $\alpha'$  formation. However, this alloy did possess an increased number of deformation/shear band intersections with  $\alpha'$  formation when compared with specimens of the same alloy at lower strains, Figs. 25, 26. Deformation substructure in the  $\delta$  also seems to have evolved further with increased strain. The bands formed by intersecting dislocations have now extended across the regions of  $\delta$ , Fig. 27. In addition, macroscopic deformation twins have been observed by light microscopy and TEM, Fig. 27a, Fig. 28. Deformation has occurred ahead of growing twins to accommodate their growth, Fig. 29(a), and in the  $\gamma$  where a twin abuts the  $\delta/\gamma$  interface, Fig. 29(b). It appears that dislocations induced by accommodation strains have interacted with dislocations from the bands in  $\delta$  to form tangles, Fig. 29(a).

It should be noted that all SAD evidence on  $\alpha'$  was consistent with a K-S orientation relationship between  $\gamma$  and  $\alpha'$ . Also single surface trace analyses of  $\alpha'$  habit planes were consistent with a  $\{225\}\gamma$  habit, within the obvious errors inherent in this kind of analysis.

#### Energy Dispersive X-ray Analysis

Energy dispersive x-ray analyses (EDS) performed on these alloys indicated partitioning of alloying elements. Chromium and molybdenum segregate to  $\delta$  and nickel to  $\gamma$ , Fig. 30. A number of EDS spectra were obtained from  $\delta$  and  $\gamma$  in Alloys 3 and 5 and subjected to a standardless ZAF semi-quantitative analysis. The results, depicted in Fig. 31, are not to be construed as fully quantitative but rather to display trends in alloying elements that affect austenite stability.\* Chromium and nickel both increase in  $\gamma$  as the volume percent  $\delta$  increases from 17.2 to 28.5.

#### DISCUSSION

##### Undeformed Specimens

These CF8M alloys, with the possible exception of Alloy 1 (1.1 volume percent  $\delta$ ), solidify with  $\delta$  as the primary phase. The micrographs of Fig. 1 represent residual  $\delta$  that remains after a  $\delta \rightarrow \gamma$  transformation. The columnar  $\gamma$  crystals observed in Fig. 2 are also the result of this  $\delta \rightarrow \gamma$  transformation and this is supported by the observation that the dendrite structure is continuous across the columnar grain boundaries, Fig. 2(b). The dendrite structure is defined by the residual  $\delta$  at dendrite spines.

---

\*Comparison of low magnification scans, that would indicate overall chemical composition, with the results of analytical chemical analysis (Table 1) indicate small discrepancies.

The observations of Rhines [22] indicate that the variations in contrast and dentate boundaries observed in Fig. 2 could be due to a mosaic or subgrain structure. The plausibility of this assertion was confirmed by TEM observations of well recovered subgrain structures, Fig. 3-6. The strains necessary to produce these subgrain structures might be derived from several sources. Strain can occur due to solidification shrinkage, strains developed during cooling of a large casting in which parts of the casting cool at varying rates, differential thermal expansion or contraction of different phases ( $\delta$  and  $\gamma$ ) and transformation ( $\delta \rightarrow \gamma$ ). The last two sources have been considered in some detail [26]. It was determined from dilatometry that a significant amount of strain was imparted to the material by the  $\delta \rightarrow \gamma$  transformation. It is probable that the total strain induced from all these sources is sufficient to account for the observed dislocation densities. The thermal activation attendant with annealing and cooling is sufficient to recover the dislocation substructure through subgrain formation. Other investigators have observed the formation of subgrains during solidification and for solid state transformation [25] and cite the fact that conservative climb of dislocations aided by pipe diffusion of vacancies can produce subgrain boundary dislocation networks very rapidly. This process is termed "knitting" and can produce all of the boundary networks observed. The evolution of a subgrain structure could also be viewed as deriving from a compromise between the tendency of the  $\gamma$  to grow along a direction of maximum heat flow and its tendency to grow more readily along certain crystallographic directions, i.e. to maintain a lattice correspondence between  $\delta$  and  $\gamma$ . The two growth directions are not necessarily parallel. The mismatch could be accommodated by the generation of subgrain structure. The succeeding discussion on lattice correspondence lends support to the notion of crystallographic directions of easy growth.

The  $\delta/\gamma$  interphase interfacial morphology, viewed via light and transmission electron microscopy, supports the existence of a lattice correspondence between  $\delta$  and  $\gamma$ . Electron diffraction evidence, in fact, confirms the existence of a K-S-type orientation relationship between  $\delta$  and  $\gamma$ , Fig. 10. The variability in the lattice correspondence has been cited by Brooks, et. al. [19] who found the lattice correspondence between  $\delta$  and  $\gamma$  in welds to vary from the Kurdjumov-Sachs to the Nishayama-Wasserman orientation relationship. The common feature of these types of orientation relationship is the parallelism between closest packed planes in the two phases, i.e.  $\{110\}_\delta // \{111\}_\gamma$ . This would seem to suggest a  $\{111\}_\gamma$  habit for the straight segments of  $\delta/\gamma$  interface but these segments of interface were observed to deviate substantially from  $\{111\}_\gamma$ . The deviation in habit for fcc:bcc boundaries has been investigated in the past [27-32]. All of these investigations emphasize the partially coherent nature of the interface for all lattice correspondences. Close matching across  $\{111\}_\gamma // \{110\}_\delta$  is actually confined to relatively small regions. The area of close matching in the interface is increased substantially by the creation of monoatomic ledges, the broad faces of which contain the regions of good fit on the next lower pair of  $\{110\}_\delta // \{111\}_\gamma$ . These are called structural ledges and account for the deviation in habit from  $\{111\}_\gamma$ . The regions on the broad faces of structural ledges in between the regions of good fit can be made partially coherent by the introduction of misfit dislocations. Therefore the  $\delta/\gamma$  interface can be viewed as the superposition of arrays of structural ledges and misfit dislocations. It should be noted that these structural ledges and misfit dislocations are sessile and therefore do not participate in growth mechanisms. The efficacy of this model in describing the  $\delta/\gamma$  interfaces being considered in this study is demonstrated by the fact that the predictions of theory [27], for a similar lattice parameter ratio of the two phases, are similar to the habit planes observed for



faceted  $\delta/\gamma$  interfaces, Fig. 11. The observation of interfacial substructure on  $\delta/\gamma$  interfaces also supports the notion of partial coherency, Fig. 12. The large steps on  $\delta/\gamma$  interfaces, observed via light microscopy (Fig. 1(b)) and TEM (Fig. 12(a)) must then be the growth ledges proposed by other investigators [27,29,30].

The existence of a K-S-type orientation relationship and a faceted  $\delta/\gamma$  interfacial morphology suggests that the general model for the  $\delta \rightarrow \gamma$  transformation previously proposed [17] is essentially an accurate description. That model proposed a transformation mechanism analogous to that of the diffusion controlled formation of proeutectoid  $\alpha$  from  $\gamma$ . The  $\delta \rightarrow \gamma$  transformation has been established as diffusion controlled [18,19] so that the model would appear to apply in that regard. The production of "lathy"  $\delta$  in austenitic welds due to a  $\delta \rightarrow \gamma$  transformation has been rationalized on the basis of an interface instability [19]. Closer scrutiny may reveal a mechanism equivalent to that described here.

### Deformed Specimens

The stress-strain ( $\sigma$ - $\epsilon$ ) behavior at 4 K of Alloys 1-5 have been determined [15,16]. The  $\sigma$ - $\epsilon$  curves of all the alloys displayed three stages of work hardening behavior, typical of metastable steels that undergo a  $\gamma \rightarrow \alpha'$  transformation [33-36]. The deformed specimens observed in this study were strained into Stage I (0.005), the beginning of Stage II (0.02) and Stage III (strain to fracture). It should be noted that the elongation was greater for the 17.2 volume percent  $\delta$  alloy than for the 28.5 volume percent  $\delta$  alloy (19% vs. 11%) but the ultimate tensile strengths were almost equal (1143 MPa vs 1164 MPa). The TEM work in this investigation confirmed that no  $\alpha'$  forms in Stage I, as noted by other workers [35,36]. This stage was associated with the generation of dislocations, deformation bands and shear bands. It was interesting that no direct evidence of  $\epsilon$ -martensite formation could be obtained via electron diffraction. The volume fraction of  $\epsilon$  should increase to a maximum and then gradually decrease with strain [33,36]. The maximum of (30-40 volume percent) occurs in AISI 304-L stainless steel at a strain of approximately 0.03 at  $T = 20^\circ\text{K}$  [33]. The maximum is expected to be less in magnitude and occur at lower strains at 4 K. Therefore  $\epsilon$  would not be expected in specimens strained to fracture. The maximum in  $\epsilon$  occurs at the onset of the transition from Stage II to Stage III (low to high rate of work hardening) [36]. It is possible that compositional effects could have suppressed formation of  $\epsilon$  by their effect on stacking fault energy. This possibility was not evaluated. An experimental reason for difficulty in detecting  $\epsilon$  via electron diffraction was the unfavorable  $\gamma$  textures introduced by preferred crystallographic growth during solidification [19]. Specimens of all alloys were characterized by a high propensity for  $\langle 100 \rangle_\gamma$  crystallographic zones near the foil normal. This is not a favorable austenite zone to detect  $\epsilon$  reflections since there is no low order  $\epsilon$  zone axis parallel to a  $\langle 100 \rangle_\gamma$  zone axis. This is due to the prevailing lattice correspondence between  $\gamma$  and  $\epsilon$ -martensite [37,38].

The dislocations produced in the vicinity of the  $\delta/\gamma$  interface during this stage of deformation (Fig. 15) may be associated with production of a population of geometrically necessary dislocations [15,39]. Geometrically necessary dislocations are generated by the microstructure in response to non-homogeneous strain i.e. matrix strain gradients in the presence of hard particles. A statistically stored dislocation density is produced by random dislocation

interactions. Whipple [15] assumed that at the outset of deformation the geometrically necessary dislocation density would be more significant than the statistically stored density and that the former should increase with volume fraction  $\delta$ . Therefore, the initial work hardening rate should increase with volume fraction  $\delta$ . This was observed. However, in the present study dislocations were observed to tangle with one another and interact with as-grown subboundaries, Fig. 13 and 16. These would seem to be processes for statistical storage of dislocations. In addition, it is uncertain what effect a 2-4  $\mu\text{m}$  diameter subgrain structure has on the initial work hardening rate. Previously produced subgrain structures have been observed to increase the flow stress of a material in a manner functionally similar to the well-known Hall-Petch grain size strengthening effect [40-43]. In fact, Sherby [41] found that well-recovered subgrain boundaries were more effective barriers to dislocation motion than subboundaries formed at lower temperatures. The additional dislocation sources at the  $\delta/\gamma$  interface that were activated in the presence of abutting subgrain boundaries might also be expected to increase the effect of subboundaries on initial work hardening, Fig. 14. It would seem that although a model based on initial generation of geometrically necessary dislocations might still be an accurate description, the transition to control of deformation behavior by statistically stored dislocations is somewhat nebulous, at least at the lowest level of strain observed in this study. It is probably not controlled by the difference between "austenite grain size" and spacing, as proposed by Whipple [15]. The variation in friction stress,  $\tau_0$ , identified by Whipple [15], may have an additional origin in the as-grown subgrain structure.

The work hardening characteristics of these alloys are also affected by  $\alpha'$  formation in Stage II. This is not accounted for by Ashby's model of plastically inhomogeneous alloys. The  $\alpha'$  formed in Stage II nucleates at shear and deformation band intersections, Figs. 19 and 20. The observations described concur with current theories of strain-induced  $\alpha'$  formation [35,37,38,44, 47-52]. Intersections are favorable sites for heterogeneous nucleation of  $\alpha'$  because of the high stress concentrations present there and because the necessary dislocation configurations for nucleation of the bcc phase are also present. According to the available literature  $\alpha'$  nucleated during straining possesses a lath morphology that extends along the length of the intersection, a K-S or Nishayama-Wasserman lattice correspondence, a single habit of either  $\{225\}_\gamma$  or  $\{259\}_\gamma$  and is bounded by  $\{111\}_\gamma$  of one of the intersecting bands. The laths grow via coalescence after repeated nucleation with straining [52]. The coalesced morphologies resemble polyhedra and will grow out of the bounding  $\{111\}_\gamma$ . Similar morphologies have been observed in this study, Fig. 19 and 20. There were regions of multiple habit variant  $\alpha'$ , Fig. 21. According to Reed [36], multiple habit variant  $\alpha'$  is associated with  $\alpha'$  that formed spontaneously on cooling. This is surprising in view of the fact that  $\alpha'$  is supposed to be virtually suppressed on quenching to 4 K [45,47].

Formation of  $\alpha'$  signals the onset of a low work hardening region. Some investigators have proposed that the  $\alpha'$  formed at this stage is non-hardening and provides "windows" for slip [35]. They cite a special variant of the K-S orientation relationship for the first formed laths. This variant results in virtual matching of  $\alpha'$  and  $\gamma$  dislocation Burgers vectors.

The fractions of  $\alpha'$  increased dramatically for both alloys in Stage III and so did the work hardening rate. It is interesting that  $\alpha'$  promotes low work hardening rates in Stage II and high work hardening rates in Stage III [3,6]. It is proposed that higher work hardening results from  $\alpha'$



formation in active slip bands and the fact that  $\epsilon$  martensite levels decrease is cited as supporting evidence. The number of deformation/shear band intersections also increased during this stage of deformation, lending support to the model for  $\alpha'$  nucleation kinetics proposed by Olson and Cohen [49]. The twin related  $\alpha'$  variants observed Fig. 24(c) have been observed by other workers [46]. These alloys only appeared to differ in the levels of  $\alpha'$  after straining to fracture. The 28.5 volume percent  $\delta$  alloy contained less  $\alpha'$ . This is puzzling since the work hardening rates were apparently equal. However, the flow stress in the 28.5 volume percent  $\delta$  alloy was higher and the elongation was less. It is possible that necking and failure occurred sooner for this alloy and therefore, less  $\alpha'$  was formed. A problem arises with this explanation in that, qualitatively, the number of deformation/shear band intersections appeared to be the same for both alloys. The analysis of Olson and Cohen [49] therefore suggests that a diminished thermodynamic driving force may be responsible for less  $\alpha'$  formation. The EDS measurements suggest increasing nickel and chromium levels in the  $\gamma$  as volume fraction  $\delta$  increases, Fig. 31. A rough calculation of the driving force for the  $\gamma \rightarrow \alpha'$  transformation,  $\Delta F^{\gamma \rightarrow \alpha'}$ , was made employing an equation due to Breedis and Kaufman [53] for Fe-Cr-Ni alloys. The calculation indicated higher austenite stability for the 28.5 volume percent  $\delta$  alloy. The austenite stability in duplex alloys must therefore be considered from the standpoint of alloy partitioning.

It is uncertain what effect the as-grown subgrain structure had on  $\alpha'$  formation. Cellular dislocation substructures that raise the strength of austenite, were observed to suppress  $\alpha'$  formation [54]. The potential effects of a subgrain structure on work hardening and  $\alpha'$  formation will have to be evaluated more fully.

In the modelling of deformation behavior in these alloys the ferrite has been assumed to be non-deforming. However, the TEM observations in the present investigation would suggest appreciable deformation during straining, although some of the dislocation substructure could have been produced by residual strains introduced during specimen reheating to room temperature after testing. The deformation twinning observed in ferrite actually requires prior deformation for nucleation of twins [55]. Twins apparently nucleate at dislocation pile-ups. It is possible that the dislocation pile-ups observed in the  $\delta$  provide nucleating sites for twins, Figs. 22 and 27. Emissary slip has been proposed as a mechanism for accommodating the high stresses in the vicinity of the tip of a twin [55]. This is observed in Fig. 29(a). The high stress at the tip of a twin that intersects the  $\delta/\gamma$  interface is accommodated by intense deformation in the adjacent  $\gamma$ , Fig. 29(b). It is uncertain whether deformation twinning affects mechanical behavior directly or what implications the prior deformation in  $\delta$  has for modelling. However, twinning has been associated with the origin of cleavage nuclei in  $\alpha$ -iron [56]. In this model interactions between emissary dislocations are proposed to induce the formation of crack nuclei. Therefore, it would appear that deformation twinning in  $\delta$  could promote fracture via cleavage cracking in  $\delta$  or failure of the  $\gamma$  in the vicinity of a  $\delta/\gamma$  interface where a twin has intersected it to produce intense accommodation strain.

## CONCLUSIONS

- (1) Residual  $\delta$  morphology is consistent with a diffusion controlled mechanism analogous to that proposed for the proeutectoid  $\gamma \rightarrow \alpha$  transformation. The habit plane of faceted segments of  $\delta/\gamma$  interface and a Kurdjumov-Sachs-type lattice correspondence are both consistent with predictions based on a semicoherent interphase interface model.
- (2) A well recovered subgrain structure was observed in  $\delta$  and  $\gamma$  for all alloys in the as-cast state. A well recovered dislocation substructure was rationalized on the basis of induced strains due to solidification, thermal contraction, differential thermal contraction and  $\delta \rightarrow \gamma$  transformation.
- (3) TEM observations indicated that low strain behavior was characterized by dislocation production in the vicinity of  $\delta/\gamma$  interfaces, dislocation-dislocation interactions and dislocation-subboundary interactions. Later stages of deformation were characterized by intersecting shear/deformation band intersections and  $\alpha'$  formation at the intersections. These observations were correlated with three stage hardening mechanisms. Differences in  $\alpha'$  formation in various alloys could be due to variations in austenite stability attendant with alloy partitioning.
- (4) Ferrite was found to deform prior to deformation twinning.

## RECOMMENDATIONS FOR FUTURE WORK

- (1) Transmission microscopy investigations of the dislocation and ledge nature of semicoherent  $\delta/\gamma$  interfaces. This would be a valuable fundamental contribution to the understanding of this generally significant interface type. The  $\delta/\gamma$  interfacial structure is probably a very significant factor affecting the ultimate  $\delta$  morphology in welds and castings.
- (2) More extensive studies of the evolution of dislocation substructure and  $\alpha'$  formation during straining over a wider range of strain and ferrite content. These could be correlated with existing theories regarding work hardening and the  $\gamma \rightarrow \alpha'$  transformation. TEM observations should be supplemented with some sort of bulk detection techniques for  $\epsilon$  and  $\alpha'$ , such as x-ray or magnetic measurements. The latter could be made in situ.
- (3) Investigate more fully the nature of deformation in  $\delta$ , deformation twinning in  $\delta$  during straining at 4K and the implications of twinning on the deformation and fracture behavior of welds and castings.

## REFERENCES

- [1] H. F. Reid and W. T. Delong: "Making Sense Out of Ferrite Requirements in Welding Stainless Steel." Met. Prog., Vol. 84 (1973), p. 73.
- [2] H. Fredriks and L. J. VanderToorn: "Hot Cracking in Austenitic Stainless Steel Weld Deposits," Br. Weld. J., Vol. 15 (1968), p. 178.
- [3] C. D. Lundin and D. F. Spond: "The Nature and Morphology of Fissures in Austenitic Stainless Steel Weld Metals" Weld J. Res. Suppl. Vol. 55 (1976), p. 356-s.
- [4] R. T. King, N. C. Cole, and G. M. Goodwin, "Creep Behavior of SMA Type 316 Weld Metal with Controlled Residual Elements," J. Pressure Vessel Technol., Vol. 98 (1976), p. 194.
- [5] L. R. Poole: "An Unwanted Constituent in Stainless Weld Metal," Met. Prog., Vol. 65 (1954), p. 108.
- [6] O. H. Henry, M. A. Cordovi, and G. J. Fischer, "Sigma Phase in Austenitic Stainless Steel Weldments," Weld. J. Res. Suppl., Vol. 34 (1955), p. 75-s.
- [7] K. E. Pinnow and A. Moskowitz: "The Corrosion Resistance of Stainless Steel Weldments," Weld. J. Res. Suppl., Vol. 49 (1970), p. 278-s.
- [8] V. N. Zemzin and G. L. Petrov: "Influence of Ferrite Content on the Properties of Austenitic Weld Metal," Svar. Proizvod., No. 5 (1967), pp. 6-8.
- [9] R. P. Reed, F. R. Fickett, M. B. Kasen, and H. I. McHenry, "Magnetic Fusion Energy Low Temperature Materials Program: A Survey," in Mat'l's Studies for Magnetic Fusion Energy Applications at Low Temperatures - I, NBSIR 78-884, (1978), pp. 245-335.
- [10] H. I. McHenry and R. P. Reed, "Structural Alloys for Superconducting Magnets in Fusion Energy Systems," Nuclear Eng. Design, Vol. 58, (1980), pp. 219-236.
- [11] R. L. Tobler, D. T. Read and R. P. Reed, "Strength and Toughness Relationship for Interstitially Strengthened AISI 304 Stainless Steels at 4 K," in Mat'l's Studies for Magnetic Fusion Energy Applications at Low Temperatures - IV, NBSIR 81-1645, (1981), pp. 37-75.
- [12] D. T. Read, H. I. McHenry, P. A. Steinmeyer, and R. D. Thomas, Jr., "Metallurgical Factors Affecting the Toughness of 316L SMA Weldments at Cryogenic Temperatures," in Mat'l's Studies for Magnetic Fusion Energy Applications at Low Temperatures - II, NBSIR 79-1609, (1979), pp. 313-352.
- [13] E. R. Szumachowski and H. F. Reid, "Cryogenic Toughness of SMA Austenitic Stainless Steel Weld Metals: Part I - Role of Ferrite," Weld. J. Weld. Res Suppl. Vol 57, (1978), pp. 325s-333s.
- [14] T. A. Whipple and H. I. McHenry, "Evaluation of Weldments and Castings for Liquid Helium Service," in Mat'l's Studies for Magnetic Fusion Energy Applications at Low Temperatures - IV, NBSIR 81-1645, (1981), pp. 273-287.
- [15] T. A. Whipple, "The Effect of Delta-Ferrite on the Mechanical Properties of CF8M Stainless Steel Castings at 4K," Mat'l's Studies for Magnetic Fusion Energy Applications at Low Temperatures - V, NBSIR 82-1667, (1982), pp. 289-317.
- [16] T. A. Whipple and E. L. Brown, "Deformation and Fracture of Stainless Steel Castings and Weldments at 4 K," in Trends in Welding Research in the U.S., ASM Conference Proc., S. A. David, ed, New Orleans, La., Nov. 1981, pp. 601-621.
- [17] E. L. Brown, "Metallography of  $\delta$ -Ferrite in Austenitic Stainless Steel Castings," in Mat'l's Studies for Magnetic Fusion Energy Applications at Low Temperatures - IV, NBSIR 81-1645, (1981), pp. 387-414.
- [18] S. A. David, "Ferrite Morphology and Variations in Ferrite Content in Austenitic Stainless Steel Welds," Weld J., Weld. Res. Vol. 60, (1981), pp. 83s-71s.



- [19] J. A. Brooks, J. C. Williams and A. W. Thompson, "Solidification of Austenitic Stainless Steel Welds," in Trends in Welding Research in the U.S., ASM Conference Proc., S. A. David, ed, New Orleans, La., Nov 1981, pp. 331-357.
- [20] E. L. Brown, T. A. Whipple and G. Krauss, "Metallography of Duplex Stainless Steel Castings," ASM sponsored symposium, St. Louis, Mo., Oct. 1982, (in press).
- [21] L. Finch, "The Influence of Ferrite and Nitrogen on Mechanical Properties of CF8M Cast Stainless steel," in Mat'ls for Magnetic Fusion Energy applications at Low Temperatures - IV, NBSIR 81-1645, (1981) pp. 337-355.
- [22] F. N. Rhines, "Evolution of Microstructure During Hot Plastic Deformation," Chapt. 10 in The Inhomogeneity of Plastic Deformation, ASM, Seminar, Oct. 1971, pp. 251-284.
- [23] M. J. Whelan, P. Hirsch, R. W. Horne, and W. Bollman, "Dislocations and Stacking Faults in Stainless Steel," Proc. Roy. Soc. A, Vol. 240, (1957), pp. 524-538.
- [24] M. J. Whelan, "Dislocation Interactions in Face-Centered Cubic Metals With Particular Reference to Stainless Steel," Proc. Roy. Soc. A, Vol. 249, (1959), pp. 114-137.
- [25] H. M. Miekkoja and V. K. Lindroos, "The Formation of Dislocation Networks," Surface Sci., Vol. 31, (1972), pp. 422-455.
- [26] J. W. Elmer, "Thermal Expansion Characteristics of Stainless Steel Welds," MS Thesis, Colorado School of Mines, Dec. 1981.
- [27] M. G. Hall, H. I. Aaronson, and K. R. Kinsman, "The Structure of Nearly Coherent fcc:bcc Boundaries in a Cu-Cr Alloy," Surface Sci., Vol. 31, (1972), pp. 257-274.
- [28] K. C. Russell, M. G. Hall, K. R. Kinsman, and H. I. Aaronson, "The Nature of the Barrier to Growth at Partially Coherent FCC:BCC Boundaries," Met. Trans., Vol. 5, (1974), pp. 1503-1505.
- [29] J.M. Rigsbee and H. I. Aaronson, "A Computer Modelling Study of Partially Coherent FCC:BCC Boundaries," Acta Met. Vol. 27, (1979), pp. 351-363.
- [30] J. M. Rigsbee and H. I. Aaronson, "The Interfacial Structure of the Broad Faces of Ferrite Plates," Acta Met., Vol. 27, (1979), pp. 365-376.
- [31] P. Kluge-Weiss and H. Gleiter, "Electron Microscopic Observations on the Structure of Dislocations in Interphase Boundaries," Acta Met., Vol. 26, (1978), pp. 117-121.
- [32] G. B. Olson, "Fine Structure of Interphase Boundaries," Acta Met., Vol. 29, (1981), pp. 1475-1484.
- [33] C. J. Guntner and R. P. Reed, "The Effect of Experimental Variables, Including the Martensitic Transformation, on the Low-Temperature Mechanical Properties of Austenitic Stainless Steels," Trans. ASM, Vol. 55, (1962), pp. 399-449.
- [34] Dieter Fahr, "Stress-and Strain-Induced Formation of Martensite and Its Effects on Strength and Ductility of Metastable Austenitic Stainless Steels," Met. Trans., Vol. 2 (1971), pp. 1883-1892.
- [35] K. Suzuki, T. Hashimoto and M. Ichihara, "An Experimental Study of the Martensite Nucleation and Growth in 18/8 Stainless Steel," Acta Met., Vol. 25, (1977), pp. 1151-1162.
- [36] R. P. Reed, "Martensitic Phase Transformations," Chapt. 9 in Materials at Low Temperatures, Reed and Clark, eds., ASM, June 1983.
- [37] J. A. Venables, "The Martensite Transformation in Stainless Steel," Phil. Mag., Vol. 7, (1962), pp. 35-44.
- [38] P. L. Mangonon and G. Thomas, "The Martensite Phases in 304 Stainless Steel," Met. Trans., Vol. 1, (1970), pp. 1577-1586.
- [39] M. F. Ashby, "The Deformation of Plastically Non-Homogeneous Alloys," in Strengthening Methods in Crystals, Halsted Press Div., John Wiley & Sons, New York, (1971), pp. 137-192.

- [40] D. Kuhlmann-Wilsdorf, "A Critical Test on Theories of Work Hardening for the Case of Drawn Iron Wire," Met. Trans., Vol. 1, (1970), pp. 3173-3179.
- [41] C. M. Young and O. D. Sherby, "Subgrain Formation and Subgrain Boundary Strengthening in Iron-Based Materials," J.I.S.I., (Sept. 1973), pp. 640-647.
- [42] C. Schwink and E. Göttler, "Dislocation Interactions, Flow Stress and Initial Work Hardening of Copper Single Crystals with [100] Axis Orientation," Acta Met., Vol. 24, (1976), pp. 173-179.
- [43] H. J. McQueen, "The Production and Utility of Recovered Dislocation Substructures," Met. Trans. A, Vol. 8A, (1977), pp. 807-824.
- [44] B. Cina, "Effect of Cold Work on the  $\gamma \rightarrow \alpha$  Transformation in Some Fe-Ni-Cr Alloys," JISI, (1954), pp. 406-422.
- [45] R. P. Reed, "The Spontaneous Martensitic Transformation in 18% Cr-8%Ni Steels," Acta Met., Vol. 10, (1962), pp. 865-877.
- [46] J. F. Breedis and W. D. Robertson, "The Martensitic Transformation in Single Crystals of Fe-Cr-Ni Alloys," Acta Met., Vol. 10, (1962), pp. 1077-1088.
- [47] R. Lagneborg, "The Martensite Transformation in 18%Cr-8%Ni Steels," Acta Met., Vol. 12, (1964), pp. 823-843.
- [48] F. Lecroisey and A. Pineau, "Martensitic Transformations Induced by Plastic Deformation in the Fe-Ni-Cr-C System," Met. Trans., Vol. 3, (1972), pp. 387-396.
- [49] G. B. Olson and M. Cohen, "Kinetics of Strain Induced Martensitic Nucleation," Met. Trans. A, Vol. 6A, (1975), pp. 791-795.
- [50] G. B. Olson and M. Cohen, "A General Mechanism of Martensitic Nucleation: Part II. FCC $\rightarrow$ BCC and Other Martensitic Transformations," Met. Trans. A, Vol. 7A, (1976), pp. 1905-1914.
- [51] S. S. Hecker, M. G. Stout, K. P. Staudhammer, and J. L. Smith, "Effects of Strain State and Strain Rate on Deformation-Induced Transformation in 304 Stainless Steel: Part I. Magnetic Measurements and Mechanical Behavior," Met. Trans. A, Vol. 13A, (1982), pp. 619-626.
- [52] L. E. Murr, K. P. Staudhammer, and S. S. Hecker, "Effects of Strain State and Strain Rate on Deformation-Induced Transformation in 304 Stainless Steel: Part II. Microstructural Study," Met. Trans. A, Vol. 13A, (1982), pp. 627-635.
- [53] J. F. Breedis and L. Kaufman, "Formation of HCP and BCC Phases in Austenitic Iron Alloys," Met. Trans., Vol. 2, (1971), pp. 2359-2371.
- [54] J. F. Breedis, "Influence of Dislocation Substructure on the Martensitic Transformation in Stainless Steel," Acta Met., Vol. 13, (1965), pp. 2359-2371.
- [55] S. Mahajan and D. F. Williams, "Deformation Twinning in Metals and Alloys," Int'l Met. Rev., Vol. 8, (1973), pp. 43-61.
- [56] A. W. Sleeswyk, "Twinning and the Origin of Cleavage Nuclei in  $\alpha$ -Iron," Acta Met., Vol. 10, (1962), pp. 803-812.



TABLE I  
Chemical Composition

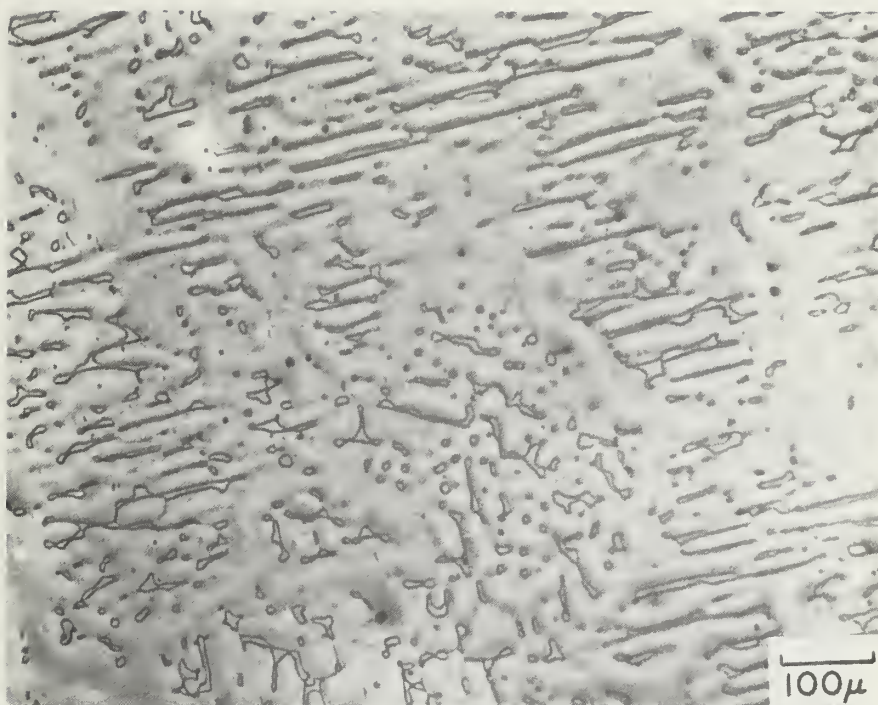
<u>Alloy</u> <u>Designation</u>	<u>C</u>	<u>N</u>	<u>Mn</u>	<u>Si</u>	<u>Cr</u>	<u>Ni</u>	<u>Mo</u>	<u>Volume</u> <u>Percent</u> <u><math>\delta</math>-ferrite</u>
K-9	0.02	-	1.06	1.10	19.33	11.67	2.14	9
K-14	0.05	-	0.83	1.25	19.50	12.20	2.69	14
K-24	0.07	-	0.52	1.32	21.48	9.48	3.18	24
1	0.06	0.05	1.10	0.59	18.04	13.24	2.12	1.1
2	0.06	0.05	0.30	1.16	19.62	10.61	2.12	8.2
3	0.06	0.05	0.36	1.13	19.23	8.25	2.16	17.2
4	0.06	0.05	0.35	0.95	20.40	8.22	2.13	23.1
5	0.05	0.05	0.39	1.11	22.54	9.84	2.26	28.5

## LIST OF FIGURES

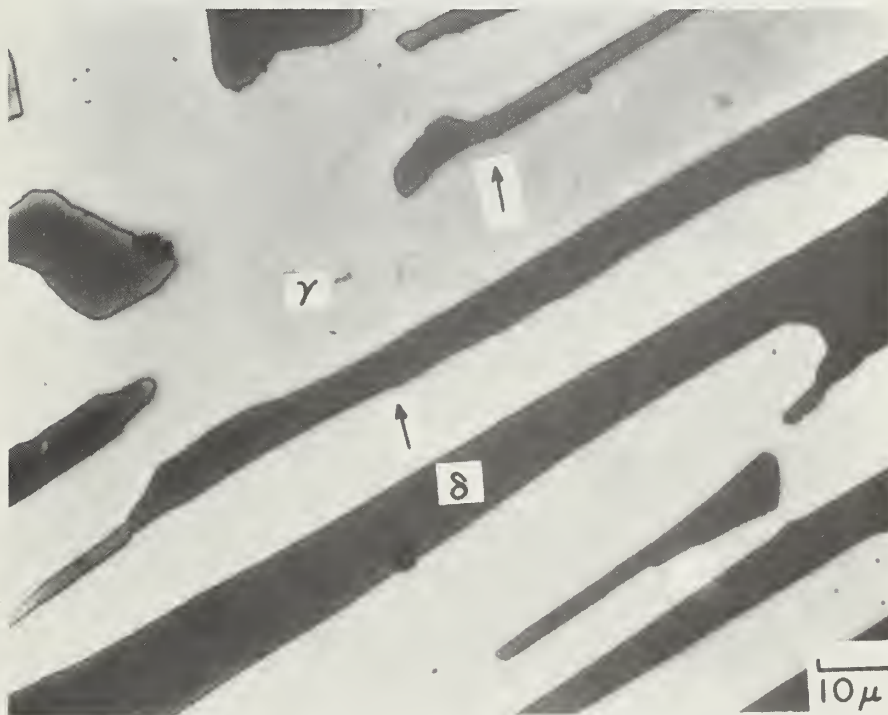
- [1]. Residual  $\delta$  morphology.
  - (a). 9 volume percent  $\delta$ , facet variants. Light micrograph, oxalic acid electroetch.
  - (b). 24 volume percent  $\delta$ , ledges on  $\delta/\gamma$  interface (arrows). Light micrograph, KOH electroetch.
- [2].
  - (a). 9 volume percent  $\delta$ , columnar  $\gamma$  crystals. Light micrograph, deposition color etch.
  - (b). 9 volume percent  $\delta$ , interiors of columnar  $\gamma$  crystals. Light micrograph, deposition color etch.
- [3]. Recovered dislocation substructures. Transmission electron micrographs.
  - (a). 1.1 volume percent  $\delta$ .
  - (b). 17.2 volume percent  $\delta$ .
  - (c). 28.5 volume percent  $\delta$ .
- [4]. 8.2 volume percent  $\delta$ , low angle boundary composed of dislocation tangles. Transmission electron micrographs.
  - (a). Bright-field.
  - (b). Weak-beam dark-field.
- [5]. 1.1 volume percent  $\delta$ , dislocation nets in subgrain boundaries. Transmission electron micrographs.
  - (a). Bright-field.
  - (b). Weak-beam dark-field.
- [6]. 28.5 volume percent  $\delta$ , recovered dislocation substructure in  $\delta$ . Transmission electron micrograph.
- [7]. 28.5 volume percent  $\delta$ , low angle boundary in  $\delta$  and cusp at boundary -  $\delta/\gamma$  interface (arrow). Transmission electron micrograph.
- [8]. 9 volume percent  $\delta$ , dislocation network attached to  $\delta/\gamma$  interface. Transmission electron micrograph.
- [9]. Dislocation debris. Transmission electron micrographs.
  - (a). 28.5 volume percent  $\delta$ , dislocations associated with sub-boundary.
  - (b). 28.5 volume percent  $\delta$ , dislocations in  $\delta$  at  $\delta/\gamma$  interface.
  - (c). 28.5 volume percent  $\delta$ , jogged dislocations and loops in  $\delta$ .
- [10].
  - (a). 9 volume percent  $\delta$ ,  $\delta/\gamma$  interface. Transmission electron micrograph.
  - (b). SAD consistent with K-S orientation relationship.
- [11]. Stereo triangle illustrating the results of single surface trace analyses of the habits of  $\delta/\gamma$  facets.
- [12]. 9 volume percent  $\delta$ , aspects of  $\delta/\gamma$  interfacial morphology and structure. Transmission electron micrographs.
  - (a). Steps on interface (arrow).
  - (b). Interfacial dislocation arrays.

- [13]. Activation of dislocation sources at  $\delta/\gamma$  interface and interaction of dislocations in vicinity of interface,  $\epsilon=0.005$ . Transmission electron micrographs.
- (a). 17.2 volume percent  $\delta$ .
  - (b). 28.5 volume percent  $\delta$ .
  - (c). 17.2 volume percent  $\delta$ ; bright-field and weak-beam dark-field.
  - (d). 28.5 volume percent  $\delta$ ; network and dislocation sources at  $\delta/\gamma$  interface.
- [14]. 17.2 volume percent  $\delta$ ,  $\epsilon=0.005$ ; dislocation source at  $\delta/\gamma$  interface - sub-boundary junction. Transmission electron micrograph.
- [15]. 17.2 volume percent  $\delta$ ,  $\epsilon=0.005$ ; higher dislocation density in  $\gamma$  at  $\delta/\gamma$  interface. Transmission electron micrograph.
- [16]. 28.5 volume percent  $\delta$ ,  $\epsilon=0.005$ ; interaction of dislocations with as-grown subgrain boundary. Transmission electron micrograph.
- [17]. 17.2 volume percent  $\delta$ ,  $\epsilon=0.005$ ; dislocation sources (arrows) in  $\delta/\gamma$  interface bowing dislocations into both phases. Transmission electron micrograph.
- [18].  $\epsilon=0.02$ , shear/deformation band intersections in  $\gamma$ . Transmission electron micrographs.
- (a). 17.2 volume percent  $\delta$ .
  - (b). 28.5 volume percent  $\delta$ .
- [19].  $\epsilon=0.02$ ,  $\alpha'$  formation (arrows) at shear/deformation band intersections in  $\gamma$ . Transmission electron micrographs.
- (a). 17.2 volume percent  $\delta$ .
  - (b). 28.5 volume percent  $\delta$ .
- [20]. 17.2 volume percent  $\delta$ ,  $\epsilon=0.02$ ; dislocations generated in vicinity of forming  $\alpha'$ . Transmission electron micrograph.
- [21]. 17.2 volume percent  $\delta$ ,  $\epsilon=0.02$ ; multi-variant  $\alpha'$  in shear/deformation bands (arrows indicate traces of two variants). Transmission electron micrographs.
- (a). Bright-field.
  - (b). Dark-field employing  $\alpha'$  reflection.
  - (c). High magnification micrograph of  $\alpha'$  in region of arrow in (a) showing substructure in  $\alpha'$  platelets and at  $\gamma/\alpha'$  interfaces. The band is composed of a bundle of faults.
- [22]. 28.5 volume percent  $\delta$ ,  $\epsilon=0.02$ ; dislocation pile-ups  $\delta$  at  $\delta/\gamma$  interface. Transmission electron micrograph.
- [23]. 28.5 volume percent  $\delta$ ,  $\epsilon=0.02$ ; twin formation in  $\delta$ . Transmission electron micrograph.
- [24]. 17.2 volume percent  $\delta$ ,  $\epsilon_{\text{fracture}}$ ; transmission electron micrographs.
- (a). Low magnification micrograph.
  - (b). High magnification micrograph of lower  $\gamma$  region.
  - (c). High magnification micrograph of upper  $\gamma$  region.

- [25]. 28.5 volume percent  $\delta$ ,  $\epsilon_{\text{fracture}}$ ;  $\alpha'$  formation at shear/deformation band intersections. Transmission electron micrographs.
- (a). Bright-field.
  - (b). Dark-field employing  $\alpha'$  reflection (arrows indicate positions of  $\delta/\gamma$  interface).
- [26]. 28.5 volume percent  $\delta$ ,  $\epsilon_{\text{fracture}}$ ;  $\alpha'$  formation at shear/deformation band intersections. Transmission electron micrographs.
- (a). Bright-field.
  - (b). Dark-field employing  $\alpha'$  reflection.
- [27]. (a) and (b). 28.5 volume percent  $\delta$ ,  $\epsilon_{\text{fracture}}$ ; dislocation bands in  $\delta$ . Transmission electron micrographs.
- [28]. 28.5 volume percent  $\delta$ ,  $\epsilon_{\text{fracture}}$ ; twins in  $\delta$ . Transmission electron micrographs.
- (a). Bright-field of twins  $T_1$  and  $T_2$ .
  - (b). Dark-field of  $T_1$  employing twin reflection.
  - (c). Dark-field employing  $\delta$  matrix reflection.
- [29]. 28.5 volume percent  $\delta$ ,  $\epsilon_{\text{fracture}}$ ; dislocation substructure produced by accommodation strains associated with  $\delta$  twinning. Transmission electron micrographs.
- (a). In  $\delta$  ahead of growing twin (at arrow in Fig. 27(a)).
  - (b). In  $\gamma$  ahead of twin (arrow).
- [30]. EDS line scans across region of  $\delta$  for Cr, Ni, and Mo indicating partitioning of elements.
- [31]. EDS determination of Ni/Cr vs  $\delta$  content.



(a). 9 volume percent  $\delta$ , facet variants. Light micrograph, oxalic acid electroetch.



(b). 24 volume percent  $\delta$ , ledges on  $\delta/\gamma$  interface (arrows). Light micrograph, KOH electroetch.

Fig. 1. Residual  $\delta$  morphology



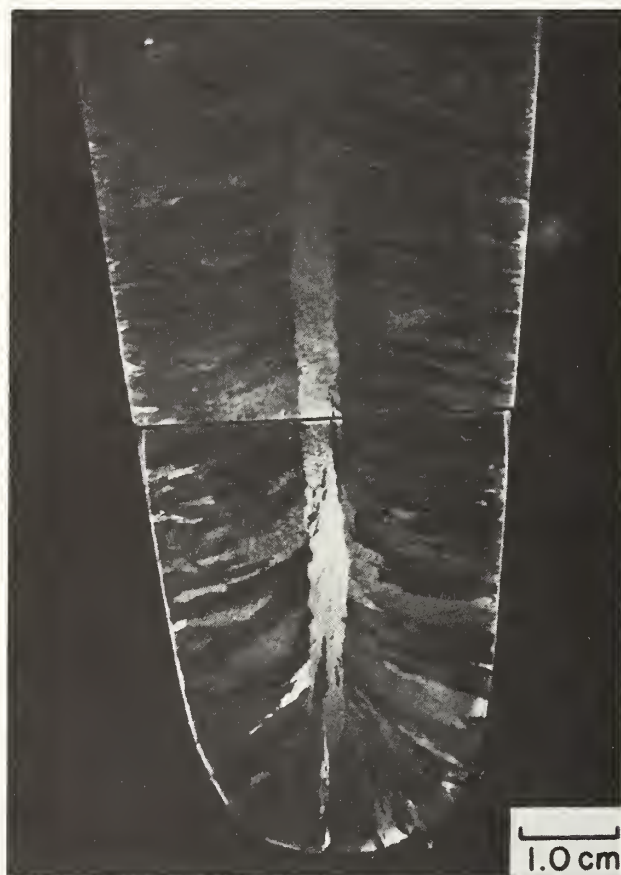


Fig. 2(a). 9 volume percent  $\delta$ , columnar  $\gamma$  crystals.  
Light micrograph, deposition color etch.



Fig. 2(b). 9 volume percent  $\delta$ , interiors of columnar  $\gamma$  crystals. Light micrograph, deposition color etch.



Fig. 3(a). 1.1 volume percent  $\delta$ .

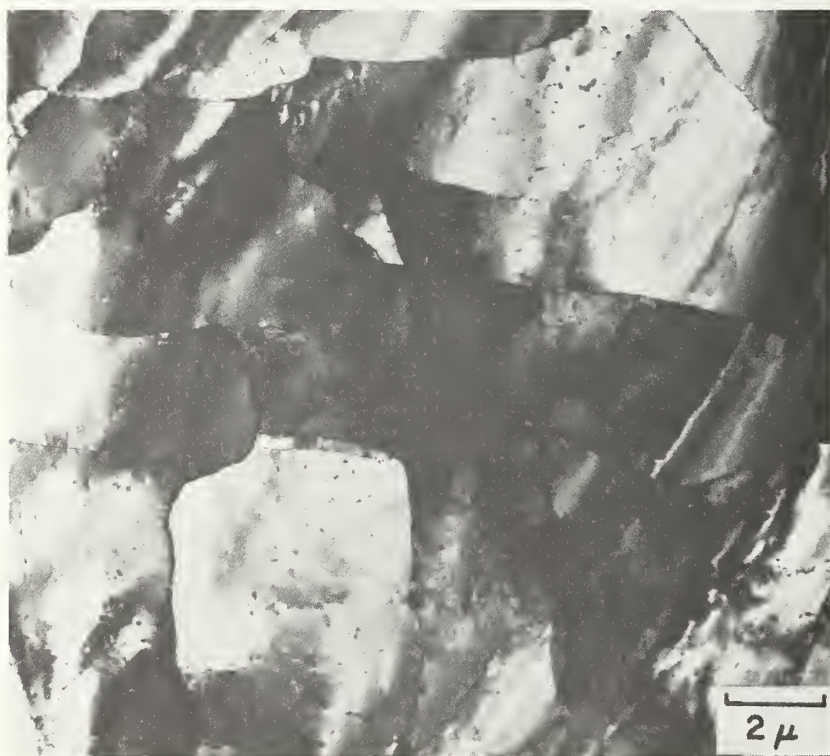


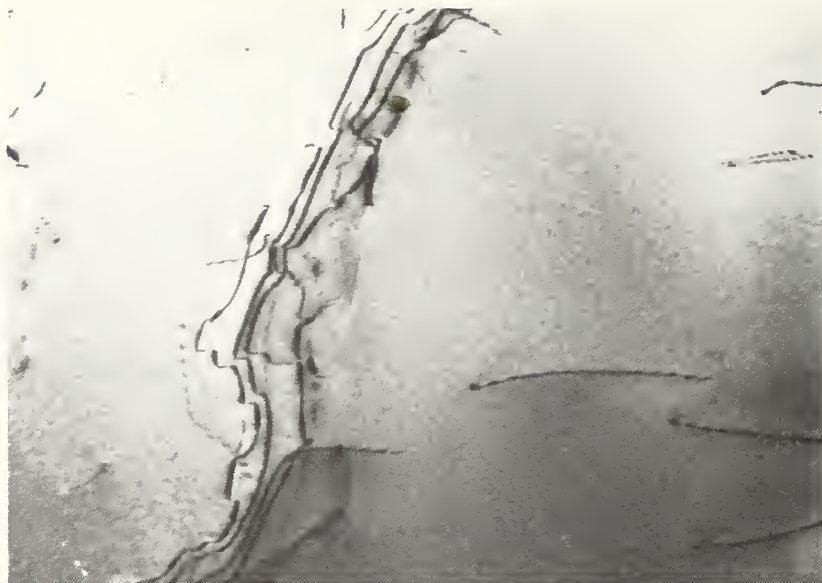
Fig. 3(b). 17.2 volume percent  $\delta$ .



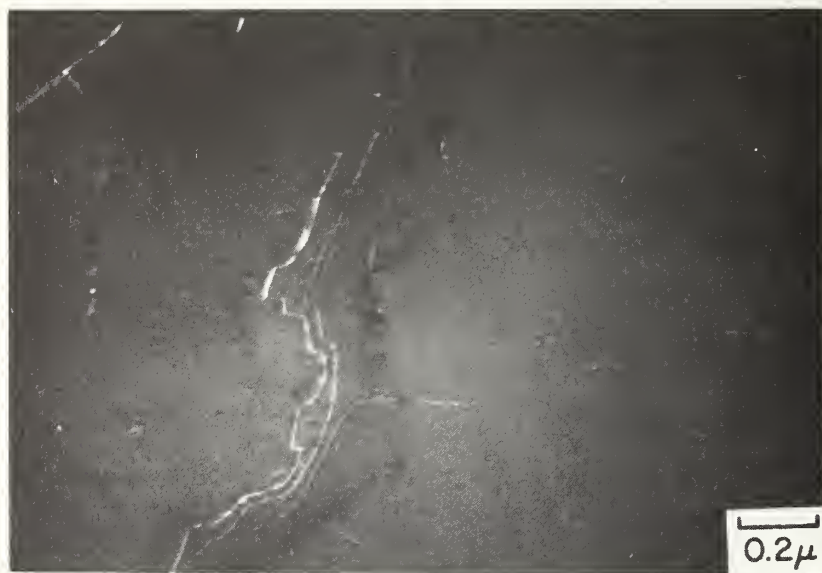
(c). 28.5 volume percent  $\delta$ .

Fig. 3. Recovered dislocation substructures.  
Transmission electron micrographs.





(a). Bright-field.



(b). Weak-beam dark-field.

Fig. 4. 8.2 volume percent  $\delta$ , low angle boundary composed of dislocation tangles. Transmission electron micrographs.

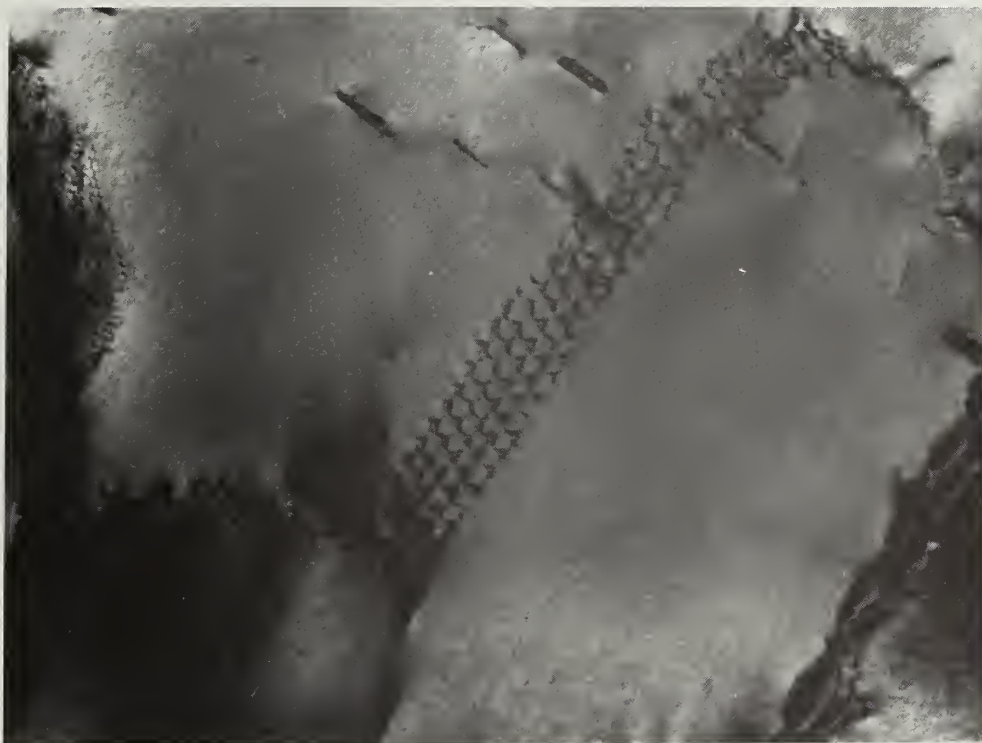
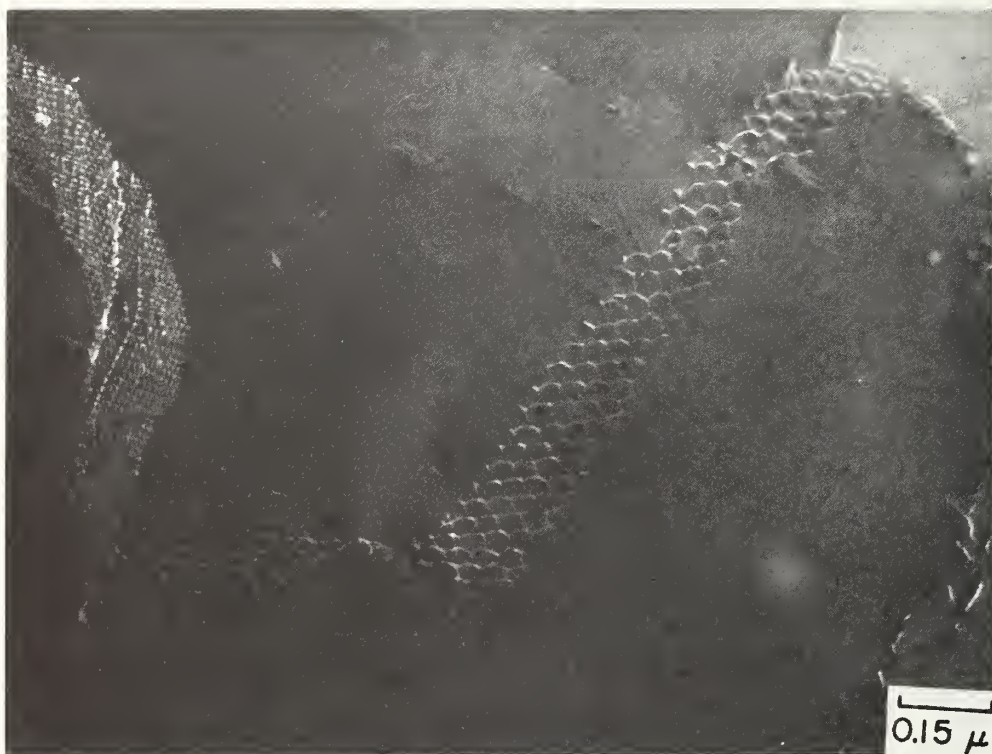


Fig. 5(a). Bright-field.



(b). Weak-beam dark-field.

Fig. 5. 1.1 volume percent  $\delta$ , dislocation nets in subgrain boundaries. Transmission electron micrographs.

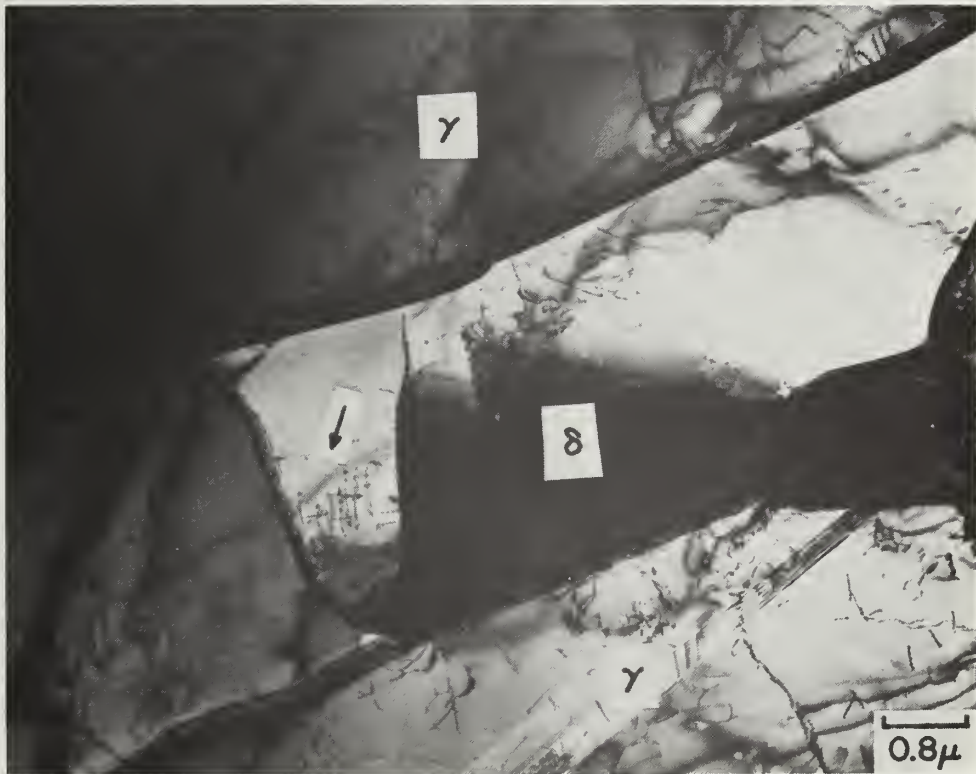


Fig. 6. 28.5 volume percent  $\delta$ , recovered dislocation substructure in  $\delta$ . Transmission electron micrograph.



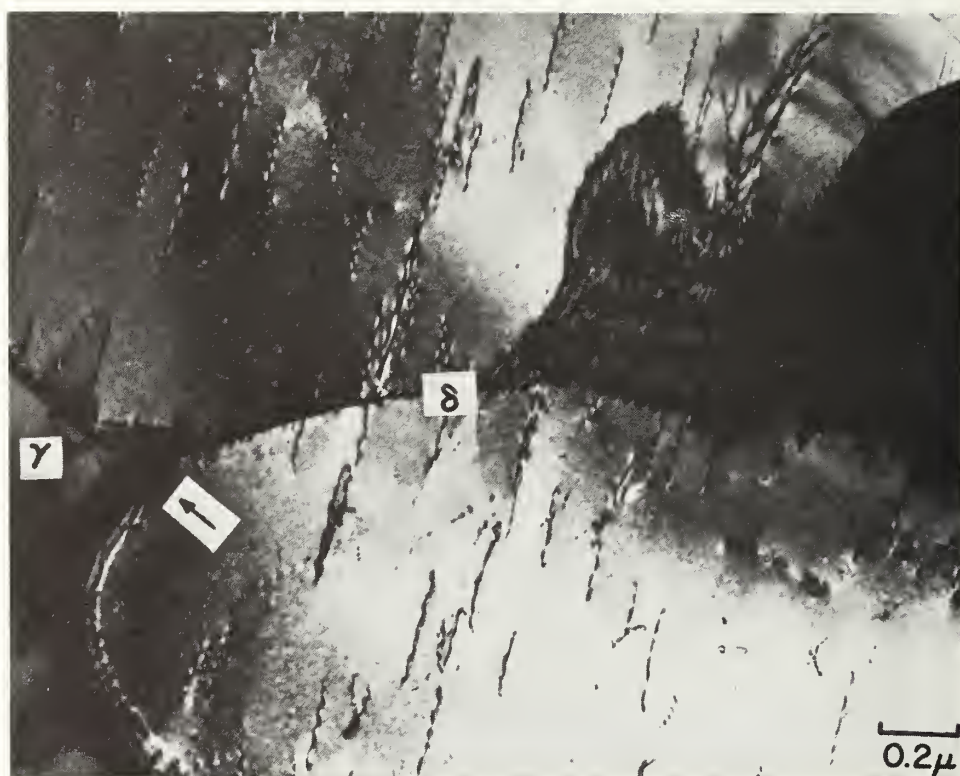


Fig. 7. 28.5 volume percent  $\delta$ , low angle boundary in  $\delta$  and cusp at boundary -  $\delta/\gamma$  interface (arrow). Transmission electron micrograph.



Fig. 8. 9 volume percent  $\delta$ , dislocation network attached to  $\delta/\gamma$  interface. Transmission electron micrograph.

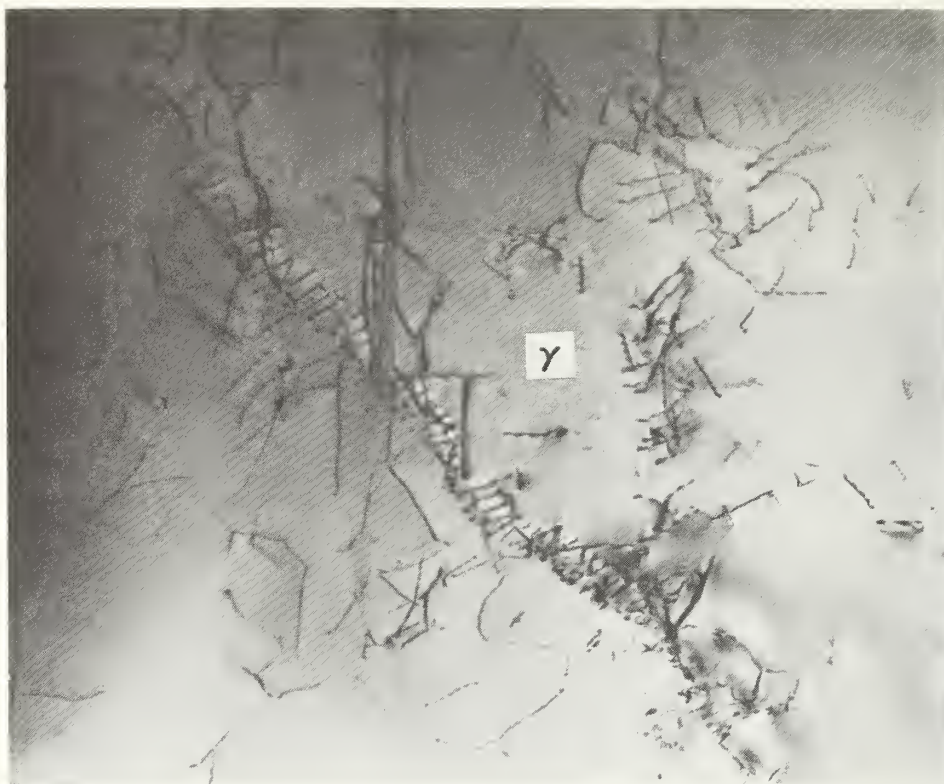


Fig. 9(a). 28.5 volume percent  $\delta$ , dislocations associated with sub-boundary.



Fig. 9(b). 28.5 volume percent  $\delta$ , dislocations in  $\delta$  at  $\delta/\gamma$  interface.



(c). 28.5 volume percent  $\delta$ , jogged dislocations and loops in  $\delta$ .  
Fig. 9. Dislocation debris. Transmission electron micrographs.





Fig. 10(a). 9 volume percent  $\delta$ ,  $\delta/\gamma$  interface. Transmission electron micrograph.

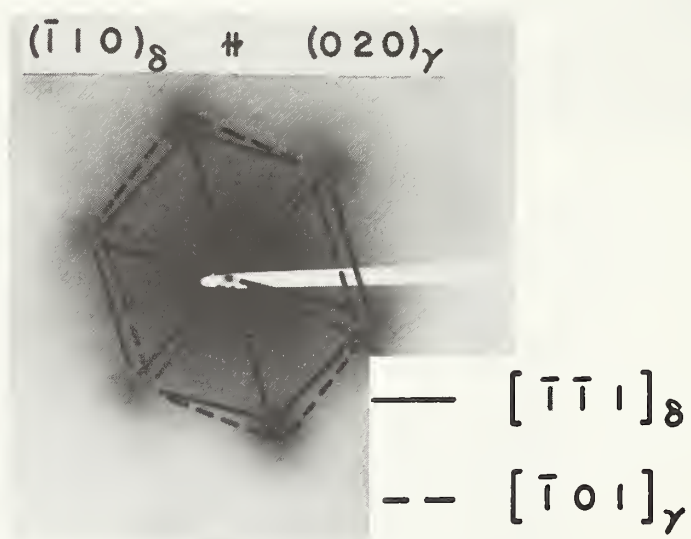


Fig. 10(b). SAD consistent with K-S orientation relationship.

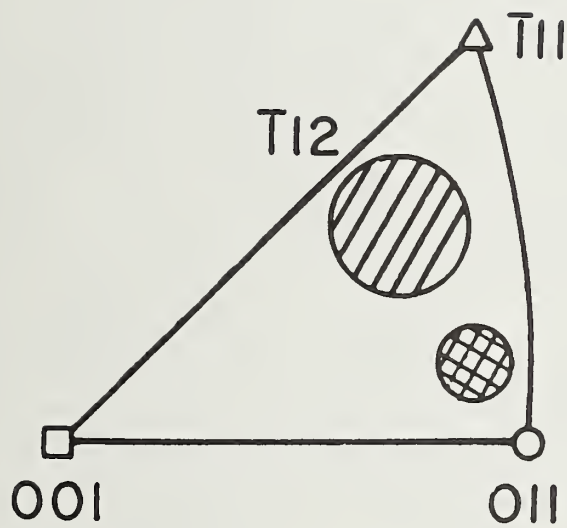


Fig. 11. Stereo triangle illustrating the results of single surface trace analyses of the habits of  $\delta/\gamma$  facets.

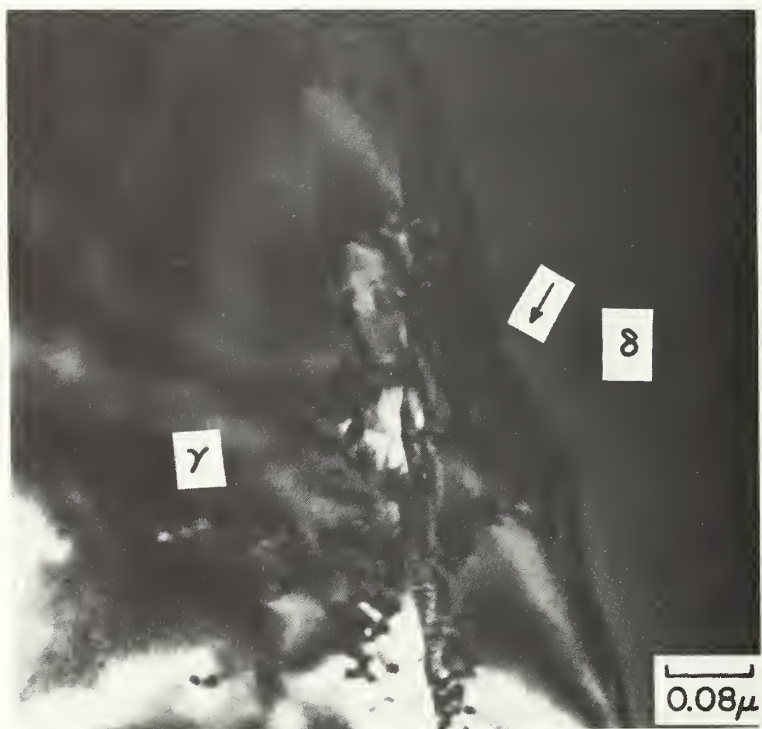


Fig. 12(a). Steps on interface (arrow).



(b). Interfacial dislocation arrays.

Fig. 12. 9 volume percent  $\delta$ , aspects of  $\delta/\gamma$  interfacial morphology and structure. Transmission electron micrographs.



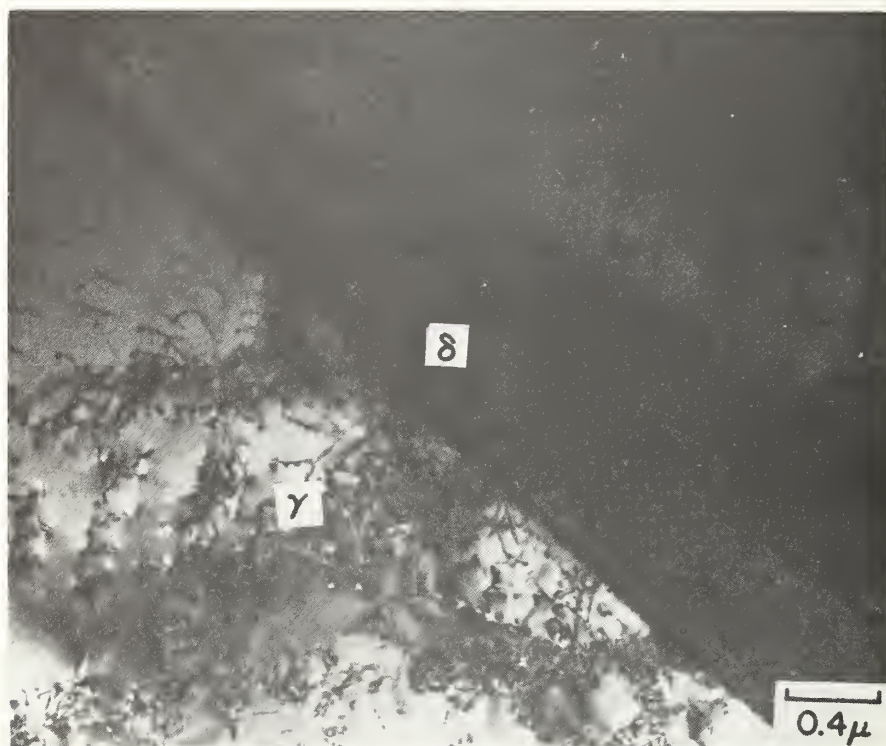


Fig. 13(a). 17.2 volume percent  $\delta$ .

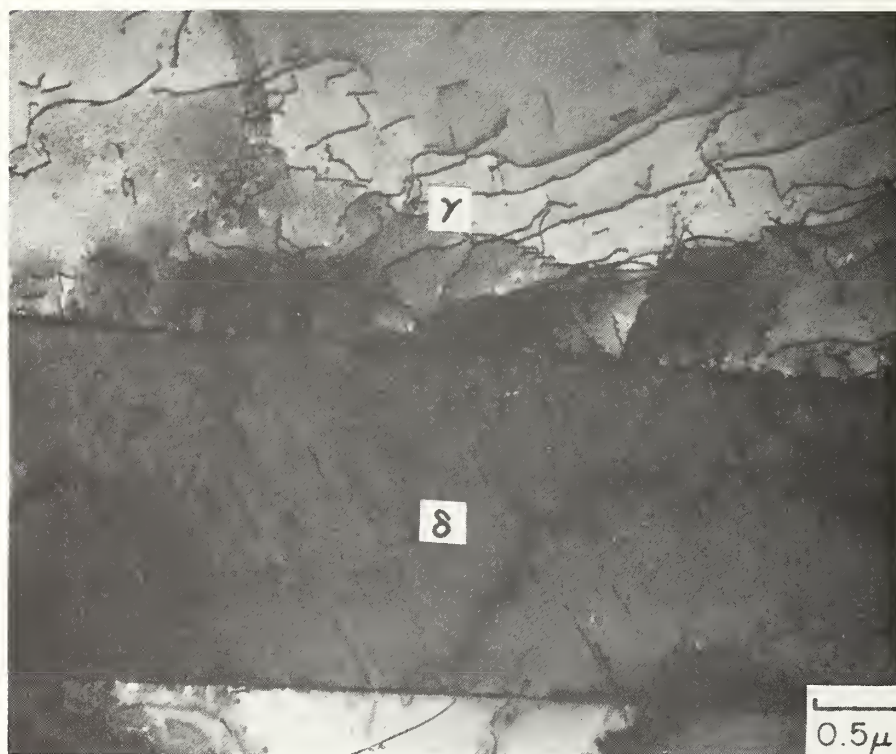


Fig. 13(b). 28.5 volume percent  $\delta$ .

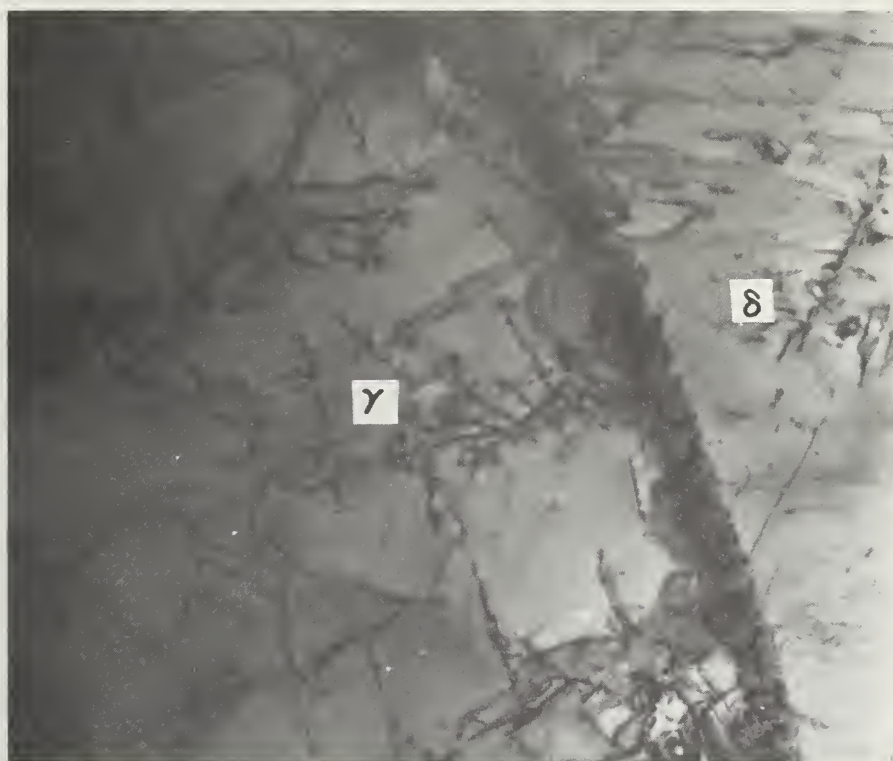
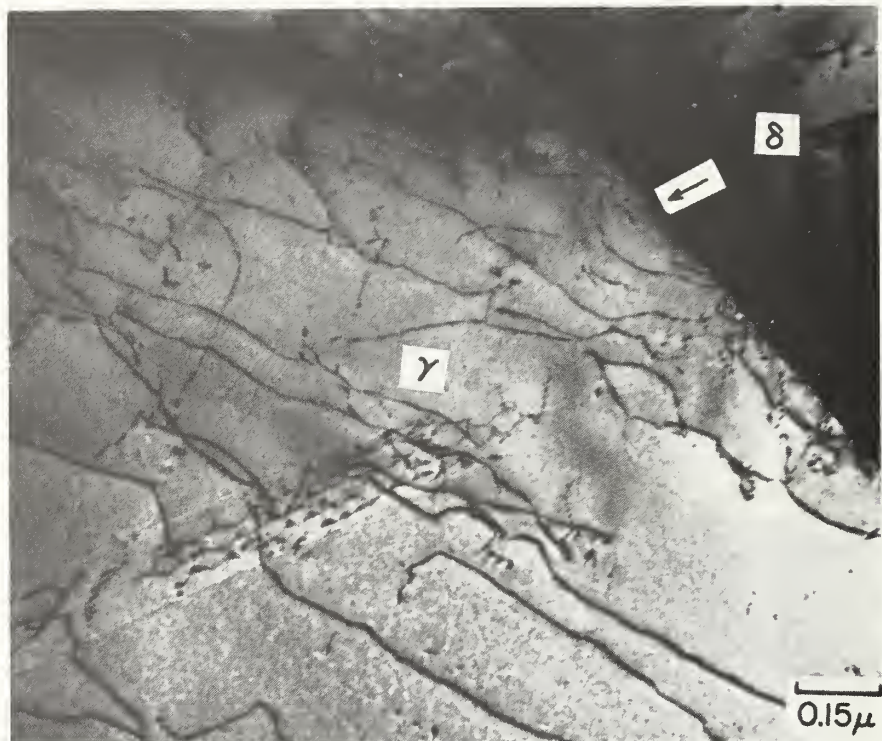


Fig. 13(c). 17.2 volume percent  $\delta$ ; bright-field and weak-beam dark-field.



(d). 28.5 volume percent  $\delta$ ; network and dislocation sources at  $\delta/\gamma$  interface.

Fig. 13. Activation of dislocation sources at  $\delta/\gamma$  interface and interaction of dislocations in vicinity of interface,  $\epsilon=0.005$ . Transmission electron micrographs.



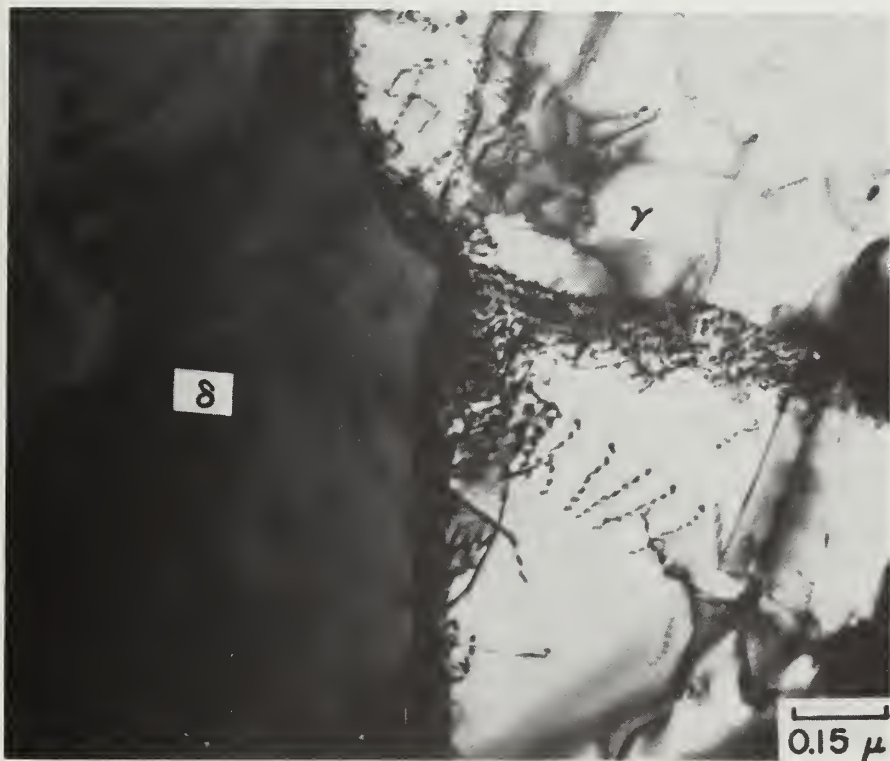


Fig. 14. 17.2 volume percent  $\delta$ ,  $\epsilon=0.005$ ; dislocation source at  $\delta/\gamma$  interface - sub-boundary junction. Transmission electron micrograph.



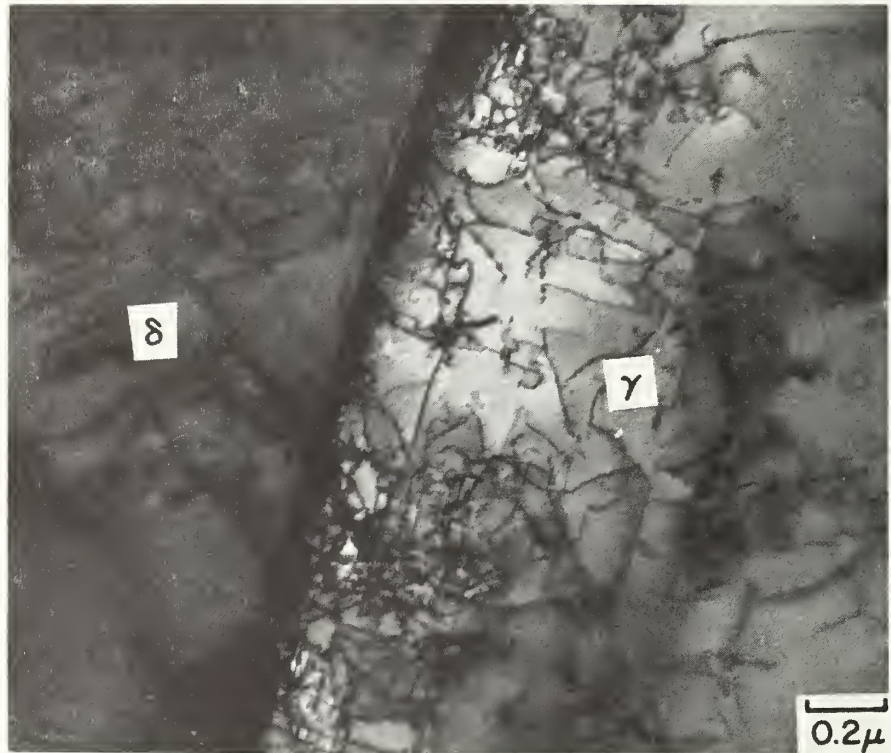


Fig. 15. 17.2 volume percent  $\delta$ ,  $\epsilon=0.005$ ; higher dislocation density in  $\gamma$  at  $\delta/\gamma$  interface. Transmission electron micrograph.

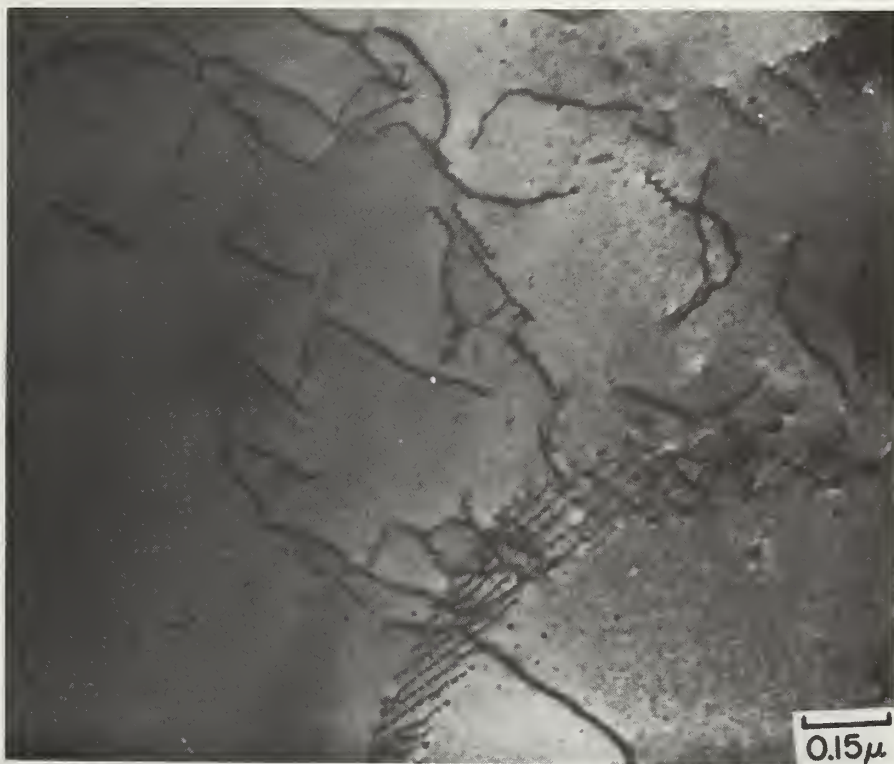


Fig. 16. 28.5 volume percent  $\delta$ ,  $\epsilon=0.005$ ; interaction of dislocations with as-grown subgrain boundary. Transmission electron micrograph.

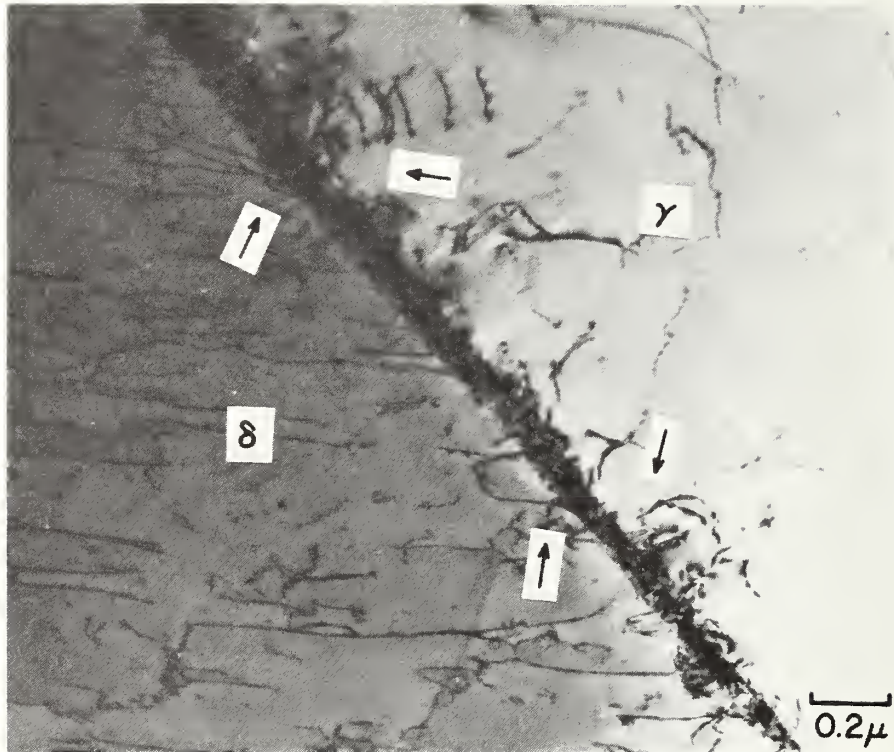


Fig. 17. 17.2 volume percent  $\delta$ ,  $\epsilon=0.005$ ; dislocation sources (arrows) in  $\delta/\gamma$  interface bowing dislocations into both phases. Transmission electron micrograph.

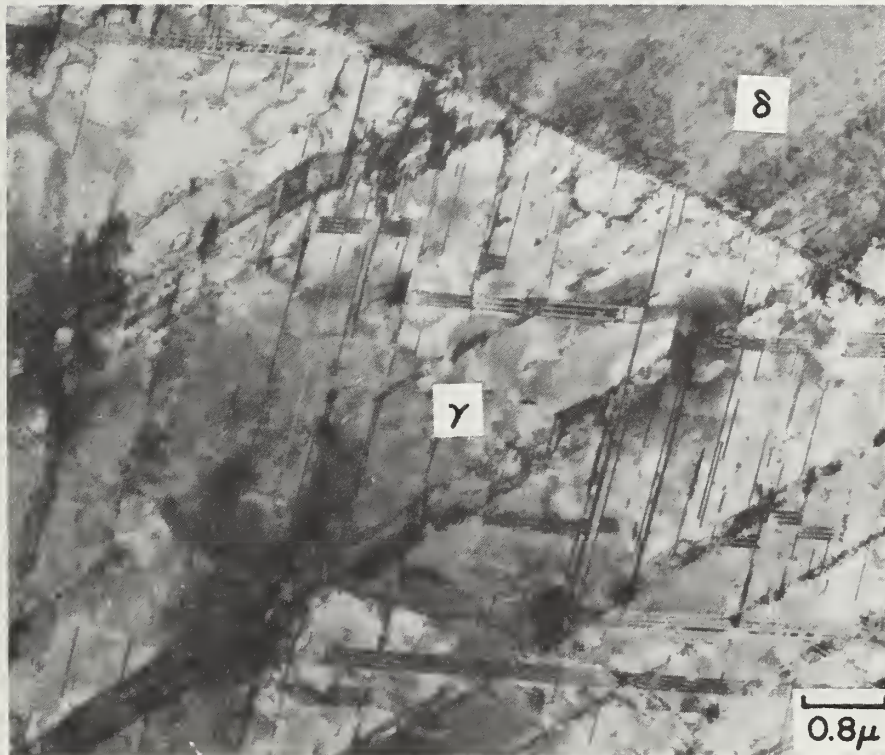


Fig. 18(a). 17.2 volume percent  $\delta$ .





(b). 28.5 volume percent  $\delta$ .

Fig. 18.  $\epsilon=0.02$ , shear/deformation band intersections in  $\gamma$ . Transmission electron micrographs.

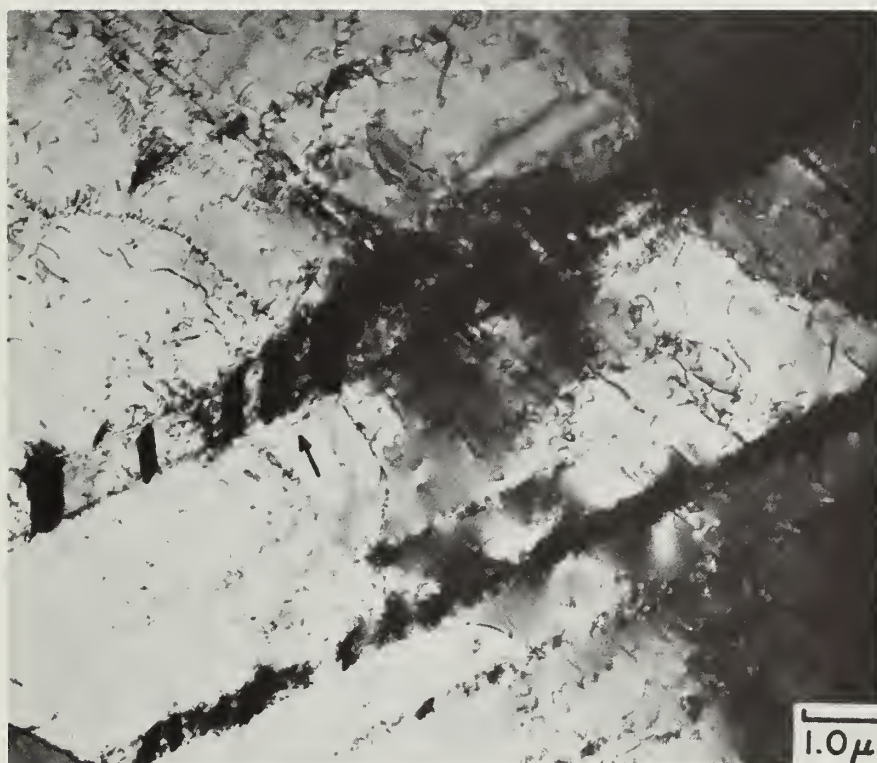


Fig. 19(a). 17.2 volume percent  $\delta$ .



(b) 28.5 volume percent  $\delta$ .

Fig. 19.  $\epsilon=0.02$ ,  $\alpha'$  formation (arrows) at shear/deformation band intersections in  $\gamma$ . Transmission electron micrographs.

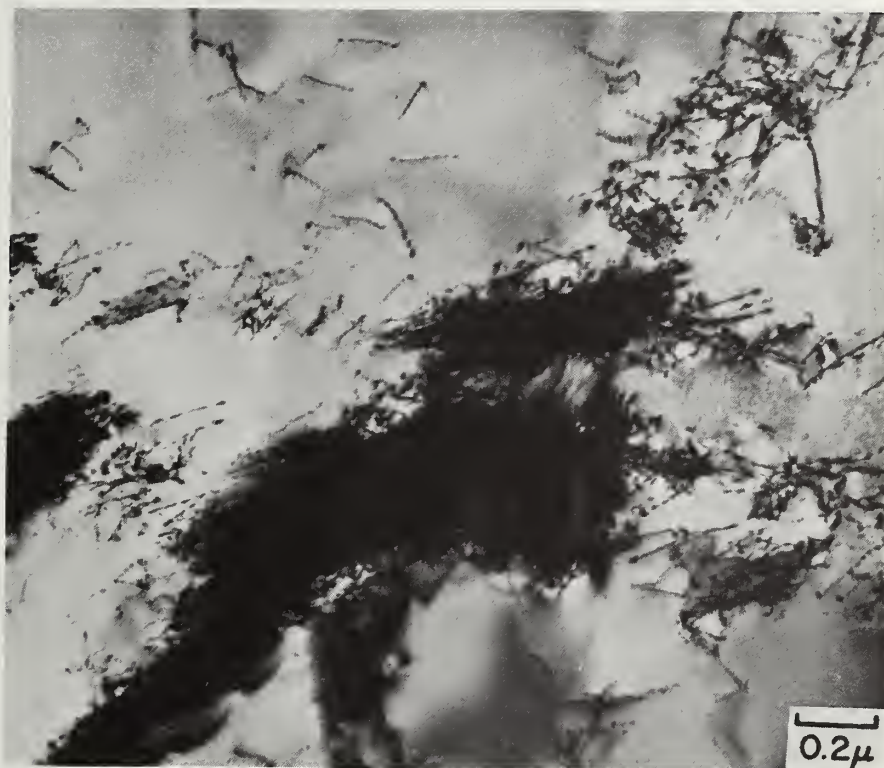


Fig. 20. 17.2 volume percent  $\delta$ ,  $\epsilon=0.02$ ; dislocations generated in vicinity of forming  $\alpha'$ . Transmission electron micrograph.

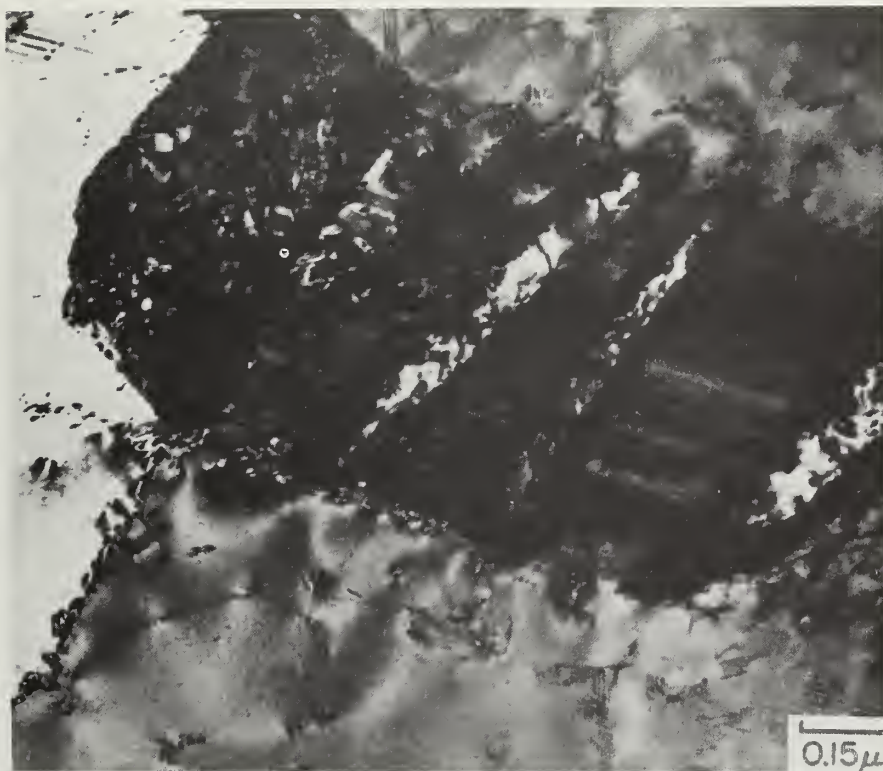




Fig. 21(a). Bright-field.



Fig. 21(b). Dark-field employing  $\alpha'$  reflection.



(c). High magnification micrograph of  $\alpha'$  in region of arrow in (a) showing substructure in  $\alpha'$  platelets and at  $\gamma/\alpha'$  interfaces. The band is composed of a bundle of faults.

Fig. 21. 17.2 volume percent  $\delta$ ,  $\epsilon=0.02$ ; multi-variant  $\alpha'$  in shear/deformation bands (arrows indicate traces of two variants). Transmission electron micrographs.

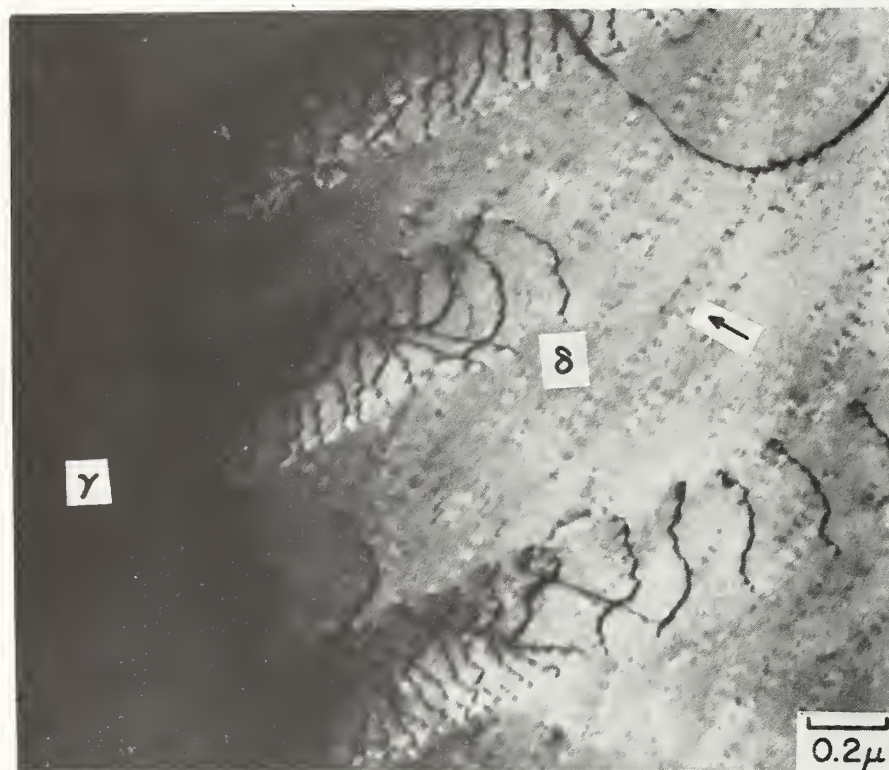


Fig. 22. 28.5 volume percent  $\delta$ ,  $\epsilon=0.02$ ; dislocation pile-ups in  $\delta$  at  $\delta/\gamma$  interface. Transmission electron micrograph.



Fig. 23. 28.5 volume percent  $\delta$ ,  $\epsilon=0.02$ ; twin formation in  $\delta$ . Transmission electron micrograph.





Fig. 24(a). Low magnification micrograph.

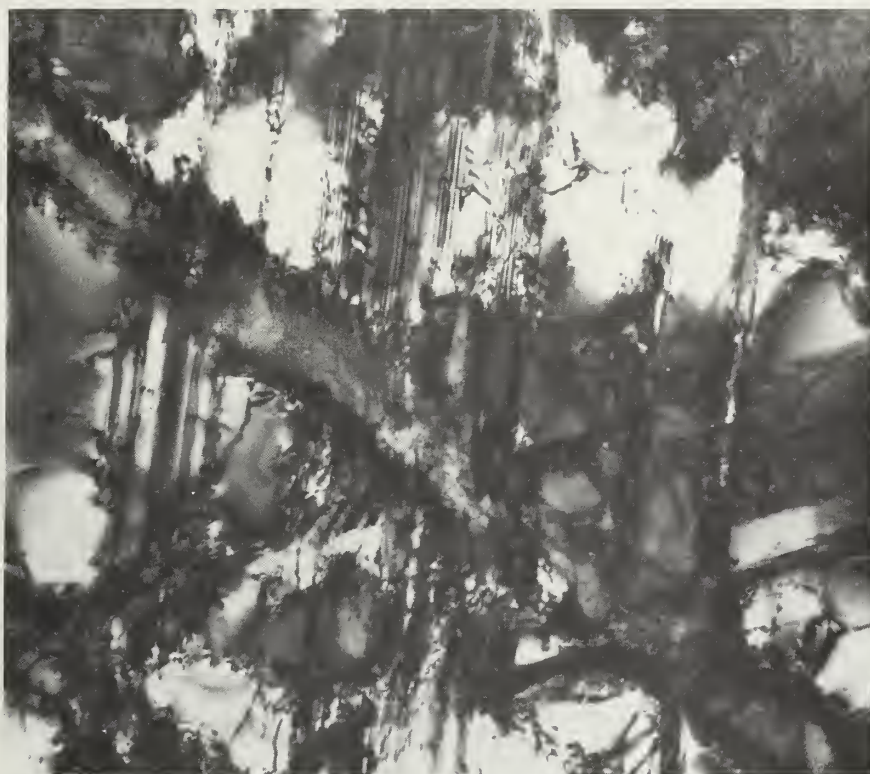


Fig. 24(b). High magnification micrograph of lower  $\gamma$  region.



Fig. 24(c). High magnification micrograph of upper  $\gamma$  region.

Fig. 24. 17.2 volume percent  $\delta$ ,  $\epsilon_{\text{fracture}}$ ; transmission electron micrographs.

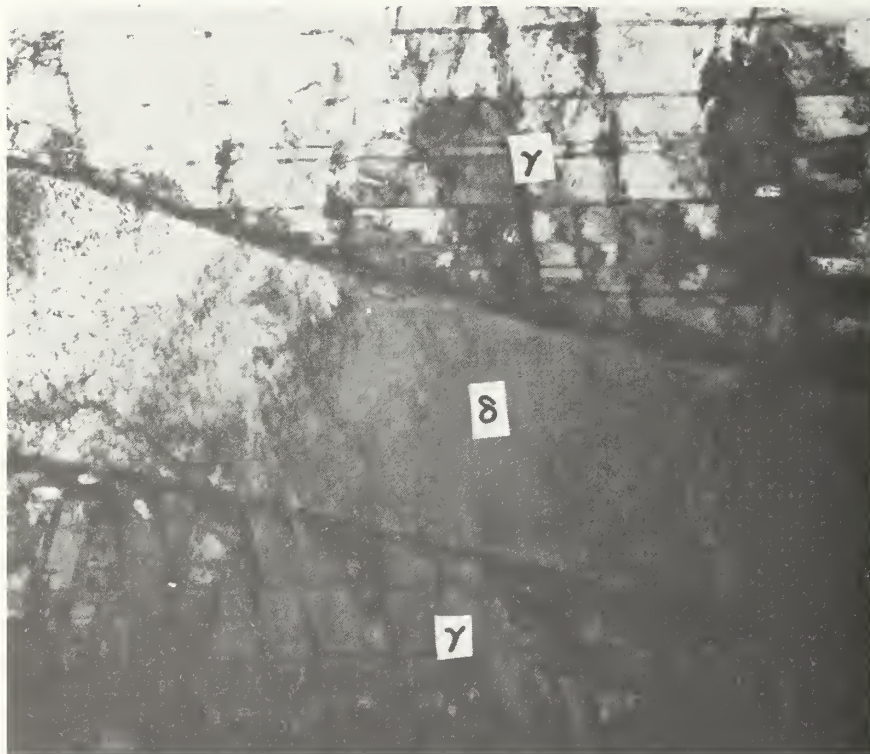
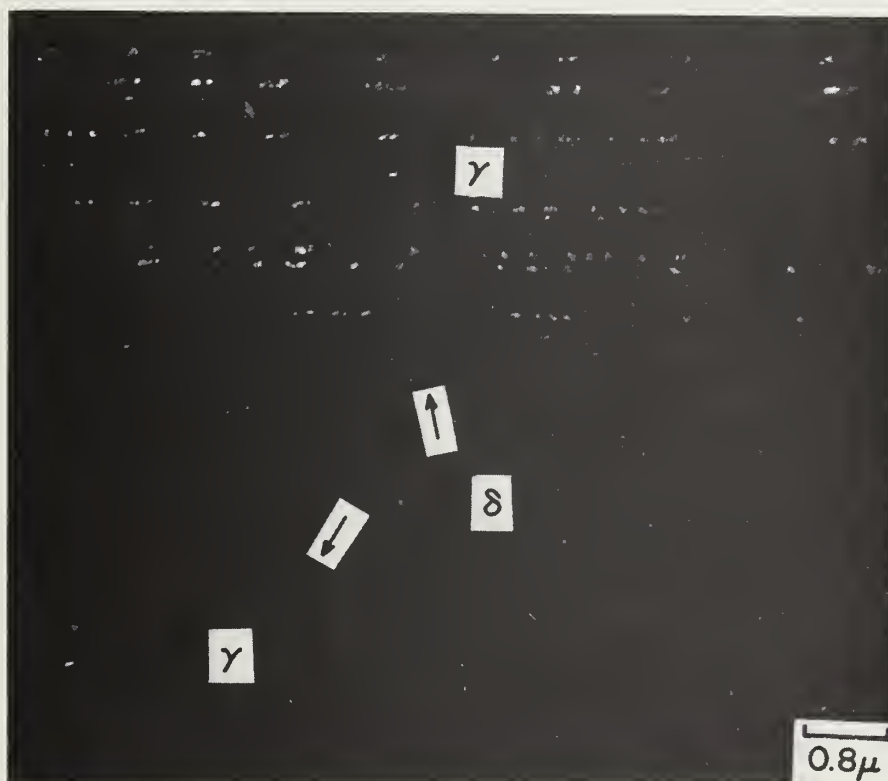


Fig. 25(a). Bright-field.





(b). Dark-field employing  $\alpha'$  reflection (arrows indicate positions of  $\delta/\gamma$  interface).

Fig. 25. 28.5 volume percent  $\delta$ ,  $\epsilon_{\text{fracture}}$ ;  $\alpha'$  formation at shear/deformation band intersections. Transmission electron micrographs.



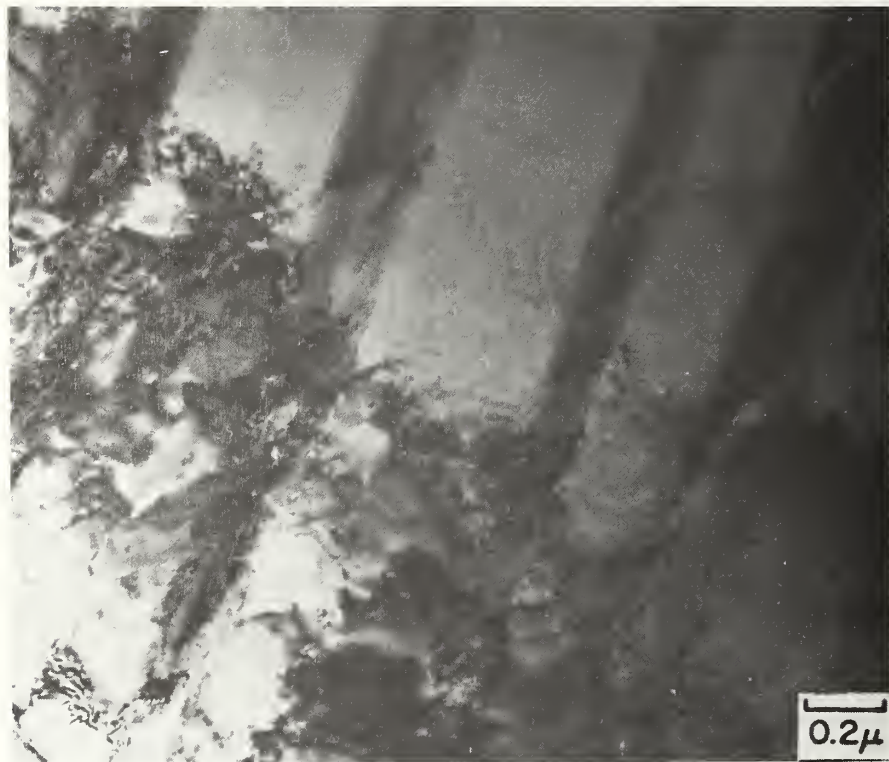
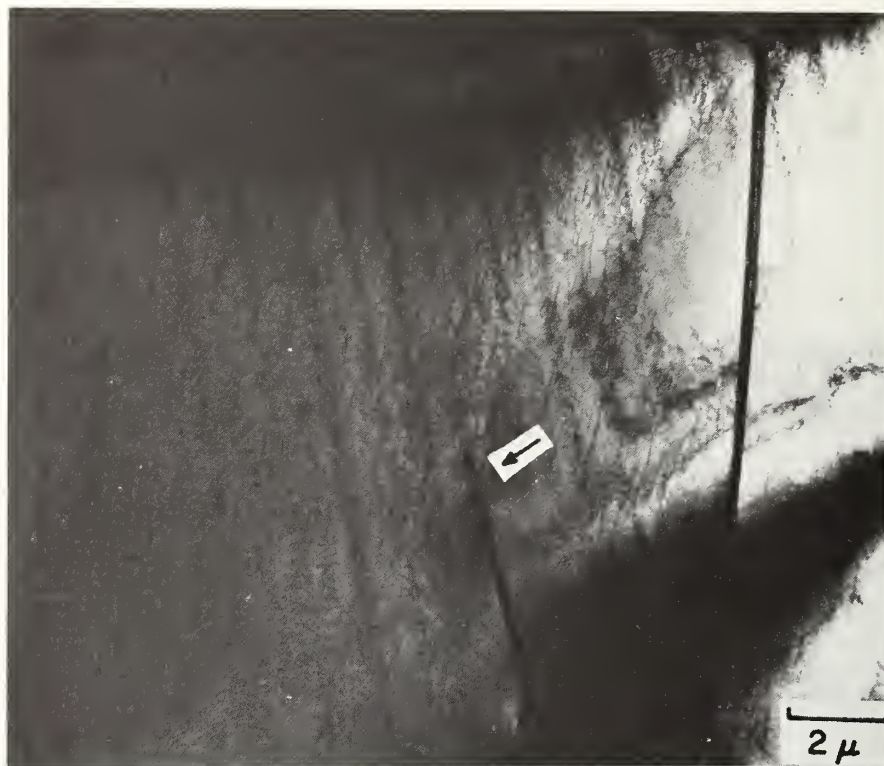


Fig. 26(a). Bright-field.

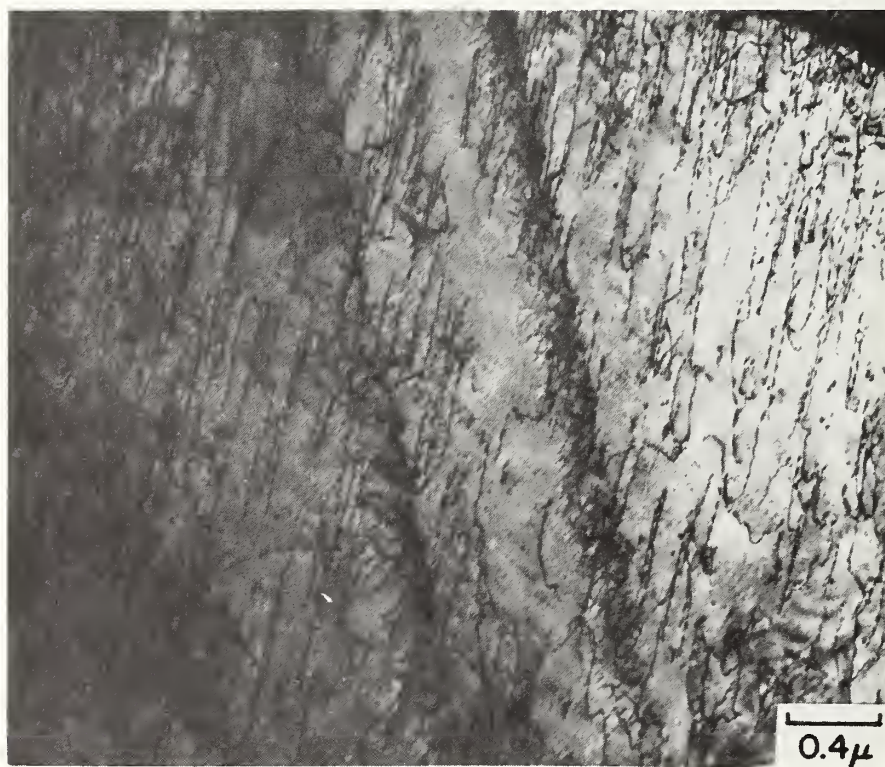


(b). Dark-field employing  $\alpha'$  reflection.

Fig. 26. 28.5 volume percent  $\delta$ ,  $\epsilon_{\text{fracture}}$ ;  $\alpha'$  formation at shear/deformation band intersections. Transmission electron micrographs.



(a)



(b)

Fig. 27. 28.5 volume percent  $\delta$ ,  $\epsilon_{\text{fracture}}$ ; dislocation bands in  $\delta$ . Transmission electron micrographs.





Fig. 28(a). Bright-field of twins  $T_1$  and  $T_2$ .



Fig. 28(b). Dark-field of  $T_1$  employing twin reflection.





(c). Dark-field employing  $\delta$  matrix reflection.

Fig. 28. 28.5 volume percent  $\delta$ ,  $\epsilon_{\text{fracture}}$ ; twins in  $\delta$ . Transmission electron micrographs.

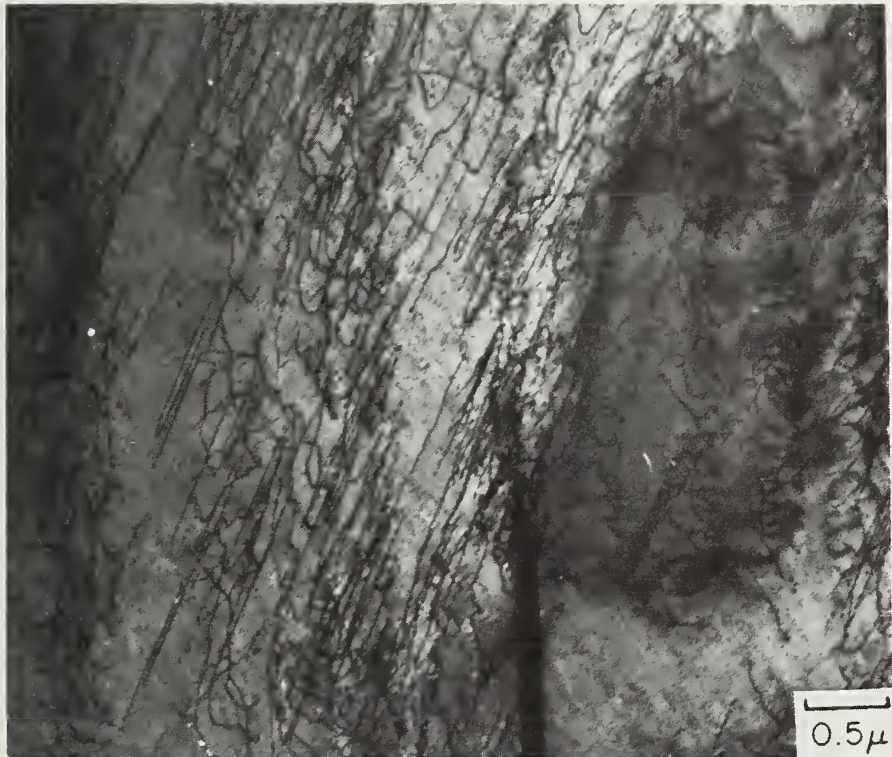
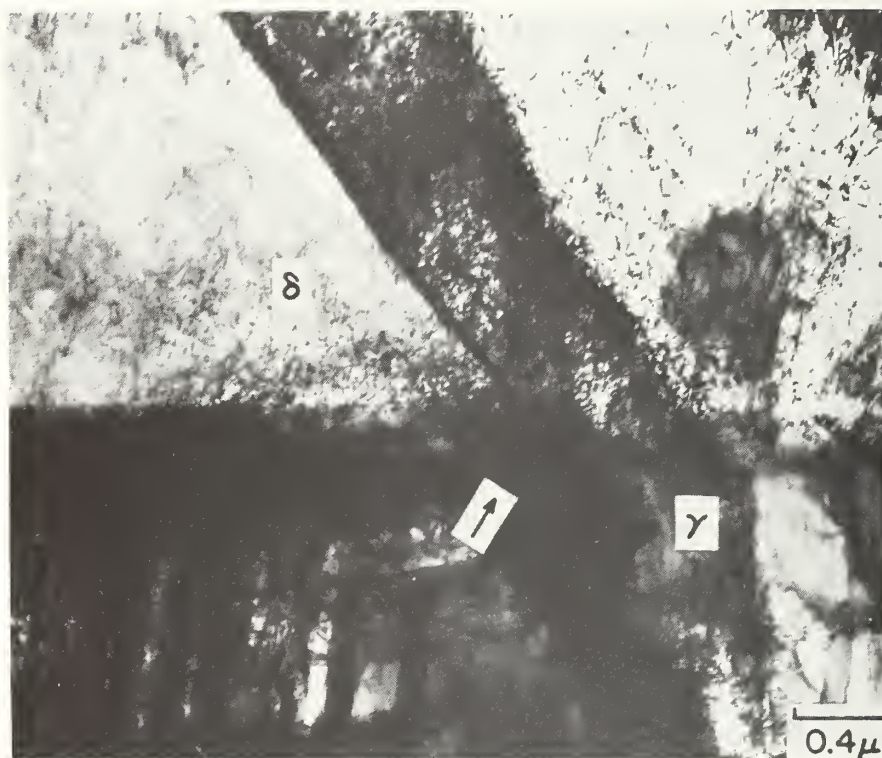


Fig. 29(a). In  $\delta$  ahead of growing twin (at arrow in Fig. 27(a)).



(b). In  $\gamma$  ahead of twin (arrow).

Fig. 29. 28.5 volume percent  $\delta$ ,  $\epsilon_{\text{fracture}}$ ; dislocation substructure produced by accommodation strains associated with  $\delta$  twinning. Transmission electron micrographs.

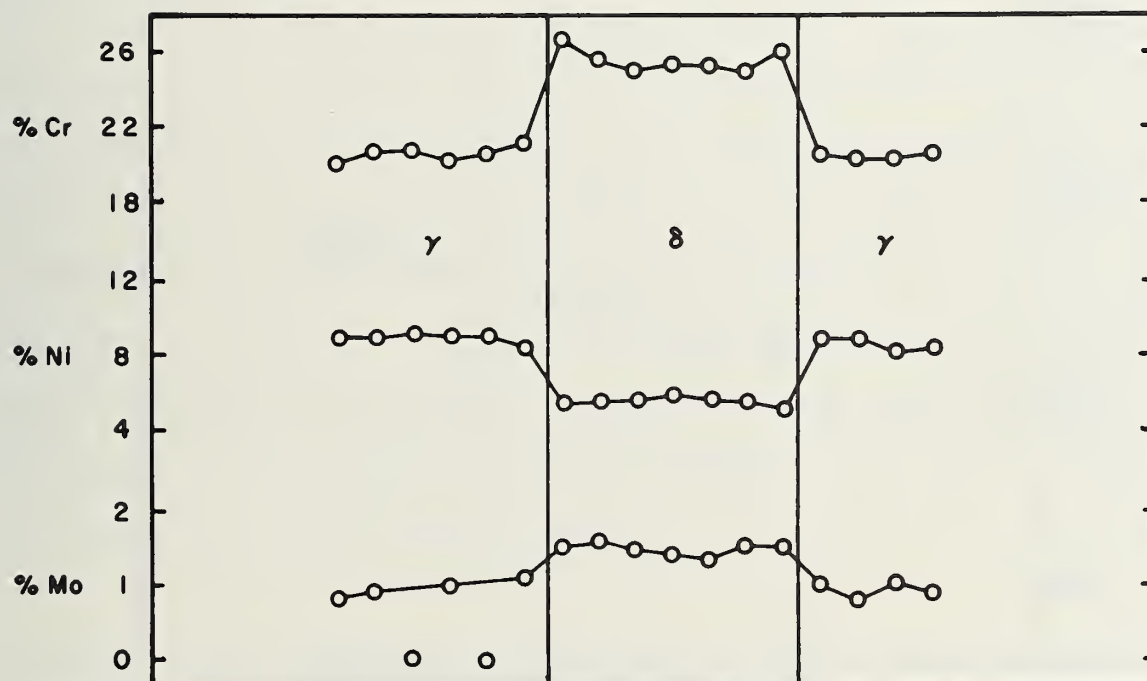


Fig. 30. EDS line scans across region of  $\delta$  for Cr, Ni, and Mo indicating partitioning of elements.



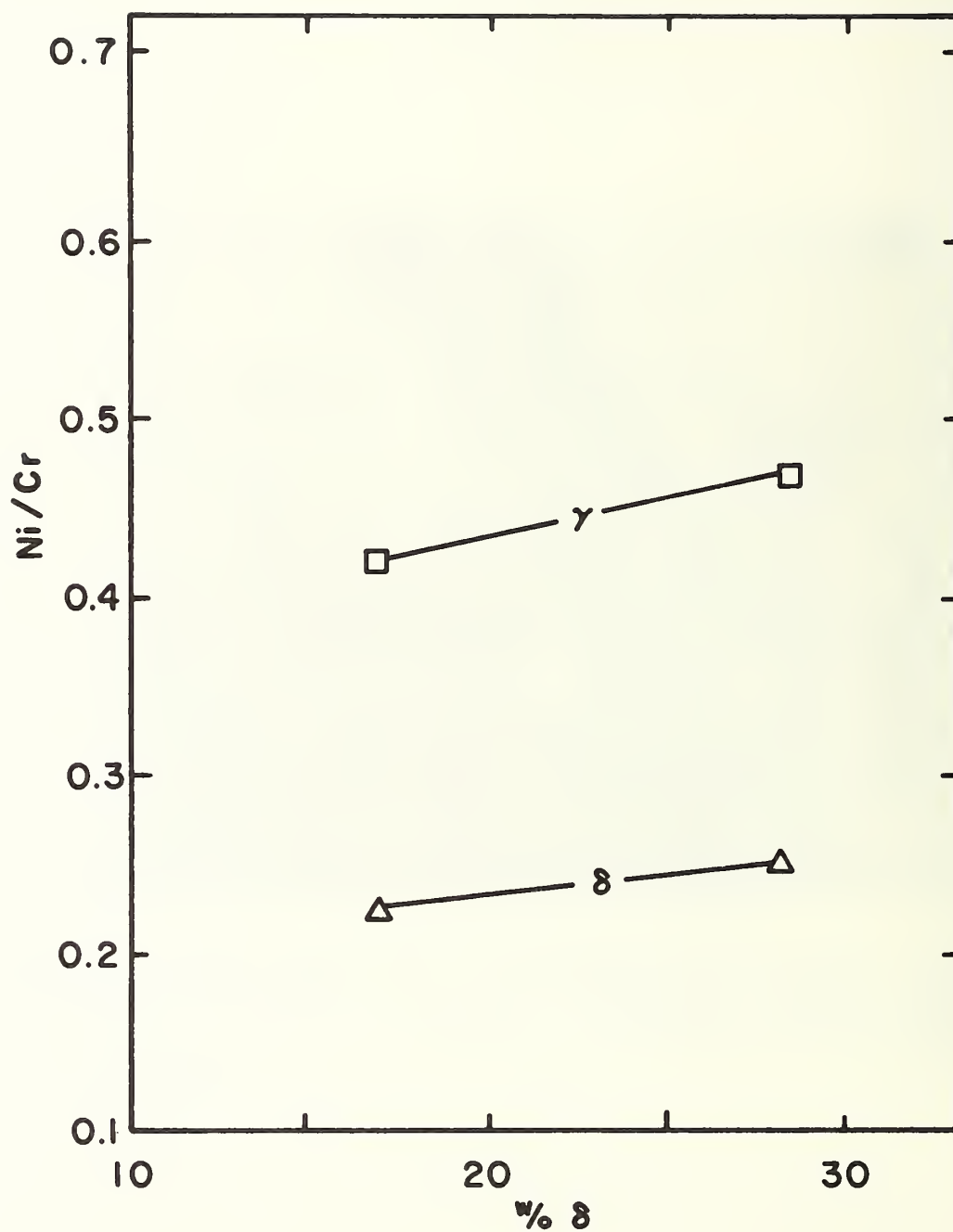


Fig. 31. EDS determination of Ni/Cr vs  $\delta$  content.

## TEXTURE IN STAINLESS-STEEL WELDS: AN ULTRASONIC STUDY

H. M. LEDBETTER, M. W. AUSTIN

Fracture and Deformation Division, National Bureau of Standards, Boulder, Colorado 80303, USA

---

We studied texture effects in five AISI 316-stainless-steel welds. We measured nine independent ultrasonic velocities along the weld's principal axes. These velocities reveal a strong texture different from the  $\langle 100 \rangle$ -fiber-type usually attributed to these materials. The texture is independent of delta-ferrite content and must contain a strong  $\langle 110 \rangle$  element related to the fcc monocrystal elastic constant  $C' = (C_{11} - C_{12})/2$ . A postulated ideal (001)[110] plate-type texture explains the range of measured longitudinal and transverse sound velocities, but not their detailed values.

Key Words: Elastic constant; sound velocity; stainless steel; texture; ultrasonics; weld



## 1. Introduction

Most metal processing produces texture, a nonrandom distribution of crystallite orientations in a polycrystal. Well-known processes that produce texture include: mechanical deformation, annealing (recrystallization), solidification, electrodeposition, vapor deposition (epitaxy), phase transformation, and welding. In each case one can identify a gradient (mechanical, thermal, electrical, and so forth) that favors one crystal orientation over another.



Texture induces anisotropic macroscopic physical and plastic properties. Thus, usual polycrystal-monocrystal relationships for quasi-isotropic (nontextured) aggregates provide only a rough guess for the macroscopic material properties. A better guess must include information concerning the orientation-distribution function of the crystallites.

In principle, any property affected by texture provides a possible tool for probing texture. For example: electrical resistivity, thermal expansivity, thermal conductivity, and so forth. But, these particular properties, which one represents as second-rank tensors, can not work for the cubic-symmetry case where they are simply direction-independent, texture-independent scalars.

A texture-probing physical property useful for all crystal-symmetry cases, including cubic, is the elastic-stiffness tensor. For the cubic case it contains three independent components: usually  $C_{11}$ ,  $C_{12}$ , and  $C_{44}$  in Voigt's contracted notation. Below, we consider the sound velocity,  $v = (C/\rho)^{\frac{1}{2}}$ , where  $\rho$  denotes mass density. In general, sound velocities are roots of the Christoffel equations:

$$\det (C_{ijkl}x_jx_k - \rho v^2\delta_{il}) = 0$$

where  $C_{ijkl}$  denotes the full fourth-rank elastic-stiffness tensor,  $x_j$  denotes components of the unit wave vector relative to cubic axes, and  $\delta_{ij}$  denotes the Kronecker delta. Thus, in an anisotropic medium,  $v$  depends on direction according to the elastic constants of the medium. Thus, in principle, one can determine the symmetry and the orientation of an anisotropic elastic body by measuring  $v$  in various directions.

In practice, one seldom uses the physical properties to study texture; usually via x-ray diffraction one obtains orientations of particular

crystallographic planes. Two references summarize the phenomenology of texture and the x-ray-diffraction approach: Wasserman and Grewen [1] and Barrett [2]. A single source dominates the description of mathematical texture-analysis: Bunge [3], which contains 302 references.

The present study used elastic constants, or, equivalently, sound velocities, to examine texture in 316-stainless-steel welds. These welds contained up to ten volume percent of delta ferrite .

## 2. Materials

From a commercial source, we obtained welds in the form of 2.5-cm plates of AISI-316 stainless steel. These were welded by a shielded-metal-arc process under the following conditions: E316L electrode, 30 amperes, 24 volts, 15-20 cm/min travel speed, 93-212°C interpass temperature, 25-33 passes. Table I gives chemical compositions. Table II gives some metallurgical properties. Further material characterization together with some mechanical-property measurements were given by Read et al. [4].

We prepared specimens for ultrasonic study by cutting, grinding, and polishing using usual metallographic procedures. These specimens were rectangular prisms measuring approximately 2.5 x 2.5 x 0.3-0.5 cm.

## 3. Sound-velocity measurements

Longitudinal-mode and transverse-mode sound velocities were determined by a pulse-echo method described in detail previously [5]. Briefly, rectangular prisms were prepared by grinding so that opposite faces were flat and parallel within 5  $\mu$ m. Quartz piezoelectric crystals with fundamental resonances between 4 and 7 MHz were cemented with phenyl salicylate to the specimens. An x-cut transducer was used for longitudinal waves and an ac-cut for transverse

waves. Ultrasonic pulses 1 to 2 cycles long were launched into the specimen by electrically exciting the transducer. The pulses propagated through the specimen, reflected from the opposite face, and propagated back and forth. The pulse echoes were detected by the transducer and displayed on an oscilloscope equipped with a time delay and a microprocessor for time-interval measurements. The sound velocity was computed by

$$v = 2\ell/t \quad (2)$$

where  $\ell$  denotes specimen length, and  $t$  the round-trip transit time. On the oscilloscope,  $t$  was the time between adjacent echoes, the first and second echoes usually being measured, and within these echoes the time between leading cycles. Elastic constants were computed from the general relationship

$$C = \rho v^2 \quad (3)$$

where  $\rho$  denotes mass density.

Extensional-mode sound velocities were determined by a Marx-oscillator method described elsewhere [6]. These measurements lead directly to Young's modulus via the relationship

$$E = 4\rho f^2 \ell^2 \quad (4)$$

where  $f$  denotes specimen resonance frequency and  $\ell$  denotes specimen length.

#### 4. Results

Figure 1 shows measured sound velocities versus ferrite content. In this figure, the first subscript indicates wave-propagation direction and the second indicates polarization direction. The dashed lines in Fig. 1 indicate the longitudinal and transverse sound velocities for nontextured 316 stainless

steel [7]. The co-ordinate system is:  $x_3$  perpendicular to welded plate,  $x_1$  along weld direction,  $x_2$  orthogonal to  $x_1$  and  $x_3$ . For specimen 5, Table III gives eight sound velocities;  $v_{23}$  could not be determined accurately and is not reported. (We assume  $v_{23} = v_{32}$ .) The set of nine velocities  $v_{ij}$  ( $i, j = 1, 2, 3$ ) correspond to all possible waves propagated and polarized along the principal axes  $x_1, x_2$ , and  $x_3$ . We measured no off-axis sound velocities. Also for specimen 5, the Young's modulus results were  $E_3 = 1.52$  and  $E_2 = 1.20 \cdot 10^{11} \text{ N/m}^2$ . Our specimens were too short along  $x_1$  to permit measurement of  $E$  along the weld direction.

## 5. Discussion

Figure 1 shows that the sound velocities and, therefore, the elastic constants of these stainless-steel welds do not vary strongly with composition. This suggests that the elastic constants of delta ferrite do not differ significantly from those of austenite. This is hardly surprising because the atomic volumes of the two phases differ by only one or two percent. Also, Ledbetter and Reed [8] showed for Fe-Ni alloys that the alpha-ferrite and austenite elastic constants do not differ dramatically.

For all cases, the longitudinal sound velocity  $v_{11}$  falls below the isotropic (nontextured) value, 0.569. This suggests the existence of texture in all the specimens. It is consistent with the  $\langle 100 \rangle$  fiber texture often suggested for these welds [9]. Ledbetter [10] calculated that a pure  $\langle 100 \rangle$  fiber texture requires  $v_{11} = 0.510$ .

One expects that cubic-symmetry crystallites in welds occur either with random orientations or with a single preferred axis parallel to the principal heat-flow direction, denoted  $x_3$ . In the  $x_1$ - $x_2$  plane, crystallites are expected to orient themselves randomly because no preferred heat-flow direction occurs in that plane. Thus, an effective fiber texture occurs with



$x_3$  being the fiber axis. Macroscopically, such a material exhibits transverse-isotropic symmetry, with five independent elastic constants. This is equivalent to hexagonal symmetry. In Voigt's contracted  $C_{ij}$  notation the symmetrical elastic-stiffness matrix is:

$$C_{ij}^H = \begin{bmatrix} C_{11}^H & C_{12}^H & C_{13}^H & 0 & 0 & 0 \\ & C_{11}^H & C_{13}^H & 0 & 0 & 0 \\ & & C_{33}^H & 0 & 0 & 0 \\ & & & C_{44}^H & 0 & 0 \\ & & & & C_{44}^H & 0 \\ & & & & & C_{66}^H \end{bmatrix} \quad (5)$$

where  $C_{66}^H = \frac{1}{2}(C_{11}^H - C_{12}^H)$ . Thus, the theoretical problem is to express the five hexagonal-symmetry elastic constants,  $C_{ij}^H$ , in terms of the three cubic-symmetry elastic constants:  $C_{11}$ ,  $C_{12}$ ,  $C_{44}$ .

Present theory does not permit calculation of the elastic constants of textured polycrystalline aggregates of cubic-symmetry crystallites. This is a special and more difficult case of determining the average elastic constants of a random polycrystalline aggregate. For this latter problem, Landau and Lifshitz [11] remind us that "there is ... no general relationship between the moduli of elasticity of a polycrystal and those of a single crystal of the same substance." The fiber-texture case involves a two-dimensional, rather than a three-dimensional, average.

However, elastic-constant bounds can be calculated for textured aggregates. In this study we calculate the Voigt (constant strain) and Reuss

(constant stress) bounds and use Hill's suggestion of an arithmetic average to estimate the elastic constants. This approach turns out to be quite reasonable because the Voigt and Reuss bounds do not differ dramatically (a maximum of 37 percent). And for the important <100>-texture case, the bounds coincide for three elastic constants:  $C_{13}^H$ ,  $C_{33}^H$ , and  $C_{44}^H$ . Thus, we know these three constants unambiguously. Kröner and Wawra [12] explain the systematics of this bounds coincidence, and they give the following expressions for the  $C_{ij}^H$ :

$$\begin{aligned}
 C_{11}^H &= C_1 + 3\beta C_3 = \frac{1}{4}(3C_{11} + C_{12} + 2C_{44}) \\
 C_{12}^H &= C_2 + \beta C_3 = \frac{1}{4}(C_{11} + 3C_{12} - 2C_{44}) \\
 C_{13}^H &= C_2 - 4\beta C_3 = C_{12} \\
 C_{33}^H &= C_1 - 8\beta C_3 = C_{11} \\
 C_{44}^H &= \frac{1}{2}(C_1 - C_2) - 4\beta C_3 = C_{44}
 \end{aligned}
 \tag{6}$$

where

$$\begin{aligned}
 5C_1 &= 3C_{11} + 2C_{12} + 4C_{44} \\
 5C_2 &= C_{11} + 4C_{12} + 2C_{44} \\
 C_3 &= C_{11} - C_{12} - 2C_{44}
 \end{aligned}
 \tag{7}$$

where

$$\beta = 1/20 \text{ for } \langle 100 \rangle \text{ fiber texture.}$$

Apparently, relationships for the  $S_{ij}$ , which give the Reuss bounds by matrix inversion, do not appear in the literature. These are:

$$S_{11}^H = \frac{1}{8}(6S_{11} + 2S_{12} + S_{44})$$

$$S_{12}^H = \frac{1}{8}(2S_{11} + 6S_{12} - S_{44})$$

$$S_{13}^H = S_{12} \tag{8}$$

$$S_{33}^H = S_{11}$$

$$S_{44}^H = S_{44}$$

$$S_{66}^H = 2(S_{11}^H - S_{12}^H) = S_{11} - S_{12} - S_{44}/2$$

In deriving these relationships, one must remember that the inverse  $C_{ijkl}^{-1}$  of a fourth-rank elasticity tensor relates to the inverse  $C_{\alpha\beta}^{-1}$  of its associated 6 x 6 matrix by a factor multiplied times  $C_{ijkl}^{-1}$ . This factor is 4 if both  $\alpha$  and  $\beta$  exceed 3, is 2 if either  $\alpha$  and  $\beta$  exceeds 3, and is 1 if neither  $\alpha$  nor  $\beta$  exceeds 3.

The most dramatic result of our measurements, as shown in Fig. 1, is the splitting of the isotropic  $v_{13} = v_{12} = 0.307$  shear velocity into two velocities  $v_{13} = 0.381$  and  $v_{12} = 0.228$ , on average. One expects the shear-wave birefringence to provide a more sensitive probe of texture than the smaller shift in the longitudinal velocity. This arises because, even for highly anisotropic cubic crystals,  $v_\ell$  depends only slightly on direction [13]. However, this particular  $v_t$  splitting is inconsistent with a  $\langle 100 \rangle$  fiber texture for which Ledbetter [10] showed that the two velocities should be 0.384 and 0.289. That is,  $v_{12} = 0.228$  is much too low for a  $\langle 100 \rangle$  fiber texture.

Departure of measurement from a  $\langle 100 \rangle$  fiber texture is shown schematically in Fig. 2. At the top, Fig. 2 gives the bounds of Voigt (upper) and Reuss (lower). Any type of texture in any amount must produce velocities

within these bounds. Our measurements meet this criterion. For the shear mode, we found velocities very close to both the upper and lower bounds, which correspond to  $C_{44}$  and to  $C' = (C_{11} - C_{12})/2$ , respectively. Thus, the fcc monocrystalline  $C_{44}$  and  $C'$  must be two of the principal elastic constants of the textured aggregate. Again, the often-suggested  $\langle 100 \rangle$  fiber texture fails as a possible texture because its elastic constants contain  $C_{44}$  but not  $C'$ . If we assume another texture element, in addition  $\langle 100 \rangle$  in the weld direction, the situation worsens, as Fig. 2 shows. The situation improves if we assume  $\langle 110 \rangle$  in the weld direction; this amounts to a (001)[110] texture. Figure 2 shows that this ideal texture explains the range of shear velocities, but not the detailed measurements without some perturbations. Possible perturbations include partial texture, a second texture, and deviations from a (001) plane or a [110] direction (or both).

## 6. Summary

The present study produced the following conclusions concerning the elastic constants and sound velocities of 316-stainless-steel welds:

1. Up to at least ten-percent delta-ferrite content, the elastic constants are independent of ferrite content.
2. All specimens exhibit texture and significant departures from quasi-isotropic physical-property values. The texture is independent of ferrite content.
3. For these materials, the usual model,  $\langle 110 \rangle$  fiber texture, fails to explain the measurements.



4. Calculated results for several other textures show that the elastic constant  $C' = (C_{11} - C_{12})/2$  or a [110] texture element, enters essentially into the weld's texture.
5. A postulated texture -- (001)[110] -- covers the range of eight measured sound velocities, but not the details of their distribution. Some other, presently unknown, element of texture must also occur.

#### Acknowledgment

This study arose from research sponsored by the U.S. DoE Office of Fusion Energy.

#### References

- [1] G. Wasserman and J. Grewen, "Texturen metallischer Werkstoffe" (Springer-Verlag, Berlin, 1962).
- [2] C. S. Barrett, "Structure of Metals" (McGraw-Hill, New York, 1952).
- [3] H.-J. Bunge, "Texture Analysis in Materials Science" (Butterworths, London, 1982).
- [4]. D. T. Read, H. J. McHenry, P. A. Steinmeyer, and R. D. Thomas, Weld Res. J. Suppl. 59 (1980) 104s.
- [5]. H. M. Ledbetter, N. V. Frederick, and M. W. Austin, J. Appl. Phys. 51 (1980) 305.
- [6] H. M. Ledbetter, Cryogenics 20 (1980) 637.
- [7] H. M. Ledbetter, Metal Sci. 14 (1980) 595.
- [8] H. M. Ledbetter and R. P. Reed, J. Phys. Chem. Ref. Data 2 (1973) 531.
- [9] B. R. Dewey, L. Adler, R. T. King, and K. V. Cook, Exper. Mech. 17 (1977) 2.
- [10] H. M. Ledbetter, in "Review of Progress in Quantitative Nondestructive Evaluation, Volume 1" (Plenum, New York, 1982) p. 619.

- [11] L. D. Landau and E. M. Lifshitz, "Theory of Elasticity" (Pergamon, London, 1959) p. 40.
- [12] E. Kröner and H. H. Wawra, Philos. Mag. A38 (1978) 433.
- [13] H. M. Ledbetter and R. L. Moment, Acta Metall. 24 (1976) 891.

Table I. Chemical compositions, weight percent, balance Fe

Specimen	Cr	Ni	Mo	Mn	C	N	Nb	Si	S	P
1	18.47	13.97	2.25	1.72	0.031	0.042	0.14	0.58	0.011	0.033
2	18.64	12.97	2.29	1.72	0.030	0.046	0.14	0.56	0.012	0.034
3	19.20	12.01	2.32	1.70	0.034	0.042	0.15	0.57	0.009	0.034
4	19.66	11.06	2.18	1.76	0.028	0.067	0.15	0.59	0.008	0.029
5	18.69	12.85	2.25	1.75	0.059	0.044	0.15	0.56	0.009	0.033

Table II. Metallurgical properties

Specimen	Ferrite (volume percent)	Ferrite Number	Mass Density (g/cm <sup>3</sup> )
1	0.13	0.12	7.932
2	4.1	4.5	7.934
3	8.5	9.2	7.921
4	10.1	11.0	7.910
5	1.2	1.3	7.930

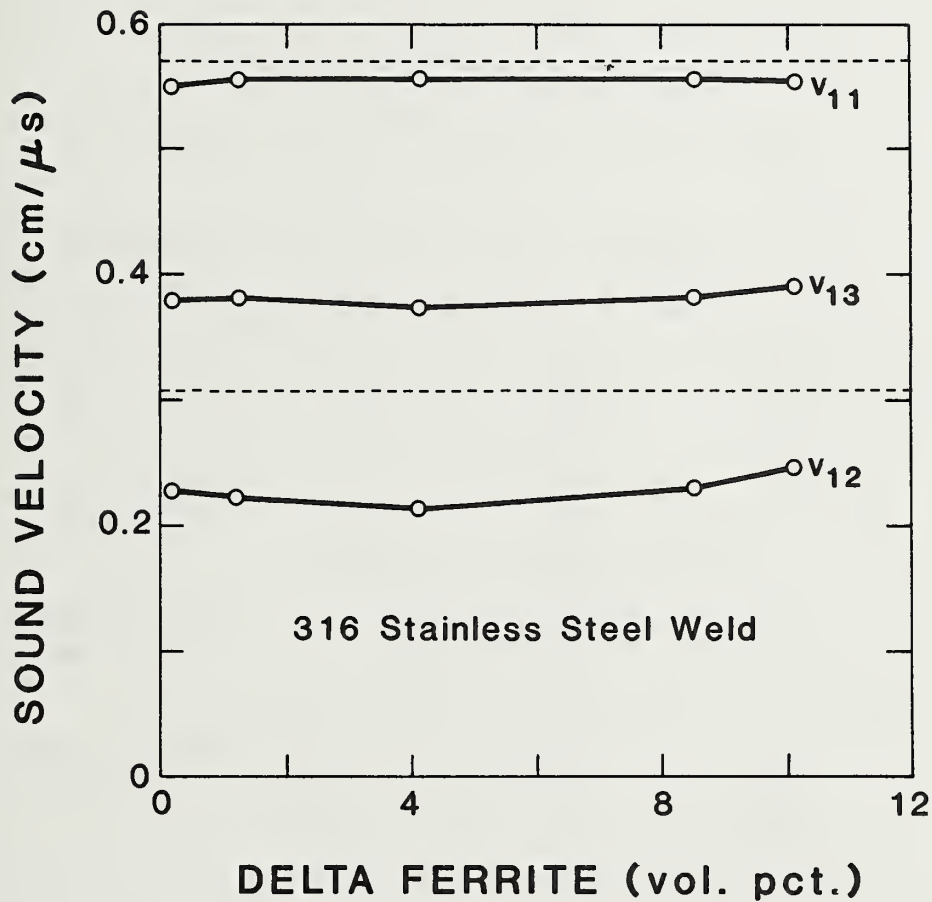
Table III. Sound velocities in specimen 5 in units of cm/ $\mu$ s

$v_{11} = 0.555$	$v_{22} = 0.568$	$v_{33} = 0.538$
$v_{12} = 0.222$	$v_{21} = 0.260$	$v_{31} = 0.363$
$v_{13} = 0.381$	$(v_{23} = 0.387)$	$v_{32} = 0.387$

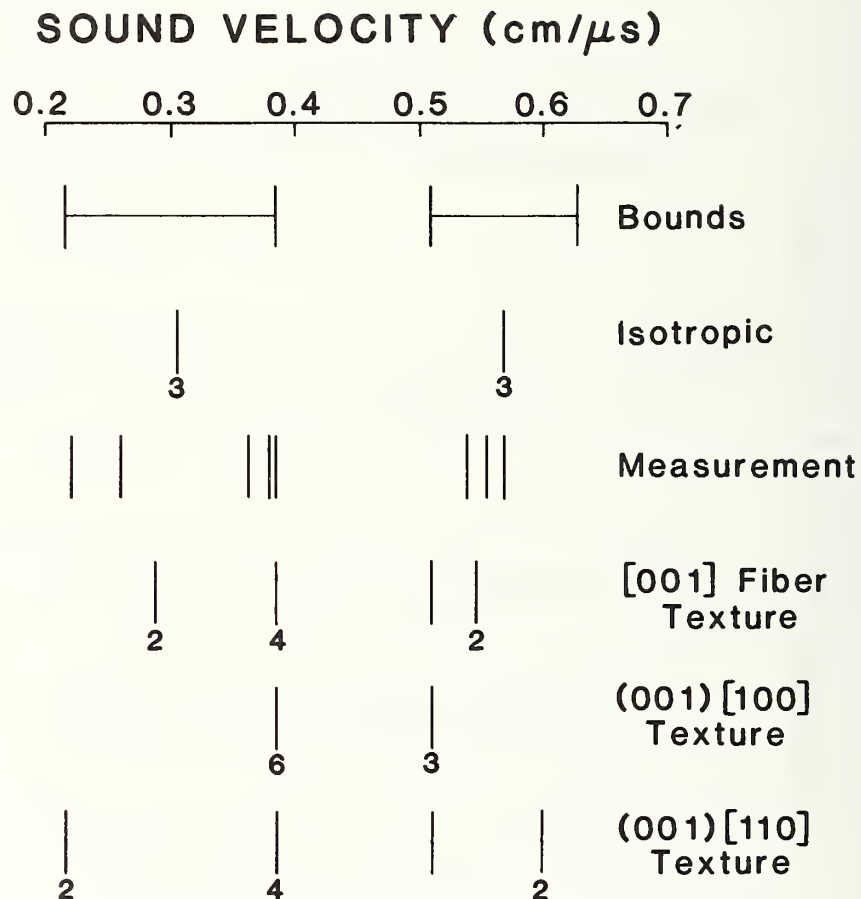


### Figure Captions

1. Longitudinal and transverse sound velocities versus delta-ferrite content for 316-stainless-steel welds. Dashed lines indicate isotropic (nontextured) velocities: upper = longitudinal, lower = transverse.
2. Longitudinal and transverse sound velocities for 316-stainless-steel welds. Small numerals indicate n-fold degeneracy.



1. Longitudinal and transverse sound velocities versus delta-ferrite content for 316-stainless-steel welds. Dashed lines indicate isotropic (nontextured) velocities: upper = longitudinal, lower = transverse.



2. Longitudinal and transverse sound velocities for 316-stainless-steel welds. Small numerals indicate n-fold degeneracy.

## ***NONMETALLICS***





## NONMETALLICS PROGRAM

LEADERS: M. B. Kasen, H. M. Ledbetter, NBS

STAFF: M. W. Austin, R. D. Kriz, R. E. Schramm, NBS

CONTRACTS: S. K. Datta, University of Colorado

### OBJECTIVES:

- (1) To measure, model, and understand the properties of composites that enter essentially into the conception, design, construction, operation, and performance of magnetic-fusion-energy equipment.
- (2) To cooperate with industry to establish and refine cryogenic-grade specifications for insulating laminates and coding systems for laminates.

### RESEARCH PAST YEAR (1982):

- (1) Kriz, Ledbetter. Ultrasonic measurement of the complete nine-component elastic-constant tensor of a woven glass-fiber/epoxy composite.
- (2) Kriz. Calculated stress distributions in a woven composite by a finite-element model.
- (3) Datta, Ledbetter, Kriz. Predicted elastic constants of transversely isotropic composites containing anisotropic fibers.
- (4) Ledbetter, Kriz. Elastic-wave surfaces in fiber-reinforced composites.
- (5) Datta, Ledbetter, Austin, Kriz. Longitudinal wave propagation in an elastic composite thin rod.
- (6) Kasen, Schramm. Screening, down to 76 K, of samples of G-10CR produced by two new manufacturers of this product.
- (7) Kasen. Continuation of a program on the standardization of cryogenic grades of insulating and structural laminates in cooperation with industry.

### RESEARCH THIS YEAR (1983):

- (1) Kriz, Ledbetter, Datta. Modeling of laminated composite elastic properties.
- (2) Ledbetter, Austin. Anisotropic thermal expansion of glass-fiber/epoxy composites: measurements and modeling.
- (3) Ledbetter, Datta. Anisotropic thermal expansion of uniaxial, fiber-reinforced composites: measurements and modeling.
- (4) Kasen. Development of improved test methods for determining the effect of cryogenic temperatures on composite material performance.



Variability in Mechanical Performance of G-10CR  
Cryogenic-Grade Insulating Laminates\*

M. B. Kasen and R. E. Schramm  
Fracture and Deformation Division  
National Bureau of Standards  
Boulder, CO 80303

ABSTRACT

An assessment is made of the variability in cryogenic mechanical performance of insulating laminates produced by five manufactureres to a common component and procedure specification. Results at 295 K and 76 K indicate that the specification is adequate to ensure the desired degree of product uniformity.

\* Published in Cryogenics, Vol. 23, No. 5, 279-280 (1983).





Five United States firms have produced a controlled grade of glass-fabric reinforced epoxy high pressure industrial laminates designated G-10CR. This laminate grade was originally intended to provide designers of superconducting magnets for magnetic fusion energy research with commercial sources of an insulating laminate having minimum performance variability at 4 K. Laminate production is controlled by component and manufacturing specifications developed cooperatively by industry and the National Bureau of Standards.<sup>1</sup> The basic mechanical, thermal, and electrical performance of this grade has been investigated;<sup>2</sup> however, little information has been available on the variability in performance of laminates produced to the specification by different companies. NBS therefore undertook to assess this variability by comparing the effect of cryogenic temperatures on tensile, compressive, and interlaminar shear properties of G-10CR products produced by the five companies. Only the warp direction of reinforcement in the plane of the laminate was considered, and testing was confined to 295 K and 76 K.

The results, obtained by procedures described elsewhere,<sup>2</sup> are summarized in Table 1. This Table reports averages, standard deviations, and coefficients of variance for the nine to eleven specimens tested in assessing each parameter. Lower tolerance limits on the properties are also reported, based on confidence limits of 99% and a confidence coefficient of 0.95. Assuming that the distribution of test results is normal, and that the materials evaluated are representative of commercial products produced by each company, there is a 95% probability that 99% of the production will produce values higher than the lower tolerance limits. The assumption of a normal distribution of strength properties may be questioned--in particular, at cryogenic temperatures where the matrix becomes embrittled. However, there were insufficient data available to justify assuming a different distribution, and the error introduced by this assumption is probably small. In Table 2, the

\*Contribution of NBS, not subject to copyright in the U.S.A.

mechanical property data are given separately for the G-10Cr products of each manufacturer.

Data on the coefficient of variation and on lower tolerance limits for tensile strain at failure are not reported because failure of the strain gages at stresses below maximum required that this parameter be estimated from a strip chart recording. This significantly reduced the accuracy of the measurements, and precluded determination of a meaningful variability.

When applied to a single production lot of G-10CR, our test procedures produced coefficients of variation of about four percent for tensile strength, Young's modulus, and shear strength, and about nine percent for compressive strength, Poisson's ratio, and failure strain. This suggests that the coefficients of variation in the present study primarily reflect uncertainties in the test procedure and intrinsic material variability. It is therefore concluded that differences in room or cryogenic mechanical performance of products produced to the G-10CR specification by different companies are probably not statistically significant. The specification therefore appears adequate to ensure the desired product uniformity. The coefficient of variation is higher at 76 K than at 295 K for most properties. This is an expected consequence of matrix embrittlement, which severely limits the operative relaxation processes, making the strength properties more sensitive to the presence of small flaws. Residual stresses combined with the possibility of microcracking also increase the variability in the elastic properties at cryogenic temperatures as compared to room temperature.

It should be emphasized that G-10CR products are highly anisotropic, the values for the warp direction of reinforcement being the highest available in the plane of the laminate. Performance in the fill direction will be substantially lower<sup>2</sup>, as will the performance for stresses applied in orientations intermediate between the warp and fill directions. Furthermore, this study was limited to evaluation of cryogenic performance at 76 K, whereas the functional use of the materials is at 4 K. Testing at 4 K would have yielded somewhat higher strengths and moduli<sup>2</sup>, but would also be expected to increase the coefficient of variation.

There is reason to believe that the average and lower tolerance limits for the compression and interlaminar shear properties in Table 1 may be somewhat lower than those representative of bulk material properties. Recent data have suggested that the compression specimen used in this study may be

sensitive to edge effects, causing premature failure. There is also reason to believe that the guillotine method used to evaluate interlaminar shear in this study yields values that are somewhat below the true bulk shear values. It is therefore probable that these values are conservative.

This work was supported by the Office of Fusion Energy, U. S. Department of Energy.

### Terminology

- $\sigma_T$  = Ultimate tensile strength
- $\sigma_C$  = Ultimate compressive strength
- $E_T$  = Young's modulus in tension
- $\nu$  = Poisson's ratio
- $\epsilon_T$  = Ultimate failure strain in tension
- $\sigma_{ILS}$  = Ultimate interlaminar shear strength

### References

1. Kasen, M. B., in Nonmetallic Materials and Composites at Low Temperatures-2, G. Hartwig and D. Evans, eds., Plenum Press, NY (1982), 327.
2. Kasen, M. B., MacDonald, G. R., Beekman, D. H., and Schramm, R. E., Adv Cryo Eng, 26 (1980) 235.

Table 1. Performance of G-10CR cryogenic-grade insulating laminates

Property	Average	Standard Deviation	Coefficient of Variation	Lower Tolerance Limit <sup>1</sup>
<u>295 K</u>				
$\sigma_T$	431 MPa	27.0 MPa	6.26%	306 MPa
$\sigma_C$	390 MPa	30.8 MPa	7.89%	254 MPa
$E_T$	27.8 GPa	1.29 GPa	4.64%	22.0 GPa
$\nu$	0.159	0.014	8.67%	0.098
$\epsilon_T$	1.97%	0.35%	---	---
$\sigma_{ILS}$	48.1 MPa	2.48 MPa	5.17%	33.7 MPa
<u>76 K</u>				
$\sigma_T$	817 MPa	71.4 MPa	8.74%	500 MPa
$\sigma_C$	703 MPa	52.1 MPa	7.41%	472 MPa
$E_T$	32.1 GPa	2.72 GPa	8.47%	20.1 GPa
$\nu$	0.208	0.023	11.2%	0.106
$\epsilon_T$	3.05%	0.395%	---	---
$\sigma_{ILS}$	68.7 MPa	5.99 MPa	8.72%	43.0 MPa

<sup>1</sup>Confidence limits 99%  
Confidence coefficient 0.95

Table 2. G-10 CR Screening

Temp, K	Young's Modulus GPa	Young's Modulus Msi	Poisson's Ratio	Ultimate Tensile Strength MPa	Ultimate Tensile Strength Ksi	Ultimate Tensile Strain, %	Ultimate Compressive Strength MPa	Ultimate Compressive Strength Ksi	Interlaminar Strength MPa	Shear (Guillotine) Ksi	Interlaminar Shear Strength (Short Beam) MPa	Interlaminar Shear Strength (Short Beam) Ksi
Manufacturer A-Warp (Production Plant)												
295	27.4 28.3	3.97 4.11	0.170 0.180	429	62.2	1.9	381 367	55.3 53.2	51.1 48.2	7.41 6.98	55.7 58.7	8.08 8.51
76	30.4 32.3	4.40 4.68	0.213 0.231	891 865	129 125	3.8 3.3	687 704	99.6 102	80.8 66.3	11.7 9.62	137 134	19.8 19.5
Manufacturer B-Warp												
295	27.8 29.2	4.03 4.23	0.154 0.157	417 421	60.5 61.1	1.7 1.6	429 414	62.2 60.0	>41.4* >43.0*	> 6.01* > 6.23*	58.9 57.6	8.54 8.35
76	33.0 35.2	4.79 5.10	0.217 0.220	872 881	126 128	3.3 3.1	682 778	98.9 113	64.3 59.3	9.33 8.60	130 135	18.9 19.6
Manufacturer C-Warp												
295	26.3 25.7	3.82 3.73	0.146 0.134	410 394	59.4 57.1	1.8 2.5	342 337	49.6 48.8	>51.4* >48.8*	> 7.40* > 7.07*		
76	32.9 29.8	4.77 4.32	0.195 0.147	763 721	111 105	2.4 2.8	733 665	106 96.5	70.3 72.4	10.2 10.5		
Manufacturer D-Warp												
295	29.0 29.6	4.21 4.29	0.174 0.151	454 477	65.8 69.2	1.8 2.6	395 360	57.3 52.2	49.2 47.7	7.14 6.92		
76	33.3 34.6	4.83 5.02	0.218 0.215	877 839	127 122	3.3 2.9	698 794	101 115	73.6 70.7	10.7 10.3		
Manufacturer E-Warp												
295	28.0 26.7	4.06 3.87	0.162 0.165	414 459	60.0 66.7	1.8 2.0	382 407	55.5 59.1	43.6 48.6	6.33 7.09		
76	35.7 35.3	5.17 5.12	0.207 0.215	731 731	106 106	2.9 2.7	657 630	95.4 91.5	61.1 69.2 66.7	8.94 10.0 9.68		

\* Broke in tension, not shear





\* EFFECT OF CRYOGENIC TEMPERATURES ON THE MECHANICAL PERFORMANCE OF  
GLASS-FABRIC-REINFORCED EPOXY AND POLYIMIDE MATRIX LAMINATES

M. B. Kasen, R. E. Schramm, and R. D. Kriz

Fracture and Deformation Division, National Bureau of Standards, Boulder, Colorado, USA

Radiation-resistant laminates are required for insulators and structural supports in the superconducting magnets of magnetic fusion energy systems. Glass-reinforced laminates fabricated with a polyimide matrix have a much higher tolerance to neutron and gamma radiation at 4 K than do laminates fabricated with an epoxy matrix. However, tests indicate that the mechanical performance of polyimide-matrix laminates is inferior to that of the epoxy type, whereas their elastic performance is superior. Fractographic studies show that the performance difference is due to a lower integrity of the polyimide-glass interface.

\* Published, Proceedings of the International Cryogenic Materials Conference, Kobe, Japan, 11-14 May 1982, Editors K. Tachikawa, A. Clark (Butterworths, UK, 1983).



## INTRODUCTION

Conventional epoxy-matrix glass-reinforced insulating laminates have been used for many years in superconducting magnet construction, but recent studies have shown that such laminates degrade rapidly when exposed to 100 kGy (1 Gray = 1 J/kg = 100 rads) of gamma radiation at 5 K [1]. Polyimide-matrix laminates degrade much less rapidly [2]; however, such laminates have disadvantages in basic performance and cost. This paper describes a program comparing the effect of cryogenic temperatures on the mechanical and elastic performance of the two laminate types. Our materials and those for the radiation tests were from the same manufacturer.

## MATERIALS AND PROCEDURES

This study compares performance of a standard bisphenol A epoxy-matrix cryogenic grade of high-pressure industrial laminate, G-10CR [3,4], with that of a laminate of similar construction utilizing a polyimide matrix, designated PG-10CR in this paper. Tensile, compressive, and interlaminar shear strength, elastic modulus and Poisson's ratio, and tensile ultimate strain were determined for each at 295 K, 76 K, and 4 K using test procedures previously described [3]. Data from two specimens of PG-10CR are compared with data from three to six specimens of G-10CR for each test condition at each temperature. Both warp and fill direction properties of the laminates were studied.

A scanning electron microscope (SEM) fractographic examination was performed on specimens of each laminate type fractured in tension, compression, and shear at each temperature to associate failure modes with property variability.

## RESULTS

### Mechanical Properties

Figure 1 illustrates the range encompassed by tests in the warp direction for the two laminate types. Tensile and compressive strength of the polyimide laminate were

found to be 20-40% lower than that of the epoxy laminate at cryogenic temperatures. Interlaminar shear strength of the polyimide laminate was lower by the same amount at all temperatures as was the strain-to-failure in tension. Young's modulus of the polyimide laminate was 10-20% higher than that of the epoxy laminate at all temperatures.

#### Fractography

Fractographic evidence suggested that the lower strength of the polyimide laminate at cryogenic temperatures was primarily due to low integrity of the polyimide-glass interface. As illustrated by Fig. 2, the polyimide laminate shattered during tensile failure at cryogenic temperatures, leaving the fibers near the fracture almost entirely devoid of resin and causing severe delamination well away from the fracture. By contrast, Fig. 3 illustrates that the epoxy laminate failed much more locally under the same conditions, with fiber bundles retaining a large amount of resin. The higher magnification views in these figures clearly show that the polyimide laminate failed cleanly at the glass surface, and the epoxy laminate failed through the resin at some distance from the glass surface. This difference in failure mode is clearly temperature dependent, since relatively little difference in tensile failure mode was found between the two laminate types at room temperature.

The lower interlaminar shear strength of the polyimide laminate is also attributable to inability of the interface to sustain appreciable shear stresses. The failure surface was again characterized by clean glass fibers and absence of the resin matrix. In contrast, the failure surface of the epoxy laminate showed a high degree of resin retention. Fractographic examination showed that the high interlaminar shear strength of the epoxy laminate at cryogenic temperatures was caused, in part, by tensile failure of some glass fibers, evidencing the ability of the glass-epoxy interface to transfer shear stresses into the fibers efficiently.

#### CONCLUSION

The inferior mechanical performance of the glass-polyimide laminate, as compared with that of the glass-epoxy laminate, is attributable to poor integrity of the glass-polyimide interface. This deficiency is exacerbated by cooling to cryogenic temperatures and is particularly damaging to the shear properties of the laminate.

#### LIST OF SYMBOLS

$T(K)$  = temperature, kelvins

$E$  = Young's modulus

$\nu$  = Poisson's ratio

$\epsilon_{TU}$  = tensile ultimate strain

$\sigma_{TU}$  = tensile ultimate stress

$\sigma_{CU}$  = compressive ultimate stress

$\sigma_{I.L.S}$  = interlaminar shear ultimate stress

#### ACKNOWLEDGMENTS

This work was supported by the Office of Fusion Energy, U.S. Department of Energy. We thank Mr. J. R. Benzinger of the Spaulding Fibre Company for providing the test materials.



# REFERENCES

- 1 Coltman, R.R., Klabunde, C.E., Kernohan, R.H., and Long, C.J. Radiation Effects on Organic Insulators for Superconducting Magnets, ORNL/TM-7077, Oak Ridge National Laboratory, Oak Ridge, Tennessee, 1979.
- 2 Coltman, R.R., Klabunde, C.E., and Long, C.J. The Effect of a 100 MGy ( $10^{10}$  rads) Gamma-Ray Dose at 5 K on the Strength of Polyimide Insulators, Report SSD No. 81-10, Oak Ridge National Laboratory, Oak Ridge, Tennessee, 1981.
- 3 Kasen, M.B., MacDonald, G.R., Beekman, D.H., and Schramm, R.E. "Mechanical, electrical and thermal characterization of G-10CR and G-11CR glass-cloth/epoxy laminates between room temperature and 4 K," A.F. Clark and R.P. Reed (eds.), in Advances in Cryogenic Engineering (Materials), vol. 26, pp. 235-244, Plenum Publishing Corporation, New York, 1980.
- 4 Benzinger, J.R. "Manufacturing capabilities of CR-grade laminates," A.F. Clark and R.P. Reed (eds.), in Advances in Cryogenic Engineering (Materials), vol. 26, pp. 252-258, Plenum Publishing Corporation, New York, 1980.

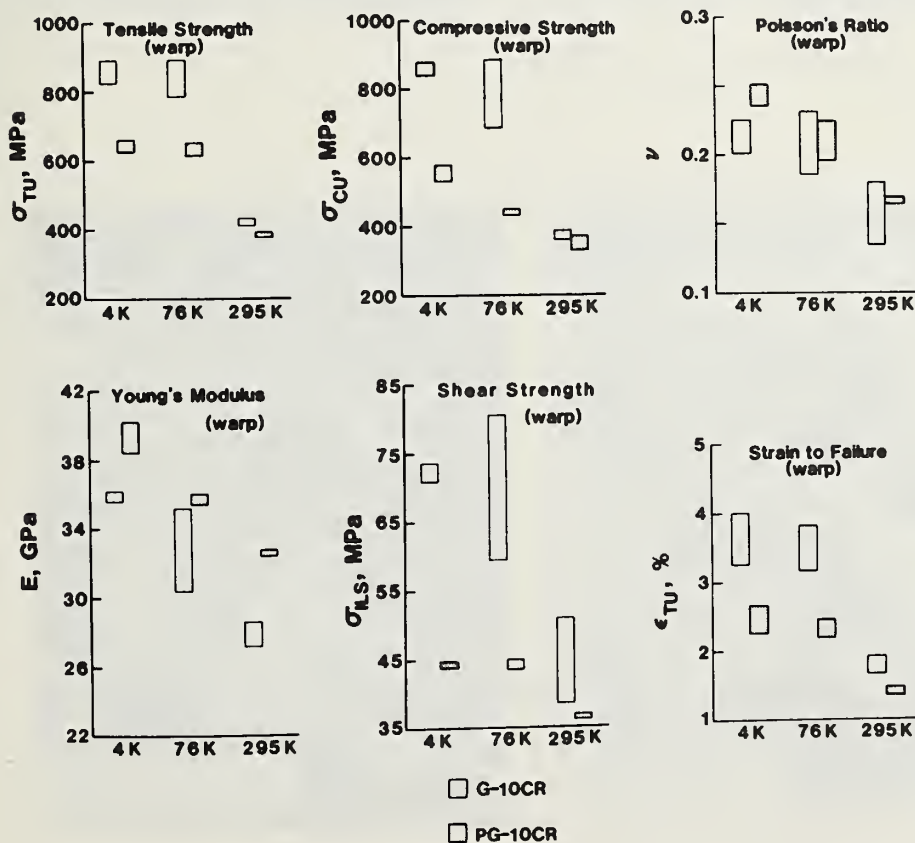


Fig. 1. Comparative range of mechanical properties for epoxy matrix (G-10CR) and polyimide matrix (PG-10CR) laminates.

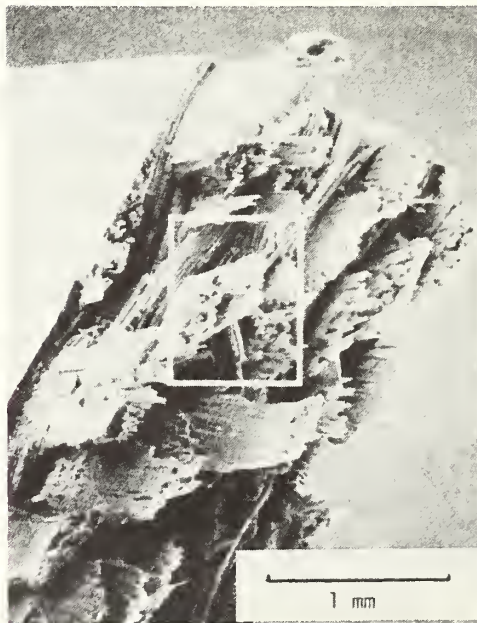


a

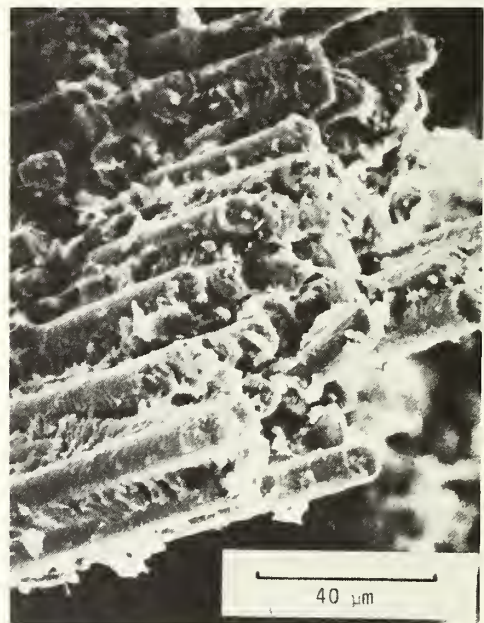


b

Fig. 2.4-K tensile failure, glass-polyimide.



a



b

Fig. 3.4-K tensile failure, glass-epoxy.

ELASTIC STIFFNESS AND LOCAL STRESSES IN WOVEN-FABRIC  
COMPOSITES AT 77 K

Ronald D. Kriz  
Fracture and Deformation Division  
National Bureau of Standards  
Boulder, Colorado 80303



Woven-fabric composites are commonly used in superconducting magnets and in containment of cryogenic liquids. Here, the mechanical response of a plain-weave laminated composite at cryogenic temperatures is studied by predicting the load-deformation response of a fundamental "unit cell". The unit cell is the smallest repeating geometrical structural unit such that 90-degree rotations about the axis normal to the fabric plane yield four identical patterns. The model assumes that generalized plane strain exists on all four faces of the unit cell. Hence the elastic response of the unit cell can be predicted by studying the three-dimensional load-deformation response within a single plane parallel to the load direction as shown in Fig. 1. Stiffness and stresses within this plane are calculated for worst-case load conditions prior to fracture. A finite-element model is used to predict unit-cell stresses and stiffnesses.

Several load conditions of tension, shear, and compression are possible. Preliminary results given here focus on tensile loads,  $N_x$ , shown in Fig. 1. The displacements within the x-z plane are linear functions of x, y, and z coordinates and out-of-plane strain,  $\epsilon_y$ :



$$\begin{aligned}
u &= a_1 + a_2x + a_3z \\
v &= a_4 + a_5x + a_6z + y\epsilon_y \\
w &= a_7 + a_8x + a_9z
\end{aligned} \tag{1}$$

where the  $a_i$  terms are evaluated in terms of nodal displacements. The in-plane and out-of-plane strains,  $\epsilon_x$  and  $\epsilon_y$ , are calculated from thin-laminate-plate theory assuming zero stresses through the thickness:

$$\epsilon_x = A_{yy}N_x / (A_{xx}A_{yy} - A_{xy}^2), \quad \epsilon_y = -A_{xy}N_x / (A_{xx}A_{yy} - A_{xy}^2) \tag{2}$$

where  $A_{xx}$ ,  $A_{yy}$ , and  $A_{xy}$  are laminate midplane stiffnesses. Here a laminate load ( $N_x=1751\text{N/cm}$ ) yields  $\epsilon_x = 0.01095$  and  $\epsilon_y = 0.001741$  with elastic properties taken from Table 1. A worst-case thermal load of  $\Delta T = -318\text{ K}$  is chosen at  $77\text{ K}$  assuming a strain-free state at  $395\text{ K}$  (cure temperature).

With these load conditions we study the elastic mechanical response and internal stress states of the unit cell. In Fig. 2 the influence of warp-fiber orientation,  $\theta$ , on the elastic response of the unit cell is shown. As expected, the elastic modulus increases with decreasing angle. Regions of highest stress concentration prior to fracture are observed along lines a-b and c-d of Fig. 1. These stress distributions are plotted in Figs. 3 and 4. As expected, larger compressive stresses are observed along line a-b of Fig. 3 with increasing warp angle. The influence of the thermal load increases the compressive stress for the  $45^\circ$  case. Stresses normal to the warp interface increase with increasing warp angle; the largest effect occurs in the matrix region. The thermal

load increases the  $45^\circ$  normal stresses in the matrix region and decreases these stresses in the fill region. Thus, the matrix region is most affected by thermal loads and warp-fiber orientations.

We continue parametric studies of the load-deformation response of the unit cell for other load cases, including the redistribution of stresses caused by the presence of cracks in the fill fiber bundles. This model permits us to evaluate other elastic properties such as shear modulus in the x-z plane. We plan to report these results later.

Table 1. Glass/epoxy properties

Isotropic constituents	Young's modulus, $E$ (GPa)	Shear modulus, $G$ (GPa)	Poisson's ratio, $\nu$
Bisphenol-A epoxy	7.16	2.768	0.293
S-glass fiber	82.22	32.55	0.263

Transversely isotropic composite	$E_l$ (GPa)	$E_t$ (GPa)	$G_{lt}$ (GPa)	$G_{tt}$ (GPa)	$\nu_{lt}$	$\nu_{tt}$
Glass/epoxy ( $V_f^*=0.5$ )	44.69	17.88	6.801	6.888	0.278	0.298

Coefficients of thermal expansion	$\alpha_l$ $\mu\text{m/m/K}$	$\alpha_t$ $\mu\text{m/m/K}$
Glass/epoxy ( $V_f^*=0.5$ )	5.963	23.39

\* Volume fraction ( $V_f$ ) of glass fibers

Subscripts : (l) indicates fiber direction and (t) indicates transverse plane

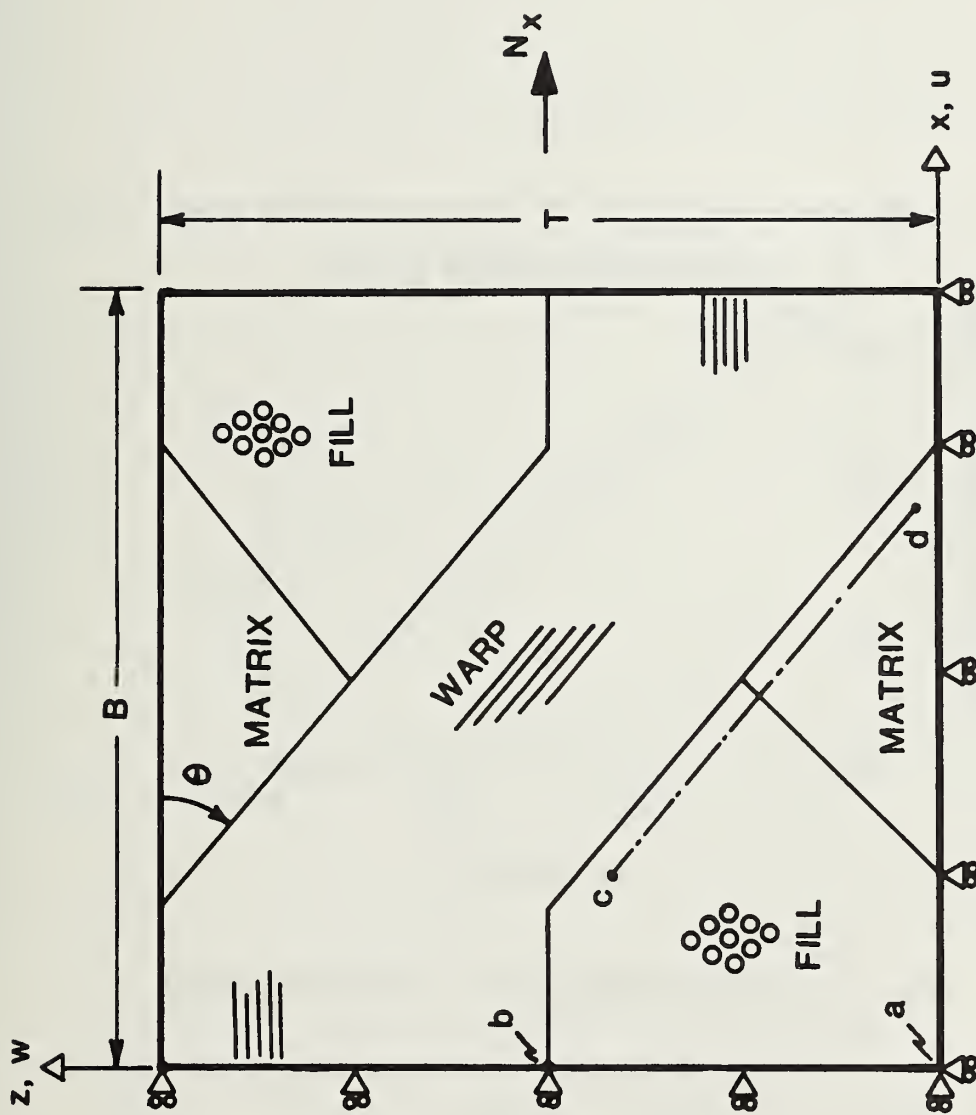


Fig. 1 Thin slice of unit cell

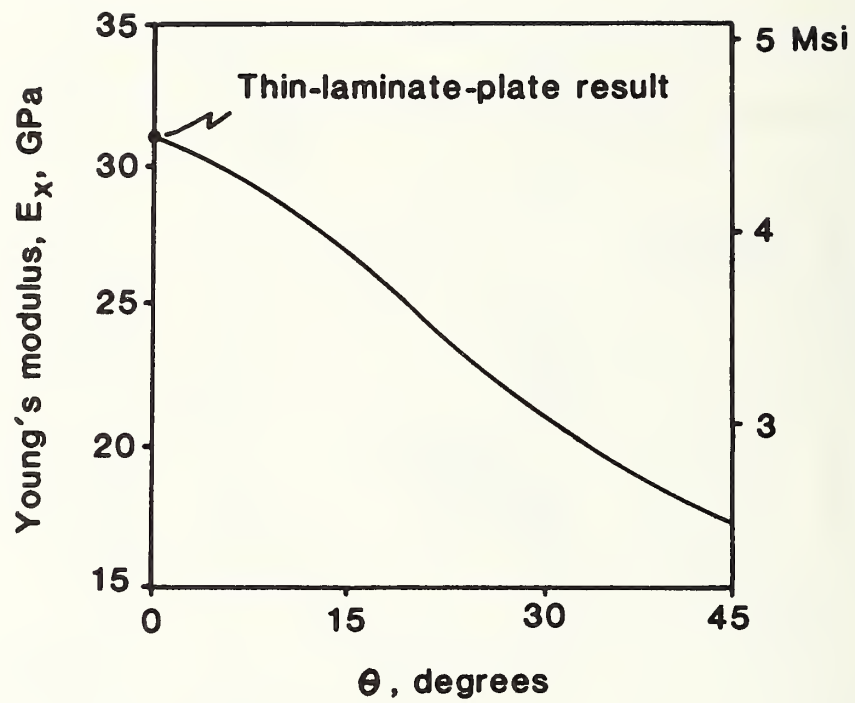


Fig. 2 Unit cell modulus in x direction (warp)



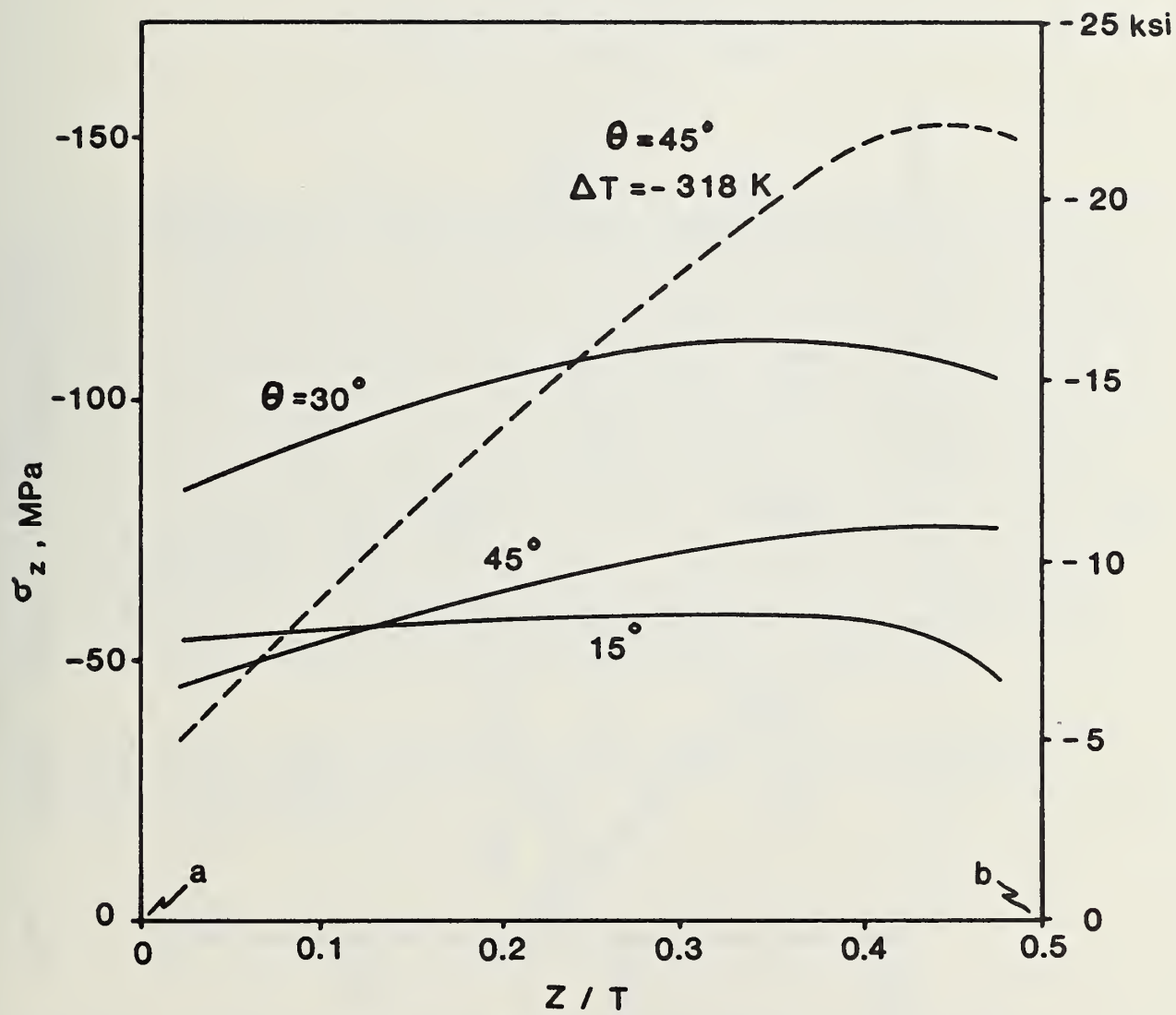


Fig. 3  $\sigma_z$  stresses along line a-b in Fig. 1.

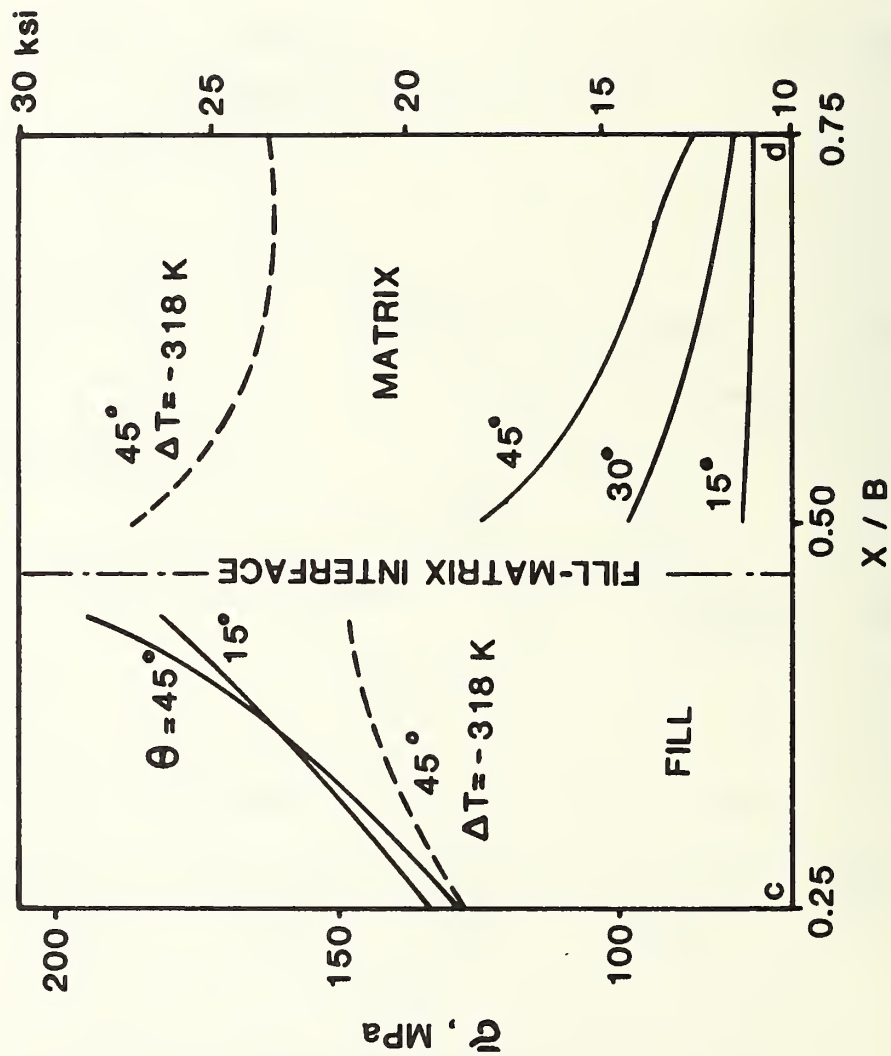


Fig. 4 Stresses normal to warp-fill interface along line c-d in Fig. 1.

# Influence of Ply Cracks on Fracture Strength of Graphite/Epoxy Laminates at 76 K

Ronald D. Kriz\*  
Fracture and Deformation Division  
National Bureau of Standards  
Boulder, Colorado 80303

## Abstract

Quasi-isotropic laminates ( $[0/90/\pm 45]_S$ ;  $[0/\pm 45/90]_S$ ) were fabricated from graphite/epoxy and quasi-statically loaded in tension at 76 K until fracture occurred. Fibers in  $0^\circ$  plies carry the largest portion of the tensile load; the weaker  $90^\circ$  and  $45^\circ$  plies crack at loads much lower than fracture strength. The effect of ply cracks on fracture of load-bearing  $0^\circ$  plies was examined to understand how defects affect laminate strength. A generalized plane-strain finite-element model was used to predict stress gradients in the  $0^\circ$  ply near the crack tip. Variations in residual stress caused by changes in temperature and absorbed moisture were included in the analysis. The experiments indicated that absorbed moisture significantly alters the fracture strength and fracture surface of a dehydrated  $[0/90/\pm 45]_S$  laminate tested at 76 K. The  $0^\circ$  plies of dehydrated laminates fractured along several  $90^\circ$  ply cracks. When moisture saturated a  $[0/90/\pm 45]_S$  laminate, a single  $90^\circ$  ply crack dominated the fracture of the  $0^\circ$  ply and the laminate fracture strength decreased 8 percent. Analysis of residual stresses indicated a higher residual stress state existed near the  $90^\circ$  ply crack when moisture was absorbed.

Submitted for publication in ASTM special technical publication from ASTM Symposium on Effects of Defects in Composite Materials, San Francisco, California, December 1982.

Key Words: finite-element; fracture; graphite/epoxy laminates; low temperatures; ply cracks; residual stress

\* NRC-NBS Postdoctoral Research Associate 1980-1982



## INTRODUCTION

When loaded in tension, graphite/epoxy laminates accumulate damage in the form of ply cracks, delaminations, fiber breaks, fiber-matrix debonding, and matrix cracks. Prior to fracture,  $0^\circ$  plies carry a larger portion of the tensile load than the weaker  $90^\circ$  and  $45^\circ$  plies. Laminate fracture occurs when fibers fracture within the load-bearing  $0^\circ$  plies.

Experimental evidence of graphite fiber breaks occurring in  $0^\circ$  plies prior to fracture was observed by Kriz [1] at room temperature. An enlargement of these fiber breaks is shown in Fig. 1. The fiber breaks observed in Fig. 1 are not influenced by the stress concentration of a  $90^\circ$  ply crack. The scatter in graphite fiber breaks is similar to those modeled by Rosen [2] for unidirectional glass/epoxy. However, Hartwig [3] observed an accumulation of graphite fiber breaks near  $90^\circ$  and  $45^\circ$  ply cracks at 76 K. Hence the presence of large residual stresses near a ply crack at 76 K can influence the fracture of  $0^\circ$  plies.

In this study, the influence of residual stress on  $0^\circ$  ply fracture was investigated for two quasi-isotropic laminates:  $[0/90/\pm 45]_S$  and  $[0/\pm 45/90]_S$ . Residual stresses were altered, prior to fracture at 76 K, by dehydrating and saturating laminates with absorbed moisture. A statistical analysis of laminate fracture populations was designed to model the weakening of load-bearing  $0^\circ$  plies. A generalized plane-strain finite-element model was used to predict variations in  $0^\circ$  ply stresses caused by mechanical and thermal-moisture loads.



## ANALYSIS

Stresses within each layer were predicted for a symmetrical laminate loaded in tension. Material response was assumed to be linear and elastic at 76 K. Hence, thermal and moisture loads were superposed with mechanical loads. The applied loads were assumed to be steady and uniform across the laminate. A typical symmetric laminate loaded in tension is shown in Fig. 2, where  $L > B \gg T$ . Each layer was assumed homogeneous with transversely isotropic elastic properties. Room-temperature and 76-K elastic properties used in the analysis are listed in Table 1. Coefficients of thermal and moisture expansion (listed in table 1) were modeled as the only contributions to residual stress. Changes in residual stress caused by variations in elastic properties were neglected.

### Generalized Plane Strain

Stresses near a ply crack tip ( $x=y=0$ ,  $z/T=0.75$ ) were predicted within the  $x$ - $z$  plane far from the laminate edges ( $y=\pm B$ ). The constraining out-of-plane strain,  $\epsilon_y$ , was modeled as the generalized strain normal to the  $x$ - $z$  plane at  $y=0$ . The strain in the load direction,  $\epsilon_x$ , was assumed to be uniform. Using classic laminate-plate theory (see Jones [5]), the strains  $\epsilon_x$  and  $\epsilon_y$  can be calculated in terms of the known laminate loads,  $N_x$ , with  $N_y = 0$ .

$$\epsilon_x = A_{yy}N_x / (A_{xx}A_{yy} - A_{xy}^2) \quad , \quad \epsilon_y = -A_{xy}N_x / (A_{xx}A_{yy} - A_{xy}^2) \quad (1)$$

where  $A_{xx}$ ,  $A_{yy}$  and  $A_{xy}$  are laminate midplane stiffnesses. Since generalized plane-strain was assumed normal to the  $x$ - $z$  plane, all six components of stress must be independent of the  $y$ -axis. Hence the equations of equilibrium reduce to

$$\frac{\partial \sigma_x}{\partial x} + \frac{\partial \tau_{xz}}{\partial z} = \frac{\partial \tau_{xy}}{\partial x} + \frac{\partial \tau_{yz}}{\partial z} = \frac{\partial \tau_{xz}}{\partial x} + \frac{\partial \sigma_z}{\partial z} = 0. \quad (2)$$

The displacement relations are derived by Talug [6] for the generalized plane-strain problem assuming laminate symmetry:

$$\begin{aligned}u(x,y,z) &= U(x,z) \\v(x,y,z) &= \epsilon_y y + V(x,z) \\w(x,y,z) &= W(x,z)\end{aligned}\tag{3}$$

where  $U$ ,  $V$ , and  $W$  are unknown displacement functions. Talug [6] derived the elliptic equations of equilibrium in terms of these unknown functions and solved for displacements near ply cracks using finite difference techniques. In this study thermal and moisture loads were included in the analysis and a finite-element model was used to solve for displacements near ply cracks.

#### Finite-Element Model

Constant-strain elements with three nodes were chosen. Hence, the required displacement fields (3) are satisfied for each element by the linear relations:

$$\begin{aligned}u &= a_1 + a_2 x + a_3 z \\v &= a_4 + a_5 x + a_6 z + \epsilon_y y \\z &= a_7 + a_8 x + a_9 z\end{aligned}\tag{4}$$

where the  $a_i$  terms are evaluated in terms of nodal displacements. Elemental stiffness and load matrices for mechanical and thermal-moisture loads were derived by Renieri [7]. A finite-element computer program was written using these elements. Because of laminate symmetry only the cross-hatched quadrant shown in Fig. 2 was modeled. The grid of elements shown in Fig. 3 was used to model stress concentrations within the  $0^\circ$  ply near the  $90^\circ$  ply crack. The dimension of the smallest element at the crack tip was less than one graphite-fiber diameter (see Region A of Fig. 3).

Traction-free boundary conditions along  $z=T$  are approximated by prescribing statically equivalent zero nodal forces. Laminate symmetry along  $z=0$  requires displacements  $w=0$ . Similarly, displacements  $u=0$  along  $x=0$  are required, except for the traction-free surface  $0.5 < z/T < 0.75$  that requires statically equivalent zero-nodal forces. In the  $x$ -direction along the surface  $x=L$  a uniform axial strain  $\epsilon_x$  is modeled by prescribing a uniform nodal displacement  $U_0 = \epsilon_x L$ .

To check the accuracy of the grid shown in Fig. 3 finite-element stresses predicted with no ply crack were compared with thin-laminate-plate theory. This comparison is shown in Table 2 when a grid aspect ratio of  $L/T=6$  is prescribed. Using the grid shown in Fig. 3, finite-element predictions of stress far from the ply crack ( $x=5L$ ) also agree well with thin-laminate-plate theory.

#### PROCEDURE

A total of 73  $[0/\pm 45/90]_s$ , 73  $[0/90/\pm 45]_s$ , and 70  $[0_8]$  specimens were fabricated from the same batch of graphite/epoxy reported in Ref. 1. All specimens were 10.2 cm long with uniform width. Quasi-isotropic laminates were 1.27 cm wide and unidirectional specimens were 0.64 cm wide. Half of the specimens of each type were exposed to 95 percent relative humidity at 343 K until no additional absorbed moisture weight gain could be measured (wet or saturated condition). The remaining specimens were dried in an oven at 338 K until no additional moisture weight loss could be measured (dry or dehydrated condition). The edges of four  $[0/\pm 45/90]_s$  and four  $[0/90/\pm 45]_s$  were polished and replicated as outlined in Ref. 8 prior to wet and dry conditioning. Thirty-five wet and thirty-five dry quasi-isotropic laminates (gage length 7.62 cm) were quasi-statically loaded in tension to fracture using a hydraulic

load controlled system. The cryogenic tension load fixture is shown in Fig. 4. A special extensometer (shown in Fig. 5) was used to measure strain over a 1.27-cm gage length with  $\pm 0.05\%$  accuracy. Glass/epoxy tabs 1.27 cm long were used to grip the quasi-isotropic specimens with a fine-mesh stainless-steel interface. The stainless-steel mesh allowed thermal contraction mismatch between graphite/epoxy specimens and glass/epoxy tabs without causing unnecessary stress concentrations. Glass/epoxy tabs were bonded to all  $[0_8]$  specimens with epoxy adhesive. No debonding was observed at 76 K.

All specimens with polished edges were loaded in increments of 445 N and replicas were taken of edge damage at room temperature after each load increment. Hence the load increment required to initiate ply cracking was recorded. Thermal cycling after each load increment resulted in no new damage.

### RESULTS AND DISCUSSION

All specimens failed at random locations between grips. There were no apparent stress concentrations near tabs that influenced fracture strength. Strengths reported in Table 3 compare well with results reported in Ref. 4. Hence strengths recorded in Table 3 are minimally influenced by test procedure. Statistical-distribution functions used to represent inherent scatter should not be chosen a priori [9]. Here we used normal and Weibull distribution functions and tested for "goodness of fit" using a chi-square test [10]. All  $[0_8]$ ,  $[0/90/\pm 45]_s$  and  $[0/\pm 45/90]_s$  specimens fit the Weibull distribution best with 80 percent confidence or better. Weibull distributions imply a weak-link effect that influences fracture strength.

The largest difference between wet and dry strengths was observed for  $[0/90/\pm 45]_s$  laminates. Weibull strength distributions for wet and dry  $[0/90/\pm 45]_s$  laminates are shown in Fig. 6. Comparison of Weibull shape



parameters  $\alpha_{WET} > \alpha_{DRY}$  indicates a more dominant weak-link effect when moisture is absorbed into the dehydrated laminate. Fracture surfaces of dry and wet conditioned  $[0/90/\pm 45]_S$  laminates are shown in Fig. 7 and 8. Figure 7 shows  $0^\circ$  ply fractures along several  $90^\circ$  ply cracks of a dehydrated laminate. When absorbed moisture saturates the laminate, a single  $90^\circ$  ply crack dominates the  $0^\circ$  ply fracture shown in Fig. 8 and the Weibull mean strength decreases 8 percent.

Stress distributions near  $90^\circ$  ply cracks were predicted with the finite-element model. The mechanical plate load,  $N_x$ , required to initiate the first  $90^\circ$  ply crack was observed at  $N_x = 273$  kN/m. Relations (1) were used to calculate strains,  $\epsilon_x = 4010$   $\mu\text{m/m}$  and  $\epsilon_y = -964$   $\mu\text{m/m}$ , which constitute the mechanical load used by the finite-element model. Stresses in dehydrated laminates loaded in tension were calculated by superposition of the mechanical stresses with residual stresses caused by a temperature change at 76 K. Stresses in saturated laminates loaded in tension were calculated by superposition of additional residual stresses caused by swelling when moisture is absorbed. Moisture weight gain was measured at 1.2 percent in the saturated state and a temperature change of -318 K was chosen, with the idealization of a stress-free state at 494 K (see Ref. 11). Using the above mechanical and thermal-moisture loads together with the elastic properties defined in Table 1, stresses near the  $90^\circ$  ply crack in a  $[0/90/\pm 45]_S$  laminate were calculated and plotted in Figs. 9 through 11.

Through-thickness variation of  $\sigma_x$  in the  $0^\circ$  ply along  $x=0$  is shown in Fig. 9. Stress in the load  $x$  direction is calculated for three cases:

1. mechanical load with no residual stresses  $\sigma_x^{MECH}$
2. mechanical load including residual thermal load  $\sigma_x^{DRY}$  (dehydrated condition),
3. mechanical load including residual thermal-moisture load  $\sigma_x^{WET}$  (saturated condition).

At position



$z/T = 0.753$  and  $x=0$  the largest  $\sigma_x$  stresses are predicted, where

$\sigma_x^{MECH} < \sigma_x^{WET} < \sigma_x^{DRY}$ . At position  $z/T = 0.766$  and  $x = 0$  the inequality of  $\sigma_x$  stresses is reversed  $\sigma_x^{DRY} < \sigma_x^{WET} < \sigma_x^{MECH}$ .

Here we assume laminate fracture is dominated by  $0^\circ$  ply fracture because the  $0^\circ$  plies carry the largest portion of the tensile load. Hence, the predicted  $0^\circ$  ply stresses  $\sigma_x^{WET}$  and  $\sigma_x^{DRY}$  were compared with the mean wet and dry fracture strengths ( $X_{WET} = 425$  MPa,  $X_{DRY} = 460$  MPa). In Fig. 9 stresses averaged within the region  $0.761 < z/T < 1.0$  for saturated (WET) laminates are larger near the crack tip than dehydrated (DRY) laminates. Hence, saturated laminates would fracture at lower tension loads. Conversely, stresses predicted in the region  $0.75 < z/T < 0.76$  indicate dehydrated laminates will fracture at lower loads than saturated laminates. Stresses predicted in the region  $0.75 < z/T < 0.761$  are located approximately one fiber diameter from the  $0/90$  interface. Hence the heterogeneous graphite/epoxy structure of the  $0^\circ$  ply can not be modeled as a continuum within the region  $0.75 < z/T < 0.76$ . Stresses predicted in this region were ignored.

Delaminations were observed only at the  $0/90$  interface near the fracture surface. However, delaminations at the  $0/90$  interface were not observed on replicas taken prior to fracture. Since delaminations occurring at the  $90^\circ$  ply crack tip will blunt the stress concentration, fiber breaks within the  $0^\circ$  ply will not occur near the crack tip. In Figs. 7 and 8 we observed broken  $0^\circ$  ply fibers near  $90^\circ$  ply crack tips. Although delaminations did not influence  $0^\circ$  ply fracture, interlaminar stresses were plotted near the  $0/90$  interface in Figs. 10 and 11. When moisture is absorbed, lower interfacial shear stress,  $\tau_{xz}$ , is predicted near the crack tip (see Fig. 10). Similarly, stress normal to the  $0/90$  interface is lower when moisture is absorbed (see Fig. 11). Hence, stresses leading to delaminations are decreased due to absorbed moisture.

Laminates with a stacking sequence of  $[0/\pm 45/90]_s$  were less affected by absorbed moisture at 76 K than  $[0/90/\pm 45]_s$  laminates. Absorbed moisture increases  $[0/\pm 45/90]_s$  laminated strength by 3.8 percent at 76 K. Fracture surfaces of dehydrated and saturated  $[0/\pm 45/90]_s$  laminates were similar;  $0^\circ$  ply fiber fractures occurred randomly and stepwise along several  $45^\circ$  ply cracks as shown in Fig. 12.

Strengths for unidirectional  $[0_8]$  specimens, shown in Table 3, scattered more than the strengths of quasi-isotropic laminates. Absorbed moisture decreases strength 12 percent at 76 K. When unidirectional graphite/epoxy is bonded to  $90^\circ$  and  $45^\circ$  plies, a constraining effect on strength was observed by Stinchcomb [12]. Strengths reported in Table 3 for  $[0, 90, \pm 45]_s$  specimens are reduced to equivalent cross-sectional areas of  $0^\circ$  plies and compared with  $[0_8]$  strengths. This comparison is justified when the  $0^\circ$  ply fracture is assumed to dominate laminate fracture strength. Unconstrained  $[0_8]$  mean strength is 23 percent lower than the fracture strength of a  $0^\circ$  ply constrained by  $90^\circ$  and  $45^\circ$  plies. Detailed discussions on constraint are given in Refs. 6 and 12.

### CONCLUSIONS

Predicted dehydrated and saturated residual stresses within  $0^\circ$  plies near ply cracks account for the observed differences in  $[0/90/\pm 45]_s$  fracture strengths, assuming  $0^\circ$  ply fracture dominates laminate fracture at 76 K. Absorbed moisture swells  $90^\circ$  and  $45^\circ$  plies and changes the residual thermal  $0^\circ$  ply stresses. When dehydrated laminates are saturated and loaded in tension at 76 K, larger residual stress exists near the crack tip. Hence saturated laminates fracture at lower tension loads. Fractographic observations confirm this prediction, where a single  $90^\circ$  ply crack is observed to dominate the

fracture of a  $0^\circ$  ply. This dominance of a  $90^\circ$  ply crack on the  $0^\circ$  ply fracture is recovered statistically, where the Weibull shape parameter,  $\alpha$ , indicates a stronger weak-link effect when  $[0/90/\pm 45]_s$  laminates are saturated. Laminate strength is increased 8 percent when dehydrated.

Laminates with the stacking sequence  $[0/\pm 45/90]_s$  are less affected by absorbed moisture at 76 K than the  $[0/90/\pm 45]_s$  laminates.

Unconstrained  $[0_g]$  unidirectional strengths are lower with more scatter when compared with constrained  $0^\circ$  ply strengths. Strength of unidirectional graphite/epoxy at 76 K was improved when constrained by crossplies.

#### ACKNOWLEDGMENTS

This work was sponsored by NRC-NBS Postdoctoral Research Program and the U.S. Department of Energy, Office of Fusion Energy.

## REFERENCES

1. Kriz, R. D., "Effects of Moisture, Residual Thermal Cure Stresses, and Mechanical Load on Damage Development in Quasi-isotropic Laminates," Doctoral Dissertation, Department of Engineering Science and Mechanics, College of Engineering, Virginia Polytechnic Institute and State University, Blacksburg, VA, Dec. 1979.
2. Rosen, B. W., "Mechanics Of Composite Strengthening," in Fiber Composite Materials, American Society for Metals, Metals Park, Ohio, 1965, pp. 37-75.
3. Hartwig, G., "Reinforced Polymers at Low Temperatures," in Advances in Cryogenic Engineering--Materials, Vol. 28, Edited by R. P. Reed and A. F. Clark, Plenum Press, New York, 1982, pp. 179-189.
4. Haskins, J. F. and Holmes, R. D., "Advanced Composite Design Data for Spacecraft Structural Applications," Technical Report AFML TR-79-4208, Air Force Materials Laboratory, Wright-Patterson Air Force Base, Ohio, October 1979.
5. Jones, R. M., Mechanics of Composite Materials, McGraw-Hill, New York, 1975, pp. 147-152.
6. Talug, A., "Analysis of Stress Fields in Composite Laminates with Interior Cracks," Doctoral Dissertation, Department of Engineering Science and Mechanics, College of Engineering, Virginia Polytechnic Institute and State University, Blacksburg, VA, August 1978.
7. Renieri, G. D., "Nonlinear Analysis of Laminated Fibrous Composites," Doctoral Dissertation, Department of Engineering Science and Mechanics, College of Engineering, Virginia Polytechnic Institute and State University, Blacksburg, VA, June 1976.
8. Stalnaker, D. O. and Stinchcomb, W. W., in Composite Materials: Testing and Design (Fifth Conference), ASTM STP 674, American Society for Testing and Materials, Philadelphia, 1979, pp. 620-641.
9. Tracy, P. G., Rich, T. P., Bowser, R., and Tramontozzi, L. R., "On the Statistical Nature of Fracture," International Journal of Fracture, Vol. 18, No. 4, April 1982, pp. 253-277.
10. Park, W. J., "Basic Concepts of Statistics and Their Applications in Composite Materials," Technical Report AFML-TR-79-4070, Air Force Materials Laboratory, Wright-Patterson Air Force Base, Ohio, June 1979.
11. Pagano, N. J. and Hahn, H. T., in Composite Materials: Testing and Design (Fourth Conference), ASTM STP 617, American Society for Testing Materials, Philadelphia, 1977, pp. 317-329.
12. Stinchcomb, W. W., Reifsnider, K. L., Yeung, P., and Masters, J., in Fatigue of Fibrous Composite Materials, ASTM STP 723, American Society for Testing Materials, Philadelphia, 1979, pp. 320-333.

## LIST OF TABLES

1. Lamina properties.
2. Comparison of finite-element and laminate-plate-theory layer stresses.
3. Weibull and normal strength distributions at 76 K.



Table 1. Lamina properties

Transversely isotropic elastic properties, GPa RT* / 76 K (% increase, Ref. 4)	$E_1$ $\frac{130}{143}$ (1.1)	$E_2 = E_3$ $\frac{9.70}{18.4}$ (2.9)	$G_{12} = G_{13}$ $\frac{5.39}{15.6}$ (1.9)	$G_{23}$ $\frac{3.25}{6.18}$ (1.9)	$\nu_{12} = \nu_{13}$ $\frac{0.308}{0.308}$ (0)
Thermal expansion coefficients, $\mu\text{m}/\text{m}/\text{K}$ Ref. 4	$\alpha_1$ $\frac{-0.128}{-0.128}$	$\alpha_2$ $\frac{8.26}{8.26}$	Moisture expansion coefficients, $\mu\text{m}/\text{m}/\%\text{H}_2\text{O}$ Ref. 1	$\beta_1$ $\frac{0.0}{0.0}$	$\beta_2$ $\frac{3710}{3710}$

\* Room-temperature (RT) elastic properties from Ref. 1.

Subscripts : (1) indicates fiber direction and (23) indicates transverse plane.

Table 2. Comparison of finite-element and laminate-plate-theory layer stresses

Layer	Stress (MPa)    Finite element / Laminate-plate theory, Ref. 5		
	$\sigma_x$	$\sigma_y$	$\tau_{xy}$
0°	4.99 / 5.09	574 / 577	0.15 / 0
90°	-117 / -117	68.9 / 69.6	0.14 / 0
45°	54.4 / 55.8	208 / 212	-94.6 / -96.5
-45°	54.2 / 55.8	208 / 212	94.2 / 96.5

Finite-element stresses averaged over four elements at each midlayer.

Table 3. Weibull and normal strength distributions at 76 K

Laminate configuration	Weibull strengths, MPa					Normal strengths, MPa		
	$\alpha$	$\beta$	Mean	Std. dev.	%*	Mean	Std. dev.	%*
[0 <sub>g</sub> ] Dry	5.07	1280	1180	267	80	1180	241	60
[0 <sub>g</sub> ] Wet	3.83	1150	1040	303	92	1040	267	80
[0/90/±45] s Dry	17.6	475	460	32.3	92	461	29.1	60
[0/90/±45] s Wet	19.0	425	425	27.7	93	425	25.2	85
[0/±45/90] s Dry	12.6	376	361	34.8	90	361	32.1	96
[0/±45/90] s Wet	16.3	387	375	28.3	50	375	25.3	70

\* Percent confidence from a chi-square test, Ref. 10.

## LIST OF FIGURES

1. Graphite fiber breaks adjacent to  $90^\circ$  ply crack in a  $[0/90/\pm 45]_S$  graphite/epoxy laminate loaded in tension at room temperature (See Fig. 19 in Ref. 1).
2. Quasi-isotropic laminate dimensions.
3. Finite-element grid.
4. Cryogenic tension test fixture.
5. Side-mounted extensometer.
6. Weibull plot of wet and dry  $[0/90/\pm 45]_S$  strengths.
7. Fracture surface of a dry  $[0/90/\pm 45]_S$  laminate.
8. Fracture surface of a wet  $[0/90/\pm 45]_S$  laminate.
9. Variation of  $\sigma_x$  through the  $0^\circ$  ply thickness above the  $90^\circ$  ply crack tip. Load cases: 1. Mechanical load  $N_x = 273$  kN/m with no residual stress (MECH), 2. Mechanical load including residual thermal load ( $-318$  K) (DRY), 3. Mechanical load including residual thermal and moisture load ( $+1.2$  percent  $H_2O$ ) (WET).
10. Variation of  $\tau_{xz}$  with  $x$  along surface  $z/T = 0.766$  above  $0/90$  interface. Load cases are the same as shown in Fig. 9.
11. Variation of  $\sigma_z$  with  $x$ , along surface  $z/T = 0.766$  above  $0/90$  interface. Load cases are the same as in Fig. 9.
12. Fracture surfaces of a wet  $[0/\pm 45/90]_S$  laminate.

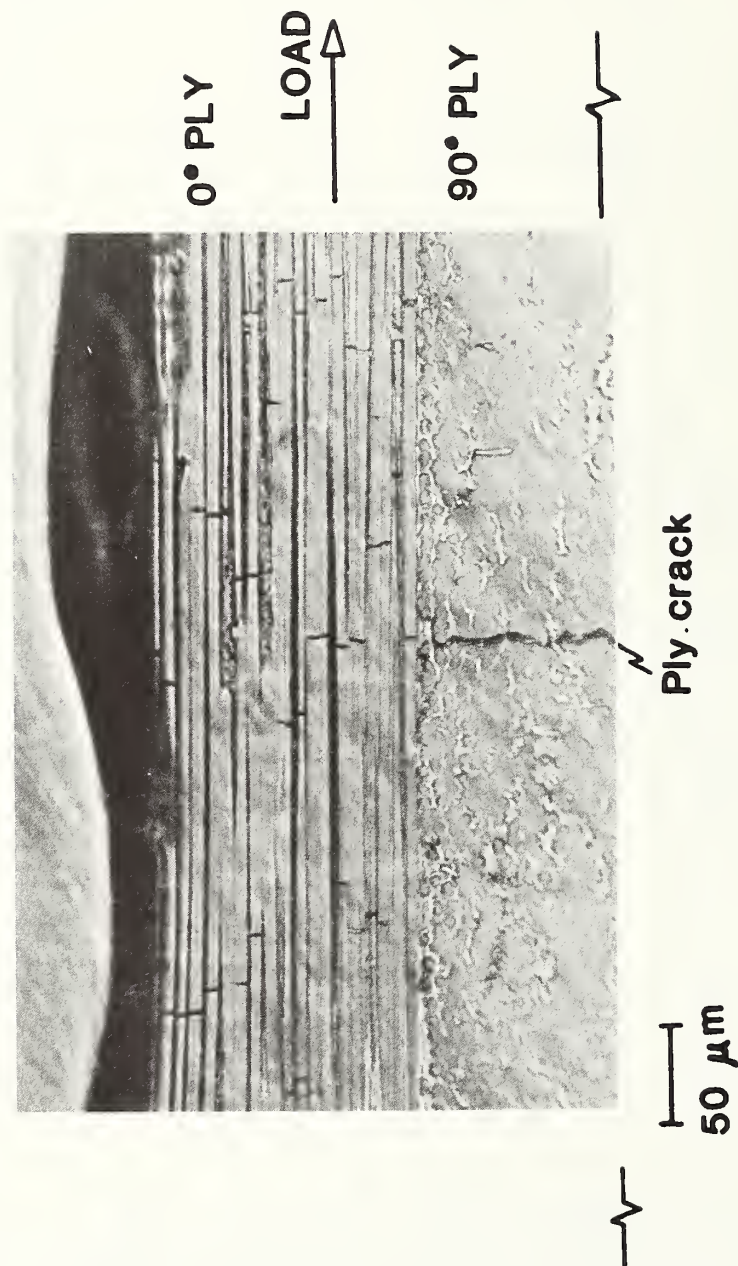


Figure 1. Graphite fiber breaks adjacent to 90° ply crack in a  $[0/90/\pm 45]_s$  graphite/epoxy laminate loaded in tension at room temperature (see Fig. 19 in Ref. 1).



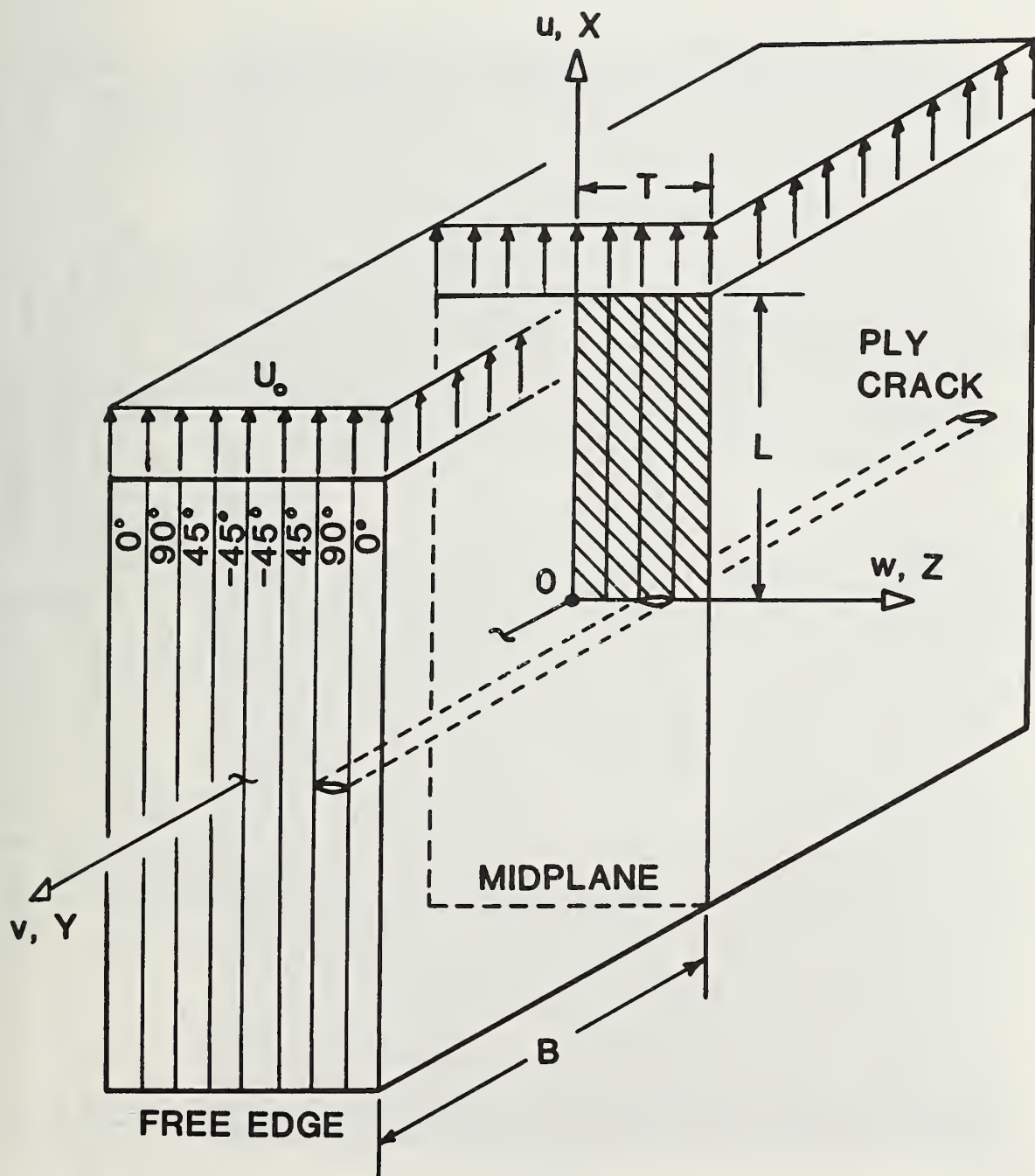


Figure 2. Quasi-isotropic laminate dimensions.

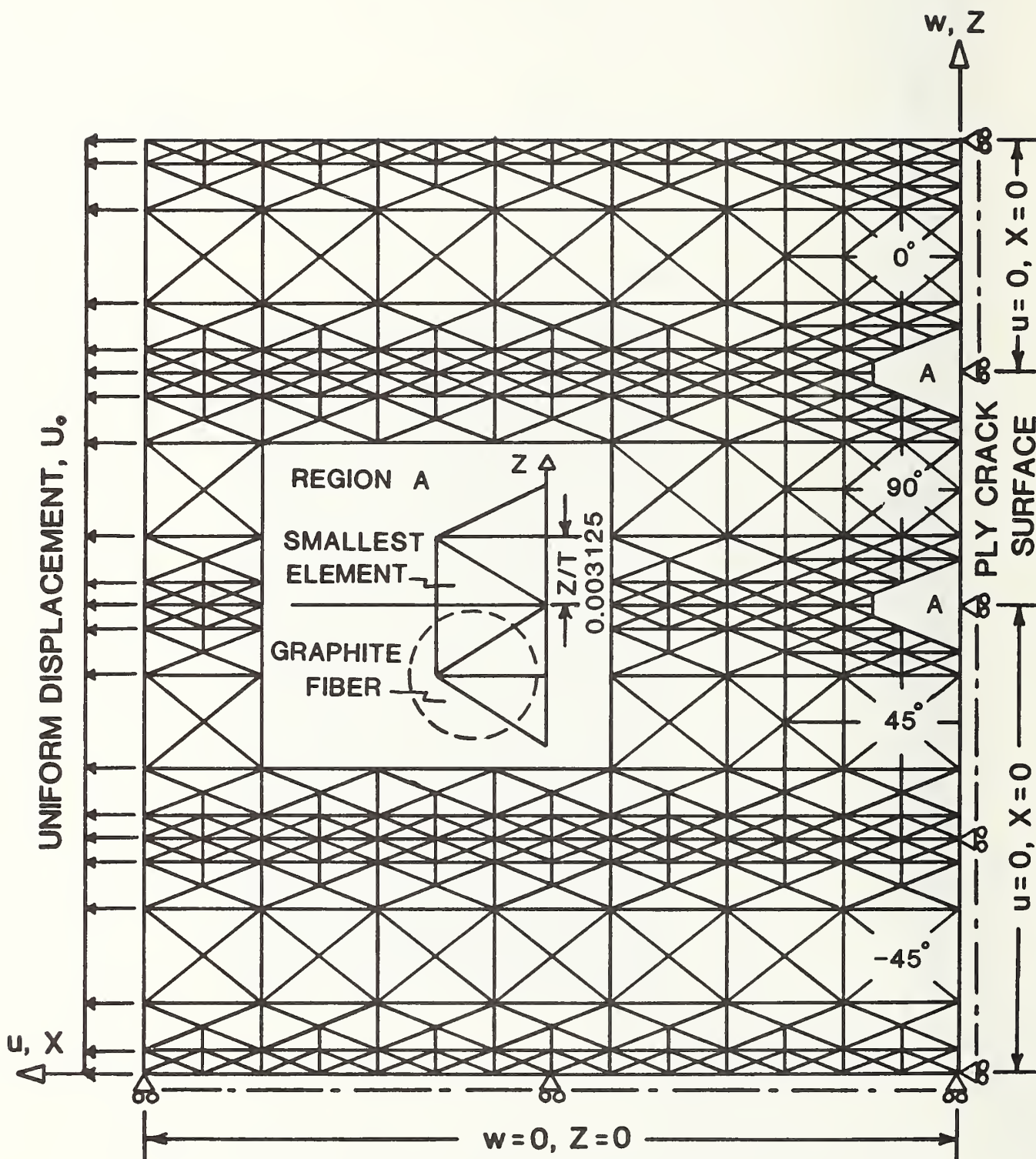


Figure 3. Finite-element grid.

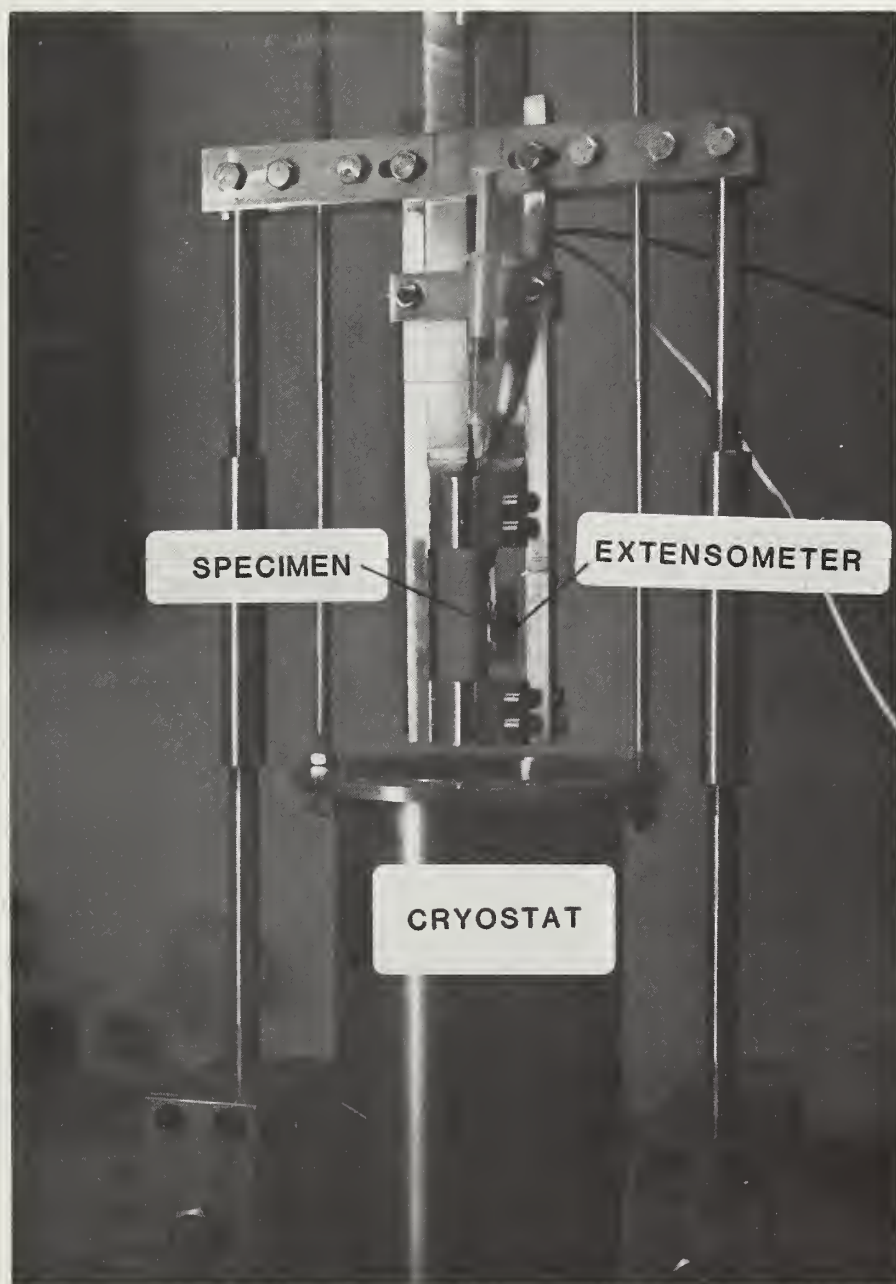


Figure 4. Cryogenic tension test fixture.

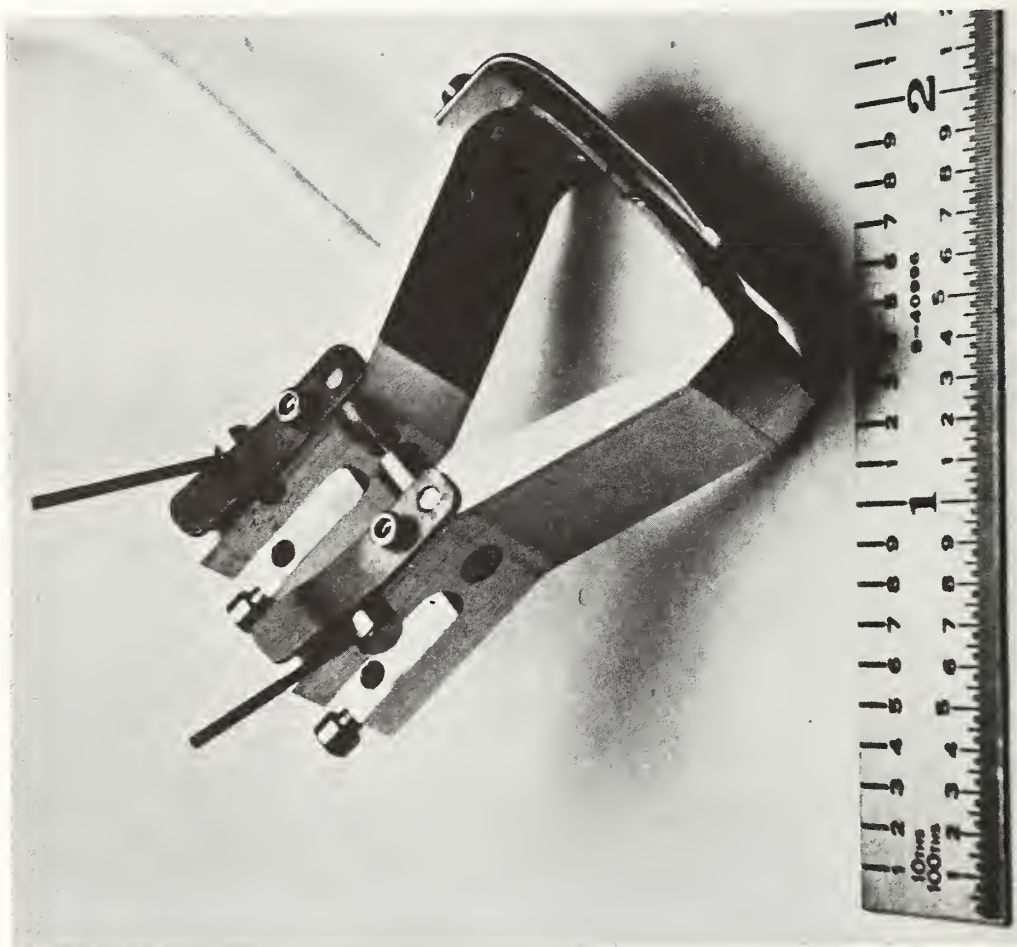


Figure 5. Side-mounted extensometer.



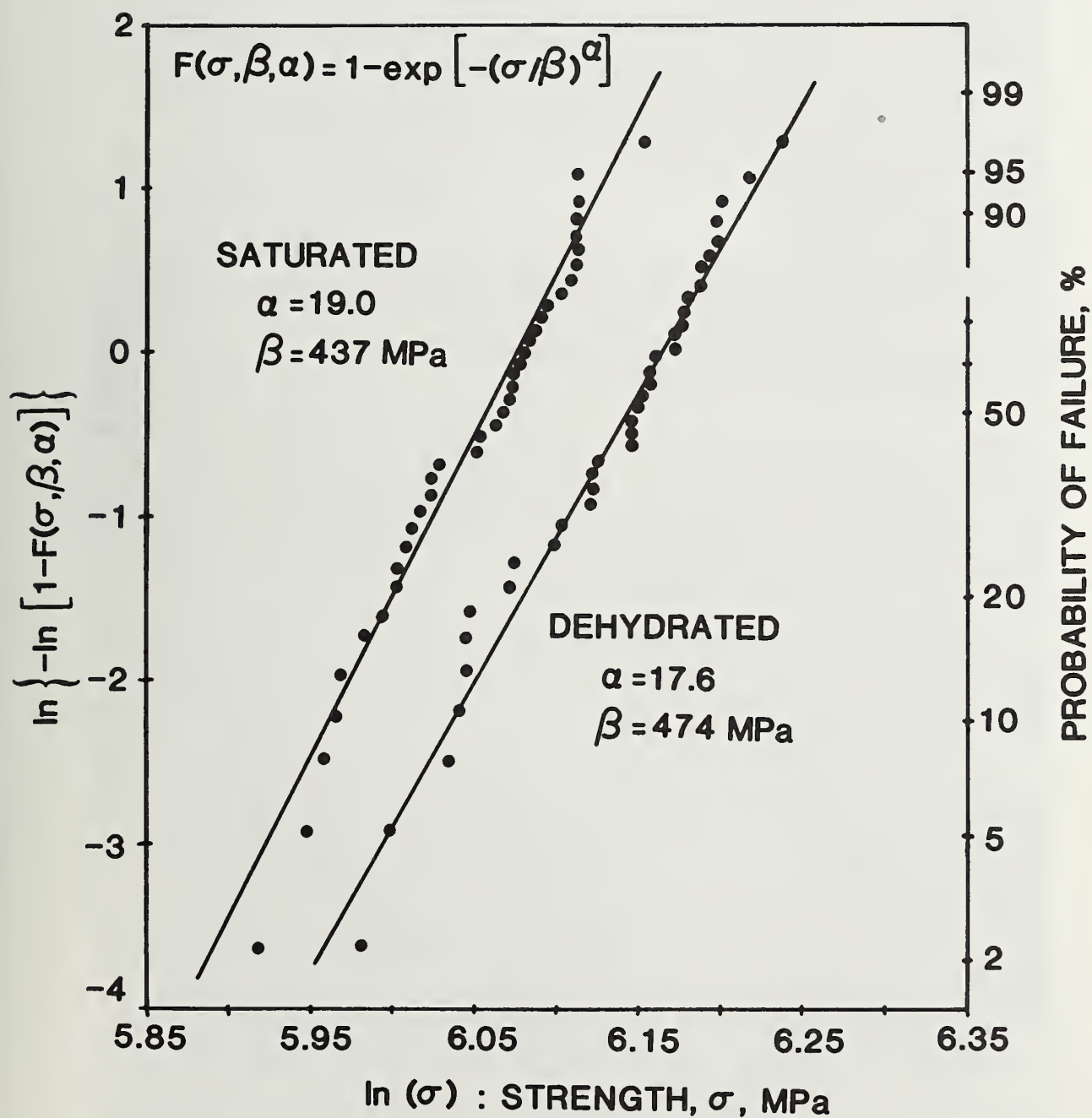
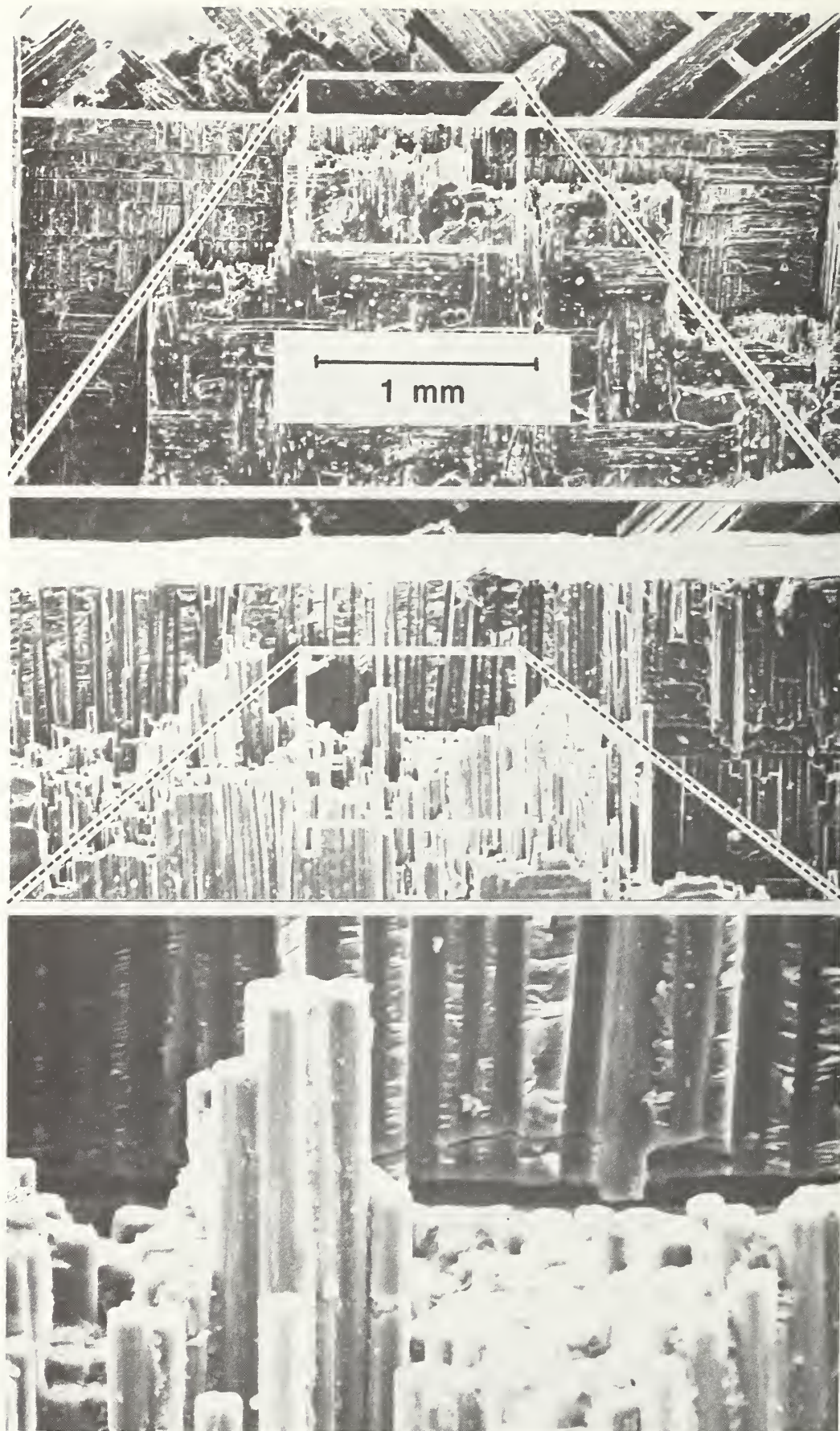


Figure 6. Weibull plot of wet and dry  $[0/90/\pm 45]_s$  strengths.



DRY



→ TENSION

Figure 7. Fracture surface of a dry  $[0/90/\pm 45]_s$  laminate.



WET

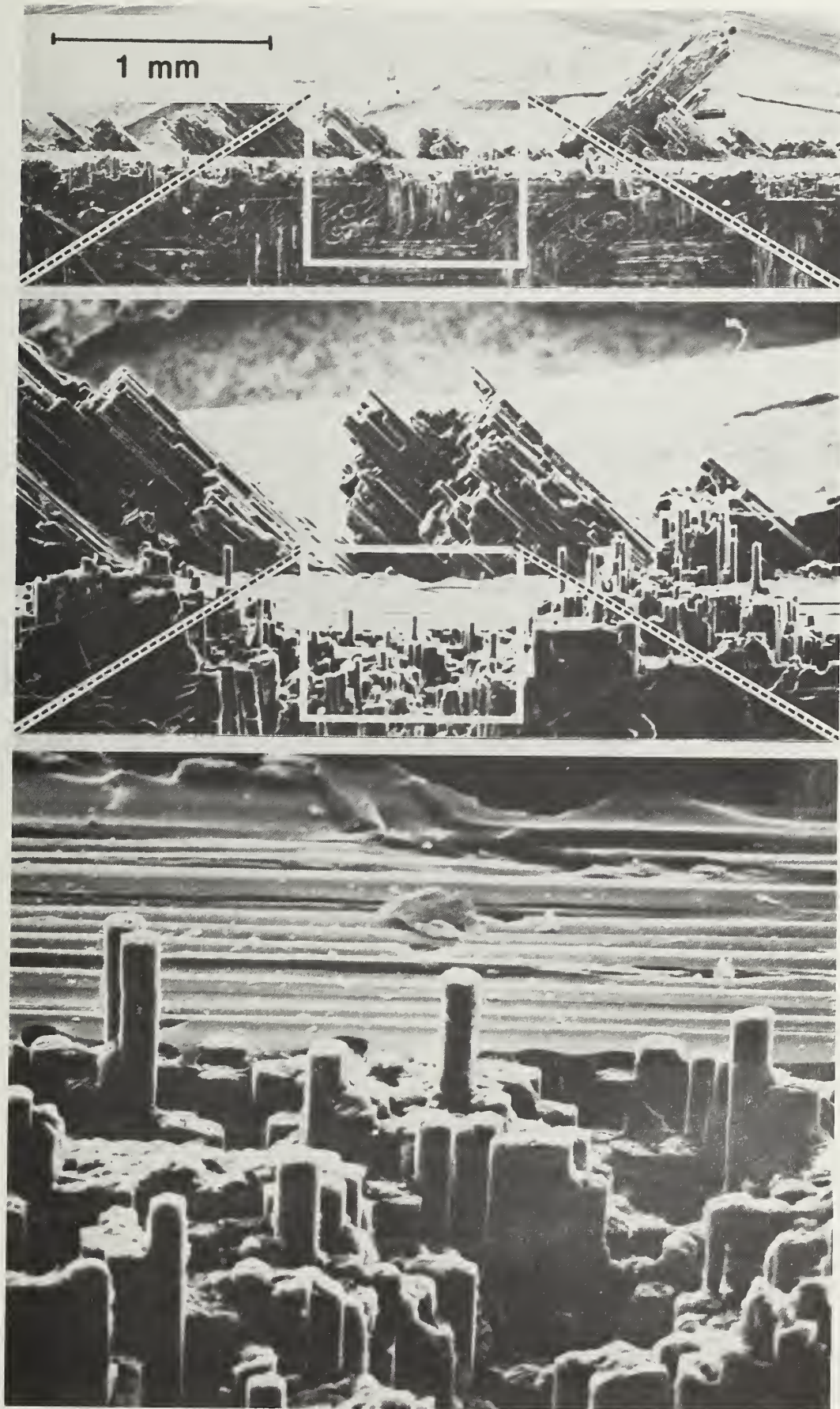


Figure 8. Fracture surface of a wet  $[0/90/\pm 45]_s$  laminate.

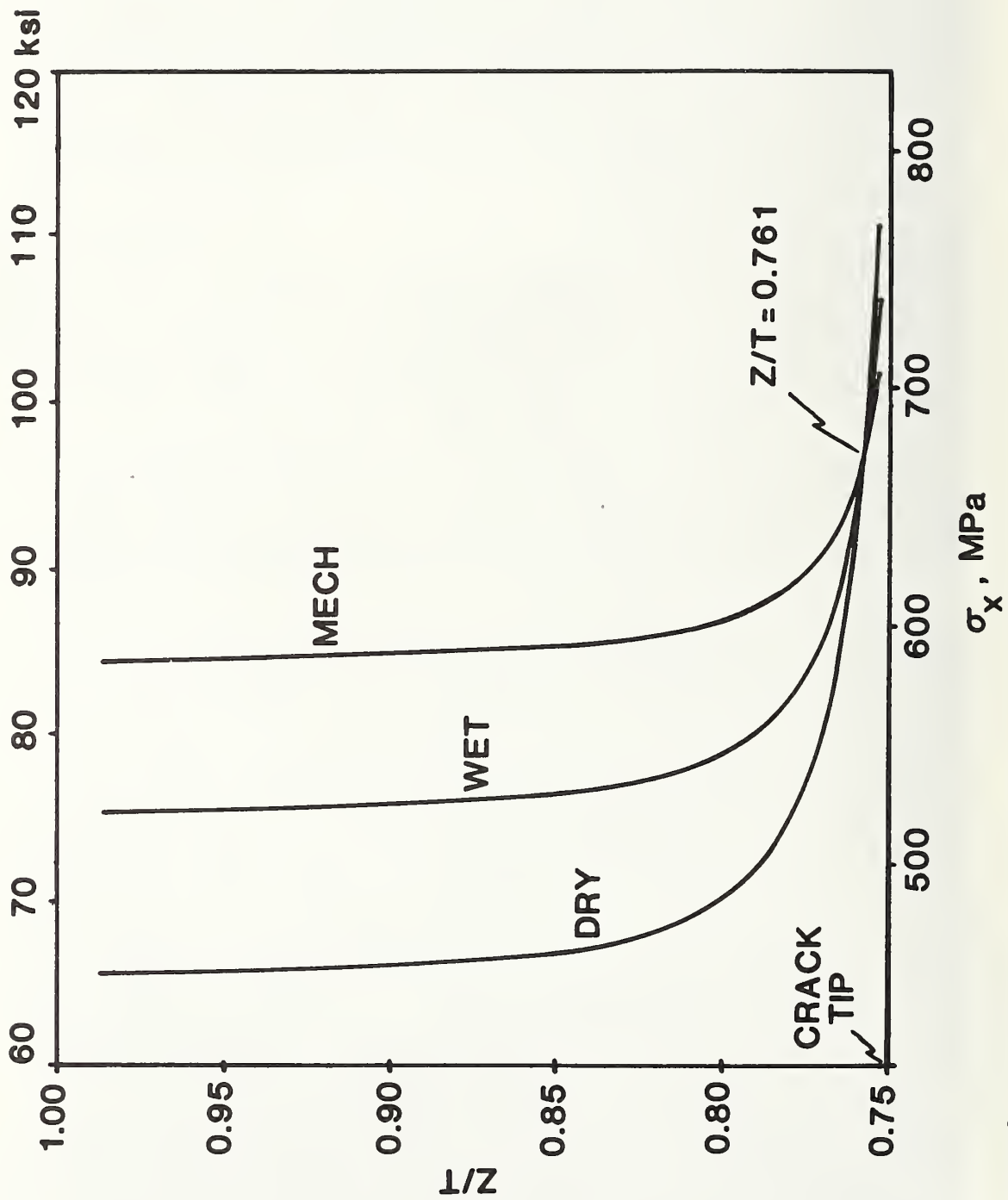


Figure 9. Variation of  $\sigma_x$  through the  $0^\circ$  ply thickness above the  $90^\circ$  ply crack tip. Load cases: 1. Mechanical load  $N = 273$  kN/m with no residual stress (MECH), 2. Mechanical load including residual thermal load ( $-318$  K) (DRY), 3. Mechanical load including residual thermal and moisture load ( $+1.2$  percent  $H_2O$ ) (WET).

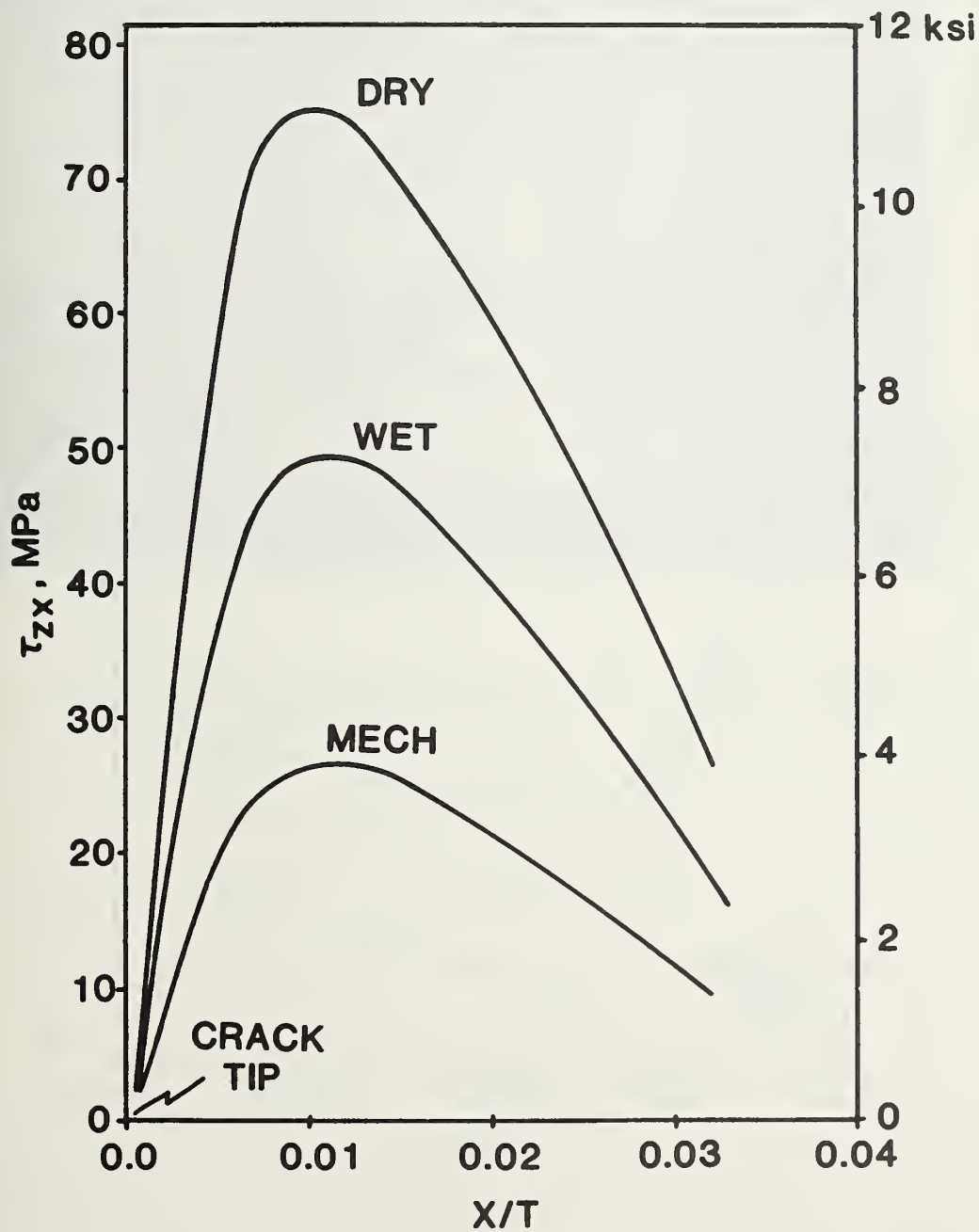


Figure 10. Variation of  $\tau_{xz}$  with  $x$  along surface  $z/T=0.766$  above 0/90 interface. Load cases are the same as shown in Fig. 9.

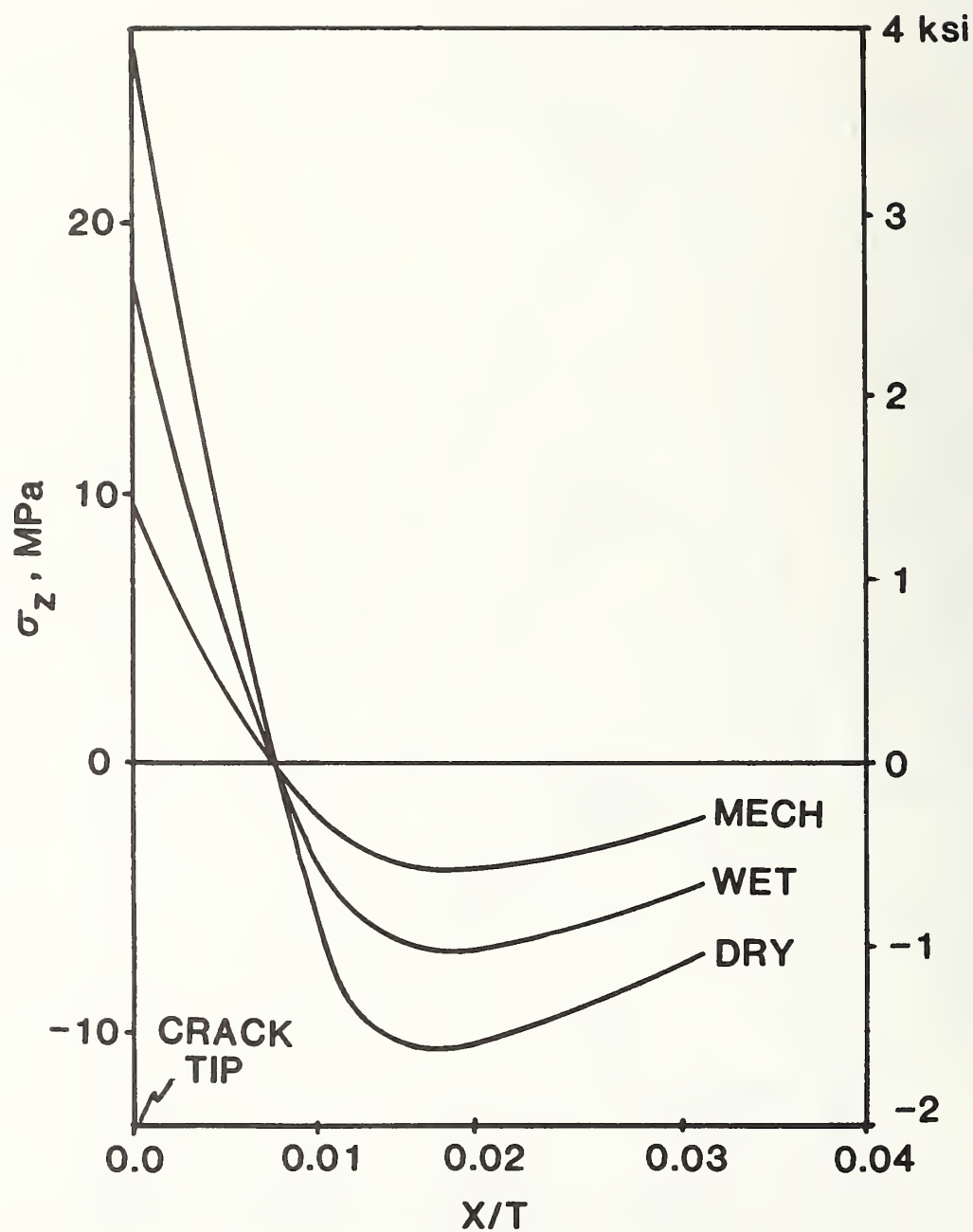


Figure 11. Variation of  $\sigma_z$  with  $x$ , along surface  $z/T=0.766$  above 0/90 interface. Load cases are the same as in Fig. 9.



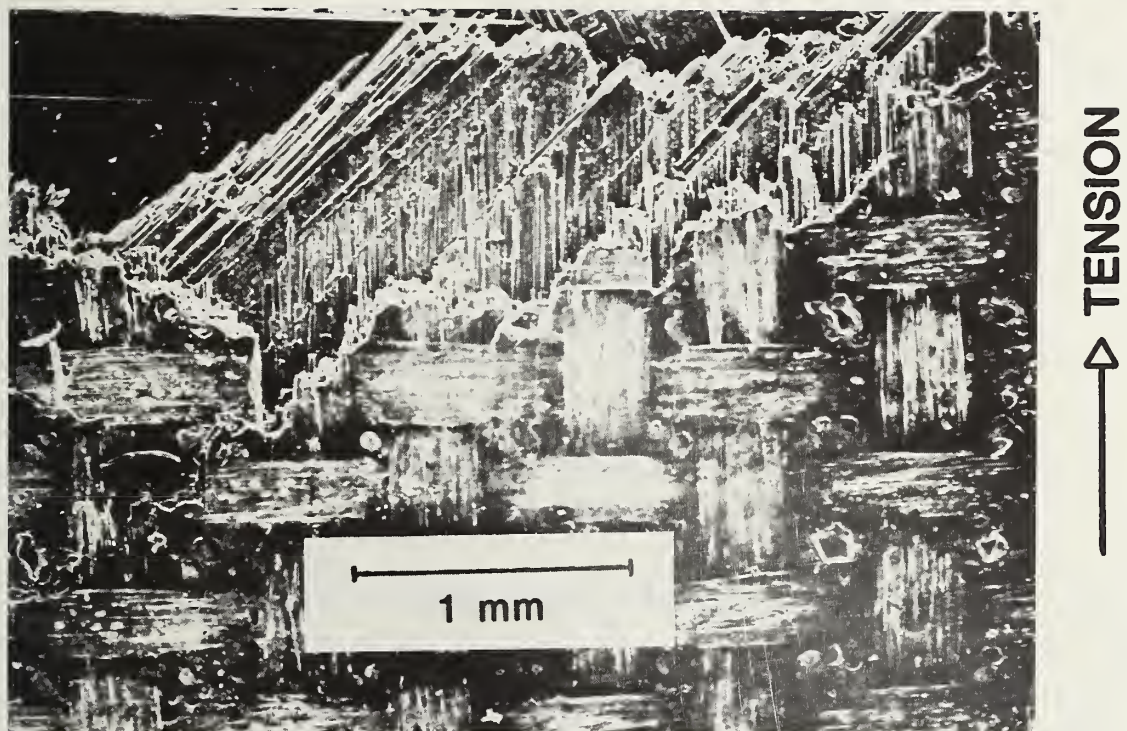


Figure 12. Fracture surfaces of a wet  $[0/\pm 45/90]_s$  laminate.



ORTHOTROPIC ELASTIC CONSTANTS OF A GLASS-FIBER-CLOTH  
EPOXY-MATRIX COMPOSITE

H. M. Ledbetter and M. W. Austin  
Fracture and Deformation Division  
National Bureau of Standards  
Boulder, Colorado 80303

ABSTRACT

We report the complete orthotropic-symmetry elastic-constant tensor for a laminated glass-fiber-cloth epoxy-matrix composite. Using a Marx-oscillator method, we determined the velocities of extensional (Young-modulus) waves in seven directions in each of the principal orthogonal planes. By a similar method, we determined velocities of torsional waves along the three principal orthogonal axes. From these twenty-two measurements, we deduced the nine-component  $S_{ij}$  elastic-compliance matrix. By matrix inversion we computed the  $C_{ij}$  elastic-stiffness matrix. Unexpected results for a shear modulus and for some Poisson's ratios suggest excessive fiber waviness in the fill direction.

Key Words: Composites; elastic constants; epoxy; glass fiber; Marx oscillator; Young's modulus



## INTRODUCTION

Not long ago, Ledbetter [1] reported an experimental study of the elastic constants of a glass-fiber-cloth epoxy-matrix laminated composite. The composite's construction led to orthotropic macroscopic elastic symmetry with three principal orthogonal directions: warp, fill, and normal. Such symmetry requires nine independent elastic constants, in contrast to two for isotropic materials.

That study suffered two deficiencies. First, specimens were taken from two separately prepared plates; thus, sample variability entered in an unknown way. Second, only six elastic constants were determined from a set of thirteen sound-velocity measurements. The remaining three resulted from some assumptions concerning increased symmetry and two of the Poisson ratios.

Continued and increased interest in this material, NEMA designation G-11CR, demanded a more thorough re-examination of the elastic constants. Here, we report the complete nine-component elastic-constant tensor based on twenty-two independent sound-velocity measurements using a Marx-oscillator method.

## EXPERIMENT

Both materials and measurement methods were described thoroughly previously [1]. For brevity we omit these here.

## RESULTS

Figures 1 through 3 show the Young's-modulus variation with angle in the three principal planes: warp-fill, fill-normal, normal-warp. Table I gives the components of the  $S_{ij}$  tensor together with the  $C_{ij}$  tensor obtained by matrix inversion. Table II recasts these as so-called engineering elastic constants. The measured torsional moduli were 0.062, 0.056, and 0.035  $\cdot 10^{11} \text{N/m}^2$  along  $x_1$  (warp),  $x_2$  (fill), and  $x_3$  (normal) directions, respectively.



## DISCUSSION

Orthotropic-symmetry materials possess nine independent elastic constants. Considering the elastic compliances, the  $S_{ij}$ , these are usually taken to be:  $S_{11}$ ,  $S_{22}$ ,  $S_{33}$ ,  $S_{44}$ ,  $S_{55}$ ,  $S_{66}$ ,  $S_{12}$ ,  $S_{13}$ ,  $S_{23}$ . Young's modulus along the  $i$  axis ( $i=1,2,3$ ) is  $S_{ii}^{-1}$ . In an arbitrary direction, Young's modulus,  $E$ , is:

$$1/E' = S'_{11} = S'_{1111} = a_{1i} a_{1j} a_{1k} a_{1l} S_{ijkl} \quad (1)$$

where primes denote a co-ordinate system rotated away from  $x_1, x_2, x_3$ ; the four indices on  $S$  are the full-tensor form necessary for tensor transformations; the  $a_{1i}$  are the direction cosines between the primed and unprimed co-ordinate systems. For orthotropic symmetry, Eq. (1) becomes

$$\begin{aligned} S'_{11} = & a_{11}^4 S_{11} + a_{12}^4 S_{22} + a_{13}^4 S_{33} + 2(a_{11}^2 a_{12}^2 S_{12} + a_{11}^2 a_{13}^2 S_{13} \\ & + a_{12}^2 a_{13}^2 S_{23}) + a_{12}^2 a_{13}^2 S_{44} + a_{11}^2 a_{13}^2 S_{55} + a_{11}^2 a_{12}^2 S_{66} \end{aligned} \quad (2)$$

For directions in the  $x_1$ - $x_2$  plane, Eq. (2) becomes:

$$S'_{11} = a_{11}^4 S_{11} + a_{12}^4 S_{22} + a_{11}^2 a_{12}^2 (2S_{12} + S_{66}) \quad (3)$$

For the  $x_2$ - $x_3$  plane:

$$S'_{11} = a_{12}^4 S_{22} + a_{13}^4 S_{33} + a_{12}^2 a_{13}^2 (2S_{23} + S_{44}) \quad (4)$$

For the  $x_1$ - $x_3$  plane:

$$S'_{11} = a_{11}^4 S_{11} + a_{13}^4 S_{33} + a_{11}^2 a_{13}^2 (2S_{13} + S_{55}) \quad (5)$$

From Eqs. (3)-(5), by measuring  $E(\theta)$  in three orthogonal planes, one obtains six elastic constants:  $S_{11}$ ,  $S_{22}$ ,  $S_{33}$ ,  $2S_{12} + S_{66}$ ,  $2S_{23} + S_{44}$ , and  $2S_{13} + S_{55}$ . To separate, for example,  $S_{12}$  from  $S_{66}$  and obtain all nine  $S_{ij}$  requires further measurements.

Torsional-modulus measurements provide the necessary information. Torsional moduli,  $T_i$ , along the principal,  $i$ , axes relate to the  $S_{ij}$  according to:

$$T_1 = 2(S_{55} + S_{66})^{-1} \quad (6)$$

$$T_2 = 2(S_{44} + S_{66})^{-1} \quad (7)$$

$$T_3 = 2(S_{44} + S_{55})^{-1} \quad (8)$$

Thus, three torsional-modulus measurements combined with  $E$  measurements versus angle in the three principal orthogonal planes lead to an unambiguous determination of all nine  $S_{ij}$ . By inversion of the six-by-six  $S_{ij}$  matrix, one obtains the  $C_{ij}$  elastic stiffnesses:

$$[C_{ij}]_{6 \times 6} = [S_{ij}]_{6 \times 6}^{-1} \quad (9)$$

Two of the three types of engineering elastic constants in Table II are readily understood because the Young modulus is simply

$$E_{ii} = S_{ii}^{-1} \quad (10)$$

and the shear moduli are simply

$$G_{23} = C_{44}, G_{13} = C_{55}, G_{12} = C_{66} \quad (11)$$

Poisson's ratio:

$$\nu_{ij} = -S_{ij}/S_{ii} \quad (12)$$

being the ratio of elastic compliances, transforms in a more complicated way. Thus,

$$\nu'_{ij} = -S'_{ij}/S'_{ii} \quad (13)$$

where  $S'_{11}$  is given by Eq. (2) and

$$\begin{aligned}
S'_{12} = & a_{11}^2 a_{21}^2 S_{11} + a_{21}^2 a_{22}^2 S_{22} + a_{23}^2 a_{13}^2 S_{33} + (a_{21}^2 a_{12}^2 + a_{11}^2 a_{22}^2) S_{12} \\
& + a_{13}^2 (a_{21}^2 + a_{22}^2) S_{13} + a_{23}^2 (a_{11}^2 + a_{12}^2) S_{23} \\
& + a_{13} a_{23} a_{12} a_{22} S_{44} + a_{13} a_{23} a_{11} a_{21} S_{55} + a_{21} a_{22} a_{11} a_{12} S_{66} \quad (14)
\end{aligned}$$

The Young's-modulus results present no surprise. We observed  $E_1 > E_2 > E_3$ , consistent with fiber packing and arrangement. The torsional moduli behave similarly,  $T_1 > T_2 > T_3$ , as expected.

The shear-modulus results present one surprise:  $G_{13}$  exceeds  $G_{23}$ . Based on fiber packing in the two directions, one expects the reverse. Tentatively, we interpret this to mean that in the fill direction ( $x_2$ ) the fibers are more wavy than in the warp direction. That is, they possess a shorter radius of curvature. Based on a finite-element model, Kriz [2] discusses such waviness effects. As expected,  $G_{12}$  exceeds both  $G_{13}$  and  $G_{23}$  because it involves tilting of the fiber-reinforced laminae, whereas  $G_{13}$  and  $G_{23}$  involve only their rigid displacement, without their deformation.

The Poisson-ratio results present several surprises. First,  $\nu_{31}$  and  $\nu_{32}$  differ by a factor of four! Again, one can interpret this as due mainly to fiber waviness in the fill direction ( $x_2$ ); the waviness permits a larger transverse strain in response to a tensile stress along  $x_3$ . Similar reasoning explains the large difference between  $\nu_{13}$  and  $\nu_{23}$ : due to lower waviness, the warp-direction fibers resist more strongly a transverse displacement, arising from a uniaxial stress along  $x_1$  or  $x_2$ . This waviness hypothesis is not consistent with the observed  $E_1:E_2$  ratio and the reported fiber-packing densities. Thus, we will conduct further studies before finally reporting on this subject.

## CONCLUSIONS

1. Defining  $x_1$  = warp direction,  $x_2$  = fill direction,  $x_3$  = normal direction, we find that the Young's moduli and torsional moduli,  $E$  and  $T$ , are ordered:  $E_1 > E_2 > E_3$  and  $T_1 > T_2 > T_3$ , as expected.

2. For the shear moduli,  $G_{12}$  exceeds  $G_{13}$  and  $G_{23}$  as expected. Surprisingly,  $G_{13}$  exceeds  $G_{23}$ . This can be explained by invoking excessive waviness (short radius of curvature) for the fill-direction fibers.

3. Peculiarities in the Poisson's ratios --  $\nu_{32}$  exceeds  $\nu_{31}$  by a factor of 4.0 and  $\nu_{23}$  exceeds  $\nu_{13}$  by a factor of 3.5 -- can be understood by the same waviness hypothesis.

4. Differences in Poisson's ratios, after correction for differences in fiber-packing density, may provide a useful tool for determining the waviness of fibers in various directions.

#### ACKNOWLEDGMENT

This study was sponsored by the U.S. DoE Office of Fusion Energy.

## REFERENCES

1. H. M. Ledbetter, to be published. Included in Materials Studies for Magnetic Fusion Energy Applications at Low Temperatures - III, NBSIR 80-1627 (June 1980).
2. R. D. Kriz, in this report.

## FIGURE CAPTIONS

- [1]. Directional variation of Young's modulus of G-11CR composite in warp-fill plane, in units of  $10^{11} \text{N/m}^2$ .
- [2]. Directional variation of Young's modulus of G-11CR composite in warp-normal plane, in units of  $10^{11} \text{N/m}^2$ .
- [3]. Directional variation of Young's modulus of G-11CR composite in normal-fill plane, in units of  $10^{11} \text{N/m}^2$ .



Table I. Elastic stiffnesses,  $C_{ij}$ , and elastic compliances,  $S_{ij}$

$ij$	$C_{ij}$ ( $10^{11} \text{N/m}^2$ )	$S_{ij}$ ( $10^{-11} \text{m}^2/\text{N}$ )
11	0.349	3.282
22	0.425	3.745
33	0.249	6.301
44	0.048	20.78
55	0.057	17.53
66	0.068	14.68
12	0.127	-0.676
13	0.090	-0.669
23	0.192	-2.641

Table II. Engineering elastic constants: E = Young modulus,  
G = shear modulus,  $\nu$  = Poisson ratio

---

$E_{11} = 0.305 \cdot 10^{11} \text{ N/m}^2$	$G_{12} = 0.068 \cdot 10^{11} \text{ N/m}^2$	$\nu_{12} = 0.206$
$E_{22} = 0.267$	$G_{13} = 0.057$	$\nu_{13} = 0.204$
$E_{33} = 0.159$	$G_{23} = 0.048$	$\nu_{21} = 0.180$
		$\nu_{23} = 0.705$
		$\nu_{31} = 0.106$
		$\nu_{32} = 0.419$

---

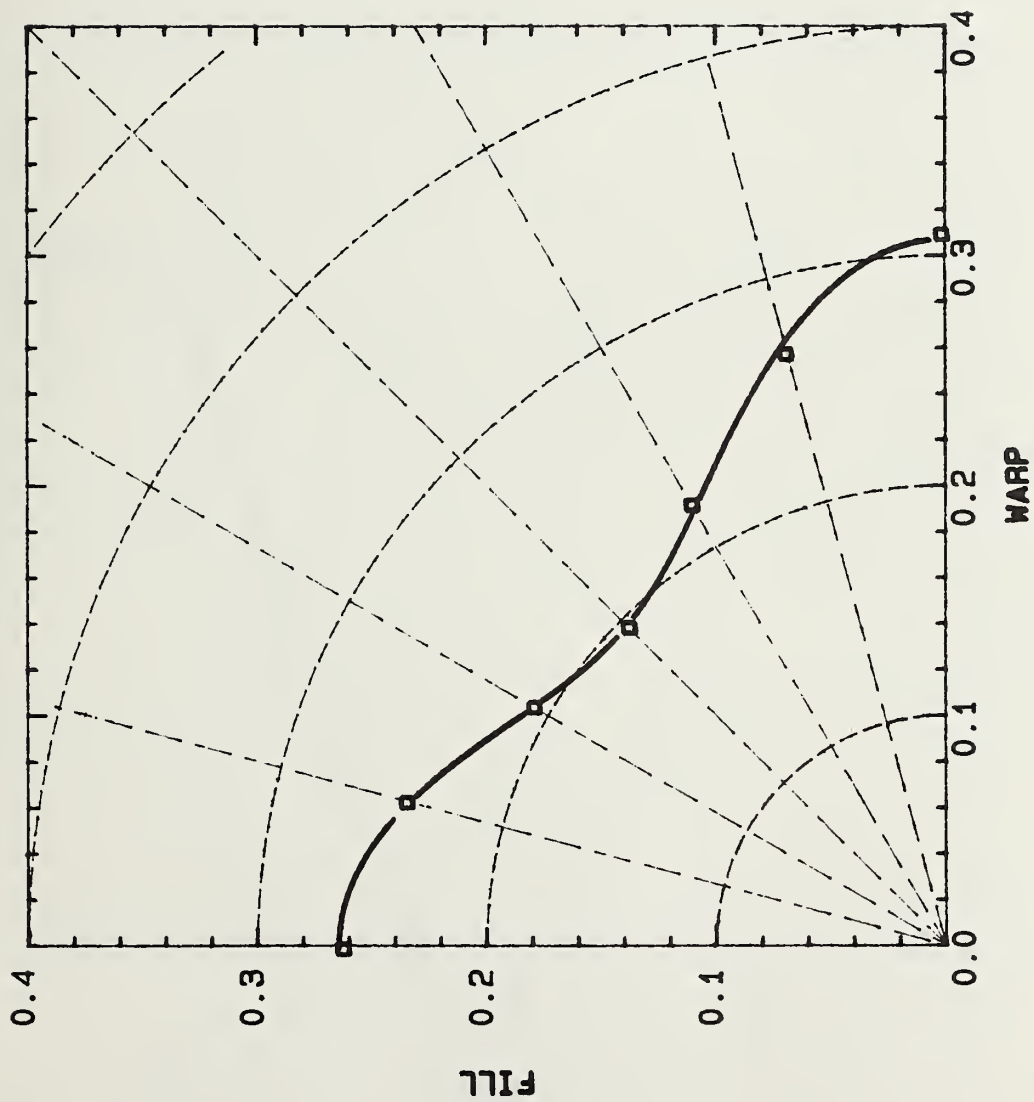


Fig. 1. Directional variation of Young's modulus of G-11CR composite in warp-fill plane, in units of  $10^{11} \text{N/m}^2$ .

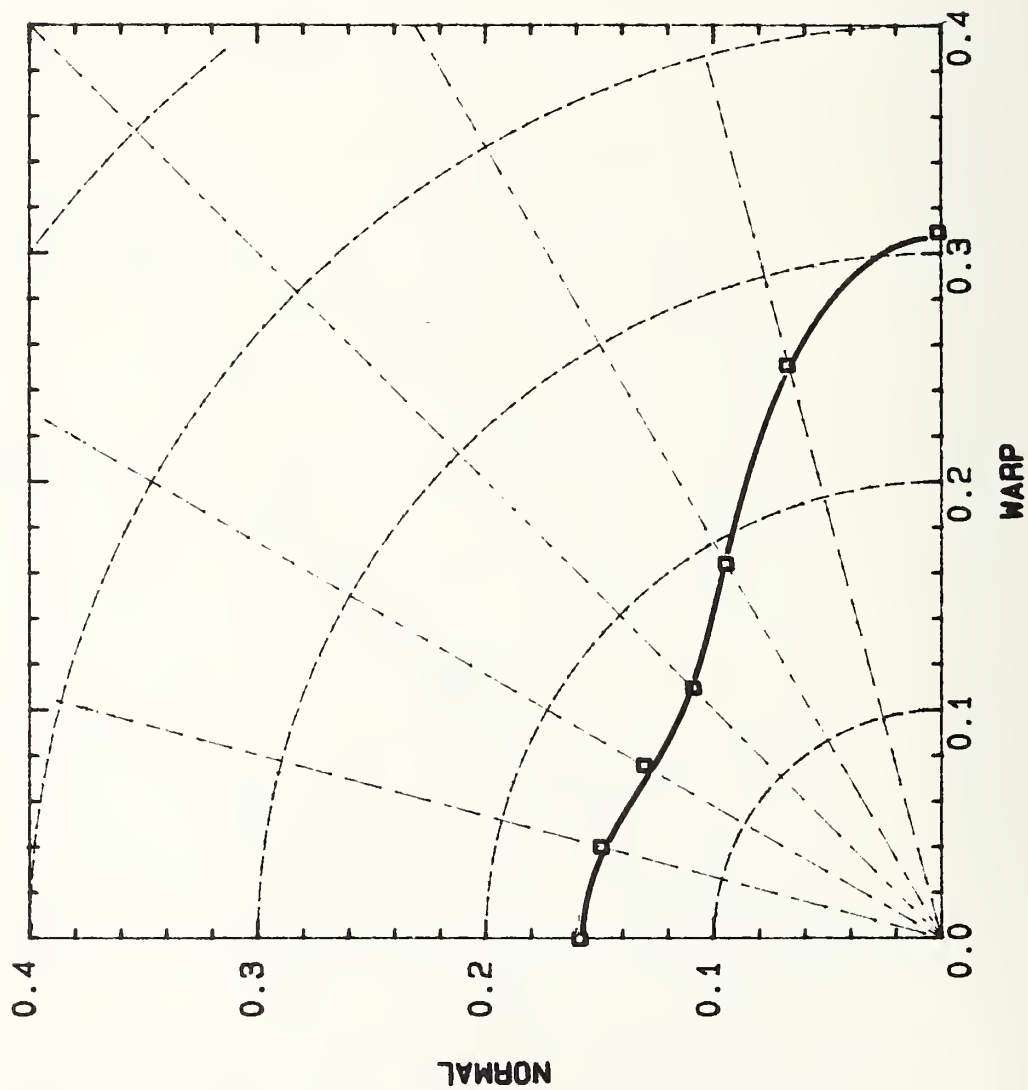


Fig. 2. Directional variation of Young's modulus of G-11CR composite in warp-normal plane, in units of  $10^{11} \text{N/m}^2$ .

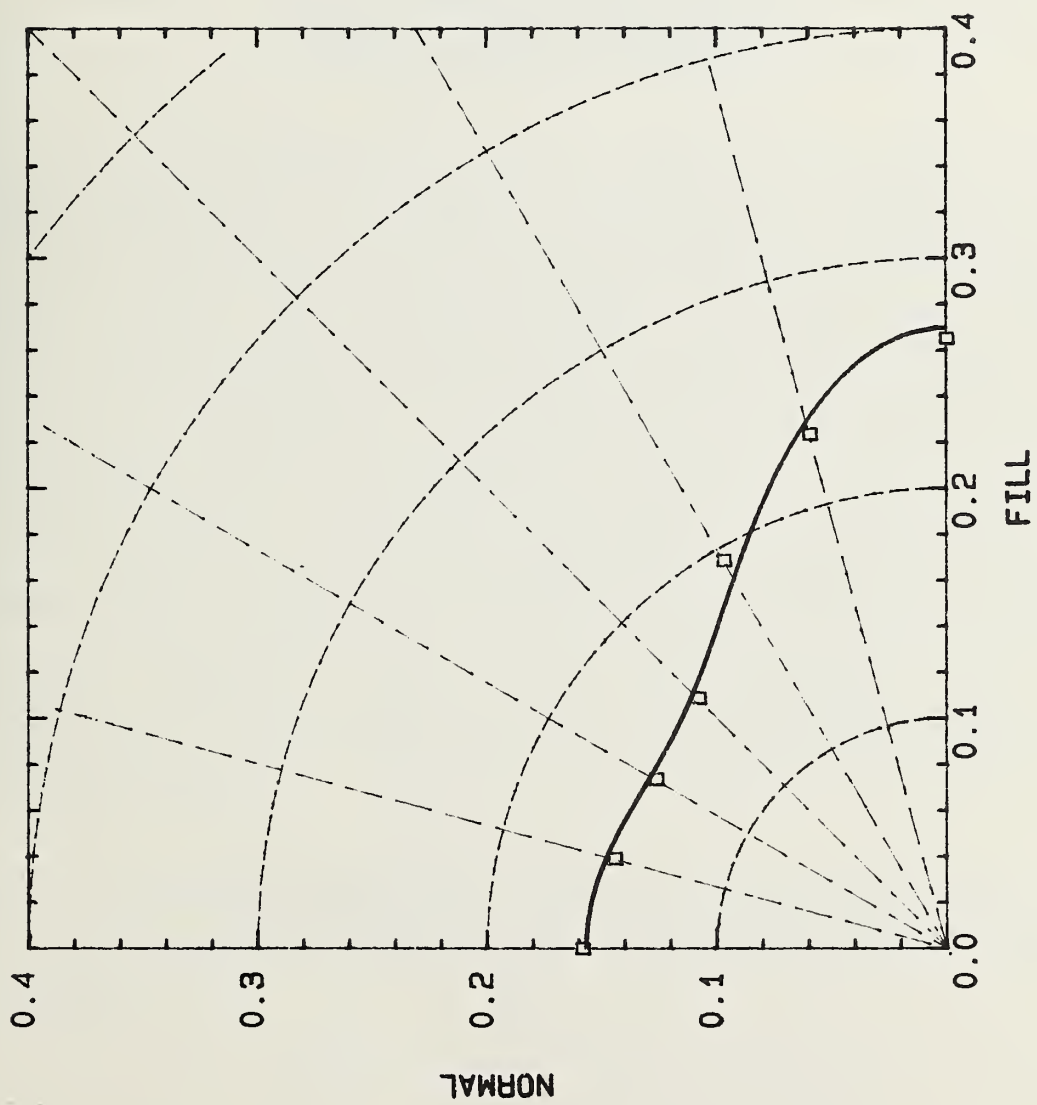


Fig. 3. Directional variation of Young's modulus of G-11CR composite in normal-fill plane, in units of  $10^{11} \text{N/m}^2$ .





Calculated Elastic Constants of  
Composites Containing Anisotropic Fibers\*

S. K. Datta  
Department of Mechanical Engineering  
University of Colorado  
Boulder, Colorado, 80309, USA

and

H. M. Ledbetter and R. D. Kriz  
Fracture and Deformation Division  
National Bureau of Standards  
Boulder, Colorado 80303, USA

By a wave-scattering method, we derive dispersion relationships for waves propagating perpendicular to continuous fibers that are oriented unidirectionally. In the long-wavelength limit one obtains relationships that predict the composite's effective static elastic constants. We compare these relationships with others derived by energy methods to obtain upper and lower bounds of the effective static moduli. We demonstrate them graphically by plotting for graphite-epoxy the predicted composite constants over the full range of fiber volume fractions. We consider the fibers to be anisotropic, but transversely isotropic. Under special conditions, the energy-method upper and lower bounds compare identically with the results of this study. The static properties are, of course, special cases of the more general dispersion relationships. Graphs are given for nine elastic constants: axial and transverse Young's and shear moduli, bulk and plane-strain-bulk moduli, and three Poisson's ratios.

Key words: Bulk modulus; composites; dispersion relationship; elastic constants; fiber reinforcement; graphite-epoxy; shear modulus; wave propagation; Young's modulus.

\* Accepted for publication, International Journal of Solids and Structures



## 1. INTRODUCTION

In recent years, both theory and observation of fiber-reinforced composites have advanced dramatically. Reviews of this subject include those on theory by Hashin [1], Sendeckyj [2], and Walpole [3], and on experiment by Bert [4].

In practice, two types of fiber reinforcement occur: continuous-fiber and short-fiber (chopped-fiber). Most studies consider only the first type, which we consider here.

Most previous studies calculated overall (effective) static elastic constants or bounds of such constants. Interested readers should see [5-14] for relevant studies. Some authors considered wave propagation in fiber-reinforced composites both for fibers in periodic arrays [15,16] and for fibers distributed randomly [17-19].

Random distributions of identical, long, and parallel fibers form the subject of the present study. We focus on the propagation of plane longitudinal and shear waves propagating perpendicular to the fibers. We use a multiple scattering approach to obtain a dispersion relationship. This relationship governs both propagation velocity and frequency of the incident wave. We make three simplifying assumptions: (1) random and homogeneous fiber distribution, (2) Lax's quasi-crystalline approximation, (3) wavelength long relative to fiber diameter. In this long-wavelength limit, one obtains effective static elastic constants that agree well with results obtained by other methods. For a graphite-epoxy composite, we consider fibers to be anisotropic, and we obtain elastic constants for all volume fractions.

## 2. FORMULATION

Consider a system of long circular cylindrical fibers embedded in an infinite matrix. We assume that the matrix is isotropic and homogeneous with Lamé constants  $\lambda$  and  $\mu$  and mass density  $\rho$  and that the fibers are transversely isotropic with the axis of symmetry coincident with the fiber axis. We consider two problems. First, the propagation of shear waves moving perpendicular

to the fibers. Here the particle motion is assumed to be parallel to the fibers. This SH-wave problem was considered in [17,19,20]. The second problem is that of propagation perpendicular to the fibers with the particle motion also perpendicular to the fibers. Details of the calculation for the first problem are given below. The second problem can be analyzed similarly, except that the algebra is much more complicated because of its vector nature.

## 2.1 SHEAR WAVE POLARIZED PARALLEL TO FIBER

Let the fibers be labeled 1, 2, ..., N and let  $(r_i, \theta_i)$  be the polar coordinates of the center  $O_i$  of the  $i^{\text{th}}$  fiber. The z axis is the fiber axis. We assume that the fibers are identical in geometry and material properties, although for the following analysis this assumption is not necessary. In a customary notation, the fiber elastic constants are denoted by  $C_{ij}$  ( $i, j = 1-6$ ). Since the fibers are assumed transversely isotropic there are only five independent constants:  $C_{11}$ ,  $C_{12}$ ,  $C_{13}$ ,  $C_{33}$ , and  $C_{44}$ .

For the problem considered in this section, the only elastic properties that enter the calculation are  $C_{44}$  and  $\mu$ . Thus, the analysis follows closely that in [16] and is a special case of that in [19], which deals with elliptical-cross-section inclusions.

Let an SH wave given by

$$u_z^{(i)} = u_0 e^{i(\beta x - \gamma t)}, \quad \beta = \gamma/c_2, \quad c_2 = \sqrt{\mu/\rho} \quad (1)$$

be incident on the medium considered. Here  $u$  represents particle displacement,  $c_2$  the shear-wave speed in the matrix, and  $\gamma$  the circular frequency.

This incident wave will be scattered by N fibers and the scattered field is given, using notation in [20], by:



$$u_z^{(s)} = \sum_{i=1}^N \hat{T}(r_i) u_z^E(r_i|r_i) \quad (2)$$

where  $u_z^E$  is the field near the  $i^{\text{th}}$  scatterer and will be called the exciting field [20]. The operator  $\hat{T}(r_i)$  operating on  $u_z^E$  gives the scattered field due to the  $i^{\text{th}}$  scatterer. It is well known, see [20], that  $\hat{T}u_z^E$  can be written

$$\hat{T}(r_i)u_z^E(r_i|r_i) = \sum_{n=0}^{\infty} \mu_n [A_{in}^1 \cos(n\phi_i) + A_{in}^2 \sin(n\phi_i)] H_n(\beta R_i) \quad (3)$$

where  $\mu_0 = 1/2$ ,  $\mu_n = 1$  ( $n > 0$ ),  $R_i$  and  $\phi_i$  are shown in Fig. 1, and  $H_n$  and  $J_n$  are Hankel and Bessel functions of the first kind. The coefficients  $A_{in}^1$  and  $A_{in}^2$  depend on the boundary conditions at the surface of the fibers and are not generally obtainable in closed form. Equation (2) can be rewritten as

$$u_z^{(s)} = \sum_{n=0}^{\infty} \mu_n [A_{in}^1 \cos(n\phi_i) + A_{in}^2 \sin(n\phi_i)] H_n(\beta R_i) + \sum_{j \neq i} \sum_{n=0}^{\infty} \mu_n [a_{jn}^1 \cos(n\phi_j) + a_{jn}^2 \sin(n\phi_j)] J_n(\beta R_j) \quad (4)$$

where

$$a_{jn}^1 = \sum_{m=0}^{\infty} \mu_m [(-1)^m (A_{j,n+m} + (-1)^n A_{j,-n+m}) e^{im\theta_{ij}} + (A_{j,n-m} + (-1)^n A_{j,-n-m}) e^{-im\theta_{ij}}] H_m(\beta r_{ij}) \quad (5)$$

$$\begin{aligned}
a_{jn}^2 = & \sum_{m=0}^{\infty} i \mu_m [(-1)^m (A_{j,n+m} - (-1)^n A_{j,-n+m}) e^{im\theta_{ij}} \\
& + (A_{j,n-m} - (-1)^n A_{j,-n-m}) e^{-im\theta_{ij}}] H_m(\beta r_{ij})
\end{aligned} \quad (6)$$

where

$$A_{ip} = \frac{1}{2}(A_{ip}^1 - iA_{ip}^2), \quad (-1)^p A_{i,-p} = \frac{1}{2}(A_{ip}^1 + A_{ip}^2).$$

The boundary conditions on the  $i^{\text{th}}$  scatterer are:

$$(u_z^{(i)} + u_z^{(s)})|_{R_i=a} = u_z'|_{R_i=a} \quad (7)$$

and

$$\mu \frac{\partial}{\partial R_i} (u_z^{(i)} + u_z^{(s)})|_{R_i=a} = C_{44} \frac{\partial u_z'}{\partial R_i} |_{R_i=a}. \quad (8)$$

Here  $u_z'$  is the field within the  $i^{\text{th}}$  scatterer and can be expanded in the form:

$$u_z' = \sum_{n=0}^{\infty} \mu_n [A_{in}^1 \cos(n\phi_i) + A_{in}^2 \sin(n\phi_i)] J_n(\beta R_i) \quad (9)$$

where

$$0 \leq R_i < a.$$

Substituting (1), (4), and (9) into (7) and (8) yields a set of equations for the unknowns  $A_{in}^1$ ,  $A_{in}^2$ ,  $A_{in}^1$ , and  $A_{in}^2$ . The solution for  $A_{in}^1$  and  $A_{in}^2$  can be written as

$$A_{in}^1 = \hat{T}_{nm}^{1v} \alpha_{im}^v, A_{in}^2 = \hat{T}_{nm}^{2v} \alpha_{im}^v \quad (10)$$

where

$$\alpha_{im}^1 = 2u_0 i^m e^{i\beta x_i} + \sum_{j \neq i}^1 a_{jm}^1, \alpha_{im}^2 = \sum_{j \neq i}^2 a_{jm}^2.$$

The repeated index implies summation over that index. It can be shown that

$$\hat{T}_{nm}^{1v} = iC_n \delta_{nm} \delta_{1v}, \hat{T}_{nm}^{2v} = iC_n \delta_{nm} \delta_{2v} \quad (\text{no sum on } n) \quad (11)$$

where

$$C_n = \frac{\mu J_n(\beta'a) \frac{\partial}{\partial a} J_n(\beta a) - C_{44} J_n(\beta a) \frac{\partial}{\partial a} J_n(\beta'a)}{C_{44} H_n(\beta a) \frac{\partial}{\partial a} J_n(\beta'a) - \mu J_n(\beta'a) \frac{\partial}{\partial a} J_n(\beta a)}$$

$$\beta' = \gamma/c_2', c_2' = \sqrt{C_{44}/\rho'}.$$

Similar expressions can be obtained for  $A_{in}^1$  and  $A_{in}^2$ .

Having the formal expressions for the scattered field we now proceed to take ensemble averages. For this purpose we assume a homogeneous fiber distribution. In this case the position of a single fiber is equally probable within the region  $S$ , the total specimen area. Hence its distribution,  $p$ , is uniform with density:

$$p(\chi_i) = \begin{cases} 1/S, & \chi_i \in S; \\ 0, & \chi_i \notin S. \end{cases} \quad (12)$$

Having the center of the  $i^{\text{th}}$  fiber at  $0_i$  the conditional probability density of the  $j^{\text{th}}$  fiber at  $\chi_j$  is:

$$p(r_j|r_i) = \begin{cases} 1/S(1-f(r_{12})), & r_2 \in S \\ 0 & , r_2 \notin S \end{cases} \quad (13)$$

where the pair correlation function  $f(r_{12})$  has the property:

$$f(r_{12}) = \begin{cases} 1, & r_{12} < 2a \\ \text{approaches } 0 & \text{as } r_{12} \text{ approaches } \infty. \end{cases} \quad (14)$$

For the purpose of this study we assume that  $f(r_{12}) = 0$ , which is asymptotically valid for small fiber concentrations. Neglecting  $f(r_{12})$  implies no pair correlations, an assumption discussed by Bose and Mal [18]. Equation (13) implies an isotropic distribution. Together with the quasicrystalline approximation made below in (17), this has been shown [21] to lead to optimum bounds. By optimum we mean with respect to the Hashin-Shtrikman variational principle [22] for isotropic distribution of spherical inclusions in an isotropic matrix. Equation (14), often called the "well-stirred" approximation, becomes invalid at high concentrations. Nevertheless, we expect from the discussion in [21] that the present study will lead to the general bounds [23,24] in the long-wavelength limit.

Taking now the ensemble average of the total field  $u_z$  we obtain:

$$\begin{aligned} \langle u_z \rangle &= (1-C)e^{i\beta x} + n_0 \int_{|r-r_i| > a} dr_i \hat{T}(r_i) \langle u_z^E(r|r_i) \rangle \\ &- n_0^2 \int_{|r-r_i| > a} dr_i \int_{|r_j-r_i| > 2a} dr_j \hat{T}(r_j) \langle u_z^E(r|r_j, r_i) \rangle \\ &+ n_0 \int_{|r-r_i| \leq a} dr_i T'(r_i) \langle u_z^E(r|r_i) \rangle \end{aligned} \quad (15)$$

where  $n_0$  is the number density of the fibers and  $C = n_0 \pi a^2$ .

$$\langle u_Z^E(r|r_i) \rangle = u_0 e^{i\beta x} + n_0 \int dr_j \hat{T}(r_j) \langle u_Z^E(r|r_j, r_i) \rangle \quad (16)$$

$$|r_j - r_i| > 2a.$$

It is seen that the first partial average of the exciting field at  $r_i$  depends on the second partial average of the same. An equation for the second partial average will depend on the third, and so on.

This hierarchy is terminated here by making the quasi-crystalline approximation that requires

$$\langle u_Z^E(r|r_j, r_i) \rangle = \langle u_Z^E(r|r_i) \rangle. \quad (17)$$

This makes (16) an integral equation for  $\langle u_Z^E(r|r_i) \rangle$ .

To solve this equation it may be assumed that

$$\langle u_Z^E(r|r_i) \rangle = \sum_{n=0}^{\infty} \mu_n [a_{in}^1 \cos(n\phi_i) + b_{in}^1 \sin(n\phi_i)] J_n(\beta R_i). \quad (18)$$

Then from (3)

$$\hat{T}(r_u) \langle u_Z^E(r|r_i) \rangle = \sum_{n=0}^{\infty} \mu_n [A_{jn}^1 \cos(n\phi_j) + A_{jn}^2 \sin(n\phi_j)] H_n(\beta R_j). \quad (19)$$

Thus we obtain:

$$a_{ip}^1 = 2u_0 i^p e^{i\beta x_i} + n_0 \int dr_j \sum_{n=0}^{\infty} \frac{1}{2} \mu_n \{ \hat{T}_{nq}^{1v} - \hat{T}_{nq}^{2v} \}$$

$$|r_i - r_j| > 2a$$



$$\begin{aligned}
& \times [H_{p-n} (\beta r_{ij}) e^{-i(p-n)\theta_{ij}} + (-1)^n H_{p+n} e^{i(p+n)\theta_{ij}}] \\
& + (\hat{T}_{nq}^{1v} + i \hat{T}_{nq}^{2v}) [H_{p-n} e^{i(p-n)\theta_{ij}} + (-1)^n H_{p+n} e^{i(p+n)\theta_{ij}}] \} a_{jq}^v \quad (20)
\end{aligned}$$

$$\begin{aligned}
a_{ip}^2 &= n_0 \int d\chi_j \sum_{n=0}^{\infty} \frac{1}{2} \mu_n \{ (\hat{T}_{nq}^{1v} - i \hat{T}_{nq}^{2v}) [H_{p-n} e^{-i(p-n)\theta_{ij}} \\
& - (-1)^n H_{p+n} e^{i(p+n)\theta_{ij}}] - (\hat{T}_{nq}^{1v} + i \hat{T}_{nq}^{2v}) [H_{p-n} e^{i(p+n)\theta_{ij}} \\
& - (-1)^n H_{p+n} e^{-i(p+n)\theta_{ij}}] \} a_{jq}^v. \quad (21)
\end{aligned}$$

Equations (20) and (21) define a pair of integral equations in the unknowns  $a_{ip}^1$  and  $a_{ip}^2$ . If it is assumed that an effective plane wave is propagating through the medium, then a solution for  $a_{ip}^v$  may be assumed in the form

$$a_{ip}^v = \chi_p^v e^{i\beta^* x_i} \quad (22)$$

where  $\gamma/\beta^*$  is the wave velocity of the plane wave.

The coefficients  $\chi_p^v$  form a set of linear homogeneous algebraic equations. These are:

$$\chi_p^1 = - \frac{2\pi n_0 a}{\beta^{*2} - \beta^2} \sum_{n=0}^{\infty} u_n i^{p-n} \hat{T}_{nq}^{1v} \chi_q^v (\Delta_{p-n} + \Delta_{p+n}) \quad (23)$$

$$\chi_p^2 = - \frac{2\pi n_0 a}{\beta^{*2} - \beta^2} \sum_{n=0}^{\infty} u_n i^{p-n} \hat{T}_{nq}^{2v} \chi_q^v (\Delta_{p-n} + \Delta_{p+n}) \quad (24)$$

where

$$\Delta_m = \left[ \frac{\partial}{\partial a} H_m(2\beta a) \right] J_m(2\beta^* a) - \left[ \frac{\partial}{\partial a} J_m(2\beta^* a) \right] H_m(2\beta a). \quad (25)$$

Because of relationships (11),  $\chi_p^1$  and  $\chi_p^2$  are uncoupled. However, for noncircular-cross-section fibers they are coupled. The dispersion equation is obtained by equating the coefficients of  $\chi_p^1$  and  $\chi_p^2$  to zero. For an arbitrary wavenumber the dispersion equation is rather complicated. We can approximate this equation by assuming that  $\beta a$  is small; this means the wavelength is long compared to the fiber diameter. For small  $\beta a$  and  $\beta^* a$  the following relationships can be obtained, which are correct to order  $(\beta a)^2$ :

$$C_0 = \frac{\pi}{4} (\beta a)^2 (\rho/\rho' - 1), \quad C_1 = -\frac{\pi}{4} (\beta a)^2 \frac{C_{44} - \mu}{C_{44} + \mu} \quad (26)$$

$$C_m = 0 \text{ for } m \geq 2$$

and

$$\Delta_m = \left( \frac{2i}{\pi a} \right) \left( \frac{\beta^*}{\beta} \right)^{|m|}. \quad (27)$$

Substituting (26) into (11), and then into (23), and using (27) one obtains:

$$i^p \chi_p^1 = \frac{2\pi n_0 a}{\beta^{*2} - \beta^2} \sum_{n=0}^{\infty} \mu_n \left(\frac{2}{\pi a}\right) i^{-n} \chi_n^1 C_n \left\{ \left(\frac{\beta^*}{\beta}\right)^{|p-n|} + \left(\frac{\beta^*}{\beta}\right)^{p+n} \right\}. \quad (28)$$

Because of (26) the infinite series can be terminated after  $n = 1$ . This yields two simultaneous homogeneous equations in  $\chi_0^1$  and  $\chi_1^1$ . Equating the determinant of the coefficients to zero gives the dispersion relationship:

$$\left(\frac{\beta^*}{\beta}\right)^2 = [1 + C(\rho'/\rho - 1)] \frac{1 - C(m-1)/(m+1)}{1 + C(m-1)/(m+1)} \quad (29)$$

where  $m = C_{44}/\mu$  and  $C$  is the fiber volume fraction.

Defining the average density as

$$\rho^* = \rho[1 + C(\rho'/\rho - 1)] \quad (30)$$

and

$$\beta^* = \gamma/c_2^*, \quad c_2^* = \sqrt{\mu_{LT}/\rho^*} \quad (31)$$

where  $\mu_{LT}$  is the effective axial shear modulus, one obtains:

$$\frac{\mu_{LT}}{\mu_m} = \frac{1 + C(m-1)/(m+1)}{1 - C(m-1)/(m+1)} \quad (32)$$

where  $m$  is the ratio of fiber and matrix shear moduli ( $\mu_{LT}'/\mu_m$ ).

Equation (32) was obtained by Hashin and Rosen [25] using the composite cylinder assemblage (CCA) model. The expression for  $\mu_{LT}$  obtained from (32) coincides with the lower (upper) bound when the fiber shear modulus,  $\mu'_{LT}$ , is larger (smaller) than the matrix shear modulus,  $\mu_m$ .

## 2.2 LONGITUDINAL AND SHEAR WAVES POLARIZED PERPENDICULAR TO FIBER

Propagation of longitudinal and shear waves polarized transverse to the fibers was studied in [18] using the same approach outlined above. It was shown that if  $\beta a$  and  $\alpha a$  were assumed small then the dispersion relationships reduce to effective longitudinal and shear moduli transverse to the fibers. These are:

$$\frac{C_{11}}{\lambda_m + 2\mu_m} = \frac{1 - CP_2(1 - \beta^2/\alpha^2) - 2C^2P_0P_2}{(1 + CP_0)[1 + CP_2(1 + \beta^2/\alpha^2)]} \quad (33)$$

$$\frac{\mu_{TT}}{\mu_m} = 1 + \frac{2C(\mu'_{TT} - \mu_m)(\lambda_m + 2\mu_m)}{2\mu_m(\lambda_m + 2\mu_m) + (1 - C)(\lambda_m + 3\mu_m)(\mu'_{TT} - \mu_m)} \quad (34)$$

where

$$P_0 = -\frac{K'_T - (\lambda_m + \mu_m)}{K'_T + \mu_m}, \quad P_2 = -\frac{(\mu'_{TT} - \mu_m)\mu_m}{\mu'_{TT}(\lambda_m + 3\mu_m) + \mu_m(\lambda_m + \mu_m)}$$

$$\alpha^2 = \gamma^2/c_1^2, \quad c_1 = \sqrt{(\lambda_m + 2\mu_m)/\rho}.$$

The effective transverse plane-strain bulk modulus,  $K_T$ , can be obtained from equations (33) and (34) as:

$$K_T = \lambda_m + \mu_m + (\lambda_m + 2\mu_m) \frac{C(K_T' - \lambda_m - \mu_m)}{(1 - C)K_T' + C\lambda_m + (1 + C)\mu_m} \quad (35)$$

where  $K_T'$  is the transverse bulk fiber modulus and the matrix Lamé constants are  $\lambda_m$  and  $\mu_m$ .

Equation (35) is the same as derived by Hashin and Rosen [25] using the CCA model. However, the CCA model does not yield an expression for the effective transverse shear modulus. Instead, bounds for the transverse shear modulus are noted. Expression (34) for  $\mu_{TT}$  is identical to the general lower (upper) bound derived for arbitrary phase geometry [23,24] if  $\mu_{TT}'$  and  $K_T'$  are larger (lower) than  $\mu_m$  and  $K_m$ , respectively, where  $K_m = \lambda_m + \mu_m$  is the plane-strain bulk modulus of the matrix.

Knowing the expression for  $K_T$  one can predict the effective longitudinal Young's modulus and Poisson's ratio using relationships derived by Hill [23]. When both fiber and matrix phases are transversely isotropic, Hill shows that:

$$E_L = E_m(1 - C) + E_L' C + \frac{4C(1 - C)(v_{LT}' - v_m)^2}{(1 - C)/K_T' + C/K_m + 1/\mu_m} \quad (36)$$

$$v_{LT} = v_m(1 - C) + v_{LT}' C + \frac{C(1 - C)(v_{LT}' - v_m)(1/K_m - 1/K_T')}{(1 - C)/K_T' + C/K_m + 1/\mu_m} \quad (37)$$

where  $E_L'$  and  $v_{LT}'$  are the axial Young's modulus and axial Poisson's ratio of the fiber. The quantities subscripted with m designate the isotropic matrix properties.



For a unidirectional fibrous composite with transversely isotropic fibers, this completes the derivation of the five independent effective elastic properties:  $K_T$ ,  $E_L$ ,  $\nu_{LT}$ ,  $\mu_{TT}$ ,  $\mu_{LT}$ . Other elastic properties of physical significance can be calculated from the five effective properties. For instance, assuming isotropy in the transverse plane, T, the Poisson's ratio,  $\nu_{TT}$ , and the Young's modulus,  $E_T$ , can be calculated from the isotropic relationships. Thus,

$$E_T = \frac{4K_T\mu_{TT}}{K_T + \psi\mu_{TT}} \quad (38)$$

$$\nu_{TT} = \frac{K_T - \psi\mu_{TT}}{K_T + \psi\mu_{TT}} \quad (39)$$

where

$$\psi = 1 + \frac{4K_T\nu_{LT}^2}{E_L}.$$

The remaining Poisson's ratio,  $\nu_{TL}$ , is calculated from the relationship obtained from the elastic-compliance symmetry condition:

$$\nu_{TL} = \nu_{LT} E_T/E_L. \quad (40)$$

If the composite behaves transversely isotropic with the unique symmetry axis along  $x_3$ , then the elastic-stiffness constants,  $C_{ij}$ , can be computed from

$$C_{11} = C_{22} = K_T + \mu_{TT} \quad (41)$$

$$C_{33} = E_L + 2\nu_{LT} C_{13} \quad (42)$$

$$C_{44} = C_{55} = \mu_{LT} \quad (43)$$

$$C_{12} = K_T - \mu_{TT} \quad (44)$$

$$C_{13} = C_{23} = 2\nu_{LT} K_T \quad (45)$$

$$C_{66} = (C_{11} - C_{12})/2 = \mu_{TT}. \quad (46)$$

One can also calculate the bulk modulus, B, from

$$B = \frac{1}{9} \sum_{i,j=1,2,3} C_{ijij} = \{E_L + 4K_T[1 + \nu_{LT}(\nu_{LT} + 2)]\}/9. \quad (47)$$

### 3. RESULTS AND DISCUSSION

The effect of fiber volume fraction, C, on the predicted elastic constants can now be demonstrated given the isotropic matrix properties and the transversely isotropic fiber properties. The matrix and fiber elastic constants, listed in Table 1, were obtained from [26] where the fiber elastic properties were extrapolated from experiments of Dean and Turner [27] using the transversely isotropic relations derived by Hashin [1]. This extrapolation of fiber properties was done with the correction  $\beta_2 = K_T^I/(K_T^I + 2\mu_{TT}^I)$  noted in [28]. The elastic properties ( $\nu_{TT}$ ,  $\nu_{TL}$ ,  $\nu_{LT}$ ,  $\mu_{TT}$ ,  $E_T$ ,  $\mu_{LT}$ ,  $E_L$ ,  $K_T$ , B) are shown in Figs. 2-5.

As noted above, the curves for  $K_T$ ,  $\mu_{TT}$ , and  $\mu_{LT}$  coincide with the general lower bounds [28] for the particular constituent properties considered here.

Of the nine elastic constants shown in Figs. 2-5,  $E_L$  best fits a simple rule of mixtures. (The correction term in (36) can be neglected.) Both  $B$  and  $\nu_{LT}$  come close to fitting this rule;  $\mu_{TT}$ ,  $K_T$ , and  $E_T$  do not differ dramatically from linearity; but  $\mu_{TT}$ ,  $\nu_{TT}$ , and  $\nu_{TL}$  do so differ. Except for  $\nu_{TT}$  and  $E_T$  all deviations from linearity are negative, that is, the curves are concave. The  $\nu_{TT}$  curve is convex. The  $E_T$  curve is convex at low fiber fractions and concave at high. This reflects the abrupt rise of  $\nu_{TT}$  at low fiber fractions combined with the slow, steady rise of  $\mu_{TT}$ . For those constants that differ strongly from a rule of mixtures, both  $\nu_{TT}$  and  $\nu_{TL}$  are fiber-property dominated while  $\mu_{LT}$  tends to be matrix-property dominated. The latter represents, of course, shear in the fiber direction.

#### 4. CONCLUSIONS

Using a multiple-scattering approach, effective elastic constants of a graphite-fiber-reinforced epoxy composite were derived in this study. Graphite fibers were assumed to be anisotropic, but transversely isotropic. It was shown that the composite can be characterized as a transversely isotropic medium. All five elastic constants characterizing the composite were calculated. These elastic constants coincide with the general lower bounds of those obtained in [1,23,24] using energy methods.

#### ACKNOWLEDGMENTS

Composites studies of H.M.L. and R.D.K. are supported mainly by the U.S. Department of Energy, Office of Fusion Energy.

## REFERENCES

1. Z. Hashin, Theory of Fiber-reinforced materials, NASA Report CR-1974 (1972).
2. G. P. Sendeckyj, Elastic behavior of composites, in Composite Materials, Volume 2, Academic (1974), pp. 45-83.
3. L. J. Walpole, Elastic behavior of composite materials: theoretical fundamentals, in Advances in Applied Mechanics, Volume 21, Academic (1981), pp. 169-242.
4. C. W. Bert, Experimental characterization of composites, in Composite Materials, Volume 8, Academic (1975), pp. 73-133.
5. J. J. Hermans, The elastic properties of fiber reinforced materials when the fibers are aligned, Proc. Koninklijke Nederlandse Akademie van Wetenschappen 70B, 1-9 (1967).
6. J. M. Whitney, Elastic Moduli of unidirectional composites with anisotropic filaments, J. Compos. Mater. 1, 188-193 (1967).
7. J. M. Bloom and D. F. Adams, Axial loading of a unidirectional composite -- anisotropic filaments, J. Compos. Mater. 3, 186-188 (1969).
8. M. D. Heaton, A calculation of the elastic constants of a unidirectional composite containing transversely isotropic fibres, J. Phys. D, 3, 672-676 (1970).
9. C. H. Chen and S. Cheng, Mechanical properties of anisotropic fiber reinforced composites, J. Appl. Mech. 37, 186-189 (1970).
10. C. H. Chen, Rectangular or square array fibrous composite with anisotropic or isotropic filament, J. Appl. Mech. 38, 710-712 (1971).
11. E. Behrens, Elastic constants of fiber-reinforced composites with transversely isotropic constituents, J. Appl. Mech. 38, 1062-1065 (1971).

12. F. Ya. Bulavs, Ya. V. Auzukalns, and A. M. Skudra, Deformation characteristics of plastics reinforced with high-modulus anisotropic fibers, *Polymer Mech.* 8, 545-552 (1972).
13. H. T. Yeh, Variational bounds of unidirectional fiber reinforced composites, *J. Appl. Phys.* 44, 662-665 (1973).
14. G. A. Ermakov, A. G. Fokin, and T. D. Shermergor, Effective moduli of elasticity for materials reinforced by anisotropic fibers, *Mech. Solids* 9, 98-104 (1974).
15. J. D. Achenbach, Generalized continuum theories for directionally reinforced solids, *Arch. Mech.* 28, 257-278 (1976).
16. M. Hlavacek, A continuum theory of fiber-reinforced composites, *Int. J. Solids Structures* 9, 1075-1085 (1973).
17. S. K. Bose and A. K. Mal, Longitudinal shear waves in a fiber-reinforced composite, *Int. J. Solids Structures* 9, 1075-1085 (1973).
18. S. K. Bose and A. K. Mal, Elastic waves in a fiber-reinforced composite, *J. Mech. Phys. Solids* 22, 217-229 (1974).
19. S. K. Datta, Propagation of SH-waves through a fiber-reinforced composite -- elliptic cylindrical fibers, *J. Appl. Mech.* 42, 165-175 (1975).
20. S. K. Datta, Scattering by a random distribution of inclusions and effective elastic properties, in Continuum Model of Discrete Systems, Solid Mechanics Study Series No. 12, University of Waterloo Press (1978), pp. 111-127.
21. J. R. Willis, Variational and related methods for the overall properties of composites, in Advances in Applied Mechanics, Volume 21, Academic (1981), pp. 1-78.
22. Z. Hashin and S. Shtrikman, On some variational principles in anisotropic and nonhomogeneous elasticity, *J. Mech. Phys. Solids* 10, 335-342 (1964).



23. R. Hill, Theory of mechanical properties of fibre-strengthened materials - I. elastic behaviour, J. Mech. Phys. solids 12, 199-212 (1964).
24. Z. Hashin, On elastic behaviour of fibre-reinforced materials of arbitrary phase geometry, J. Mech. Phys. Solids 13, 119-134 (1965).
25. Z. Hashin and B. W. Rosen, The elastic moduli of fiber-reinforced materials, J. Appl. Mech. 31, 223-232 (1964).
26. R. D. Kriz and W. W. Stinchcomb, Elastic moduli of transversely isotropic graphite fibers and their composites, J. Exper. Mech. 19, 41-49 (1979).
27. G. D. Dean and P. Turner, The elastic properties of carbon fibers and their composites, Composites 4, 174-180 (1973).
28. Z. Hashin, Analysis of properties of fiber composites with anisotropic constituents, J. Appl. Mech. 46, 546-550 (1979).

### List of Figures

- Fig. 1. The coordinate system.
- Fig. 2. Predicted axial Young's and shear moduli.
- Fig. 3. Predicted transverse Young's and shear moduli.
- Fig. 4. Predicted bulk modulus and plane-strain bulk modulus.
- Fig. 5. Predicted Poisson's ratios.

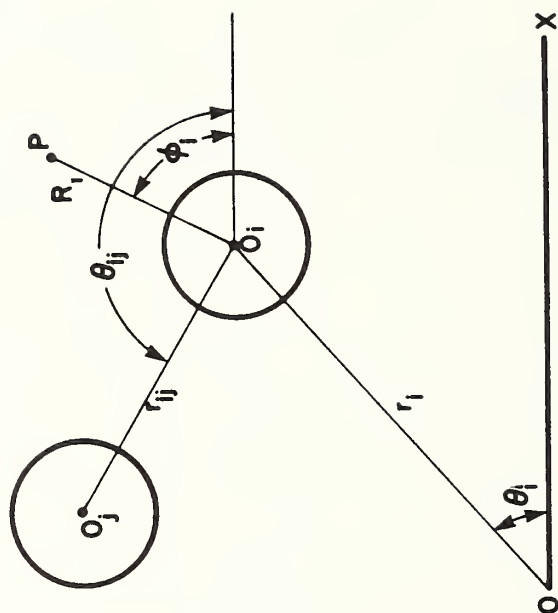


Fig. 1. The coordinate system.

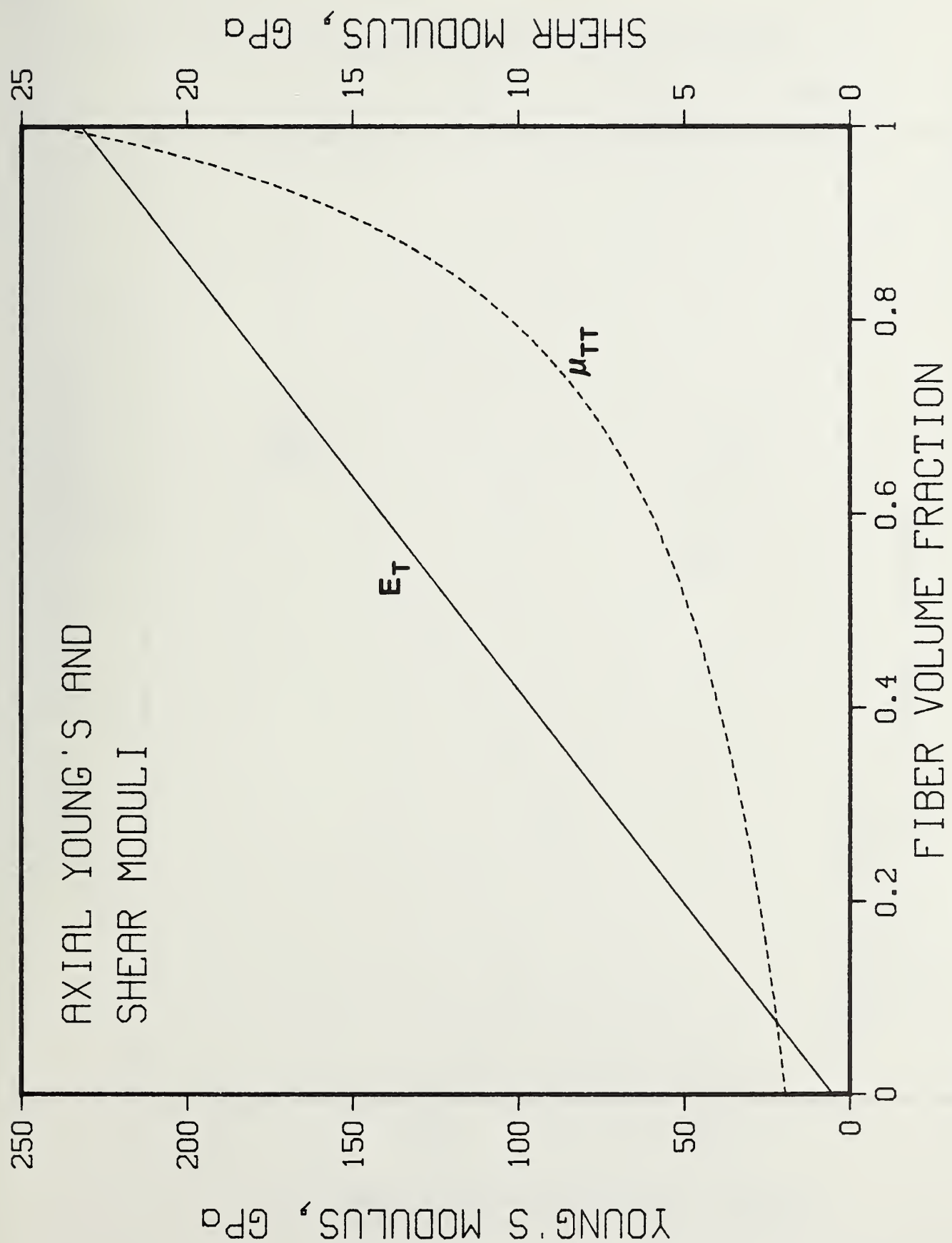


Fig. 2. Predicted axial Young's and shear moduli.

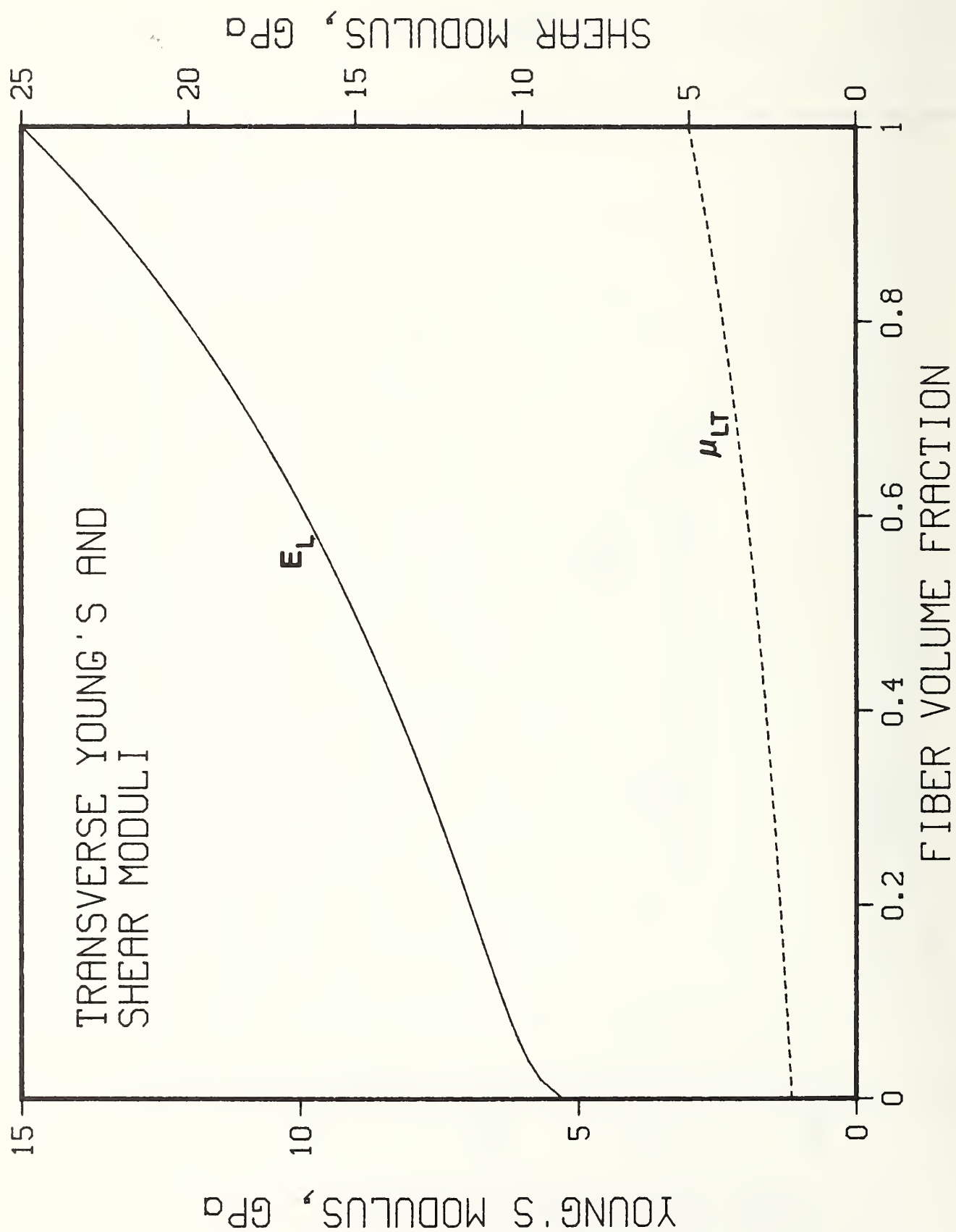


Fig. 3. Predicted transverse Young's and shear moduli.



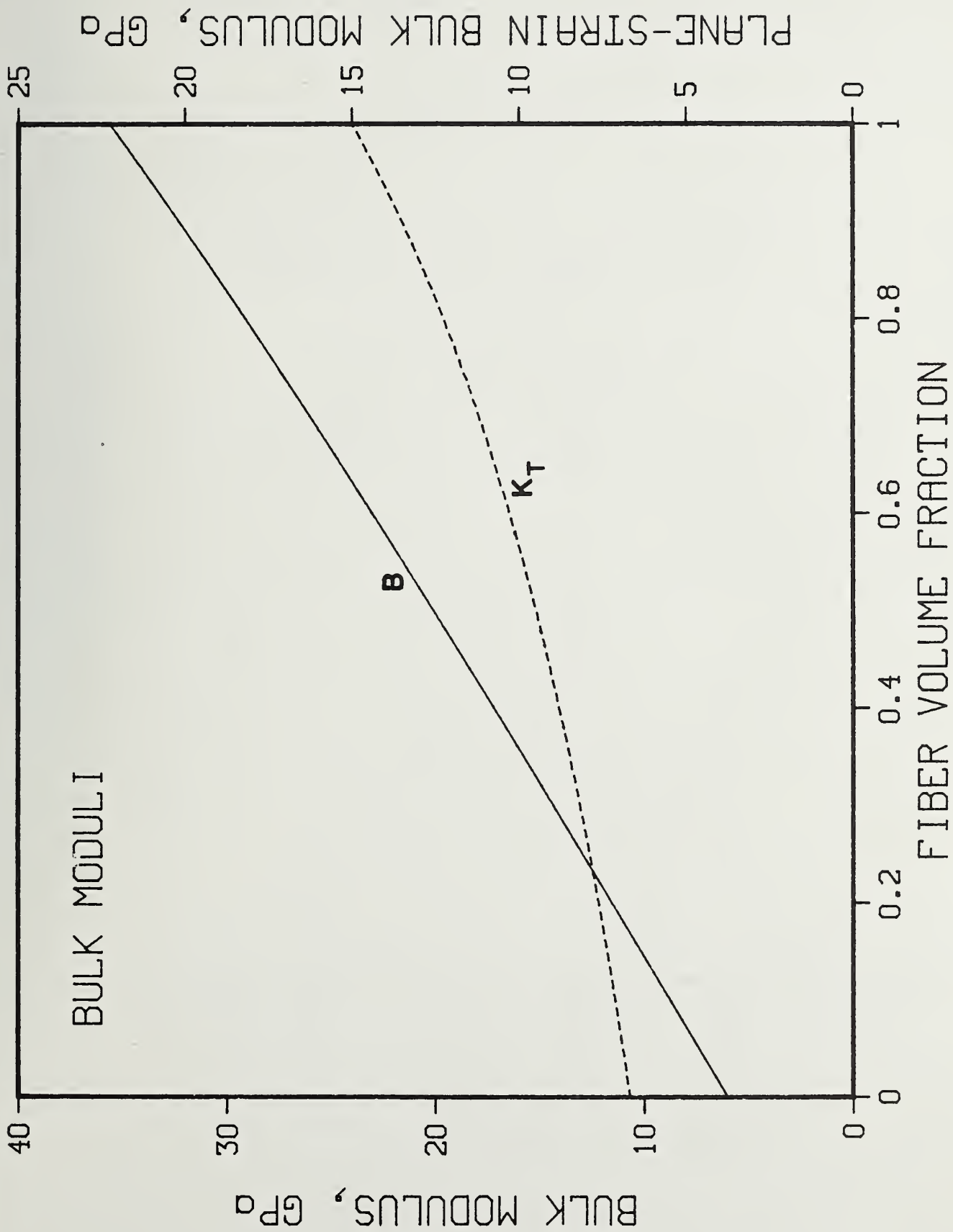


Fig. 4. Predicted bulk modulus and plane-strain bulk modulus.

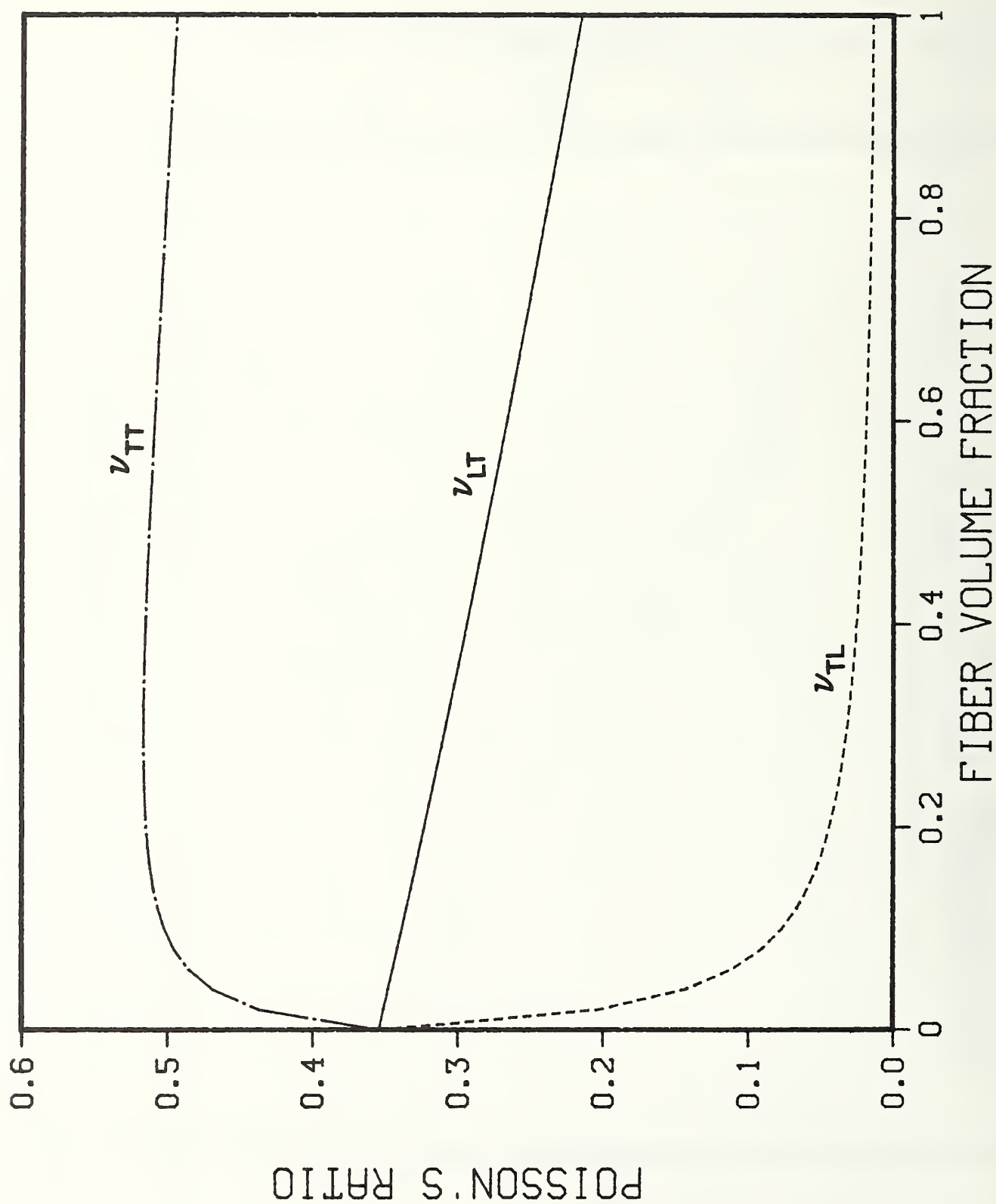


Fig. 5. Predicted Poisson's ratios.

# ***TECHNOLOGY TRANSFER***



## TECHNOLOGY TRANSFER PROGRAM

LEADER: N. J. Simon, NBS  
STAFF: P. O. Chavez, NBS

### OBJECTIVES:

- (1) To hold a biennial workshop in the autumn of alternate years. Major topics include design overviews of fusion energy projects with respect to low-temperature material needs and reviews and data on structural alloys, composites, and weldments.
- (2) To produce and distribute an annual report as well as monthly highlight reports to OFE/DoE.
- (3) To prepare handbook pages and supporting documentation on low-temperature mechanical and physical properties of structural materials for superconducting magnets. The pages are to be distributed to workshop attendees and others in the low-temperature materials applications community. The pages will also be presented for inclusion in the "Materials Handbook for Fusion Energy Systems."

### RESEARCH PAST YEAR (1982):

- (1) "Materials Studies for Magnetic Fusion Energy Applications-V," NBSIR 82-1667, 490 pages (May 1982), editors R. P. Reed and N. J. Simon, has been sent to the Technology Information Center, ORNL, and approximately one hundred copies have been requested by other interested persons.
- (2) Handbook pages and supporting documentation covering mechanical and physical properties of AISI 316 stainless alloys and Fe-21Cr-6Ni-9Mn have been distributed in preliminary draft form to interested persons. These pages (410 in total) have also been submitted to the "Materials Handbook for Fusion Energy Systems."
- (3) Efforts were undertaken to encourage international cooperation in research to develop radiation-resistant laminates to meet requirements for the Engineering Test Reactor (M. B. Kasen, NBS). See discussion and letter on following pages.

### RESEARCH THIS YEAR (1983):

- (1) Current plans are to hold the biennial low-temperature materials workshop again in October 1983.
- (2) "Materials Studies for Magnetic Fusion Energy Applications-VI," NBSIR 83-1690, 466 pages (1983), editors R. P. Reed and N. J. Simon, is the current edition of the annual report.
- (3) The AISI 316 handbook pages are currently in the review process for "Materials Handbook for Fusion Energy Systems," and the Fe-21Cr-6Ni-9Mn handbook pages will enter the review process later this year.
- (4) Preparation of AISI 304N and 304LN handbook pages will be completed this year. Preparation of handbook pages on the aluminum alloys 2219 and 5083 will be started.
- (5) Efforts to develop international cooperation in research to develop radiation-resistant laminates will continue. See discussion following (M. B. Kasen, NBS).



## INTERNATIONAL COOPERATION IN RESEARCH TO DEVELOP RADIATION-RESISTANT LAMINATES

During the past year, an independent program entitled "Development of Organic Insulators for Fusion Magnets" has been established under the DoE Office of Magnetic Fusion Energy. The program participants (LANL, ORNL, MIT, and NBS) have the task of developing radiation-resistant laminates suitable for use in the Engineering Test Reactor (ETR), for which construction is expected to begin in 1988. A complimentary program to refine cryogenic nonmetallic test specimens and techniques has also been independently established under a subcommittee of the Metals Properties Council. A common element in both programs is the desire to develop international cooperation in the research efforts. This was informally begun by conversations between interested parties from the United States, Japan, Germany, and England during the 1982 ICEC9/ICMC conference in Kobe, Japan. The attached letter outlining the United States programs and proposing an initial step in implementing such cooperation is an outgrowth of that meeting.

December 2, 1982

this letter sent to names checked on the attached list

Dear

There is an expanding awareness of the need to develop nonmetallic insulators suitable for use in superconducting magnets for magnetic fusion energy applications. The required research is complicated by the need to subject specimens to high neutron fluences at 4 K, and by the difficulty in evaluating insulator degradation in such an environment. Few facilities are available for conducting such work, and experimental costs are high. It is therefore recognized that close cooperation between laboratories and individuals pursuing such research would be mutually beneficial.

This subject was informally discussed during the 1982 ICEC9/ICMC conference in Kobe, Japan, in a group composed of Prof. Hitoshi Yamaoka (Kyoto U.), Dr. Shigihiko Nishijima (Osaka U.), Dr. David Evans (Rutherford and Appleton Labs., UK), Dr. Gunther Hartwig (Kernforschungszentrum, W. Ger.), and myself. It was agreed that the first effort should strive for agreement on specimen design to facilitate intercomparison of results of irradiation programs. I agreed to coordinate the U.S. participation in this effort. However, I have delayed further communication until the present time because we have been in the process of structuring several programs having a bearing on the subject. This has now been done.

The purpose of this letter is to summarize the objectives of these programs for you and others who have an interest in such research, and to solicit suggestions for ways in which mutually beneficial cooperative efforts might be implemented between these programs and your activities.

We have now begun a six year program to develop organic insulators capable of meeting the anticipated requirements of the magnetic fusion energy Engineering Test Reactor (ETR) which is anticipated to enter the design and construction phase about 1988. This program is sponsored by the Office of Fusion Energy of the U. S. Department of Energy (DoE). It is the outcome of a series of meetings and workshops held over the last few years, the most recent being on September 8-9 of this year. Direct participants in this program are:

Dr. Marvin Cohen, DoE, Contract Monitor  
Dr. Ralph R. Coltman, Oak Ridge National Laboratory (ORNL)  
Dr. George F. Hurley, Los Alamos National Laboratory (LANL)  
Dr. Herbert Becker, Plasma Fusion Center, Massachusetts Institute of Technology (MIT)  
Dr. Maurice B. Kasen, National Bureau of Standards (NBS)

As presently structured, the program will initially address several questions that have arisen concerning insulator behavior under simultaneous stress and irradiation. The next objective would be to identify and standardize the best insulator materials based on the results of irradiation test programs. Eventually, we believe that the suitability of such materials must be verified by testing magnet components in a simulated magnet environment.

Some questions to be initially addressed are:

1. Does the majority of the structural damage to insulators occur during irradiation at 4 K or during warmup following irradiation?
2. How does degradation under neutron irradiation at 4 K differ from that produced by gamma irradiation?
3. Is it necessary to evaluate insulator performance under combined stress and irradiation at 4 K?
4. What is the effect of different types of structural damage on electrical insulating performance at 4 K?
5. Will the allowable radiation fluence be limited by damage to the insulators or to the superconducting stabilizer?

The ORNL studies will continue their evaluation of gamma irradiation effects using their low temperature irradiation facility (LTIF) to assess the effect of warmup on damage accumulation in epoxy. ORNL will also continue studies of the effect of irradiation on the magnetoresistance of copper stabilizing materials. The LANL studies are addressing the question of the relative effect of neutron and gamma irradiation on insulators. Materials similar to those studied by ORNL are being irradiated at the IPNS-1 accelerator base neutron source at the Argonne National Laboratory (ANL). The MIT studies are concentrating on the interaction between the geometrical aspects of insulator design and the properties of the insulators themselves. The current interest is in characterizing the performance of insulators under compression normal to the reinforcement direction. My work at NBS will involve selection and characterization of materials required by the other participants for their test programs, cooperating with the others in post-irradiation failure analysis, and in stimulating international cooperation in the overall effort. I am pleased to report that the value of such cooperation has been recognized as an integral part of the program.

A second and somewhat complimentary program addresses the need to improve and standardize cryogenic test methods. This effort is being organized by a subcommittee of the Metals Properties Council (both nonmetallic and metallic materials are being addressed). Two organizational meetings have thus far been held, resulting in the establishment of a nonmetallics committee consisting of Dr. Herbert Becker (MIT), Dr. James Gauchel (Owens-Corning Research Laboratory), and myself. Dr. Gauchel has elected to work on development of a flexural test specimen optimized for use in material performance screening. Dr. Becker has chosen to address the development of an improved technique for measuring interlaminar shear strength.

We would welcome your active participation in any aspect of either of these programs. However, as we discussed at Kobe, perhaps the best way to begin a cooperative effort would be to investigate the possibility of establishing commonality in specimens used to screen the effects of cryogenic irradiation so as to facilitate meaningful exchange of test data between laboratories. As suggested in Kobe, an exchange of test specimens might be a proper first step. On our part, Dr. Gauchel has offered to provide samples of his proposed specimen configuration that can be forwarded to you. His specimen looks very interesting in that it can be easily and inexpensively manufactured in any laboratory, any desired fiber content can be easily and precisely obtained, its size lends itself to efficient screening under cryogenic irradiation, and I understand that the configuration facilitates analysis of test results in terms of structural factors. We would, of course, solicit your suggestions for alternate configurations.

I also suggest that it might be beneficial for each of us to have a more detailed understanding of the ongoing and planned activities of the various individuals working on this problem. If each of you would take the time to prepare a brief summary of your activities and plans, I would be pleased to combine them into a single document and distribute it to all parties.

The attached list includes those individuals who to my knowledge are working in this area or have indicated an interest in cooperative efforts. I shall be sending a copy of this letter to each of them. Please let me know if there are others who you believe should be added to the list.

Sincerely,

M. B. Kasen  
Fracture and Deformation Division



## Distribution List

Dr. Saburo Takamura  
Solid State Physics Laboratory No. 2  
Japan Atomic Energy Research Laboratory  
Tokai Research Establishment  
Tokai-Mura, Ibaraki-ken 319-11  
Japan

Dr. Kenzo Kadotani  
Senior Researcher, Nonmetallics  
Hitachi Research Laboratory  
Hitachi Ltd.  
4026 Kuji-chuo, Hitachi-shi  
Ibaraki-ken 319-12  
Japan

Prof. Hitoshi Yamaoka  
Research Reactor Institute  
Kyoto University  
Kumatori, Osaka-shi 590-04  
Japan

Dr. Toichi Okada  
Institute of Science and Industrial Research  
Osaka University  
Ibaraki, Osaka 567  
Japan

Dr. David Evans  
Chemical Technology Division R34  
Rutherford Appleton Laboratory  
Chilton, Didcot  
Oxon OX11 0QX  
England

Dr. Günther Hartwig  
Institut für Technische Physik  
Kernforschungszentrum, Karlsruhe  
Postfach 3640  
7500 Karlsruhe  
West Germany

Dr. George F. Hurley M.S. 546  
Los Alamos National Laboratory  
P. O. Box 1663  
Los Alamos, NM 87545

Dr. Ralph R. Coltman  
Building 3115  
P. O. Box X  
Oak Ridge National Laboratory  
Oak Ridge, TN 37840



Dr. Herbert Becker  
MIT Plasma Fusion Center  
167 Albany Street  
Cambridge, MA 02139

Dr. Marvin Cohen  
Office of Fusion Energy  
Materials and Radiation Branch M.S. G-234  
U. S. Department of Energy  
Washington, DC 20545

Dr. James Gauchel  
Owens-Corning Fiberglass Research Center  
P. O. Box 415  
Granville, OH 43023

Dr. Ursula Kreibich  
Ciba-Geigy Research Laboratory  
Ciba-Geigy AG  
CH-4002 Basel  
Switzerland

Dr. Maurice B. Kasen  
Fracture and Deformation Division 562  
National Bureau of Standards  
Boulder, CO 80303

## ACKNOWLEDGMENT

The editors wish to express their appreciation to Diane Bieber, JoAnne Wilken, and Peggy Chavez for their work in preparing the manuscript.

Marilyn Stieg removed many of the inconsistencies, grammatical errors, and awkward usages of language. The editors are responsible for those that remain.

U.S. DEPT. OF COMM. <b>BIBLIOGRAPHIC DATA SHEET</b> <i>(See instructions)</i>	<b>1. PUBLICATION OR REPORT NO.</b> NBSIR 83-1690	<b>2. Performing Organ. Report No.</b>	<b>3. Publication Date</b> May 1983
<b>4. TITLE AND SUBTITLE</b> Materials Studies for Magnetic Fusion Energy Applications at Low Temperatures--VI			
<b>5. AUTHOR(S)</b> R. P. Reed and N. J. Simon, Editors			
<b>6. PERFORMING ORGANIZATION</b> <i>(If joint or other than NBS, see instructions)</i> NATIONAL BUREAU OF STANDARDS DEPARTMENT OF COMMERCE WASHINGTON, D.C. 20234			<b>7. Contract/Grant No.</b>  <b>8. Type of Report &amp; Period Covered</b>
<b>9. SPONSORING ORGANIZATION NAME AND COMPLETE ADDRESS</b> <i>(Street, City, State, ZIP)</i> Department of Energy Office of Fusion Energy Washington, DC 20545			
<b>10. SUPPLEMENTARY NOTES</b> Related earlier reports: NBSIR 81-1645, NBSIR 80-1627, NBSIR 79-1609, NBSIR 78-884, NBSIR 82-1667 <input type="checkbox"/> Document describes a computer program; SF-185, FIPS Software Summary, is attached.			
<b>11. ABSTRACT</b> <i>(A 200-word or less factual summary of most significant information. If document includes a significant bibliography or literature survey, mention it here)</i> This report contains results of a research program to produce material property data that will facilitate design and development of cryogenic structures for the superconducting magnets of magnetic fusion energy power plants and prototypes. The program was conceived and developed jointly by the staffs of the National Bureau of Standards and the Office of Fusion Energy of the Department of Energy; it is managed by NBS and sponsored by DoE. Research is conducted at NBS and at various other laboratories through subcontracts with NBS. The reports presented here summarize the sixth year of work on the low-temperature materials research program. Highlights of the results are presented first. Research results are given for the four main program areas: structural alloys, weldments and castings, nonmetallics, and technology transfer. Objectives, approaches, and achievements are summarized in an introduction to each program area. The major portion of the program has been the evaluation of the low-temperature mechanical and physical properties of stainless steel base metals, welds, and castings, with particular emphasis on the nitrogen-strengthened stainless steels. Developmental steels with manganese additions are also under investigation. Codes and standards development received increased emphasis this year, especially as related to low-temperature property measurements. Work has been done of the standardization of industrial laminates for low-temperature applications and on the measurement of nonmetallic composite properties at cryogenic temperatures. Modeling of the elastic and fracture behavior of woven fiber-reinforced composites has been initiated this year.			
<b>12. KEY WORDS</b> <i>(Six to twelve entries; alphabetical order; capitalize only proper names; and separate key words by semicolons)</i> alloys; austenitic steels; castings; composites; cryogenic properties; low temperatures; mechanical properties; nonmetallics; elastic properties; stainless steels; structural alloys; weldments.			
<b>13. AVAILABILITY</b> <input checked="" type="checkbox"/> Unlimited <input type="checkbox"/> For Official Distribution. Do Not Release to NTIS <input type="checkbox"/> Order From Superintendent of Documents, U.S. Government Printing Office, Washington, D.C. 20402. <input checked="" type="checkbox"/> Order From National Technical Information Service (NTIS), Springfield, VA. 22161			<b>14. NO. OF PRINTED PAGES</b> 436 <b>15. Price</b> \$32.50







